NASA TECHNICAL MEMORANDUM

NASA TM X-73360

APOLLO-SOYUZ TEST PROJECT – COMPOSITE OF MSFC FINAL SCIENCE REPORT

Space Processing Applications Task Team

January 1977

NASA

George C. Marshall Space Flight Center
Marshall Space Flight Center, Alabama

MSFC - Form 3190 (Rev June 1971)

4740

1 Report No	2 Government Accession No	3 Recipient's Catalog No
NASA TM X-73360		

4 Title and Subtitle	5 Report Date
Apollo-Soyuz Test Project — Composite of MSFC Final Science Report	January 1977
	6 Performing Organization Code
7 Author(s)	8 Performing Organization Report No
	10 Work Unit No
9 Performing Organization Name and Address	
George C. Marshall Space Flight Center Marshall Space Flight Center, Alabama 35812	11 Contract or Grant No
	13 Type of Report and Period Covered
12 Sponsoring Agency Name and Address	Technical Memorandum
National Aeronautics and Space Administration Washington, D.C. 20546	14 Sponsoring Agency Code

15 Supplementary Notes

Prepared by Advanced Projects Office, Program Development

16 Abstract

This report summarizes the experimental procedures of nine experiments conducted during the Apollo-Soyuz Test Project mission from July 15 to July 24, 1975, and presents the investigators' conclusions and recommendations based on these experiments. The experiments reported on herein are:

- Experiment MA-011, Column Electrophoresis on the Apollo-Soyuz Test Project — Section I
- Experiment MA-014, Electrophoresis Experiment — Section II
- Experiment MA-041, Surface Tension Induced Convection in Encapsulated Liquid Metals in a Microgravity Environment — Section III
- Experiment MA-044, Monotectic and Syntectic Alloys — Section IV
- Experiment MA-060, Quantitative Determination of Zero-Gravity Effects on Electronic Materials Processing — Germanium Crystal Growth with Simultaneous Interface Demarcation — Section V
- Experiment MA-070, Zero-G Processing of Magnets — Section VI
- Experiment MA-085, Crystal Growth from the Vapor Phase — Section VII
- Experiment MA-131, Zero-Gravity Growth of NaCl-LiF Eutectic — Section VIII
- Experiment MA-150, Germanium — Silicon Solid Solutions — Section IX

17 Key Words (Suggested by Author(s))	18 Distribution Statement

19 Security Classif (of this report)	20 Security Classif (of this page)	21 No of Pages	22 Price
Unclassified	Unclassified	472	NTIS

For sale by National Technical Information Service, Springfield, Virginia 22151

PREFACE

Space materials processing is a young technology which is defined as the use of the unique aspects of the space environment to process materials that cannot be made on Earth. The primary reason for exploring the potentialities of space materials is to learn how to take advantage of the effects of very low gravity for modifying the properties of materials. The most direct result of reduced gravity is the elmination of thermal convection, sedimentation of heavier particles, and bouyancy of lighter particles or bubbles in a fluid.

A primary objective of the Apollo-Soyuz Test Project was to conduct the materials processing scientific experiments during the mission. Nine of those experiments are reported herein. The information contained in this document was reproduced from reports supplied by the experiment investigators. Information concerning each of the experiments reported on is contained in a separate section, and the experiment procedures as well as the investigators' conclusions and recommendations are included. The information contained in this document was edited to provide consistency in the presentation, where necessary.

The experiments conducted on the Apollo-Soyuz Test Project mission cover a wide range of scientific interest. NASA obtained the participation of other government agencies and domestic and foreign organizations in planning the experiments and studying the results. The mission and the experiment program were overwhelmingly successful.

TABLE OF CONTENTS

SECTION I

COLUMN ELECTROPHORESIS ON THE APOLLO-SOYUZ TEST PROJECT

EXPERIMENT MA-011

By R. E. Allen, P. H. Rhodes, Milan Bier,[1] Fortunato J. Micale,[2] John W. Vanderhoff,[2] Carel J. van Oss,[3] P. E. Bigazzi,[4] G. H. Barlow,[5] G. V. F. Seaman,[6] and R. J. Knox[6]

1. Veterans Administration Hospital, Tucson Arizona 85713
2. Center for Surface and Coatings Research, Lehigh University, Bethlehem, Pennsylvania 18015
3. Department of Microbiology, State University of New York at Buffalo, Buffalo, New York 14214.
4. Department of Pathology, University of Connecticut Health Center, Farmington, Connecticut 06032.
5. Scientific Division, Abbott Laboratories, North Chicago, Illinois 60064.
6. University of Oregon Health Sciences Center, Portland, Oregon 97201.

TABLE OF CONTENTS

LIST OF ILLUSTRATIONS

LIST OF ILLUSTRATIONS (Concluded)

LIST OF TABLES

INTRODUCTION

The possibility of using space as a place where scientific experiments can be conducted and unique products returned is not a consideration in the minds of many scientists. The reason is, obviously, the lack of access to this unusual environment. There has been, however, a continuing effort to probe space and explore the possibilities of advances that can be accomplished there.

Most biological materials, when dissolved or suspended in a selected aqueous medium, have a characteristic electric charge, and the migration velocity per unit electric field strength (defined as the electrophoretic mobility of the material) is thus fixed [I-1]. If the mobility difference between biological species is small, separation can be enhanced by increasing the length of the column. Electrophoresis was originally conducted in liquid media, or free solutions, but problems arose because of disturbances in the bulk of the fluid. Two major causes of these disturbances were sedimentation of the particles or solute being separated and thermal convection generated by Joule heating of the column during electrophoresis. Although various techniques have been developed to overcome these problems on Earth, the elimination of gravity-induced sedimentation and thermal convection can be accomplished best in the near-zero-g environment of space.

Electrophoresis in a free fluid was first demonstrated in space during the Apollo 14 mission [I-2]. This electrophoresis experiment used three materials of different molecular weight, deoxyribonucleic acid (DNA), hemoglobin, and soluble dyes. The separations were photographed periodically during electrophoresis in 10 cm (4 in.) long by 0.64 cm (0.25 in.) diameter cylindrical columns. Before operation of the apparatus, the sample materials were isolated in small cavities of a plastic slide, this slide arranged for insertion in a slot intersecting the separation columns. The experiment was initiated in orbit by pushing the slide so that the sample cavities coincided with the separation columns. The diameter of the sample cavity was made slightly smaller than the column diameter so that electrophoresis of the sample would occur away from the walls, where electroosmotic streaming would be less intense. The results showed that a separation was measured between the two dyes, and operation of the fluid and electrical systems was normal. The overall results indicated the validity of fluid electrophoresis; therefore, plans were made and hardware developed for a second demonstration during the Apollo 16 mission.

The Apollo 16 electrophoresis demonstration was performed using the basic operating elements of the Apollo 14 experiment, but a nonbiological standard sample material, polystyrene latex, was used [I-2]. These stable, nondegradable particles were used as models for living cells. Latex particles of similar zetapotential but of two different sizes, and thus, due to their different ratios of size to thickness of double layer, of different electrophoretic mobilities [I-3], were run separately and collectively to provide comparative data. An automatically operated camera, mounted rigidly on the apparatus, photographed a clock, a thermometer, a column current meter and the position of the migrating materials. These photographs provided better technical data on electrophoresis in space than had been obtained previously. The sample insertion mechanism was redesigned to provide for a more reliable release of the samples in the columns. These results showed that a clear separation of the two sizes of polystyrene latex particles was not obtained because of the electroosmosis. Electrophoresis did occur in the columns containing single species of the latex particles. The photographs clearly show distinct boundaries and sharply defined fronts. The deleterious effects of gravity-induced sedimentation and thermal convection on particle electrophoresis can be seen by comparing the results of the Apollo 16 electrophoresis demonstration with those of ground experiments [I-4]. These advantages of the space environment for cell separation processes were further confirmed in the demonstration experiment on isotachophoresis of erythrocytes conducted aboard Skylab 4 [I-5].

For the Apollo-Soyuz Test Project (ASTP), experiment plans included reuse of the parts of the Apollo 14 and Apollo 16 systems that operated correctly, improvement of the techniques used to accomplish sample insertion, elimination of the charge condition along the column walls, and avoidance of bacterial degradation by using proven sterile techniques. A sample insertion technique was devised to ensure precise injection of the sample into the electrophoresis column without affecting the properties of the sample or disturbing the fluid column. The Apollo 14 method of inserting a thin rectangular vane containing cylindrical sample disks into the column was slightly modified and used. Buffer leakage and bubble formation were avoided by specific design techniques. Each sample disk was kept frozen and the entire insertion slide was stored at liquid-nitrogen 77 K (-196°C) temperature [I-6]. The ASTP experiment was designated MA-011.

EXPERIMENT SAMPLE SELECTION

The samples selected for MA-011, Electrophoresis Technology Experiment, were fixed red blood cells, human lymphocytes, human kidney cells, and fresh human and rabbit red blood cells. The MA-011 experiment involved two different types of electrophoresis — zonal electrophoresis and isotachophoresis. There were eight columns processed during the experiment. The order that the samples were processed and processing technique utilized is presented in Table I-1. The samples selected and their importance are as follows.

TABLE I-1. COLUMNS AND SAMPLES PROCESSED IN SPACE

Number of Columns	Type of Electrophoresis	Sample
1	Zonal	Fixed[a] Rabbit, Human, Horse Red Blood Cells
2	Zonal	Human Lymphocytes
3	Zonal	Human Kidney Cells
4	Isotachophoresis	Fresh Rabbit, Human Red Blood Cells
5	Zonal	Same as Column 1
6	Zonal	Same as Column 2
7	Zonal	Same as Column 3
8	Isotachophoresis	Fixed[a] Rabbit, Human Red Blood Cells

a. Formaldehyde fixed red blood cells.

Fixed Red Blood Cells

To assess the resolution and sharpness of the bands formed by electrophoresis in space, a well-characterized particle specie was required. Although polystyrene latexes were the model particles for the Apollo 16 demonstration, the red blood cells used on the ASTP flight (erythrocytes fixed in a formaldehyde fixative) provide an almost indestructible sample material resistant to mechanical stress, hemolytic agents and surface modification. These fixed red blood cells are stable for months under varying temperature conditions, and extensive electrophoresis mobility measurements of the cells using a variety of buffers have been published [I-7]. Each type of cell was selected to be morphologically distinguishable under microscopic examination. The red color of the cells makes them clearly distinguishable in photographs.

Lymphocytes

The interest in specific lymphocytes stems from the increased emphasis in the field of immunology. Initial interest in immunology grew out of the knowledge that persons who survive an infectious disease seldom contract that disease again. The two major types of immune mechanisms are humoral and cellular. Humoral immunity is characterized by the circulating antibodies that originate from B lymphocytes. Cellular immunity is mediated by means of T lymphocytes and is responsible for delayed allergic and transplant-rejection reactions. With the increasing emphasis on cell interactions and the cellular basis of immunology, a simple method of obtaining pure fractions of cells from heterogeneous populations is desirable. From examination of microelectrophoretic data, differences in cell surface charge are known to exist and differences in electrophoretic mobility have been measured [I-8 through I-11]. The significance of the cell separation is of great practical and theoretical importance. Many unresolved questions in immunology depend on the availability of pure lymphocyte subpopulations; such subpopulations are needed to study the nature of the interaction between B and T cells in antibody formation, and the nature of the recently described interaction between the classes of T cells in reactions of cell-mediated immunity. More specifically, interest has developed in the clinical use of various soluble lymphocyte products (lymphokines) in a manner analogous to the use of antisera. Several other lymphocyte products, such as the factors modifying inflammatory cell behavior, are also important. The fractionation of these different lymphokines depends on the earlier separation of the specific lymphocyte populations responsible for their production. To date, none have been fractionated to any significant extent.

Kidney Cells

The isolation and production of the enzyme urokinase (UK) have interested biomedical laboratories for more than 20 years [I-12]. This enzyme is capable of effecting the conversion of plasminogen to plasmin. This conversion is necessary to accomplish blood clot lysis. Originally, UK was extracted from urine; however, at least 1500 l of urine were required to produce a single UK unit dose consisting of 4 million CTA (Committee on Thrombolytic Agents) units. Another source was subsequently discovered; UK has been isolated from cultures of cells located in the cortex of the kidney as follows. Human fetal kidneys are trypsinized to disperse the cells and then tested for viability. The cells are grown out in cultures on mass tissue propagators from which the UK is harvested. Currently, the demand for UK greatly exceeds the capability for its production. Bernik and Kwann in 1969 observed that only approximately 5 percent of the cells in the cortex of the kidney produce UK [I-13]. Obviously, if these "producing cells" could be isolated and subjected to subculturing techniques, a twenty-fold increase in the yield — with a corresponding reduction in the cost — of this drug might result.

Electrophoresis has been used to try to isolate these "producing cells." The disadvantages of separation on Earth are the loss of resolving power due to sedimentation of the cells and convective mixing due to the heating effects of electrophoresis. Under zero-g conditions, these disadvantages should be eliminated or minimized.

As outlined, the kidney cell portion of Experiment MA-011 consisted of taking to orbit a mixture of frozen human kidney cells, separating them by electrophoresis, refreezing the resulting bands, and returning them to Earth. They were then grown out in tissue culture and assessed for UK production. In addition, extensive analyses were conducted to characterize the separated cells. The information from these analyses, as well as these data from the tissue culturing, has contributed to the understanding of this very important source of UK.

DESCRIPTION OF THE APPARATUS

The experiment equipment consisted of four major elements: (1) an electrophoresis unit (EU), (2) a cryogenic freezer (CF), (3) eight experiment columns (six for electrophoresis and two for isotachophoresis), and (4) eight

sample slides containing the experiment specimens. In addition to this experiment hardware, performance of the experiment required the following items of support equipment: (1) a 70 mm electric camera, (2) an 80 mm lens and extender tube, (3) an intervalometer, and (4) an EU power cable. In addition to the sample slides actually used, several control slides containing samples of the biological materials were stored in the CF at launch. They remained there throughout the ASTP mission to allow assessment of the effects of space flight on the biological materials.

A detailed description of each major hardware element and its subelements is provided in the following paragraphs.

Electrophoresis Unit

The EU (Fig. I-1) was the apparatus in which the experiment was performed. External envelope dimensions of the unit (cover closed), excluding mounting lugs and fasteners, were 20.32 by 20.32 by 40.64 cm (8 by 8 by 16 in.). Launch weight was 13.61 kg (30 lb). The EU was designed to be mounted to the Electrophoresis Experiment (MA-014) adapter rack near command module locker A-6 with four thermally stable fasteners. Subassemblies provided by the EU were as follows:

1. Controls and displays

2. Fluorescent light assembly for illumination of the experiment columns during processing

3. Thermoelectric (TE) module for cooling and freezing the electrophoresis columns

4. Self-contained power supplies that required only an external 208 Vac (115 V line-to-neutral), three-phase, 400 Hz connection

5. Buffer solution

6. Buffer solution circulation pump

7. Phase separator assemblies for removing gases liberated in the buffer solution

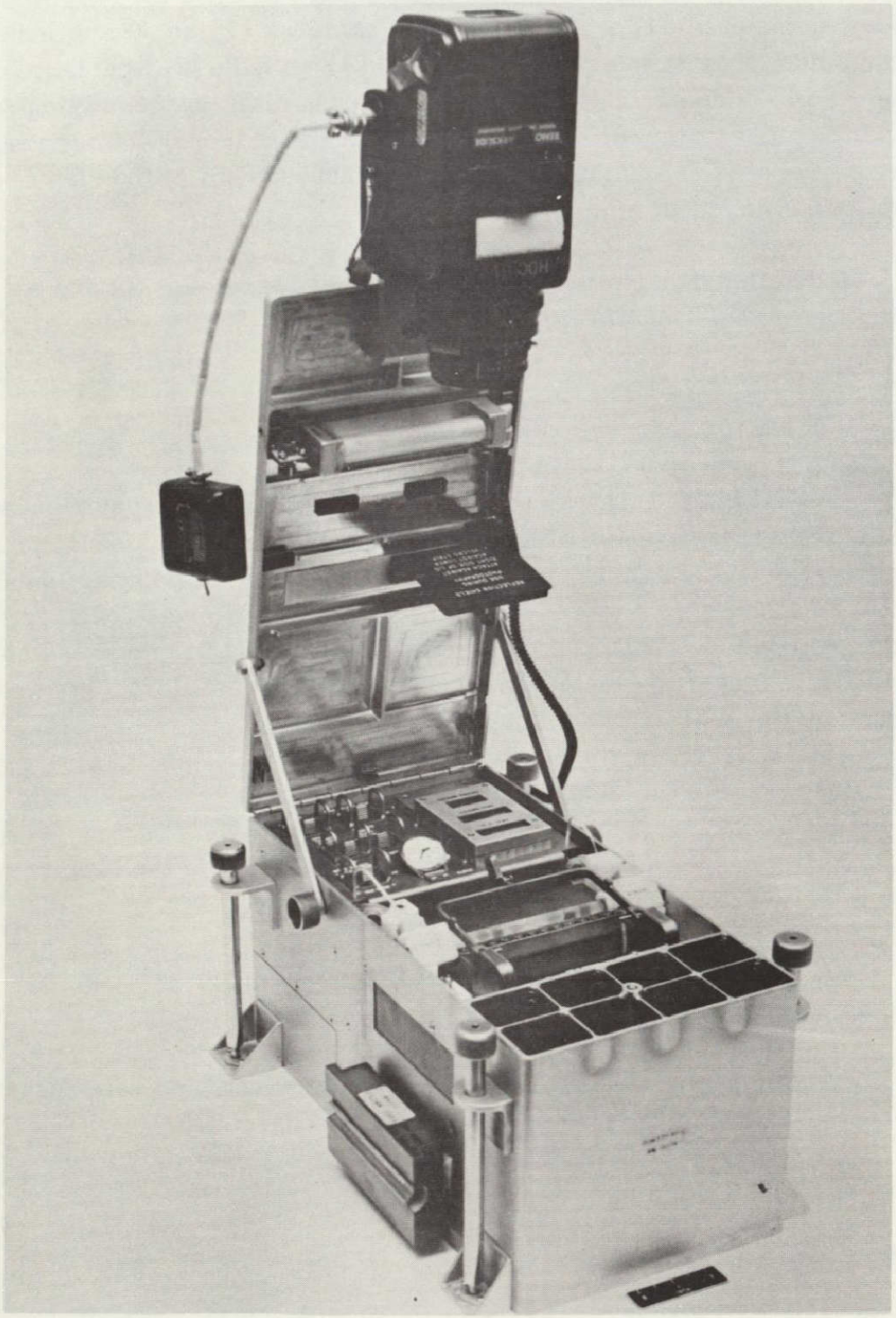

Figure I-1. EU showing camera, photographic shield and column in the operational position (the thermal cover used for columns 2, 3, 6, and 7 is shown on the left side of the unit).

8. Electrical circuitry and plumbing required by the experiment

9. Cover with one knurled screw fastener latch to protect the EU when not in use

10. Camera attachment assembly for mounting the camera to the EU cover

11. Individual storage compartments for eight experiment column assemblies.

The EU control and display panel (Fig. I-2) is described as follows. In the ON position, the POWER switch energizes the fluorescent light assembly and the EU digital displays and also activates the TE module cooling blower.

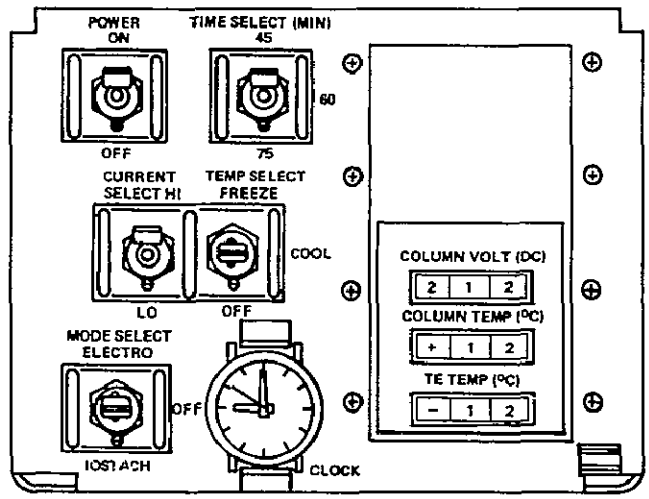

Figure I-2. EU control and display panel.

The TEMP SELECT switch has positions FREEZE, COOL, and OFF. The FREEZE position is selected to freeze the electrophoresis column after each electrophoresis separation has been accomplished. A TE temperature controller allows a minimum temperature of approximately 233 K (-40°C). When the COOL position of the switch is selected, the temperature controller will control the TE units to temperatures as high as 278 K (5°C). The switch is placed in the position at the beginning of viable cell electrophoresis separations and remains in COOL until the separation is accomplished. Because

performance of the isotachophoresis portion of the experiment required neither cooling nor freezing of the column, the OFF position was used for isotachophoresis.

The MODE SELECT switch has positions ELECTRO, OFF, and ISOTACH. The ELECTRO position is selected to perform the electrophoresis. When the ISOTACH position of the switch is used to perform the isotachophoresis, the buffer pump, which is not needed for this part of the experiment, does not operate.

The TIME SELECT (MIN) switch is used to select a time period of 45, 60, or 75 min for experiment operation.

The CURRENT SELECT switch is used to select the level of current flow through the experiment column to either 4.00 mA (HI) or 1.31 mA (LO). The electrophoresis samples were processed with the switch in the HI position, while the LO position was used for isotachophoresis.

The COLUMN VOLT (DC) digitally displays the voltage sensed across the experiment column electrodes. The range of the display is from 0 to 99 V in increments of 1 V, with an accuracy of ±2 percent.

The TE TEMP (°C) displays the temperature of the TE module assembly cold plate. The range of this display is from -99° to 99°C in increments of 1°C, with an accuracy of ±2 percent.

The purpose of the EU clock (a commercial panel-mounted wristwatch) is to enable time correlation of the photographs taken during the experiment process. A metric scale is mounted next to the experiment column cradle. The scale is marked from 0 to 130 mm in 1 mm increments to provide distance information in photographing the biological specimens as the specimens move through the column during the experiment. A portable fluorescent light assembly mounted on the EU cover supplied the illumination required both for viewing the electrophoresis and isotachophoresis processes in the experiment columns and for photography. The fluorescent light tube, contained inside a polycarbonate tube for protection, is permanently bonded to its electrical receptacles.

The EU contains a TE assembly consisting of four three-stage TE coolers to remove heat from the electrophoresis columns during the experiment and to freeze the columns after each separation has been performed. The four coolers

are mounted on a heat sink that is cooled by a flow of 0.09 m^3/s (190 ft^3/min) free air by a 208 Vac, three-phase blower. The cradle holding the electrophoresis columns during the experiment is attached to the TE assembly cold plate. The cold plate contains a thermistor device to sense the cold plate temperature. A thermal cover joins the column cradle to provide thermal continuity around the periphery of the column. The thermal cover is designed to remain in place for all freezing operations and during electrophoresis of lymphocytes and human kidney cells. The column assemblies can be isolated from the TE cradle by using special thermal spacers or slide devices.

A buffer solution reservoir is mounted on a removable tray that forms a part of the EU structure. The tray is attached to the EU by screw fasteners. The reservoir contains a cylindrical rubber diaphragm with ahemispherical end and has a buffer solution capacity of 57.7 ml. The buffer solution enters the reservoir from a phase separator assembly and is then delivered from the reservoir to the buffer solution pump. The reservoir was covered with a hydrophobic felt cover to ensure containment of the buffer solution if the diaphragm ruptured.

A double peristaltic pump, mounted on one side of the EU removable tray assembly next to the buffer solution reservoir, circulates the buffer solution through the fluid system to allow removal by the phase separators of gas bubbles generated at the electrophoresis column electrodes. The pump receives buffer solution from one side of the fluid system (e.g., the column anode side) and circulates it to the other end of the column (Fig. I-3). The capacity of the pump is 35 ml/min.

Two phase separator assemblies were located on the EU removable tray assembly. The phase separators are identical and consist of two cylindrical membranes. One membrane is hydrophilic (porous polyethylene) and the other is hydrophobic (porous polytetrafluorethylene). The buffer and gas mixture enters between the membranes. The hydrophobic membrane allows passage of gas to either the cabin atmosphere or the hydrogen adsorber, and the hydrophilic membrane allows passage of liquid to the storage reservoir. One separator is connected to the column anode side of the fluid system and removes the oxygen gas liberated in the buffer solution at the anode. The oxygen is vented to cabin air. The other separator is connected to the cathode side of the fluid system and removes hydrogen gas liberated at the cathode. The hydrogen is then routed to the hydrogen adsorber assembly. The separator assemblies return the liquid buffer solution to the reservoir.

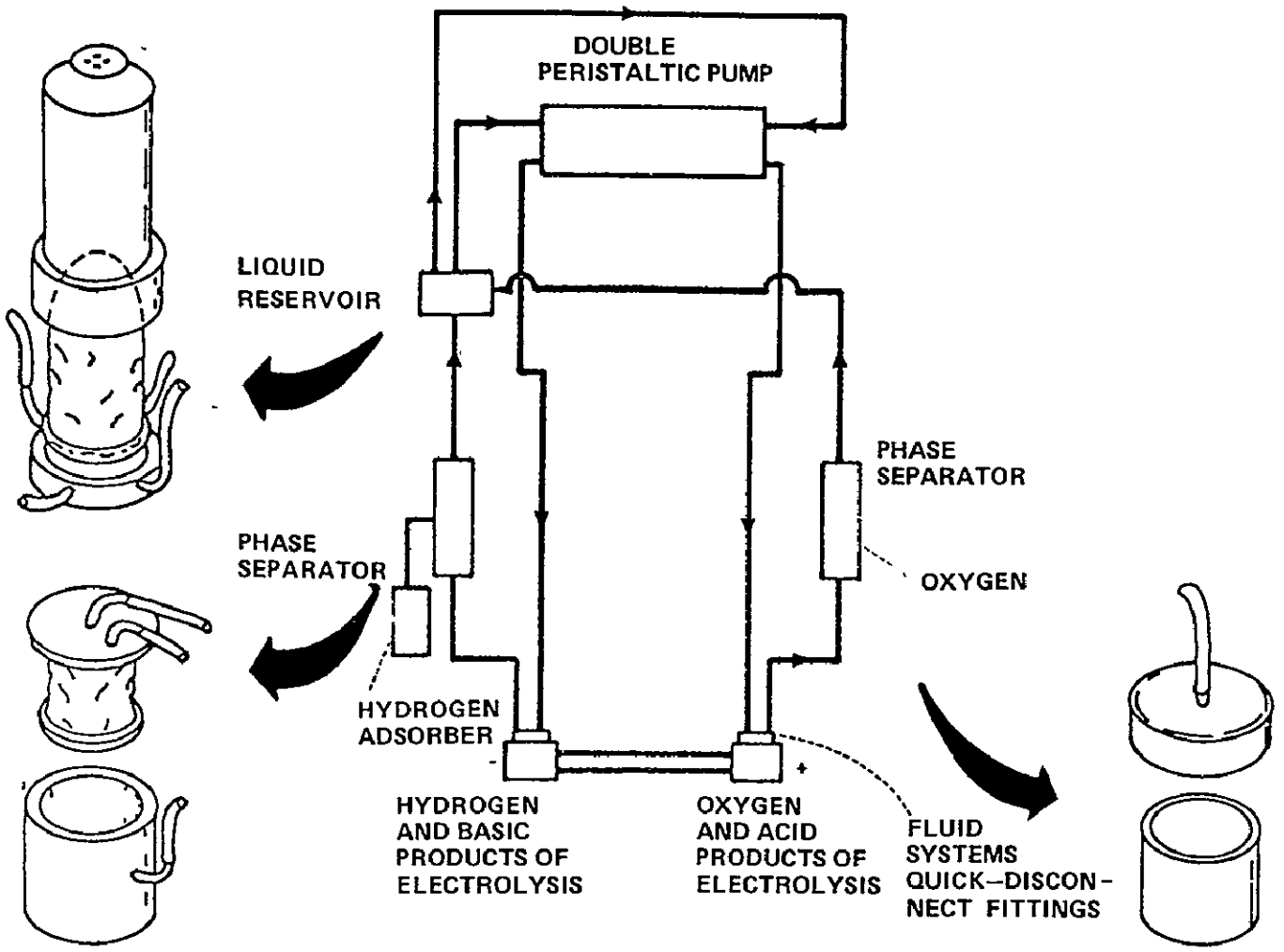

Figure I-3. Electrophoresis fluid system schematic.

The hydrogen adsorber assembly is connected to the phase separator assembly to remove hydrogen bubbles from the buffer solution. The hydrogen gas is adsorbed on a mixture of precipitated palladium (palladium black) and silica gel contained in a fine-filament fiberglass bag in the adsorber canister.

Cryogenic Freezer

The CF (Fig. I-4) was used to contain the experiment samples before insertion into the experiment columns for processing and to maintain the frozen electrophoresis columns after the separations had been accomplished. The sample slides were launched in the CF, and the frozen electrophoresis columns were returned to Earth in the CF.

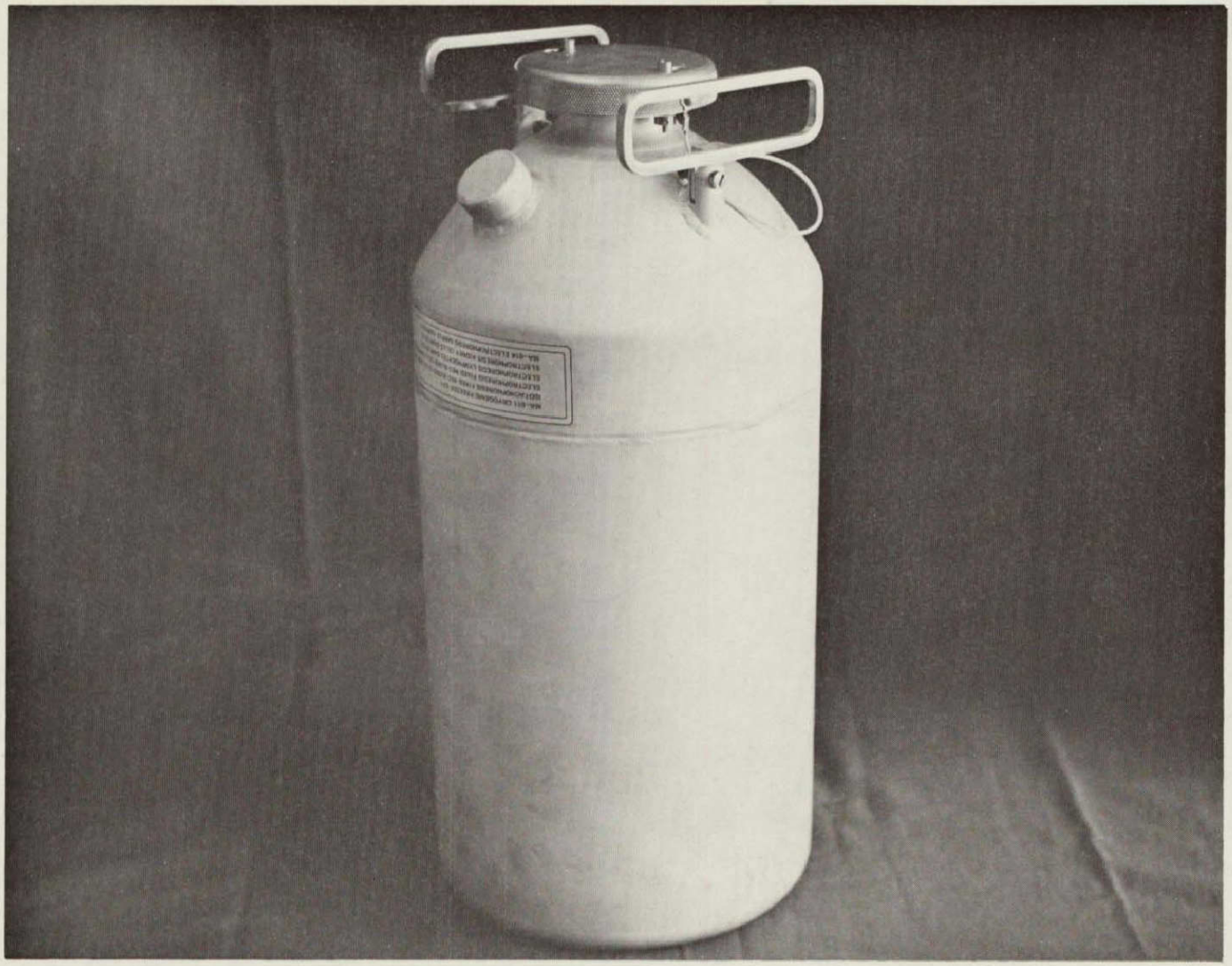

Figure I-4. CF used to transport samples to orbit and to return frozen columns to Earth (note tether cord on cap to prevent separation during orbital operations).

The CF consists of two concentric flasks. The space between the flasks is evacuated for thermal insulation. The inner flask has an outside diameter of 31.12 cm (12.25 in.) and has a cavity to accommodate a cylindrical sample storage canister with dimensions of 4.98 cm (1.96 in.) diameter and 48.26 cm (19 in.) length. The maximum launch weight of the CF, when charged with liquid nitrogen, is 10.4 kg (22.9 lb).

The cooling medium used in the CF was liquid nitrogen vapors. The liquid nitrogen was contained in a saturated absorbent of the inner flask. The CF maintained the samples at a temperature no higher than 188 K (-85°C) for 20 days. The sample canister had space for eight experiment sample slides with samples, one experiment sample column for the German Electrophoresis Experimsne (MA-014), and three cylindrical cavities for return of the electrophoresis columns (two columns per cavity).

Electrophoresis Columns

Six electrophoresis columns were stowed in individual compartments at one end of the EU. Each column consisted of a transparent Pyrex glass tube 0.953 cm (0.375 in.) outside diameter by 0.635 cm (0.25 in.) inside diameter. The tube was 15.25 cm (6 in.) long and was split lengthwise and rejoined with a composite RTV 140/RTV 560 silicone seam to allow for expansion of the buffer solution when the electrophoresis columns were frozen. A thermistor bonded to the tube wall at the center of the length of each tube was used to monitor the column temperature for display on the EU COLUMN TEMP (°C) display.

The inside surfaces of the glass columns were stringently cleaned, coated with Z-6040 (γ-glycidoxypropyltrimethoxysilane, Dow Corning) and then coated with methylcellulose to obtain a stable, biocompatible surface with close to zero zetapotential [I-14]. The zetapotential of an electrophoresis column is that electric potential at a surface of shear between the two parts of the double ionic layer formed by surface ions in the coating and ions of the opposite charge in the fluid which are attracted toward the surface ions [I-1]. Confirmation of the adequacy of the coating was obtained by experimentally determining the electrophoretic velocity of fixed red blood cells in the coated columns. The ends of the tubes were plugged with a fritted glass disk containing a 3 percent agarose gel. The columns were filled before flight with a sterile buffer solution. Each column was sealed in a laminated bag that was then placed in a

fine-filament fiberglass bag (Fig. I-5). This laminated bag consisted of a 0.05 mm layer of polyvinylidene chloride with 0.03 mm of polyethylene on each side. Attached to the laminated bag was a wiper used to wipe the female electrical connectors before column installation. Each end of the electrophoresis column has an electrode chamber assembly containing a platinum electrode, a printed circuit electrical connector, and a mating EU buffer solution connector.

The electrode chamber assemblies were removable for disposal after the column had been frozen on the EU. The electrode chamber assembly containing the column cathode had a cavity into which the sample slide was inserted for experiment operation. A blank slide was contained in the cavity before experiment operation. The blank slide had a 0.13 cm (0.05 in.) inside diameter threaded hole used for preflight filling of the column with buffer solution. The opening was sealed after filling.

The buffer (A-1) used in the zonal electrophoresis columns consisted of a mixture of 1.76 mmol Na_2HPO_4, 0.367 mmol KH_2PO_4, 6.42 mmol NaCl, 0.336 mmol Na_2EDTA, 222 mmol glucose, and 514 mmol glycerol in water. It had a hydrogen-ion concentration (pH) of 7.30 ± 0.10 at 293 K (20°C) and a calculated ionic strength of 0.0097 mol/liter. At 298 K (25°C), the conductivity was 0.96 mmho/cm; the density, 1.022; and the dynamic viscosity, 0.00111 N-s/m^2 (0.0111 poise). The buffer was demonstrated to be compatible with the column coating, all components of the EU system, and the candidate materials to be flown on the mission. The average mobilities of fixed rabbit, human, and horse red blood cells in this buffer were 1.60, 1.96, and 2.60 m/s/V/cm, respectively.

Isotachophoresis Columns

Two isotachophoresis columns were stowed in individual compartments in the EU. Each column consisted of a glass tube having dimensions of 0.97 cm (0.38 in.) outside diameter, 0.64 cm (0.25 in.) inside diameter, and 15.24 cm (6 in.) length. Each end of the tube had an assembly containing a flat, disk-shaped, three-lobed electrode (one electrode assembly with a silver anode and the other with a palladium cathode), a rubber diaphragm, and a printed circuit electrical connector. The design of the columns had to be slightly modified from those used for zonal electrophoresis, due to the special requirements of isotachophoresis. Some of the features of the Skylab 4 isotachophoresis module [I-5] were also incorporated. It should be emphasized that these modifications

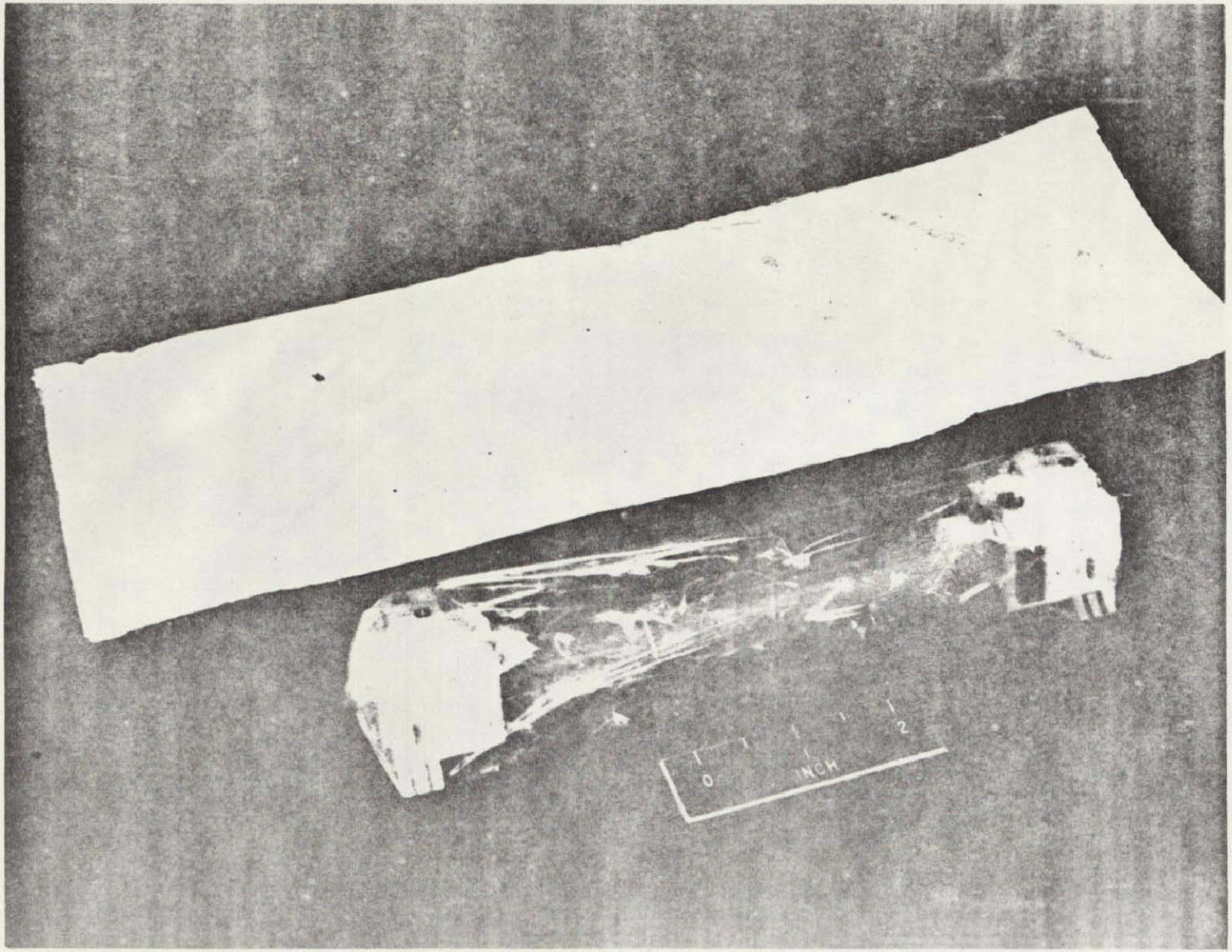

Figure I-5. Column shown bagged in polyvinylidene chloride bag to prevent air exchange (the bagged column was inserted in the larger fiberglass bag for protection of flammability).

notwithstanding, the columns were not optimal for isotachophoresis, as the observation channel was unnecessarily long, and the electrode buffer volumes too small. The modifications represented only the best achievable compromise consonant with the basic design of the flight apparatus. Figure I-6 illustrates the differences between the two models of columns employed.

The assembly containing the palladium cathode had a cavity into which the sample slide was inserted for experiment operation. A blank slide was contained in the cavity before processing the columns. The blank slide had two 0.13 cm (0.05 in.) inside diameter threaded holes used to fill the column with buffer solution before flight.

The isotachophoresis occurred in a column containing a leader buffer consisting of the following components: 0.62 ml of 85 percent phosphoric acid in 500 ml water, with 42 grams of dextrose and 276 grams of glycerol, adjusted to a pH of 7.4 in 1 liter of distilled water. The terminator buffer contained 2 grams of serine, 42 grams of dextrose, and 276 grams of glycerol, adjusted to pH 8.2 in 1 liter of glass distilled water.

Sample Slides

Each sample to be processed during the experiment was mounted in a slide assembly (Fig. I-7). Before processing, the slides were stowed in the CF sample canister. Each slide assembly was contained in a tetrafluoroethylene cover 0.13 mm (0.005 in.) thick that had a removal tab 5.08 cm (2 in.) long of the same material. The slides were removed from the CF sample canister by grasping the removal tab and pulling the slide out of the canister. Every two slides removed from the canister exposed a return storage space in the canister for two electrophoresis columns. In addition to the slides to be processed, four "control" slides with sample material were stowed in spaces on the circumference of the sample canister. Two control slides contained lymphocytes and two contained kidney cells. These "control" slides were designed to assess the effects of the environment on the viable sample materials; they were returned to Earth without processing. The slides containing the lymphocytes were labeled A and C, while those containing kidney cells were labeled B and D.

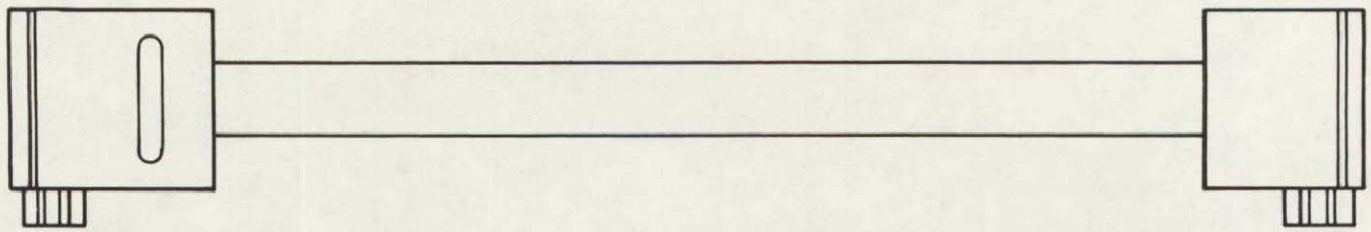

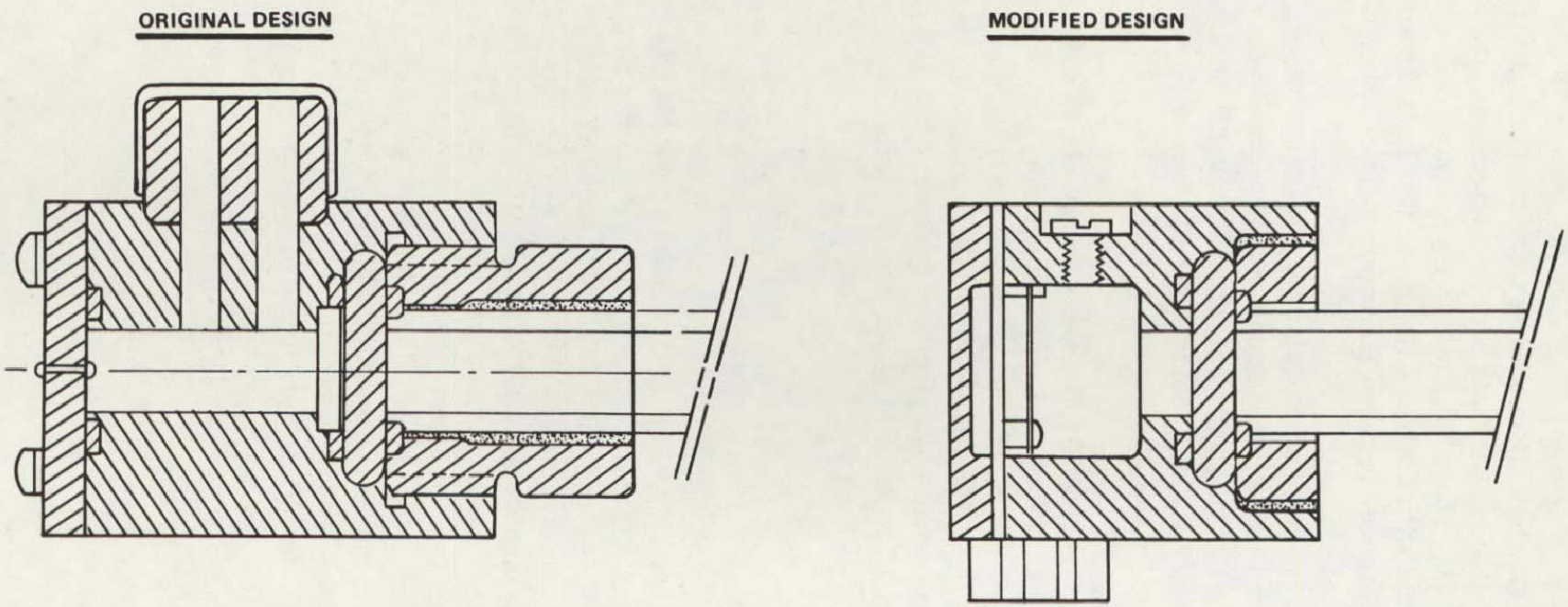

Figure 6. Modifications employed from the zonal electrophoresis column (original design) to the isotachophoresis column (modified design).

Figure I-7. Sample slide containing frozen sample (these samples were kept at liquid nitrogen temperature until processed).

Each sample slide was numbered to correspond to the appropriate column. The slides were removed from the canister and inserted into the experiment column electrode (cathode) chamber assembly for processing in numerical order. Each slide was discarded together with the electrode chamber assemblies after each electrophoresis column was frozen for return. The entire isotachophoresis column was discarded after processing.

Slicing Device

After the electrophoretic separation was completed the columns were frozen on the TE module by the astronauts and returned to Earth in the CF. It was then necessary to slice these frozen samples into uniform sections for subsequent analyses. In slicing the columns, several critical requirements had to be satisfied, as noted: (1) the frozen columns had to be sliced at 233 K (-40°C) or colder; (2) contamination from slicing mechanism must be minimized, e.g., heating and particulates from the cutting device; (3) the slices had to be between 0.5 mm and 5.0 mm in length; (4) each slide had to be contained aseptically, and (5) the slicing procedure had to be recorded photographically. After a thorough search of the literature, no existing device was found that could satisfactorily meet all of these requirements. Therefore, a device was designed, constructed, and tested for this specific purpose [I-5]. As shown in Figure I-8, the slicing assembly consisted of an extraction assembly where the frozen flight column was placed. The extraction rad was used to push the ice column into a teflon tube contained in the slicing assembly. After proper alignment, the razor blade was used to slice "coins" of the frozen column. The 5 mm "coins" were captured, bagged, and stored at 77 K (196°C). The entire slicing assembly was operated in a laminar flow hood and operated in a sterile manner. Subsequent analyses of the cultured kidney cells proved that no detectable contamination resulted from the operation of this device.

MA-011 EXPERIMENT OPERATIONS

An electrophoresis or isotachophoresis column was removed from its storage location and installed on the EU column cradle. Fluid couplings were secured to each electrode chamber of the electrophoresis columns only. Then, the proper sample slide with a forzen sample was removed from the CF and inserted into the column. The 70 mm camera, mounted on the EU cover,

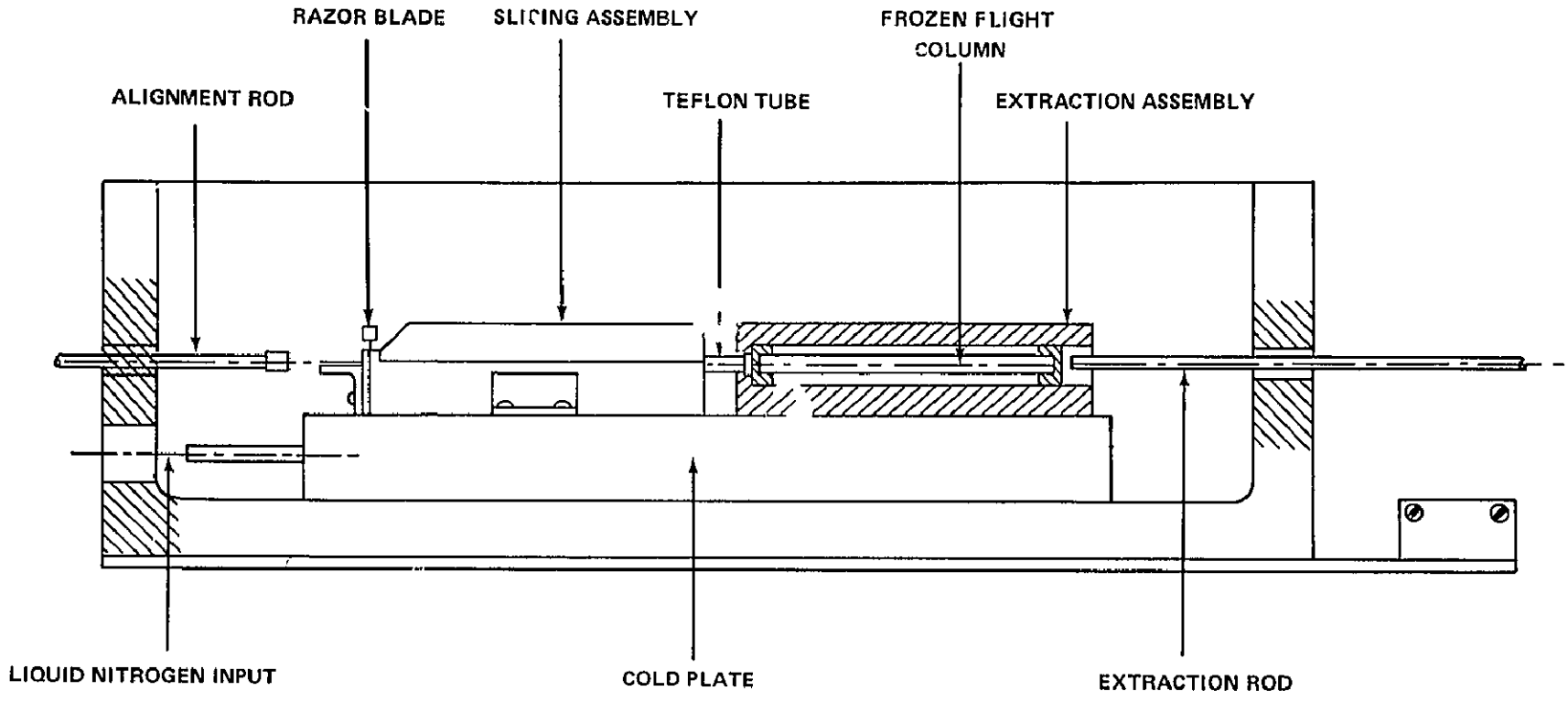

Figure 8. Cross section of slicing device.

photographed the experiment column during a run. After each electrophoretic separation was completed, the column was frozen in place on the EU by the TE module. The frozen column was removed from the column cradle, the electrode chambers were removed and discarded, and the column was placed in the CF for return to Earth. Isotachophoresis specimens were neither frozen nor returned but only photographed during processing.

RESULTS

The EU, CF, and the data collection assembly met the required objectives with satisfactory experimental results. The fluid connect lines (located in the electrode housings) of some of the columns were clogged during assembly. Without a fluid purge of the electrode housing, chemical and gas products of electrolysis accumulated in the electrode region. This accumulation triggered changes in the buffer which were manifested as column voltage fluctuations and pH changes in the column fluid. These anomalies were seen in columns 2, 5, and 6. Operations of the other columns appeared normal.

The order of the experimental results that follow are reported according to the order that the samples were processed. The electrophoresis experiments are given first; the isotachophoretic runs are reported in the last section.

Electrophoresis

The analyses of the electrophoretic columns containing fixed rabbit, human, and horse red blood cells (columns 1 and 5) consisted of mobility tests and morphological examinations. There were both flight photographs and the sliced samples with which to work.

The number of red blood cells loaded in the sample slide was 5.22×10^6 rabbit cells/0.06 ml, 3.44×10^6 human cells/0.06 ml, and 7.26×10^6 horse cells/0.06 ml. The volume of the sample slide was 0.06 ml for an electrophoresis slide.

FLIGHT PHOTOGRAPH ANALYSIS

Three major questions were posed for the flight photograph analysis:

1. Was electroosmosis eliminated?

2. Did the bands migrate at rates predicted from the ground-based experiments?

3. Did the total migration of the bands agree with the predictions?

A major problem in the preparations for the flight experiment was the elimination of electroosmosis. If present, the fluid flow due to electroosmosis would cause the cells in the center of the flight column to travel faster than those near the column wall. This effect produces "bullet" shaped bands and reduces the resolution capability of the apparatus. A methycellulose coating technique was used to coat the inside walls of the electrophoresis column to eliminate electroosmotic flow [I-14]. Following coating, electoosmotic flow as reduced from approximately 4.5 μm/s/V/cm to less than 0.3 μm/s/V/cm. Within this level of electroosmotic flow (0.3 μm/s/V/cm) the bands were predicted to be spread to approximately 2.5 times the length computed for zero electroosmotic flow after 60 min of run time. Not all of this spread would be observable to the naked eye since at the boundaries the concentrations of cells would be lower than the threshold for direct visualization.

In subsequent examinations of the flight photographs, two indications of electroosmosis were investigated: (1) a curvature of band front boundaries which became more pronounced as the run time increased, and (2) longitudinal spread of the bands in excess of that predicted in the absence of electroosmotic flow.

The band fronts were planar in appearance with no signs of pronounced curvature for column 1. Problems which might interfere with this visual assessment are the following: (1) the optical aberration in viewing bands through a cylindrical tube wall, (2) the haziness of the flight photos, and (3) the definition of the band boundaries as seen by the naked eye. However, again, the band fronts appeared planar on visual inspection of the flight photographs.

The spreading behavior of the bands were analyzed by plotting the displacement of the band boundaries from the sample slide as a function of run time. The data were collected by visual examination of 20 flight photographs taken at 3 min intervals during the 60 min run of column 1. The band widths at 60 min were taken from the straight curve fits to the boundary migration data. The results are presented in Table I-2. The bands were slightly more compressed than expected. Thus, it is concluded that no band spreading occurred that was due to electroosmosis through visual examination.

The electrophoretic mobility of the particles in the band boundaries was computed from the plot of band boundary migration versus run time. The data in Table I-2 shows that the calculated mobility at 25°C for the fast band was 2.36 for the band front and 2.21 m/s/V/cm for the rear boundary which are slightly lower than the predicted average of 2.38 μm/s/V/cm for horse cells as observed in ground-based analytical particle electrophoresis. The front of the slower band complex corresponded to the mean value for human cells of 1.94 μm/s/V/cm, but the rear boundary had a mobility of 1.70 which is higher than the 1.56 average value observed for rabbit red cells in the ground-based experiments. The predicted red cell band intensities as a function of migration distance from the sample slide are shown in Figure I-9. This figure was constructed from observed electrophoretic mobility distributions for each of the red cell populsions and the number of each cell type loaded in the sample slide at MSFC. The straight curve establishes the mobilities, U_e^{25}, measured at 258 K (25°C) in A-1 buffer during ground-based experiments. The right-hand ordinate gives the percentage of the total number of cells in the sample slide found in each bar of the histogram. From the figure it can be seen that the location of visibly dense bands should be: rabbit 70 to 81 mm, human 88 to 100 mm, and horse 105 to 123 mm.

TABLE I-2. OBSERVED AND PREDICTED BAND WIDTH VALUES OF THE FORMALIN-FIXED RED BLOOD CELLS

Band	Band Width (mm)		Electrophoretic Mobility (25°C) (μm/s/V/cm)	
	Observed	Predicted	Observed	Predicted
Fast (Horse)	8 to 10	15 to 18	2.21 to 2.36	2.38
Slower Band Couples (Human + Rabbit)	20	30	1.70 to 1.96	1.56 to 1.94

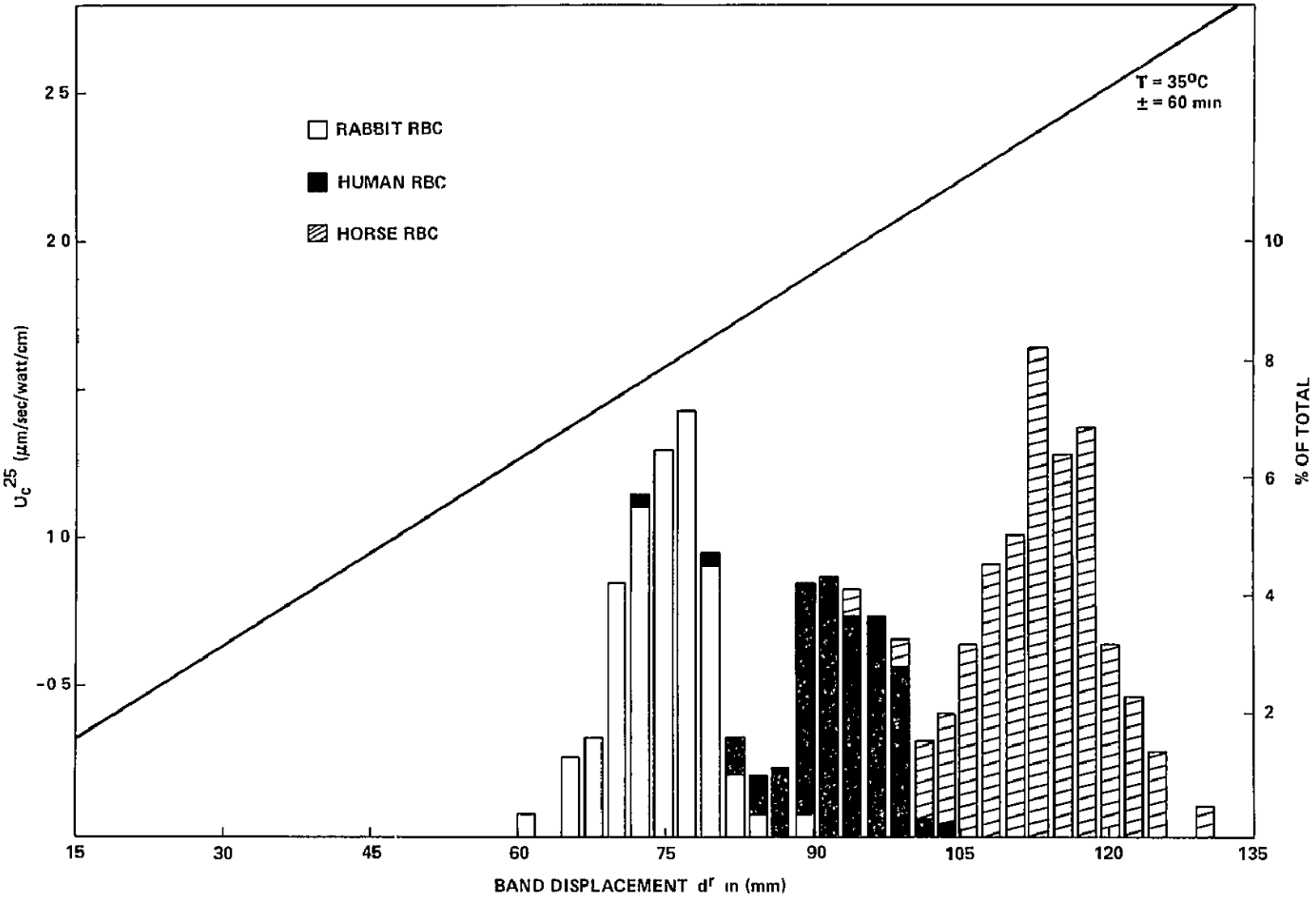

Figure 9. Predicted band intensities at various migration distances.

The observed band locations for column 1 at 60 min are compared with the predicted locations in Figure I-10. The observed band locations were taken from the plot of band migrations versus run time since the visualization of the bands was difficult at the end of the run. The fast band corresponded well with the predicted location for horse red cells and the front of the slower band complex corresponded with the predicted human red cell location. The rear boundary of the slower band complex was 1 to 1.5 cm further into the tube than predicted for rabbit cells. Overall, the bands were slightly more compressed than expected and the separation between horse and human cells was greater than predicted.

The analysis of the flight photographs showed good general agreement between the observed migration behavior of the red cell bands and the predicted behavior. Small discrepancies were found which have not yet been explained. Some of these may relate to factors not included in the predictive model of the experiment such as radial and longitudinal thermal gradients in the flight column, the compression of the voltage field in the sample disk aperture, and red cell concentration effects.

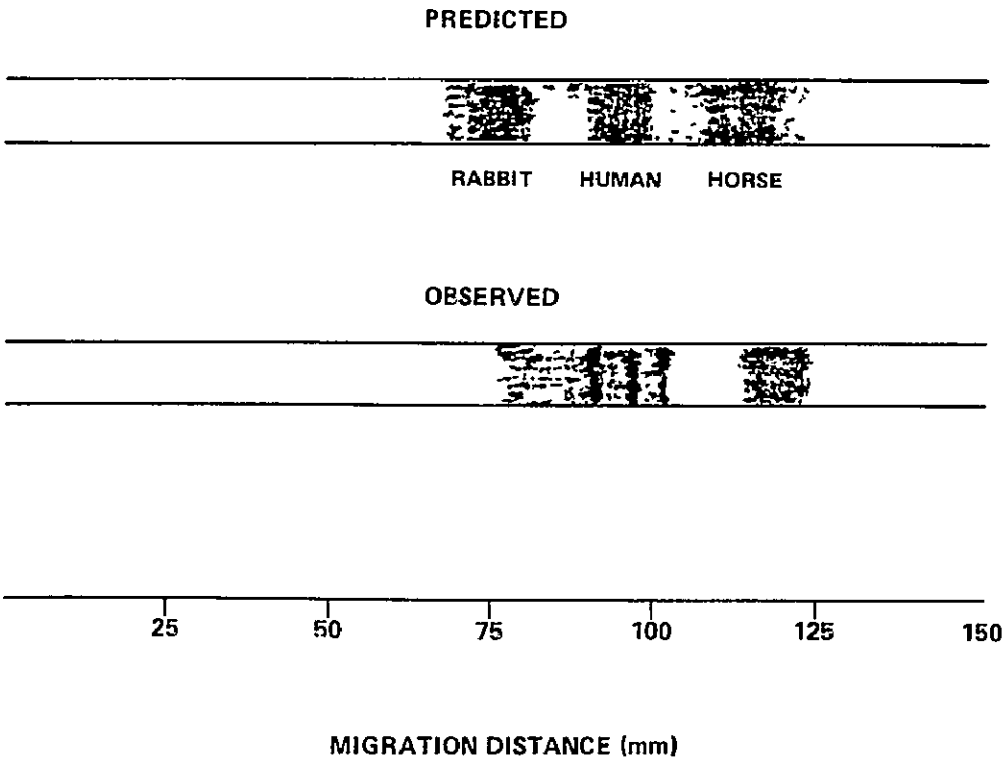

Figure I-10. Visually predicted and observed migration of formalin-fixed red blood cells (the observed migration of cells are from column 1 of the flight experiment).

In column 5, two specific instances of sudden disruption of boundaries can be seen in the flight photographs (Figs. I-11 to I-14). These disruptions occurred between the time of the photographs shown in Figures I-13 and I-14. The disruptions probably were caused by random motion of the apparatus or perhaps of the spacecraft.

During the sample slicing operation for column 1, the column walls fractured and the column was distorted. The samples were collected in the hope that minimal mixing and contamination had occurred. In the case of column 5, the flight experiment had not functioned properly due to blockage of the electrode buffer circulation ports. This was thought to produce a fluid flow through the electrophoresis column which opposed the direction of particle migration and carried electrolysis products into the column. The sample slicing was carried out as planned for column 5.

The calculated recovery of fluid volume was 75 percent for column 1 and 93 percent for column 5. The histograms of cell count versus the computed distance from the column sample slide are shown for columns 1 and 5 in Figures I-15 and I-16, respectively.

In Figure I-15, only six fractions were obtained from the region of the column containing the red cell bands. These were placed in the sample histogram starting from the anode end of the column from the sample slide, since 25 percent of the column fluid had not been recovered and the earlier sample slices were shown to contain consistently less volume than calculated. The histogram agreed well with the locations of cells in the flight photographs, but this agreement may be fortuitous since cell typing and electrophoretic data indicated considerable mixing of cell types. The recovery of cells was 70 percent of the theoretical value.

In Figure I-16, no discrete bands were shown in the histogram for column 5 which agrees with the flight photographs. The recovery of cells was 90 percent of the theoretical yield. The front of the continuous band was located at 80 mm in the flight photos in contrast to the location of the cells in the sample slices where the front was at approximately 60 mm. In sample slices 7 to 10 the pH decreased from 7.9 to 6.5 and reached values of 3 to 4 in slices at larger migration distances.

The cells in three sample slices from each column were examined by analytical particle electrophoresis to find whether they displayed the electrophoretic mobility distributions expected from their locations in the flight column. Data were collected for 100 cells from each sample.

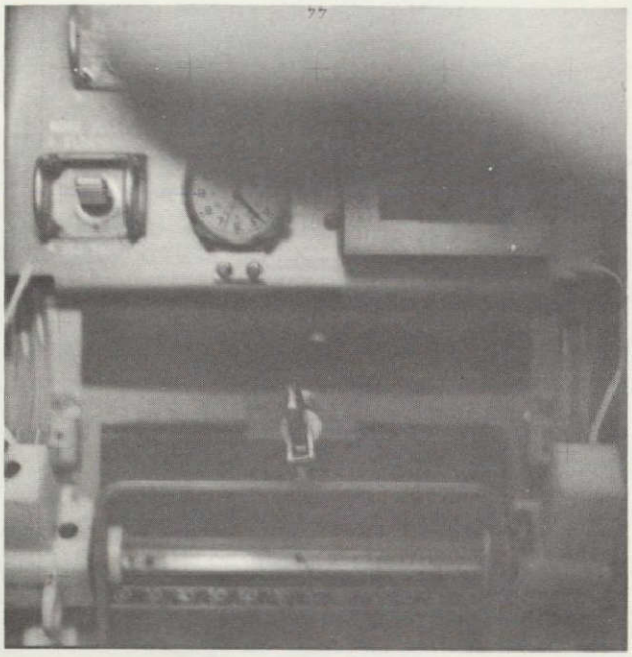

Figure I-11. Flight photograph of electrophoresis column 5 (AST-26-2182).

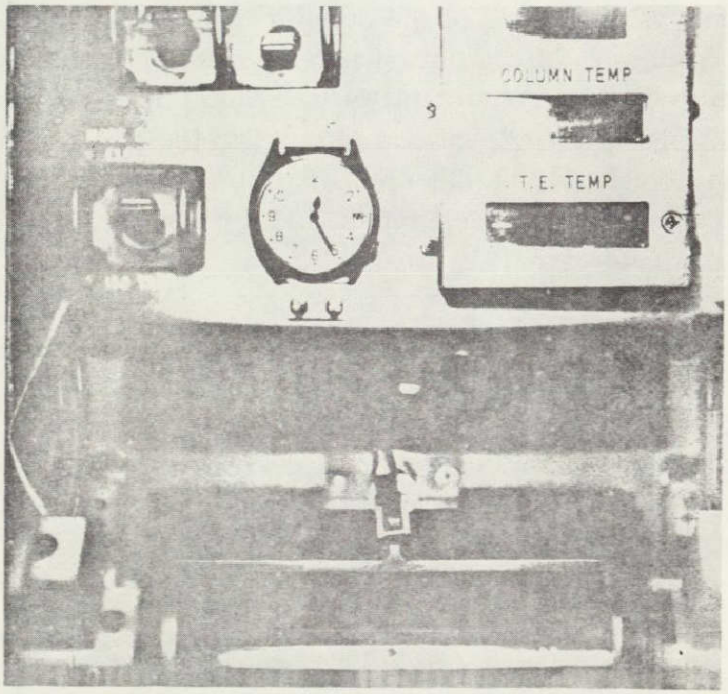

Figure I-12. Flight photograph of electrophoresis column 5 showing disruption of boundaries (AST-26-2183).

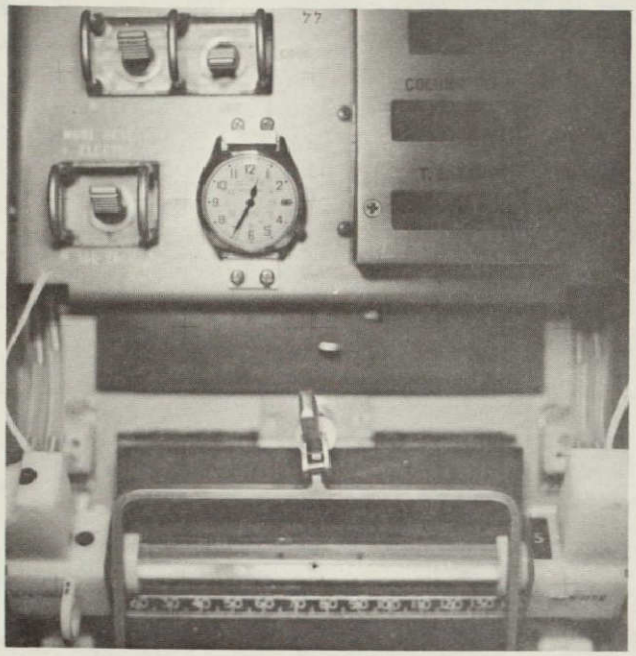

Figure I-13. Flight photograph of electrophoresis column 5 (AST-26-2186).

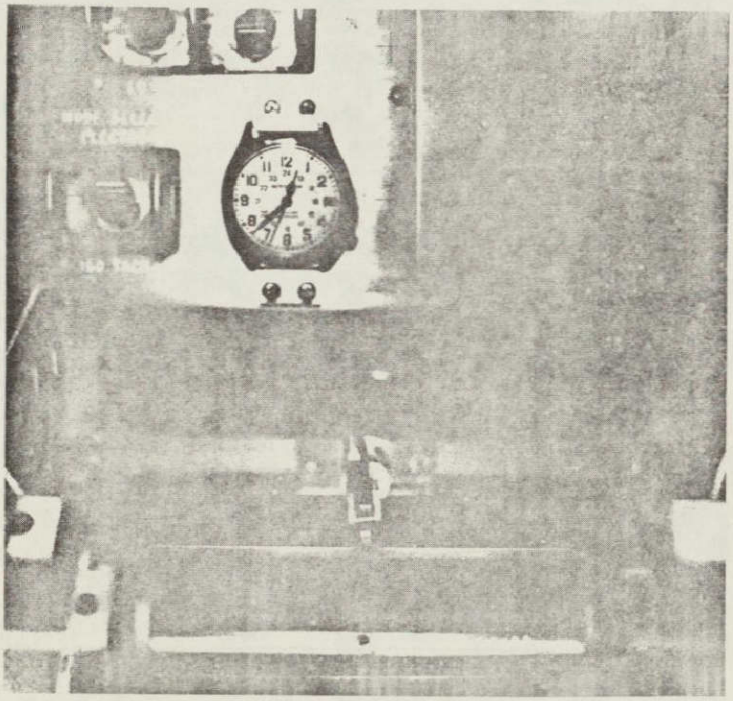

Figure I-14. Flight photograph of electrophoresis column 5 showing disruption of boundaries (AST-26-2187).

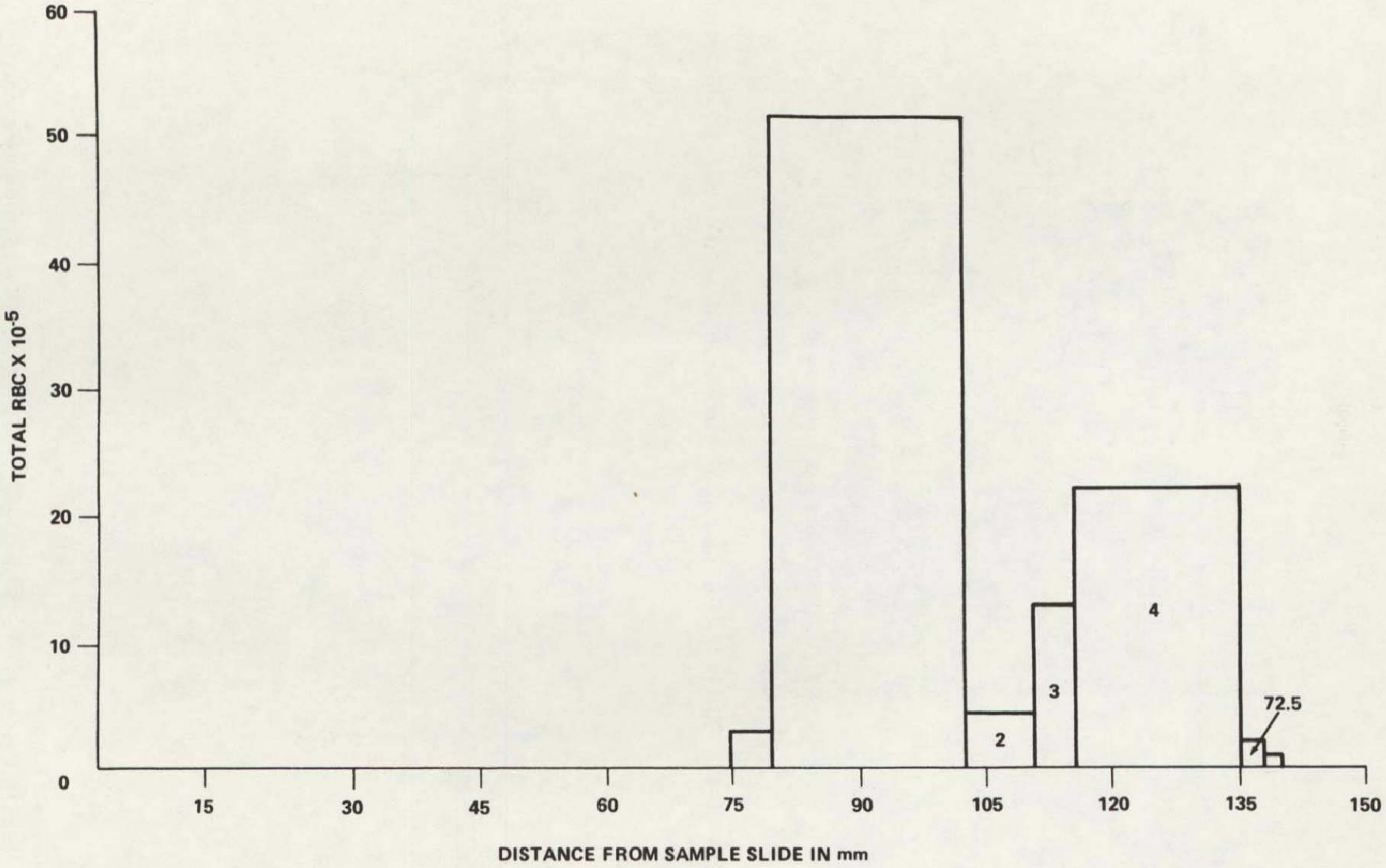

Figure 15. Cell count histogram from column 1.

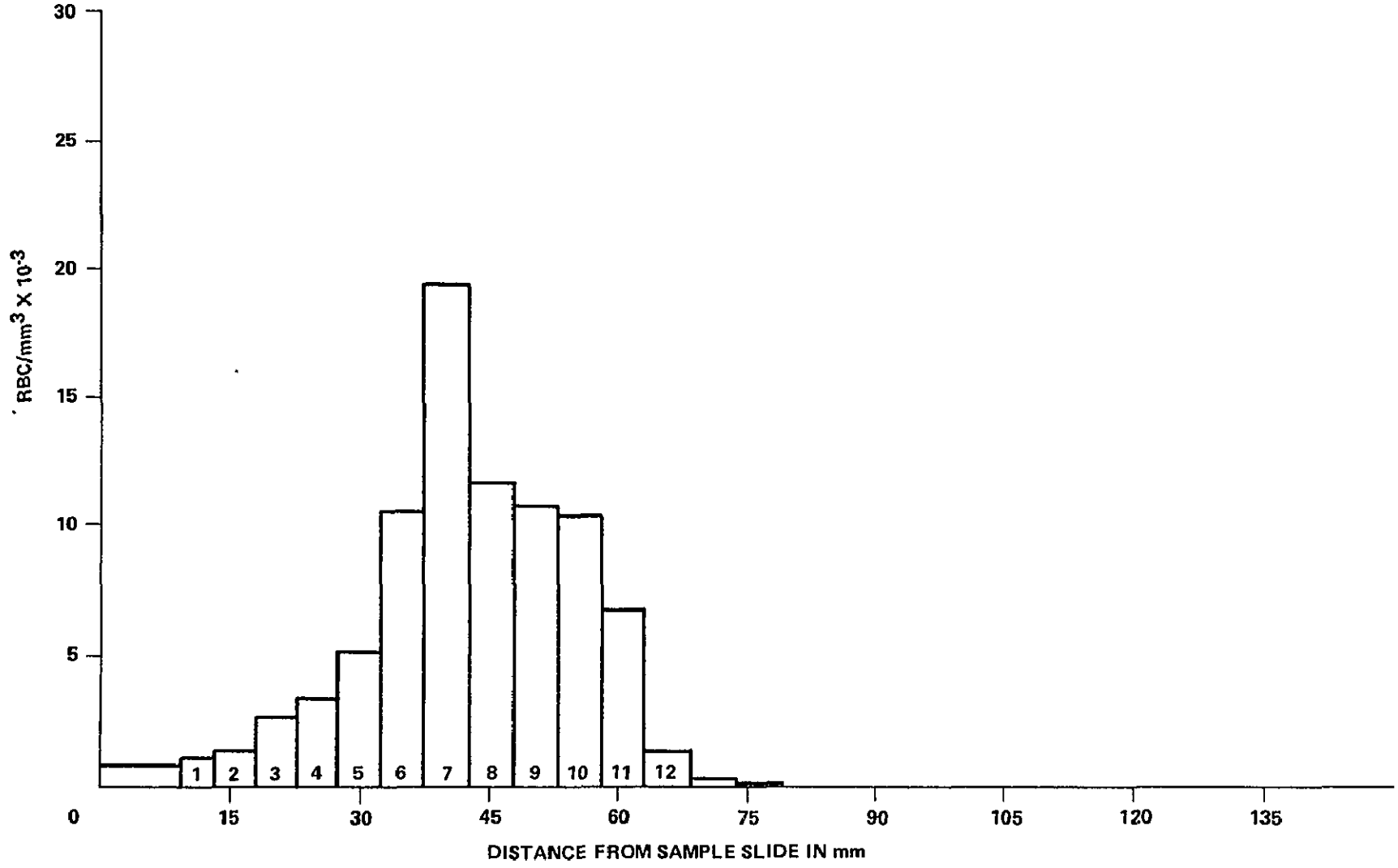

Figure 16. Cell count histogram from column 5.

The results for column 1 sample slices 1, 3, and 4 were disappointing, since all had similar electrophoretic mobilities and did not show the expected trends. Their mean mobilities were all in the range from 2.05 to 2.17. This suggested that the cells had either been mixed, contaminated during the column breakage, or mixed prior to freezing. The cells in sample slices 5, 8, and 11 from column 5 showed a trend from lower to higher electrophoretic mobilities, respectively, but the separation was not large.

Estimations were made of the numbers of each cell type from the electrophoretic mobility data. These were in general agreement with the morphological typing estimations made (Figs. I-17 and I-18). For column 1, the typing data showed similar distributions of the three cell types in each of the sample slices in contrast to the expected behavior. This supported the suggestion that the samples had been mixed when the column broke or prior to freezing. As the data show, in column 5, there were enrichments of rabbit cells in the slow region of the band (cathode end of column) and horse cells in the fast region (anode end of column) as expected.

The results of the post-flight sample slice analyses indicate that the samples from column 1 are of little use in interpreting the behavior of the flight experiment. The column 5 data show partial separation of cells according to their electrophoretic mobilities.

Conclusions

Electroosmosis, which is a major obstacle to successful electrophoretic separations in a closed cylindrical tube apparatus, was eliminated in the ASTP electrophoresis experiment. The coating techniques developed for this purpose significantly increased the resolution capability of the EU and will be useful for ground-based and future space electrophoretic applications. The red blood cell test samples behaved essentially as predicted from ground-based studies. The bands were planar and showed no signs of unexpected longitudinal spreading. Therefore, the MA-011 EU has demonstrated the capability of separating small volumes of sample cells on the basis of their electrophoretic mobilities.

SLICED SAMPLES

Human Lymphocytes

Approximately 1.5×10^7 human lymphocyte cells were loaded into the 0.06 ml volume of each sample slide. Migration of the cells was not detected in either column. In column 2, current was established for less than 3 min

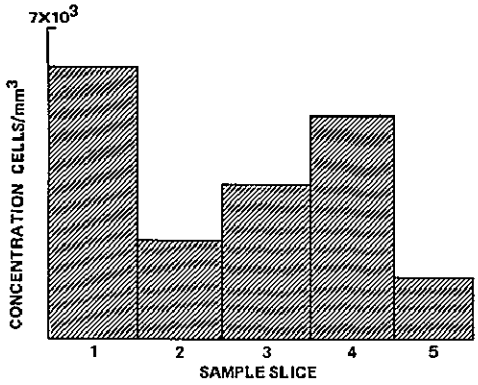

SAMPLE SLICE	CELL TYPE		
	RABBIT	HUMAN	HORSE
MOBILITY PERCENT			
1	19	22	59
3	11	17	72
4	12	38	50
MORPHOLOGY PER 100 CELLS			
1	17	26	57
3	19	48	33
4	15	31	54

Figure I-17. Mobility and morphological data from column 1.

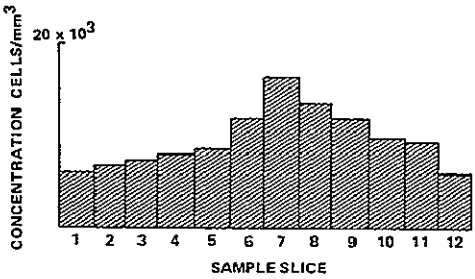

SAMPLE SLICE	CELL TYPE		
	RABBIT	HUMAN	HORSE
MOBILITY PERCENT			
5	18	60	22
8	24	48	28
11	23	42	35
MORPHOLOGY PER 100 CELLS			
1	56	38	6
2	66	31	3
3	60	40	0
4	64	36	0
5	36	57	7
6	47	41	12
7	31	32	37
8	17	41	41
9	12	27	61
10	11	23	66
11	10	34	56

Figure I-18. Mobility and morphological data from column 5.

because of fluid line blockage, which resulted in the formation of gaseous products around the electrodes. These gas bubbles blocked current and prevented operation of the experiment. In addition, the cell viability was only 6 percent (Table I-3). No explanation can be found for this observation, as the pH of the column fluid varied from 6.69 to 6.85.

In column 6, current existed for approximately 30 min. In this case, the electrode housings were returned, and an investigation confirmed that the right electrode chamber fluid lines were blocked. This condition resulted in an acid pH throughout the column. The pH of the fluid in column 6 was 2.54 on the cathode end, 2.28 in the center, and 2.21 on the anode end. As would be expected, the viability of the lymphocytes was only 1 percent (Table I-4).

In addition, the control cells that were taken to orbit but not thawed, showed an unusually low viability (Tables I-3 and I-4). It is deduced that because of the small size of the control slides these lymhocytes froze and thawed faster than the prescribed rate. In preflight tests, the cells showed routinely a recovery of 55 to 63 percent viability when frozen and thawed using the sample keys. These sample keys are much larger than the control slides, although their cell-compartments are of the same size.

Conclusion

These data are not adequate for any conclusions related to the feasibility of space electrophoresis of human lymphocytes. As a spin-off from this work, however, the freezing of human granulocytes, by the same method developed for the freezing of human lymphocytes for ASTP, appears most promising and is being pursued further. The viability of human granulocytes using the ASTP method after freezing and thawing is approximately 82 to 86 percent. In addition, their phagocytic activity appears undiminished. Also, during simulation of and in preparation for the flight experiments, a 1 g method for preparative cell electrophoresis was developed, permitting the separation of the fastest-migrating cells (the T-lymphocytes) in a pure state [I-16].

Human Kidney Cells

In the human kidney cell experiments, approximately 2.0×10^6 cells were loaded into the sample slide. Only column 3 was electrophoresed in orbit. During orbital operations, the processing of column 7 was discontinued.

TABLE I-3. CELL COUNT AND VIABILITY RESULTS OF HUMAN LYMPHOCYTES FROM COLUMN 2

Number of Fraction	Weight (Vial + Teflon Collar + Cells)	Count per Sample	Viability
Left End	6.1430	364 000	6 %
1	6.1103	44 800	6 %
2	6.1232	50 800	0 %
3	6.1555	1 120	0 %
4	6.1418	0	—
5	6.2016	560	0 %
6	6.1406	0	—
7	6.1630	0	—
8	6.1239	0	—
9	6.1673	0	—
10	6.0990	0	—
11	6.1507	0	—
12	6.1528	0	—
13	6.1325	0	—
14	6.1862	0	—
15	6.1787	0	—
16	6.1547	0	—
17	6.1273	0	—
18	6.2091	0	—
19	6.1998	0	—
20	6.2064	0	—
21	6.1465	0	—
22	5.9932 (No Collar)	0	—
23	6.1728	0	—
24	6.2326	0	—
25	6.1354	0	—
26	5.9526 (No Collar)	0	—
Right End	6.1723	0	—
Ground Control A	6.2813	1 420 000	46 %
Flight Control A	6.2794	3 620 000	13 %

TABLE I-4. CELL COUNT AND VIABILITY RESULTS OF HUMAN LYMPHOCYTES FROM COLUMN 6

Number of Fraction	Weight (Vial + Teflon Collar + Cells)	Count per Sample	Viability
Left End	6.1921	392 000	0 % Clumps
1	6.0849	427 000	1 %
2	6.2056	856 000	0 % Clumps
3	6.1272	851 200	0 %
4	6.1692	6 160	0 %
5	6.1974	0	—
6	6.1590	0	—
7	6.1146	0	—
8	6.1595	0	—
9	6.1164	0	—
10	6.0714	0	—
11	6.1408	0	—
12	6.1269	0	—
13	6.1780	0	—
14	6.1360	0	—
15	6.1626	0	—
16	6.1623	0	—
17	6.1975	0	—
18	6.1532	0	—
19	6.1966	0	—
20	6.1834	0	—
21	6.2268	0	—
22	6.1181	0	—
23	6.2654	0	—
24	6.1395	0	—
Right End	6.2239	0	—
Ground Control C	3.1232	1 290 000	19 %
Flight Control C	3.1480	2 360 000	14 %

The frozen slices obtained from column 3 were thawed rapidly at 310K (37°C), centrifuged, and resuspended in growth media. These fractions were weighed, tared, and the pH determined (Table I-5). An aliquot was taken for viable cell count and based on this information, the cells were cultured. The distribution of viable cells is shown in Figure I-19. As shown, approximately four subpopulations of cells can be identified.

TABLE I-5. WEIGHTS AND pH OF SAMPLE SLICES FROM COLUMN 3

Fraction					
R	1.4292	1.1061	None	0.3231	7.25
L	1.3623	1.08425	None	0.27805	7.05
1	1.3483	1.11375	0.0855	0.15400	7.8
2	1.3381	1.0926	0.0944	0.15110	7.9
3	1.3150	1.0861	0.08695	0.14195	7.8
4	1.3612	1.1047	0.08955	0.16695	7.8
5	1.3521	1.09775	0.09115	0.16320	7.85
6	1.3350	1.0905	0.08625	0.15825	7.6
7	1.3290	1.09205	0.08850	0.14845	7.85
8	1.3568	1.104	0.09030	0.16250	7.75
9	1.3573	1.0943	0.09105	0.17195	7.75
10	1.3350	1.0869	0.09005	0.15805	7.85
11	1.3581	1.11405	0.08970	0.15435	—
12	1.3749	1.10465	0.09260	0.17765	7.65
13	1.3301	1.08585	0.08805	0.15620	7.55
14	1.3156	1.10695	0.01765	0.10100	7.45
15	1.2970	1.08865	0.07495	0.13340	7.5
16	1.3154	1.08785	0.08830	0.13925	7.65
17	1.4090	1.10985	0.09510	0.20405	7.25
18	1.3296	1.0915	0.08805	0.14975	—
19	1.2915	1.0854	0.08585	0.12015	7.45
20	1.3240	1.08645	0.08840	0.14915	—
21	1.3443	1.0908	0.09235	0.16115	—
22	1.3714	1.10855	0.09590	0.16695	7.45
23	1.3494	1.09885	0.08825	0.16230	—
24	1.3408	1.09785	0.08660	0.15635	—
25	1.3829	1.09895	0.09850	0.18545	—
26	1.2727	1.1061	0.04690	0.11970	7.4

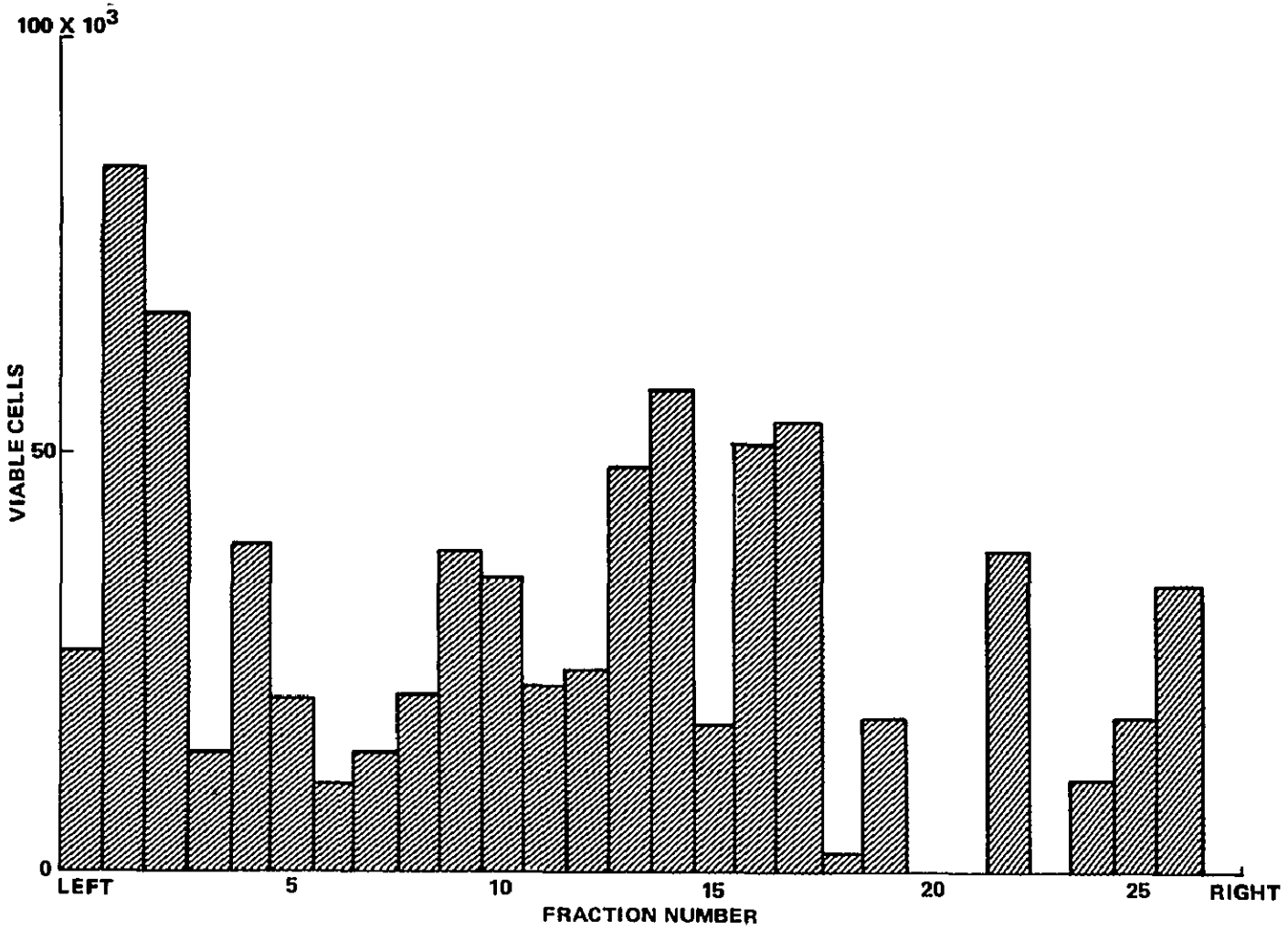

Figure I-19. Histogram of viable kidney cells for each sample slice in column 3.

After 28 days, only fractions 11 to 19 had reached confluency. The other fractions were removed from the culture plates and tested for urokinase activity by fibrin plate method [I-17] and showed no fibrinolytic activity. The disposition of the subcultures is shown in Tables I-6 and I-7. Those cells that were put on production media were tested for urokinase activity at various times. The cells that were subcultured were removed from the dishes with EDTA and then recultured.

TABLE I-6. DISPOSITION OF KIDNEY CELL SUBCULTURE FROM COLUMN 3

Number of Fraction	Condition	Disposition
14-1	Confluent	To Subculture
14-1	Confluent	To Production
16-1	50% Confluent	To Production
16-1	50% Confluent	Reculture[a]
17-1	Confluent	To Subculture
17-1	Confluent	To Production
19-1	Confluent	To Subculture
19-1	Confluent	To Production

a. No growth resulted from this subculture.

Table I-8 presents the results of the urokinase production obtained with the primary and subculture 1 cells after 35 days on production. There is an obvious enrichment of urokinase activity in fraction 15. An increased production is also seen in several other fractions. Control experiment with the same cells cultured using ground-base conditions gave the value of 0.28 UK units per 100 cells. The subculture 2 cells did not produce urokinase when placed on production media. Part of the cells from subculture 2 were analyzed for electrophoretic mobility distribution and the results of three such fractions are shown in Figures 20, 21, and 22. The cells of subculture 1 were also tested for the presence of human granulocyte conditioning factor (HGCF) and the results are presented in Table I-9. It is evident that the highest concentration of these HGCF producing cells was in a separate band (fraction 17).

TABLE I-7. DISPOSITION OF CONFLUENT KIDNEY CELL SUBCULTURE 2 FROM COLUMN 3

Number of Fraction	Condition	Disposition
14-2	Confluent	To Production
14-2	Confluent	To Mobility[a]
17-2	Confluent	To Production
17-2	Confluent	To Mobility
19-2	Confluent	To Production
19-2	Confluent	To Mobility

a. Electrophoretic mobility determination.

TABLE I-8. UNITS OF UROKINASE PRODUCED FROM PRIMARY AND SUBCULTURE -1 KIDNEY CELLS (THESE KIDNEY CELLS WERE SEPARATED IN FLIGHT COLUMN 3)

Number of Fraction	UK Assay Units/Disk	Viable Cells $\times 10^5$	UK Units 100 cells
Primary			
11	45	0.07	0.64
13	535	0.696	0.77
15	240	0.12	2.0
17	225	0.744	0.3
B Control[a]	61	0.068	0.9
D Control[a]	81	0.288	0.3
Subculture 1			
14-1	85	0.60	0.14
16-1	124	0.132	0.94
17-1	205	0.9	0.23
19-1	359	0.222	1.62

a. Samples taken as controls on the ASTP mission.

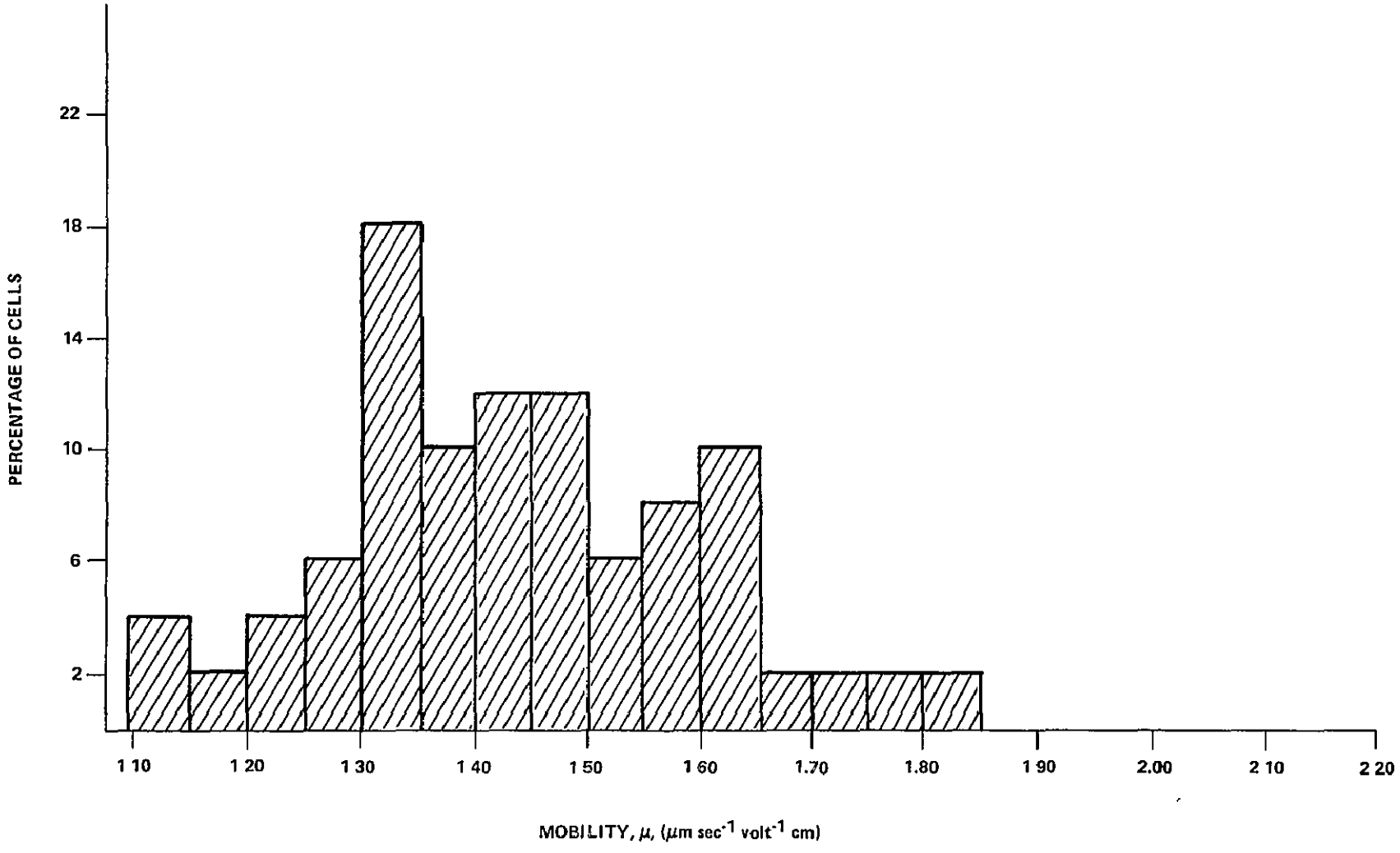

Figure I-20. Analytical electrophoretic mobility distribution on cell subculture 2 of fraction number 14.

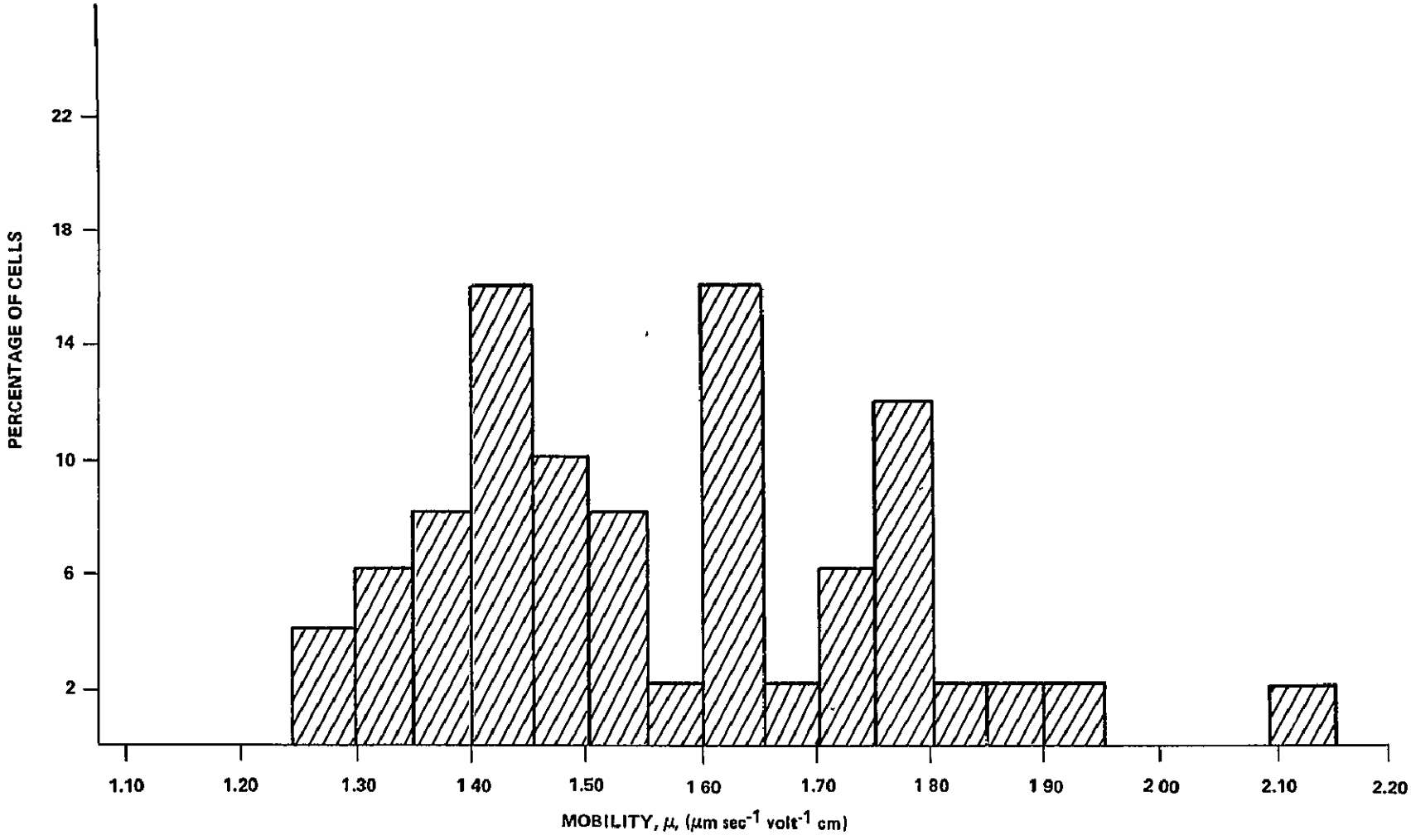

Figure 21. Analytical electrophoretic mobility distribution on cell subculture 2 of fraction number 17.

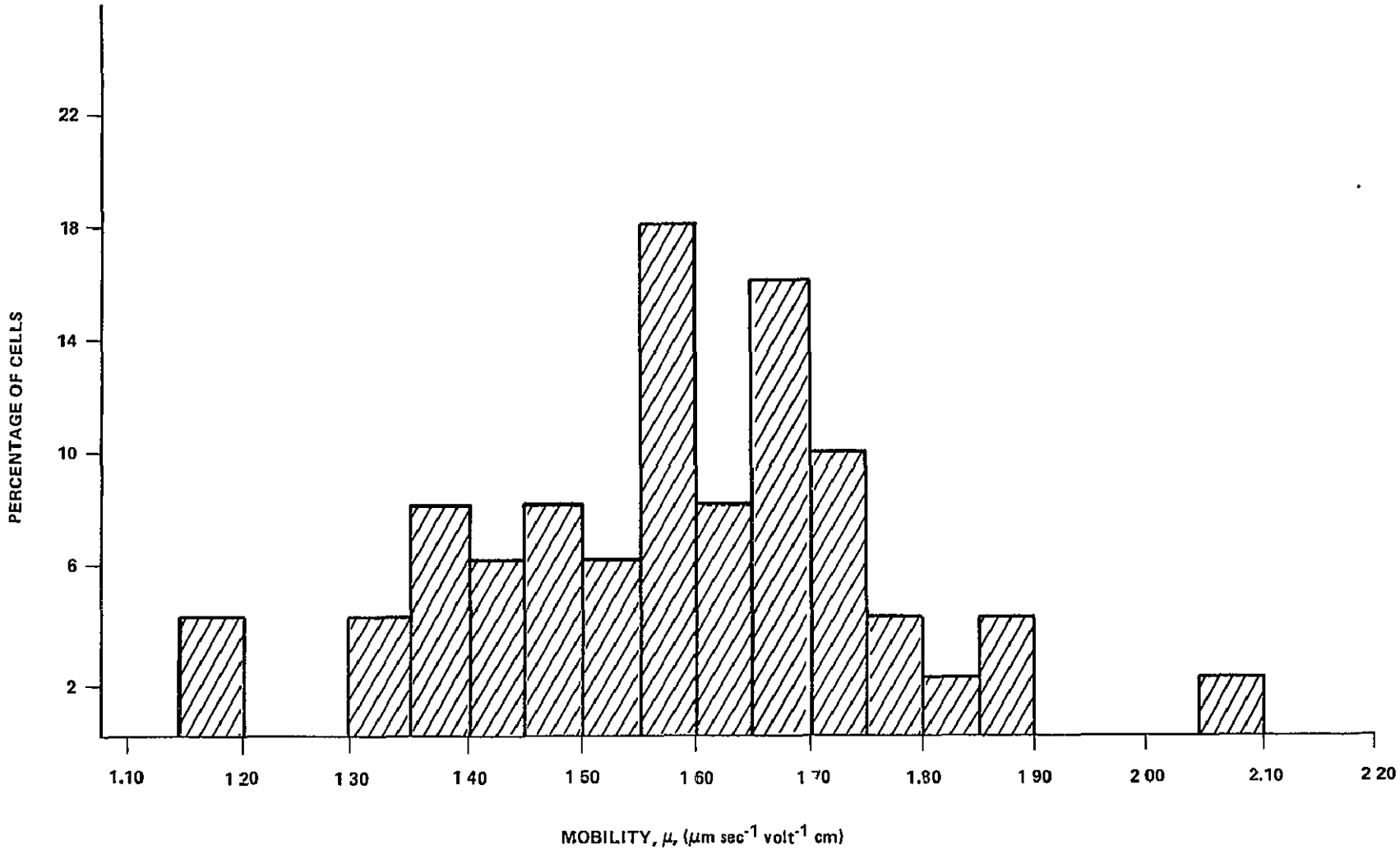

Figure I-22. Analytical electrophoretic mobility distribution on cell subculture 2 of fraction number 19.

TABLE I-9. LEVELS OF HUMAN GRANULOCYTE CONDITIONING FACTOR (HGCF) FOUND FROM VARIOUS FRACTIONS OF SUBCULTURE -1 (THIS SHOWS THE CONCENTRATION OF HGCF WAS FROM FRACTION 17 WHILE FRACTION 15 CONTAINED THE HIGHEST CONCENTRATION OF UROKINASE PRODUCING CELLS)

Number of Fraction	HGCF (Colonies Formed)[a]
14-1	40
16-1	65
17-1	123
19-1	0

a. Colonies formed corrected for control plate.

These results show that cells can be separated under sterile conditions and returned from orbit in such a manner that they retain their ability to grow in culture. The electrophoresis in space showed good separation of the kidney cells into subpopulations. The results indicated that there were at least 3 and maybe 4 subpopulations. These results are in agreement with the best data obtained using the endless belt electrophoresis. While subpopulations have been observed using the endless belt apparatus, sterile collection of these bands has proved to be impossible. Even though each fraction from the ASTP flight showed viable cells by the stain technique [I-18] and they all attached to the glass surface, only a few fractions (between 11 and 20) multiplied. The reason for this is not known. The only possible explanation is that the "non-growers" were more sensitive to unfavorable conditions and, therefore, could not recover to grow in culture.

During the final quarter of this program, analyses were made for erythropoietin activity. All assays were performed using Erythropoietin Standard Step 3 (CMRL), lot number 3005-1 from Connaught Labs. This standard had a potency of 2.2 units/mg. The harvest from the primary, subculture 1, and from subculture 2 was assayed for erythropoietin activity. The results reported in Table I-10 are the average of two sets of assays. The results are most encouraging as the peak activity for erythropoietin is found in fraction 14. As will be remembered, this is a different fraction than for either urokinase (fraction 15) or HGCF peak (fraction 17). These data indicate that a different subpopulation of cells is responsible for each activity assayed.

TABLE I-10. UNITS OF ERYTHROPOIETIN PRODUCED FROM PRIMARY, SUBCULTURE 1, AND SUBCULTURE 2 KIDNEY CELLS (THE KIDNEY CELLS WERE SEPARATED IN FLIGHT COLUMN 3)

Number of Fraction	Erythropoietin Activity (units/ml)
Controls[a]	
B	0.8
D	0
Primary	
13	Inhibitory
15	
17	
Subculture 1	
14-1	1.1
17-1	0.9
19-1	1.65
Subculture 2	
14-2	5.0
17-2	2.0
19-2	1.0

a. Samples taken as controls on the ASTP mission.

Conclusions

These data indicate an enrichment of urokinase producing cells in the area centering around fraction 15. These results can be interpreted to show an incomplete resolution between a producing cell population and a nonproducing population. Considering the fact that the experimental conditions, e.g., buffer run time, etc., were not optimized for kidney cells but generalized for three different separations, these results are not surprising. This lack of optimization is probably why the cells failed to produce further than subculture 2, when normally under optimized growth conditions the cells produce to subculture 7.

It also appears that the bands that produced HGCF and erythropoietin do not coincide with that band of cells that produces urokinase. This is a very interesting finding and indicates that these products are most likely not produced by the same cell.

The analytical mobility data of the subculture 2 show each fraction of this stage to have a rather broad distribution. This is rather disappointing in that one would anticipate a rather sharp mobility distribution. This is probably explained by the fact that the starting fraction is heterogeneous and the cell attachment and growth pattern are random events which can broaden at each reculture level. It also must be remembered that the mobility data were conducted on subculture 2 cells and not on the original cells separated during the ASTP flight. More analyses should help prove this point and are in progress.

Isotachophoresis

Isotachophoresis (ITP) is a relatively new technique of electrophoretic separation in which a discontinuous electrolyte system is used at the site of sample injection [I-5, I-19]. The boundaries between species of different mobility are sharply defined and stabilized by electrical forces. The boundaries are highly self-recuperative and will reform if stirred or disrupted by other factors, including convection. The concentration of each substance within a compartment is uniform and remains constant throughout the run once the separation has been achieved. Because of this uniformity, higher concentrations of components can be handled with no deterioration of the sharp boundaries. The buffer in front of the sample is called the "leading buffer" and the buffer that is behind the inserted sample is the "terminator buffer."

On the negative side, the sample compartments are contiguous to each other and never separate to form an intermediate zone of clean buffer. If separation is desired, a so-called "spacer ion" of suitable intermediate mobility has to be added. As will be seen later, this is of crucial importance for ITP. A further complication is that the heating of the column is not uniform, i.e., the progressively lower mobility compartments are exposed to proportionately higher potential gradients to ensure identical mobility. The temperature is a complicated function of both radial cooling and frontal migration of each compartment. Highest temperature is reached in the terminator buffer. This has caused considerable concern in the design of the ASTP experiment and caused us to limit both the field applied and the duration of each experiment to an absolute minimum that was deemed compatible with sample resolution.

Because of the sharpness of ITP boundaries, giving rise to equally steep concentration, i.e., density gradients, gravity effects are even more difficult to overcome than in zone electrophoresis. Thus, protein ITP was always conducted only in gels, and at the beginning of the planning of the ASTP experiment there was no ground-based apparatus of any kind in which cell ITP could be carried out. Thus, the ASTP experiment provided a unique opportunity to study cell ITP.

Approximately six months before actual flight time, a new apparatus for cell ITP was developed as a result of the extensive ground-based research. It utilized boundary stabilization through rotation of a horizontal tube, and the apparatus, named Rotofor, permitted the first ground-based work on cells isotachophoresis. Unfortunately, the lead time for preparation of the ASTP experiment was too short to permit as thorough an evaluation as one would have wished.

From the beginning of the planning for the ASTP experiment, the possibility of processing either fixed or fresh red cells was considered. The freezing of fixed cells presents no problems, but the freezing of fresh cells is more difficult. While low temperature storage of erythrocytes is well documented, the particular requirements of ITP called for a freezing mixture with low overall electrolytes and substitution with a buffer suitable for ITP. This latter requirement posed the greatest problem. Many of the usual leader/terminator buffers, while compatible with the freezing of the red cells, caused cell aggregation during an actual ITP run. Using the Rotofor instrument, nonaggregating buffers were eventually found. In addition, the proposal to use liquid nitrogen as the freezing agent, together with the prescribed method of thawing (direct contact of the frozen cells with buffer at ambient temperature), imposed further limitations on the method of freezing red cells. The toxicity of dimethyl sulfoxide, widely used in red cell preservation, precluded its use in the manned flight experiment. Clycerol, therefore, seemed the most suitable cryoprotectant, especially in view of its electrophoretic inertness.

The primary buffer variables investigated were concentrations of glycerol and concentrations of dextrose which were found to be necessary to preserve isotonicity in the freezing mixture. In addition, the influence on red cell recovery of variable cooling rates was studied. While the full report on sample handling covers several pages, it will suffice to report here that good recovery (60 percent) of fresh red cells could be obtained using a freezing mixture containing 4.2 percent dextrose and 2.8 to 3.5 M glycerol. Since these results were based on a freezing temperature of 194 K (-79°C), the study was extended by using liquid nitrogen for freezing. It was found that over a wide range of red

cell concentrations in the freezing mixture, 5 percent to 50 percent hematocrit, no modification in the composition of the cryoprotectant was necessary.

A ground-based problem encountered in ITP of red cells was their aggregation. This aggregation was initially absent but would become apparent several minutes after application of the current and increased progressively during a run. A number of leader/terminator buffer combinations were tried, including 2-amino-2 (hydroxymethyl-1, 3-propanediol) hydrochloride, acetate or cacodylate as leader, and threonine, and alanine and asparagine as terminator. All of these caused aggregation. The combination which avoided aggregation was the use of phosphate as leader and serine as terminator.

Using nonfrozen red blood cells in phosphate-serine buffer systems, ITP separation of cells from hemoglobin (or various added dyes) was easily achieved. Characteristically, sharp boundaries were always obtained proving that these cells do behave analogously to proteins or other ionic constituents in ITP. Fractionation of mixtures of sheep and rabbit, or human and rabbit cells, i.e., separation into two clearly defined zones was, however, not achieved. Again, the customary assortment of spacers was used, including ampholines and amino acids. The addition of ampholines caused spreading of boundaries, proving that at least some ampholine fractions possessed mobilities comparable to the two cell populations. Lack of visible separation can be interpreted in terms of an interaction between the red cells and ampholine, resulting in randomization of cell mobilities. The situation was radically different with frozen mixtures of fresh cells. These readily separated on ITP even without the addition of any spacers. As freezing always results in partial hemolysis of the cell population, this was interpreted as showing that hemolysis liberated a spacer of suitable mobility to act as a spacer. No attempts were made to characterize this spacer. Attempts to use the supernatant from frozen fresh cells to separate fixed cells were not productive. It was, therefore, proposed on the ASTP experiment to fly one sample of fixed cells and one sample of frozen fresh cells.

ITP column 4 was processed using rabbit and human formalin-fixed red blood cells. The concentration of these cells, when loaded, was the same as that for columns 1 and 5. The volume of live red blood cells loaded into the sample slide (number 8) was provided in the following manner. Human and rabbit cells were prepared at a 40-percent hematocrit each. Equal volumes of each concentration were loaded into the sample slide. The final concentration was 450×10^6 cells/0.098 ml. The ITP sample slides had a slightly larger volume (0.098 ml) than that of the electrophoresis slides (0.06 ml).

On the day of the space experiment, two sample slides containing duplicate samples of the fresh frozen flight cells were removed from liquid nitrogen, thawed, examined for free hemoglobin and submitted to ITP in the Rotofor, using aliquot portions of the flight buffer. Free hemoglobin was found to correspond to a hemolysis of 52 percent of cells, considerably higher than the usual hemolysis of less than 20 percent, routinely observed in prior experiments. The decreased recovery of cells did not affect the ASTP experiment, as sufficient cells survived to form good bands, and, indeed, the cell mass was clearly visible in both ground-based and ASTP runs. One may have expected the formation of a third ITP band containing free hemoglobin. Unfortunately, the ITP run in the Rotofor, under conditions of amperage and duration mimicking the conditions of the flight, did not result in the expected separation of the two cell populations and/or hemoglobin. The migration distance was also lower than expected, the sample migrating only 30 mm in the 45 minutes. The boundaries were diffuse and did not present the usual sharp fronts of other ITP cell runs. At the time of this experiment, there was no explanation as to the lack of sample resolution. The lack of characteristically sharp boundaries is frequently observed during early stages of ITP before the sample is fully resolved and a steady state is reached. Lack of boundary sharpness is particularly pronounced in presence of large amounts of ampholines, which provide a continuous mobility spectrum spacer. Migration velocity is also usually reduced during the resolving period of a mixture containing large amounts of ampholines and visible samples frequently appear to remain stationary, while in fact, higher mobility ampholine fractions are advancing into their proper position along the column.

Thus, this ground-based control experiment had all the appearances of ITP of a sample in presence of a great excess of ampholines. At this time, only limited importance was assigned to this ground-base control experiment. The limited amount of available control-frozen cells prevented the exploration of this cell behavior. In view of the similarly reduced migration velocity of the cells in the ASTP experiment, this control experiment proved to be highly significant. Its implication will be discussed, correlating it with the increased hemolysis of the sample.

EVALUATION OF THE PHOTOGRAPHIC RECORD OF THE FLIGHT EXPERIMENT

ITP of the formalin-fixed red blood cells was run in column 4. Photographs taken at various times are shown in Figures I-23 through I-26. The photographic record is not as good as hoped because the film was underexposed and the visibility is particularly poor at the two ends of the column. The photographs were taken at intervals of 3 min. The first frame showed the

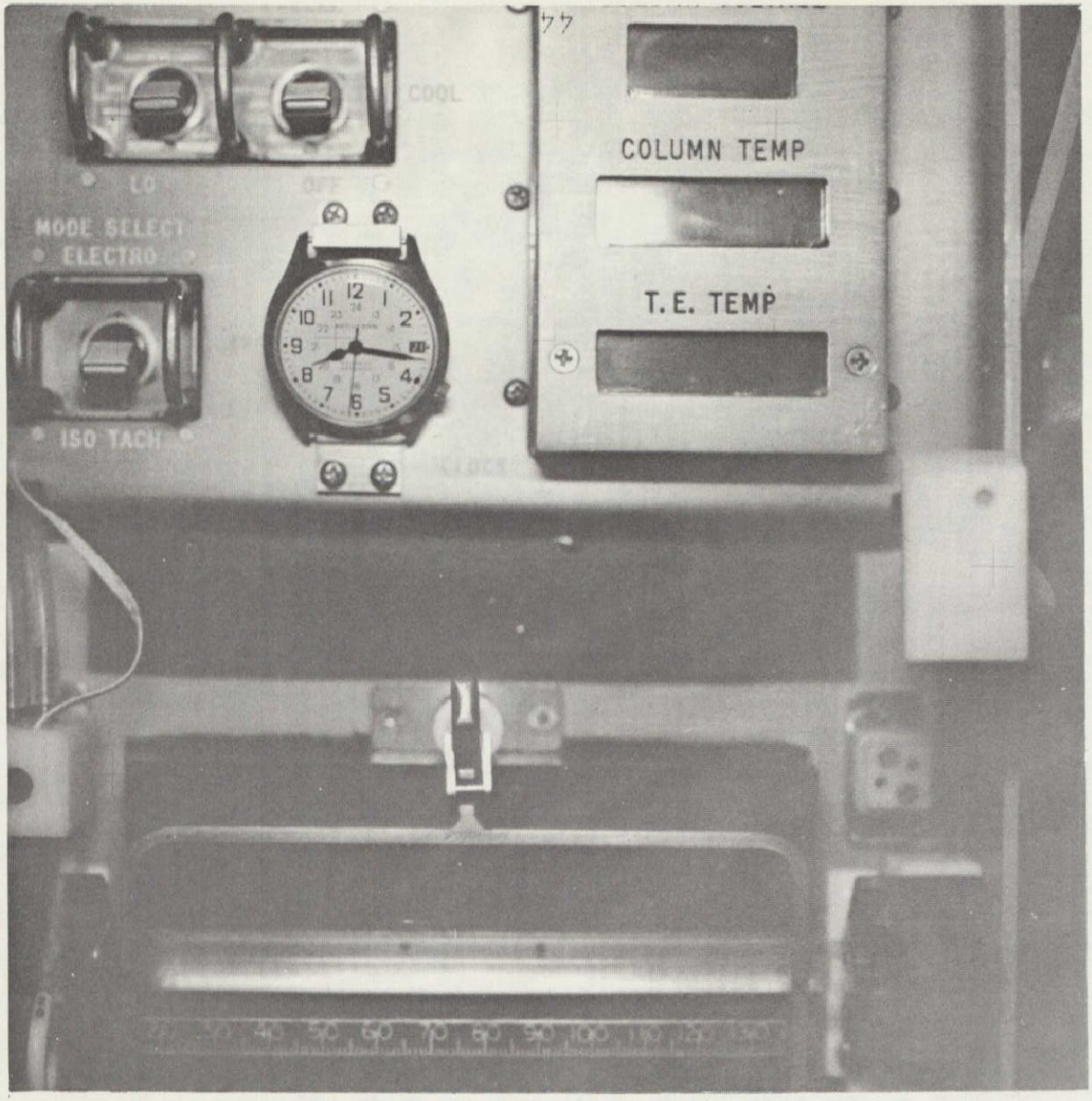

Figure I-23. Flight photograph of column 4 after 31 min of ITP (sample is formalin-fixed rabbit and human red blood cells).

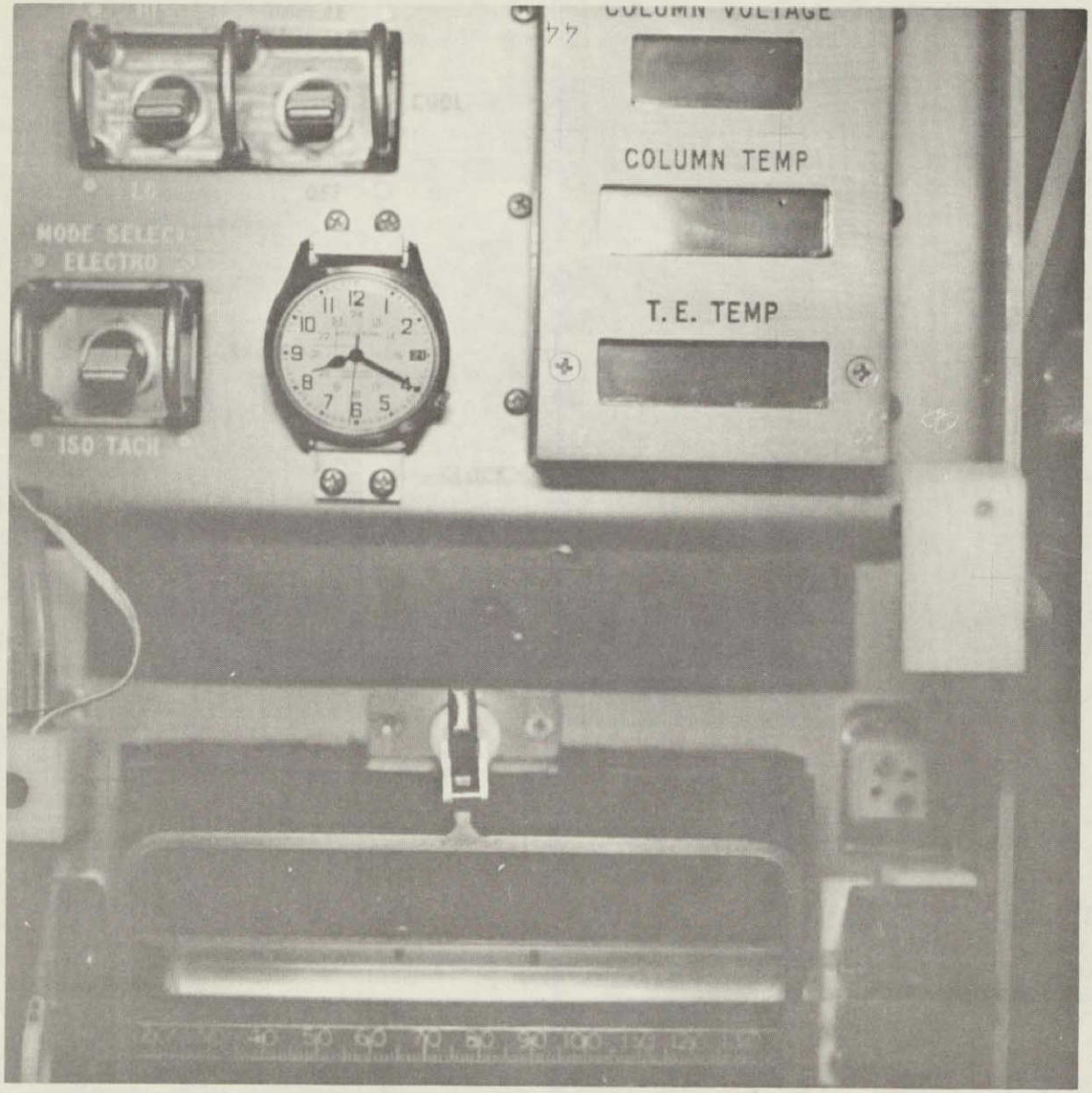

Figure I-24. Flight photograph of column 4 after 34 min of ITP.

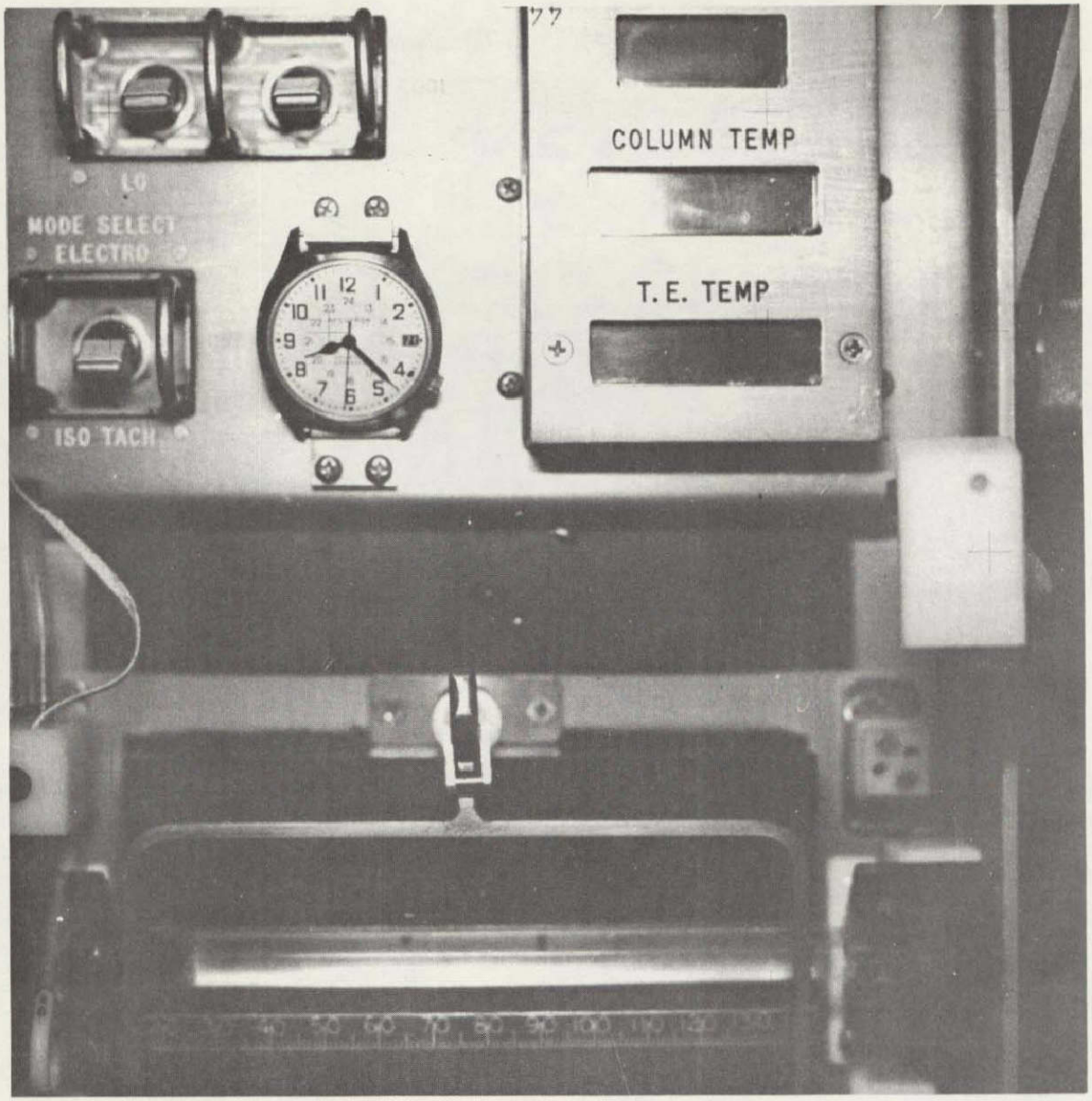

Figure I-25. Flight photograph of column 4 after 37 min of ITP.

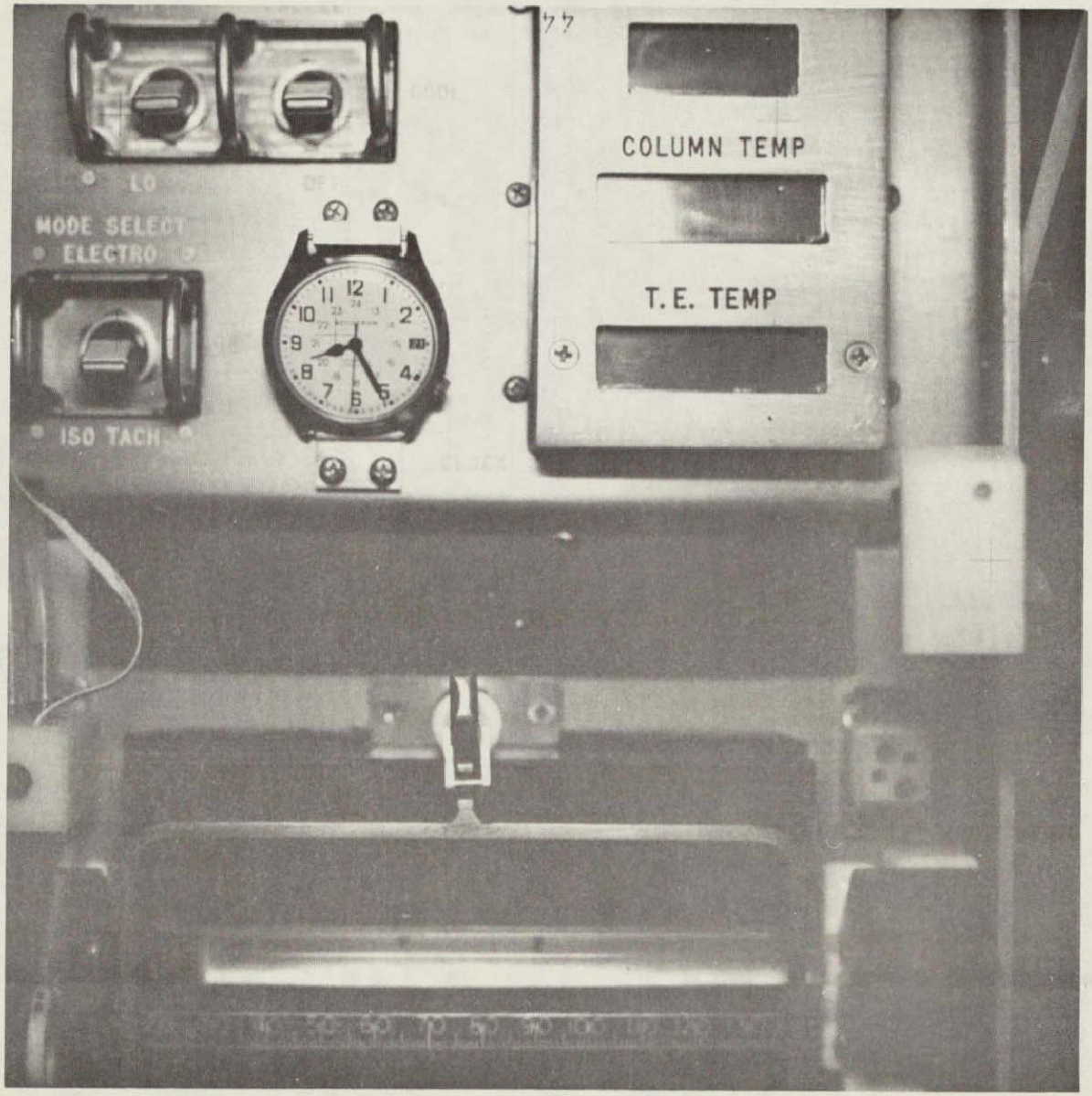

Figure I-26. Flight photograph of column 4 after 40 min of ITP.

current off; the following frames, covering a time span of 40 min, showed the current on and the last 3 frames are with the current off again. Thus, it is not certain if the current was on for 40 or 46 min or for some interim time period, as no record was made at precisely when the switches were turned on and off. The migration velocity appears to be 10 mm in 9 min or very close to the predicted velocity of 1 mm/min. A different velocity is obtained, however, if the whole time span of migration is taken into account. The last photograph was taken at a minimum of 40 min (Fig. 26) and maximum of 43 min of migration; thus, the overall migration rate was 0.725 or 0.675 mm/min, depending on the exact time of current application. This represents a substantially lower migration rate than expected.

The first visible boundary (Fig. I-23) appears slightly fuzzy, but the last boundary, four frames later, is sharp and flat, as expected to be found in ITP. The initial voltage was 113 V, final voltage 133 V, this increase being characteristic of ITP. The predicted initial voltage on the basis of the ground-based experiment would have been 106 V; thus, in this regard, there is excellent agreement.

The ITP of fresh-frozen cells occurred in column 8 (Figs. I-27 through I-30). The quality of the photographs is somewhat better than in the first ITP run, and the column is visible past the 15 mm mark. In the case of column 8, the experiment was repeated twice by the astronauts; the first portion of the run showed no current was applied, and consequently, no migration occurred. For reasons unknown, the run was repeated and the remaining time span of 39 min showed the current to be on. This second run was initiated, however, at least 70 min after insertion of the sample specimen into the column. Thus, there is considerable uncertainty as to the position of the sample at the beginning of the run. Figures I-27 through I-30 show the presence of two minor air bubbles in the column, at approximately 20 mm and 36 mm marks. In Figure I-27, a typically sharp front boundary of the red cell mass is visible at the 20 mm position. The boundary is not flat, however, but appears to be tilted toward the air bubble. In Figure I-30, the boundary appears straighter, though slightly rounded, and is at the 25 mm position. Thus, the migration rate appears to be 0.55 mm/min, considerably less than the anticipated rate of 1 mm/min. Overall migration rate from the beginning of the run is 0.64 or 0.60 mm/min. The initial voltage was 121 V (it dropped to 109 V) and increased then to a maximum of 138 V. This transient drop in voltage is unexpected, but the overall voltage is within the expected range.

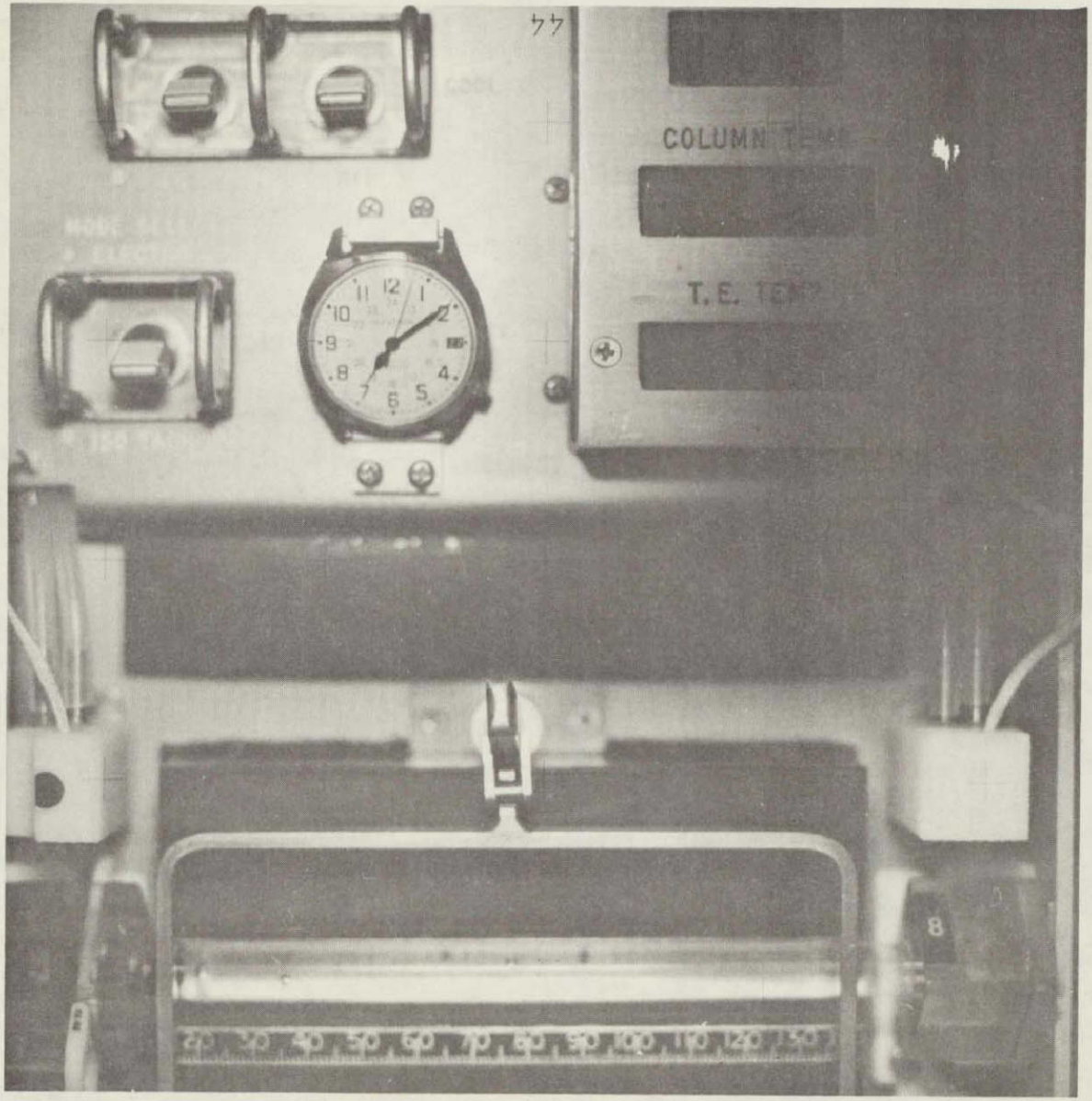

Figure I-27. Flight photograph of column 8 after 30 min of ITP (sample is fresh frozen rabbit and human red blood cells).

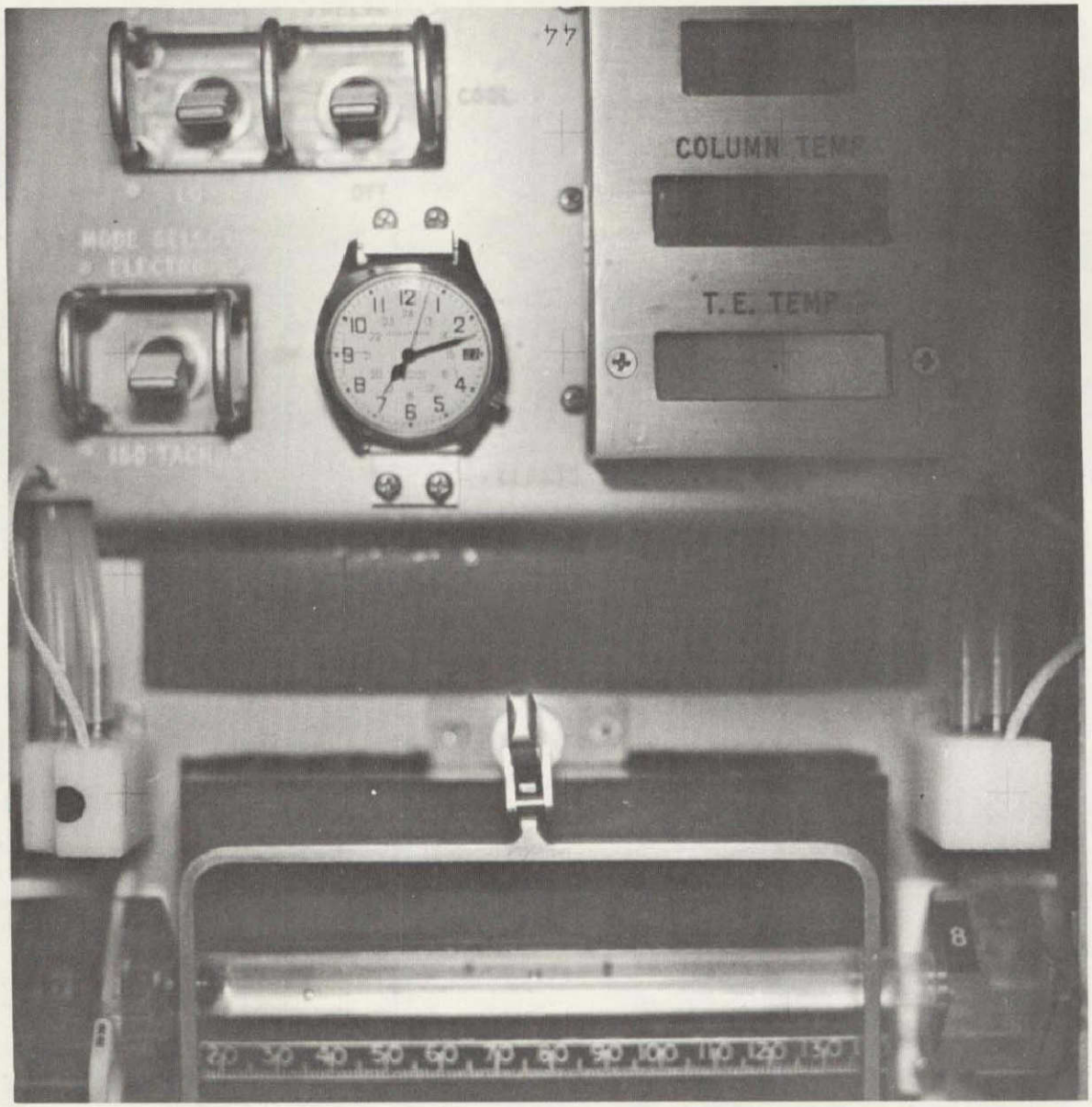

Figure I-28. Flight photograph of column 8 after 33 min of ITP.

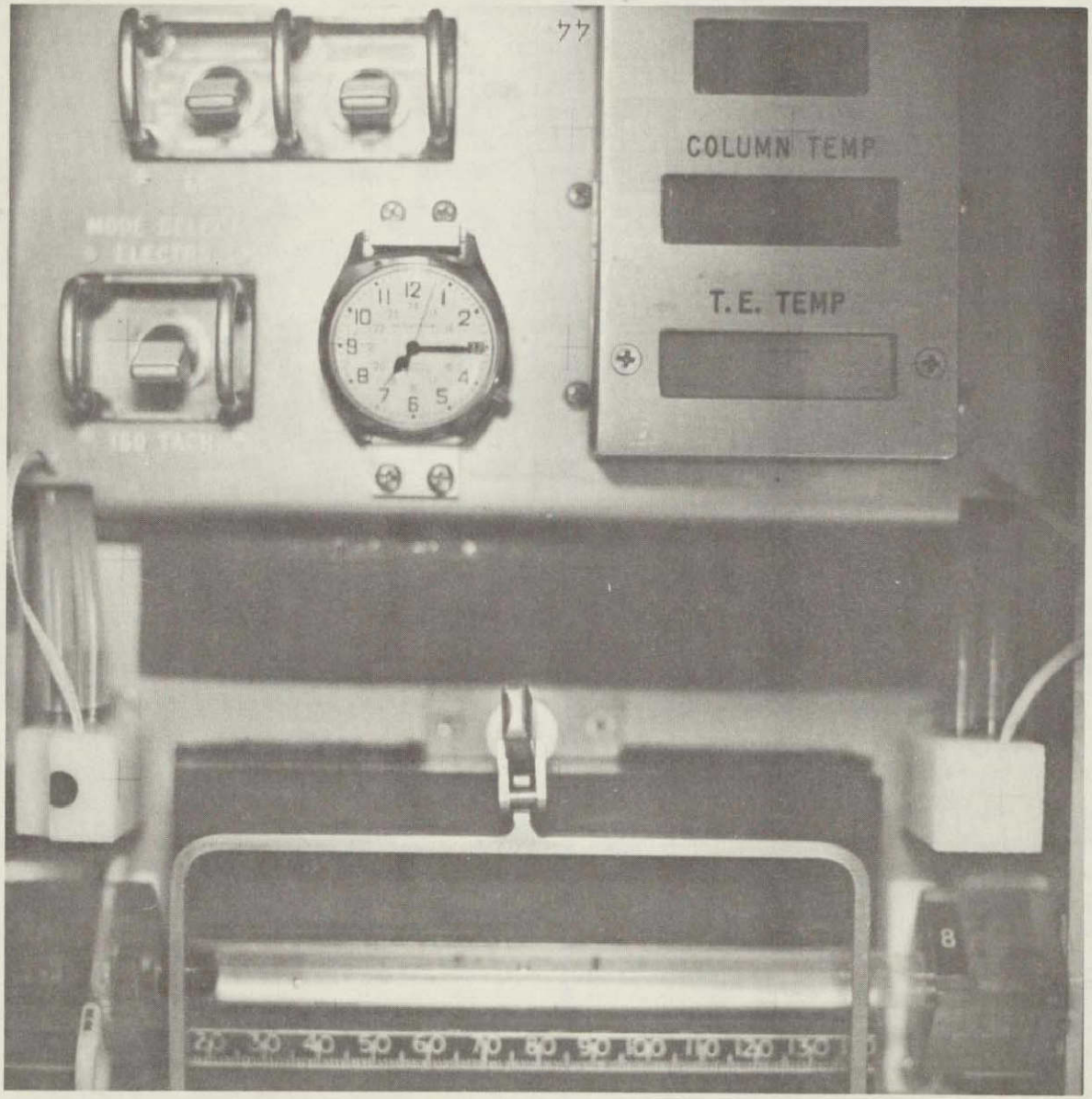

Figure I-29. Flight photograph of column 8 after 36 min of ITP.

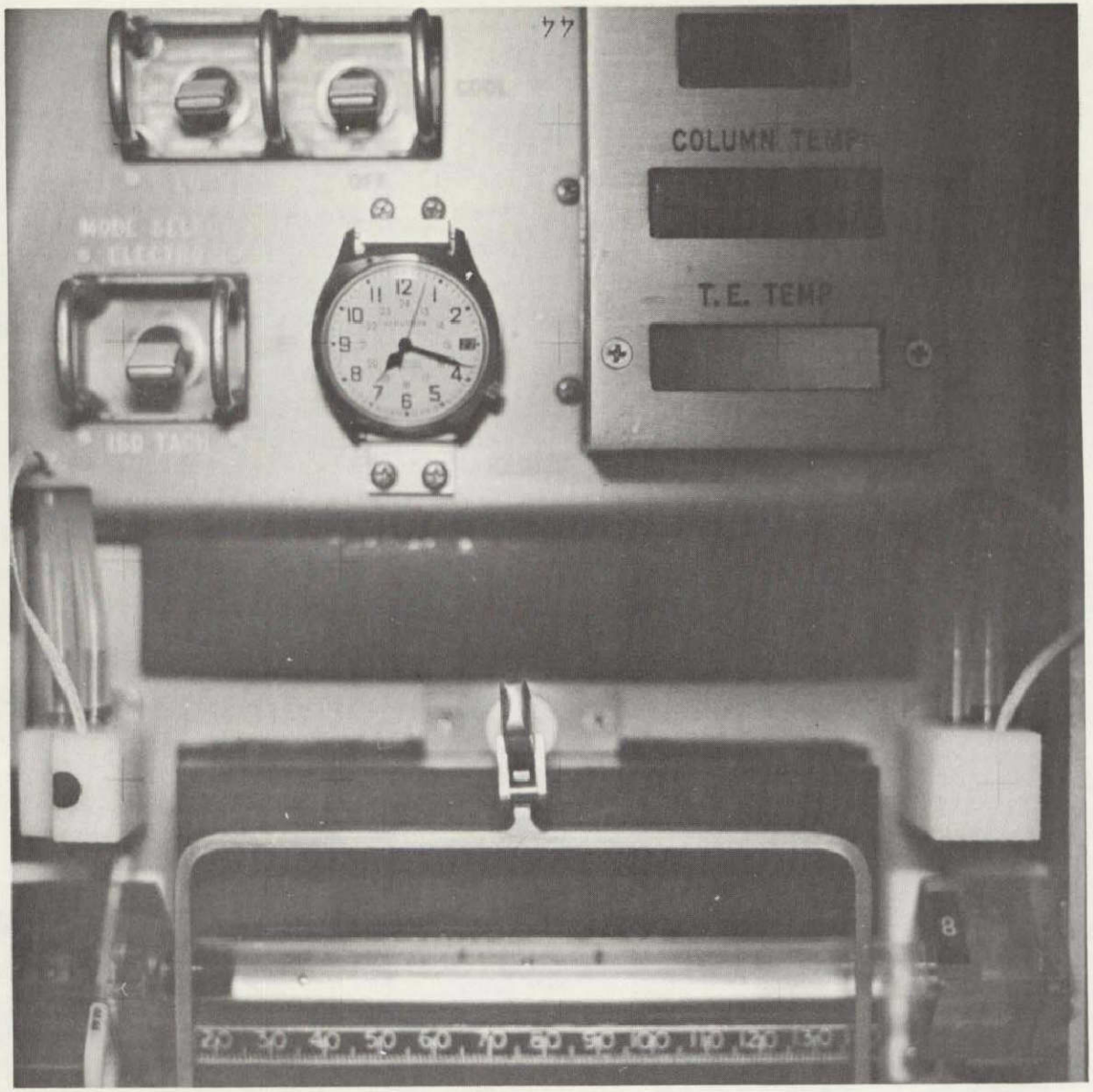

Figure I-30. Flight photograph of column 8 after 39 min of ITP.

CONCLUSIONS

It is clear that both of the ITP runs were essentially successful. Unfortunately, full expectations were not realized; there is only evidence of the frontal boundaries but no rear boundaries are visible, and therefore, no separation claims can be concluded. In retrospect, the plans were far too cautious in limiting the duration of the run to 45 min. This time was insufficient to bring the ITP bands into full view. The caution was predicted by the calculated and experimentally observed temperature rise in ground-based experiments. A better photographic record may have provided some indications of possible emergence of the rear boundary, or the expected intercompartmental boundaries in the fresh cell sample.

An overall migration rate of 1 mm/min was predicted for both samples. The last 4 frames of the fixed cells confirm this migration rate, but the overall migration rate appears to be substantially lower than expected (presumably only 0.675 mm/min). With the fresh cells, the migration rate was still lower, being in the range of 0.55 to 0.64 mm/min, depending on mode of calculation.

Interpretation of these mobility differences is difficult because there are several possible contributing factors: (1) there is an inherent uncertainty concerning overall duration of each run because the exact time of power application was not recorded, (2) for column 8, there appear to be unexplained periods of power fluctuation, and (3) the position of the sample at the beginning of the fresh cell run is uncertain, as previously mentioned, due to the insertion of the sample at least 70 min before the onset of migration. Thus, it is not certain whether during either of the ITP experiments the photographs taken at 3 min intervals represent a true record of run times. It is conceivable that power may have been flickering, but this was not seen during ground-based runs. While measurements of advancing fronts in the fixed cell show constant increments, this is not the case with the fresh cell run.

One has to assume, therefore, that none of the above factors contributed to the observed reduction in migration velocity. That is, the same reduction in migration of the fresh cells in the ground-base control experiment was obtained when carried out in the Rotofor using a duplicate of the flight sample. It will be remembered that this sample had an unusually high hemolysis. The reason for this high hemolysis is inexplicable. During the month prior to submission of flight samples, the cell preparation and freezing procedures were conducted numerous times, with innumerable individual samples, and uniform results were obtained. The separation of the two cell populations in frozen fresh cell ITP is predicated, however, on the liberation of an unidentified spacer. It is

entirely possible that the freezing procedure liberates not only a colorless spacer with intermediate mobility between the two populations, but also a spacer with a mobility higher than that of the human cells. Thus, a leading band of colorless spacer may be present. Increased hemolysis may account for greater quantity of either spacer, and thus result in slower initial migration rate, while the components of the mixture are resolved. As was previously mentioned, this occurs whenever an excess of ampholines is used. Thus, the reduced rate of fresh cell migration may have been caused by excessive hemolysis, the sample not having reached a steady state in the time allotted.

A similar explanation may account for the discrepancy in the migration rate of fixed cells. That is, there may have been colorless fast ions in the sample, thus retarding initially the migration rate of these cells. The sample, however, achieved a steady state of migration by the time the photographic record was obtained, as is judged by the cells migration velocity.

In summary, the two ITP experiments did not run for sufficient time to permit visualization of rear or intercompartmental boundaries. Nevertheless, the experiment shows the advantage of ITP in the sharpness of the frontal boundary, and concentration of the migrating zones. Thus, the main potential advantage of ITP is the quality of sample it may fractionate. With cells, however, one must specify that the future of ITP depends on finding proper spacers.

DISCUSSION AND CONCLUSIONS

This experiment represents a milestone in the history of separation processes for space. The significance, however, not only is centered on the specific return of the viable urokinase producing kidney cells, but also for the first time all general aspects necessary to transport samples to orbit, conduct a separation, and return a viable product to Earth were addressed.

The red blood cell separations served as the first controls ever successfully run on the same space mission with unknown samples. The red cells were easily visible from the flight photographs and proved the operation of the flight unit in orbit. In addition, control samples of kidney cells and lymphocytes were carried on this experiment. Subsequent analyses proved that no unusual phenomena of space flight affected their viability, morphology, or ability to produce their specific product — a most significant observation as production facilities are being considered for future missions.

The only disturbing factor of this flight experiment was the failure of some of the columns. The blockage in the electrode housing fluid system caused the most damaging results, i.e., pH perturbations which reduced cell viability. Because of this, we did not separate the lymphocytes carried to orbit. It must be emphasized that this problem was not related to the lymphocytes. No doubt these cells will be flown again on another mission.

The kidney cell separation was most encouraging, not only because viable cells were carried to orbit, processed, returned and cultured, but also because the cells which were separated appear to be product specific. That is, from some bands, urokinase appears to be the prime product the cells produce, while in entirely different bands, human granulocyte conditioning hormone and erythroprotein are the prime products of the cells. This finding is especially important in the case of urokinase as one considers the need for this drug. In addition, this information will no doubt encourage other investigators to consider zero-g experimentation where separation and subsequent cell culturing can be used to isolate a particular cell and then increase the number of cells brought back from space through culturing.

The ITP experiment was essentially successful. The sharpness of the boundaries and the concentration of the migrating zones demonstrated the potential advantage of the ITP technique in space. With further work on the definition of suitable spacers that can be used with cells, no doubt this procedure will allow for separations that cannot be accomplished on the ground.

No conclusions written concerning the MA-011 experiment can be considered to be complete without a discussion of the hardware that made this experiment possible. The EU allowed for not only two different types of separations to be conducted but also for a multiple run condition. That is, not only were eight different columns processed in the EU, but the requirements for cooling, freezing, current, fluid connections and run time were varied in orbit. Even with two different crewmen operating the experiment over a two-day period near the end of a complicated and tiring mission program, no contamination was introduced to the columns or to the fluid system. In addition, the CF used to transport the samples to orbit and to bring back the frozen glass columns performed as designed. While it is planned for future flights to carry viable samples to orbit in a fluid state, nevertheless, the method of freezing the cells used on the MA-011 proved to be a satisfactory means of transporting, handling, and inserting the samples.

The future of separation experiments in space is a most encouraging one. The 1976 timeframe will usher in the Rocket Program where separation experiments and hardware concepts can be flown. In 1979, the Space Shuttle will begin

its flights. The operational Shuttle flights to follow are projected to be flown on a regular basis — an opportunity not afforded scientists since the Apollo Program. In 1983 and beyond, plans are being made to develop orbital Space Stations. These Stations will remain in orbit which will allow for more orbital time for continuing advancements. The discoveries which will result promise to stimulate innovative ideas from all who are involved in this venture.

ACKNOWLEDGMENTS

We thank the many people involved in the planning, design, and fabrication of this experiment, especially Dr. W. J. Patterson, Ms. F. E. Scott, Mr. B. H. Nerren, Mr. R. J. Harwell, and Dr. R. S. Snyder at the Marshall Space Flight Center. We appreciate the meticulous performance of this experiment in space by Astronauts D. K. Slayton and T. P. Stafford.

REFERENCES

I-1. Shaw, D. J.: Electrophoresis. Academic Press, New York 1969.

I-2. McKannan, E. C.; Krupnick, A. C.; Griffin, R. N.; and McCreight, L. R.: Electrophoresis Separation in Space — Apollo 14. NASA Technical Memorandum TMX-64611, 1971.

I-3. Wiersema, P. H.; Loeb, A. L.; and Overbeek, J. T. G.: Calculation of the Electrophoretic Mobility of a Spherical Colloid Particle. J. Colloid and Interface Science, vol. 22, 1966, pp. 78-99.

I-4. Snyder, R. S.; Bier, M.; Griffin, R. N., Johnson, A. J., Leidheiser, H.; Micale, F. J.; Ross, S.; and van Oss, C. J.: Free Fluid Particle Electrophoresis on Apollo 16. Separation and Purification Methods, vol. 2, 1973, pp. 259-282.

I-5. Bier, M.; Hinckley, J. O. N.; and Smolka, A. J. K.: Potential Use of Isotachophoresis in Space. Protides of the Biological Fluids, 22nd Colloquim, H. Peeters (ed.), Pergamon Press, New York, 1975, pp. 673-678.

I-6. Allen, R. E.; Barlow, G. H.; Bier, M.; Bigazzi, P. E.; Knox, R. J.; Micale, F. J.; Seaman, G. V. F.; Vanderhoff, J. W.; van Oss, C. J.; Patterson, W. J.; Scott, F. E.; Rhodes, P. H.; Nerren, B. H.; and Harwell, R. J.: Electrophoresis Technology Experiment MA-011. NASA Technical Memorandum TMX-58173, 1976, pp. 20-1 — 20-23.

I-7. Seaman, G. V. F.: Electrokinetic Behavior of Red Cells. Red Blood Cell, vol. 2, D. N. Surgenor (ed.), Academic Press, New York, 1975.

I-8. Wioland, M.; Sabolovic, D.; and Burg, C.: Nature New Biology, vol. 237, 1972, pp. 274-275.

I-9. Zeiller, K.; Pascher, G.; and Hannig, K.: Hoppe-Seyler's Z. Physiol. Chem., vol. 351, 1970, pp. 435-447; vol. 352, 1971, pp. 1168-1170.

I-10. Zeiller, K. and Hannig, K.: Hoppe-Seyler's Z. Physiol. Chem., vol. 352, 1971, pp. 1162-1167.

I-11. Donald, D.; Hutchinson, F.; Macleod, T. J.; and Raffle, E. J.: Electrophoretic Mobility of Human Lymphocytes — an Investigation of the Techniques of Cytopherometry. J. Immunological Methods, vol. 6, 1974, pp. 151-516.

REFERENCES (Concluded)

I-12. White, W. F.; Barlow, G. H.; and Mogen, M. M.: The Isolation and Characterization of Plasminogen Activators (Urokinase) from Human Urine. Biochemistry, vol. 5, 1966, pp. 2160-2169.

I-13. Bernik, M. B. and Kwaan, H. C.: Plasminogen Activator Activity in Cultures from Human Tissues. An Immunological and Histochemical Study. J. Clinical Investigation, vol. 48, 1969, pp. 1749-1753.

I-14. Patterson, W. J.: Development of Polymeric Coatings for Control of Electro-Osmotic Flow in ASTP MA-011 Electrophoresis Technology Experiment. NASA Technical Memorandum TMX-73311, 1976.

I-15. Nerren, B. H.; Goodlett, H. L.; and Bond, J. B.: Development of a Slicing Device for Apollo-Soyuz Test Project, Electrophoresis Technology Experiment, MA-011. NASA Technical Memorandum, 1976 (in press).

I-16. Gillman, C. F.; Bigazzi, P. E.; Bronson, P. M.; and van Oss, C. J.: Preparative Electrophoresis of Human Lymphocytes. I. Purification of Non-immunoglobulin Bearing Lymphocytes by Electrophoretic Levitation. Prep. Biochem., vol. 4, 1974, pp. 457-472.

I-17. Brakman, K.: Fibrinalysis: A Standardized Fibrin Plate Method and a Fibrinolytic Assay of Plasminogen. Scheltema and Holkema, 1967.

I-18. Phillips, H. J.: Tissue Culture, Methods and Applications, Kruse and Patterson (eds.), Academic Press, 1973, p. 406.

I-19. Haglund, H.: Isotachophoresis — A Principle for Analytical and Preparative Separation of Substances such as Proteins Peptides, Nucleotides, Weak Acids, Metals. Science Tools, vol. 17, 1970, pp. 1-28.

SECTION II

ELECTROPHORESIS EXPERIMENT

EXPERIMENT MA-014

By K. H. Hannig,[1,2] H. Wirth,[1] and E. Schoen[3,4]

1. Max-Planck-Institut für Biochemie Munich
2. Principal Investigator
3. Messerschmitt-Bölkow-Blohm GmbH Munich
4. Project Manager of Experiment Hardware

TABLE OF CONTENTS

TABLE OF CONTENTS (Concluded)

LIST OF ILLUSTRATIONS

LIST OF TABLES

ABSTRACT

A continuous free-flow electrophoresis study was conducted during the Apollo-Soyuz Test Project mission to investigate and evaluate the increase in sample flow rate and sample resolution achievable in space. This electrophoresis technique is one of the most valuable methods to separate and analyze biological particles, such as living cells, without decreasing their biological activity. Gravity-induced thermal convection and sedimentation limit the effectiveness of separation by this method. The electrophoresis equipment was designed for the separation of four mixtures of biological cells with variable sample flow rates, buffer flow rates, and electric field gradients. Separation quality was assessed by measuring the light from a quartz lamp through the electrophoresis channel and onto a photodiode system.

The data evaluation indicates that all monitored systems operated correctly during the experiment. The optical system produced a light that was too bright to discern true cell distributions, but final analysis of scientific data by computer processing shows the expected distribution of separated cells.

INTRODUCTION

The scientific requirements of the electrophoresis experiment (EPE) on the Apollo-Soyuz Test Project (ASTP) flight resulted from a study concerning the application of electrophoresis in future biological experiments on Spacelab. That study examined the possibility of separating vital cells or other biological materials in the space environment.

To understand the specific function of cells and their membrane systems, research is needed concerning the problem of separation and characterization of particles performing individual functions. Of particular importance in studying cooperative interactions in biological processes is the isolation of the interacting systems in the most homogeneous and still functioning form. These problems are not only of a fundamental theoretical interest but are also of practical importance to elucidate normal and pathological processes in biology.

The reason for using electrophoresis to investigate these problems concerns the properties of the cell membrane surface, which is the site of many important biological phenomena. Transformation and differentiation processes are often accompanied by changes of the cell surface charge density. Charge density, however, determines the electrophoretic behavior, i.e., the electrophoretic mobility. Therefore, electrophoresis is a highly efficient

method of separating cells or other biological particles according to functional criteria. Furthermore, cell electrophoresis is one of the few physicochemical processes that can be applied to living cells without producing damage or loss of viability.

Because electrophoresis is established as one of the most effective separation methods used in biological study, it is considered an essential tool for investigation in space. The expectation was that the separation capability would be increased at zero-g, resulting in new applications that depend on improved resolution.

The EPE concept was based on a new electrophoretic principle known as "carrier-free continuous-deflection electrophoresis" (free-flow electrophoresis). The technique was developed by K. Hannig at the Max Planck Institut and is patented in Germany and the United States. By this method (Fig. II-1), the sample to be separated is introduced continuously into a separation chamber in

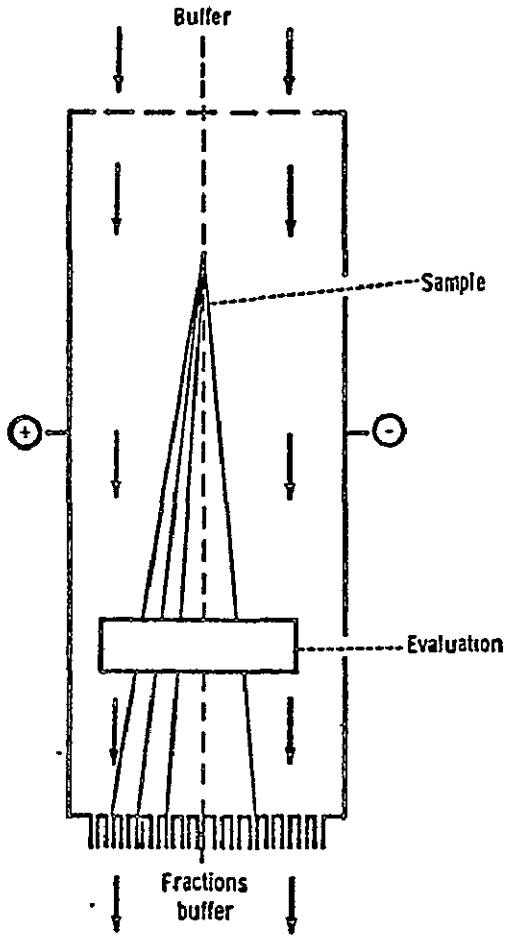

Figure II-1. Illustration of the principle of free-flow electrophoresis.

which a buffer solution flows laminarly. An electric field is generated perpendicular to the direction of flow. Particles having different surface charge densities are deflected from the flow direction of the buffer by an angle determined by the flow rate and the electrophoretic mobility of the particles. After leaving the lower end of the separation chamber, the separated zones can be collected continuously or analyzed by evaluating the deflection and the density distribution of the fractions.

EFFICIENCY OF FREE-FLOW ELECTROPHORESIS

The decision advantages of free-flow electrophoresis result from the principle of continuous operation in a flowing medium. In contrast to most of the usually applied foil or gel electrophoresis methods, this method does not accomplish stability by an open-pore carrier medium, but rather permits the medium to flow freely in a narrow gap. To obtain the necessary stability, the capillary forces at the gap walls are used. Under one-g conditions, this method succeeds when the gap width is less than 1.0 mm. This width is also sufficient for an undisturbed electrophoretic migration of larger particles in the electrical field. Unlike the discontinuous electrophoresis method that is stabilized by porous media, the range of application of electrophoresis for preparative purposes can be expanded to include bulk colloidal mixtures such as suspensions of viruses, bacteria, and cells and their membrane systems. A further advantage of electrophoresis in flowing medium with continuous operation is that the samples to be examined can be quickly exchanged without interrupting the experimental process.

The capability of quickly switching to the optimal experimental conditions combined with a completely automated operation makes this electrophoretic principle applicable to routine analytical separation problems. Thus, it would be possible to separate as many as 100 samples/h to obtain analytical data concerning the composition of the samples to be examined.

As in every physical process, the effectiveness of free-flow electrophoresis is limited by some methodologically determined disturbances. In the use of electrophoresis under zero-g conditions, it is necessary to distinguish between effects caused by gravitation (i.e., sedimentation and thermal convection) and effects independent of gravitation. Under zero-g conditions, sedimentation and convection can be eliminated, thus, a higher throughput with larger separation chamber gap dimensions can be obtained.

The resolution of electrophoretic separation is, however, hindered by a methodologically caused band broadening, which also exists under zero-g conditions. The band-broadening effects result primarily from (1) the Poisseuille velocity profile of the liquid curtain, (2) the electro-osmotic velocity profile, and (3) the temperature gradient through a liquid curtain thickness; the temperature gradient increases with liquid curtain thickness and electric power (Fig. II-2). The thermal diffusion caused by the extremely short separation times in free-flow electrophoresis can be ruled out.

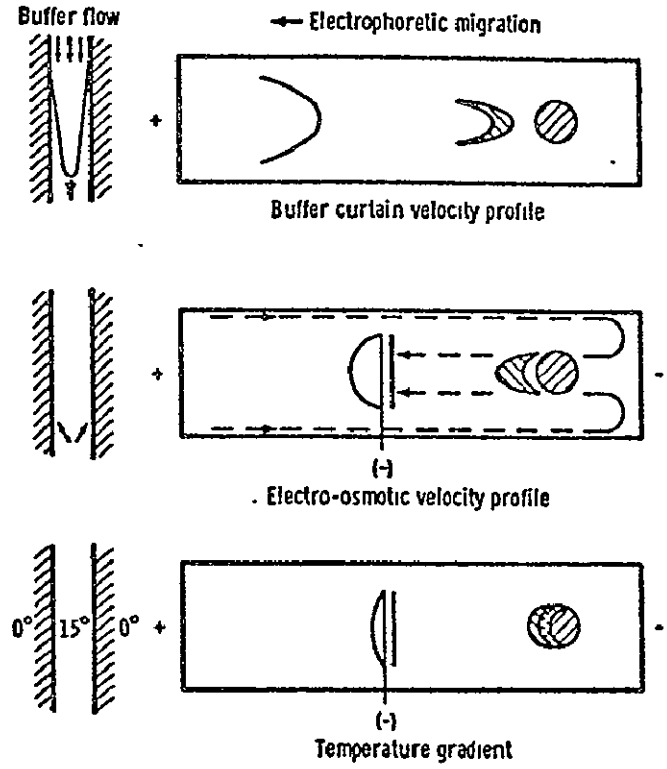

Figure II-2. Band-broadening effects in free-flow electrophoresis.

The extent of the previously mentioned effects on the resulting band broadening has been theoretically and experimentally examined. The results are reported in Reference II-1, from which the following remarks were taken:

> An analytical Free-Flow Electrophoresis apparatus permitted easy observation of all these parameters. It could be shown that the opposing tailing effects of electro-osmosis, and the temperature gradient to the effect of the velocity profiles can be compensated for by appropriate adjustment of the chamber wall zeta potential. (The velocity profile of the liquid curtain

flow causes a tailing of the separated bands in the direction of electrophoretic migration, whereas the electro-osmotic velocity profile counteracts this effect.) The experiments showed that there are additional broadening effects due to other not clearly defined parameters. It was observed that the sample inlet geometry plays a considerable role in band broadening. The practical relevance of this observation is that band broadening is reduced if samples are centered in the middle of the liquid curtain. Furthermore, sample bandwidths should be adjusted to values with a starting bandwidth of less than half the liquid curtain thickness. Under such conditions, the bandwidth was reduced so as to approach theoretical values.

These considerations and the experimental results reveal decisive advantages of free-flow electrophoresis, as opposed to static systems, regarding obtainable separation sharpness and sample throughput. However, one limitation occurs if the method of "isoelectric focusing" or "isotachophoresis" is applied for special separation problems. Because of the discontinuous buffer systems required (pH or ion strength gradients), the free-flow system appears to be less suitable.

ELECTROPHORESIS UNDER ZERO-G CONDITIONS

The efficiency of electrophoresis under one-g conditions is limited. Gravity effects such as heat convection, sedimentation, and buoyancy limit the application with respect to flow rates and resolution. To avoid convection under one-g conditions, the cross section and dimensions of the electrophoresis separation chamber must be kept small. (The thickness of the buffer film is normally 0.5 to 1 mm.) Under zero-g conditions, there are theoretically no limits in this respect. However, one limit is set by the need for effective removal of the Joule heat, especially when working with biological materials. (Depending on environmental conditions, this limit occurs at a layer thickness of 5 to 10 mm.) Considering this limitation, with a possible tenfold larger buffer film thickness, an increase of up to tenfold in sample throughput can be achieved because of the lack of convection disturbances.

A simultaneous improvement of separation sharpness is, however, not to be expected. As previously discussed, the factors influencing separation sharpness in the EPE are essentially methodological and are not dependent on gravitation. An optimization of separation sharpness can be achieved under one-g conditions if the experimental requirements are fulfilled (suitable separation chamber wall potential and less sample throughput).

The significance of applying electrophoresis in the Spacelab as the preferred separation method for sensitive biological material becomes particularly evident in connection with important biological experiments conducted under zero-g conditions. The use of electrophoresis may assist in clarifying many phenomena, such as growth, metabolism, genetics, and immune responses, which occur differently in zero-g conditions than in one-g conditions. The two main purposes for conducting electrophoresis experiments in space are (1) to analyze purity and to isolate samples for medical and biological research and (2) to develop separation methods for commercial and other applications on a preparative scale.

Many proposals also merit further investigations. These proposals concern the effect of gravity on cell functions and the ability of cells or whole organisms to adapt to changes in gravity. One example is the cultivation of cells, the investigation of their synthesis efficiency, and their contact inhibition without gravity. Assuming that it is possible to isolate highly purified cell populations grown under zero-g conditions, the state of weightlessness will offer an excellent opportunity to examine the phenomena of cell differentiation and the exchange of information between different cells.

Some of the necessary operational conditions can be tested only with complete absence of sedimentation. The clarification of these phenomena is not only of great scientific interest but also of practical significance for the regulation of detailed biological processes.

The importance of new findings of this kind for medicine can be anticipated. These investigations require a separation method that allows separation of the carriers of specific syntheses or of the synthesis products themselves. This purpose may be fulfilled in Spacelab by using electrophoretic separation methods. However, the applicability of space electrophoresis for the production of biological material for commercial purposes cannot yet be predicted. At this point, researchers are just learning how electrophoresis in space is to be used. The EPE can therefore be essentially regarded as a pilot experiment.

The primary purposes of EPE and the problems to be clarified were as follows:

1. Applicability of electrophoresis in space

2. Performance of separation experiments with greater throughput

3. Investigation of temperature and velocity effects with a chamber of larger gap width

4. Investigation of separation capability in zero-g conditions

5. Proof of the possibility of separating preparative quantities of living cells

6. Determination of necessary modifications in the construction of the apparatus for use in space.

METHODS AND PROCEDURES

Equipment Design

The design goal for the EPE apparatus (Fig. II-3) was to develop experimental equipment meeting the ASTP spacecraft requirements. The apparatus functions automatically, requiring minimal crew intervention. Known biological samples were used, and it was not necessary to collect the separated biomaterial fractions. An optoelectronic analysis of the separation was performed. A preparative separation was not used. A quantitative evaluation (by use of an optical system) is sufficient to determine the applicability of the method and to study the sharpness of separation.

The separation chamber is the primary portion of the apparatus. It consists of two cooling plates that are adjusted to be exactly parallel to supply laminar flow and form a gap of approximately a 28 to 3.8 mm cross section. Along the sides, electrodes (180 mm long) provide the electric field perpendicular to the chamber buffer flow. The electrodes are separated from the chamber buffer by ion-exchange membranes. The electrodes are located in channels purged by the electrode buffer to remove the hydrogen and oxygen (H_2 and O_2) gases generated by the electrolytic processes. The gases are separated from the fluid and absorbed by means of catalysis. The fluid flow is kept constant by controlled pumping at a rate sufficient to transport the total volume of gas generated. The electrode buffer is separated from the cell buffer, which has a lower concentration, by the two ion-exchange diaphragms.

During the experiment sequence the walls of the separation chamber were cooled, and the temperature was controlled at the operational condition 278 ± 3 K ($5 \pm 3°$C). The buffer leaves the storage container and enters the separation chamber somewhat upstream of the sample inlet to achieve a constant laminar flow in the separation chamber parallel to the electrodes. After having passed the separation chamber, the mixture of sample and chamber buffer entered the waste container, which is combined with the storage container but separated by a membrane. The angle of deflection for a particular particle was determined by the separation buffer flow rate and the field gradient. The program included two flow rates for each sample, so that the influence of buffer velocity could be studied.

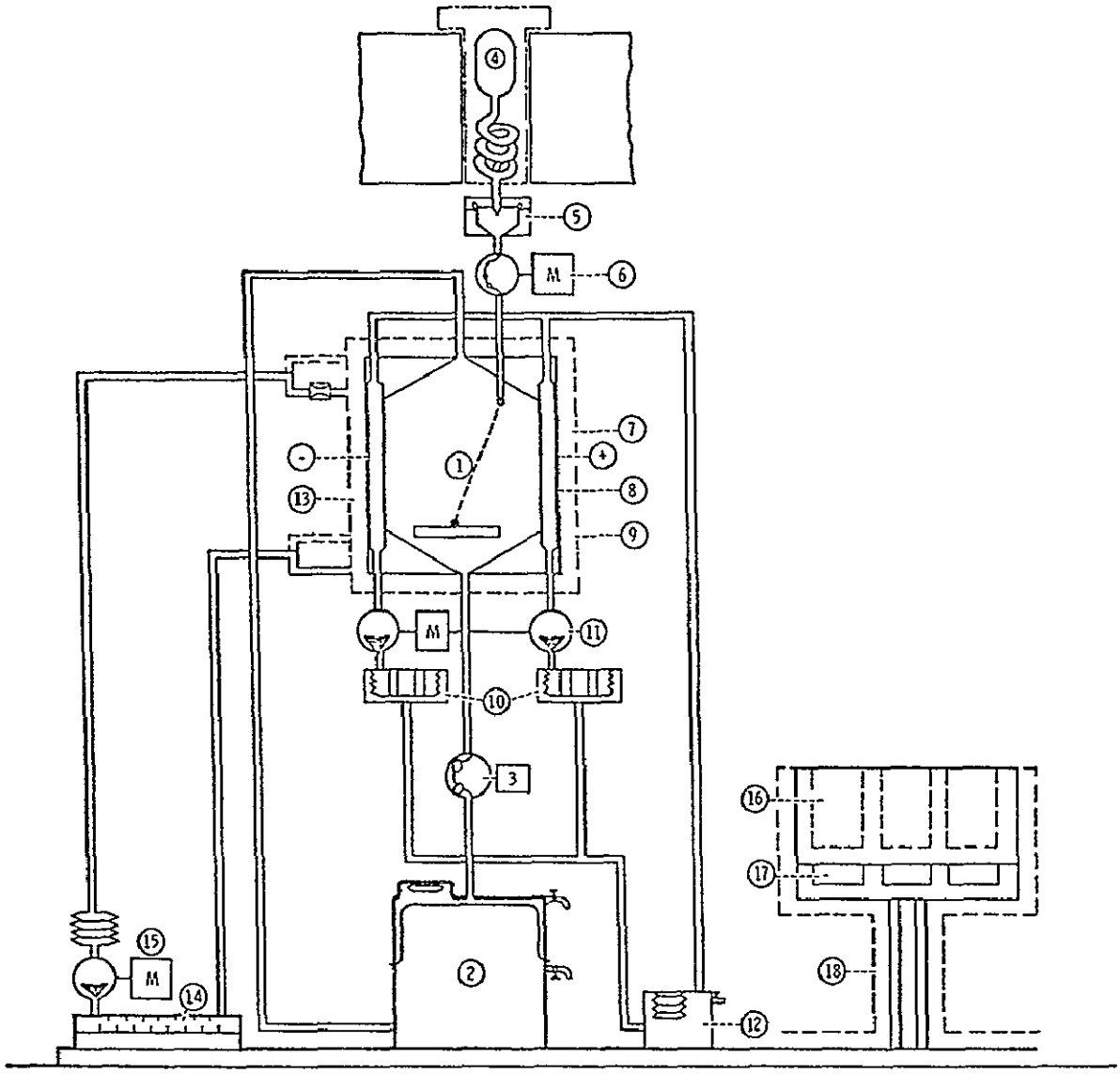

BUFFER SYSTEM
(1) SEPARATION CHAMBER
(2) CHAMBER BUFFER/WASTE CONTAINER BY DIAPHRAGM
(3) PERISTALTIC PUMP AND MOTOR FOR BUFFER FLOW

SAMPLE SYSTEM
(4) SAMPLE CONTAINER (EXCHANGEABLE)
(5) SAMPLE INLET
(6) PERISTALTIC PUMP AND MOTOR FOR SAMPLE FLOW

ELECTRODE SYSTEM
(7) ELECTRODE CHAMBER
(8) ELECTRODES
(9) ION-EXCHANGE MEMBRANES
(10) PHASE SEPARATORS ($O_2 + H_2$) AND GAS ABSORBERS (PALLADIUM BLACK)
(11) GEAR PUMP AND MOTOR FOR ELECTRODE PURGING
(12) ELECTRODE BUFFER CONTAINER

CHAMBER COOLING SYSTEM
(13) SEPARATION CHAMBER COOLING PLATES
(14) PELTIER HEAT EXCHANGER
(15) GEAR PUMP AND MOTOR FOR COOLANT FLOW

FREEZER SYSTEM
(16) SAMPLE STORE
(17) PELTIER COOLING UNIT
(18) HEAT TRANSFER PLATE

Figure II-3. Functional diagram of experiment.

The sample containers were designed so that no air entered the circuit and none of the samples were split when the containers were inserted into the equipment. The containers have a volume of 2 ml, consist of a metal tube with handling knob, and are totally gold plated. On the upper end, they are closed by a pressure exchange membrane and seal. The lower end has a bore connected to a needle with a valve that is opened by inserting the container into the sample inlet closed by a rubber seal.

The sample containers were stored in a freezer at 273 to 278 K (0 to +5°C). For experimental operation, they are removed from the freezer and inserted into the equipment so that the sample flow entered the buffer flow. This flow was directed by a peristaltic pump similar to that of the buffer flow circuit.

The separation was evaluated by optoelectronic methods. By this method, a narrow slit across the downstream end of the separation chamber, parallel to the electric field, is illuminated. The light passes through the quartz plates of the separation chamber and is attenuated as a function of the density of the biomaterial distribution. On the other side of the chamber, the light intensity, related to the cell density, is measured with a photodiode array.

Experiment Electronics

The experiment equipment was programed and controlled by electronic units that performed the following functions.

1. Control of the flow rates, i.e., motor speeds for driving the pumps

2. Power supply

3. Program sequencing, which provided the program of the experiment operations

4. Thermoelectric temperature control

5. Self-check and NO GO indications

6. Data acquisition, evaluation, and processing

7. Data recording

8. Switching and displaying of experiment operations and experiment states.

The primary purpose of the program sequencer was to operate the experiment automatically as much as possible, thereby reducing crewmember participation. The program sequencer was designed to perform the following functions (Fig. II-4).

1. Timing of functions such as precooling or purging

2. Generating nominal values for voltage and flow rates according to the sequence step

3. Collecting and processing GO/NO GO information from experiment subsystems

4. Switching subunits "on" or "off" according to the program

5. Providing time, frequency, and voltage references.

All experimental data were recorded in digital form by two redundant tape recorders that were integrated into the experiment. Both recorded digital data at a bit rate of 2.5 kilobits/s.

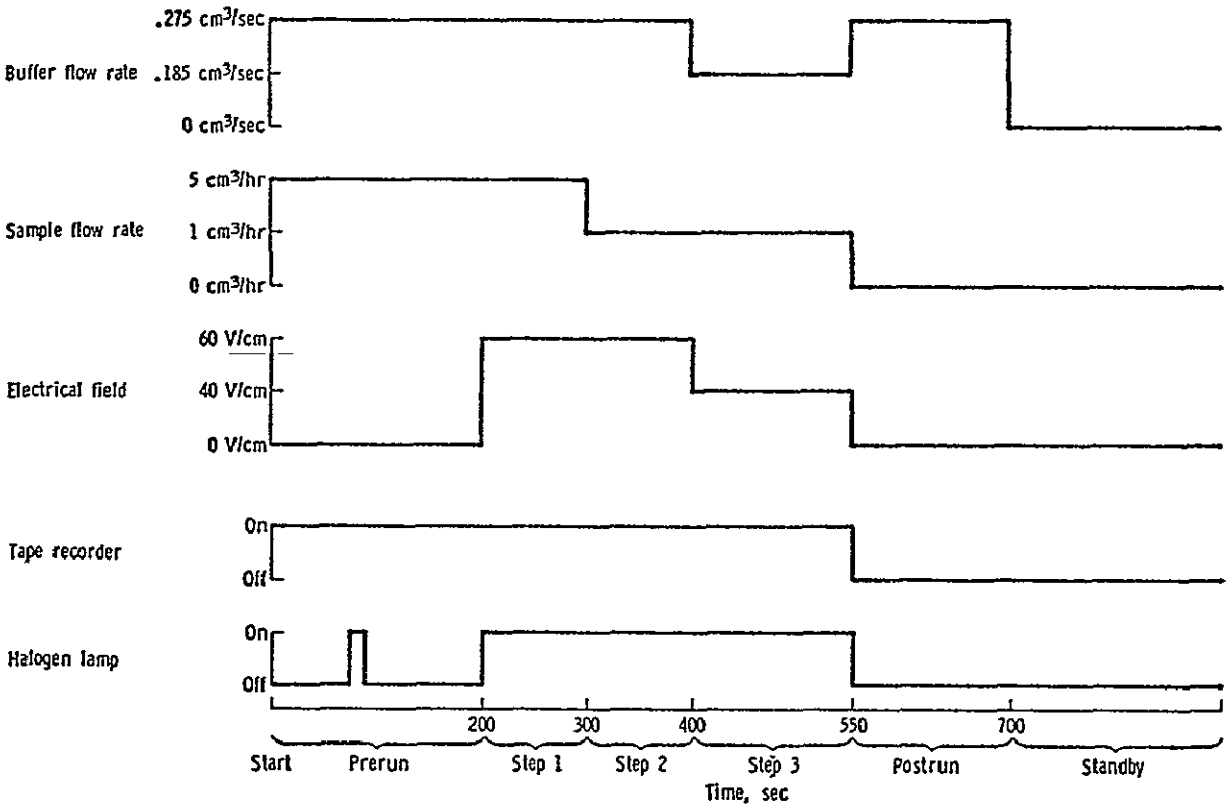

Figure II-4. Electrophoresis experiment sequence.

FLUID CIRCUITS

The experiment incorporates four independent fluid circuits:

- The chamber buffer circuit is used to provide laminar flow for the chamber buffer which passes from the sample inlet to the quartz window through the separation chamber. The buffer is stored in the chamber buffer container which at the same time serves to collect the waste chamber buffer leaving the separation chamber. The container halves are separated by a diaphragm which prevents waste buffer from mixing with unused buffer. Thus, the buffer circuit has a constant volume, so that there is no need for complicated volume and pressure compensating systems.

- The sample circuit is used to ensure defined insertion of the biological samples into the separation chamber.

- With the aid of the electrode buffer circuit the gases produced at the electrodes are transported to the phase separator where they are separated from the fluid and absorbed by means of catalysis.

- The coolant circuit is used to keep the temperature of the separation chamber constant (+5°C wall temperature).

Chamber buffer and sample flow is achieved by means of peristaltic pumps (Fig. II-5). The coolant and electrode buffer are fed using gear pumps (Fig. II-6).

ELECTRONICS

The following major problems must be solved through electronic equipment (Fig II-7):

1. Drive and rpm control of motors

2. Control of experiment sequence

3. Temperature control of sample freezer and separation chamber

4. Data acquisition, processing, and storage

5. Automatic functional check of systems and indicators (GO/NO GO).

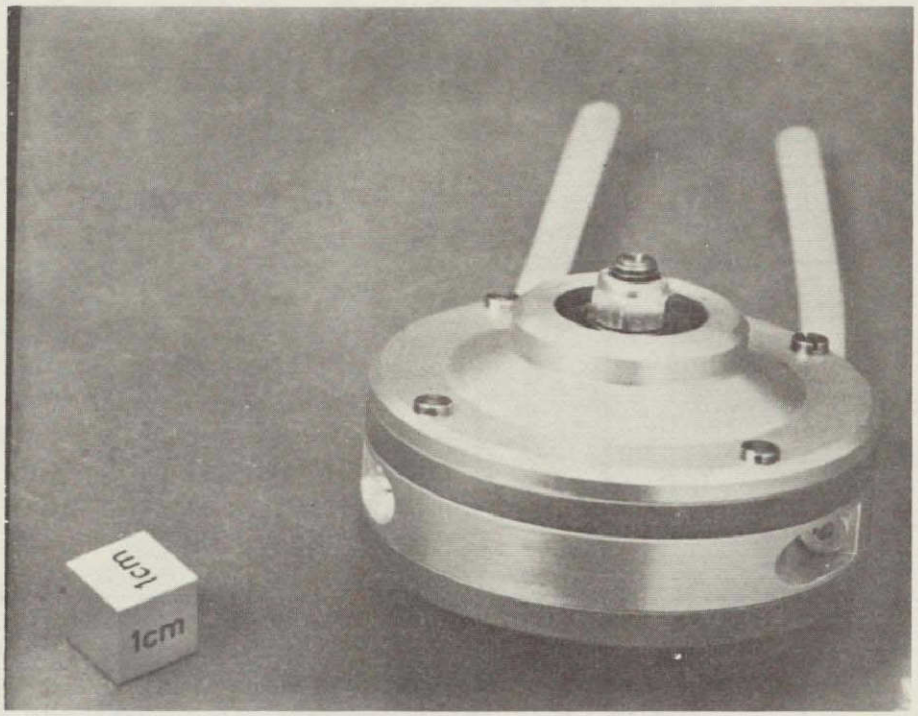

Figure II-5. Complete peristaltic pump, weight of approximately 150 g, as used in chamber buffer circuit and in sample circuit.

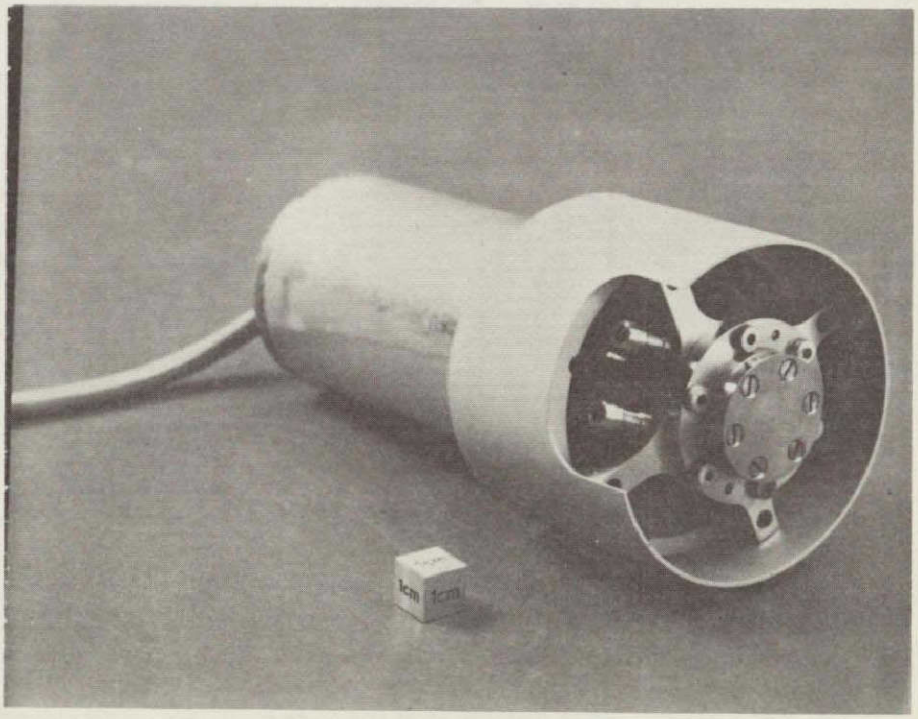

Figure II-6. Gear pump complete with motor as used in electrode buffer circuit and in coolant circuit.

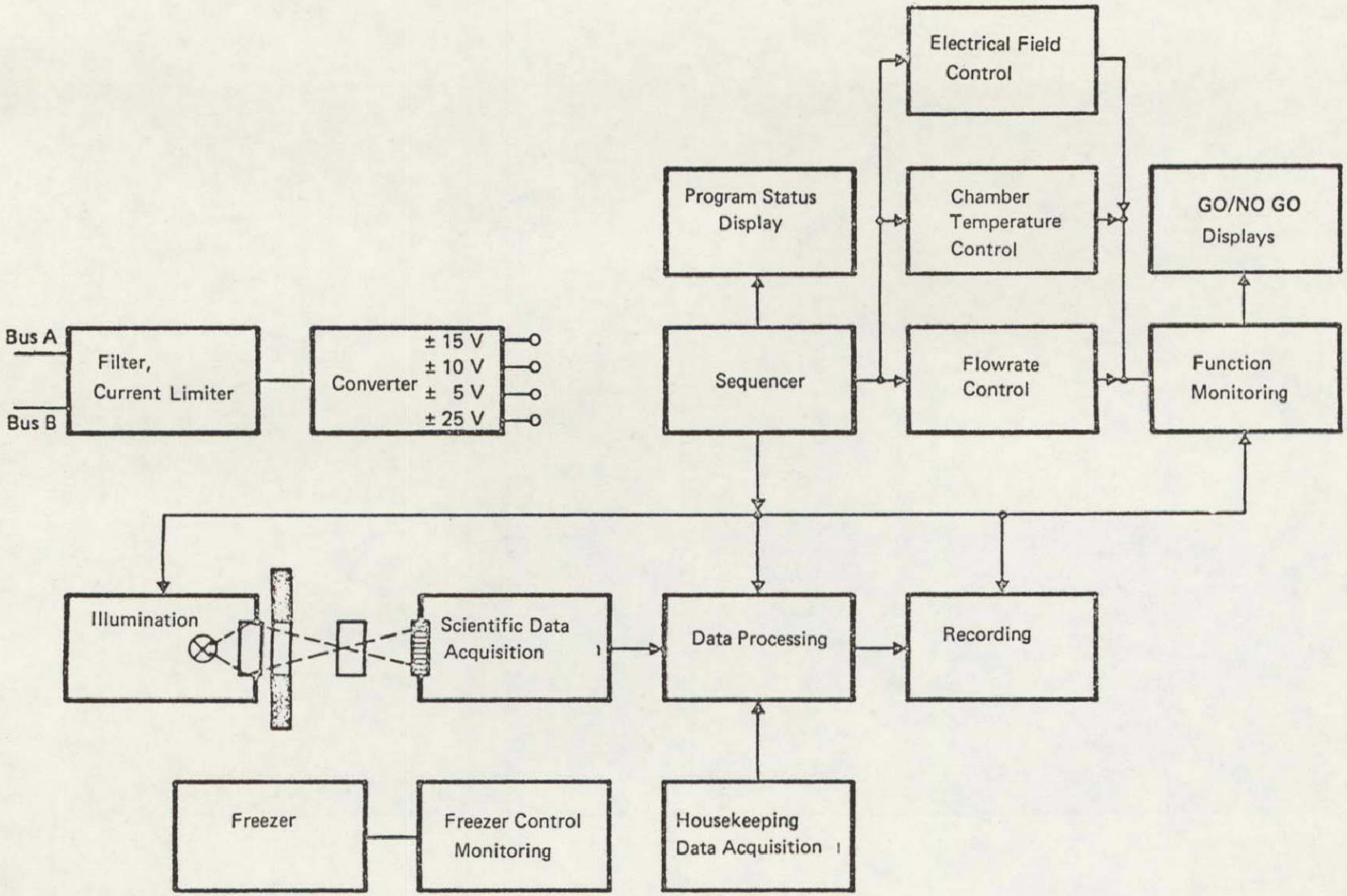

Figure II-7. Electronic block diagram.

ACQUISITION OF SCIENTIFIC DATA

The scientific data are obtained through measurement of the absorption of short-wave light passing through the separation chamber to reach the line of measurement (Fig. II-8). After having passed the quartz window of the separation chamber, light from a filtered source is focused onto the optical center of a lens with the aid of a condenser. An image of this line of measurement is projected onto a photodiode array measuring the local brightness of the individual image points.

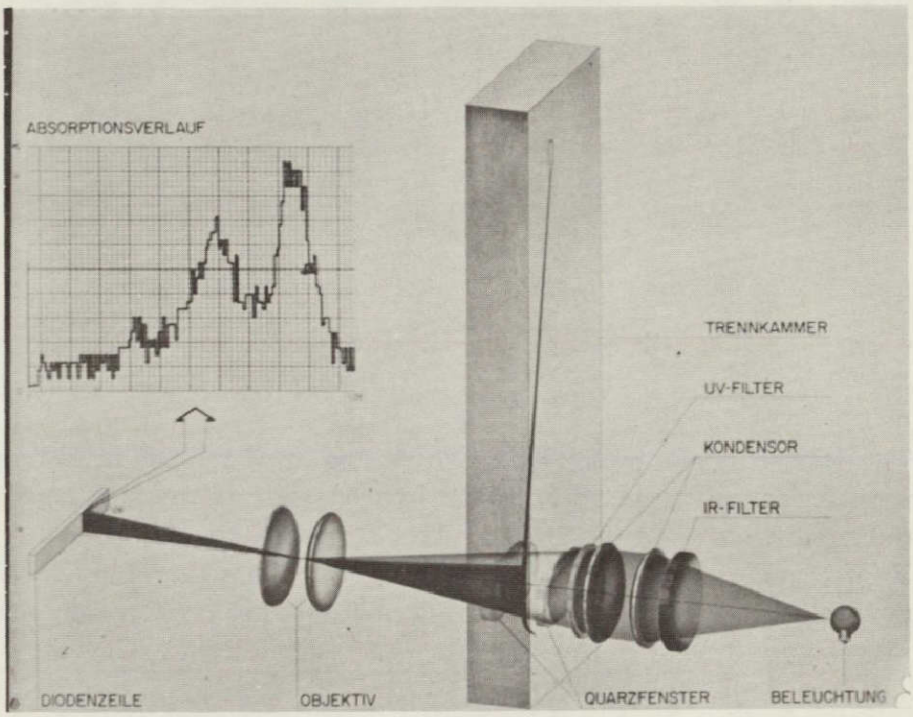

Figure II-8. Principle of sample absorption measurement.

The photodiode array (Fig. II-9) comprises 128 photodiodes, 12.5 mm in length. Their photo voltages are successively scanned and recorded in digital form on a magnetic tape as a measure of the local brightness. The data rate is approximately 2.5 kilobits/s with a brightness resolution of approximately 1 percent per step.

SAMPLES

The equipment was designed for successive runs of a total of four samples. Each sample had a volume of 1.6 cm^3 usable for analysis.

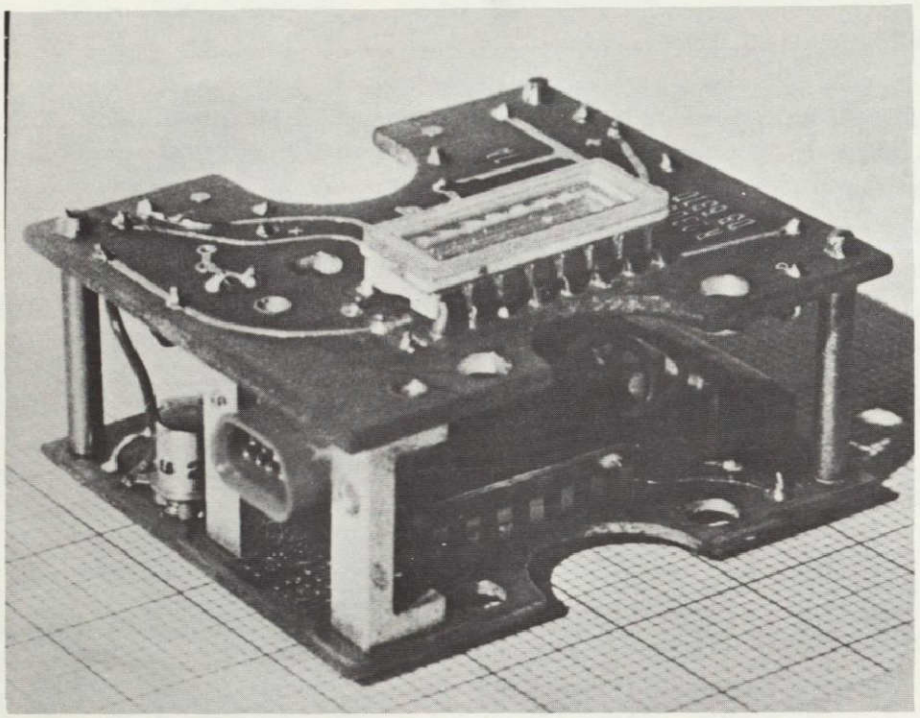

Figure II-9. Photodiode array integrated into shift register and amplifier unit.

The first three samples were stored at +4°C in a sample freezer in the experiment. The fourth sample stored in a freezer in the space vehicle was kept at the temperature of the liquid nitrogen until use. Since the crew had to insert and exchange the samples, the containers were designed such that simple and easy handling was ensured, fulfilling at the same time the functional requirements concerning (1) no entrance of air when inserting the samples into the sample inlet and (2) no escape of fluid when exchanging the samples.

EXPERIMENT SEQUENCE

To determine the effects of the individual parameters, the essential parameters influencing the separation were changed in several steps. Each sample was subjected to the same sequence:

- During the prerun the sample circuit was refilled with sample fluid and any possible remainders of the previous sample were removed from the separation chamber.

- During experiment step 1 the various settings were made:

- Electric field: 60 V/cm
- Buffer flow rate: 275 μl/s
- Sample flow rate: 5 ml/h.

- During step 2 the sample flow rate was decreased from 5 ml/h to 1 ml/h, maintaining the two other conditions.
- During step 3 the electric field intensity and the buffer flow rate were reduced to two-thirds of their original values, keeping the flow rate constant (1 ml/h).

The experiment sequence is shown in Figure II-4.

OVERALL EXPERIMENT

The components of the experiment were mounted on a baseplate which also accommodated the heat exchanger and the Peltier elements for control of the chamber temperature (Figs. II-10 through II-12).

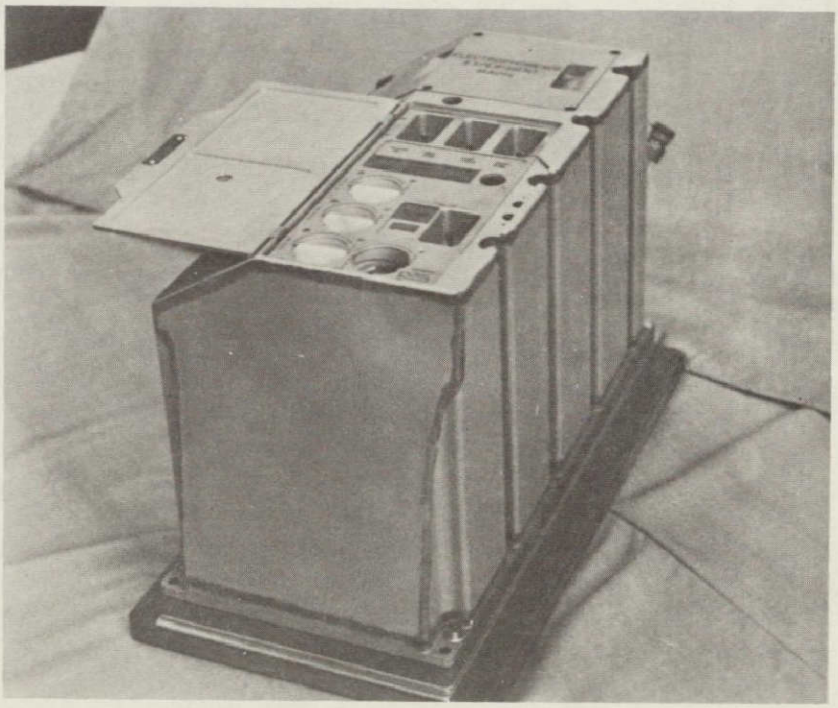

Figure II-10. MA-014 electrophoresis flight unit, cover for control protection opened.

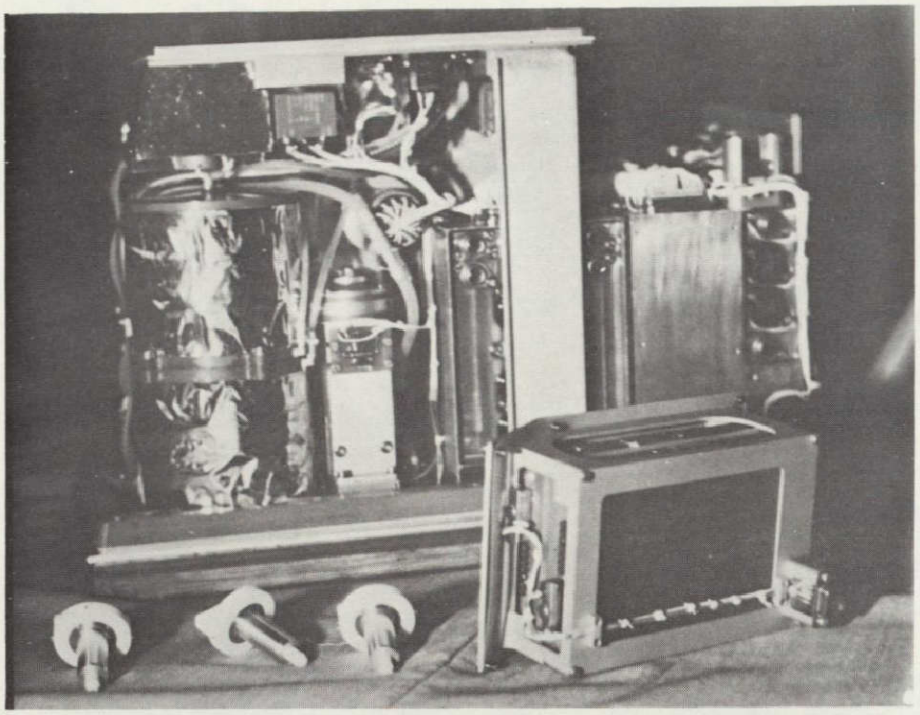

Figure II-11. Experiment opened with sample container and tape recorder module in the foreground [components of the experiment shown are the 1.3 1 buffer container (left), the buffer pump with motor and the electrode buffer pump (center), the electronic components (right)].

Special consideration was given to the design to ensure that:

1. The equipment was capable of functioning satisfactorily with the cover removed.

2. All components could be exchanged as easily as possible.

3. The major maintenance work such as sterilizing the fluid circuits and fueling the systems can be performed with the cover closed.

Cell Sample Preparation

The following samples were prepared for the electrophoresis experiment:

1. Rat bone marrow cells

2. Mixture of human and rabbit erythrocytes

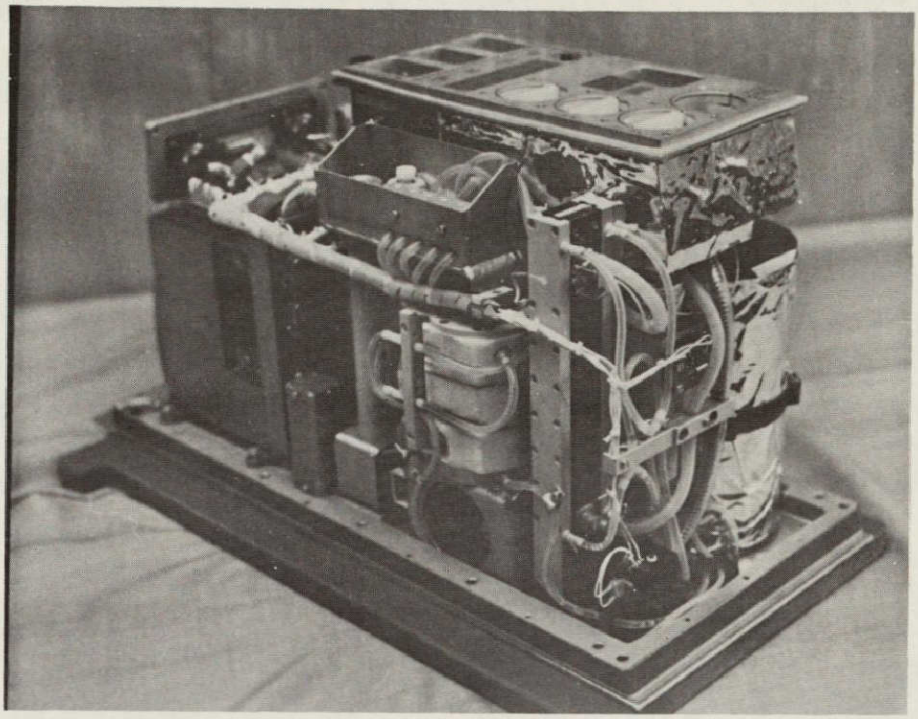

ON THE RIGHT SIDE IS THE BUFFER CONTAINER; ABOVE IT IS THE SAMPLE FREEZER AND THE CONTROL PANEL WITH SAMPLE CONTAINERS INSTALLED. IN THE FOREGROUND IS THE SEPARATION CHAMBER WITH THE HOSE CONNECTIONS FOR BUFFER, COOLANT, AND SAMPLES. BELOW ARE PARTS OF THE OPTICAL SYSTEM. ADJACENT TO THE SEPARATION CHAMBER IS THE ELECTRODE BUFFER CONTAINER AND ABOVE IT IS THE SERVICE BOARD FOR FUELING AND VENTILATION. THE PHASE SEPARATOR IS SHOWN BELOW THE SERVICE BOARD.

Figure II-12. Experiment front.

3. Rat spleen cells

4. Rat lymph node cells with the addition of human erythrocytes as markers (sample 4 was the only frozen sample).

With the exception of sample 2 (erythrocytes), all samples were freshly prepared on July 14, 1975, 15 to 20 h before lift-off. They were stored at 277 K (4°C) for approximately 45 h before the start of the experiment. Sample 2 (erythrocytes) had been prepared 2 weeks in advance at the Max Planck Institut für Biochemie in Munich, and the cells were preserved by fixation in 2 percent glutaraldehyde. The preparation of cells from different lymphatic organs was accomplished under sterile conditions (autoclaved material, clean bench) at 277 K (4°C) at the NASA John F. Kennedy Space Center (KSC) laboratory.

Bone marrow cells of rate (Wistar) were prepared, and cells were flushed out of the bones with Puck TC solution combined with 2.5 percent bovine

serum albumin (33 percent) by using a syringe. A single cell suspension was prepared by passing the cells through a plastic syringe without a needle several times. The cells were then washed twice (150 g, 10 min) with the same buffer and finally resuspended in ampholine buffer.

Cells from spleen and lymph nodes of the rates were prepared by teasing the organs in Puck TC solution at 277 K (4°C) with injection needles. Cells were washed twice with the same solution (150 g, 10 min), filtered through cotton wool, and resuspended in ampholine buffer.

For sterile tests, cell suspensions and buffer solution were spread on blood agar dishes and incubated for 5 h at 301 K (28°C). This test, as well as light microscopical control, showed no bacterial contamination of cell suspensions and buffer solutions. The viability of the prepared cells (tested with trypan-blue exclusion test) was more than 90 percent in each sample.

All containers of the flight unit were sterilized with formaldehyde (2.5 percent) and washed five times with 20 ml of sterile ampholine buffer. A special apparatus for filling the sample containers was sterilized in the same way. At 4 days before Apollo lift-off, the special "deep freezing container" was filled with a 0.8 ml mixture of rat lymph node cells (25×10^6 cells/ml) and human erythrocytes (30×10^6 cells/ml) and kept in liquid nitrogen. At 14 h before Apollo lift-off, the other three sample containers were filled with 1.4 ml of the following preparations:

1. A mixture of fixed human erythrocytes (30×10^6 cells/ml) and fixed rabbit erythrocytes (50×10^6 cells/ml)

2. Native bone marrow cells of the rat (80×10^6 cells/ml)

3. Native spleen cells of the rat (80×10^6 cells/ml).

The exact composition of all buffer systems used for cell preparation and for electrophoretic separation is shown in Table II-1.

RESULTS

The experiment began on schedule on July 16, 1975, at 32:40 ground elapsed time (GET) and lasted for one complete Earth orbit until 34:25 GET. Radio communication from the Apollo spacecraft confirmed that, according to the signal lamps, all functions were operating properly.

TABLE II-1. BUFFER SOLUTION[a]

Description	Electrode Buffer	Chamber Buffer	Ampholine Buffer
Substance, g/l			
Triethanolamine	5.16	1.71	—
Potassium Acetate	0.90	0.30	0.61
Glucose	0.90	14.61	—
Sucrose	—	7.88	—
Calcium Acetate	—	0.033	0.05
Magnesium Acetate	—	0.46	—
Glycine	—	—	21.55
Ampholine (pH 3.5 to 10)	—	—	20 000
Characteristic			
Conductivity, μmho	2500	900	900
Osmolarity, mOsmol	—	≈300	≈300
pH	7.2	7.2	7.2

a. Buffer solutions mixed with distilled water.

Evaluation of Housekeeping Data

The housekeeping data serve to prove that the experiment is functioning correctly during the mission. The data were examined individually and compared with the values recorded in the course of qualification testing of the equipment (December 1974). In this way, apart from the functional proof, a good statement can be made as to the functional reliability of the equipment for a relatively long period. The results are summarized in Table II-2 and Figure II-13 and discussed in the following under separate headings.

PROGRAM

The program sequencer was functioning satisfactorily during all four runs. Program sequence and schedule were as planned (Fig. II-13).

TABLE II-2. RESULTS OF HOUSEKEEPING DATA EVALUATION

Word No.		Nominal From/To	Mission From/To	Qualification From/To	Remarks
004	EPE Sequence Prerun/Part I/II	OK	OK	OK	See Figure II-16.
005	EPE Sequence Part III	OK	OK	OK	See Figure II-16.
134	Reference Voltage	9.9/10.1 V	9.96/9.98 V	10.00 V	See Figure II-16.
135	Chamber Temperature	3/7°C	4/7.5°C	4/6°C	See Figure II-16.
136	Coldplate Temperature	5/7°C	5.8/6.3°C	—	
137	Amplifier Supply	14.2/15.8 V	15.05 V	5.0 V	
138	Amplifier Supply	-14.2/-15.8 V	-14.8 V	-14.8 V	
139	Logic Supply	9/11 V	+9.8 V	9.95 V	
140	Recorder Supply	4.5/5.5 V	4.75/5.0 V	4.8 V	
141	Diode Array Supply	24.0/25.0 V	24.7/24.8 V	-25.0 V	
142	Motor Supply	20/27 V	20.8/23.6 V	22.5 V*	*KSC — Test on 10/1/75
143	Electrical Field, 60 V/cm	58/62 V/cm	61/61.7 V/cm	61 V/cm	
144	Electrical Field, 40 V/cm	39/41 V/cm	40 V/cm	41 V/cm	
145	Peltier Current	0/100%	10/85%	10/85%	See Figure II-16.
146	Lamp Supply	—	—	—	No Results
147	Reference Voltage	9.9/10.1 V	10.00/10.01 V	-10.01 V	
148	Reference Voltage	9.9/10.1 V	10.0 V	-10.00 V	
149	Reference Voltage	9.9/10.1 V	10.02/10.026 V	9.99 V	
150	Reference Voltage	9.9/10.1 V	10.00 V	10.00 V	
151	Display Supply	4.5/5.5 V	4.70 V	5.05 V	
152	Auxiliary Motor Supply	20/28 V	22/26 V	24.2 V*	*KSC — Test at 10/1/75
157/158	Speed Motor 2	OK	OK	OK	
159/160	Speed Motor 1	OK	OK	OK	No NO GO During Mission
161	GO/NO GO Events	OK	OK	OK	

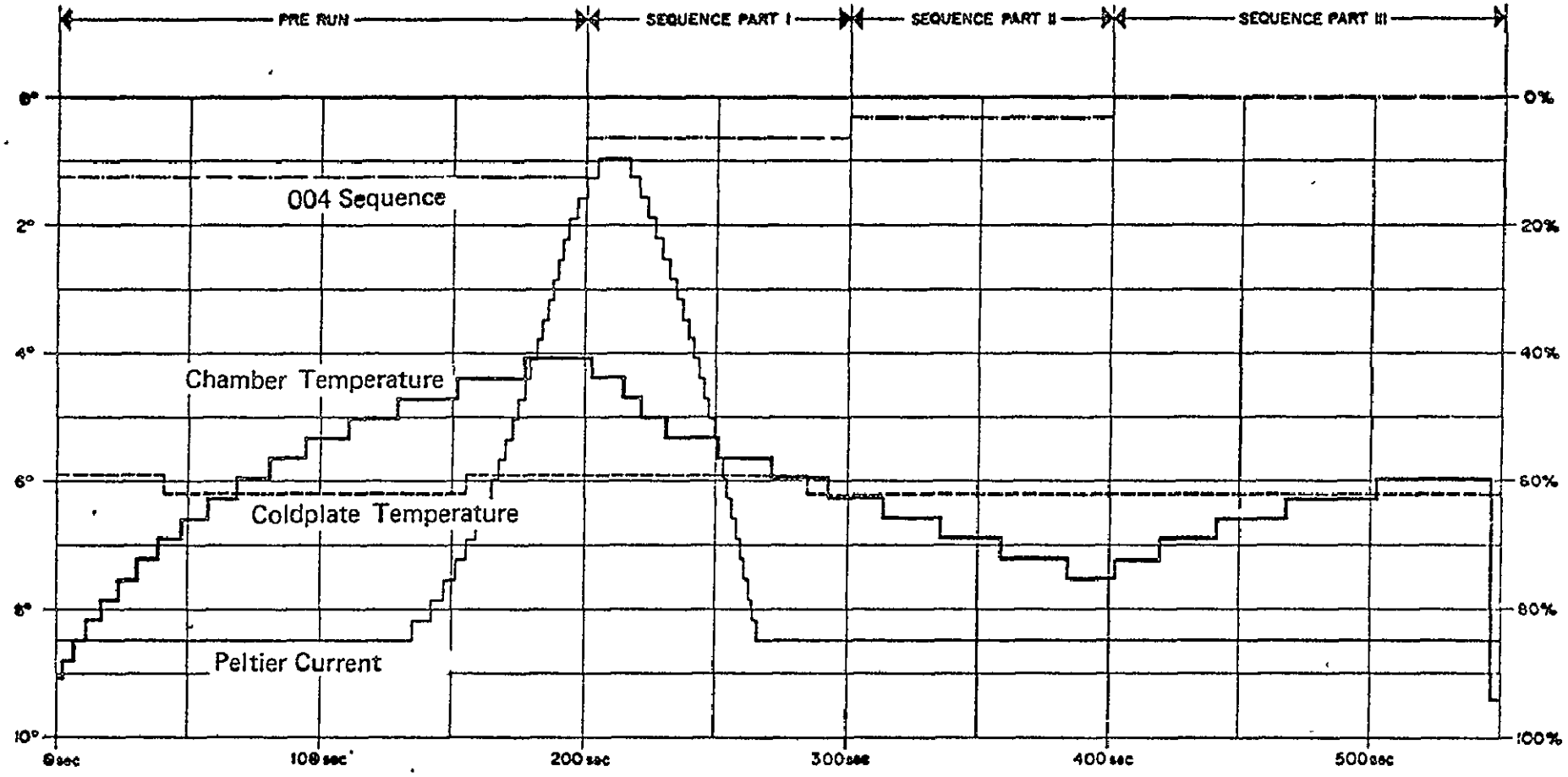

Figure II-13. Temperature behavior of experiment during mission (applicable for all four samples).

CHAMBER COOLING

The controller used for chamber cooling was functioning properly. During precooling in the prerun the chamber was cooled to +4.1°C for each sample, this minimum value being reached toward the end of the "prerun" program step. From program part I to the end of part II the temperature control circuit was overloaded during all the four sample runs. The chamber temperature rose beyond the nominal value of +5°C to +7.8°C (sample 1), 7.5°C (samples 2 and 3), and 7.2°C (sample 4), respectively. The maximum value was reached in each case at the end of part II.

In part III the chamber temperature was again reduced continuously to final values of 5.9°C. The circuit was no longer overloaded and would reach its nominal temperature, as shown through the extrapolation. The latter behavior differing from that in part I and part II was due to the more than 50 percent reduction in heat transformation during part III of the sequence.

In the course of testing a certain improvement of the temperature behavior was recognizable which, as experience has shown, results from desalting of the electrode buffer, thus causing a decrease in the conductivity of this buffer with the operating time.

Overloading of the temperature control circuit during parts I and II of the sequences was a result of:

1. The conductivity of the chamber buffer was set to 800 μs/cm at a temperature of 10° for the mission. Desalting of the electrode buffer, in principle, results in an approximate 10 percent increase in the conductivity of of the chamber buffer within the separation chamber, so that a mission conductivity of approximately 880 μs/cm was obtained. As compared with the nominal value (750 μs/cm), a current increase of 18 percent or a power increase of approximately 35 percent was achieved.

2. Upon completion of the hardware design, the conductivity of the electrode buffer was increased to 2500 μs so that the electrode buffer cross section no longer affected the overall resistance of the separation chamber. This led to another current increase of approximately 10 percent, as compared with the nominal value (20 percent power increase).

3. The modification of the cooling pump brought about a 30 percent reduction in coolant flow rate, so that the stability reserve preventing the coolant circuit from overloading was used up.

The assessments based on the performance parameters thus modified have shown that the cooling system behavior must be as shown during the mission.

As indicated in Table II-3, the temperatures as a whole did not exceed the prescribed performance limits.

TABLE II-3. TEMPERATURE BEHAVIOR OF EXPERIMENT

	Initial Chamber Temperature	Minimum Temperature (End of Prerun)	Minimum Temperature (End of Part II)	Minimum Temperature (End of Part III)
Sample 1	9.4	4.1	7.8	5.9
Sample 2	9.1	4.1	7.5	5.9
Sample 3	9.1	4.1	7.5	5.9
Sample 4	9.4	4.1	7.2	5.9

ELECTRIC FIELDS

The prescribed field voltages in both ranges, i. e., 60 V/cm and 40 V/cm, were maintained with a high degree of accuracy during all four sample runs (Table II-2).

SUPPLY VOLTAGES

The supply voltages were within the prescribed tolerance range; minor deviations of the mission data from the comparison values obtained during qualification testing are irrelevant.

ILLUMINATION

As a result of the weightlessness the circuit process in the halogen lamp was disturbed so that the helix temperature during the mission was higher than that under one-g conditions. To obtain information about the excessive lighting, the transient phenomena of the illumination unit were determined at the commencement of each lamp check performed prior to each mission sequence, and the final lighting value was defined through extrapolation.

The transient phenomena of the illumination unit are shown in Figure II-14. Assuming that the transient follows the exponential law, the following equation applies approximately:

$$y = y_{\infty} (1 - T\dot{y})$$

Time constant T_1 is then given by

$$T_1 = \frac{1}{\dot{y}_1} \left[1 - \frac{y_1}{y_{1\infty}} \right]$$

Assuming that the time constant T_1 of the curve for normal lighting and that of the curve for excessive lighting are approximately equal, a conditional equation is obtained for the final value $y_{2\infty}$ from the curve for excessive lighting,

$$y_{2\infty} = \frac{y_2}{1 - \left(1 - \frac{y_1}{y_{1\infty}} \right) \frac{\dot{y}_2}{\dot{y}_1}}$$

Using the values shown in the diagrams,

$y_1 = y_2 = 0.7$ (lower end of measuring range)

$\dot{y}_1 = 1.677 \cdot 10^{-3}$ 1/s (with $y_1 = 0.7$)

$\dot{y}_2 = 2.5..2.85 \cdot 10^{-3}$ 1/s (with $y_2 = 0.7$)

$y_{1\infty} = 0.95$ (final value of normal curve).

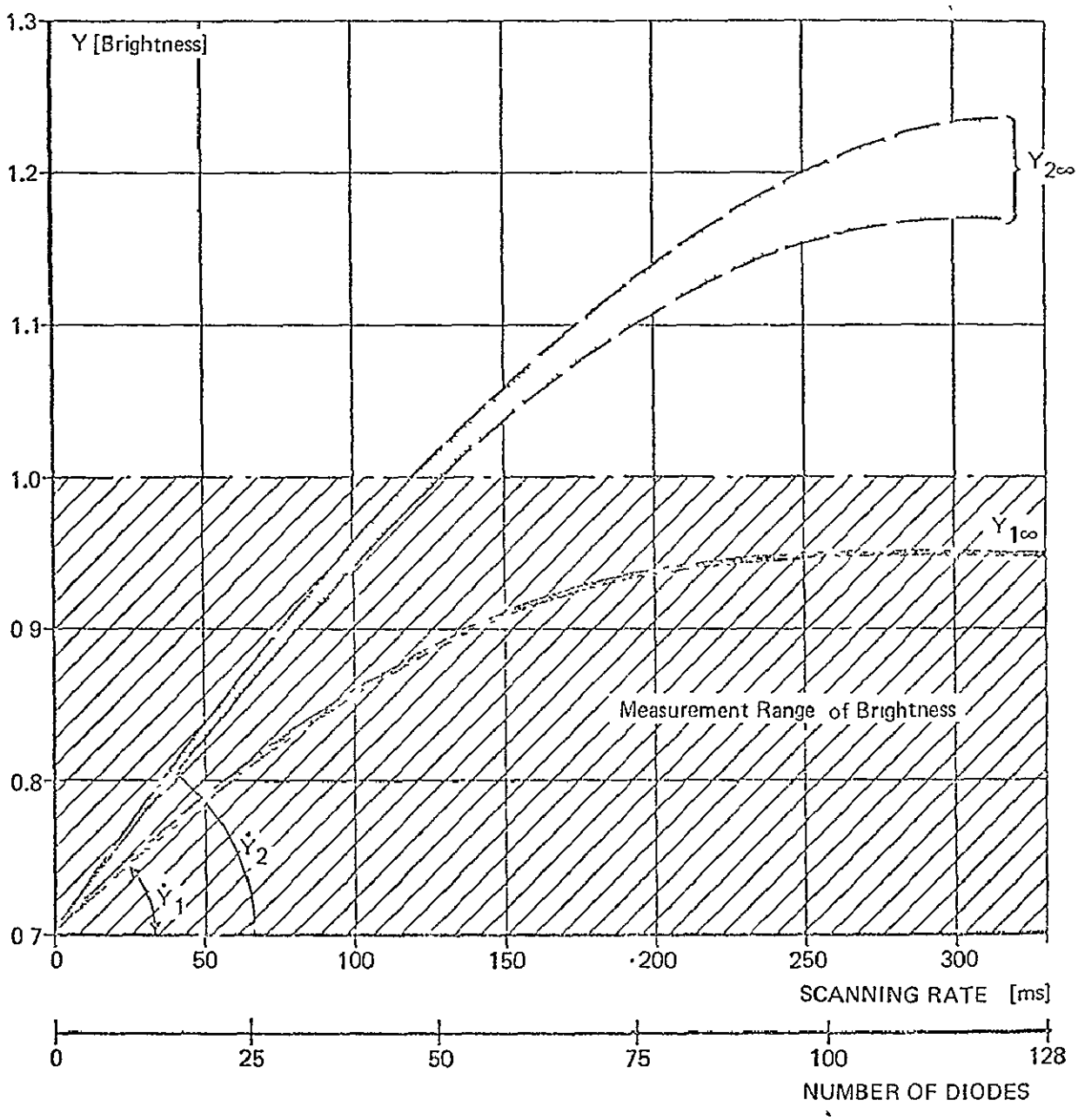

$Y_{1\infty}$ = Final value at nominal exposure
$\dot{Y}_1$ = Derivative at nominal exposure
} During preinstallation test

$Y_{2\infty}$ = Final value at over exposure
$\dot{Y}_2$ = Measured derivative at over exposure
} During mission

Figure II-14. Transient behavior of illumination system.

The probable final value of the photodiode array subjected to excessive lighting is given by

$$1.18 \leqq y_{2\infty} \leqq 1.27 \quad .$$

REFERENCE VOLTAGES

The reference voltages registered on channels 136 and 147 through 150 are decisive for the reproducibility of the data. The deviations of the reference voltages from the values obtained during qualification testing show the level of confidence of the calibration curves. None of the voltages revealed a deviation larger than 3.6 percent, so that the calibration sheets established for the experiment data during qualification testing could be used without any corrections.

LAMP VOLTAGE

After a modification of the illumination system performed on a short-term basis, adaptation of the brightness sensor from 40 W to 10 W was abandoned for cost and schedule reasons as agreed with the customer, so that no data were supplied by this channel.

MOTOR SPEEDS OF PERISTALTIC PUMPS

The motor speeds were within the prescribed tolerance range. Since stepper motors were used, only two stable states are possible, which means that the motors either run at nominal speed or they do not run at all. In addition, the NO GO indicators and the event combination (in channel 161) confirmed that the motors were operating correctly.

NO GO AND STATUS CHECKS

No NO GO was recorded throughout the mission. The experiment status was displayed as requested by the program.

INTERFACES

The cold plate temperature ranged between 5.9 and 6.2°C throughout the mission.

The terminal voltages of bus A and bus B were within the prescribed tolerance range, as derived from the evaluation of channels 142 and 152 (uncontrolled voltages).

TAPE RECORDING

The tape recordings could be read correctly by the unit tester. The synchronization and bit errors were smaller than 1 percent. Of the total of 7,500 frames, approximately 50 frames could not be read. The errors essentially were due to data failures during starting and stopping of the tape recorder at the beginning and end of the sequences (four samples and preinstallation test).

Evaluation of Scientific Data

The scientific data revealed that the light for the optical detection of the separation must have been too bright. The lamp check showed excessive lighting resulting in a saturation of the photodiodes in the optical detection system. The quantitative estimate of error revealed that the light must have been 35 percent too bright, although the lamp check indicated normal functioning during the preinstallation check. For this reason, only absorptions above 25 percent were registered. This amount corresponds to the maximum expected absorption of the separated fraction zone.

In the entire separation process, no "true" cell distribution curve was obtained. The baseline of registration in all cases was above the maximum absorption obtained in the peaks. Because of this finding, an analysis of the experiment seemed at first to be impossible. However, during the stationary phase of the separation (after adjustment to constant experimental conditions), i.e., during the 90 s separation time, irregularly occurring pulses (called "events") were recorded. This pattern reflected the expected course of the separation curves (Fig. II-15). These pulses seemed to be caused by cell aggregation in the region of the separated bands. This assumption was confirmed in the following two ways:

1. An aliquot of the sample used in the ASTP flight was separated under the same conditions on mission day at KSC in an identical apparatus under one-g conditions (electrophoresis engineering model, EM, with a 0.7 mm buffer film thickness). In addition to the expected cell distribution curves (Fig. II-15), analysis of this undisturbed tape showed stray pulses caused by cell aggregation that had a greater absorption. The accumulation at the same location (frequency distribution of the events) during a separation time of approximately 2 min yielded distribution curves (Fig. II-15).

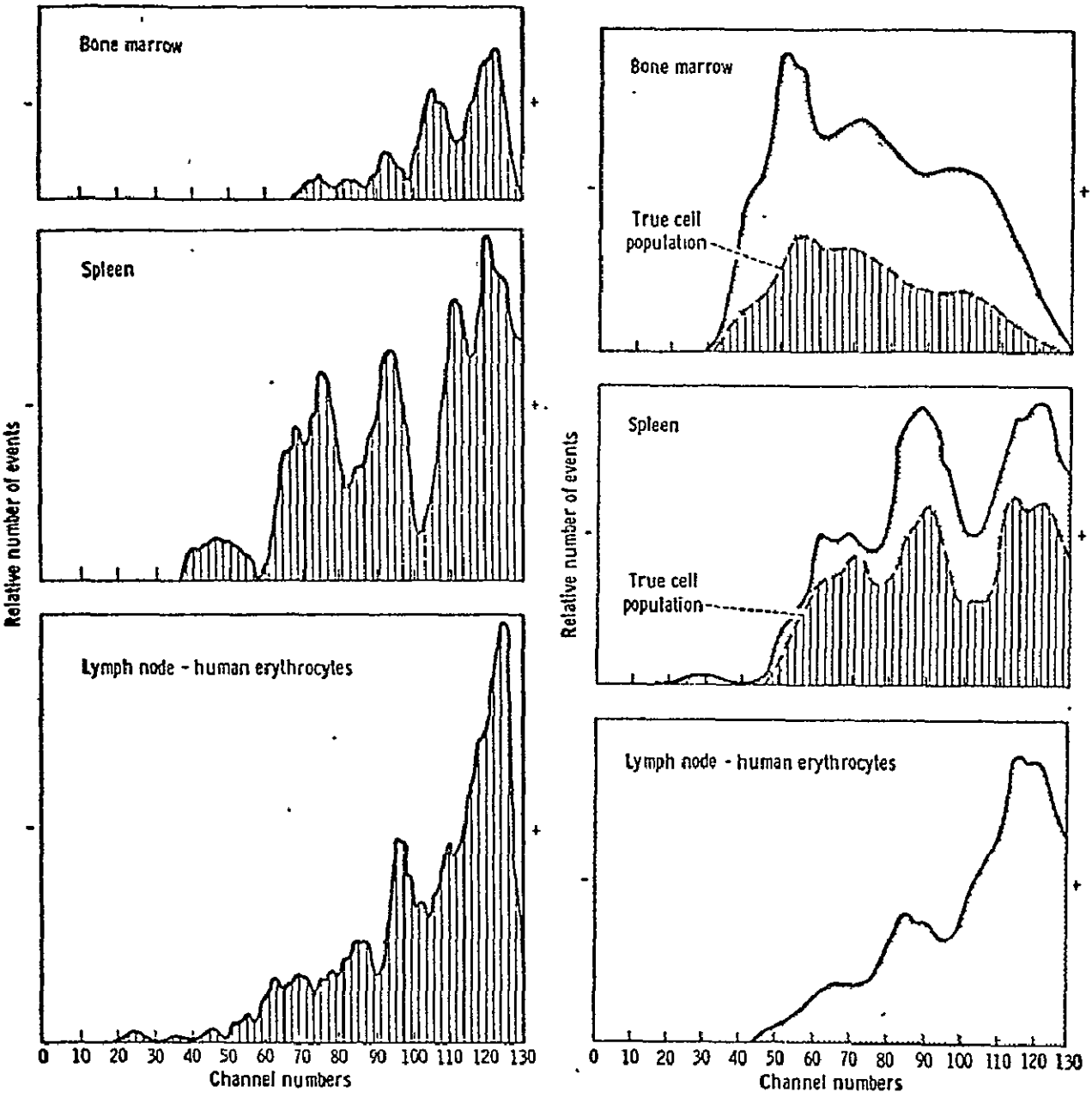

(a) Zero-g conditions.

(b) One-g conditions.

Figure II-15. Sample separation under zero-g and one-g conditions.

2. To check this finding and to obtain a reliable interpretation, such separations were repeated many times with the EM apparatus, and each experiment was performed and evaluated with normal and increased lighting. It was clearly established that only the analysis of the periodically occurring cell aggregations at the measuring location was representative of the actual cell distribution. The difficult evaluation and coordination of indirect information was performed with the aid of a data processing computer.

Based on these studies, assertions can be made regarding the following samples:

1. Bone Marrow Cells — Although only a few events (73) could be analyzed because of the tendency of these cells to form no aggregations, the distribution curve is that of an excellent separation.

2. Mixture of Human and Rabbit Erythrocytes — Because of the weak tendency of these fixed cells to form aggregations, insufficient information was available for computation.

3. Spleen Cells — The best result was obtained with this sample. The amount of information (358 events) was sufficient to identify fine details of the separation. The separation in erythrocyte peak can sometimes be indicated in good separations under normal one-g conditions as well. This finding indicates an essentially good separation sharpness under zero-g conditions.

4. Lymph Node Cells with the Addition of Human Erythrocytes (Frozen Sample) — A large number of events (549) were detected. A good separation effect, similar to sample 3, was inferred here as well as under zero-g conditions.

Postflight Examination

Postflight examination of the flight unit, which took place in Munich, yielded the following information:

1. All housekeeping data were within the tolerance range.

2. The buffer and sample amounts corresponded to the required specification according to the volume measurement carried out.

3. Buffer samples collected in the container revealed no extraordinary bacterial contamination despite the long storage period. Microscopic investigation for the presence of cell particles in the separation buffer (collection container) was positive.

4. The expected remainder of the cell suspension, more than 3 months old, was found in the examined sample containers. However, the gold-plated containers revealed unexpected corrosion.

5. All buffer tube systems were intact and penetrable. The pump systems were still fully operational.

This information clearly reveals that the course of the buffer and sample and the electronic system must have operated accurately. Surprisingly, the error in the optical detection system shown by the tape (saturation of the photodiodes) was at first not identifiable. Both the current and the voltage of the lamp were normal. By contrast, the light intensity measured by the diode array was, as expected, too low becaude of turbidity. The cause of this phenomenon can be considered as either a fault in the electrical contact arising during the flight or an increase in lamp helix temperature arising under zero-g conditions. The latter could be explained by the absence of thermal convection in the gas-filled tube.

SUMMARY

The applicability of free-flow electrophresis under zero-g conditions of the space flight was confirmed. The technical problems arising from the special environmental conditions in a Spacelab can be controlled. This observation applies to the technical concept of the EPE apparatus as well as the manual operation by crewmembers. In particular, it was demonstrated that the buffer flow systems operated despite the more difficult conditions imposed by a closed system. The effective removal of gases from the electrode buffer (electrolytic products) by the measures used was a necessary part of this experiment.

In a separation chamber of large cross section, the temperature conditions required for biological material could be fulfilled. The same applies for the correct laminar buffer flow.

A sample throughput greater than tenfold was achieved by the expansion of the separation chamber cross section possible in space flight and with otherwise similar chamber dimensions. [In the fast sequence (Fig. II-4, step 1), 7×10^6 cells/min were separated.] Despite the error that occurred in the optical detection system, it was demonstrated that the separation sharpness corresponded at least to that of analytical separations under one-g conditions. Whether an improved separation sharpness is possible with a fivefold decreased sample insertion rate (Fig. II-4, steps 2 and 3), in contrast to one-g conditions,

could not be determined because of the reduced source of information (sensitivity) caused by the lamp error. This is of little importance because such measurements can also be conducted under one-g conditions, as already shown. Also, the separation sharpness depends on other influences as well (e.g., zeta potential on the wall).

The possibility of separating living cells under zero-g conditions was demonstrated. The cell aggregations that formed in the cell suspensions need not correspond to a decrease in cell viability.

REFERENCE

II-1. Hannig, K.; Wirth, H.; Neyer, B.; and Zeilter, K.: Theoretical and Experimental Investigations of the Influence of Mechanical and Electrokinet Variables on the Efficiency of the Method. Z. Physiol. Chem., vol. 356, August 1975, pp. 1209-1223.

BIBLIOGRAPHY

Schoen, E.: Elektrophorese-Experiment. MA-014 in ASTP Final Report No. URW-87/75, November 1975.

SECTION III

SURFACE TENSION INDUCED CONVECTION IN ENCAPSULATED LIQUID METALS IN A MICROGRAVITY ENVIRONMENT

EXPERIMENT MA-041

By R. E. Reed,[1] W. Uelhoff,[2] and H. L. Adair

1. Deceased.
2. Guest scientist from Institut fur Festkörperforschung, Kernforschungsanlage Julich, BRD.

Contract No. W-7405-eng-26

SOLID STATE DIVISION

ASTP EXPERIMENT MA-041
"SURFACE TENSION INDUCED CONVECTION IN ENCAPSULATED LIQUID METALS IN A MICROGRAVITY ENVIRONMENT" - FINAL REPORT

R. E. Reed†, W. Uelhoff* and H. L. Adair

†Deceased.

*Guest scientist from Institut fur Festkörperforschung, Kernforschungsanlage Jülich, BRD.

OAK RIDGE NATIONAL LABORATORY
Oak Ridge, Tennessee 37830
operated by
UNION CARBIDE CORPORATION
for the
ENERGY RESEARCH AND DEVELOPMENT ADMINISTRATION

CONTENTS

ASTP EXPERIMENT MA-041
"SURFACE TENSION INDUCED CONVECTION IN ENCAPSULATED LIQUID METALS IN A MICROGRAVITY ENVIRONMENT" - FINAL REPORT

R. E. Reed, W. Uelhoff and H. L. Adair

ABSTRACT

This experiment was designed to detect possible convection caused by a steplike compositional variation in a liquid metal in a microgravity environment. Wetting and nonwetting ampoules were used to try to determine the extent of the stirring effects if they were present. Since stirring effects can be caused by temperature gradients, the temperature gradients for this experiment were minimized.

Steplike compositional variation was created by pressure bonding a lead-0.05 atom percent gold alloy to pure lead. Two diffusion temperatures (923 K and 723 K) were used; if no stirring effects were present, it was hoped that the liquid diffusion parameters for gold in lead could be obtained.

Two identical experimental arrangements were used to compare the transport mechanisms of gold in liquid lead in unit gravity and microgravity environments.

INTRODUCTION

In the absence of gravity, stirring in a liquid due to density differences caused by thermal or compositional gradients is suppressed. However, other mechanisms resulting in natural convection in microgravity environment exist and have been described elsewhere.[1] One of

the most important mechanisms for liquid metals is surface tension driven convection (Marangoni effect) which becomes predominant in the low-gravity environment. In this case, surface tension differences caused by compositional or temperature gradients have been demonstrated to cause stirring in liquids during experiments performed aboard Skylab. Compositional gradients were created by adding soap solution or grape juice to a large water globule. This caused vigorous fluid motion for some moments after the addition. Also, evidence of stirring was detected in the sphere forming[2] and welding[3] experiments involving electron beam heating; this type of heating causes very steep temperature gradients.

The present experiment was designed to detect possible convection caused by steplike compositional variation in a liquid metal contained in both wetting and nonwetting ampoules. The general concept of the investigation was to set up a liquid diffusion couple of lead and Pb-0.05 atom percent gold alloy in a microgravity environment. The couples were to be in the molten state for about two hours which would allow the gold to diffuse on the order of 2.5 cm. If there were no convective stirring effects between the lead and Pb-0.05 atomic percent gold alloy, then a normal concentration-distance profile for the gold would be found in the diffusion couples. Since there were two diffusion temperatures (923 K and 723 K), it should be possible to estimate the liquid diffusion parameters for gold in lead. If there are convective stirring effects, then these effects should be found by the autoradiographic technique used for the diffusion analysis. The extent of the convective stirring effects (if present) were to be determined by examination of the wetting and nonwetting containers.

Surface tension induced convection could be expected if the specimens were not in contact with the ampoule walls. However, if the specimens touch the walls, the interface tension between the alloy and pure lead should not be able to create a convection effect according to the fluid dynamic theories that state there should be zero flow at the walls.[4] On the other hand, the zinc self-diffusion experiment[5] indicated that a little convection occurred in liquid zinc contained in a nonwetting capsule that was heated in a temperature gradient on

the order of 45 K/cm. The change in surface tension (not interface tension) with temperature has been reported to be in the range of -0.09 to -0.25 ergs $\cdot$ cm^{-2} $\cdot$ $(K)^{-1}$ for zinc.[6] This means a surface tension change of about 0.5 to 1.5 percent per centimeter in the zinc self-diffusion experiment could have occurred.

THE LEAD-GOLD SYSTEM

There were three major reasons for selecting a Pb/Pb-0.05 at. % gold diffusion couple for this experiment.

1. The melting point of lead (600 K) was low enough to provide a convenient temperature range for liquid diffusion while 0.05 atomic percent gold would be initially soluble in lead upon solidification. Any subsequent precipitation of Pb_2Au would be *in situ* thus still providing a marker for the original position of the gold. If the precipitation reaction is sluggish enough, the gold could be in solid solution at room temperature. Figure 1 is the portion of the lead-gold phase diagram of interest to this experiment. The calculated solubility line shown in Figure 1 is based on data from reference 7.

2. The nuclear properties of lead and gold make it an ideal diffusion couple to study by neutron activation techniques. Determination of the gold distribution in the lead matrix can be done by autoradiography. In this case samples were neutron irradiated in the center hole of the D_2O tank of the Bulk Shielding Reactor at Oak Ridge National Laboratory in essentially a pure thermal flux of 1.2×10^{12} neutrons/sec $\cdot$ cm^2. The nuclear data of interest for the lead and gold are shown in Table 1. After neutron activation the distribution of the gold was detected by placing a polished section of the sample on a nuclear emulsion

plate that is sensitive to 0.96 MeV electrons. By calibrating the emulsion sensitivity to β^- radiation using samples of lead containing known amounts of gold, quantitative analyses of the gold concentration in the experimental samples was made using a microphotometer to read the plates. This technique has been used successfully at ORNL for determinations of tungsten and tantalum in niobium.[8]

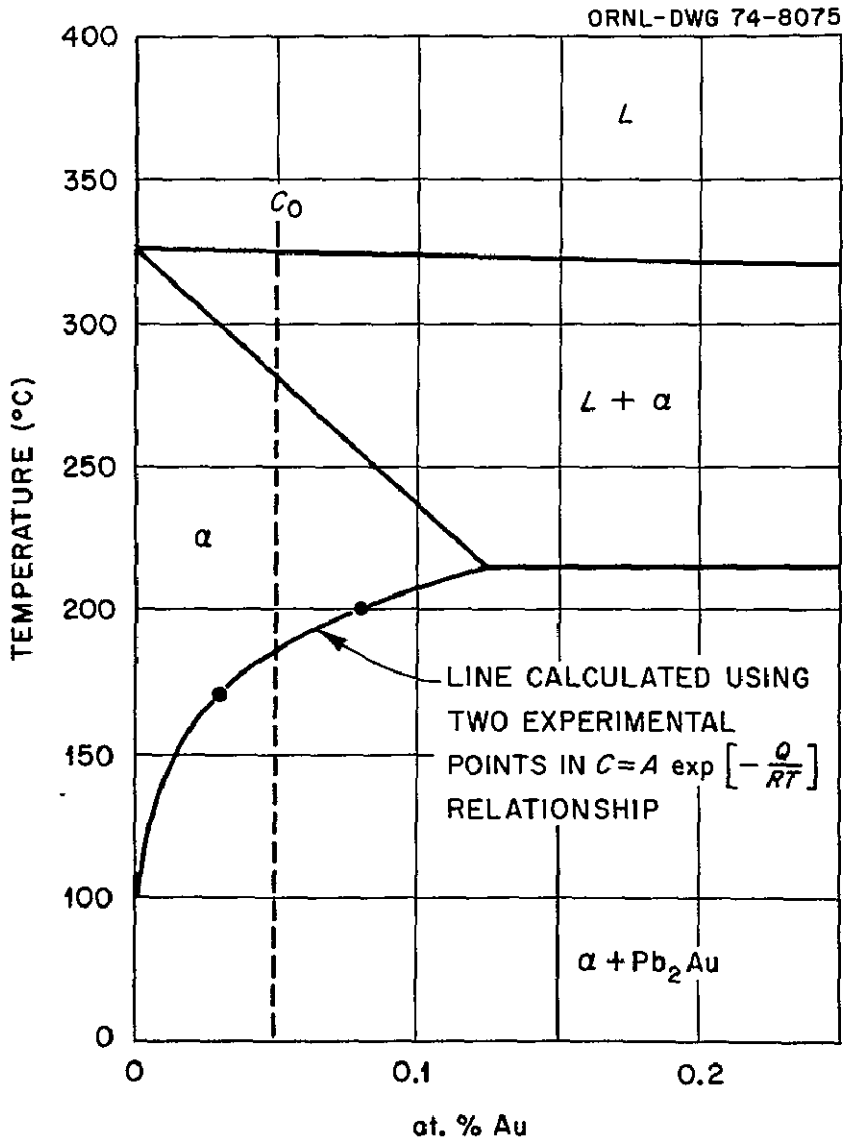

Figure 1. The lead-rich portion of the lead-gold binary phase diagram.[7]

3. It is believed that the lead-gold system has large variations of surface tension with changes in composition. The variation of surface tension with temperature ($d\sigma/dT$) is well known for lead from the melting point to about 1373 K.[9] In fact, $d\sigma/dT$ ranges from -0.062 to -0.120 ergs $\cdot$ cm^2 $\cdot$ $(K)^{-1}$. The variation of surface tension with composition ($d\sigma/dc$) has not been determined for the lead-gold system. However, a similar system, tin-copper, has been studied.[10] For tin-copper, a slight negative deviation from a linear relationship was found. Thus assuming a linear relationship between the surface tension of lead (395 erg $\cdot$ cm^{-2}) and gold (1125 erg $\cdot$ cm^{-2}) at a common temperature of 1373 K, $d\sigma/dc$ can be estimated to be about 7.3 erg $\cdot$ cm^{-2} $\cdot$ $(at.\ \%)^{-1}$. The interfacial energies for the alloy-graphite, lead-graphite, alloy-mild steel, and lead-mild steel systems are not known.

Table 1. Nuclear Data for Lead and Gold

Property	Lead	Gold
Nuclear Reaction	$^{208}Pb(n,\gamma)^{209}Pb$	$^{197}Au(n,\gamma)^{198}Au$
Abundancy	^{208}Pb 52.3%	^{197}Au 100%
Thermal Neutron Cross Section, Barns	0.0005	99
Radionuclide	^{209}Pb	^{198}Au
Type Decay	β^-	β^-
β^- Energy, MeV	100% 0.64	96% 0.96
Radionuclide Half-Life	3.3 hr	64.8 hr

EXPERIMENTAL DESIGN

A schematic representation showing the arrangement of the specimens in the multipurpose electric furnace is shown in Figure 2. Because of longitudinal heat flow in the furnace upon heating and cooling, the specimens melted from left to right with reference to the representation, Figure 2, and solidified in the reverse direction; as is shown, a total of six specimens were used in the experiment aboard Apollo-Soyuz. The furnace and the cartridges which contained the specimen ampoules were constructed such that each ampoule would experience minimum temperature gradients. Two of the three flight cartridges contained specimens loaded in graphite containers. The two cartridges were identical except for the fact the lead and 0.05 at. % gold alloy in one cartridge (Flight Cartridge 2) was located on the end which melted first; in the other

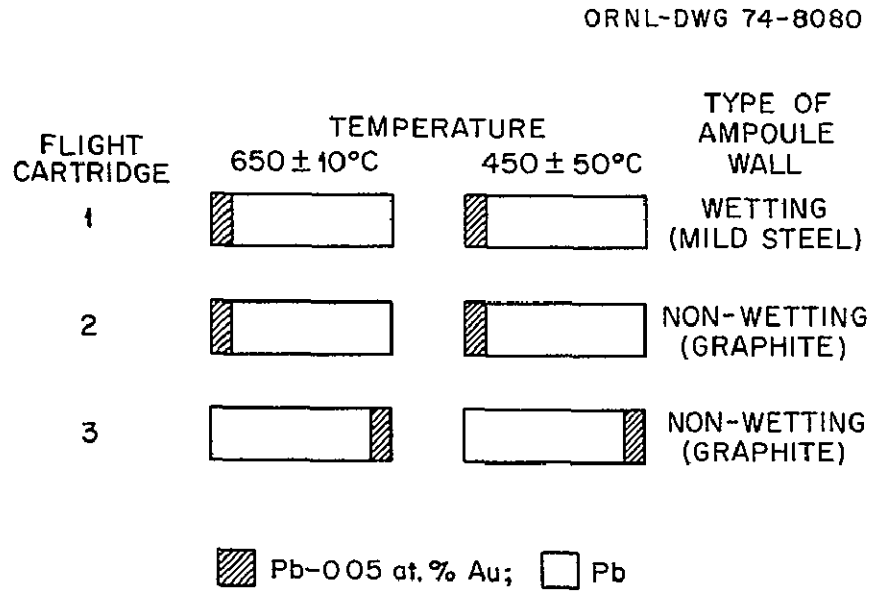

Figure 2. Schematic arrangement of specimens in Experiment ASTP MA-041.

cartridge (Flight Cartridge 3) the alloy was located on the reverse end of the specimen and thus melted last and solidified first. This arrangement was designed to determine if there was melting or solidification effects on the gold concentration profile. Flight Cartridge 1 (Figure 2) contained two specimens in a steel capsule with the lead-gold alloy aligned such that it melted first. An identical specimen arrangement to the one just described was used for ground base tests to provide comparison between the different transport mechanisms in liquid metals processed in space and in a unit gravity environment.

Dimensions of the actual specimens are shown in Figure 3. The total specimen length was approximately 3 cm and the diameter was approximately 1 cm. The 3-millimeter thick Pb-0.05 at. % gold alloy disk was cold-pressure welded to the pure lead. It should be noted that the total diffusion distance available was approximately 3 cm.

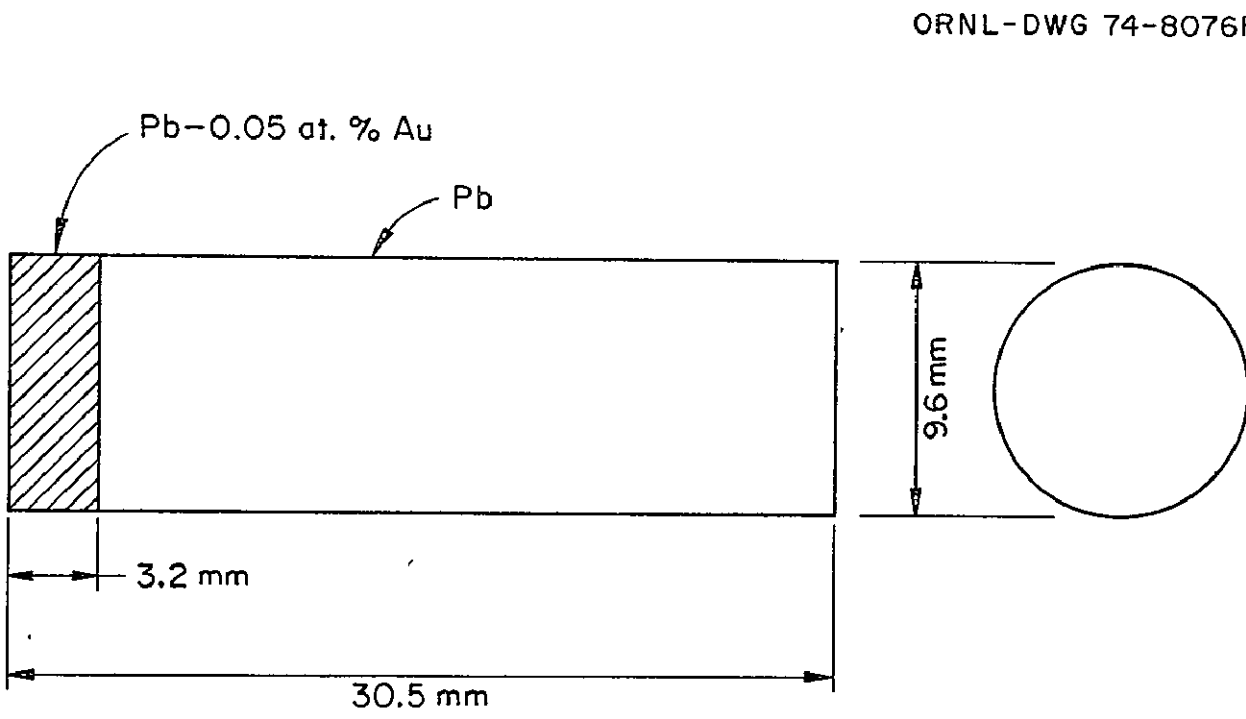

Figure 3. ASTP MA-041 specimen geometry.

Ampoules (mild steel and stainless steel lined with graphite) used for the specimens described in this report are shown in Figures 4 and 5, respectively. In the graphite lined container, quartz cloth disks were placed at each end to provide some padding for normal handling movements and to adjust the void space in the ampoule. Originally it was anticipated that the time the specimen would be in the liquid state would be approximately two hours for specimens attaining the 923 K temperature while specimens heated to 723 K would be molten approximately one hour. Liquid diffusion data for gold in lead is not available. However, by using the results from the zinc self-diffusion experiment performed on Skylab,[11] it was possible to estimate some diffusion distances for this experiment. Figures 6 and 7 give the calculated gold concentration-distance profiles for a geometry consisting of a 3 mm thick disk of Pb-0.05 at. % gold alloy bonded to pure lead to form a cylindrical specimen 3 cm long. These concentration-distance profiles were calculated using the solution for an extended source of limited extent from reference 12. The source width is h = 3 mm, the diffusion temperatures were 673 and 923 K for Figures 6 and 7, respectively. The

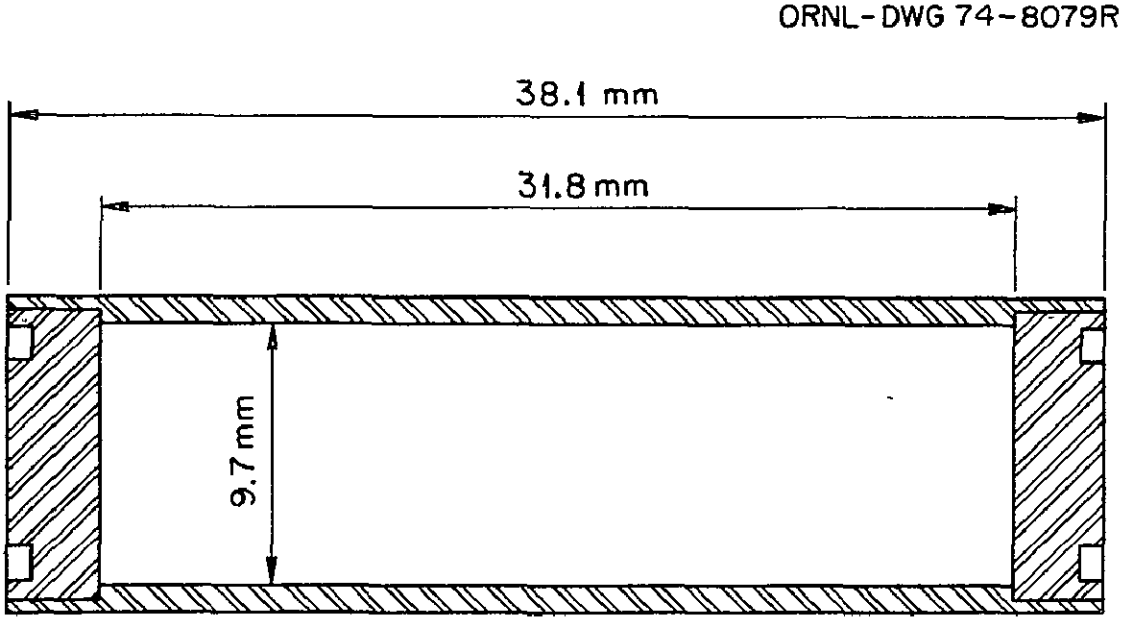

Figure 4. Ampoule assembly for B-type specimen capsules (Type 1015 steel).

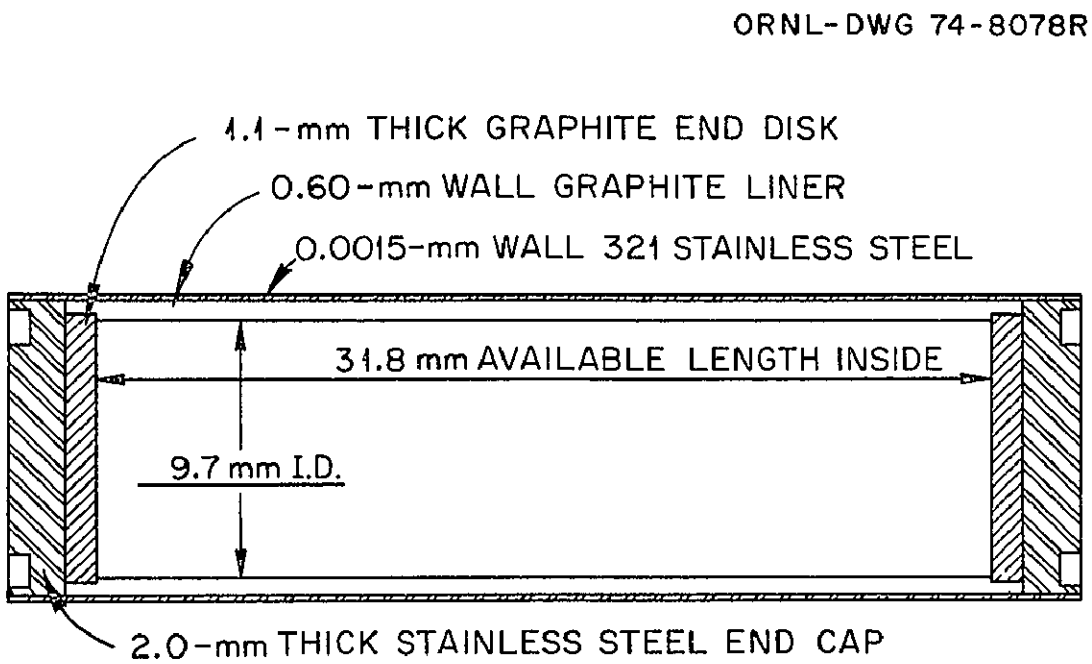

Stainless Steel–Graphite Ampoule Assembly.

Figure 5. Ampoule assembly for A and A-R specimens.

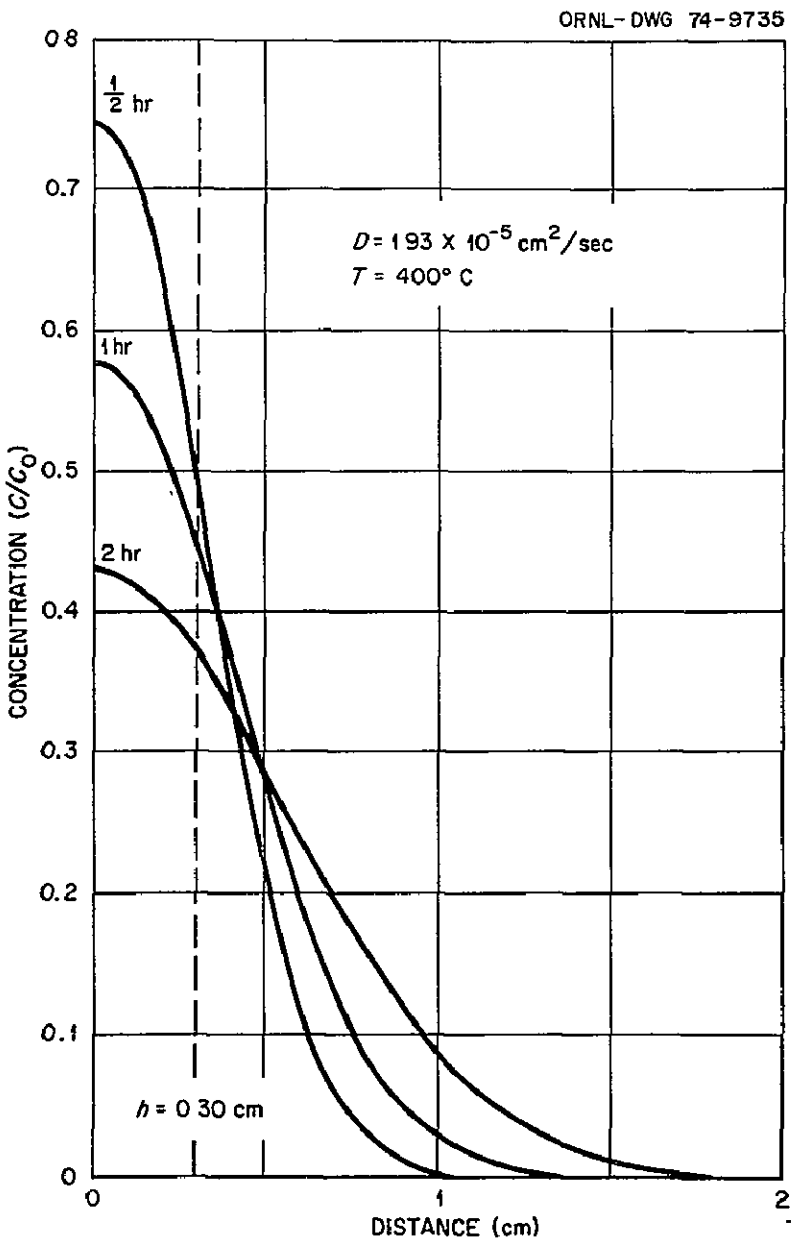

Figure 6. Concentration-distance profile calculated using the solution for an extended source of limited extent.[12] Source width, h = 3 mm, diffusion temperature = 400°C, diffusivity value, D, calculated from zinc self-diffusion data.[11]

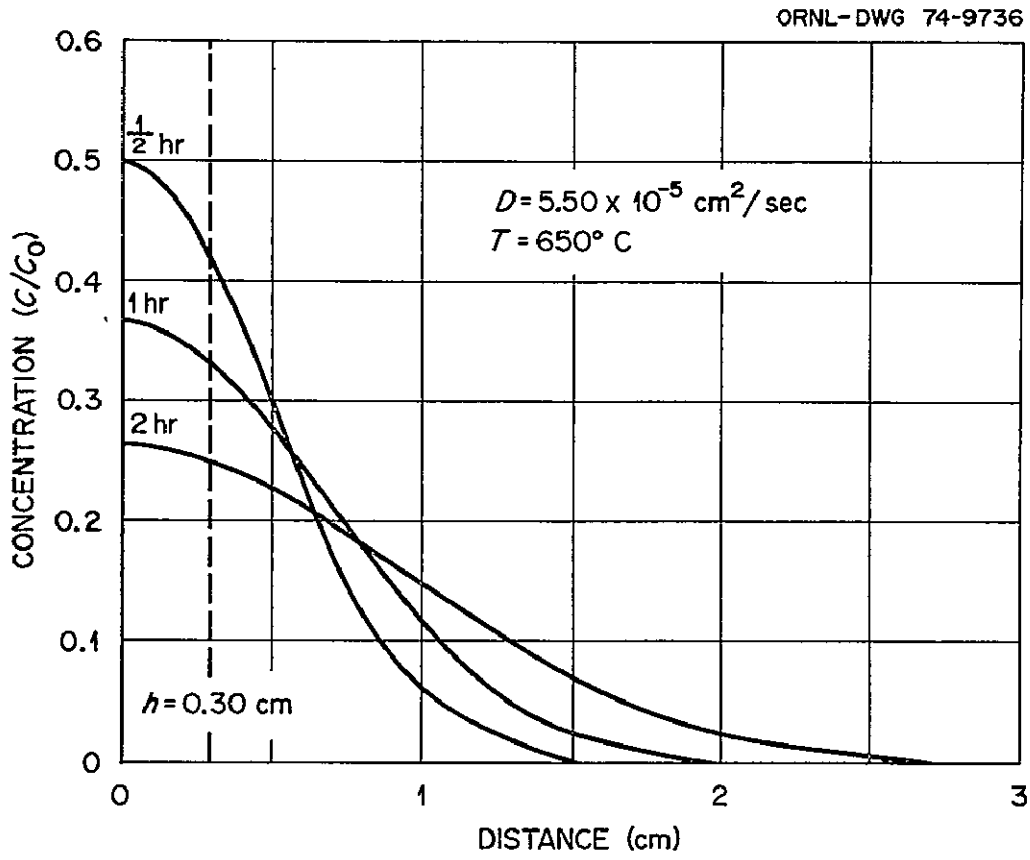

Figure 7. Concentration-distance profile calculated using the solution for an extended source of limited extent.[12] Source width, h = 3 mm, diffusion temperature = 650°C, diffusivity, D, calculated from zinc self-diffusion data.[11]

diffusivity value, D, is calculated from the zinc self-diffusion results of reference 5. Figure 6, which assumes an effective diffusion temperature of 673 K, shows that diffusion distances of about 1.5 cm would be achieved in one hour. Figure 7, calculated for 923 K, indicates a diffusion distance of 2.7 cm would be expected within two hours at temperature. Assuming C_0 (initial concentration of gold in lead) to be 500 atomic ppm, the gold concentration in the pellet would be reduced to 215 and 130 atomic ppm at 673 and 923 K, respectively. These estimated distances and concentrations were within the limits of the experimental design capabilities.

GROUND BASE AND SPACE FLIGHT THERMAL CHARACTERISTICS OF THE MULTIPURPOSE ELECTRIC FURNACE AND OTHER IMPORTANT EXPERIMENTAL PARAMETERS

Temperature-time data monitored on the mission were obtained by measurements made on the heat-leveler block of the multipurpose furnace (Figure 8). Subsequent to flight, a ground base test was made in which the space flight furnace operation was duplicated since its operation during the actual experiment was different from that originally planned. The thermal characterization analyses to obtain the temperature-time

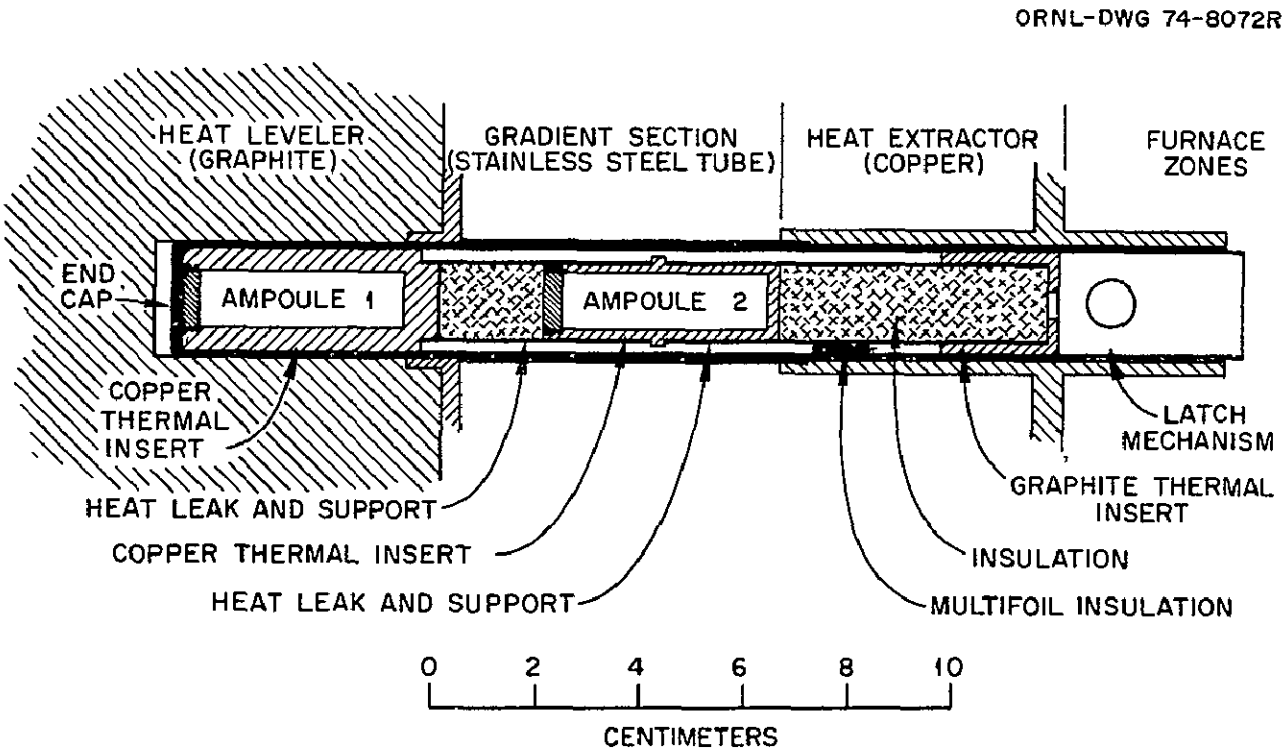

Figure 8. ASTP MA-041 advanced flight cartridge designed by Westinghouse Corporation.

history for the specimen ampoules both space flight (SF) and ground base (GB) samples were made by Teledyne Brown Engineering and the results are shown in Tables 2 through 5.[13] Relative node locations described in Tables 2 through 5 are shown in Figure 9. The temperature-time curves are shown in Figures 10 through 13. Table 6 lists the heating and

cooling rates for both ground base and space flight specimens at 600 K; these rates are based on the slopes of the temperature curves for nodes 312 and 322 (Figure 9). The approximate solidification rates for both the ground base and space flight samples were determined by dividing the change in temperature per unit time by the change in temperature per unit length. The results are shown on page 20.

Table 2. Ampoule A Temperature Profile and Gradient at Selected Times in GBT-25

Experiment Event	Temperature K					Ampoule Gradient* (K/cm)
	Node 410	Node 311	Node 312	Node 313	Node 414	
Pre-Melt	604.9	599.6	599.1	598.7	598.4	1.7
Start Soak**	816.9	811.2	810.3	809.6	809.2	2.0
Mid Soak	925.5	922.6	922.0	921.3	921.0	1.2
End Soak*** (ES)	928.5	925.7	925.1	924.4	924.1	1.1
ES + 10 min.	899.2	897.4	896.9	896.3	895.9	0.9
ES + 30 min.	827.8	825.9	825.6	825.1	824.9	0.8
ES + 60 min.	739.2	737.8	737.4	737.1	736.9	0.6
Pre-Solidification	603.8	602.8	602.7	602.4	602.3	0.4

*Ampoule gradient = (T 410 - T 414)/3.81.

**Soak started 70 min. after furnace on.

***Soak ended 115 min. after furnace on.

Table 3. Ampoule B Temperature Profile and Gradient at Selected Times in GBT-25

Experiment Event	Temperature K					Ampoule Gradient* (K/cm)
	Node 420	Node 321	Node 322	Node 323	Node 421	
Start Soak**	545.2	545.1	542.3	540.1	540.1	1.3
Pre-Melt	599.9	599.8	596.8	594.2	594.1	1.5
Mid Soak	691.4	691.2	687.7	684.7	684.6	1.8
End Soak*** (ES)	700.7	700.5	697.0	694.1	693.9	1.8
ES + 10 min.	657.9	657.8	654.3	651.4	651.3	1.7
ES + 30 min.	650.4	650.3	647.7	645.5	645.4	1.3
Pre-Solidification	605.2	605.1	602.6	600.8	600.4	1.3
ES + 60 min.	600.5	600.4	598.2	596.4	596.3	1.1

*Ampoule gradient = (T 410 - T 414)/3.81.

**Soak started 70 min. after furnace on.

***Soak ended 115 min. after furnace on.

Table 4. Ampoule A Temperature Profile and Gradient at Selected Times in Flight

Experiment Event	Temperature K					Ampoule Gradient* (K/cm)
	Node 410	Node 311	Node 312	Node 313	Node 414	
Pre-Melt	600.6	595.4	594.8	594.7	594.5	1.6
Start Soak**	922.3	919.7	919.2	918.6	918.3	1.1
Mid Soak	932.7	930.3	929.8	929.2	928.9	1.0
End Soak*** (ES)	936.1	933.8	933.3	932.8	932.5	0.9
ES + 10 min.	886.0	884.0	883.5	883.0	882.7	0.9
ES + 30 min.	840.3	839.7	839.3	838.8	838.6	0.5
ES + 60 min.	718.9	717.5	717.2	716.9	716.8	0.6
Pre-Solidification	604.6	603.7	603.5	603.3	603.2	0.4

*Ampoule gradient = (T 410 - T 414)/3.81.

**Start soak 95 min. after furnace on.

***End soak 127 min. after furnace on.

Table 5. Ampoule B Temperature Profile and Gradient at Selected Times in Flight

Experiment Event	Temperature K					Ampoule Gradient* (K/cm)
	Node 420	Node 321	Node 322	Node 323	Node 421	
Pre-Melt	597.3	597.2	594.4	592.0	591.9	1.4
Start Soak**	675.1	674.9	671.3	668.2	668.1	1.8
Mid Soak	701.3	701.1	697.5	694.5	694.4	1.8
End Soak*** (ES)	710.7	710.5	707.1	704.1	704.0	1.8
ES + 10 min.	650.2	650.0	646.7	643.8	643.7	1.7
ES + 30 min.	631.3	631.2	628.5	625.8	625.7	1.5
Pre-Solidification	603.5	603.4	601.5	600.6	600.1	0.9
ES + 60 min.	582.7	582.7	581.0	579.5	579.5	0.8

*Ampoule gradient = (T 420 - T 421)/3.81.

**Start soak 95 min. after furnace on.

***End soak 127 min. after furnace on.

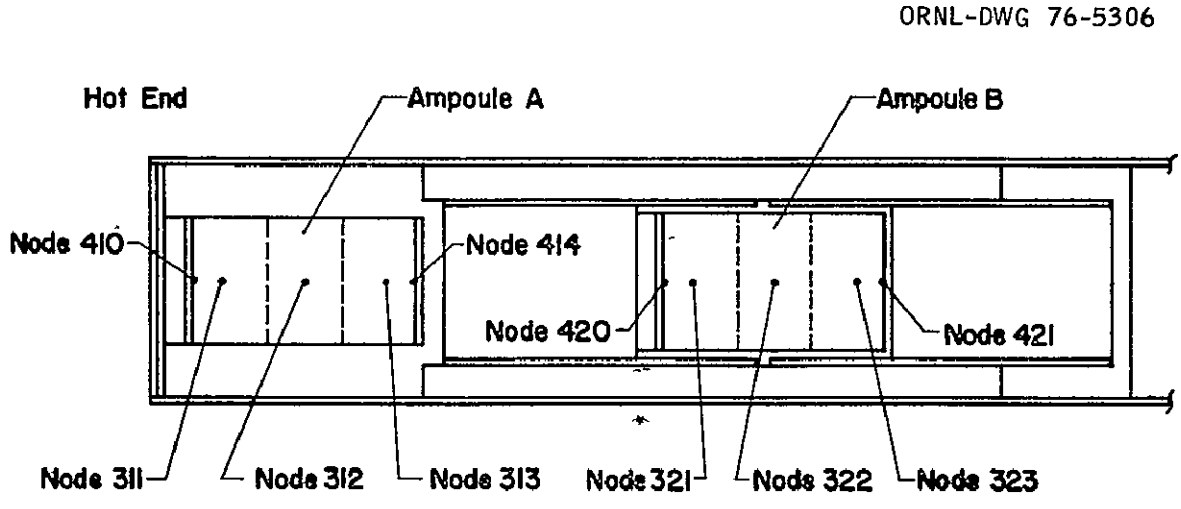

Figure 9. Schematic representation of the relative node locations used in both ground base and space flight thermal analyses. Ampoules A and B represent the 923 K and 723 K temperature zones of the multi-purpose electric furnace, respectively.

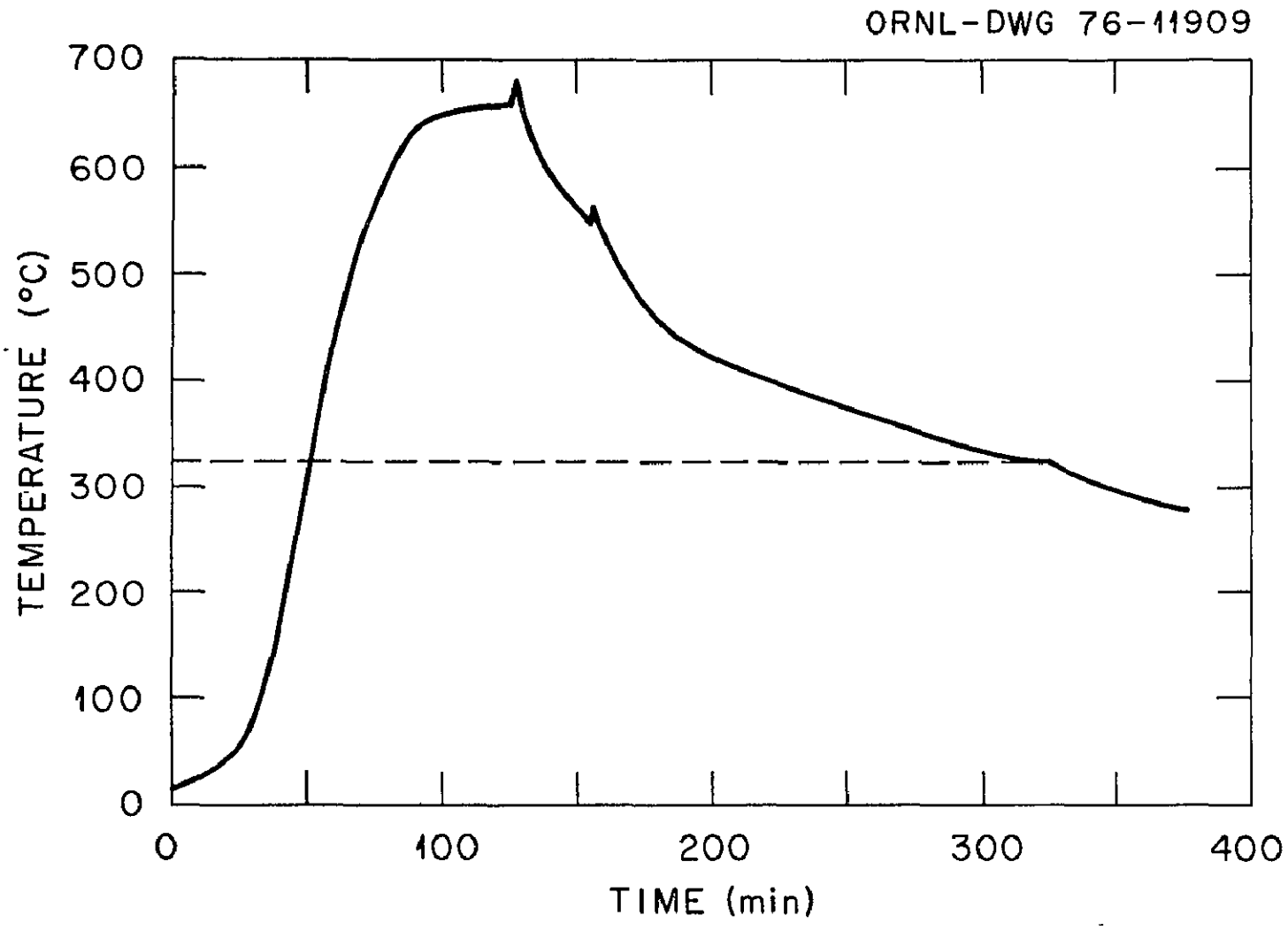

Figure 10. Temperature-time history for the 923 K space flight specimens. The dotted line is at 600 K, the melting point of lead.

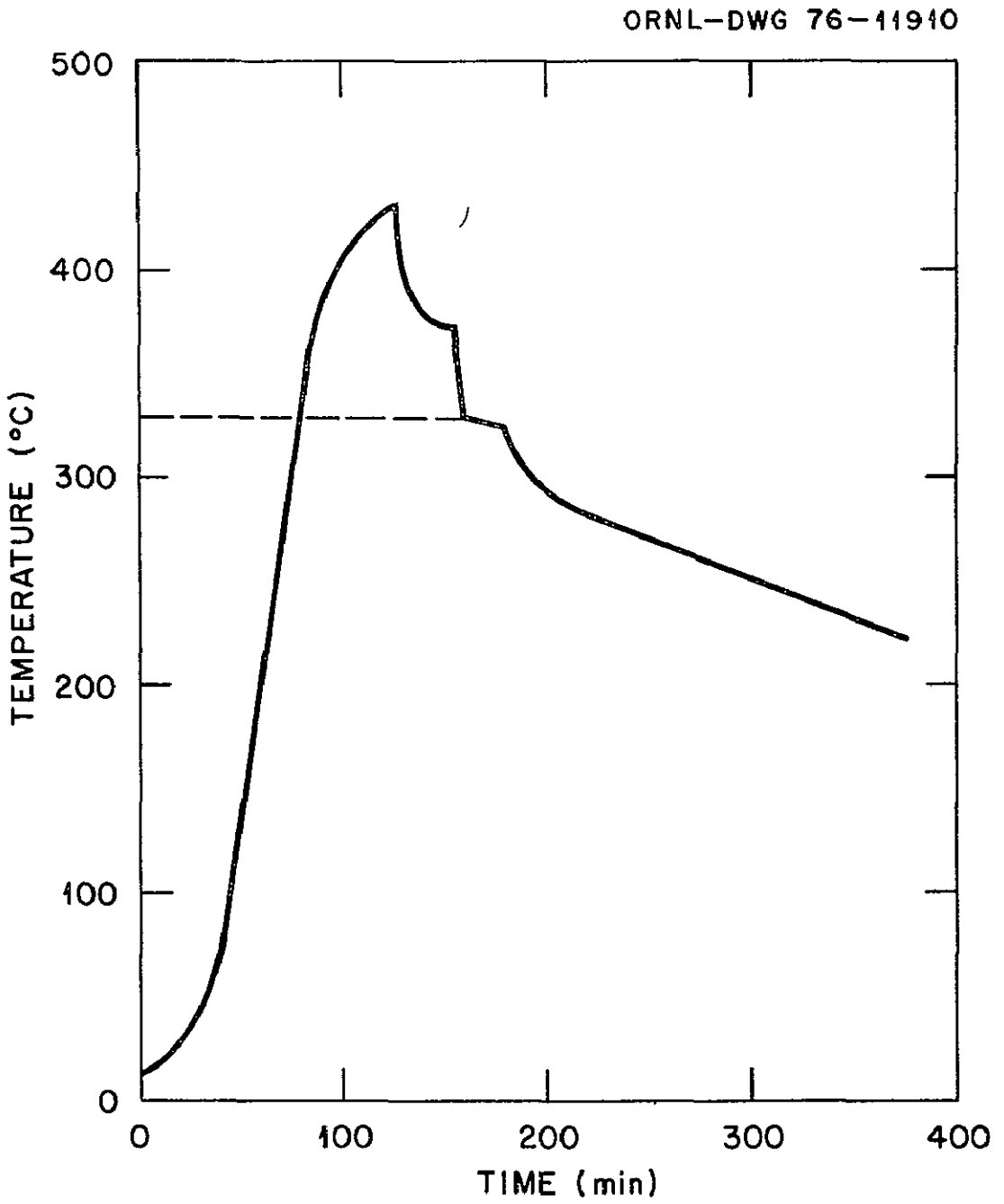

Figure 11. Temperature-time history for the 723 K space flight specimens. The dotted line is at 600 K, the melting point of lead.

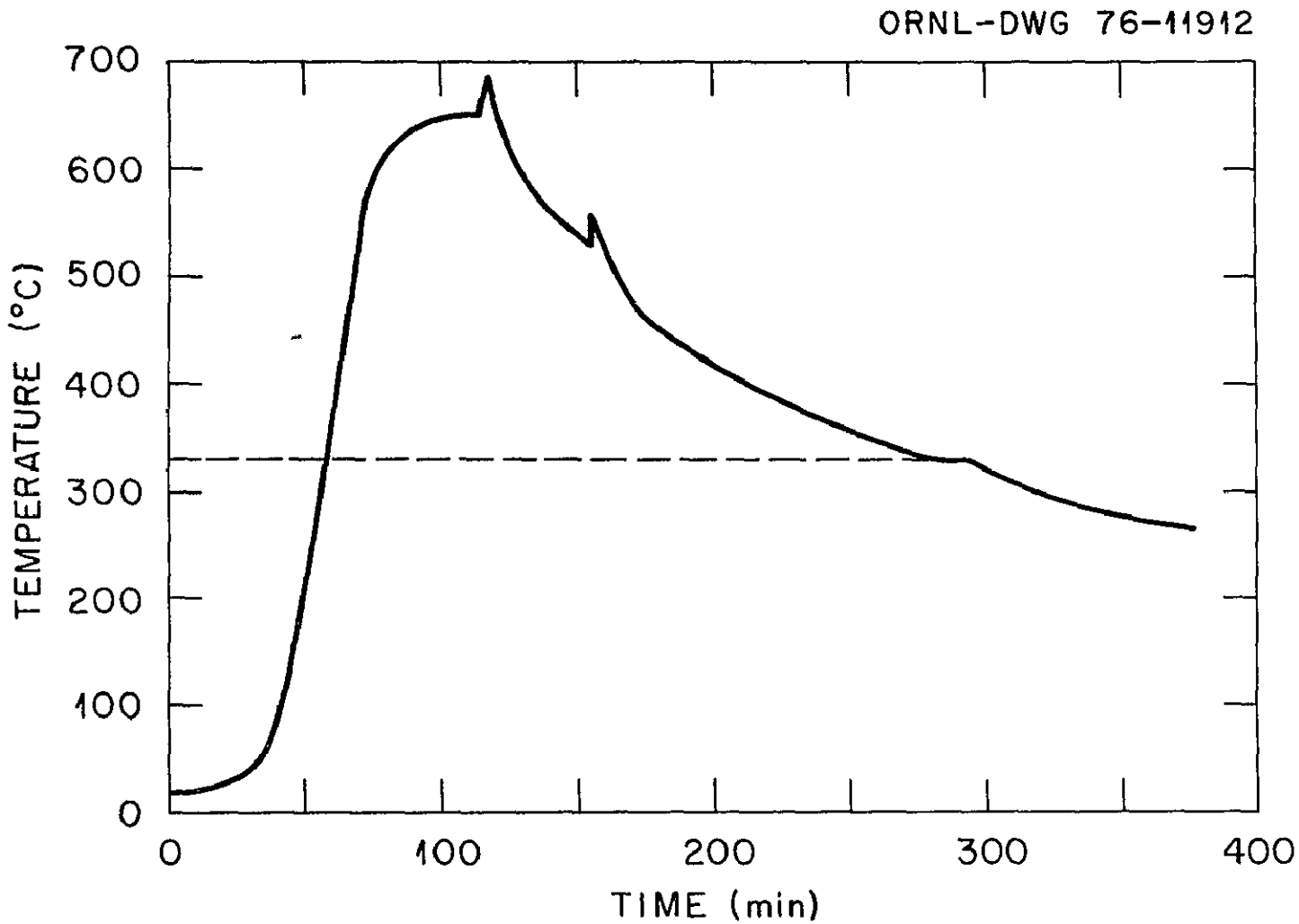

Figure 12. Temperature-time history for the 923 K ground base specimens. The dotted line is at 600 K, the melting point of lead.

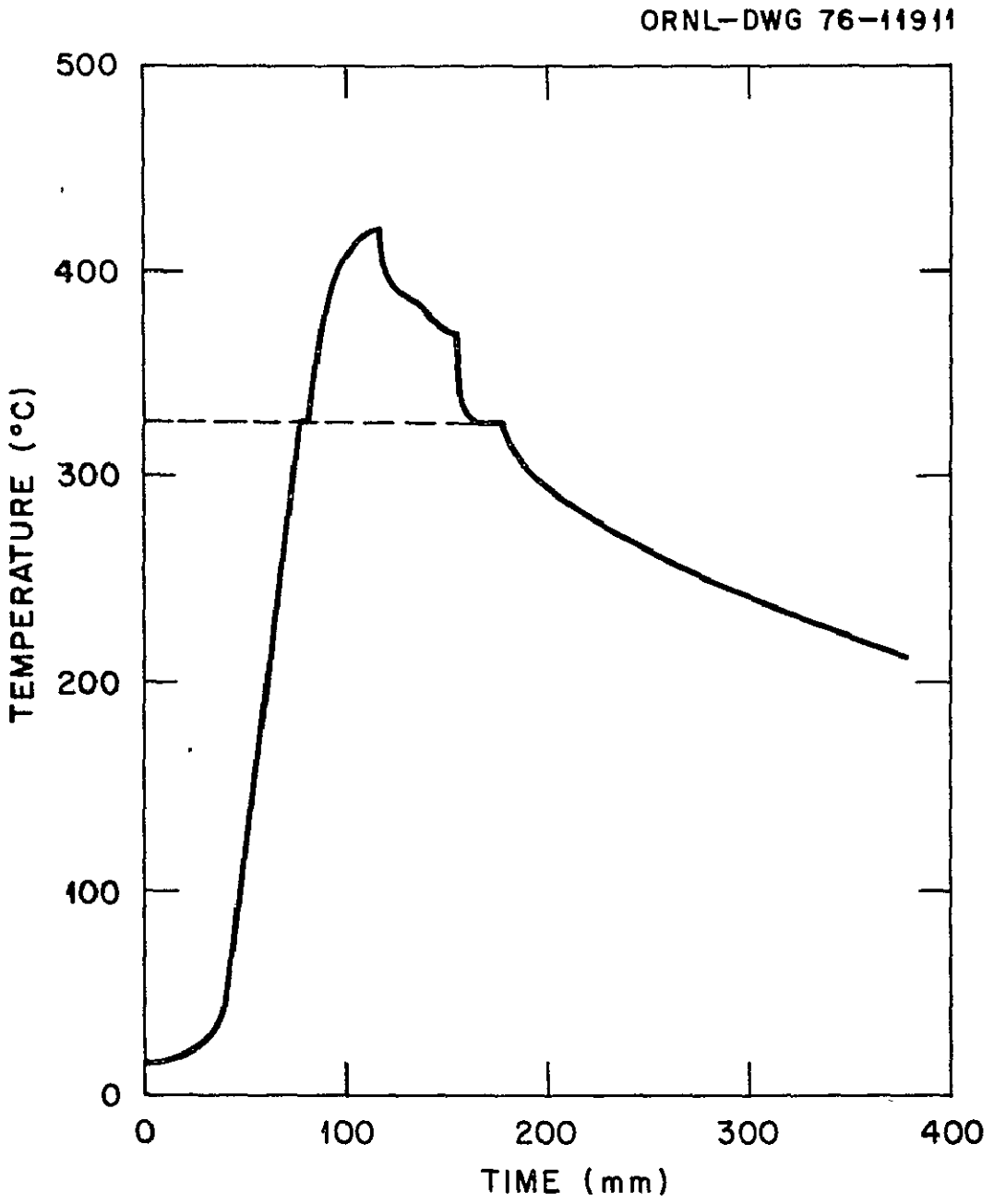

Figure 13. Temperature-time history for the 723 K ground base specimens. The dotted line is at 600 K, the melting point of lead.

Table 6. Heating and Cooling Rates for Ground Base and Space Flight Specimen Ampoules

Characteristic	Ground Base Temperature History* (GBT-25 - Teledyne Brown Engineering)		Space Flight Temperature History** (Teledyne Brown Engineering)	
	923 K Zone	723 K Zone	923 K Zone	723 K Zone
Heating Rate at 600 K (K/min.)	7	2	11	4
Cooling Rate at 600 K (K/min.)	1	10	1	5

*Heating and cooling rates based on the slopes of the temperature curves at 600 K at nodes 312 and 322 for GBT-25.[13]

**Heating and cooling rates based on the slopes of the temperature curves at 600 K at nodes 312 and 322 for the space flight ampoules.[13]

1. 2.5 cm/min. for the 923 K temperature zone ground base samples,
2. 9.0 cm/min. for the 723 K temperature zone ground base samples,
3. 2.5 cm/min. for the 923 K temperature zone space flight samples,
4. 6.0 cm/min. for the 723 K temperature zone space flight samples.

It was determined from the flight analyses that the ampoules A and B (Figure 9) were in the liquid phase for 268 and 82 min., respectively. In the GBT-25 experiment the samples remained in the liquid phase 226 and 77 min. for ampoules A and B, respectively.[13] Some additional experimental values that must be considered in the experimental analyses are listed below.

1. Relative density difference between the alloy and the lead was 1.76×10^{-4}.
2. The equilibrium distribution coefficient of gold in lead is nearly 0.3.
3. Cooling rates were in the range of 1 to 10 K/min.
4. The temperature gradient was purposely kept small so as to maintain a constant temperature diffusion rate and was in the range of 0.4 to 2.0 K/cm (Tables 2 through 5).
5. Calculated solidification velocity was in the range of 2.5 to 9 cm/min.

The previous experimental values are summarized in Table 7.

The average acceleration of the space flight specimens (SFS) during the experiment was <0.1 milligees; maximum acceleration was caused by the thrusters but was <6 milligees for time periods of 15 milliseconds.

Table 7. Important Experimental Values

Terms	Symbol	Value(s)
$\frac{\text{Alloy Density-Lead Density}}{\text{Lead Density}}$	$\frac{\Delta\rho}{\rho}$	1.76×10^{-4}
Equilibrium Distribution Coefficient	K	0.3
Cooling Rates	dT/dt	1 - 10 K/min.
Temperature Gradient	G	0.4 - 2.0 K/cm
Solidification Velocity	V	2.5 - 9 cm/min.

SAMPLE PREPARATION FOR POST-MISSION ANALYSES

Sample numbers for each specimen used in both the ground base and space flight experiments are shown in Tables 8 and 9. After completion of the melting experiments (both ground base and space flight) the samples were returned to the Oak Ridge National Laboratory (ORNL) for sectioning and subsequent analysis. After removal from the ampoules, specimens A and A-R were potted in epoxy for longitudinal sectioning. Since the B specimens were contained in the mild steel ampoules which should have been wet by the molten alloy, the ampoules were mounted in epoxy resin and the ampoules, together with the B alloy specimens, were sectioned longitudinally. The epoxy potting material was then dissolved and each sample together with seven lead-gold alloy calibration disks were then remounted in a 5-cm diam epoxy mount and metallographically polished.

The samples were irradiated in the Bulk Shielding Reactor (BSR) at ORNL for 4 hr in essentially a pure thermal flux of 1.2×10^{12} neutrons/sec $\cdot$ cm^2. During irradiation both ^{209}Pb and ^{198}Au are formed. The activity of interest is ^{198}Au which decays by the emission of 0.960 MeV beta particles with a half life of 64.8 hr. The ^{209}Pb formed during the irradiation is essentially nonexistent after approximately 24 hr since the thermal neutron cross section for forming ^{209}Pb from ^{208}Pb is small and the ^{209}Pb half life is only 3.3 hr. After the radioactive nuclides decayed for 24 to 30 hr, autoradiographs of the specimens were made.

Autoradiographs were made in complete darkness in the same darkroom in which the film was developed subsequent to exposure. The polished face of the mount was placed face down on Kodak Industrial Type "R" X-Ray film, an ultrafine grain, single emulsion film. Exposures were made for 8, 16, 32, 64, 128, and 256-min. durations. The film is sensitized by β^- emission from the gold in the lead. Since the range of the 0.960 MeV β^- in lead is approximately 0.4 mm, only the gold concentration in this layer thickness is detected.

Table 8. Sample Number, Container Type, Temperature Region and Pb-0.05 at. Percent Gold Location for Space Flight Specimens

Container Type	Temperature Region, Lead-Gold Alloy Location and Sample Numbers	
	923 K Zone	723 K Zone
Graphite	* | 11-A	* | 21-A
Graphite	13 A-R | *	17 A-R | *
Mild Steel	* | 12-B	* | 21-B

*Pb-0.05 at. percent gold.

Table 9. Sample Number, Container Type, Temperature Region and Pb-0.05 at. Percent Gold Location for Ground Base Specimens

Container Type	Temperature Region, Lead-Gold Alloy Location and Sample Numbers	
	923 K Zone	723 K Zone
Graphite	* | 17-A	* | 14-A
Graphite	11 A-R | *	20 A-R | *
Mild Steel	* | 13-B	* | 15-B

*Pb-0.05 at. percent gold.

Originally seven lead-gold standards of 0, 20, 52, 91, 217, 277, and 393 at. ppm gold were used. The arrangement of the standards and specimen for the first irradiation is as shown in Figure 14. Beta scattering from the standards distorted the gold concentration profiles in both the GB and SF specimens in the area of the specimens adjacent

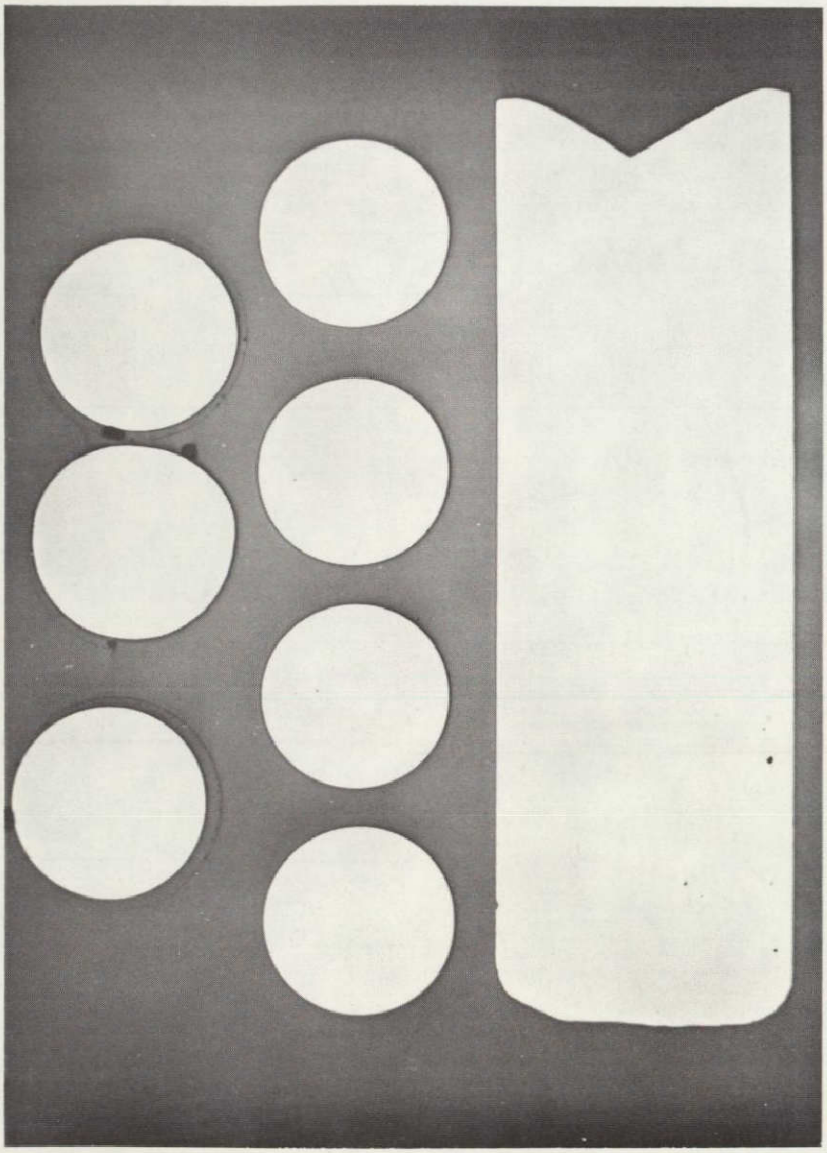

Figure 14. A macrograph of the longitudinally cut surface of Space Flight Specimen 17 A-R and seven lead-gold standards mounted in epoxy resin.

to the standards. In addition, beta scattering influenced the radiation values obtained for each standard. Thus, to eliminate the beta scattering problem, two epoxy mounts were necessary; one contained the lead-gold standards and one contained the specimen. This arrangement is shown in Figure 15. The 277 and 393 at. ppm gold standards were not used because the original irradiation verified that all the gold concentrations in the specimens were below these values.

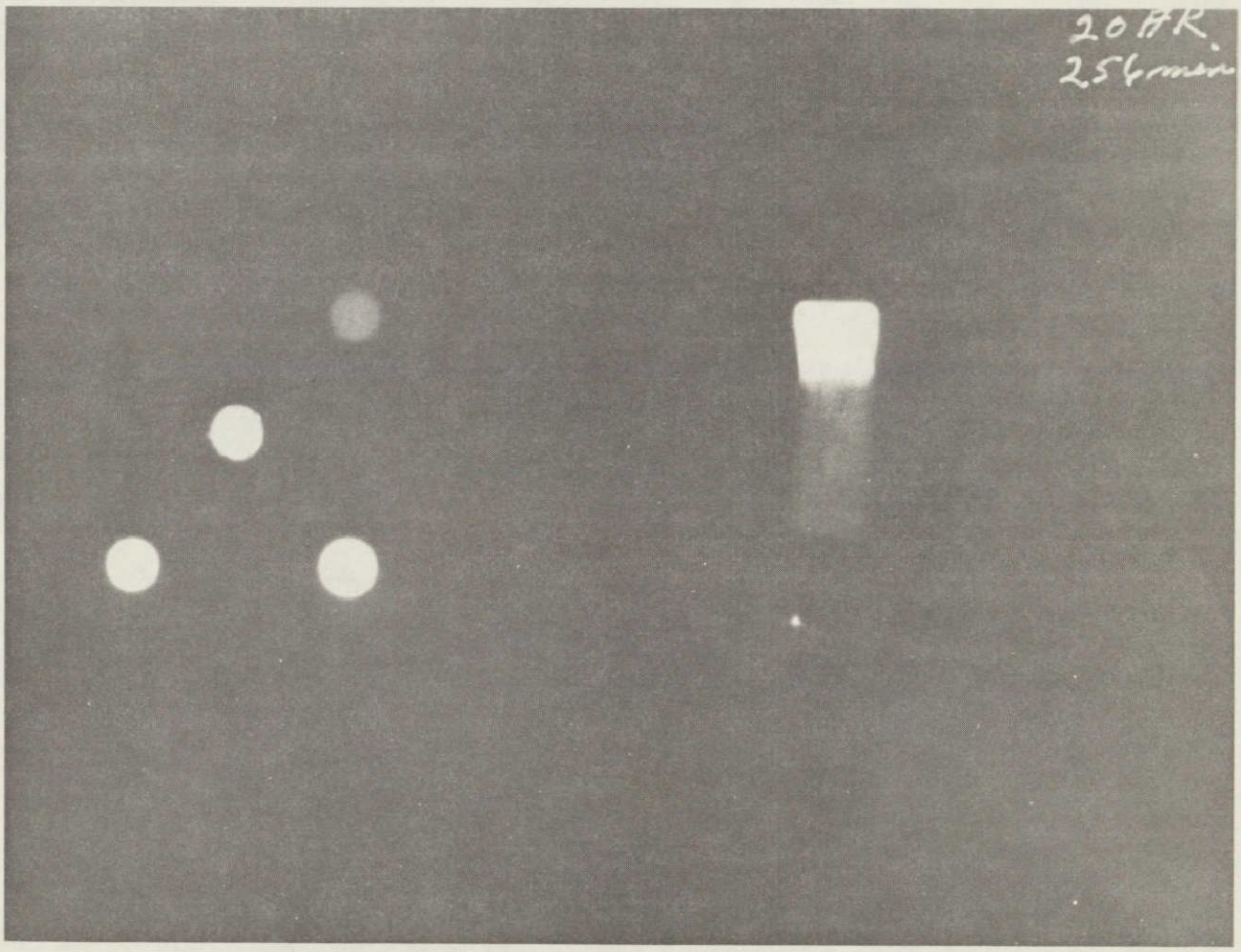

Figure 15. A print taken from a deliberately overexposed autoradiograph showing the relative locations of the lead-gold standards and the specimen during the autoradiography. Light areas indicate gold activity.

EXAMINATION OF EXTERIOR AND LONGITUDINAL CUTS OF GROUND BASE AND SPACE FLIGHT SPECIMENS

A visual examination of both the GB and SF specimens after the removal from the ampoules, revealed no evidence of oxidation. The exterior surfaces of the A and A-R GB specimens are shown in Figures 16 through 21. The side view of GB specimens 17 A and 14 A is shown in Figure 16. The specimens were mounted vertically in the multipurpose electric furnace and were located in the 923 and 723 K temperature

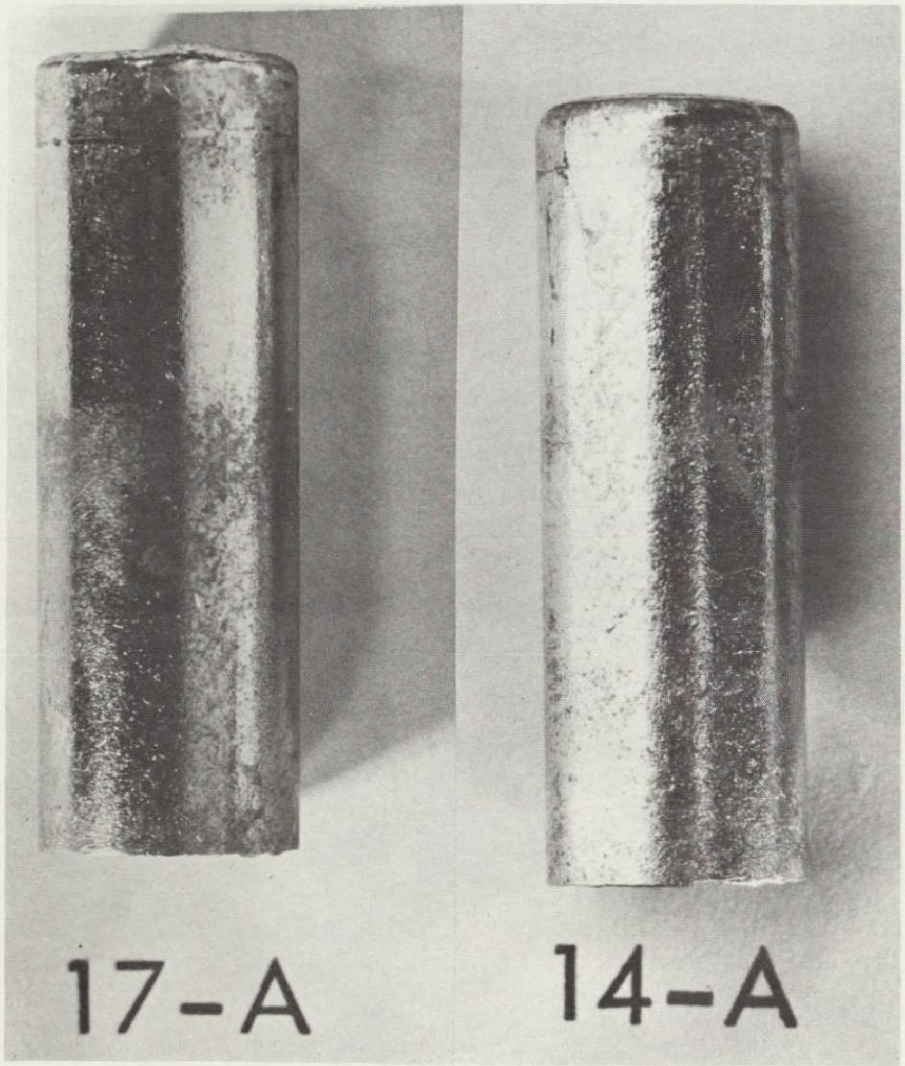

Figure 16. Photograph of ground base specimens 17 A and 14 A which were located in the 923 K and 723 K temperature zones of the multipurpose furnace, respectively. Samples solidified from the bottom to top in ampoules with nonwetting walls. Samples are approximately 1-cm diam.

zones, respectively. The samples melted from the top to the bottom (Figure 16) and upon cooling solidified in the reverse direction. As is shown, the original bond interface of the lead-gold disks can still be discerned at the top of each specimen. In addition, both specimens show the expected sharp corners at the base.

A bottom view of 17 A and 14 A is shown in Figure 17. This figure shows the sharp corners as well as ripples due to the quartz spacer cloth. Figure 18 shows the top view of GB specimen 17 A. Evidence of a solidification pipe can be seen which was not evident for 14 A.

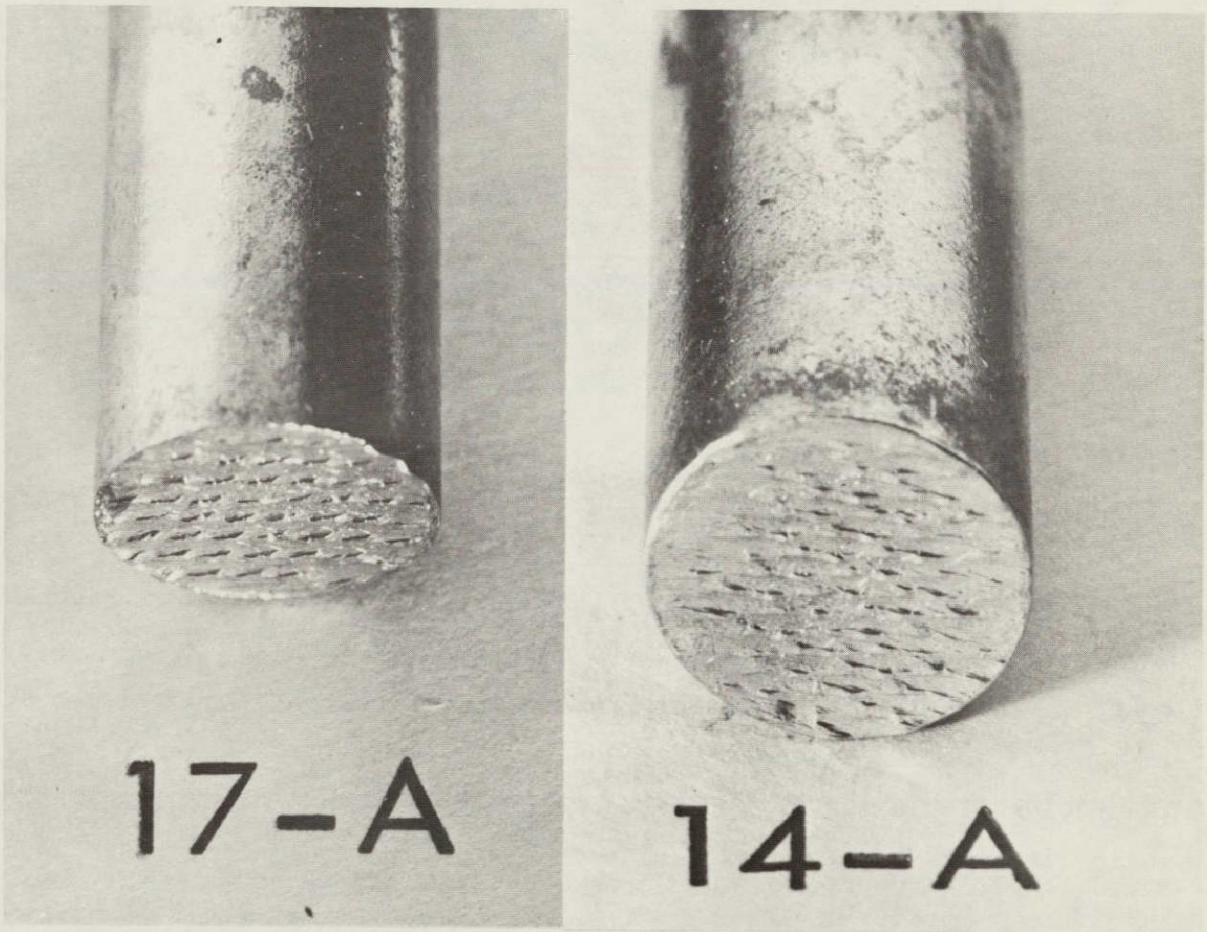

Figure 17. Photograph of the bottom ends of ground base specimens 17 A and 14 A.

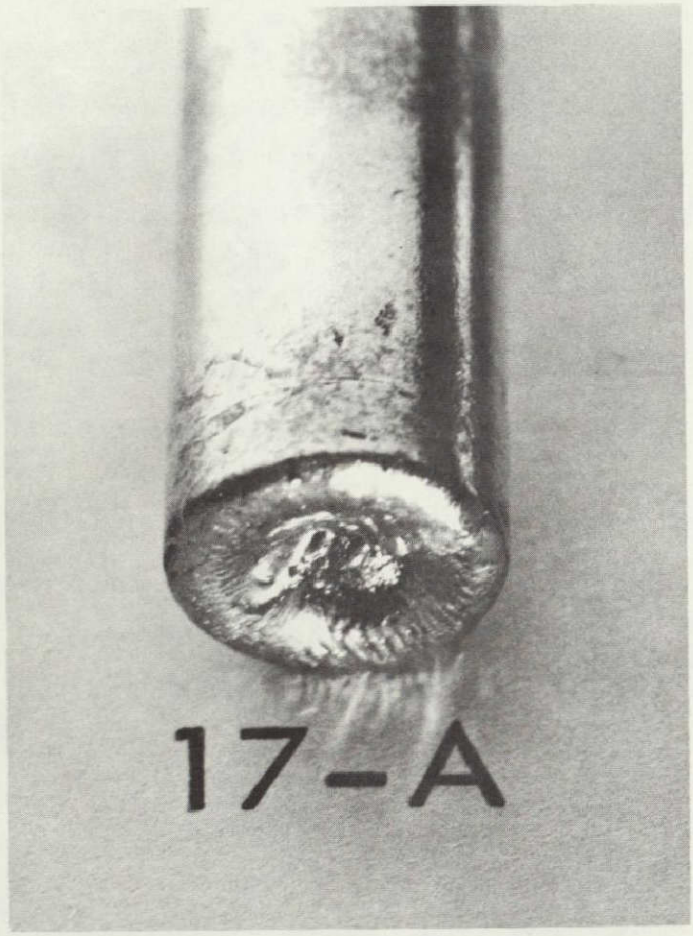

Figure 18. Photograph of the top end of ground base specimen 17 A.

A side view of GB specimens 11 A-R and 20 A-R is shown in Figure 19. As for the previous specimens (17 A and 14 A), 11 A-R and 20 A-R were mounted vertically in the multipurpose electric furnace and were located in the 923 and 723 K temperature zones, respectively. However, the lead-gold alloy disks were located at the bottom and melted last and solidified first. Again, one can see the original bond interface and the square corners at the bottom of the specimen. The top view of 11 A-R and 20 A-R is shown in Figure 20. Evidence of a solidification pipe can be seen for 11 A-R but not for 20 A-R. A bottom view of the two specimens can be seen in Figure 21. Characteristics to note are the ripples due to the quartz spacer cloth and the lead-gold bond interface.

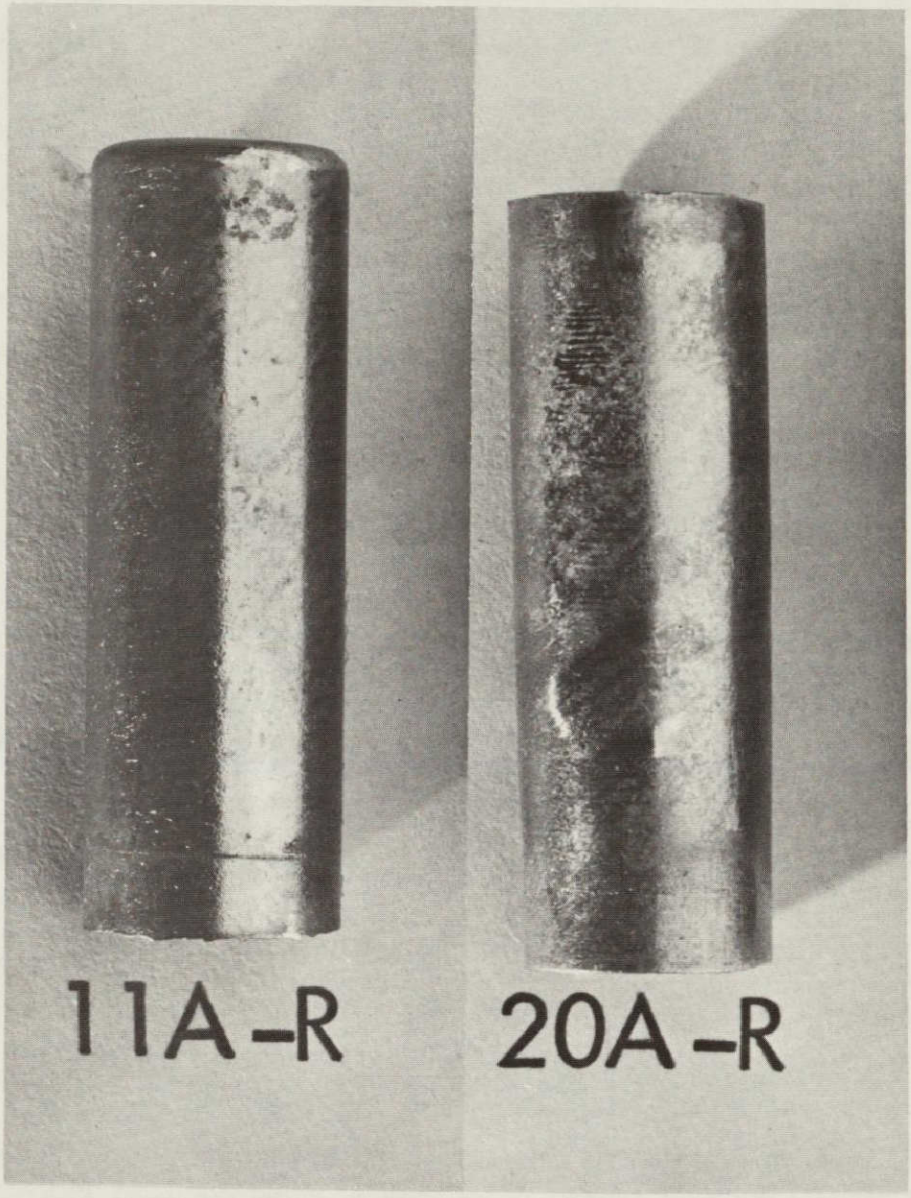

Figure 19. Photograph of ground base specimens 11 A-R and 20 A-R which were located in the 923 K and 723 K temperature zones of the multipurpose furnace, respectively. Samples solidified from the bottom to top.

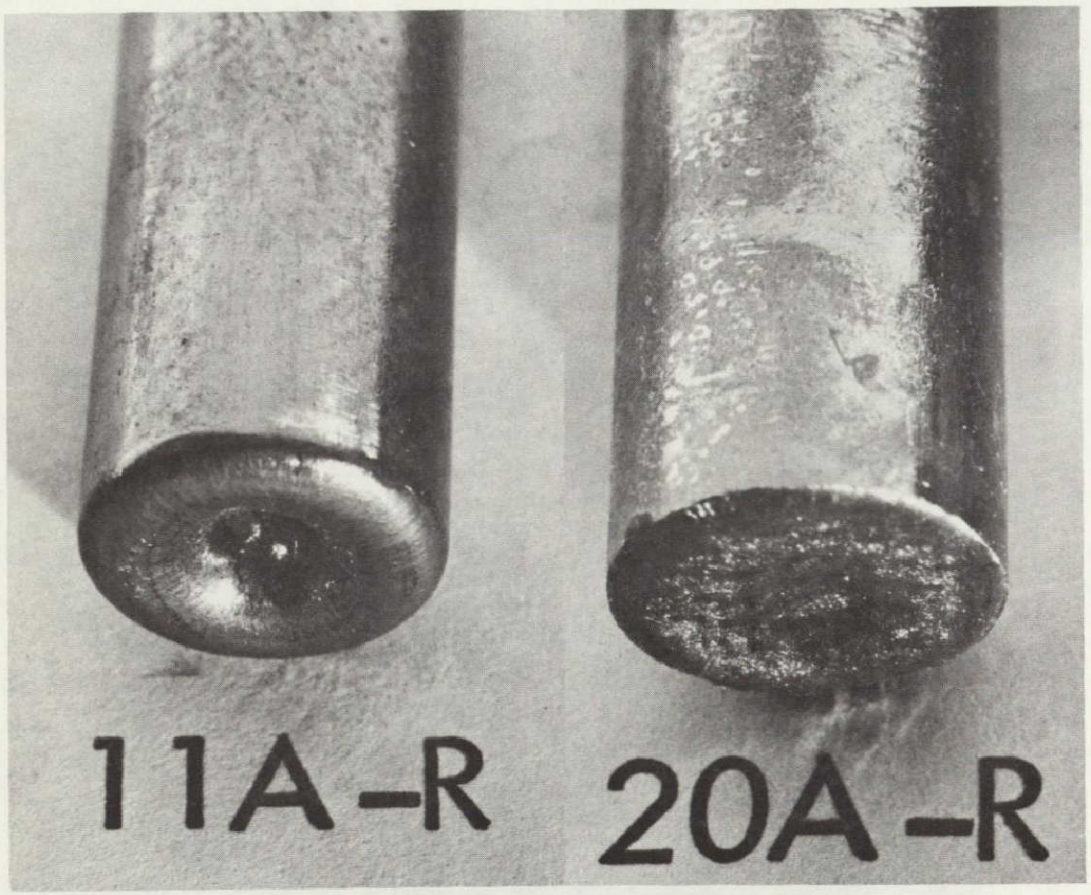

Figure 20. Photograph showing a top view of ground base specimens 11 A-R and 20 A-R.

Macrographs of the metallographically polished longitudinal surfaces of GB specimens 17 A, 11 A-R, 14 A, and 20 A-R are shown in Figures 22 through 25, respectively. The solidification pipe is clearly seen for the two 923 K specimens which are shown in Figure 22 and Figure 23. The 723 K specimens shown in Figures 24 and 25 show very square corners and no evidence of solidification pipes.

The exterior surfaces of the A and A-R SF specimens are shown in Figures 26 through 31. A side view of SF specimens 11 A and 21 A is shown in Figure 26. Cellular structure at the top of the specimen is evident for 11 A which was located in the 923 K temperature zone, but it is not as evident for the 723 K zone specimen (21 A). The specimens melted from the top to the bottom (Figure 26) and solidified in the reverse direction. An end view of 11 A and 21 A is shown in Figure 27. The space flight samples have rounded edges and no evidence of ripple

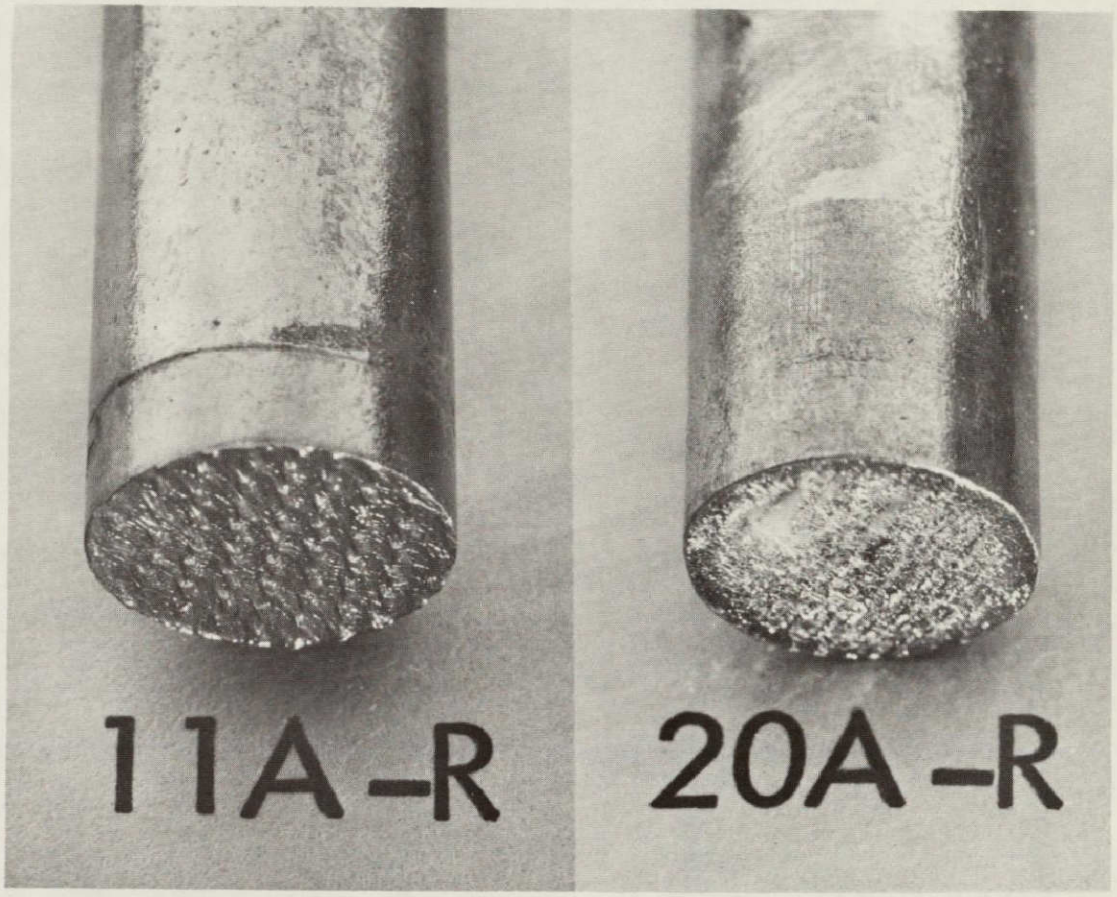

Figure 21. Photograph showing bottom views of ground base specimens 11 A-R and 20 A-R.

marks from the quartz spacer cloth. An end view showing the lead-gold alloy disk region for SF specimen 11 A is shown in Figure 28. The cellular structure and the lead-gold bond interface are clearly distinguished.

A side view of SF specimens 13 A-R and 17 A-R is shown in Figure 29. Again one can see the cellular structure for the 923 K temperature zone specimen (13 A-R) in the gold rich region at the bottom. This is not evident for the 723 K zone specimen (17 A-R). An end view (opposite from the lead-gold alloy disk) in Figure 30 shows evidence for

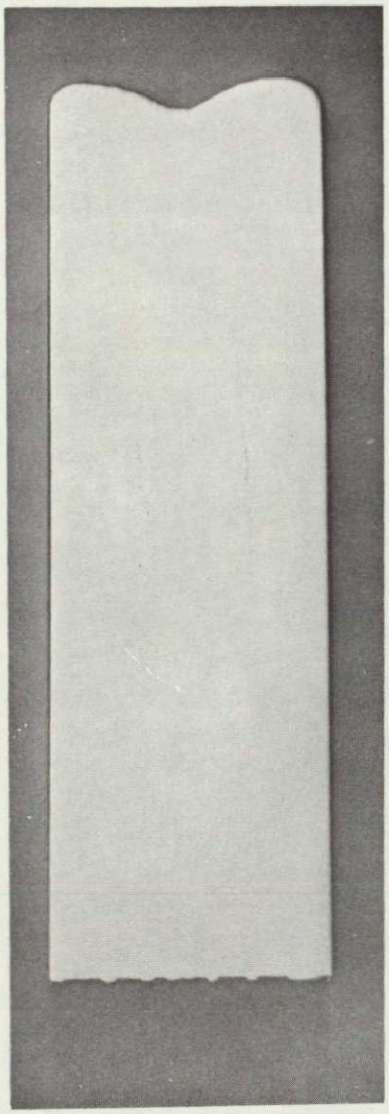

Figure 22. Macrograph of the as-polished 17 A ground base specimen. The specimen was in the 923 K temperature zone and solidified from bottom to top in a nonwetting ampoule. The lead-gold alloy was originally located at the top. The specimen is approximately 1 cm diam.

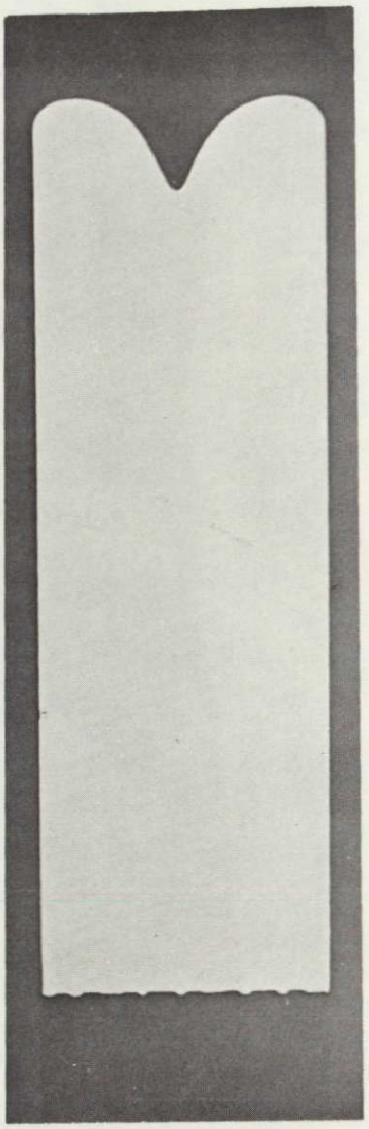

Figure 23. Macrograph of the as-polished 11 A-R ground base specimen. The specimen was in the 923 K temperature zone and solidified from bottom to top in a nonwetting ampoule. The lead-gold alloy was originally located at the bottom.

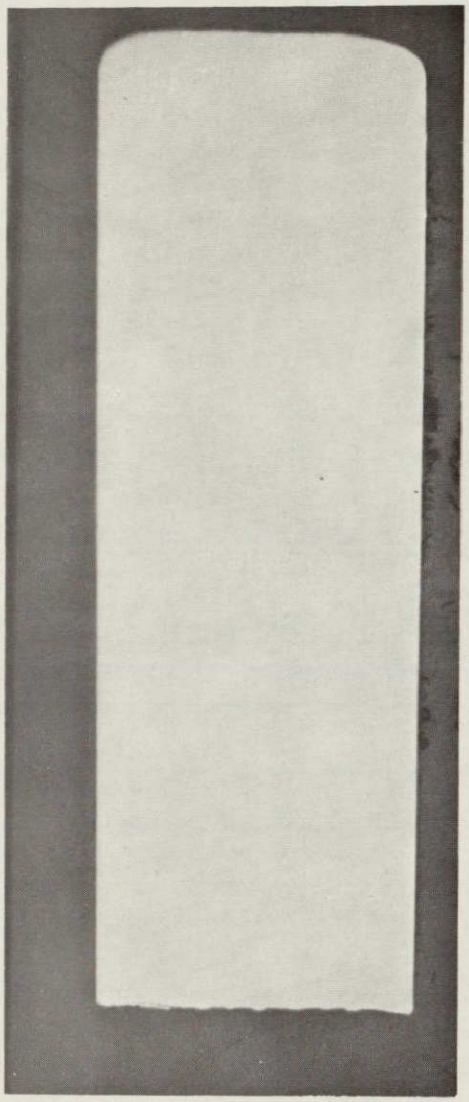

Figure 24. Macrograph of the as-polished 14 A ground base specimen. The specimen was in the 723 K temperature zone and solidified from bottom to top in a nonwetting ampoule. The lead-gold alloy was originally located at the top.

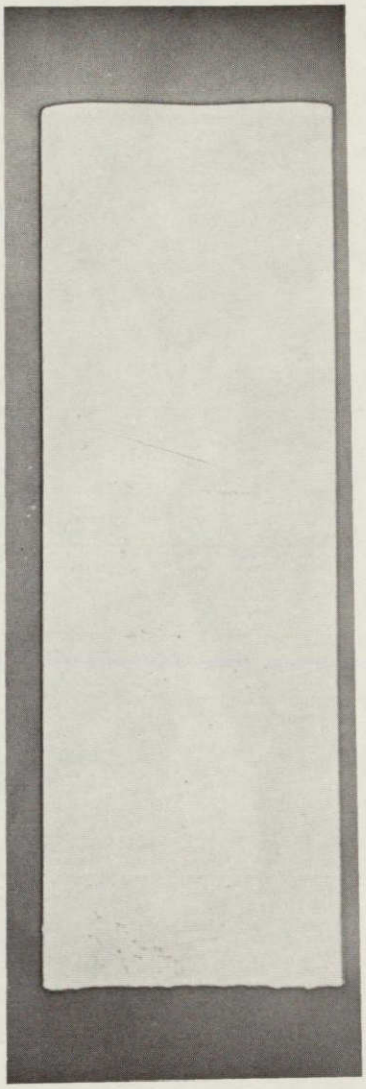

Figure 25. Macrograph of the as-polished 20 A-R ground base specimen. The specimen was in the 723 K temperature zone and solidified from bottom to top in a nonwetting ampoule. The lead-gold alloy was originally located at the bottom.

Figure 26. Photograph of space flight specimens 11 A and 21 A which were located in the 923 K and 723 K temperature zones of the multipurpose electric furnace, respectively. Samples solidified from the bottom to the top in ampoules with nonwetting walls. The original lead-gold alloy was located at the top.

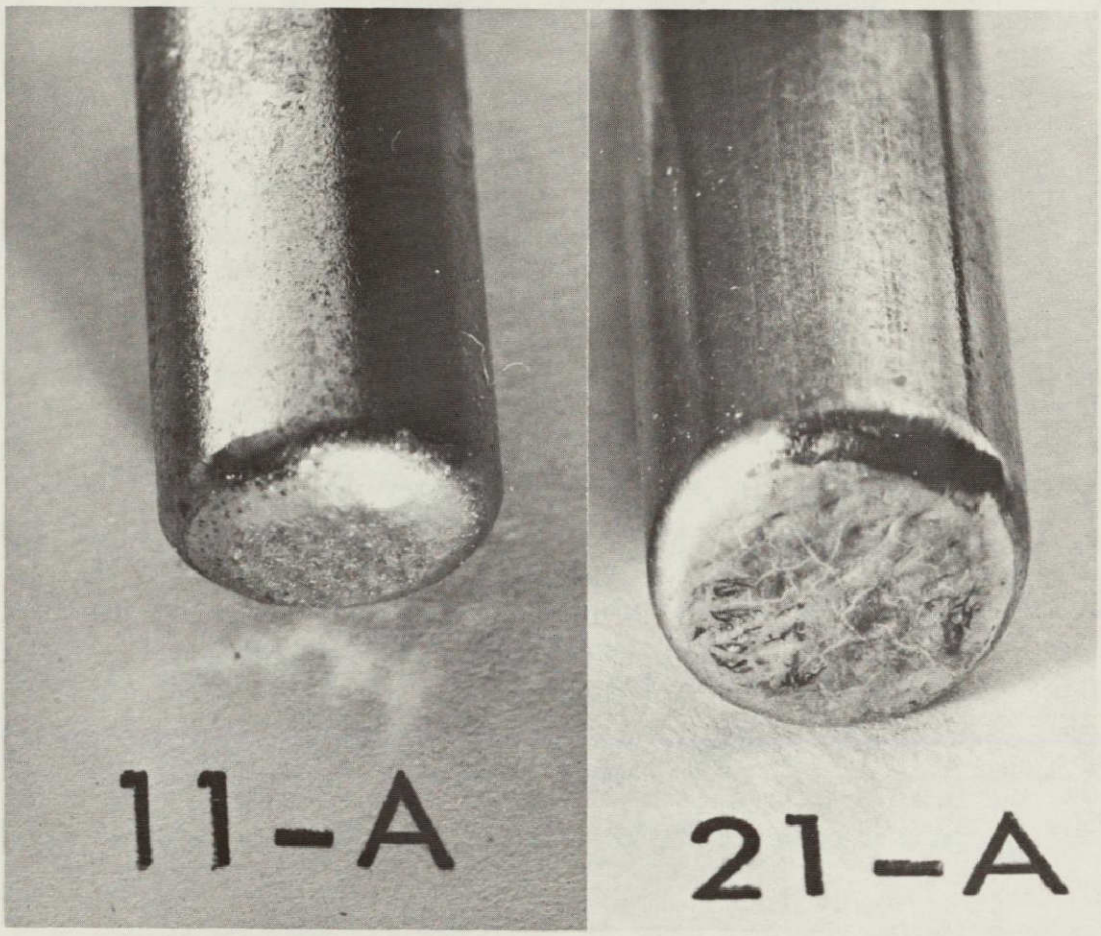

Figure 27. Photograph showing an end view of space flight specimens 11 A and 21 A which were located in the 923 K and 723 K temperature zones of the multipurpose furnace, respectively. This end of the specimens melted last and solidified first. The samples were contained in nonwetting ampoules.

Figure 28. Photograph showing the original lead-gold alloy end of space flight specimen 11 A which was located in the 923 K temperature zone. This end melted first and solidified last.

solidification pipes for both specimens. The lead-gold alloy region for the two specimens (13 A-R and 17 A-R) is shown in Figure 31. Recall this end of the specimen melted last and solidified first. The cellular structure and the lead-gold bond interface can be seen for both specimens.

Macrographs of the polished surfaces of the SF specimens are shown in Figures 32 through 35. The macrograph for SF specimen 11 A, in Figure 32, shows the expected rounded corners. This specimen was located in the 923 K temperature zone. The A-R SF specimen from the same temperature zone is shown in Figure 33. Again, as for 11 A, rounded

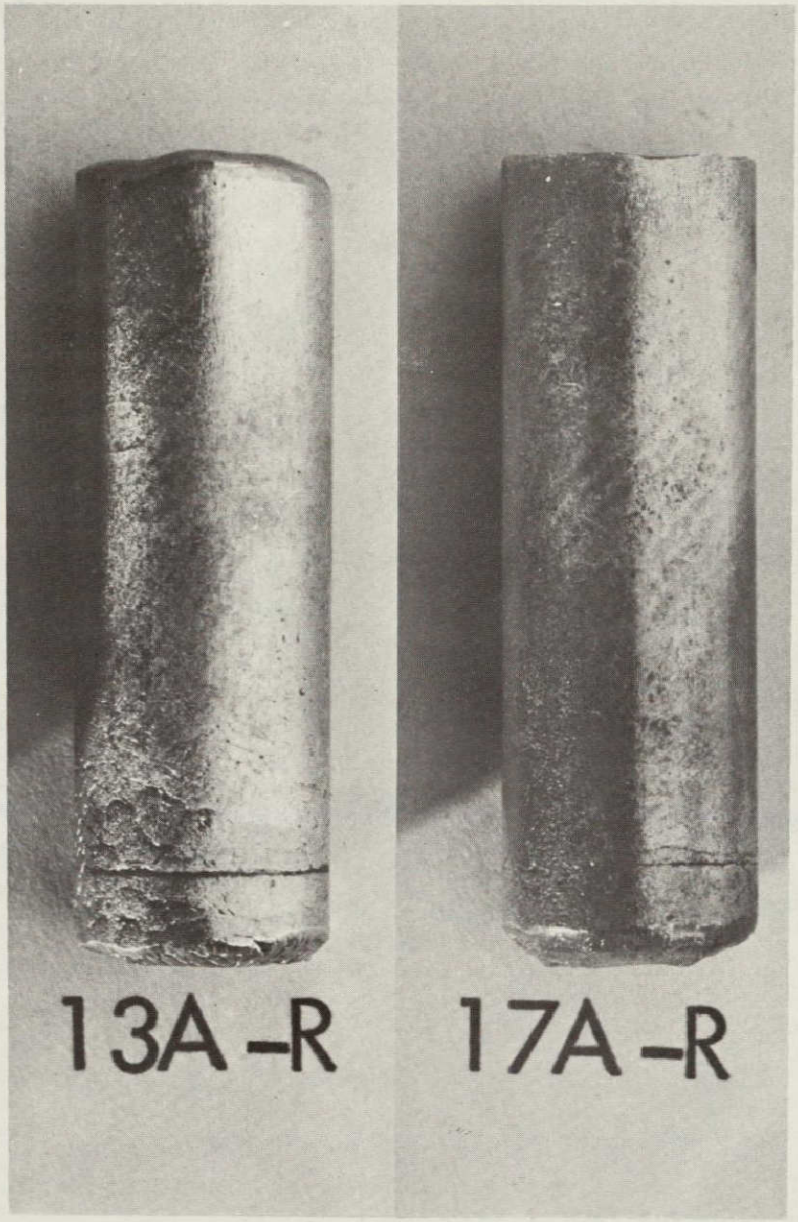

Figure 29. Photograph of space flight specimens 13 A-R and 17 A-R which were located in the 923 K and 723 K temperature zones, respectively. The original lead-gold alloy region was located at the bottom. Solidification direction was from bottom to top. The specimens were contained in nonwetting ampoules.

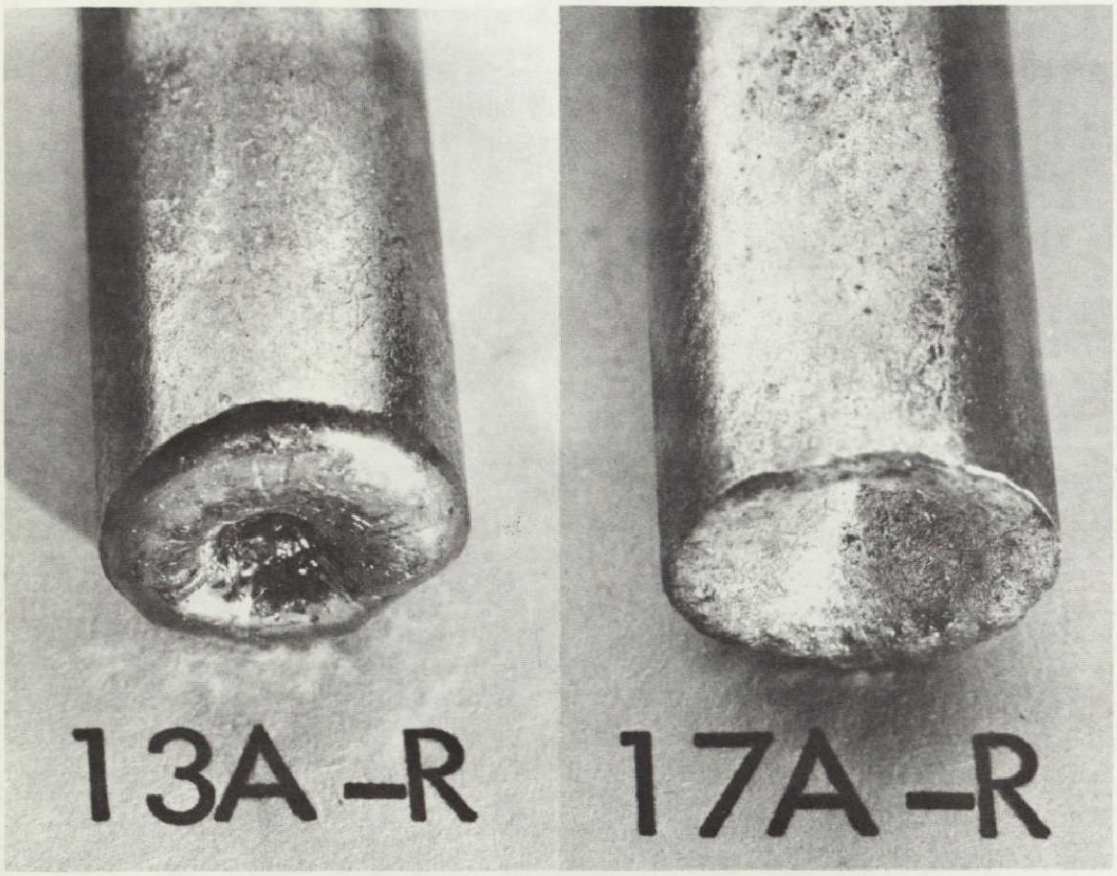

Figure 30. Photograph showing an end view of space flight specimens 13 A-R and 17 A-R from the 923 K and 723 K temperature zones, respectively. Melting direction was from bottom to top.

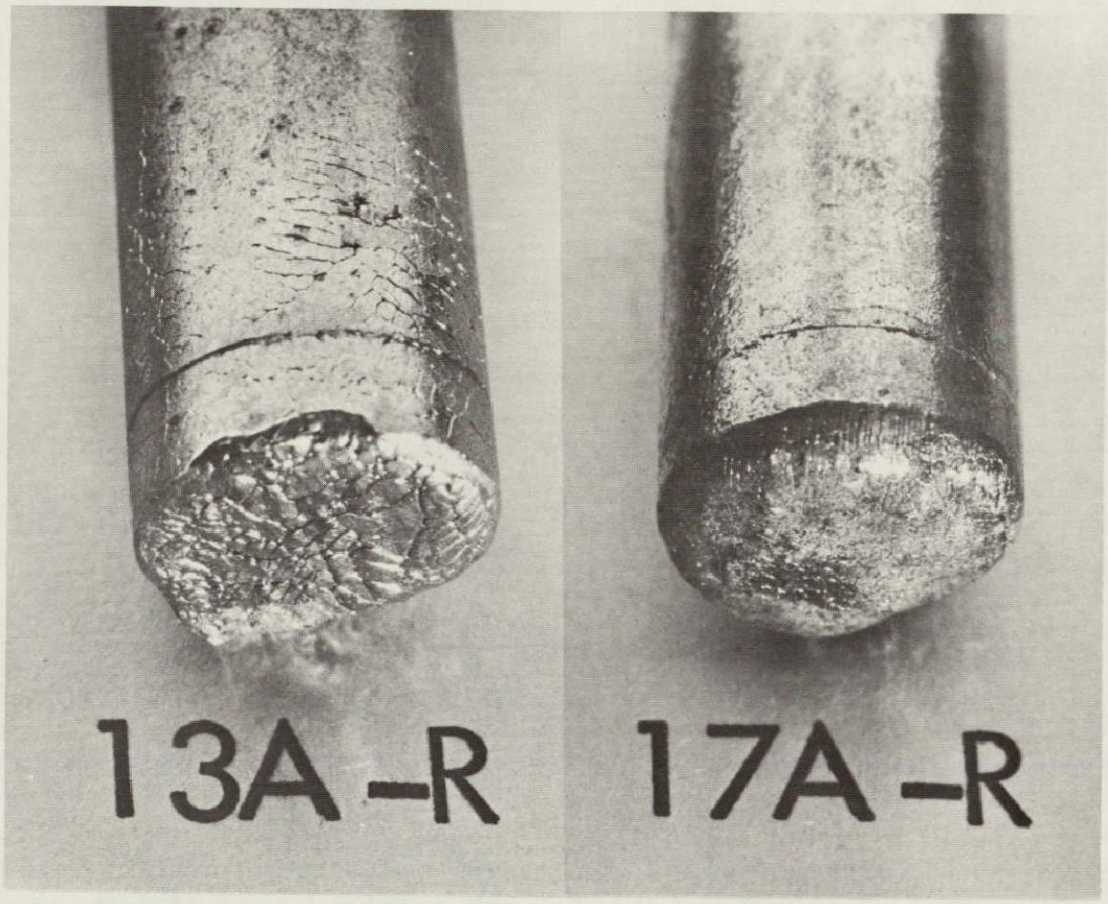

Figure 31. Photograph of an end view of space flight specimens 13 A-R and 17 A-R which shows the original lead-gold alloy region. Specimens solidified from the bottom to the top.

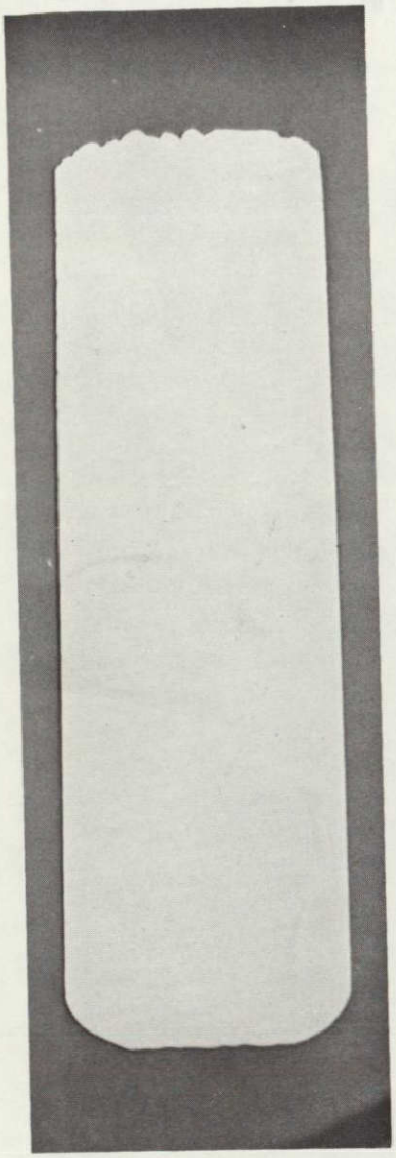

Figure 32. Macrograph of the as-polished 11 A space flight specimen. The specimen was in the 923 K temperature zone and solidified from bottom to top in a nonwetting ampoule. The original lead-gold alloy was located at the top.

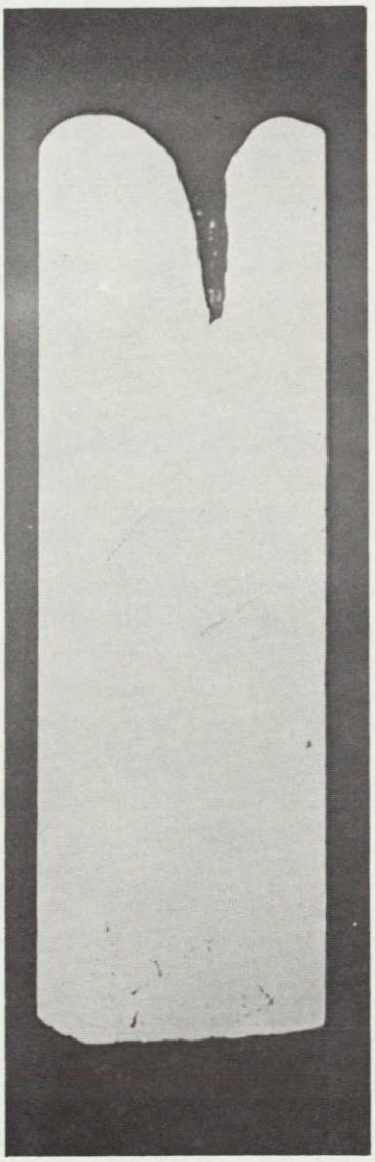

Figure 33. Macrograph of the as-polished 13 A-R space flight specimen. The specimen was in the 923 K temperature zone and solidified from bottom to top in a nonwetting ampoule. The original lead-gold alloy was located at the bottom.

corners can be seen. In addition, a large solidification pipe was formed at the top of the specimen. Macrographs of the longitudinal cuts of the 723 K temperature zones A and A-R SF specimens are shown in Figures 34 and 35, respectively. These specimens have similar characteristics to those described for the 923 K zone SF specimens.

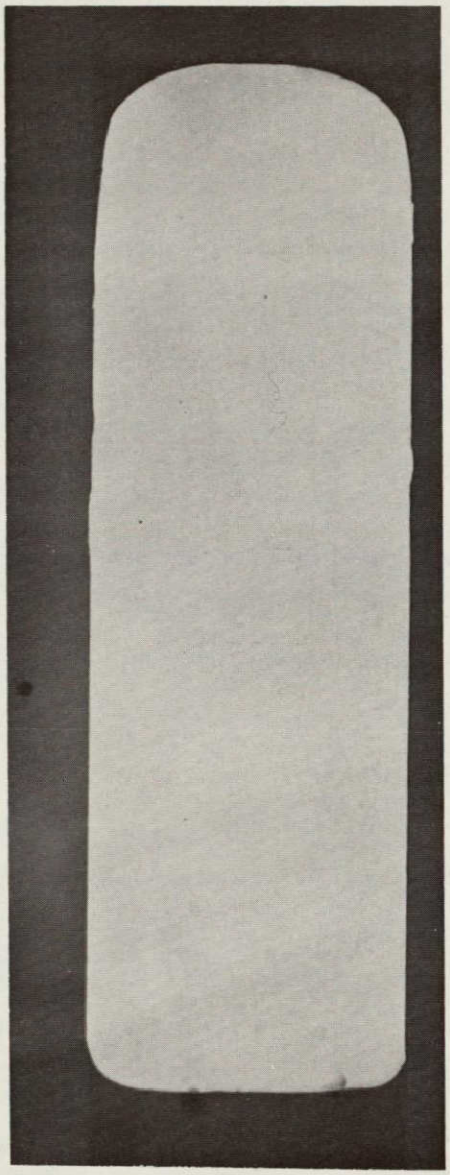

Figure 34. Macrograph of the as-polished 21 A space flight specimen. The specimen was in the 723 K temperature zone and solidified from bottom to top in a nonwetting ampoule. The original lead-gold alloy was located at the top.

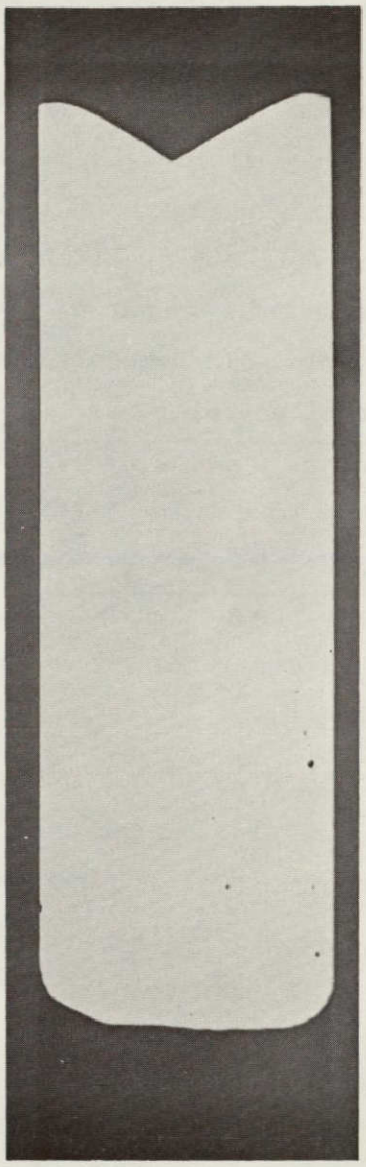

Figure 35. Macrograph of the as-polished 17 A-R space flight specimen. The specimen was in the 723 K temperature zone and solidified from bottom to top in a nonwetting ampoule. The original lead-gold alloy was located at the bottom.

GOLD CONCENTRATION DETERMINATION

The gold concentration as a function of location was determined by using the Image Data Processing System (IDAPS) at the Marshall Space Flight Center, Huntsville, Alabama. Before scanning the autoradiograph of the specimen, the autoradiograph of the standards, which had been irradiated and autoradiographed at the same time as the specimen, was scanned to establish a calibration curve that related transmittance to gold concentration. This was done automatically by the computer-based IDAPS. By using the calibration curve, a table which related all gray values for each specimen to gold concentrations was established. This permitted the output of the densitometer scan of each specimen to be stated in gold concentration units rather than gray values. The scanning interval normally used for each specimen was 70 microns although a scanning interval of 12.5 microns was used for some selected magnified regions to examine specimen microstructure as will be shown. The integration time normally used was 80 microseconds with a signal to noise ratio of 34 decibels. For the magnifications, an integration time of 1200 microseconds was used with a corresponding signal to noise ratio of 46 decibels.

The highly sophisticated IDAPS provided many unique possibilities for analyzing the autoradiographs. For this experiment, gold concentration values for all specimens were obtained and stored on magnetic tape for present and future analysis. For a quick and easier understanding of the gold distribution in the specimens, pseudocolors were assigned to particular gold concentration ranges. Using this method, pseudocolor representations showing the gold distribution were obtained. The color scheme used for all specimens is as shown in Table 10.

Table 10. Color Scheme Relating Pseudocolors to Gold Concentrations

Pseudocolor	Gold Concentration (at. ppm)	Percentage of Original Gold Concentration
Black	0- 5	0- 1.0
Yellow	6- 10	1.2- 2.0
Blue-Green	11- 20	2.2- 4.0
Red	21- 40	4.2- 8.0
Green	41- 80	8.2-16.0
Purple	81-120	16.2-24.0
Dark Blue	121-160	24.2-32.0
Orange	161-254	32.2-50.8

GOLD CONCENTRATION DISTRIBUTIONS FOR GROUND BASE SPECIMENS

The pseudocolor representations of the gold distributions in the type A-R and A GBS are shown in Figures 36 through 39. Figure 36 shows GBS 11 A-R from the 923 K zone which had the original alloy disk located at the bottom. Each large division shown is approximately 0.24 cm. As can be seen, a large portion of the gold remained at the bottom. In examining the gold concentration results, one should be aware that a characteristic of the autoradiographic technique is that an "edge" effect occurs when recording the radioactive disintegrations on film. This edge effect is caused by the symmetry of the radioactive disintegrations and is more predominant for β^- particles than α particles since the range of β^- particles in various materials is longer. Thus at the extreme edge of the samples one can see a slight decrease in gold concentration recorded which is simply a characteristic of the process. The edge effect for all specimens is $\leq$0.4 mm which is the approximate range of the 960 keV ^{198}Au β^- in lead.

Thermal soak time for specimen 11 A-R (Figure 36) was approximately 230 min. and it is clearly evident that mixing was incomplete. The flow direction is probably indicated by the red color and mixing probably occurred in the upper portion of the sample. The pseudocolor representation of the gold distribution for the 723 K GBS which had the original

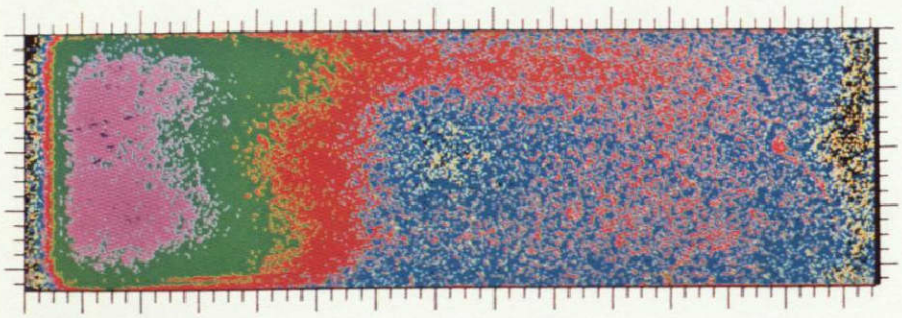

Figure 36. Pseudocolor representation of gold concentrations in ground base specimen 11 A-R. The pseudocolors are defined in Table 10. The specimen was mounted vertically in the multipurpose furnace with the original lead-gold alloy (left side of specimen shown) located at the bottom.

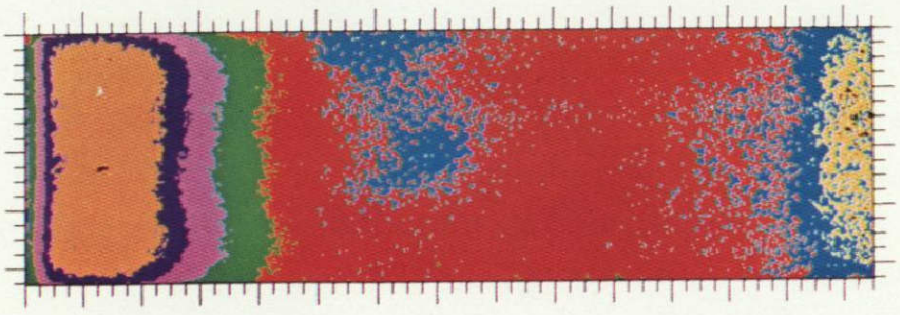

Figure 37. Pseudocolor representation of gold concentrations in ground base specimen 20 A-R. The pseudocolors are defined in Table 10. The specimen was mounted vertically in the multipurpose furnace with the original lead-gold alloy (left side of specimen shown) located at the bottom.

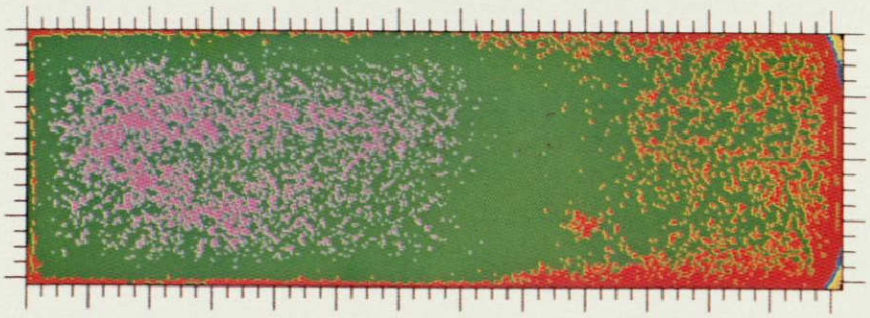

GB 14A 450 DEG. C

(--- MELTING DIRECTION

Figure 38. Pseudocolor representation of gold concentrations in ground base specimen 14 A. The pseudocolors are defined in Table 10. The specimen was mounted vertically in the multipurpose furnace with the original lead-gold alloy (right side of specimen shown) located at the top.

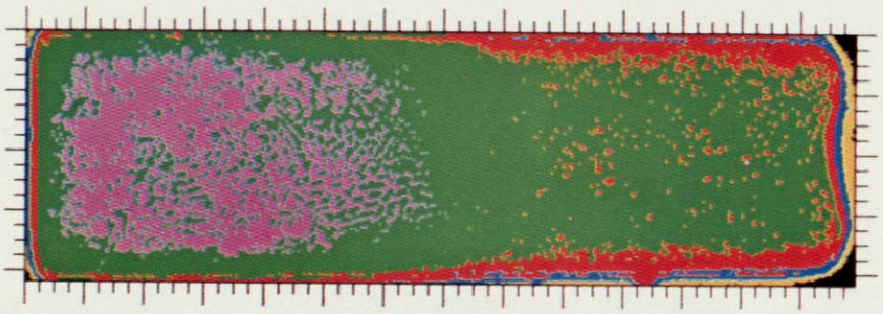

GB 17A 650 DEG. C

(--- MELTING DIRECTION

Figure 39. Pseudocolor representation of gold concentrations in ground base specimen 17 A. The pseudocolors are defined in Table 10. The specimen was mounted vertically in the multipurpose furnace with the original lead-gold alloy (right side of specimen shown) located at the top.

alloy located at the bottom is shown in Figure 37. Again it can be seen that most of the gold remained at the bottom of the specimen.

Surprising results were obtained for the GBS with the alloy located at the top. Specimens having soak temperatures of 723 and 923 K are shown in Figures 38 and 39, respectively. Most of the gold "dropped" to the bottom creating nearly the same gold distribution for the two temperature zones. Almost identical isograms for the two specimens are shown in Figures 40 and 41.

EXPLANATION OF GOLD CONCENTRATION DISTRIBUTION PROFILES FOR GROUND BASE SPECIMENS

There are at least two possible explanations for the gold movement to the bottom in specimens 14 A and 17 A, Figures 38 and 39, respectively.

1. Sedimentation effect: assumes an equal distribution of gold in the specimen is obtained and subsequently gravity causes the gold to settle to the bottom. An estimation of this effect shows that the density difference and gold concentrations are much too low for this to occur.

2. System instability: as was shown by Verhoeven,[14] fluid systems with heavier materials at the top can sustain only a certain concentration gradient ($\Delta C/\Delta Z$) before becoming unstable. The concentration gradient can be obtained from the following equation:

$$\Delta C/\Delta Z = \frac{(R_s)_c \cdot \nu \cdot D}{g \cdot \alpha' \cdot r^4} \qquad (1)$$

The terms in the previous equation (except r which is the radius of the specimen) are defined in Figure 42. In the beginning of our experiment the concentration gradient was infinite, thus the gold would be predicted to flow downward to reduce the gradient. Using Equation 1 one can calculate the distance (ΔZ) the material must flow to reach the critical

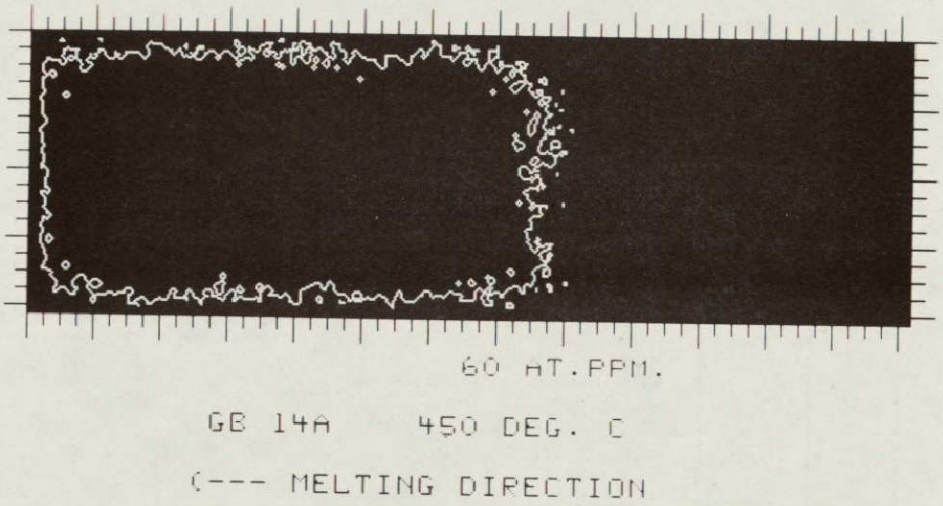

Figure 40. Isogram showing the 60 at. ppm gold concentration region for ground base specimen 14 A.

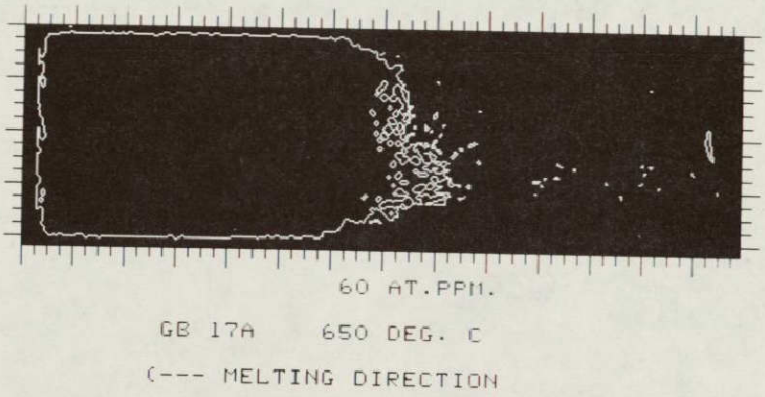

Figure 41. Isogram showing the 60 at. ppm gold concentration region for ground base specimen 17 A.

ORNL - DWG 76 - 10055A

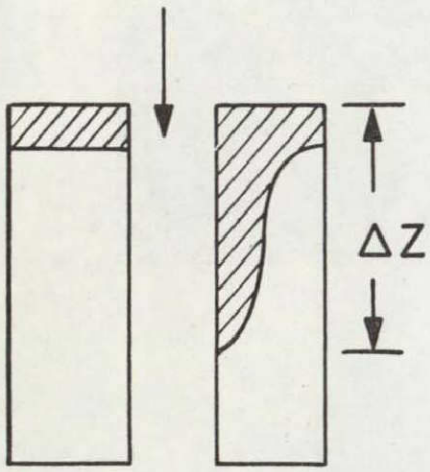

$$\frac{\Delta C}{\Delta Z} = \frac{(R_S)_C \cdot \nu \cdot D}{g \cdot \alpha' \cdot r^4}$$

$(R) = 68$ CRITICAL RAYLEIGH-NUMBER

$\nu = 1.73 \cdot 10^{-3} \frac{cm^2}{sec}$ KINEMATIC VISCOSITY

$D \approx 4 \cdot 10^{-5} \frac{cm^2}{sec}$ DIFFUSION CONSTANT

$g = 981 \frac{cm}{sec^2}$ GRAVITY ACCELERATION

$\alpha' = \frac{1}{\rho} \cdot \frac{d\rho}{dC} = 0.4$

$\Delta Z = 2.63 \cdot 10^3$ cm

Figure 42. Explanation for the gold movement to the bottom of ground base specimens 14 A and 17 A on the basis of the stability analysis of Verhoeven.

concentration gradient. Calculation of ΔZ yields a predicted distance of 2.6×10^3 cm. Thus, there seems to be little doubt that the movement of the gold was caused by system instability.

GOLD CONCENTRATION DISTRIBUTIONS FOR SPACE FLIGHT SPECIMENS

Gold concentration pseudocolor representations used for the A and A-R SFS from the 923 K temperature zone are shown in Figures 43 and 44, respectively. Recall that for specimen 11 A, the lead-gold alloy melted first and solidified last with the reverse being true for specimen 13 A-R. In both specimens, there are curved radial gold concentration profiles with the larger amount of gold at the cylinder axis and gradually decreasing toward the wall. Isograms for specimens 11 A and 13 A-R are shown in Figures 45 and 46, respectively; the isograms show the 5, 10, 20, 40, and 80 at. ppm gold concentration lines. To the right of the 5 ppm concentration line the concentration decreases to 0 and to the left of the 80 ppm concentration line, the gold concentration increases to approximately 140 ppm for 11 A and approximately 115 ppm for 13 A-R. Although approximately 120 axial gold concentration profile lines were obtained for each specimen, only the central lines are shown. As can be seen from Figures 47 and 48, which represent the central axial gold concentration lines from specimens 11 A and 13 A-R, respectively, the gold diffusion distance was slightly less for specimen 13 A-R. The ordinates in Figures 47 and 48 represent the percentage of gold with respect to the initial concentration (500 at. ppm); the amount of gold at any point can be obtained by multiplying the ordinate by 500. The abscissa corresponds to a particular column number which can readily be converted to distance in millimeters since there are 14.5 columns/mm.

Gold concentration pseudocolor assignments used for SFS 21 A and 17 A-R, which were located in the 723 K temperature zone of the multi-purpose electric furnace are shown in Figures 49 and 50, respectively. Gold diffusion into these specimens is approximately equal as can be seen from the central axial gold concentration lines shown in Figures 51 and 52. Curved radial gold concentration profiles are clearly evident

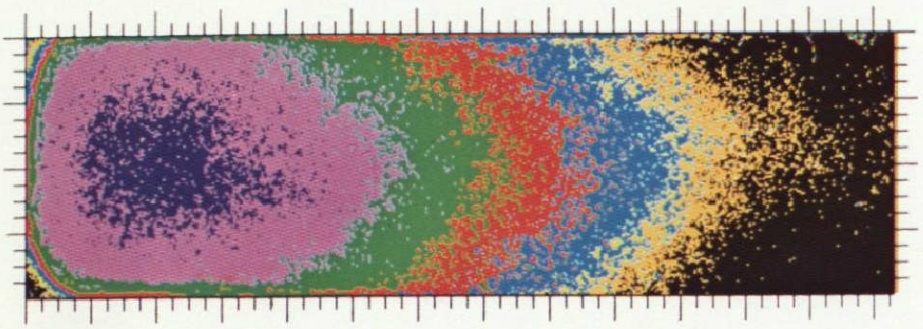

Figure 43. Pseudocolor representation of gold concentrations in space flight specimen 11 A. The pseudocolors are defined in Table 10. The original lead-gold alloy was located on the left side of the specimen.

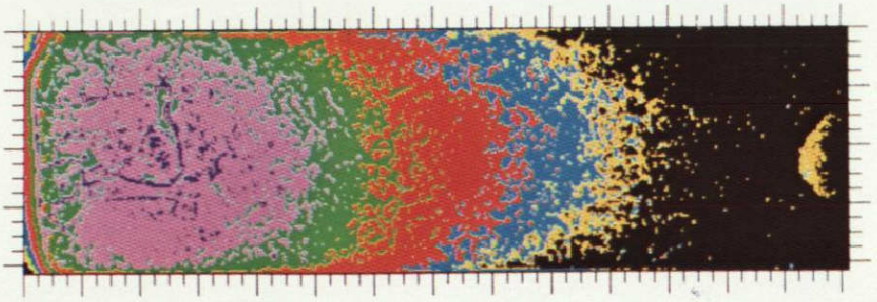

Figure 44. Pseudocolor representation of gold concentrations in space flight specimen 13 A-R. The pseudocolors are defined in Table 10. The original lead-gold alloy was located on the left side of the specimen.

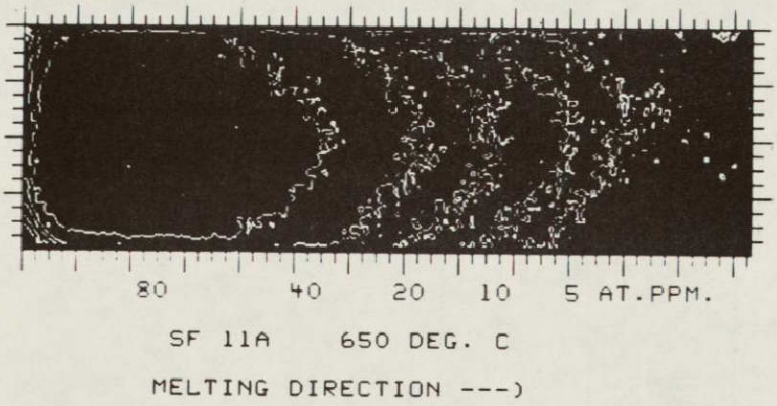

Figure 45. Isogram showing the 5, 10, 20, 40, and 80 at. ppm gold concentration regions for space flight specimen 11 A.

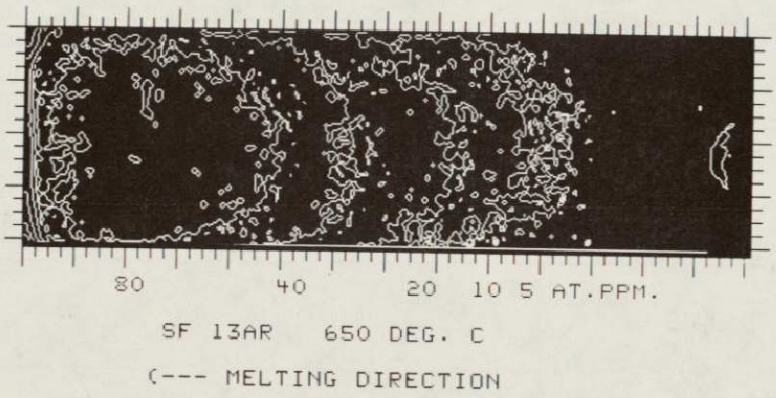

Figure 46. Isogram showing the 5, 10, 20, 40, and 80 at. ppm gold concentration regions for space flight specimen 13 A-R.

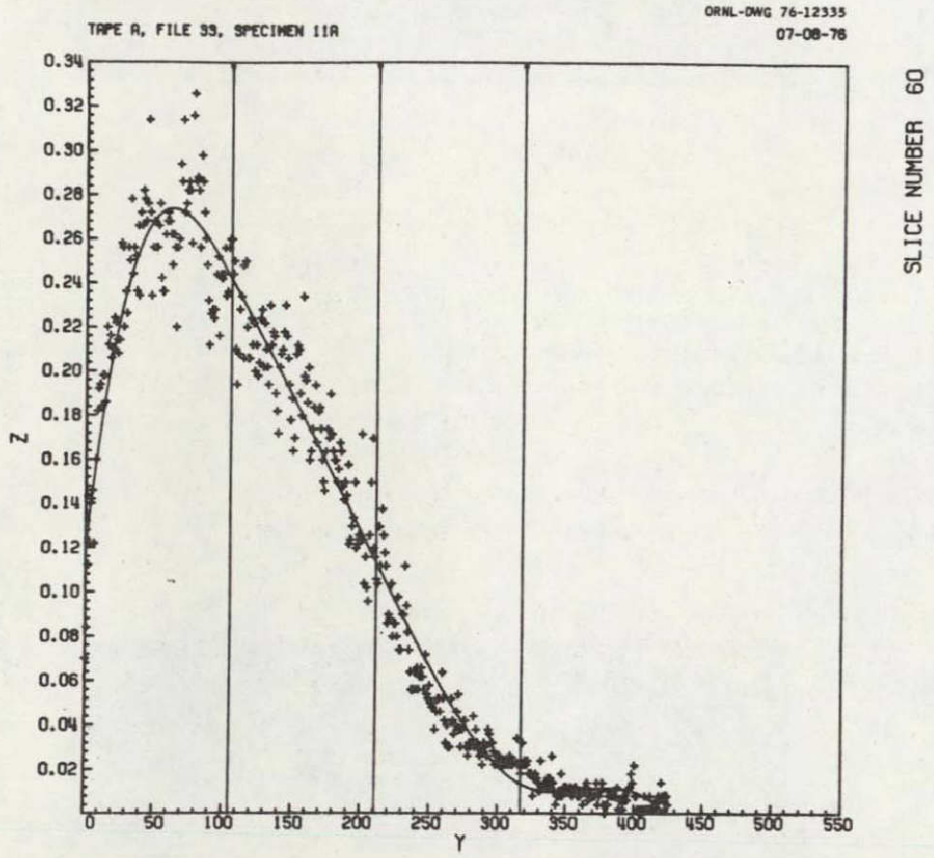

Figure 47. Central axial gold concentration line for space flight specimen 11 A. The ordinate represents the percentage of gold with respect to the initial concentration (500 at. ppm). The abscissa corresponds to a particular column number which can readily be converted to distance in millimeters since there are 14.5 columns/mm. All data points (approximately 420) are shown.

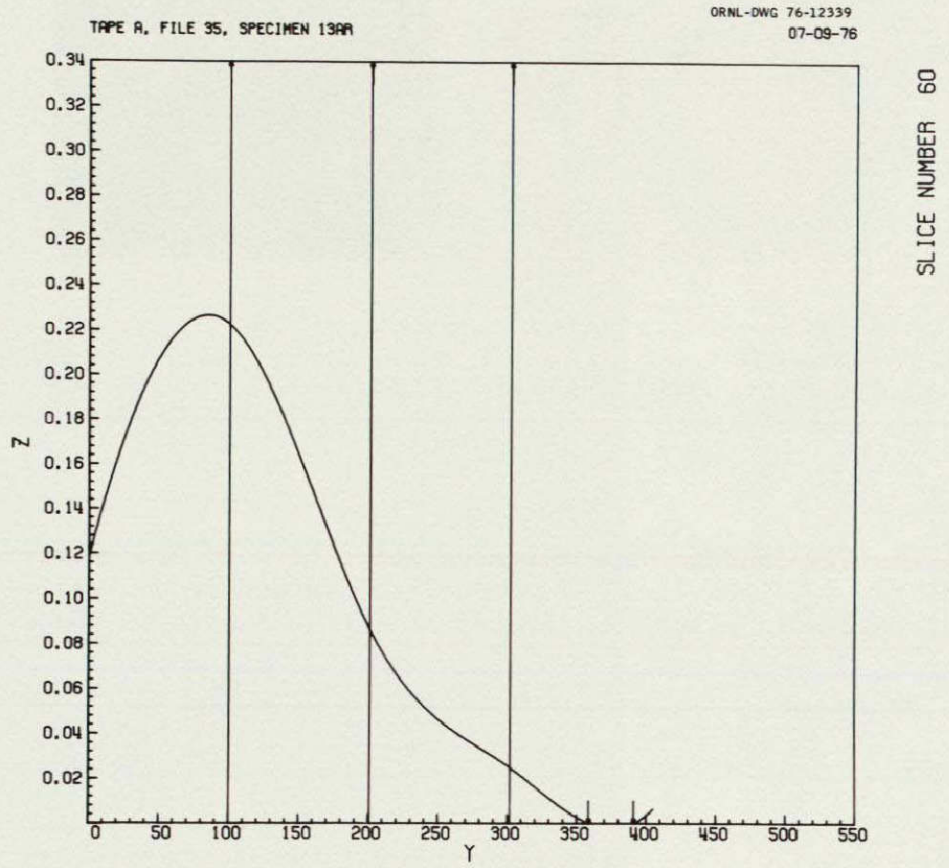

Figure 48. Central axial gold concentration profile for space flight specimen 13 A-R. The ordinate represents the percentage of gold with respect to the initial concentration (500 at. ppm). The abscissa corresponds to a particular column number which can be converted to millimeters by dividing by 14.5.

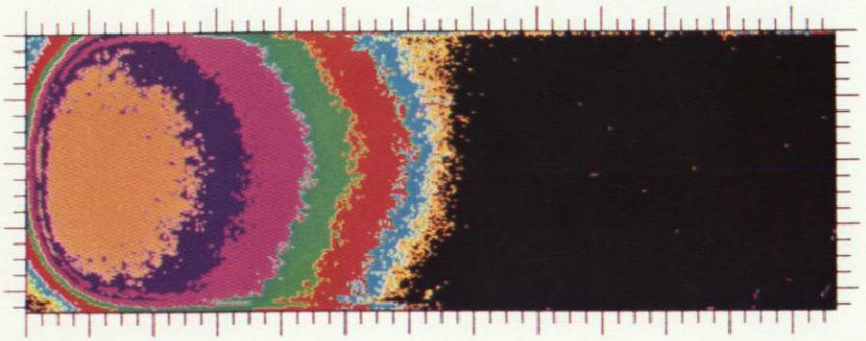

Figure 49. Pseudocolor representation of gold concentrations in space flight specimen 21 A. Pseudocolors are defined in Table 10. The original lead-gold alloy was located at the left side of the specimen.

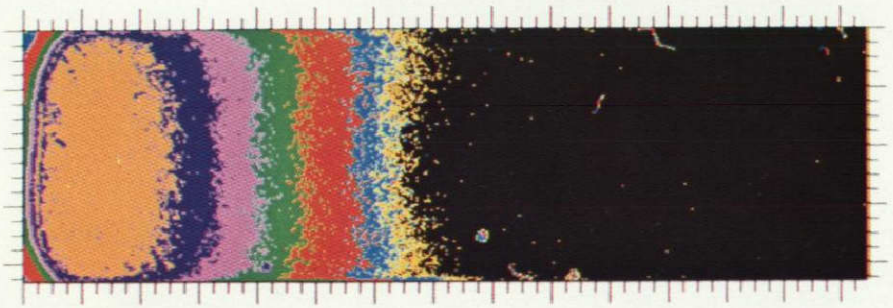

Figure 50. Pseudocolor representation of gold concentrations in space flight specimen 17 A-R. Pseudocolors are defined in Table 10. The original lead-gold alloy was located at the left side of the specimen.

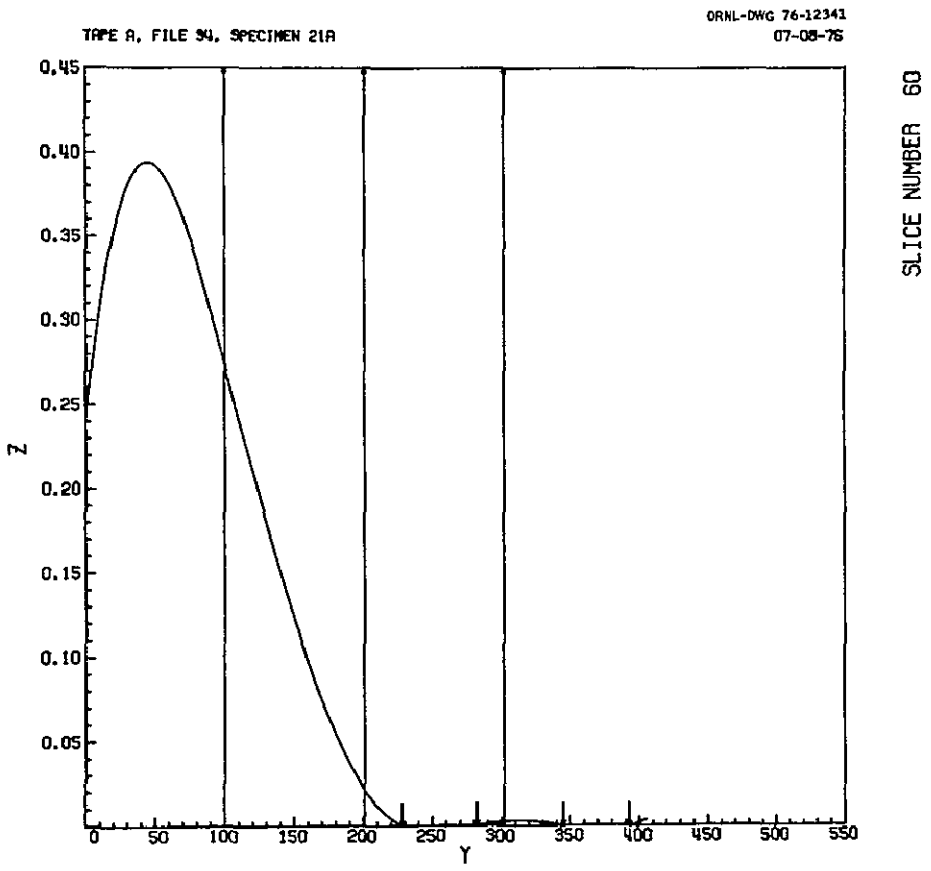

Figure 51. Central axial gold concentration profile for space flight specimen 21 A. The ordinate represents the percentage of gold with respect to the initial concentration (500 at. ppm). The abscissa corresponds to a particular column number which can be converted to millimeters by dividing by 14.5.

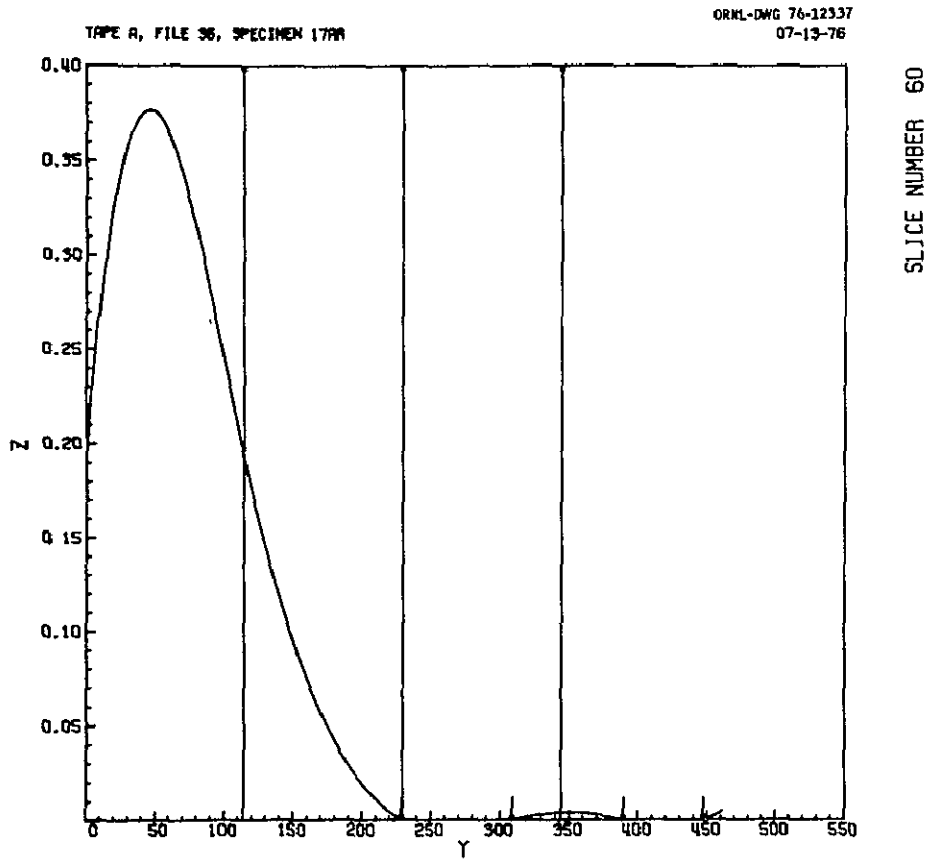

Figure 52. Central axial gold concentration profile for space flight specimen 17 A-R. The ordinate represents the percentage of gold with respect to the initial concentration (500 at. ppm). The abscissa corresponds to a particular column number which can be converted to millimeters by dividing by 14.5.

for both specimens but appear to be greater for SFS 21 A. The only apparent difference between the A and A-R specimens from the 923 and 723 K temperature zones is that the gold diffusion distance for 13 A-R is slightly less than that for 11 A and that the radial concentration curvature is slightly greater for specimen 21 A than for specimen 17 A-R. A number of SFS slices were examined for all the SF specimens to determine the location of the maximum gold concentration. The results are shown in Tables 11 through 14. It appears fairly certain that the maximum C/C_0 values for the 923 K specimens was shifted further into the samples than for the 723 K specimens.

Table 11. Specimen 11 A - Data Used to Locate Gold Concentration Maximum

Segment No.	Longitudinal Location (mm)	Maximum C/C_0
6	4.5	0.207
12	4.3	0.219
18	4.3	0.230
24	4.2	0.243
30	4.3	0.247
36	4.3	0.255
42	4.3	0.270
48	4.3	0.272
54	4.2	0.274
60	4.3	0.274
66	4.6	0.273
72	4.7	0.273
78	4.7	0.268
84	4.7	0.261
90	4.7	0.254
96	4.8	0.239
102	4.5	0.237
108	4.7	0.223
114	4.7	0.210
120	4.8	0.173

Table 12. Specimen 21 A - Data Used to Locate Gold Concentration Maximum

Segment No.	Longitudinal Location (mm)	Maximum C/C_0
6	3.6	0.270
12	3.4	0.304
18	3.4	0.324
24	3.4	0.342
30	3.3	0.352
36	3.2	0.360
42	3.2	0.388
48	3.1	0.388
54	3.1	0.389
60	3.1	0.395

Table 13. Specimen 17 A-R - Data Used to Locate Gold Concentration Maximum

Segment No.	Longitudinal Location (mm)	Maximum C/C_0
6	3.8	0.329
12	3.9	0.349
18	3.4	0.363
24	3.4	0.365
30	3.3	0.370
36	3.3	0.370
42	3.3	0.374
48	3.2	0.379
54	3.1	0.379
60	3.1	0.378

Table 14. Specimen 13 A-R - Data Used to Locate Gold Concentration Maximum

Segment No.	Longitudinal Location (mm)	Maximum C/C_0
6	4.1	0.170
12	4.1	0.172
18	5.0	0.189
24	4.7	0.196
30	4.5	0.218
36	4.1	0.212
42	5.0	0.211
48	5.2	0.221
54	5.2	0.229
60	5.6	0.226
66	5.9	0.232
72	6.3	0.217
78	6.2	0.223
84	4.9	0.236
90	5.6	0.219
96	5.6	0.220
102	4.8	0.223
108	4.8	0.214
114	4.7	0.218
120	4.5	0.204

DIFFUSION ANALYSIS

If there were no convective stirring effects present during the period when the samples were molten, then a normal diffusion concentration-distance profile would be expected. As shown in Figures 47, 48, 51, and 52, the right side of the concentration profiles for the central slices of the SF specimens resemble those that would result essentially from diffusion. Thus, an attempt was made to calculate the diffusion constant, D_0, and activation energy, A, for the liquid diffusion of gold in lead by assuming the coefficient of diffusion, D, to be given by

$$D = D_0 \, e^{-\frac{A}{RT}} \qquad (2)$$

where

R = gas constant = 1.987 cal/mol K,

T = temperature.

Due to a malfunction in the helium quenching process, the SF specimens stayed molten longer than was initially anticipated. As is shown in Figures 10 through 13, the temperature was not constant but decreased at a slow rate during the cool-down process. To solve this problem, according to Crank[15], one uses the solutions of the diffusion differential equation

$$\frac{\delta C}{\delta T^*} = \frac{\delta^2 C}{\delta x^2} \tag{3}$$

where

C = concentration

x = diffusion distance

$$T^* = \int_0^t D(t')dt', \text{ and} \tag{4}$$

t = time.

Substituting Equation 2 into Equation 4 gives

$$T^* = D_0 \int_0^t e^{-\frac{A}{RT(t')}} dt'. \tag{5}$$

Solving Equation 2 with the boundary conditions

1. extended source of length, h, and constant concentration, C_0,

2. finite specimen length, l,

one obtains[16]

$$\frac{C}{C_0} = 1/2 \sum_{n=-\infty}^{\infty} \left[\text{erf} \frac{(h + 2nl - X)}{2\sqrt{T^*}} + \text{erf} \frac{h - 2nl + X}{2\sqrt{T^*}} \right]. \tag{6}$$

It is evident that T^* (Equation 5) is a function of the temperature-time history of the specimens. Since the specimens in this experiment were located in two temperature zones, there are two temperature-time histories. Thus, there are two T^* values,

$$T_1^* = D_0 \int_0^{t_1} e^{-\frac{A}{RT_1(t')}} dt' \tag{7}$$

and

$$T_2^* = D_0 \int_0^{t_2} e^{-\frac{A}{RT_2(t')}} dt'. \tag{8}$$

One method of determining the activation energy is to define a function, G(A), given by

$$G(A) = \frac{\int_0^{t_1} e^{-\frac{A}{RT_1(t')}} dt'}{\int_0^{t_2} e^{-\frac{A}{RT_2(t')}} dt'} = \frac{T_1^*}{T_2^*} . \tag{9}$$

Using this function, the quotient of the experimentally determined values of T_1^* divided by T_2^* defines the actual value of G. Using the calculated values for the function G(A) shown in Figure 53, one should be able to determine the activation energy for the lead-gold system.

Equation 6 was used to obtain the best fit for the concentration profiles for the central slices of the four SF specimens neglecting the six lowest concentration values shown on the experimental curves. An example of such a fit for SFS 13 A-R is shown in Figure 54. The T^* values obtained for the four SF specimens are shown in Table 15.

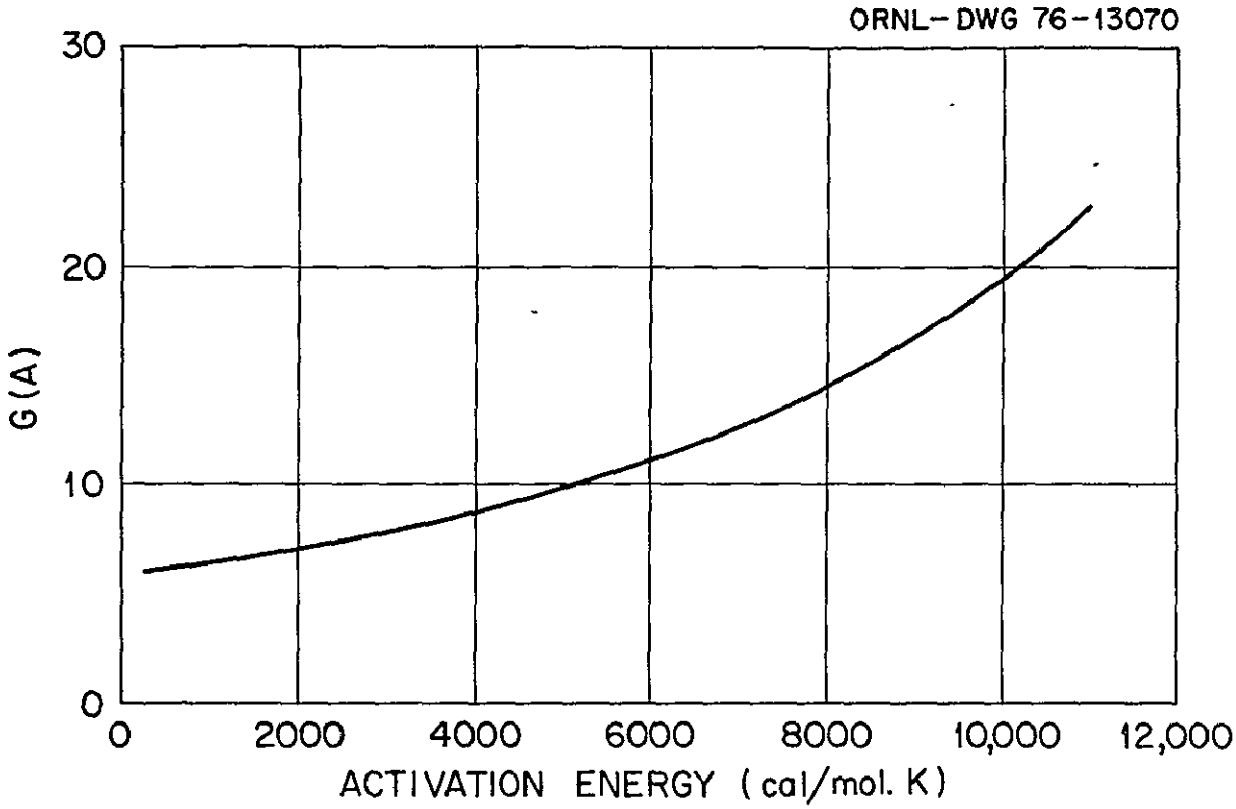

Figure 53. A graphic solution of Equation 9 for the two temperature-time histories of this experiment and different activation energies.

Table 15. T^* Values for the Four SF Specimens

SF Specimen	Temperature Zone (K)	T^* (cm^2)
11 A	923	0.39
13 A-R	923	0.48
21 A	723	0.16
17 A-R	723	0.16

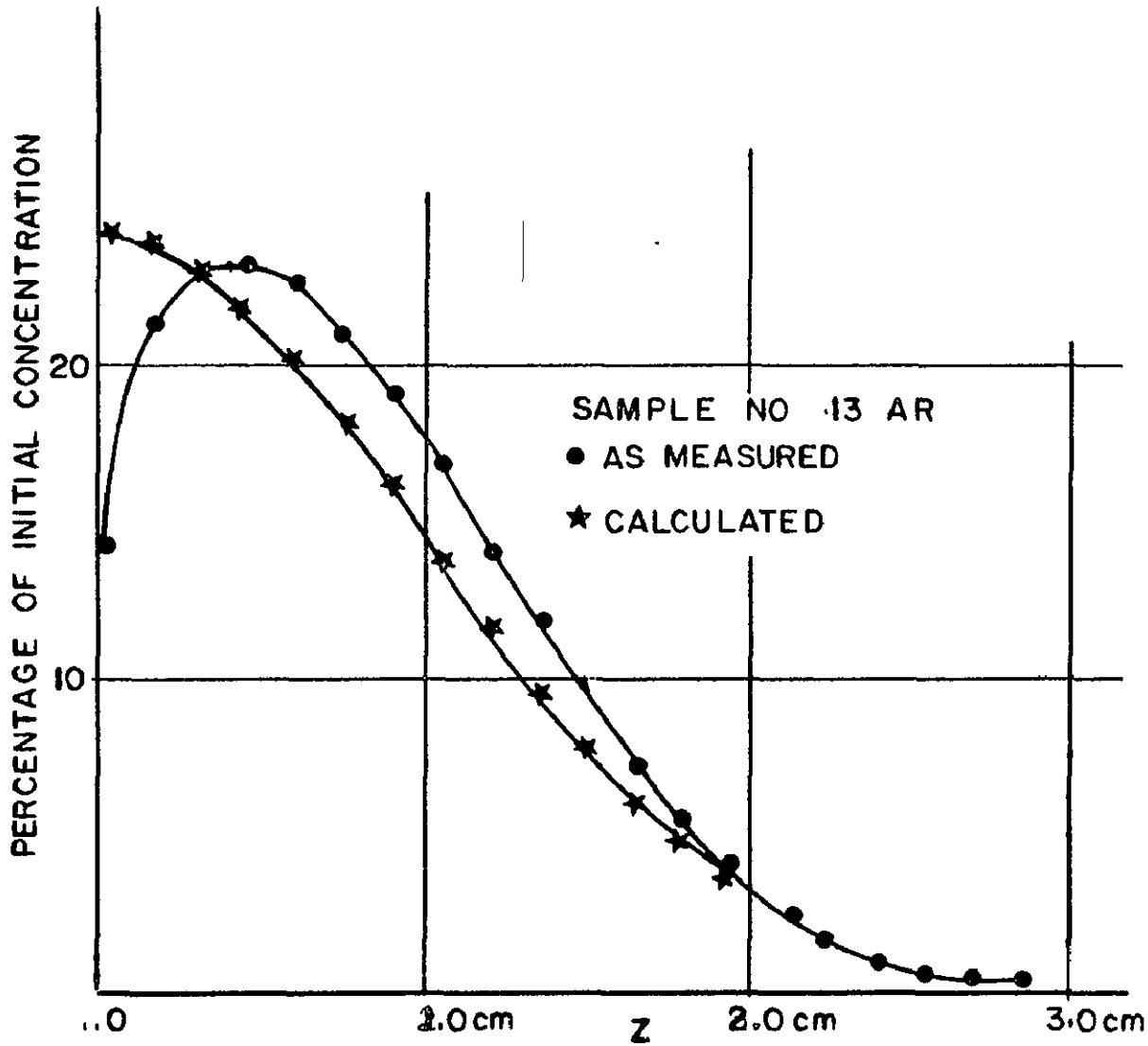

$$\frac{\partial C}{\partial T^*} = \frac{\partial^2 C}{\partial X^2}$$

$$T^* = \int_0^t D(t')\,dt'$$

$$T^* = 0.48\ cm^2$$

Figure 54. Comparison of experimental and calculated diffusion profiles for space flight specimen 13 A-R. The calculated curve was obtained from Equation 6.

Taking the average value for the two temperature zones and using Equation 9, a value of 2.12 is obtained for G(A). Figure 53 indicates that the corresponding activation energy would be extremely small (or negative). This low value does not appear reasonable since the reported activation energies for most liquid diffusion systems are >1000 cal/mol K[17].

To clarify the discrepancy, the zinc self-diffusion data taken from the Skylab experiment[18] was used in conjunction with the two temperature-time histories for this experiment to calculate concentration profiles. The calculated concentration profiles, using a D_0 value = 9.17×10^{-4} and an activation energy of 5160 cal/mol K, are compared with the experimental concentration profiles for SF specimens 11 A and 21 A in Figures 55 and 56, respectively. Curves 1 and 2 in Figures 55 and 56 represent the experimental values. Curve 1 represents the actual gold

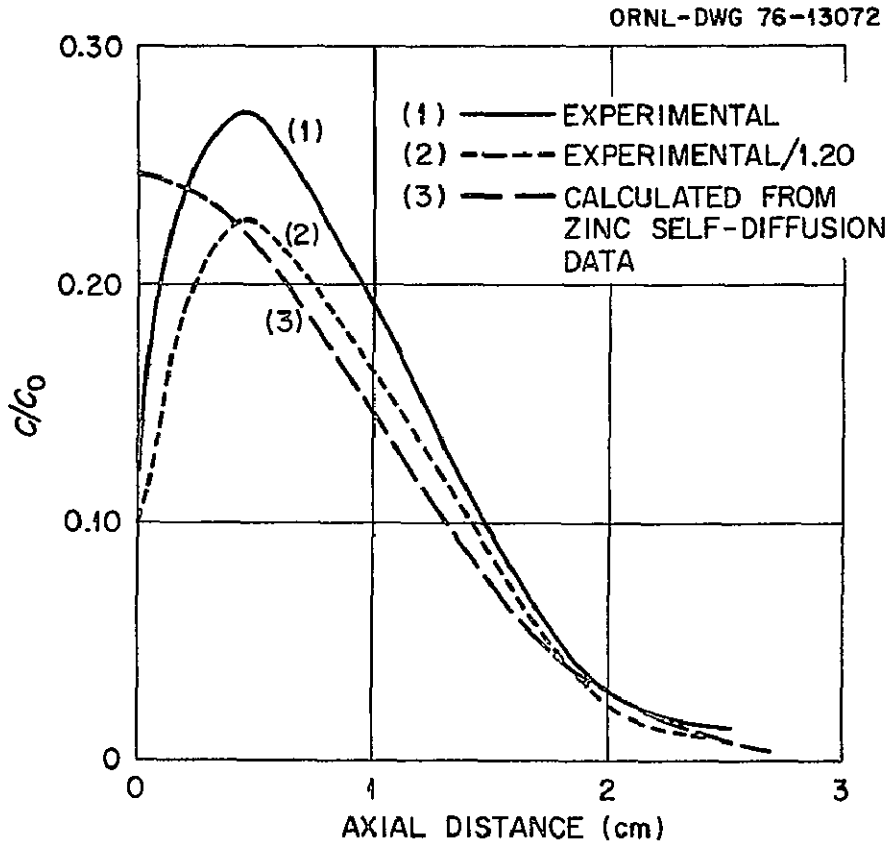

Figure 55. Comparison of experimentally determined gold concentration values with calculated values for space flight specimen 11 A using the zinc self-diffusion data and Equation 6.

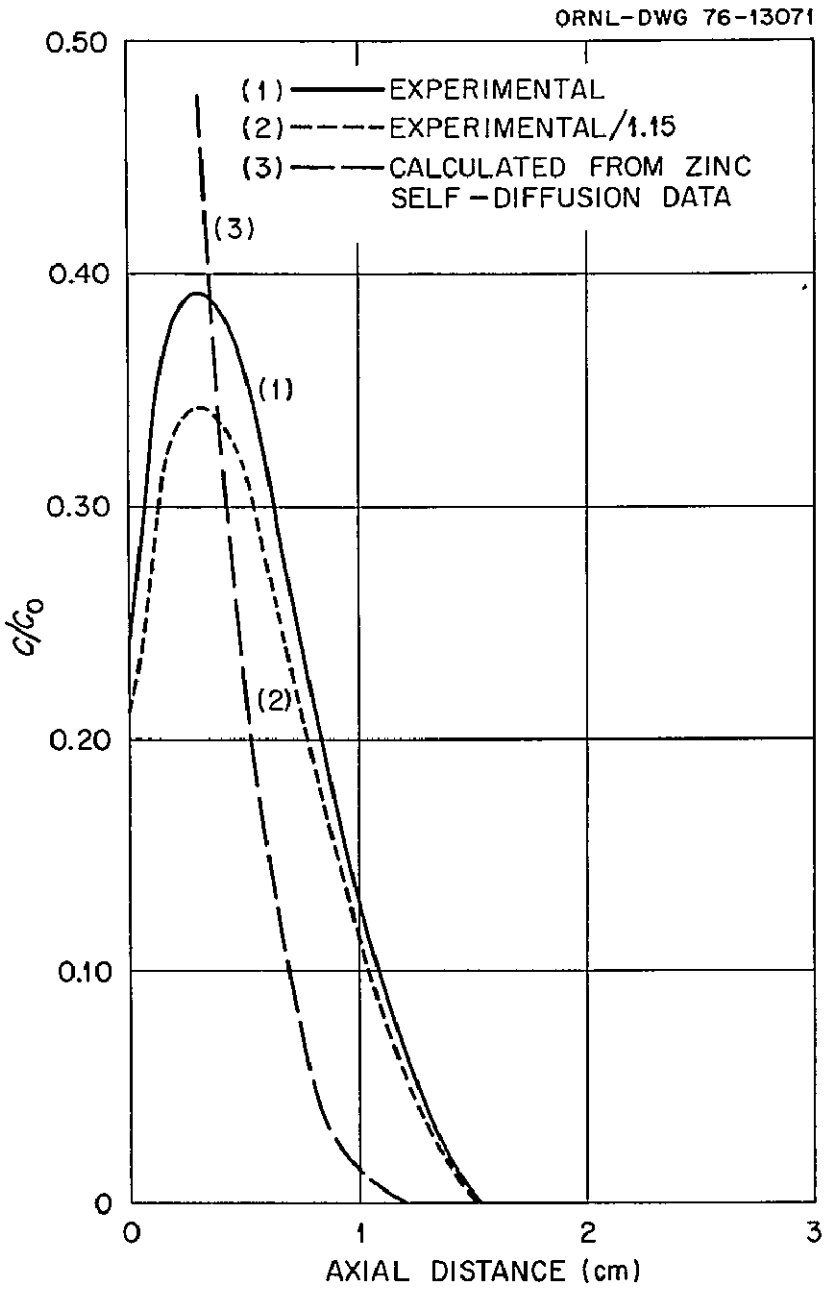

Figure 56. Comparison of experimentally determined gold concentration values with calculated values for space flight specimen 21 A using the zinc self-diffusion data and Equation 6.

concentration in the central slice. Since there was an increased gold concentration in the central region of the SF specimens, it was thought that perhaps the true diffusion curve would be better represented by a curve adjusted to show no gold increase. Thus, curve 2 was obtained by

adjusting the experimental values by the amount that the gold concentration was increased in the central region. It is evident that the calculated values for the 923 K SFS (Figure 55) are in good agreement with the adjusted experimental values, whereas Figure 56 shows that the diffusion process is much faster than that calculated from the zinc self-diffusion data. Assuming the temperature-time histories for both temperature zones are correct, there seems to be another mass transport mechanism which occurs predominantly in the beginning. This mechanism is not as evident for the longer soak time since it is obscured by the diffusion process. It is obvious that more than diffusion occurred, thus it is not possible to obtain the true diffusion activation energy and the gold diffusion constant from this experiment. Possible transport mechanisms which could lead to our observed results will be considered in the next section.

POSSIBLE EXPLANATIONS FOR GOLD CONCENTRATION DISTRIBUTION PROFILES FOR SPACE FLIGHT SPECIMENS

It seems evident that the concentration distribution of the gold in the SF specimens is not determined simply by diffusion. Independent of the previously discussed diffusion results, there are additional reasons for this conclusion:

1. Occurrence of a maximum gold concentration in the region of the original lead-gold alloy disk as was shown in Tables 11 through 14,
2. Curved gold concentration profiles in the radial direction for all the SF specimens as shown in Figures 43, 44, 49, and 50, and
3. An increase in the gold concentration in the axial regions.

Increase in gold concentration in the axial region was determined by calculating the total gold content in each radial segment and dividing by the initial concentration of the lead-gold alloy, 500 at. ppm, e.g.,

in Figure 57, the axial gold concentration increase for SFS 11 A is shown. The ordinate represents the total gold content in each segment divided by the initial concentration and the abscissa shows the location of each segment of the specimen with respect to the sample axis which is set equal to 0. A 20 percent gold concentration increase in the central region was observed for 11 A (Figure 57) with a corresponding concentration decrease in the outer radial portions of the specimen. The axial gold concentration increases in SF specimens 13 A-R, 21 A and 17 A-R are shown in Figures 58, 59, and 60, respectively.

The following mechanisms were considered in trying to understand the gold concentration distribution in the SF specimens.

1. Melting Effects

   Radial temperature gradients comparable to longitudinal temperature gradients known to exist might cause variations in gold concentration. Although the magnitudes of the radial temperature gradients are not known, one would expect a difference in the gold concentration profile for the A and A-R SF specimens since the melting occurred in opposite directions. However, since the curvature of the gold concentration is the same for both A and A-R SF specimens, this explanation is assumed to be invalid.

2. Solidification Effects

   a) Interdendritic flow - According to Mehrabian[19] et al., the curved concentration profiles could be the result of interdendritic flow. However, an examination of the microstructure revealed no dendritic solidification. Curved gold concentration profiles were observed even in the low gold concentration regions (0-5 ppm) where dendritic solidification would not be expected. Thus, this explanation seems infeasible.

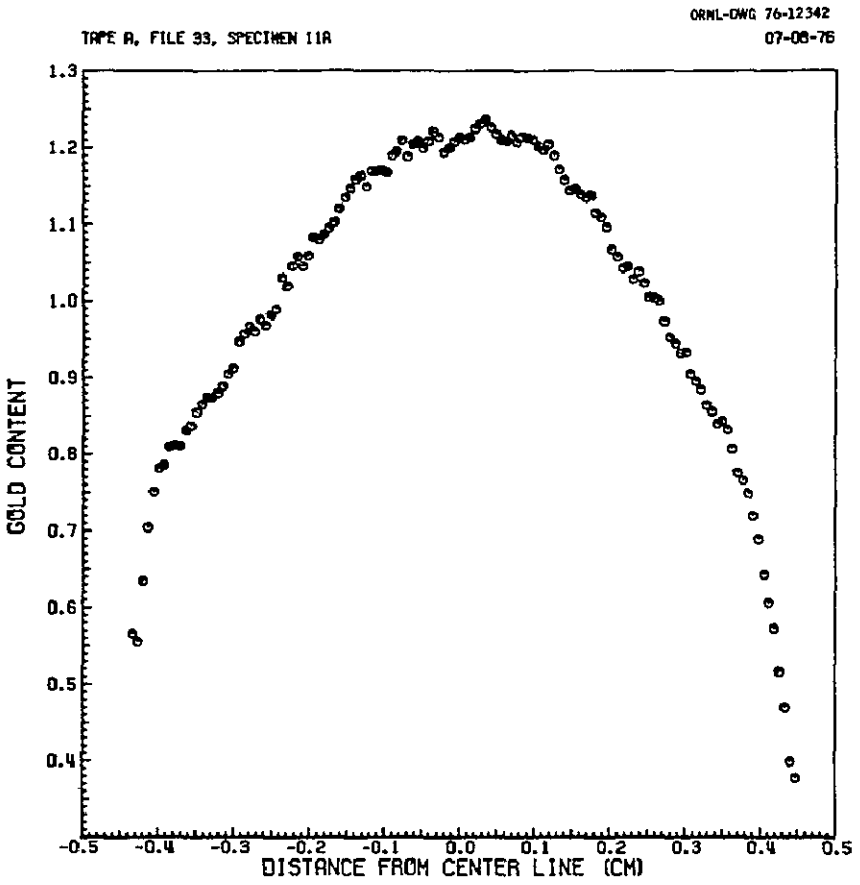

Figure 57. Enhancement of gold in the axial region of space flight specimen 11 A which was located in the 923 K temperature zone. The ordinate represents the percentage of gold for each slice compared to the initial concentration (500 at. ppm). The abscissa represents the radial location of each slice compared to the central slice.

b) Volume shrinkage - Volume shrinkage during solidification in the presence of curved interfaces generally could cause radial concentration distortion. However, in this case one would expect opposite radial concentration profile curvature for the A and A-R specimens. Thus, even though the volume shrinkage for lead is 3.1 percent, it apparently had no effect on the final gold concentration profiles.

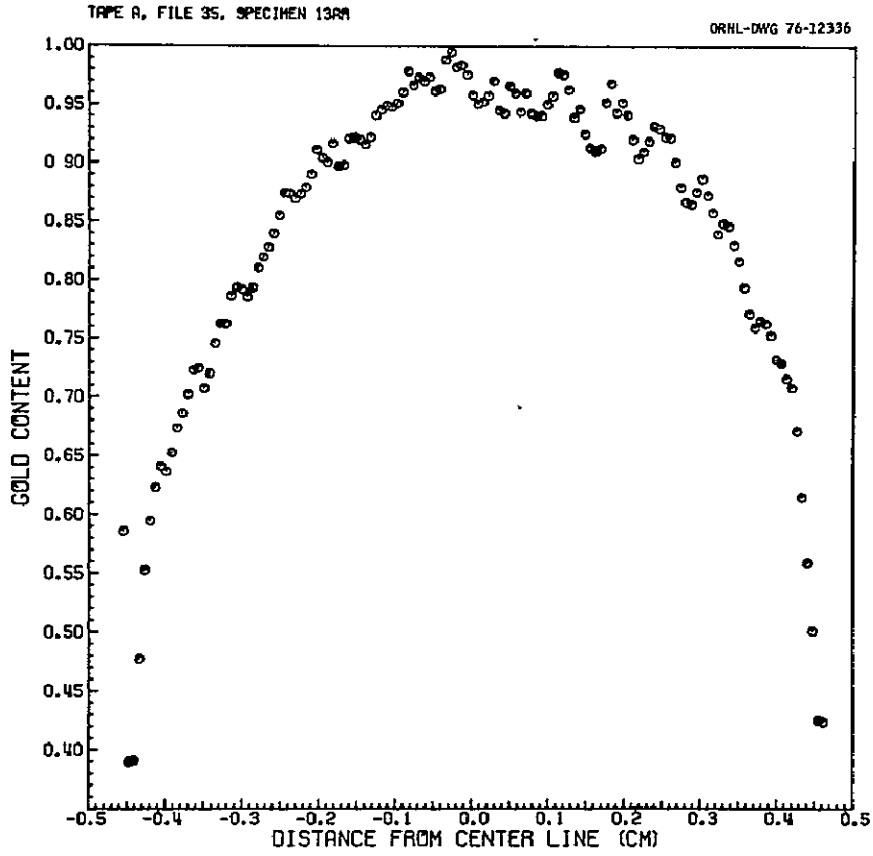

Figure 58. Enhancement of gold in the axial region of space flight specimen 13 A-R which was located in the 923 K temperature zone. The ordinate represents the percentage of gold for each slice compared to the initial concentration (500 at. ppm). The abscissa represents the radial location of each slice compared to the central slice.

Thus, the experimental arrangement of the A and A-R specimens made it possible to exclude melting or solidification effects as an explanation for the curved gold concentration profiles.

3. Flow Effects While in the Liquidous State

a) Radius-dependent diffusion - Radius-dependent diffusion may occur as the result of a radial temperature gradient but if there was a radial gradient due to the furnace design, one would assume a higher temperature at the surface of the

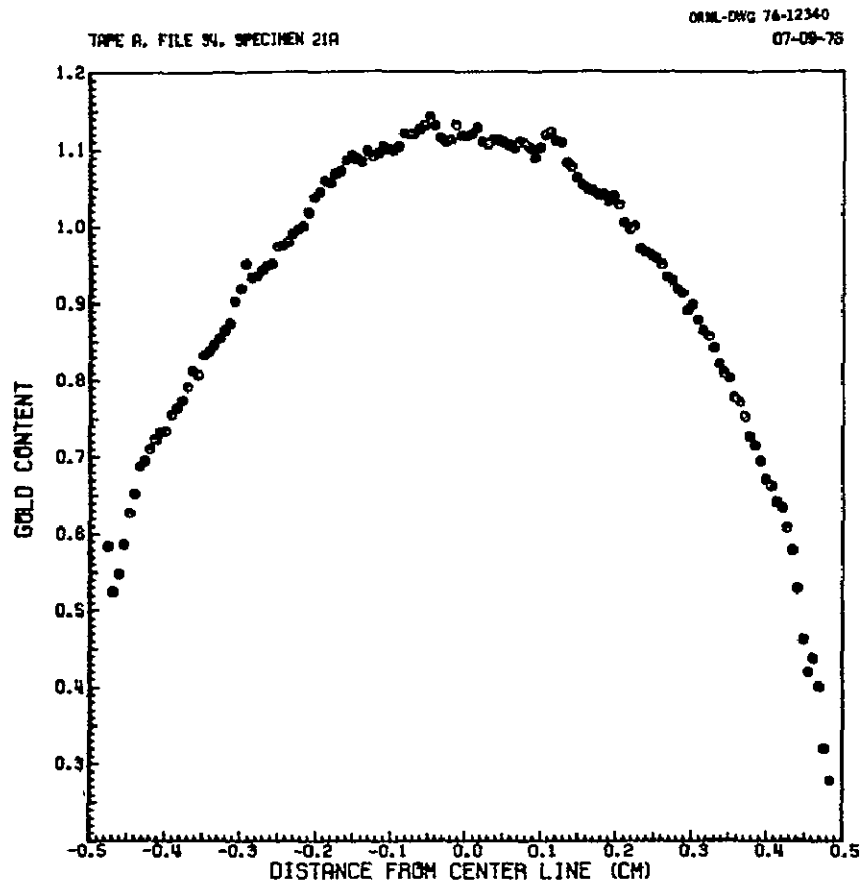

Figure 59. Enhancement of gold in the axial region of space flight specimen 21 A which was located in the 723 K temperature zone. The ordinate represents the percentage of gold for each slice compared to the initial concentration (500 at. ppm). The abscissa represents the radial location of each slice compared to the central slice.

specimen. In this case diffusion would be faster in the surface region which would create a resultant concentration curvature opposite to that observed.

b) Flow caused by gas pressure differences - Pressure difference between the meniscus at the left side and right side of the specimen could cause a flow of all the material in one direction. Therefore, the curved concentration profiles are probably not caused by pressure differential since

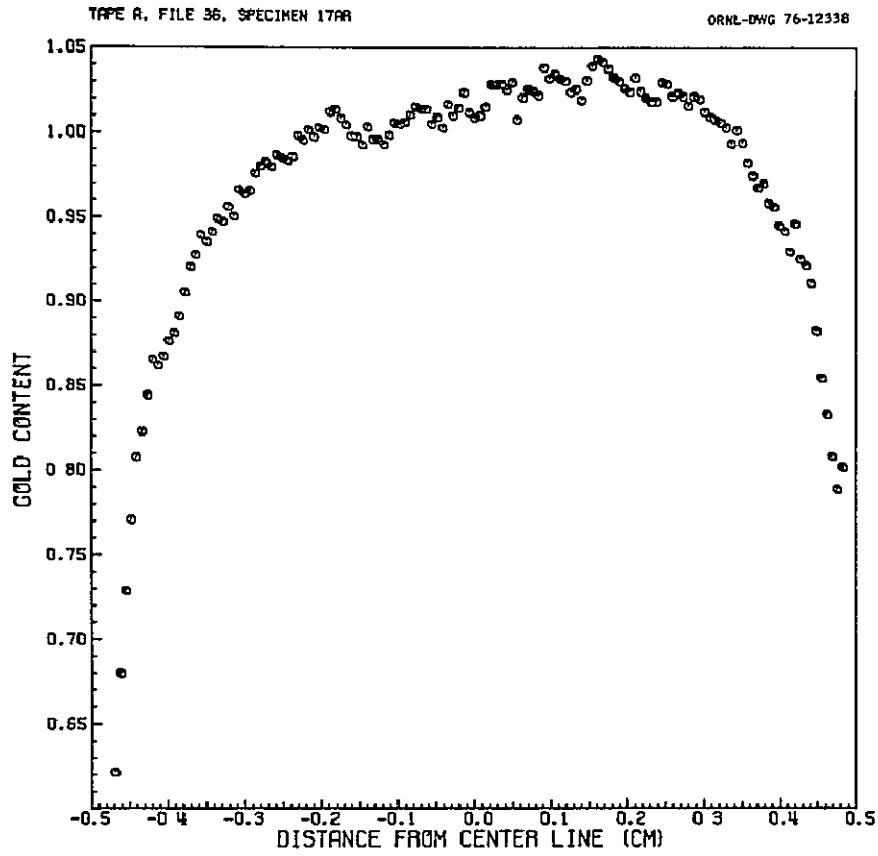

Figure 60. Enhancement of gold in the axial region of space flight specimen 17 A-R which was located in the 723 K temperature zone. The ordinate represents the percentage of gold for each slice compared to the initial concentration (500 at. ppm). The abscissa represents the radial location of each slice compared to the central slice.

1. all material would necessarily flow in the same direction, and

2. the specimens were sealed in the ampoules in a vacuum of 10^{-6} torr.

c) Meniscus forming induced flow - Meniscus induced flow could have played a part in forming the curved gold concentration profiles. The equilibrium form of the meniscus in a nonwetting container under zero gravity is a half sphere.

Under this assumption, during the melting process, some material from the outer region would flow to the central region to form the equilibrium shape. Material flow would occur toward the center of the specimen and part of the material would flow back, forming the flow patterns shown in Figure 61. In our experiment such an effect was probably less than other effects since the development of the meniscus was impeded by the confining walls of the capsule.

d) Marangoni effect induced flow - Experimental results can be explained by assuming induced material flow was caused by either a difference in the interfacial energies between the alloy-graphite or lead-graphite, or a difference in the surface tensions of the alloy and pure lead according to the contact conditions which will be discussed later. Assuming the interfacial tension of alloy-graphite to be greater than that of lead-graphite, convection could occur after melting in the region and in the direction shown in Figure 62 to decrease the difference in the interfacial tensions or surface tensions. Lead would be transported in the region near the walls to the alloy region, thus diluting the latter region. A corresponding flow would occur in the specimen center in the opposite direction causing the alloy to flow into the pure lead region.

An estimate of the Marangoni number was obtained from the equation

$$M_a = -\Delta\gamma \cdot \frac{L}{\eta \cdot \psi} \qquad (10)$$

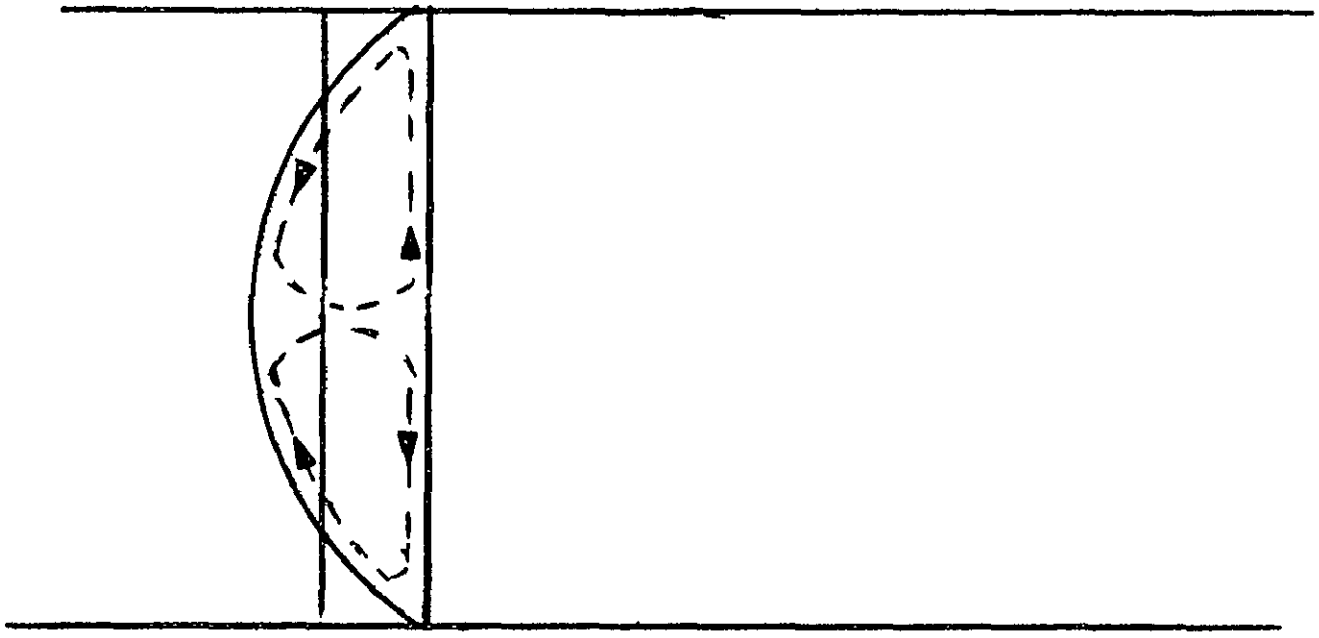

Figure 61. Schematic representation of the flow pattern for meniscus-forming induced flow.

ORNL-DWG 76-10056

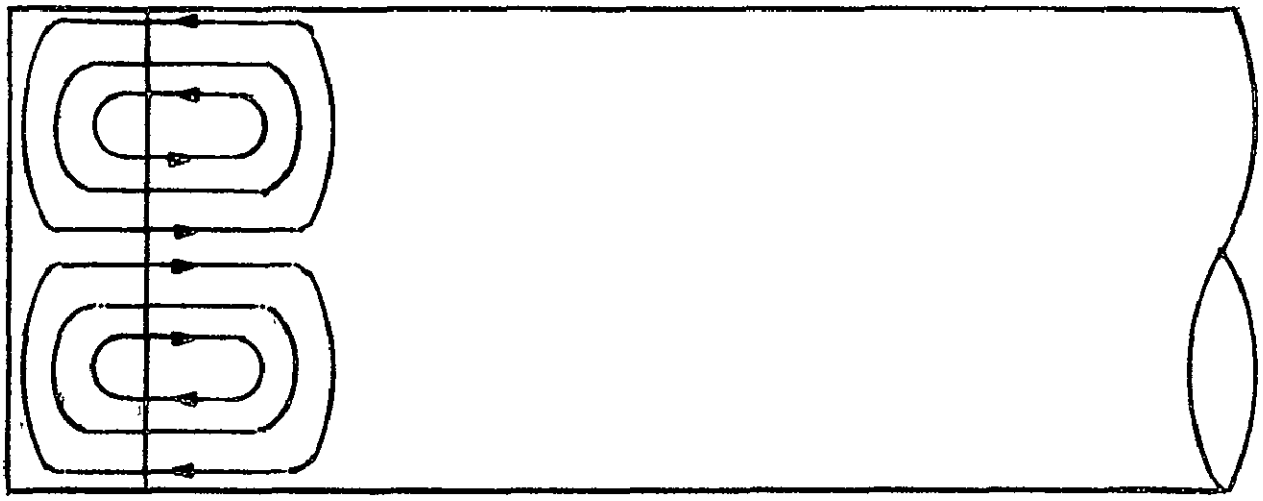

$$Ma = \Delta\gamma \cdot \frac{L}{\eta \cdot \chi}$$

$$Ma = 97 \quad (L = 1\,cm \quad \Delta\gamma = 0.37\ dynes \cdot cm^{-1})$$

Figure 62. Schematic representation of the flow patterns arising from the Marangoni effect.

where

M_a = Marangoni number

$\Delta\gamma$ = surface tension difference

L = specimen diameter

η = viscosity

ψ = heat diffusivity,

with

$$\psi = \frac{\lambda}{\rho C_v} \tag{11}$$

where

λ = heat conductivity

ρ = density

C_v = specific heat for constant volume.

Estimation of the Marangoni number was made using available surface tension values of the similar copper-tin system. The estimated value of 97 for the 723 K specimens supports the above argument since the critical Marangoni number for zero-gravity is zero.

The Marangoni effect can, in fact, explain all of the experimental observations, such as the gold concentration minimums, occurrence of a gold concentration maximum (not at the beginning of the alloy as in a normal diffusion experiment, but at some distance from the end of the specimen), and the low gold concentrations in the outer radial regions of the specimens. In addition, smaller curvatures for the lower temperature specimens can be explained by the same mechanism since the viscosity at the lower temperature is greater which would result in a lower flow velocity.

Additional support for induced flow resulting from the Marangoni effect can be found in at least three other experiments:

1. Indium Self-Diffusion Under Unit Gravity[20] - The capillary method was used to study indium self-diffusion over a wide temperature range. Curved concentration profiles were observed. Nachtrieb[21] explained these results by radial segregation of the indium tracer isotope which in our opinion is very unlikely based on isotope separation theory.

2. Liquid Zinc Self-Diffusion at Near-Zero Gravity[22] - Zinc-65 was pressure bonded to zinc and placed inside a carbon lined tantalum ampoule. Samples remained in the liquid state for one hour. Zinc (^{65}Zn) concentration profiles were determined by sectioning the specimens and gamma-counting each

segment to determine the ^{65}Zn concentration. Results indicated curved concentration profiles in the radial direction which Ukanwa attributed to surface diffusion, capillary attraction or some sort of surface phenomena.

3. Tea Diffusion Experiment in Near-Zero Gravity[23] - A tea solution was placed in an ampoule containing water and the diffusion process was monitored. Curved concentration profiles were visually observed by the astronauts aboard Skylab, but no quantitative data were obtained.

We believe the results of the first two experiments can better be explained by Marangoni-effect induced flow which results from surface tension gradients induced by temperature gradients, while in the last experiment the interfacial or surface tension gradient was caused by concentration differences.

The greatest flaw in the previous explanation is that, according to hydrodynamic theories, Marangoni-effect induced flow should only occur on "free" surfaces. In this experiment and the three experiments referred to above, it must be assumed that the liquid touched the container walls. Thus, flow caused by interfacial tension gradients can only occur if one assumes a non-zero flow velocity at the walls. According to Screven[24] and Richardson[25], this is a violation of the zero-slip boundary condition. On the other hand, we believe there are some reasons for doubting the zero-slip boundary conditions in space. The degree of contact of the nonwetting fluid may be different for zero gravity than for unit gravity. The fluid may have only partially contacted the ampoule wall, thus free surfaces could have existed over small regions. The degree of contact is influenced by the different pressures in the fluid. If, in fact, the Marangoni-effect induced flow in this experiment was not hindered by total contact, we can assume, in this case, that flow was caused by the difference in the surface tensions rather than the interfacial tensions.

The best explanation at this time for the experimental results is that a flow induced by the Marangoni effect did occur. We would suggest that investigations should be made concerning the validity of the non-zero boundary condition in zero gravity with nonwetting materials and different surface structures for the container walls.

MILD STEEL CAPSULES

The gold concentration distribution for the specimens in the mild steel containers was similar to that obtained for the specimens in graphite containers. Macrographs of the longitudinal cut surfaces of mild steel-contained GB and SF specimens are shown in Figures 63 through 66. As shown by the meniscus shapes, the contact angle in all GB and SF cases is >90°. Rough measurements of contact angles indicate a tendency for nonwetting for the GB specimens and nearly total nonwetting for the space flight specimens.

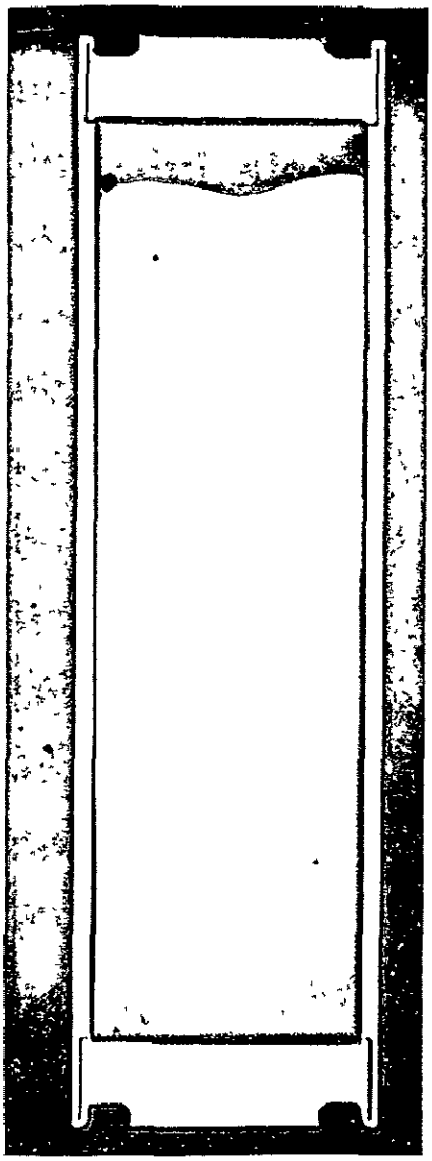

Figure 63. Macrograph of the as-polished 13 B ground base specimen contained in a mild steel ampoule. The specimen was mounted vertically in the 923 K temperature zone. The original lead-gold alloy was located at the top. Melting direction was from top to bottom.

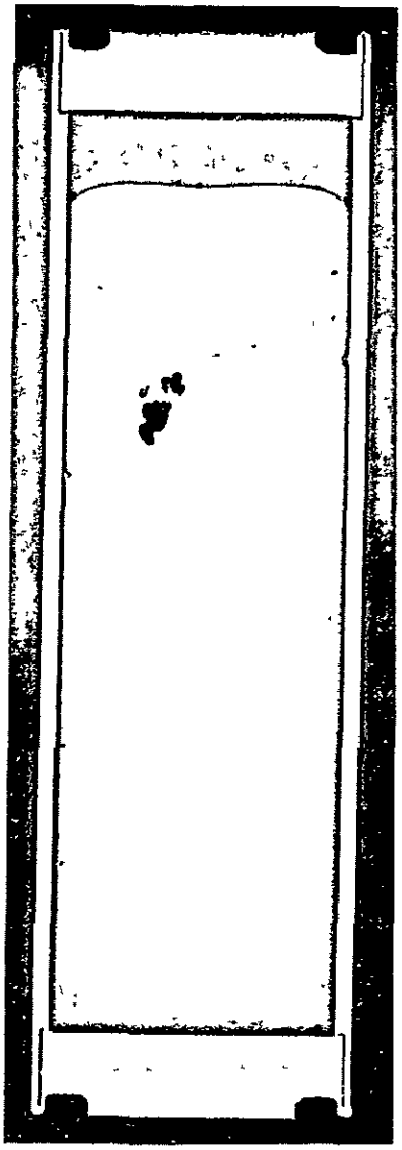

Figure 64. Macrograph of the as-polished 15 B ground base specimen contained in a mild steel ampoule. The specimen was mounted vertically in the 723 K temperature zone. The original lead-gold alloy was located at the top. Melting direction was from top to bottom.

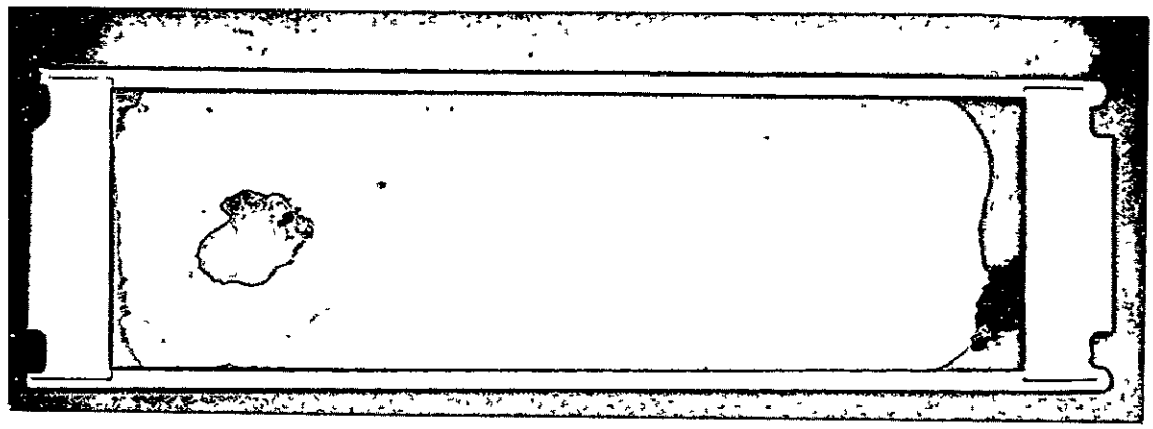

Figure 65. Macrograph of the as-polished 12 B space flight specimen contained in a mild steel ampoule. The specimen was located in the 923 K temperature zone and melted from left to right. The original lead-gold alloy was located in the vicinity of the large void.

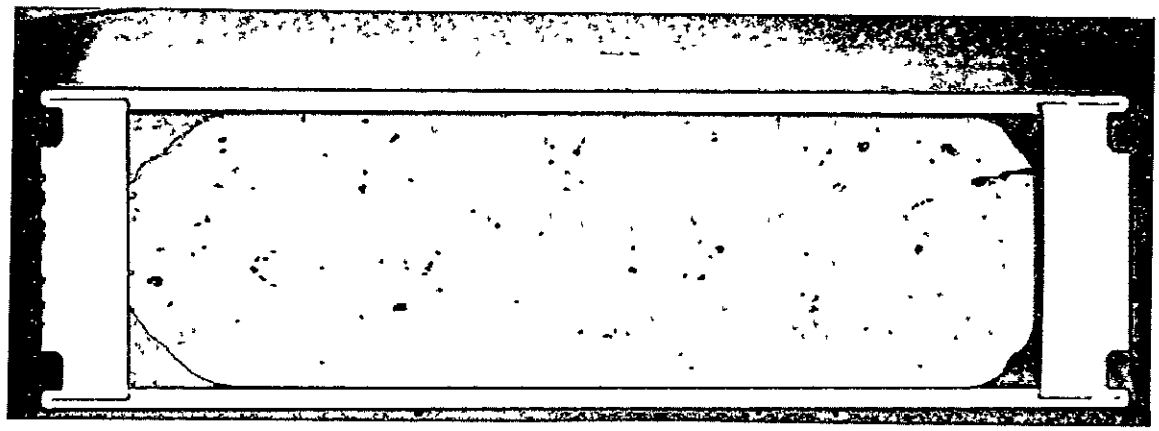

Figure 66. Macrograph of the as-polished 21 B space flight specimen contained in a mild steel ampoule. The specimen was located in the 723 K temperature zone and melted from left to right. The original lead-gold alloy was located on the left side of the specimen as shown. Dark spots are oxide deposits on the surface.

MICROSTRUCTURE

Initial investigations revealed no systematic differences in the microstructure of the GB and SF specimens. Selected areas in the autoradiographs of two SF and one GB specimen were magnified for an examination of the microstructure. The observed microstructures can be classified as follows:

1. Grain and subgrain boundaries,
2. Well developed cell structure, and
3. Diffuse-little structure.

These microstructures are shown in Figures 67, 68, and 70, respectively. Each large division in the figures represents approximately 0.7 mm. Figure 67 shows an enlargement of a selected area in the gold-rich region of Figure 44 (SFS 13 A-R) which contains grain and subgrain boundaries. The pseudocolor assignment is as shown in Table 10. Segregation of gold at the grain boundaries is shown by the orange color and represents at least a 60 percent increase over the amount of gold in the adjacent grain region. One also can observe that segregation in the grain boundaries is not homogeneous.

Well-developed cell structure is shown in Figure 68 which is an enlargement of a selected area in the center of Figure 39 (GBS 17 A). The pseudocolor assignment for the gold concentrations in Figure 68 is shown in Table 16. Quantitative gold concentration data for the magnified region of GBS 17 A is shown in Figure 69 for a slice taken parallel to the melting direction. Gold concentration values (at. ppm) are shown along the ordinate. The abscissa represents the column number where the corresponding linear distance between two columns on the sample is 0.0175 mm.

The slice shown in Figure 69 was located approximately 9.5 large divisions from the top of Figure 68. The average cell size calculated from the slice is approximately 0.3 mm. In addition, further examination of the slice reveals a segregation increase of gold at the cell walls of

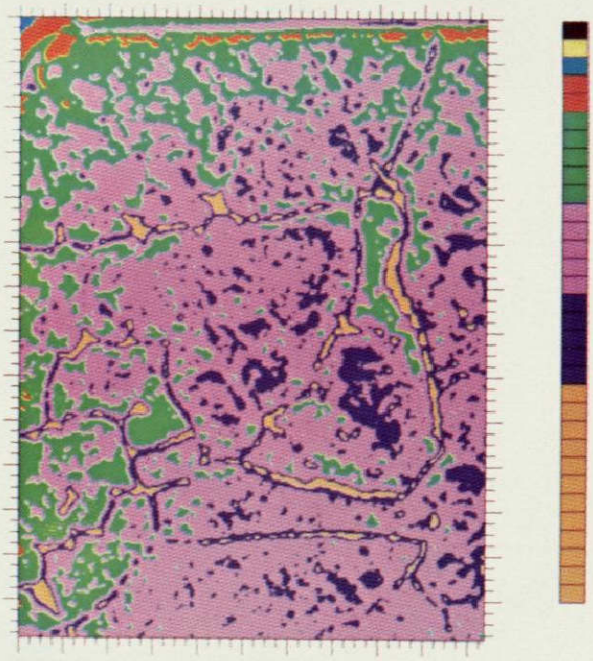

Figure 67. Magnification of an area from the gold-rich region of space flight specimen 13 A-R used to examine microstructures. The pseudocolor-gold concentration assignments are shown in Table 10.

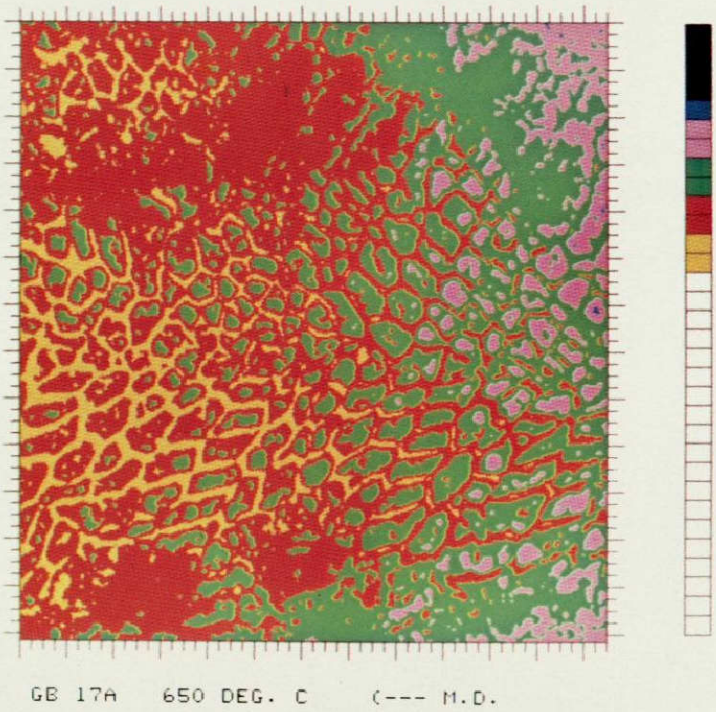

Figure 68. Magnification of an area from ground base specimen 17 A used to examine microstructures. The pseudocolor-gold concentration assignments are shown in Table 16.

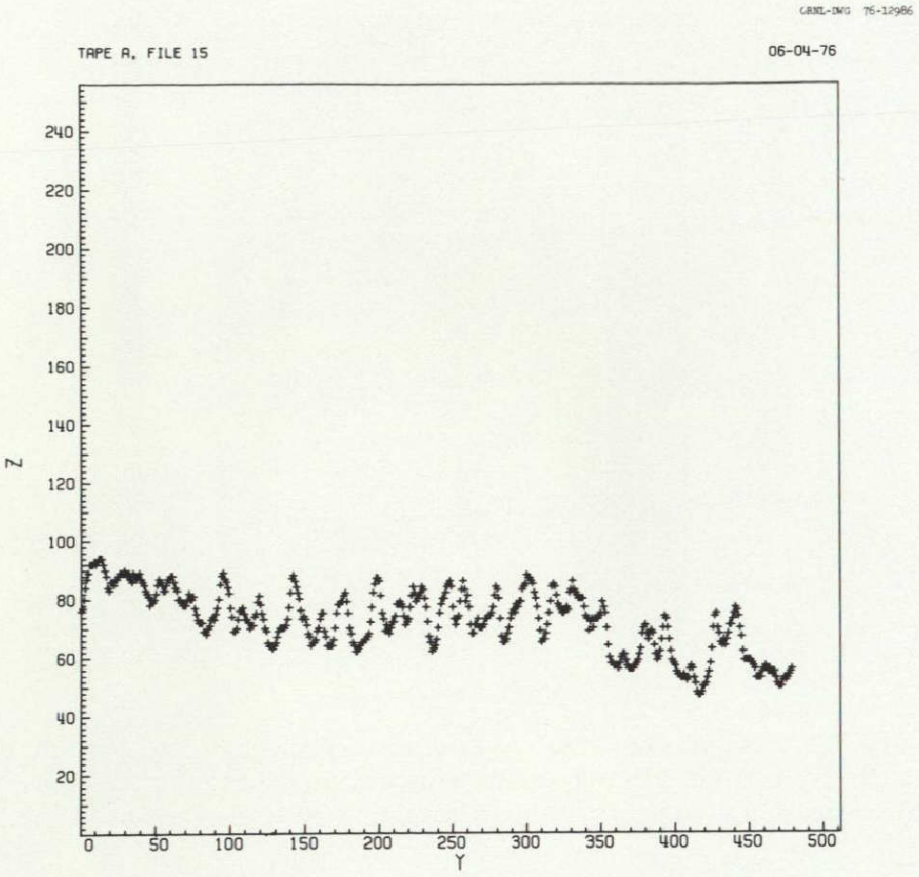

Figure 69. Gold concentration data for a slice parallel to the melting direction for ground base specimen 17 A. The ordinate gives the gold concentration (at. ppm) and the abscissa represents the column number where the distance between two columns is 0.0175 mm.

Table 16. Color Scheme Relating Pseudocolors to Gold Concentrations for GBS 17 A Magnification

Pseudocolor	Gold Concentration (at. ppm)	Percentage of Original Gold Concentration
Black	0- 24	0- 4.0
Blue	25- 40	5.0- 8.0
Pink	41- 55	8.2-11.0
Green	56- 70	11.2-14.0
Red	71- 85	14.2-17.0
Yellow	86-100	17.2-20.0

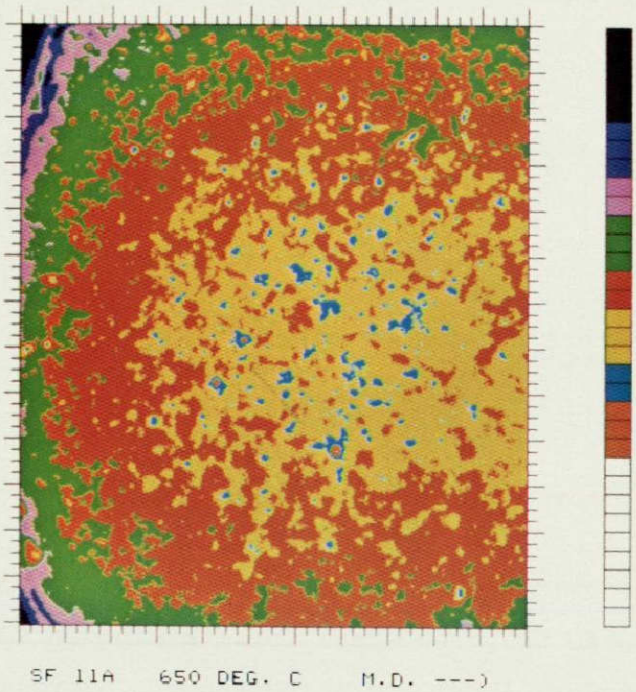

Figure 70. Magnification of an area from space flight specimen 11 A. The pseudocolor-gold concentration assignments are shown in Table 17.

approximately 50 percent compared to the cell interior. Both Figures 68 and 69 show that the cell walls are not very sharp, but are broadened either during formation or by diffusion in the solid. An enlargement of a selected area in the gold-rich region of SFS 11 A (Figure 43) is shown in Figure 70. The pseudocolor representation of the gold concentrations for this magnification is shown in Table 17. As one can see there is very little structure present.

Results obtained for the three magnifications represent only a beginning in the examination of the microstructure of both GB and SF specimens.

Table 17. Color Scheme Relating Pseudocolors to Gold Concentrations for SFS 11 A Magnification

Pseudocolor	Gold Concentration (at. ppm)	Percentage of Original Gold Concentration
Black	0- 40	0- 8.0
Dark Blue	41- 60	8.2-12.0
Purple	61- 80	12.2-16.0
Green	81-100	16.2-20.0
Red	101-120	20.2-24.0
Yellow	121-140	24.2-28.0
Light Blue	141-160	28.2-32.0
Red-Brown	161-180	32.2-36.0

SUMMARY

The purpose of this experiment was to observe compositional-induced convection effects. Convection effects were observed but were not sufficiently large to bring about total mixing in the space flight specimens. However, they were large enough to prohibit analysis of the pure diffusion process. The most plausible explanation for the flow phenomena observed is convection induced by the Marangoni effect; if this explanation is in fact correct, a violation of the no slip condition must be assumed. Results for the ground base specimens were totally different from those melted in space, with convection being a dominant factor.

Expected wetting of the mild steel capsules did not occur in space and only a partial wetting occurred for the ground base specimens.

Initial investigation of the microstructures revealed no systematic differences for GB and SF specimens. Segregation resulted in an increase in gold concentration of approximately 50 to 60 percent in the cell walls and grain boundaries.

PROPOSED ADDITIONAL INVESTIGATIONS

1. Measurement of surface and interfacial tensions for our system components since these values are still unknown.
2. A detailed investigation and comparison of the GB and SF specimen surfaces to determine if there is a difference in contact behavior.
3. Investigation of the no-slip boundary condition especially for nonwetting liquid metals in gravity and a gravity-free environment.
4. Experiments to determine if there exists a difference in the wetting behavior for liquids in unit and zero gravity environments.

ACKNOWLEDGMENTS

Many Oak Ridge National Laboratory personnel have helped in obtaining the results contained in this report. The authors would like to acknowledge J. F. Emery and K. J. Northcutt of the Analytical Chemistry Division for handling all the neutron irradiations. The authors also gratefully acknowledge J. A. Carter and J. C. Franklin, Analytical Chemistry Division, for the many helpful discussions and assistance in making the initial densitometer measurements and to J. D. Sheppard of the Reactor Division, H. C. Schweinler of the Health Physics Division, and E. H. Kobisk of the Solid State Division, for helpful discussions concerning the experimental results. Appreciation is expressed to B. C. Leslie and W. H. Farmer of the Metals and Ceramics Division who did the metallography, C. W. Nestor of the Computer Sciences Division for assistance in putting the data into the desired format, and to C. A. Culpepper, K. B. Campbell, H. E. Harmon, and W. E. Evans of the Solid State Division for making the autoradiographs. In addition, the authors acknowledge the assistance and helpful discussions of R. Ruff, T. Rathz, J. Watkins, and C. Schaffer of the Marshall Space Flight Center, Huntsville, Alabama.

REFERENCES

1. Grodzeka, P. G., Bannister, T. C.: Proceedings of the AIAA 12th Aerospace Sciences Meeting, AIAA Paper No. 74-156, Washington, D. C., January 30-February 1, 1974.

2. Larson, D. J.: Proceedings of the 3rd Space Processing Symposium, Skylab Results, Vol. 1, Marshall Space Flight Center, April 30-May 1, 1974, pp. 101-113.

3. McKannan, E. G., Poorman, R. M.: Ibid., pp. 85-100.

4. Richardson, S.: On the No-Slip Boundary Condition, J. of Fluid Mechanics (1973), Vol. 59, Part 4, pp. 707-719.

5. Ukanwa, A. O.: Proceedings of the 3rd Space Processing Symposium, Skylab Results, Vol. 1, Marshall Space Flight Center, April 30-May 1, 1974, pp. 425-442.

6. Semenchenko, V. K.: Surface Phenomena in Metals and Alloys, Pergamon Press, New York, 1961, pp. 403-404.

7. Hansen, M.: Constitution of Binary Alloys, McGraw-Hill Book Company, New York, 1958, pp. 222-224.

8. Reed, R. E.: J. of Crystal Growth 19, (1973), pp. 61-64.

9. Semenchenko, V. K.: Surface Phenomena in Metals and Alloys, Pergamon Press, New York, 1961, pp. 8 and 400.

10. Semenchenko, V. K.: Surface Phenomena in Metals and Alloys, Pergamon Press, New York, 1961, p. 258.

11. Ukanwa, A. O.: Proceedings of the 3rd Space Processing Symposium, Skylab Results, Vol. 1, Marshall Space Flight Center, April 30-May 1, 1974, p. 440.

12. Crank, J.: The Mathematics of Diffusion, Oxford at the Clarendon Press, London, 1956, pp. 11-14.

13. Key, W. S.: Technical Letter ASD-EP 44-22716, Teledyne Brown Engineering, December 16, 1975.

14. Verhoeven, J. D.: Convection Effects in the Capillary Reservoir Technique for Measuring Liquid Metal Diffusion Coefficients, Transactions of the Metallurgical Society of AIME, Vol. 242, September 1968, pp. 1937-1942.

15. Crank, J.: The Mathematics of Diffusion, Oxford at the Clarendon Press, London, 1956, p. 9.

16. Crank, J.: The Mathematics of Diffusion, Oxford at the Clarendon Press, London, 1956, p. 15.

17. Nachtrieb, N. H.: Self-Diffusion in Liquid Metals, Proceedings of the International Conference on the Properties of Liquid Metals Held at Brookhaven National Laboratory, Upton, New York, September 1966, p. 316.

18. Ukanwa, A. O.: Proceedings of the 3rd Space Processing Symposium, Skylab Results, Vol. 1, Marshall Space Flight Center, April 30-May 1, 1974, p. 440.

19. Mehrabian, R., Keane, M., and Flemings, M. C.: Interdendritic Fluid Flow and Macrosegregation, Metallurgical Transactions, Vol. 1, May 1970, p. 1209-1220.

20. Coreri, G., Paoletti, A., and Vincentini, M.: Nuovo Cim., 10, 1958, p. 1088.

21. Nachtrieb, N. H.: Self-Diffusion in Liquid Metals, The Properties of Liquid Metals, Proceedings of the International Conference Held at Brookhaven National Laboratory, Upton, New York, September 1966, p. 314.

SECTION IV

MONOTECTIC AND SYNTECTIC ALLOYS

EXPERIMENT MA-044

By L. L. Lacy[1,2] and C. Y. Ang[1,2]

1. George C. Marshall Space Flight Center, Marshall Space Flight Center, Alabama
2. Co-Principal Investigators

TABLE OF CONTENTS

LIST OF ILLUSTRATIONS

LIST OF ILLUSTRATIONS (Concluded)

LIST OF TABLES

ABSTRACT

The flight test furnace run of the monotectic and syntectic alloys experiment was successfully performed during the Apollo-Soyuz Test Project mission in July 1975. Examination of the returned sample cartridges and the formal comparative characterization of the low-g and one-g processed samples of lead-zinc and aluminum antimonide have been completed. The results for aluminum antimonide show that polycrystalline and multiphased material can be homogenized in space under low-g conditions. In terms of reduction of the unwanted second phase, the low-g samples show a homogeneity improvement by factors from 4 to 20 over their one-g counterparts. Furthermore, small amounts of the second phase were formed only along parts of the grain boundaries of the flight samples, whereas the ground-based samples show major grains of the second phase. These encouraging results show promise in the possible commercial utilization of space for the containerless zone melting and leveling of aluminum antimonide for solar cell applications.

Microstructural study on the lead-zinc flight samples shows that complete interdiffusion of lead and zinc had not been achieved, even though the flight data indicated a soak temperature in the miscible region that was 40 K above the published consolute temperature. Dispersion of lead particles in the zinc matrix was observed in both the low-g and one-g samples of lead-zinc. A chemical analysis of cut sections shows that the distribution of lead in zinc in the flight sample follows a diffusional process with a diffusion coefficient of approximately 3×10^{-6} cm/s^2, which is approximately two orders of magnitude smaller than that for miscible liquid metals. However, the one-g samples of lead-zinc show a uniform dilute concentration of lead in the zinc matrix, indicating that sedimentation removed most of the lead phase after it was introduced by convective mixing. The lead-zinc investigation illustrates that the quiescent low-g conditions of orbital flight provide an ideal environment for studying the relative importance of convective, sedimentation, and diffusional processes that are difficult to study separately on Earth.

INTRODUCTION

Certain potentially useful alloys or material systems are difficult to synthesize on Earth because of sizable differences in specific gravity of the constituents in a molten state, which result in undesirable buoyancy and convection influences during homogenization of the melts as well as during the initial stages of solidification and grain growth. Consequently, the near zero-g condition in space processing was the primary motivation for this experiment.

Furthermore, significant discoveries related to microsegregation and kinetics of lattice defects, made as a result of the Skylab experiment [IV-1], have strengthened the belief in the value of continuing space processing experimentation for future space manufacturing activities.

The purpose of this experiment was to investigate the effects of weightlessness on the melting and solidification of two material systems, lead-zinc (Pb-Zn) and aluminum antimonide (AlSb). The objectives were: (1) to investigate phase segregation effects in low-g for the immiscible binary Pb-Zn and (2) to determine the influences of low-g solidification on the microstructural homogeneity and stoichiometry of the semiconducting compound AlSb. This report presents a comprehensive summary of evaluation results for two flight samples, two ground-based test (GBT) samples, and two prototype test (PT) samples of each material. Additional samples were used for specific tests such as chemical analyses.

EXPERIMENT CONCEPT AND PROCEDURES

The PbZn monotectic system [IV-2] (Fig. IV-1) is characterized by the large miscibility gap $L_1 + L_2$, where two liquid phases can coexist over a large compositional and temperature range. This system is also characterized by a large density difference between Pb (11.7 g/cm^3) and Zn (7.14 g/cm^3). In the Earth's gravity field, preventing gravity separation between Pb and Zn upon solidification is difficult. Negating the effects of gravity in space processing should lead to an optimum mixing of the two phases, resulting in a dispersion of fine particles of superconducting Pb in a zinc-rich composition. Previous results of Skylab experiments [IV-1, IV-3] and experiments performed using the MSFC drop tower [IV-4—IV-6] indicated that stable dispersions of immiscible liquids can be prepared in low-g, whereas similar dispersions prepared on Earth are rapidly separated by such gravity-dependent influences as creaming, flocculation, and coalescence. The composition selected for the experiment was 20 at.% Pb and 80 at.% Zn as shown by the heavy vertical line in Figure IV-1. This composition is equivalent to a weight percent of 44.2 Pb and 55.8 Zn or a volume percent of 33.2 Pb and 66.8 Zn.

The PbZn samples were prepared from materials five-ninths pure that were premelted by heating (850°C) the samples above the consolute temperature of the binary (795°C) for 10 min. Metallographic examination of the PT and GBT samples indicated good interfacial bonds between the gravity-separated layers. To obtain the low-g dispersions of Pb in Zn, the material was again heated 40°C above the published value of the consolute temperature and allowed

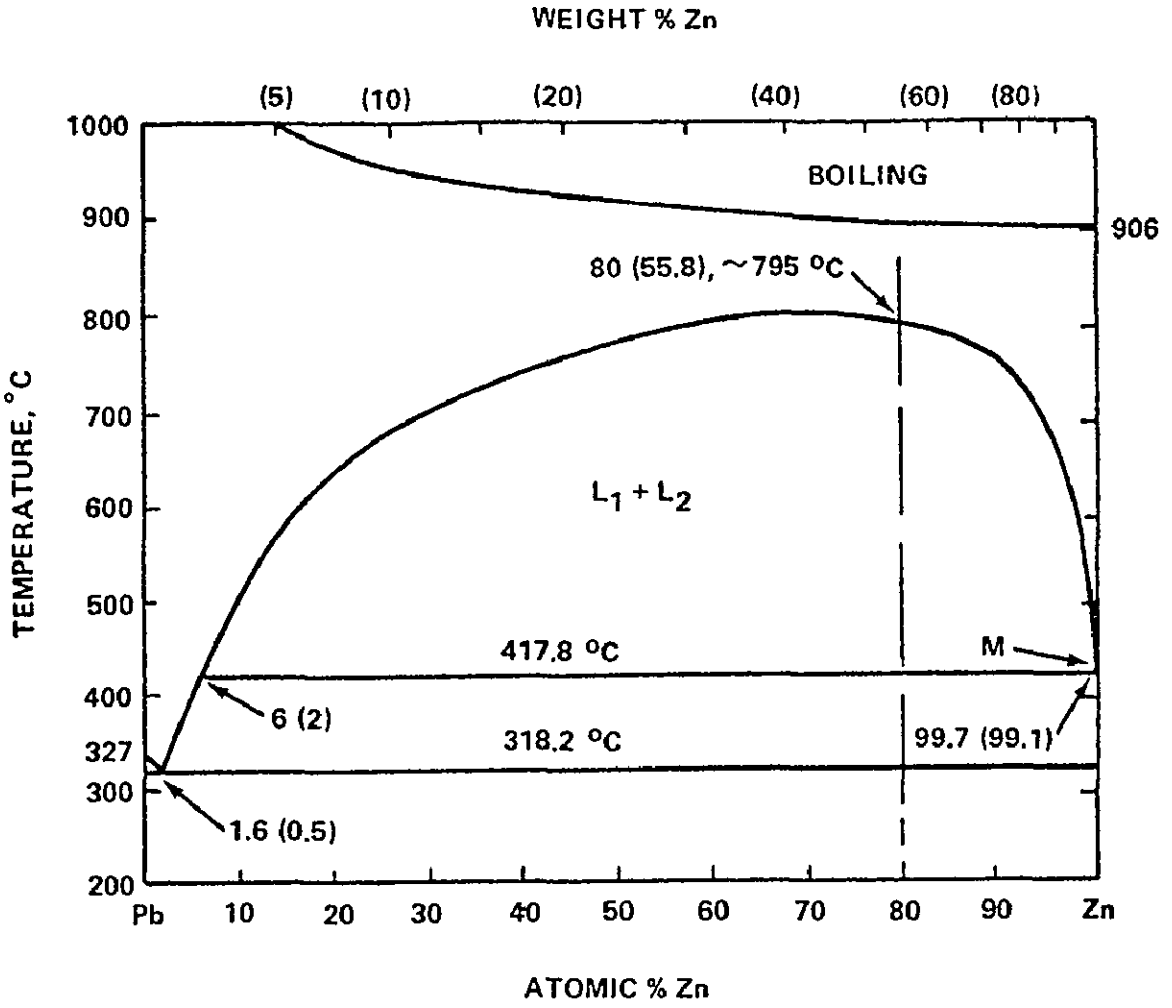

Figure IV-1. Phase diagram for PbZn.

to interdiffuse for 1.5 h. A thermal history of PbZn for both the GBT and flight test is shown by the lower curve in Figure IV-2. Preflight diffusion analysis indicated that the liquid binary should be easily homogenized into a single liquid phase within this time interval. During the cool-down portion of the thermal history, it was anticipated that small lead-rich liquid particles would continuously nucleate and grow in a Zn-rich liquid phase until the monotectic temperature was reached. Therefore, it was the objective of this investigation to study the low-g diffusion and kinetics of such dispersions.

The AlSb system (Fig. IV-3) has been neglected for many years among the III-V semiconducting compounds that are characterized upon solidification by a syntectic transformation of two molten constituents to a constant composition intermetallic compound (at.% of 50 Al and 50 Sb). The reasons for this neglect have been difficulties [IV-7] in synthesizing a stoichiometrically

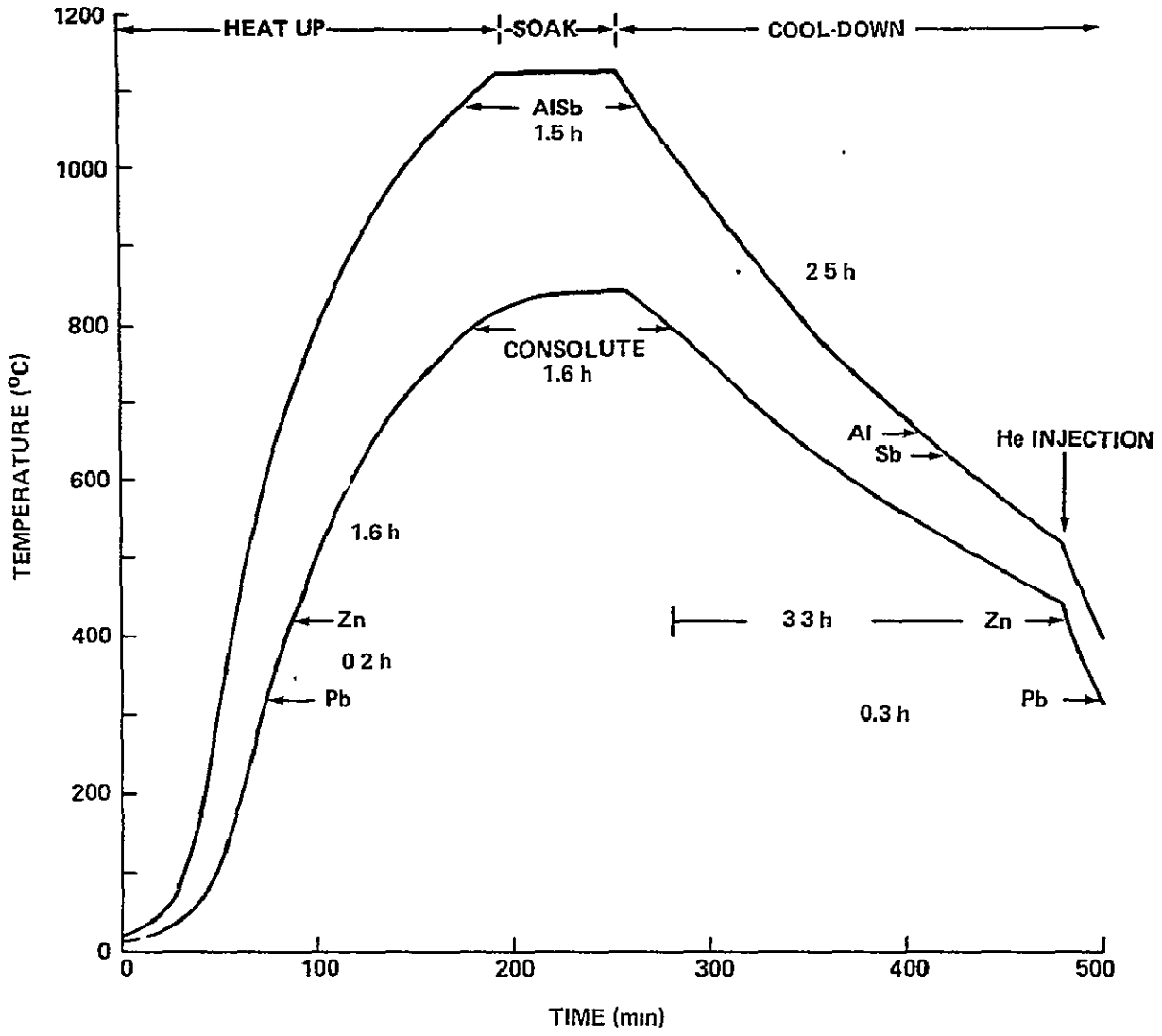

Figure IV-2. Thermal history for AlSb and PbZn.

homogeneous compound and the problems of high reactivity of the material to moisture. With an energy gap of 1.62 eV, AlSb has been theoretically analyzed as a highly efficient solar cell material [IV-8, IV-9] which may be 30 to 50 percent more efficient than silicon.

A typical grain of the best commercially available polycrystalline AlSb can be seen in Figure IV-4. In addition to the compound phase, the material consists of Al- and Sb-rich phases. A chemical analysis of a 2 g sample of this starting material indicated that macroscopically the material has the correct stoichiometric composition of 50.00 at.% of each element and no more than 0.001 wt.% oxygen content. In space processing, the compositional homogeneity may be enhanced by minimizing the very large density difference between

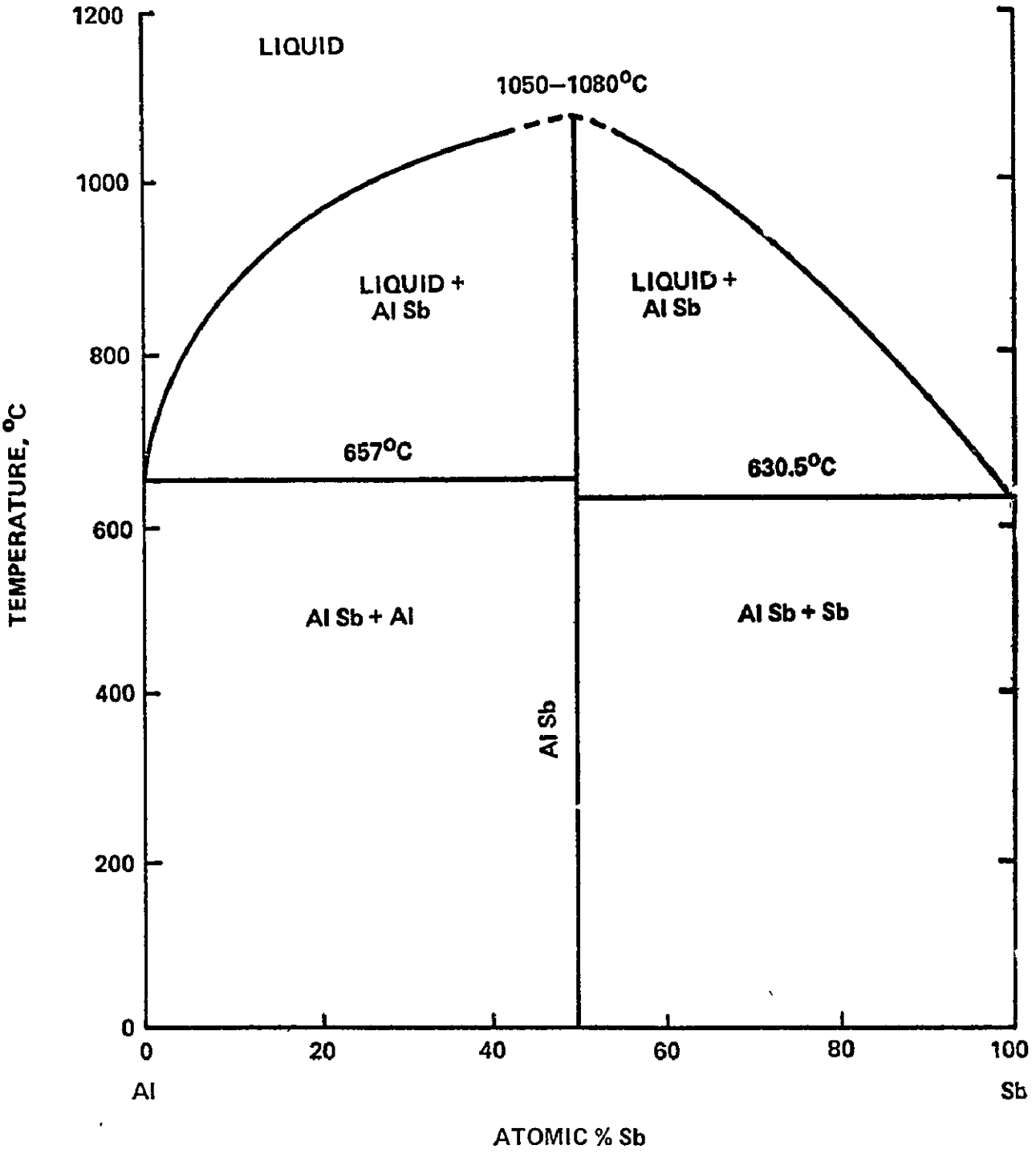

Figure IV-3. Phase diagram of AlSb.

Figure IV-4. Typical grain of AlSb starting material.

constituents (2.7 g/cm^3 for Al and 6.62 g/cm^3 for Sb) in the molten state and during crystallite formation upon cooling. Electromotive potential considerations suggest that Al- and Sb-rich phases observed in polycrystalline AlSb synthesized on Earth could cause the high reactivity to moisture. It was therefore the objective of this investigation to determine if low-g liquid-state homogenization and solidification would improve the microstructural and compositional homogeneity of the best commercially available polycrystalline AlSb. A thermal history of the AlSb samples for both the flight and GBT samples is given by the upper curve of Figure IV-2. The experiment consisted of heating samples of polycrystalline AlSb 50°C above the melting temperature (1080°C) for 1 h.

A detailed description of sample preparation and experiment design for the ampoules and cartridges can be found in References IV-10 and IV-11. Briefly stated, the AlSb and PbZn samples were thermally cycled in the multipurpose furnace on the Apollo-Soyuz Test Project (ASTP), which had three furnace cavities each providing a short hot zone and a longer gradient zone. As depicted in Figure IV-5, each furnace cartridge contained one AlSb and one PbZn ampoule. Except for the difference in size, the two types of ampoules were similarly constructed. All sample preparation and ampoule assembly steps, from graphite crucible capping to tungsten-inert-gas welding of the stainless steel containers, were carried out within an atmosphere of ultrapure argon gas. Similarly assembled sample cartridges were thermally processed on the ground under one-g conditions for comparative characterization purposes. The post-ASTP and post-ground test examination of cartridges and ampoules, including the quick-look evaluation of a limited number of samples, has been previously reported [IV-10, IV-11]. Only data and illustrations from the previous reports that were considered germane to the discussions are reintroduced in this report.

EXPERIMENTAL RESULTS AND DISCUSSIONS

Although the common denominator for both the AlSb and PbZn experiments is the study of effects of low-g on liquid-state heat treatment and solidification, the two types of material systems are quite different in terms of phase equilibria, phase transformations, and anticipated microstructure and properties. Therefore, the experimental results and analyses of the two materials are presented separately in the following discussion.

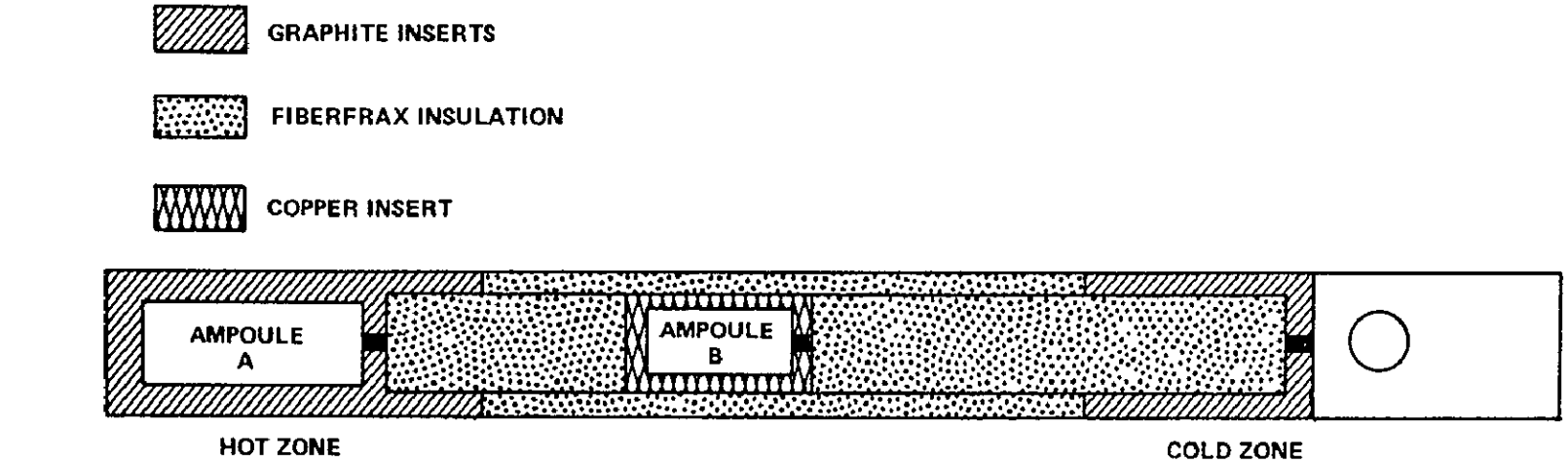

a. Simplified schematic of stainless steel cartridge assembly.

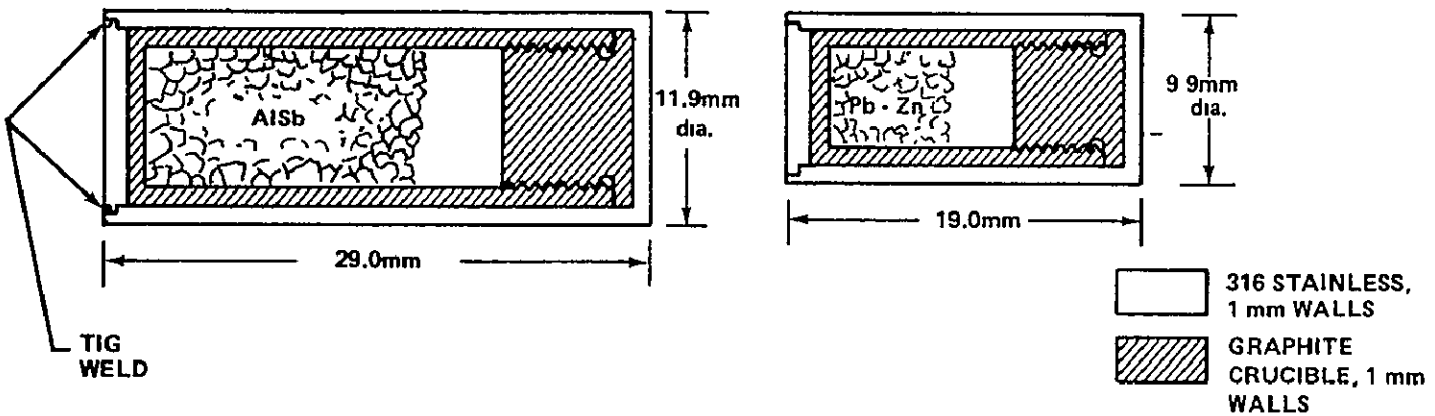

b. Ampoule A (AlSb).

c. Ampoule B (PbZn).

Figure IV-5. Schematic of cartridge assembly and ampoules.

THERMAL HISTORY

The soak temperatures of the flight and GBT samples were determined by using thermocouples attached directly to the experiment ampoules in instrumented PT's. Ampoule temperatures in the PT's were determined as a function of two temperatures simultaneously measured inside the multipurpose furnace. The two temperatures measured in the furnace are at the hot end and cold end of the experiment cartridges. Thus, the thermal history of the flight and GBT samples, shown in Figure IV-2, was indirectly calculated from the measured furnace temperature data, shown in Figure IV-6. In Figure IV-6 the hot and cold end furnace data for the flight and GBT cartridges are compared. The data on Figure IV-6 indicate that both the flight and GBT samples had essentially equivalent thermal histories.

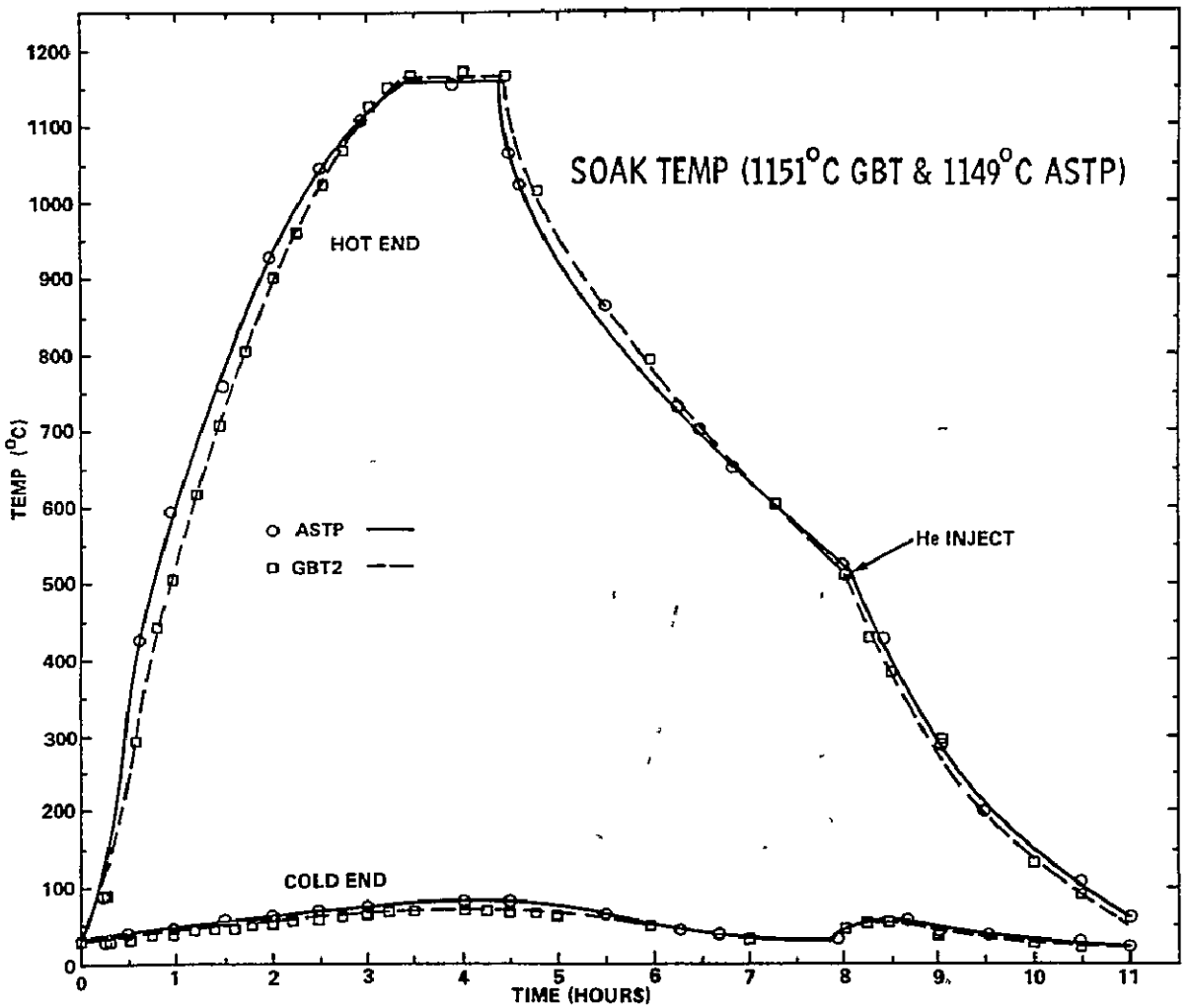

Figure IV-6. Hot end and cold end temperatures of experiment cartridges.

POSTFLIGHT EVALUATION AND CHARACTERIZATION

Postflight evaluation and characterization of the flight and GBT samples is given in Table IV-1. A detailed discussion of task 1 and task 2 and a quick-look metallographic assessment of one flight (A185) and one prototype (A127) sample of AlSb are given in Reference IV-10. A preliminary analysis of one flight sample (A185), one GBT sample (A141), and two PT samples of AlSb can be found in Reference IV-11. This report reviews the completed characterization of the samples previously mentioned plus additional flight, GBT, and PT samples. The characterization tasks to be discussed include metallography, quantitative microstructural analysis, scanning electron microscopy/energy dispersive X-ray analysis (SEM/EDAX), electrical resistivity measurements, X-ray diffraction studies, and chemical and ion-microprobe mass analysis (IMMA).

METALLOGRAPHY AND QUALITATIVE MICROANALYSIS

A comparison of the microstructures of low-g and one-g samples is presented in Figure IV-7. The typical unetched microstructure of low-g homogenized AlSb, as represented by ASTP samples A185 and A164 in Figures IV-7(a) and IV-7(b) respectively, shows that the very small amounts of a second phase (light) are formed along parts of the boundaries of the primary grains (dark) of AlSb compound. In contrast Figures IV-7(c) and IV-7(d), representing the typical microstructures of the PT and GBT AlSb samples respectively, show large amounts of the secondary phases not unlike the microstructure of the starting material (Fig. IV-4). Figures IV-8(a) and IV-8(b) are pseudocolored photographs of Figures IV-7(a) and IV-7(c) in which surface artifacts have been eliminated and the computer-aided technique of digital imaging analysis (DIA) has been used to more clearly present compositional homogeneity. The red areas of the photograph represent the AlSb compound, and the blue areas represent a second phase (Al-rich for the flight sample and Sb-rich for the one-g sample). For these two selected photomicrographs, the area fraction of the secondary phase is 21.6 percent in the one-g sample and 1.7 percent in the flight sample.

Major improvements in microscopic homogeneity are quite evident in the flight samples. The energy dispersive X-ray maps of the one-g and low-g samples, shown respectively in Figures IV-9 and IV-10, qualitatively identify the gray phase as the compound AlSb and the white phase as an Al-rich phase (in the SEM, the secondary phase appears lighter than the compound phase). Figure IV-11 is a pseudocolor representation of the low-g and equivalent one-g microstructure using DIA. An analysis of the area fraction of the second phase

TABLE IV-1. POSTFLIGHT EVALUATION AND CHARACTERIZATION PLAN

Evaluation	AlSb	PbZn
Cartridge Examination (Task 1)		
Photography	X	X
Radiography (Preflight and Postflight)	X	X
Disassembly	X	X
Ampoule Examination (Task 2)		
Photography	X	X
Radiography	X	X
Leak Tests (Helium)	X	X
Weighing	X	X
Sample Characterization (Task 3)		
Removal	X	X
Weighing	X	X
Stereoscopic Examination (10X to 100X)	X	X
Macrophotography (2X to 10X)	X	X
SEM[a] Topography (60X to 1000X)	(b)	X
Surface EDAX[c]	(b)	X
Microstructure (Metallography)	X	X
Quantitative Microstructural Analysis	X	X
SEM/EDAX (Qualitative and Quantitative)	X	X
Microhardness Testing	X	(b)
Resistivity (Four-Point Probe)	X	X
X-Ray Diffraction	X	X
Chemical and Spectral Analysis	X	X
Microchemical Analysis (Ion-Microprobe)	X	X
Diffusion Analysis	X	X

a. Scanning electron microscope.

b. No evaluation.

c. Energy dispersive X-ray analysis.

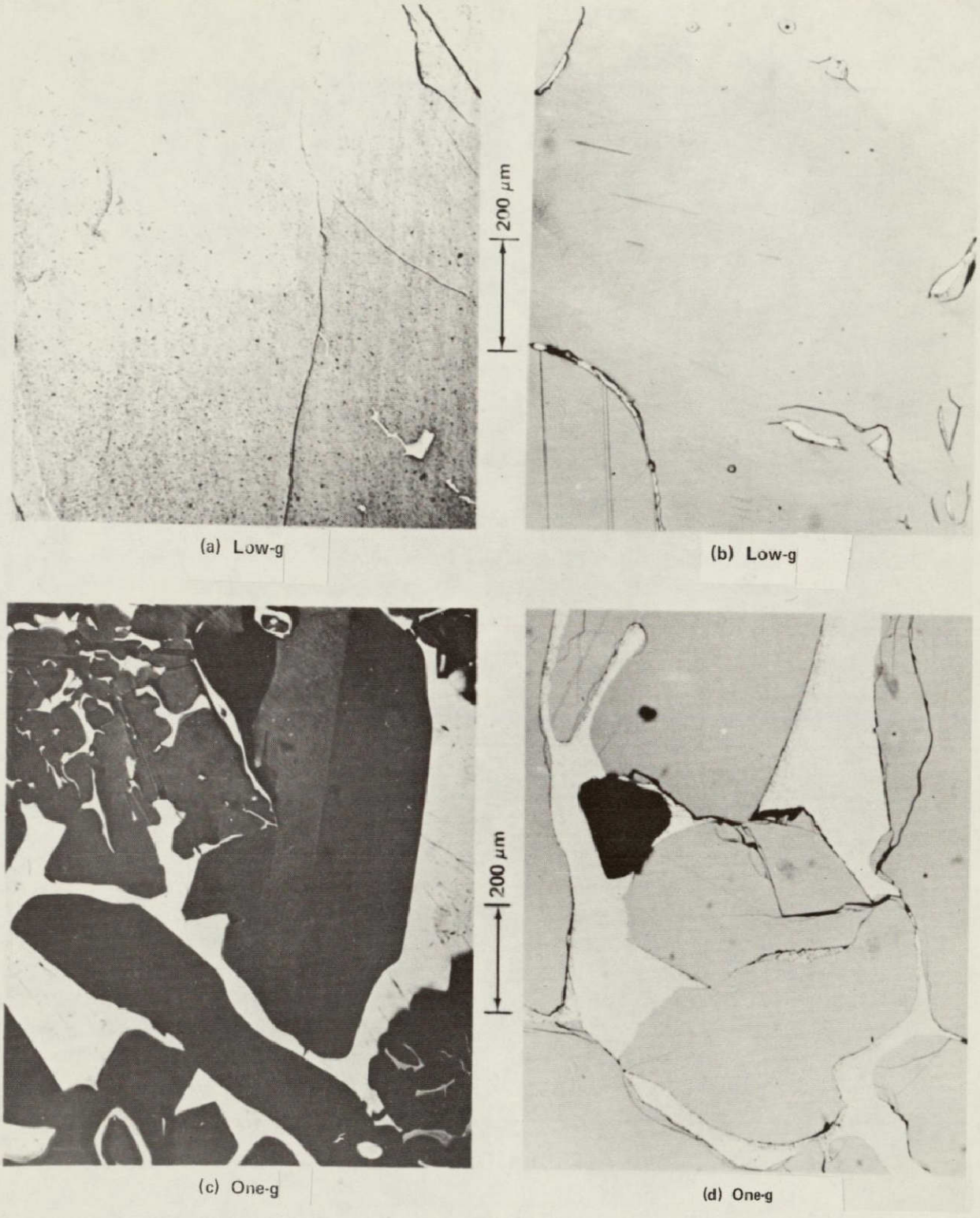

Figure IV-7. Microstructures of low-g and one-g AlSb samples.

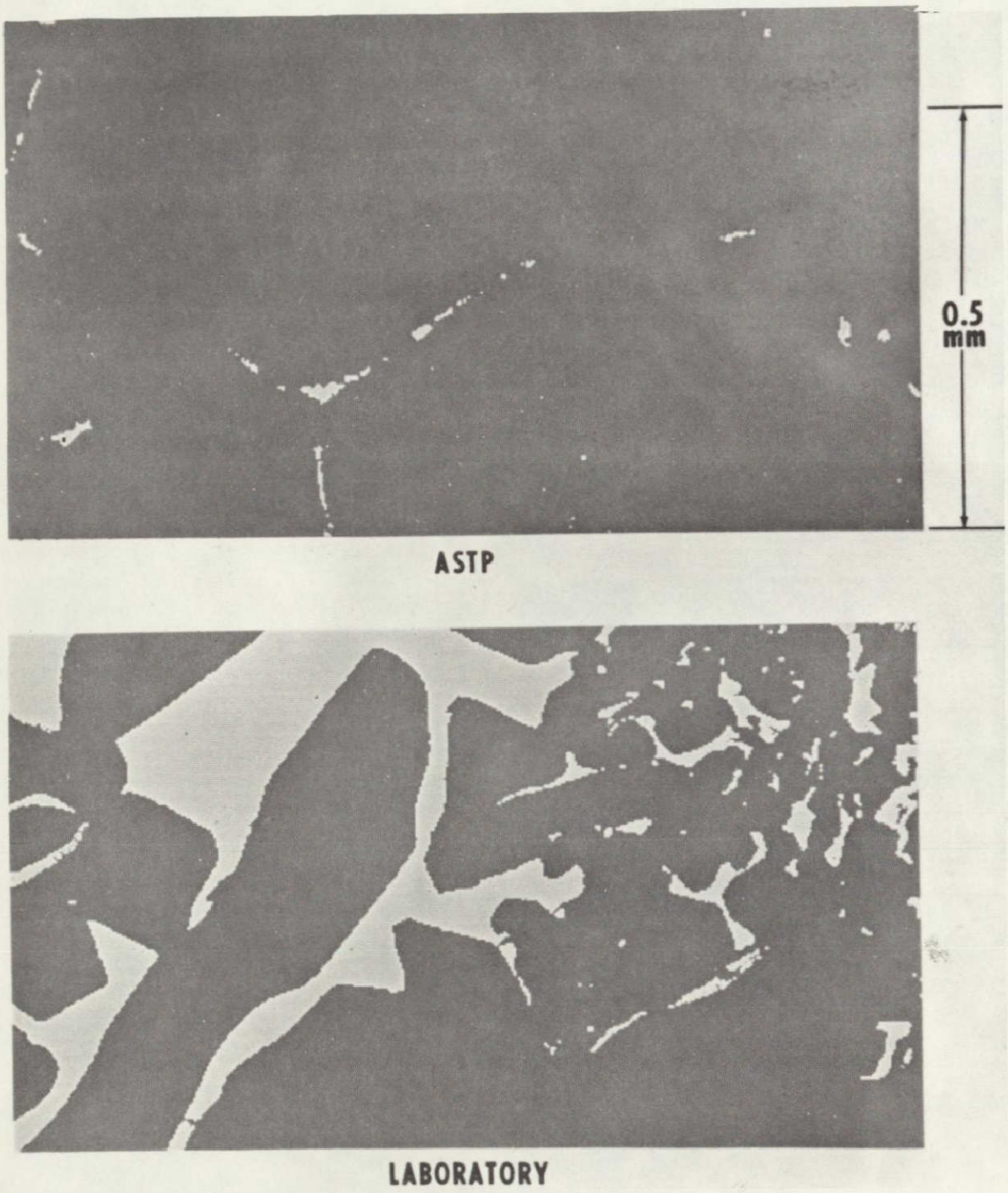

Figure IV-8. Pseudocolored microstructures of flight and prototype tested AlSb samples.

Figure IV-9. EDAX map of GBT AlSb sample.

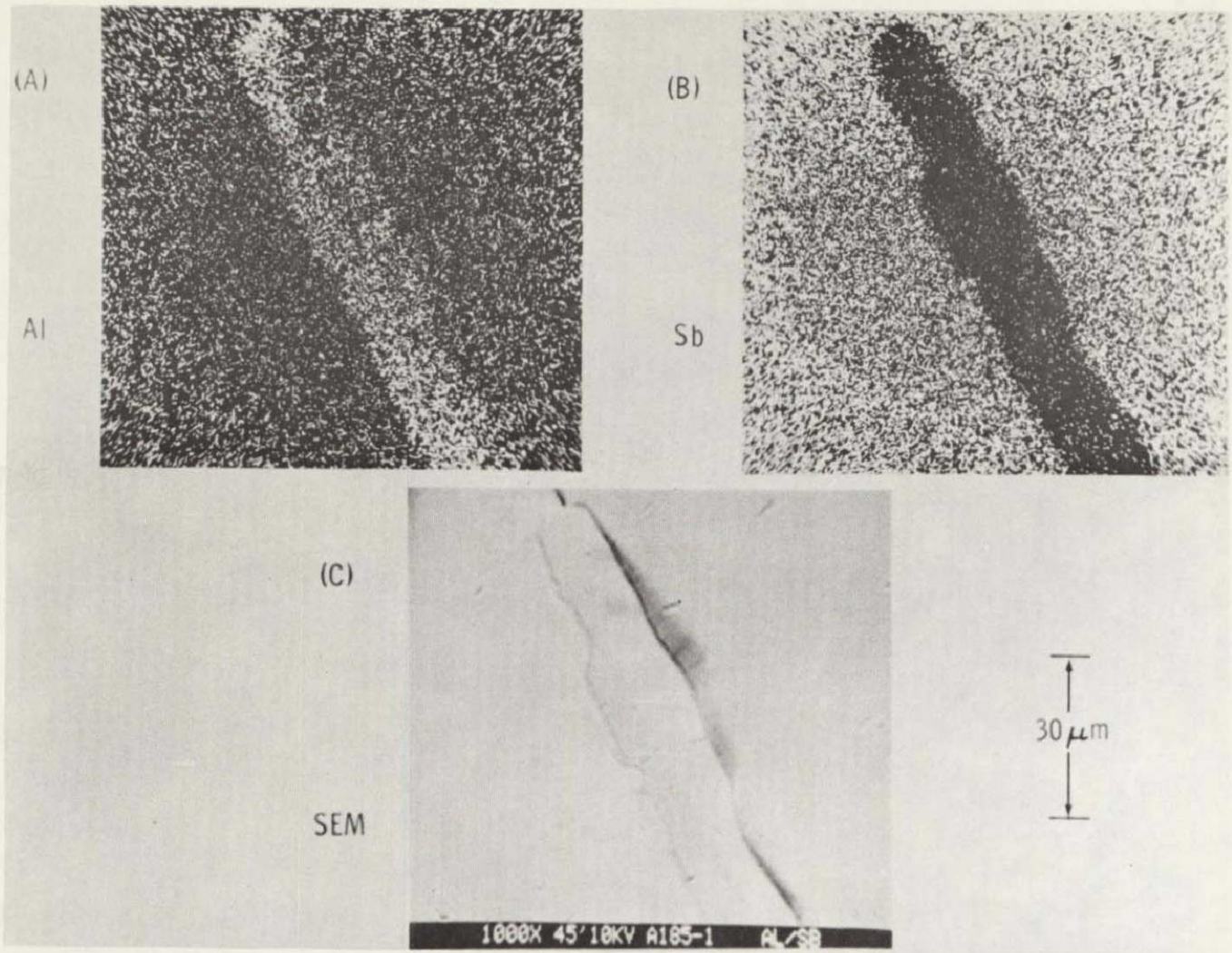

Figure IV-10. EDAX map of flight AlSb sample.

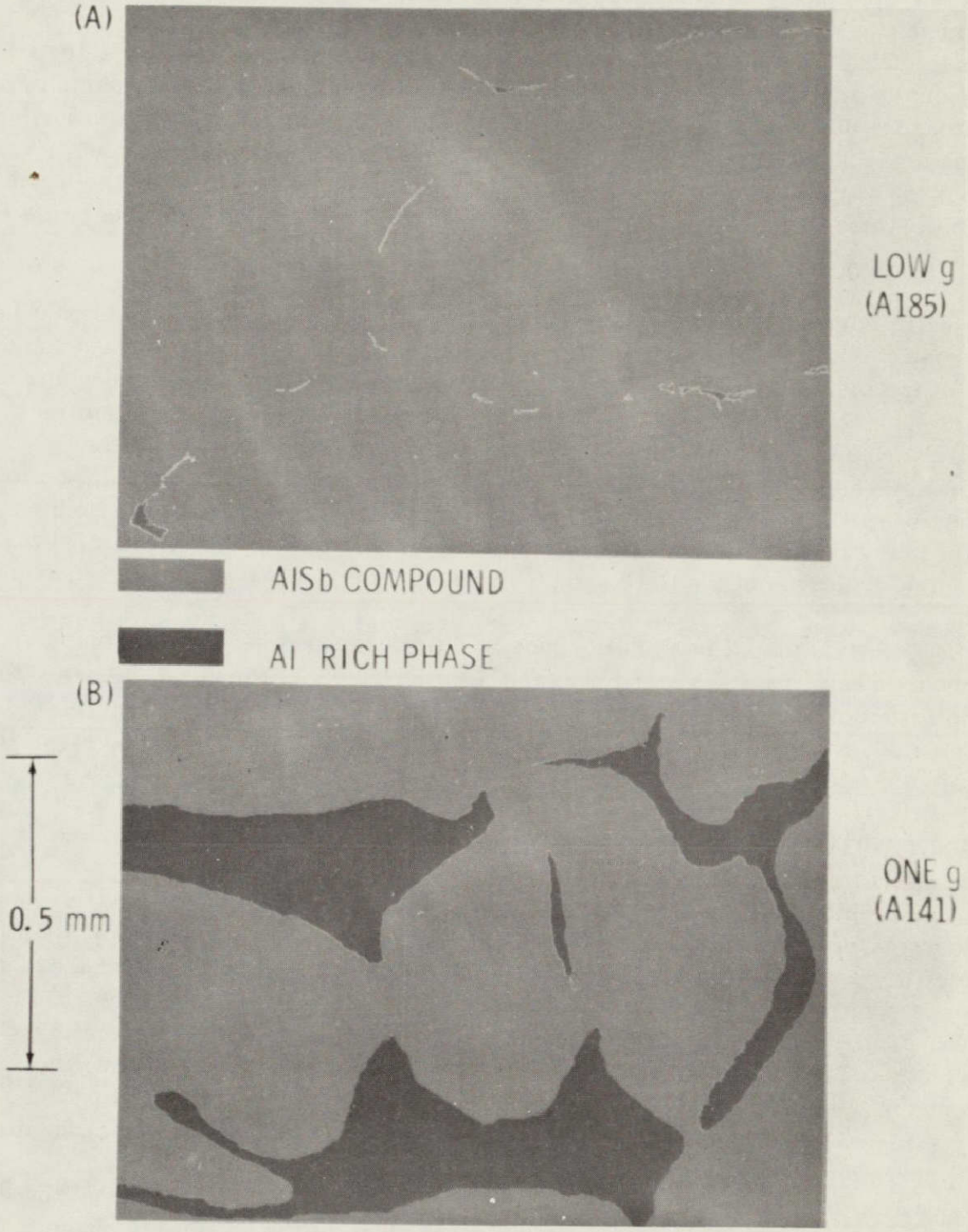

Figure IV-11. Pseudocolored microstructures of flight and GBT AlSb samples.

for these two photomicrographs reveals that the flight sample has 1.1 percent of the Al-rich phase as compared to 25.2 percent for the GBT sample. Thus, for these two selected areas, the Al-rich phase has been reduced by a factor of 23 in the flight sample. Although the photomicrographs represent two selected locations of approximately 1 mm^2 surface area for the flight and GBT sample, the microstructures typify the salient features of what is observed on a microscopic scale in other parts of the samples. That is, only a small amount of a secondary phase is found along parts of the AlSb grain boundaries for the flight sample, whereas major grains of a secondary or satellite phase are observed in the GBT sample.

To compare the homogeneity of the flight, GBT, and PT samples on a macroscopic scale, Figure IV-12 is presented to show the relative location and size of the primary compound phase (red) and secondary phases (blue) using a 20 μm scan across the sample surfaces. The major improvement in macroscopic homogeneity of the flight sample is again evident. The size of the secondary phases for the PT and GBT sample can vary from below 20 μm up to 1 mm, whereas the size of the secondary phase can vary from 3 to approximately 30 μm in the flight sample. The 20 μm scan was taken near the bottom of the PT sample, the top of the GBT sample, and near the hot end of the flight sample.

There is also a large difference in microhardness between the primary compound phase and the second phase. Microhardness readings taken on a PT sample section indicate that the AlSb phase has a Vickers number of approximately 400, whereas the softer second phase has a hardness number of approximately 60.

QUANTITATIVE MICROSTRUCTURAL AND CHEMICAL ANALYSIS

To obtain a more quantitative comparison of the microstructure, a continuous series of photomicrographs (100X) was taken across the sectional surface of flight sample A185 and GBT sample A141. An area analysis for the secondary phase, obtained from the photomicrographs, is shown in Figure IV-13. The area fraction of the secondary phase varies from approximately 2 percent to 22 percent for the GBT sample. As shown in Figure IV-13, the secondary phase is nonuniformly distributed on a macroscopic scale for the GBT sample. For the flight sample the area fraction varies from approximately 0.7 percent to approximately 2 percent. Thus, the flight sample is macroscopically much more homogeneous than the GBT sample. Note also that the worst location of the flight sample contains no more of the secondary phase than the best location of the GBT sample. As also shown in Figure IV-13, the ratio of the average area fraction for the GBT sample to the average area fraction

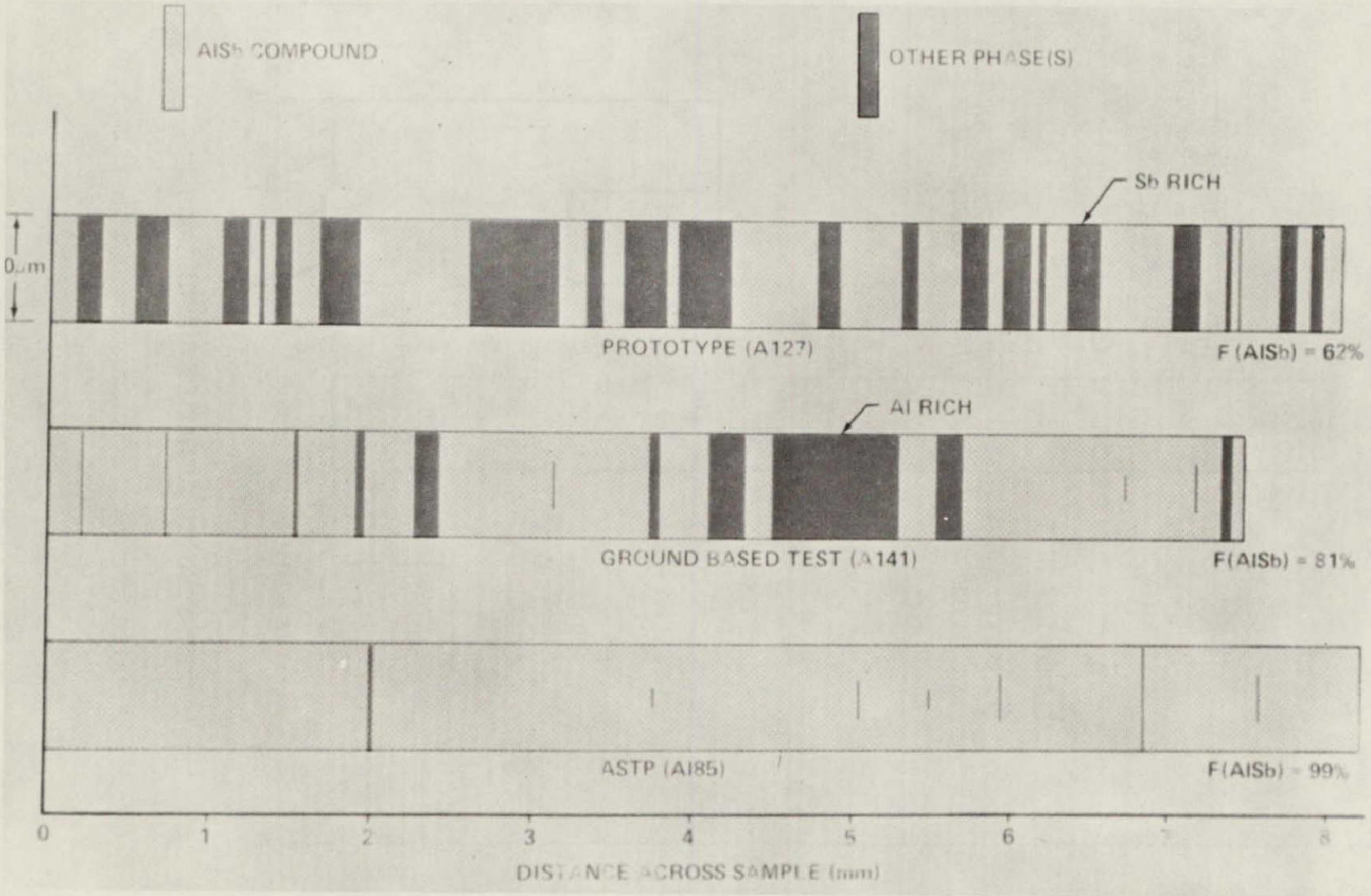

Figure IV-12. Distribution of compound and secondary phases across low-g and one-g AlSb samples.

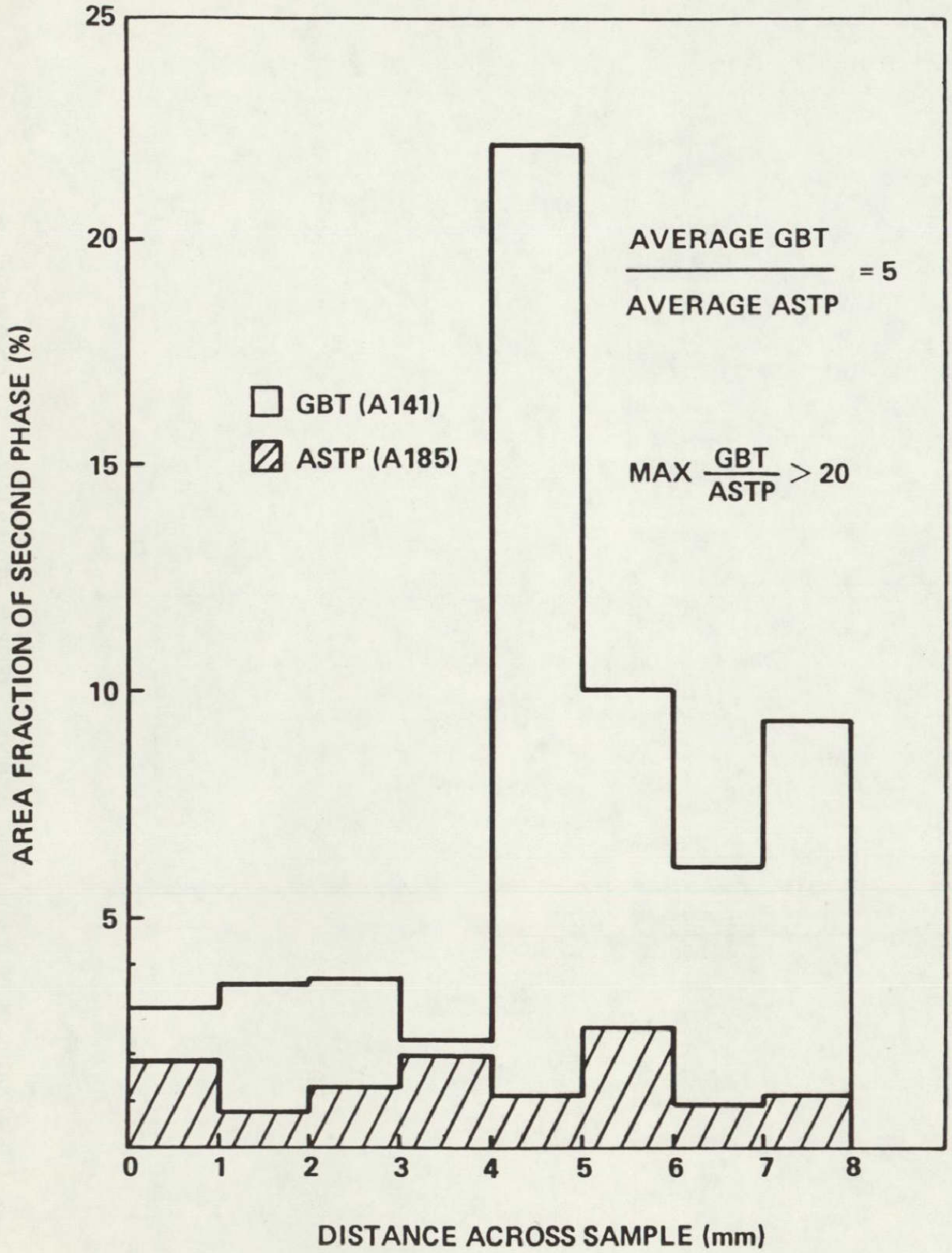

Figure IV-13. Area fraction of secondary phases across flight and GBT AlSb samples.

of the flight sample is 5.1. One photomicrograph each from the GBT and flight samples was selected to quantitatively compare the microscopic homogeneity of the material. For these selected regions of the samples, the area fraction of the AlSb compound phase was determined as a function of measuring area. The results are shown in Figure IV-14, where it can be seen that the flight sample is also more homogeneous in terms of the microscopic areas examined. The average size of the secondary phase was determined for the same photomicrographic data, and the results are shown in Figure IV-15. On the average, the secondary phase is 33 times larger in the GBT sample than in the flight sample.

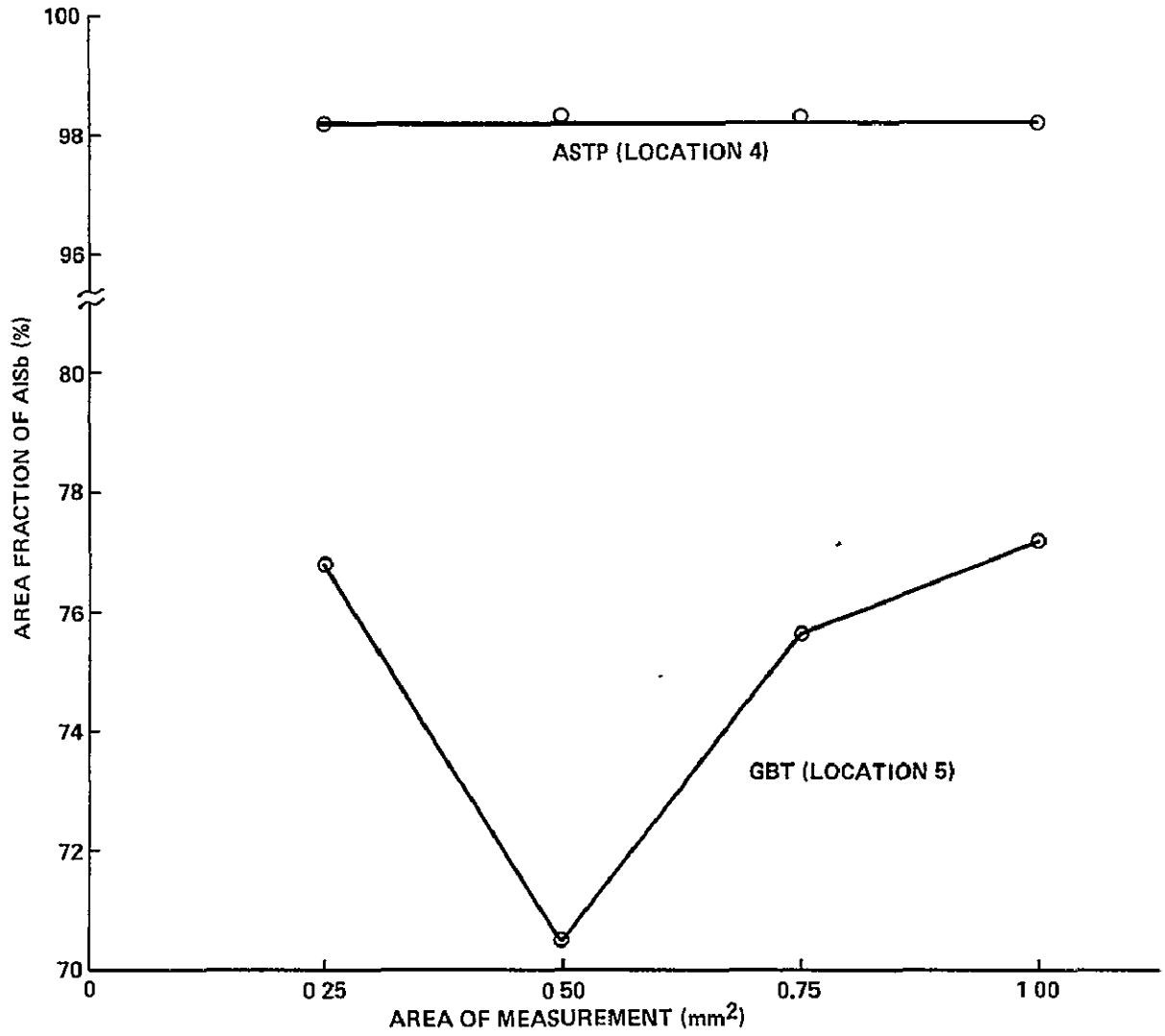

Figure IV-14. Area fraction of compound phase as a function of measured area.

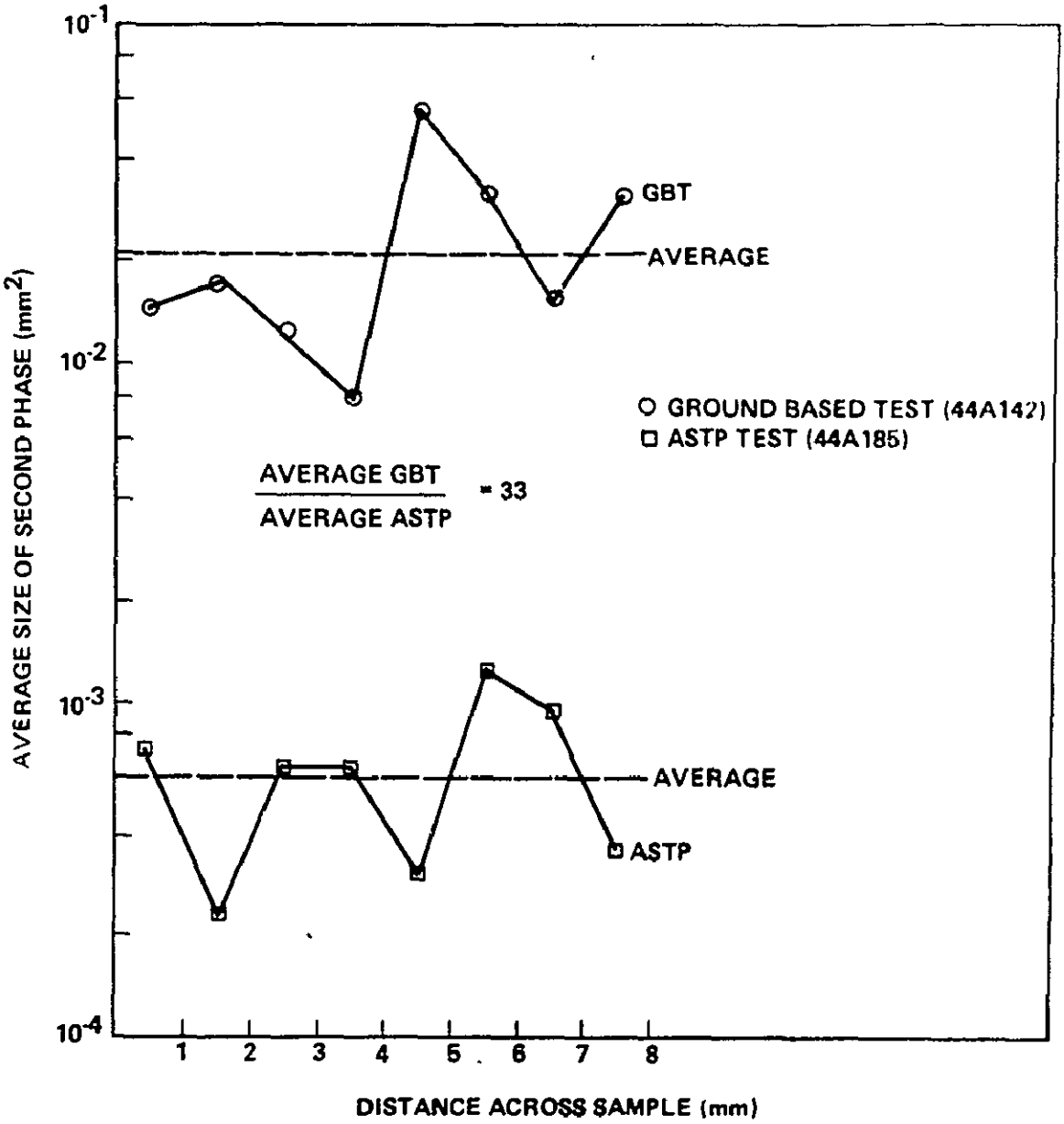

Figure IV-15. Comparison of average size of secondary phases.

A similar quantitative microstructural analysis was performed on flight sample A164 and GBT sample A142. In this comparison, the worst area of the flight sample was selected, and the average reduction in the second phase is 2.2 times. The distributions of the second phase across representative segments of the two samples are plotted in Figure IV-16.

A third GBT sample (A165) was cut into five wafers that were analyzed for their aluminum content using the method of atomic absorption analysis.

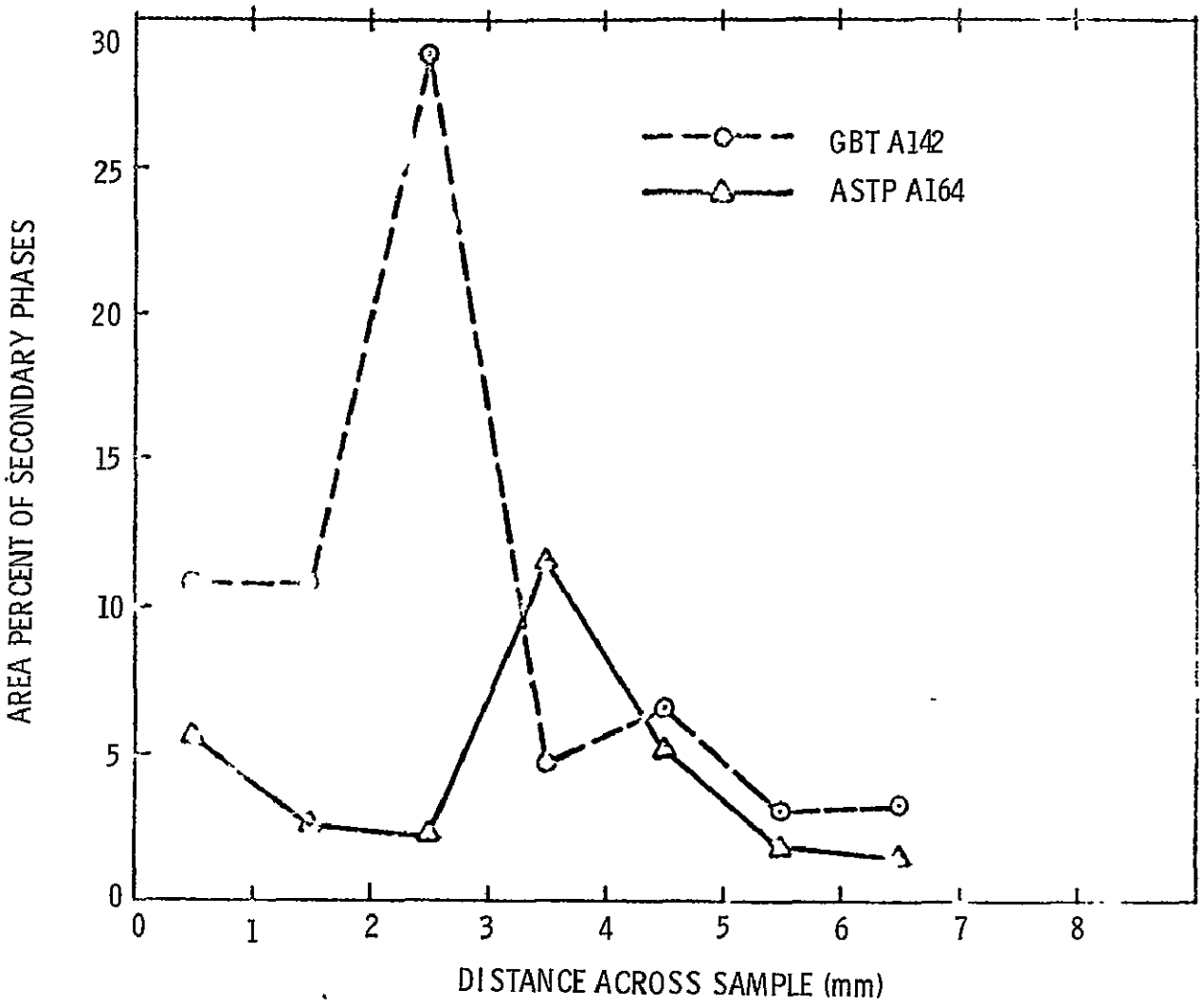

Figure IV-16. Comparison of area fraction of secondary phases for the worst region of flight sample A164 and a typical region of GBT sample A142.

Results of this quantitative analysis are plotted in Figure IV-17 as a function of distance from one end of the sample to the other end. It should be noted that the average Al content in this one-g processed sample is approximately 1 at.% higher than the theoretical value and that there is a compositional variation from end to end, perhaps due to the influence of gravity during liquid-phase homogenization.

Because the initial SEM/EDAX results gave indications of variation in composition of the two microstructural phases in various samples, an effort has been initiated to use the IMMA for quantative chemical determination on a microscale. The preliminary IMMA results on PT sample A132 are plotted in

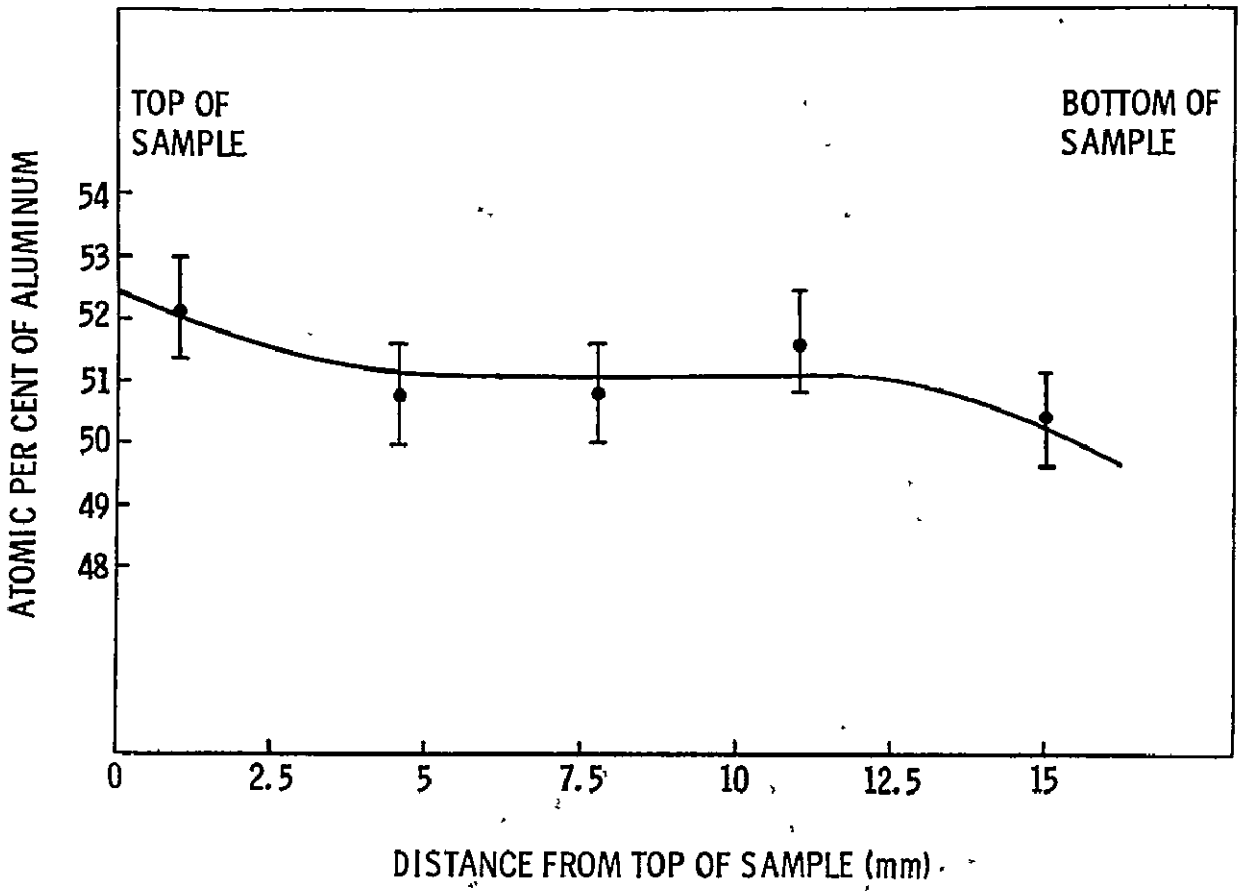

Figure IV-17. Aluminum content in GBT AlSb sample (A165).

Figure IV-18 in terms of ratios of Al^+ to Sb^+ ions sputtered off from the two phases at three locations. Since a "standard" has yet to be introduced, these results are considered as semiquantitative in nature. Nevertheless, the differences in the Al/Sb ratios are significant, indicating that the second phase in this sample has varying compositions from one end of the sample to the other and that the AlSb "compound phase" may have a homogeneity range not unlike many other intermetallic compounds such as Cu_3As, AgZr, BeCo, AlLi, or $AlPd_2$.

IMMA ion maps for Sb^+ in the second phases for a low-g and one-g sample are compared in Figure IV-19. This comparison shows that in the flight sample the small amount of residual second phase is almost pure Al, whereas in the GBT sample the Al-rich phase does contain significant concentrations of Sb.

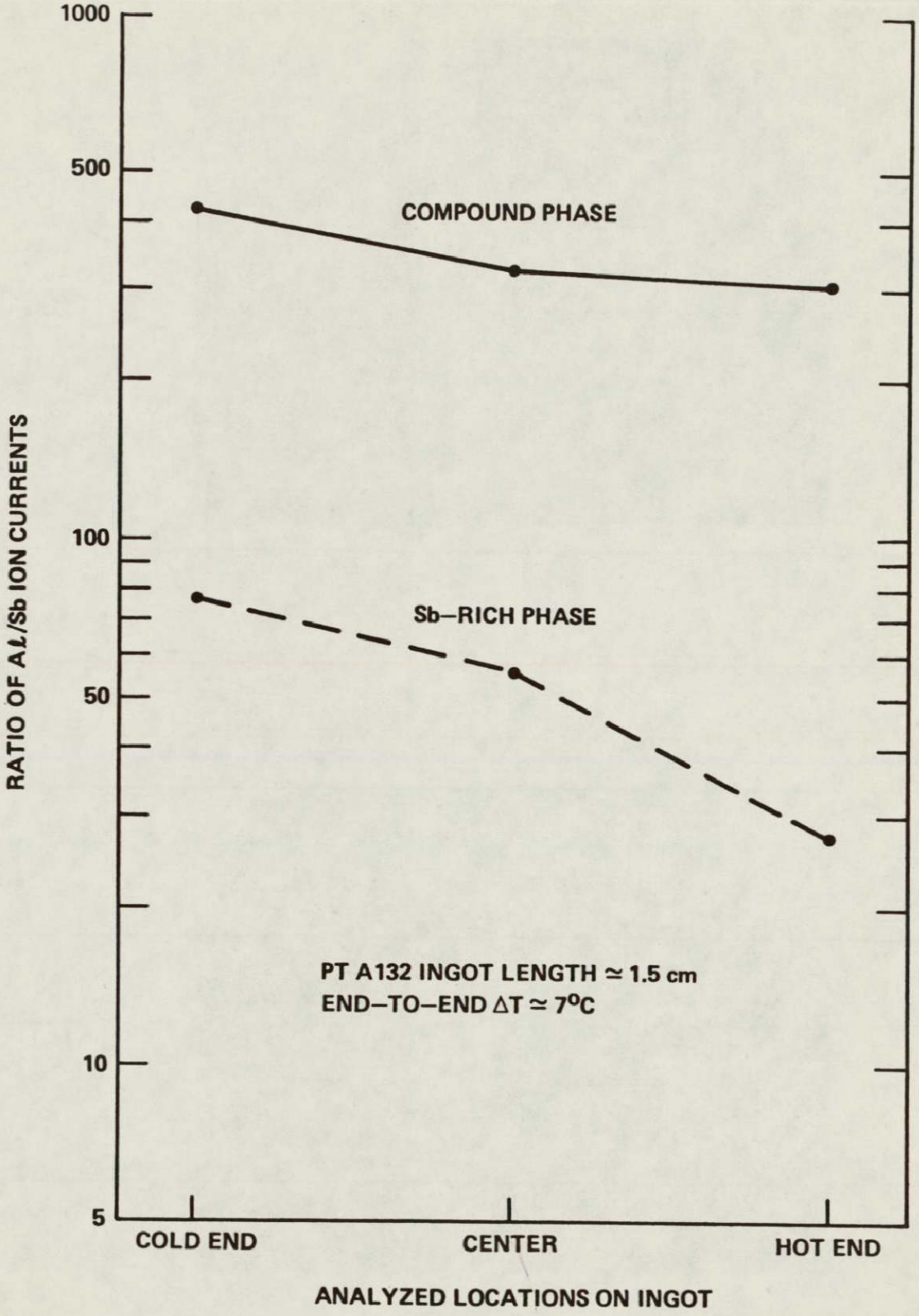

Figure IV-18. IMMA Al/Sb ratios in PT AlSb sample.

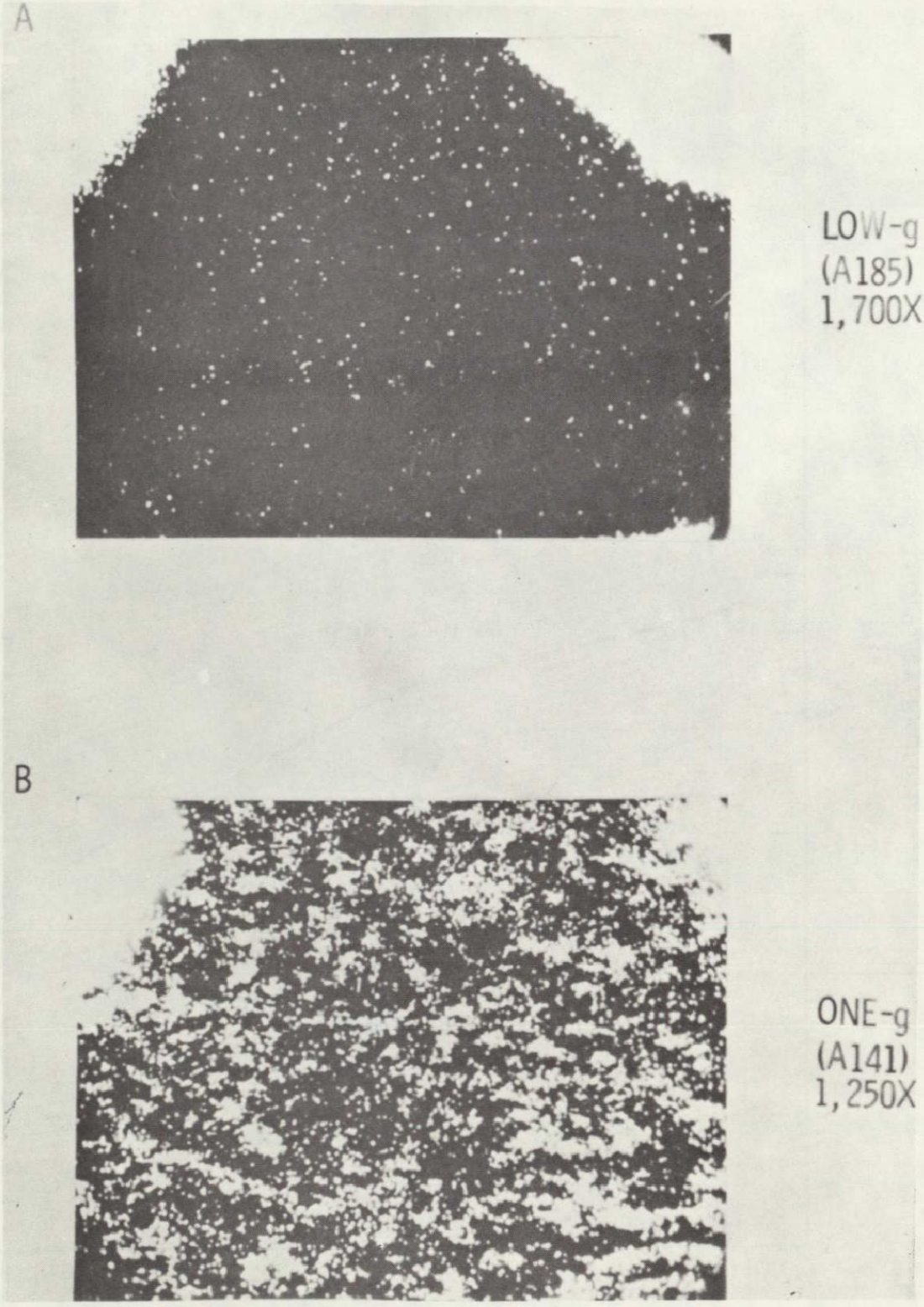

Figure IV-19. IMMA Sb^{+} ion maps for Al-rich phase of flight and GBT AlSb samples (the white areas in the top corners are the AlSb compound phase).

ELECTRICAL RESISTIVITY

Aluminum antimonide is a III-V semiconducting compound with a typical resistivity (p-type) of 10 to 100 Ω-cm. The Alrich or Sb-rich phases are metallic and should have resistivity values in the range of 10^{-4} to 10^{-6} Ω-cm (i.e., the resistivity of the secondary phases would depend upon their precise composition and previous history). Thus, the average resistivity of the AlSb samples would be very sensitive to the relative fraction of the primary compound phase and the secondary phases, since the compound phase has a resistivity that is six orders of magnitude larger than the resistivity of the secondary phases. Likewise, those samples which have the largest values of resistivity should contain the highest fraction of the compound phase.

By measuring the resistivity on a cut and polished surface of the sample using a four-point probe, the localized values of resistivity will be a sensitive indication of the quality for the sample at various locations within the material. The electrical resistivity of two prototype samples and one flight sample was determined by using a four-point probe to measure approximately 10 to 20 values at different locations on each sample. The results are shown in Table IV-2. The typical or average value of resistivity found for the flight sample was 12 Ω-cm, which indicates that the flight sample consisted almost entirely of the compound phase. The minimum or "worst" value of resistivity of 0.03 Ω-cm found in the flight sample is still a factor of 3 to 10 greater than typical values observed in the two prototype samples. The prototype samples had typical resistivity values in the range of 3×10^{3} to 9×10^{-3} Ω-cm, which is three orders of magnitude less than expected for the pure compound phase but several orders of magnitude larger than expected for the secondary phases. Thus, the resistivity measurements tend to support the results and conclusions of the microstructural studies. That is, the flight sample shows major improvements in compositional homogeneity. Additional measurements will be made on the GBT samples.

TABLE IV-2. RESISTIVITY OF AlSb SAMPLES

Sample	Typical Value (Ω-cm)	Minimum Value (Ω-cm)
Flight (A185)	12	0.03
Proto 2 (A132)	0.009	0.003
Proto 1 (A127)	0.003	0.002

X-RAY DIFFRACTION STUDIES

A small amount of material was filed off the outside surface of the top and bottom of one flight sample (A164), the middle of one GBT sample (A141), the bottom of one prototype sample (A124), and two locations from a single crystal of AlSb. The single crystal, which actually consisted of several twins or large single crystalline grains, was obtained from the Battelle Memorial Institute for the purpose of comparative characterization. This crystal is probably unique, since the authors have not been able to find any other single crystals of AlSb. X-ray diffraction images, using the Debye-Scherrer technique, were made with CuK_{α} radiation through an Ni-filter. An optimum exposure time of 2 h was chosen after verification that a 4 h exposure time did not reveal any more lines but, instead, increased the background fluorescence. The primary results of this analysis are summarized in Table IV-3.

TABLE IV-3. X-RAY DIFFRACTION STUDY OF AlSb SAMPLES

Sample (Location)	Lattice Constant (Å)[a]	Notes
Flight A164		
Top	6.133	AlSb Lines
Middle	6.134	AlSb Lines
GBT 2 A141 (Middle)	6.133	AlSb Lines
Proto 2 A124 (Bottom)	6.135	AlSb + Sb Lines
BMI single crystal		
No. 1	6.136	AlSb Lines
No. 2	6.136	AlSb Lines
Published Data [IV-12]	6.1355 ± 0.0001	

a. Accuracy of ±0.003 Å.

All samples except the PT 2 sample A124 revealed only the AlSb compound lines. The bottom part of PT 2 sample A124 had eight additional lines that could be identified as Sb lines. As expected, the lattice constant of AlSb for all samples was the same to within an accuracy of ±0.003 Å and agreed with the best published data [IV-12] and the data of the single crystal. A careful

measurement of the highest reflection lines indicated that the primary phase was always forming at 50 ± 1 at.% stoichiometric composition. That is, to within an accuracy of 1 at.%, the composition of the compound does not appear to vary between samples or depend upon the amount or nature of the secondary phases.

LIQUID STATE HOMOGENIZATION AND DIFFUSIONAL ANALYSIS

The observation that the ASTP samples have a much smaller amount of the secondary or satellite phases seems to suggest that at low-g intermetallic diffusion dominates in the liquid state homogenization process, whereas at one-g convection-induced segregation hampers the process of compositional homogenization. The results obtained can be explained by assuming that the melts obtained in low-g are relatively well homogenized within the 1.5 h of available diffusion time, but that the melts obtained in one-g are still relatively inhomogeneous. The inhomogeneities that seem to exist in the Earth-based melts are probably caused by the large differences in densities that exist between the Al-rich or Sb-rich phases found in the best commercially available starting material (Fig. IV-4).

With the above premises, a liquid state homogenization model for the AlSb system may be postulated to analyze the relative importance of gravity and diffusion. Since the starting material consists of Al-rich, Sb-rich, and AlSb phases, it will take some time for liquid state diffusion to homogenize the material at every location within the melt. If during this time, the Al- and Sb-rich liquid phases are separating or segregating by gravity-driven convection caused by differences in density, the compositional inhomogenetics within the melt may increase. To determine which is the dominant process, we may define a liquid state homogenization number, H, as

$$H = \frac{\text{convective or segregation distance}}{\text{diffusion distance}}$$

If, $H \gg 1$, gravity will dominate; if $H \approx 1$, gravity will have a smaller effect; and if $H \ll 1$, diffusion will dominate. Consider a region of the melt whose typical size is ℓ and has a density difference $\Delta\rho$ from the surrounding AlSb melt, then

$$\Delta\rho \cong \rho_{AlSb} - [C\rho_{Al} + (1 - C)\rho_{Sb}] \qquad (1)$$

where C is the concentration of Al in the inhomogeneous region. If we use a Stoke's law type model to specify the convective distance and Fick's law type model to specify the diffusional distance, then

$$H \cong \frac{\ell^2 \Delta \rho g}{5\nu} \sqrt{\frac{t_s}{D}} \quad , \tag{2}$$

where ν is the viscosity of the primary fluid phase and t_s is the total soak time for a melt with a diffusion rate D. To determine the relative influence of gravity to diffusion, consider a conservative analysis that would tend to underestimate the gravitational influences by $\ell \leq 0.2$ mm, $C \approx 0.9$, $D \approx 10^{-4}$ cm^2/s, $\nu \leq 10$ poise, and $\Delta\rho \approx 2$ g/cm^3; then $H \gtrsim 100$ for the ground-based test and $H \lesssim 0.1$ for the flight test (assuming 10^{-3} g).

Thus, these calculations would tend to indicate that convection plays an important role in maintaining any inhomogenities that may exist in Earth-based AlSb melts. However, if the inhomogenities are localized and if the starting material is on the average macroscopically 50 at.% of each element, the calculations would tend to indicate that the melt should rapidly homogenize by liquid state diffusion in a low-g environment.

These simple calculations serve to identify the difficulties of maintaining homogeneous Earth-based melts. It should also be understood that part of the effects observed in this experiment may occur during the nucleation, growth, and solidification of the compound phase.

Lead-Zinc Immiscible

MISCIBILITY GAP IN THE PbZn SYSTEM

The PbZn system is a classical monotectic binary that is characterized by a large liquid miscibility gap in the temperature-composition phase diagram (Fig. IV-1). Thermodynamically speaking, the two liquids within the immiscible region do not obey the regular solution laws and exhibit large positive deviations from Raoult's linear relationship between activity and concentration. In this miscibility gap, on an atomic scale, the dipole-dipole attractive forces between like atoms (or ions) are much greater than between unlike species. With the large difference in specific gravity (Pb/Zn = 11.4/7.14), macroscopic sedimentation of the heavier Pb liquid occurs when the binary melt is held quiescently on Earth in the miscibility gap.

As described previously, the composition selected for the experiment is 20 at.% Pb or 33.2% Pb by volume. For this composition, the consolute temperature (immiscible to miscible transition point) is approximately 795°C. The starting sample configuration was a layered ingot achieved by heating Pb on top of Zn in the graphite crucible at 850°C for 10 min, resulting in the sedimentation of Pb through the Zn. Reheating samples of this type at low-g for 60 min at a temperature 50°C higher than the consolute temperature should promote miscible liquid interdiffusion. By solidifying the thoroughly interdiffused liquids under low-g conditions, a microstructure consisting of a dispersion of superconducting Pb in the Zn matrix was postulated.

The following discussions will bring to light two important phenomenological observations that must be taken into consideration in future investigations (on Earth as well as in space) of immiscible systems similar to PbZn. The first observation is that microscopically complete and total separation of Pb and Zn is difficult to achieve under one-g conditions. The second observation is that under low-g conditions whereby convection is minimized, the liquid diffusion coefficient within the miscibility gap is smaller than commonly found for miscible metals.

Because of small convection currents, precise measurements of liquid diffusion parameters in Earth experiments are extremely difficult. However, it is generally agreed that diffusion rates of liquids are orders of magnitude greater than those for the solid phases of the same components. It is also recognized that although the intermolecular geometry of diffusing liquids is not well understood, some geometric order does exist in liquids as far as nearest neighbors are concerned. If one assumes that a range of liquid diffusion lengths exist, an analysis of the root mean square (rms) distance covered by atoms as a function of time will lead to an expression similar to that for the long range atomic motion in one-dimensional solid diffusion. This liquid diffusion motion in terms of rms distance covered is

$$\overline{x^2} = 2\,Dt \quad , \tag{3}$$

where D is the liquid diffusion coefficient. The available experimental data reported in the literature show that liquid metal diffusion coefficients all fall within the range of 10^{-5} to 10^{-4} cm^2/s. It was on the basis of this knowledge that optimum mixing of Pb and Zn at 850°C was postulated for the soaking period of 1 h in the ASTP experiment.

The difference between diffusion profiles in miscible liquids (i.e., temperature $T >$ consolute temperature T_C) and immiscible liquids ($T < T_C$) is shown in Figure IV-20. The models in Figure IV-20 represent the expected diffusion profiles at times $t_\infty > t_2 > t_1$ for liquids diffusing from a well defined interface starting at time t_0. For miscible liquids, the original interface should quickly disappear or become modified and the concentration gradient should vary continuously and smoothly throughout the sample. After a sufficient time lapse (identified as t_∞), the two liquids should homogenize into one liquid phase. In

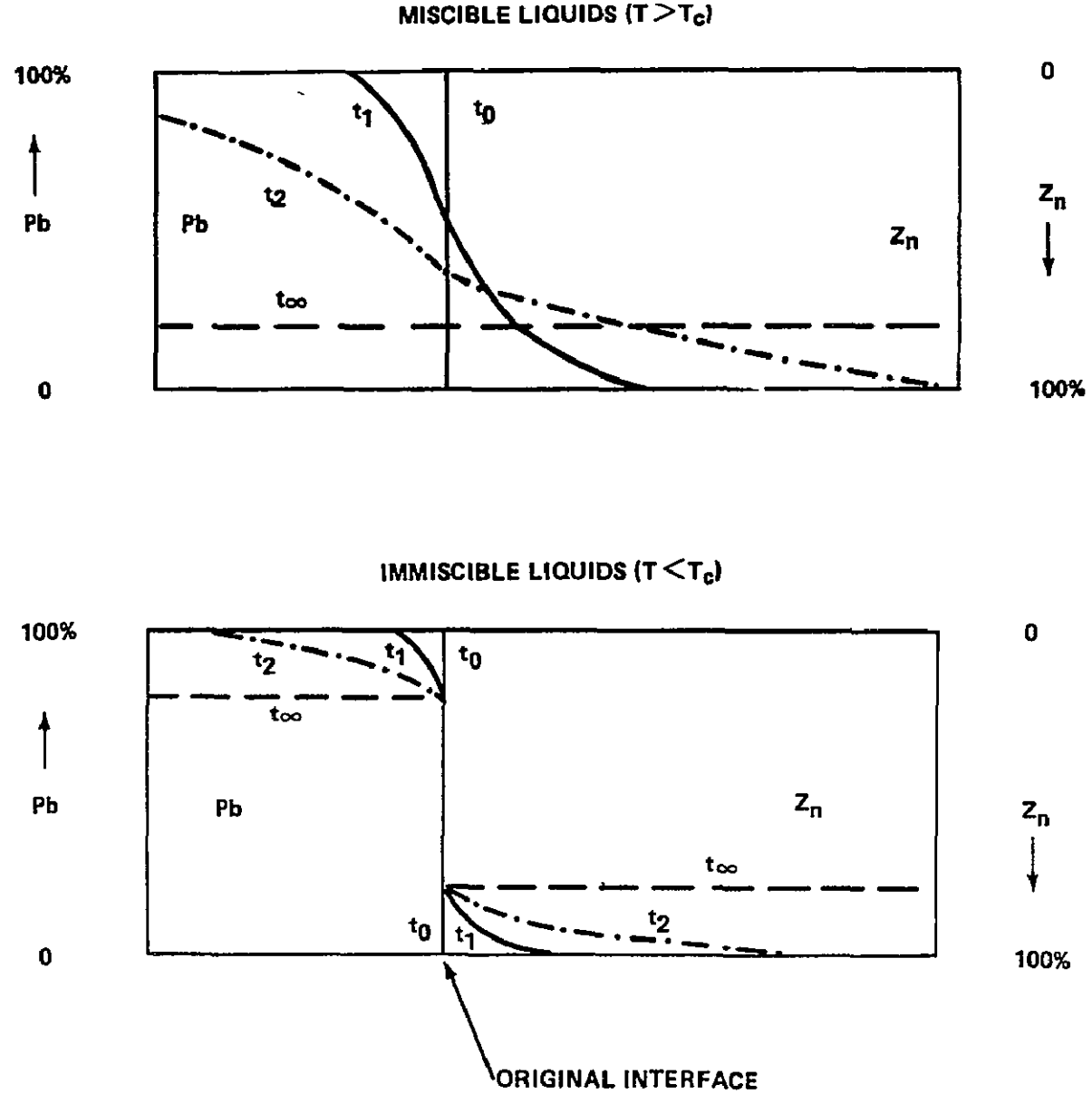

Figure IV-20. Low-g PbZn liquid state diffusion models.

contrast to miscible liquids, the model at the bottom of Figure IV-20 indicates that the original interface should persist for immiscible liquids even for long diffusion times (t_∞) and that there should be a discontinuity in the concentration gradient at the interface. Within the miscibility gap, the diffusion profiles on both sides of the interface would probably approach those for solid state diffusion as described by the second Fick's law for change in solute concentration C, as a function of time and distance,

$$\frac{\partial C}{\partial t} = D \frac{\partial^2 C}{\partial x^2} \quad , \tag{4}$$

where D is again the diffusion coefficient. By analyzing the concentration of Pb in Zn away from the interface, it should be possible to determine whether the analytical data agree with a solution of equation (4) in the form of

$$C = C_o \left[1 - \text{erf}\left(\frac{x}{2\sqrt{Dt}} \right) \right] \quad , \tag{5}$$

where C_o is the maximum solubility of Pb in Zn and x is the distance from the interface. In the following discussion of the results, it will be seen that the PbZn system is still immiscible in near zero-g at a temperature that is 40°C higher than the published value of the consolute temperature and that the diffusion coefficient is one or two orders of magnitude smaller than usually found in Earth-based liquid metals experiments.

METALLOGRAPHY AND MICROANALYSIS

The GBT samples show almost total and complete separation of the Pb and Zn phases. This can be seen in Figure IV-21(a) for a polished and etched (5 percent HNO_3) sample. Surprisingly, the ASTP samples also show major separation of the Pb-rich and Zn-rich phases as shown in Figure IV-21(b). Consistent with the immiscible liquids model of Figure IV-20, the original Pb/Zn interface is evident. An SEM of the interface on the flight sample can be seen in Figure IV-22(c). A corresponding microchemical map of Zn and Pb, using EDAX, can be seen also in Figures IV-22(a) and IV-22(b). There appears to be a sharp discontinuity in the Pb or Zn concentrations at the interface. The black particles in the upper part of Figure IV-22(c) are Pb particles dispersed in a Zn matrix.

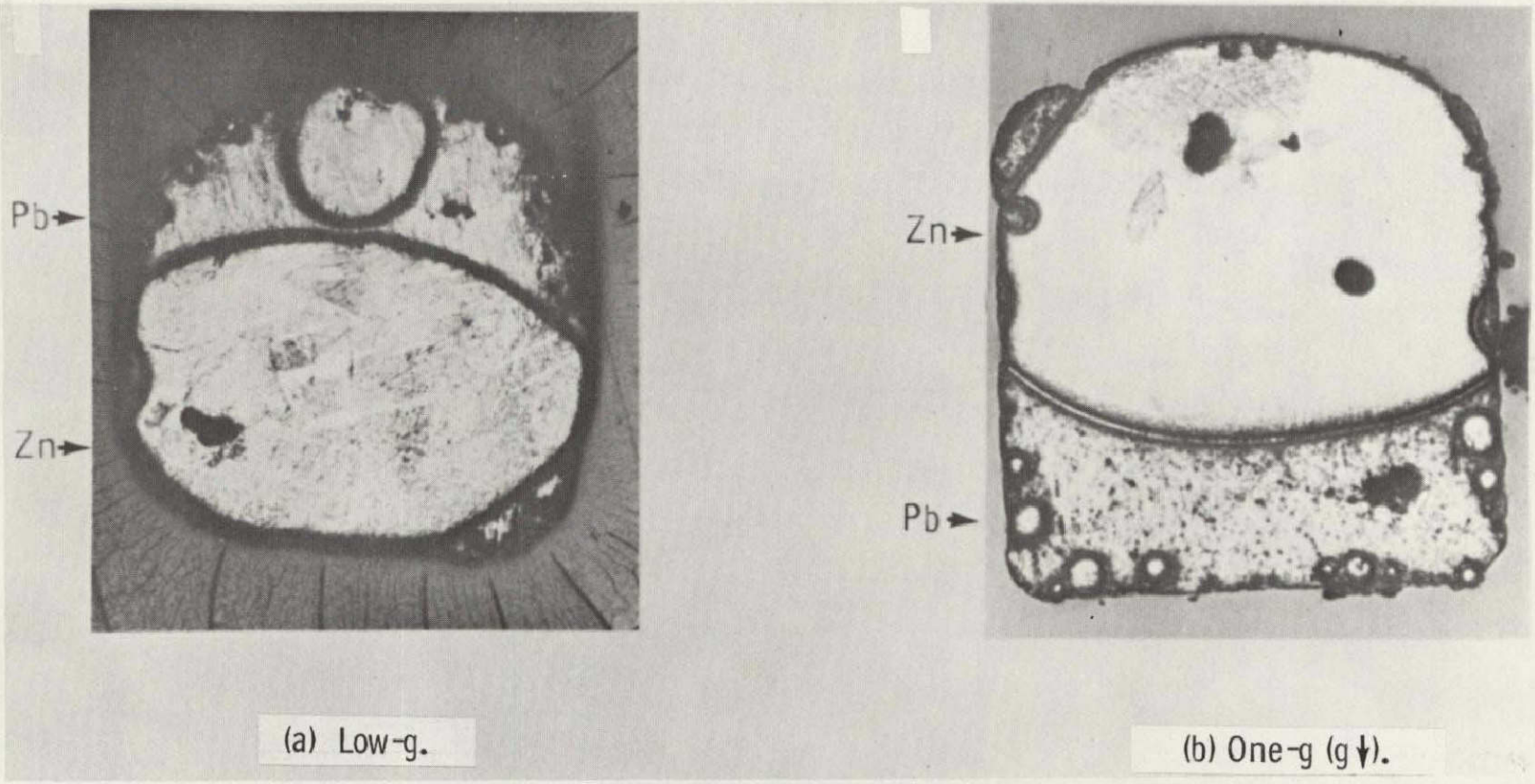

Figure IV-21. Photomacrographs of PbZn flight and GBT ingots (the Pb-rich and Zn-rich portions of the GBT ingots are reversed due to sedimentation).

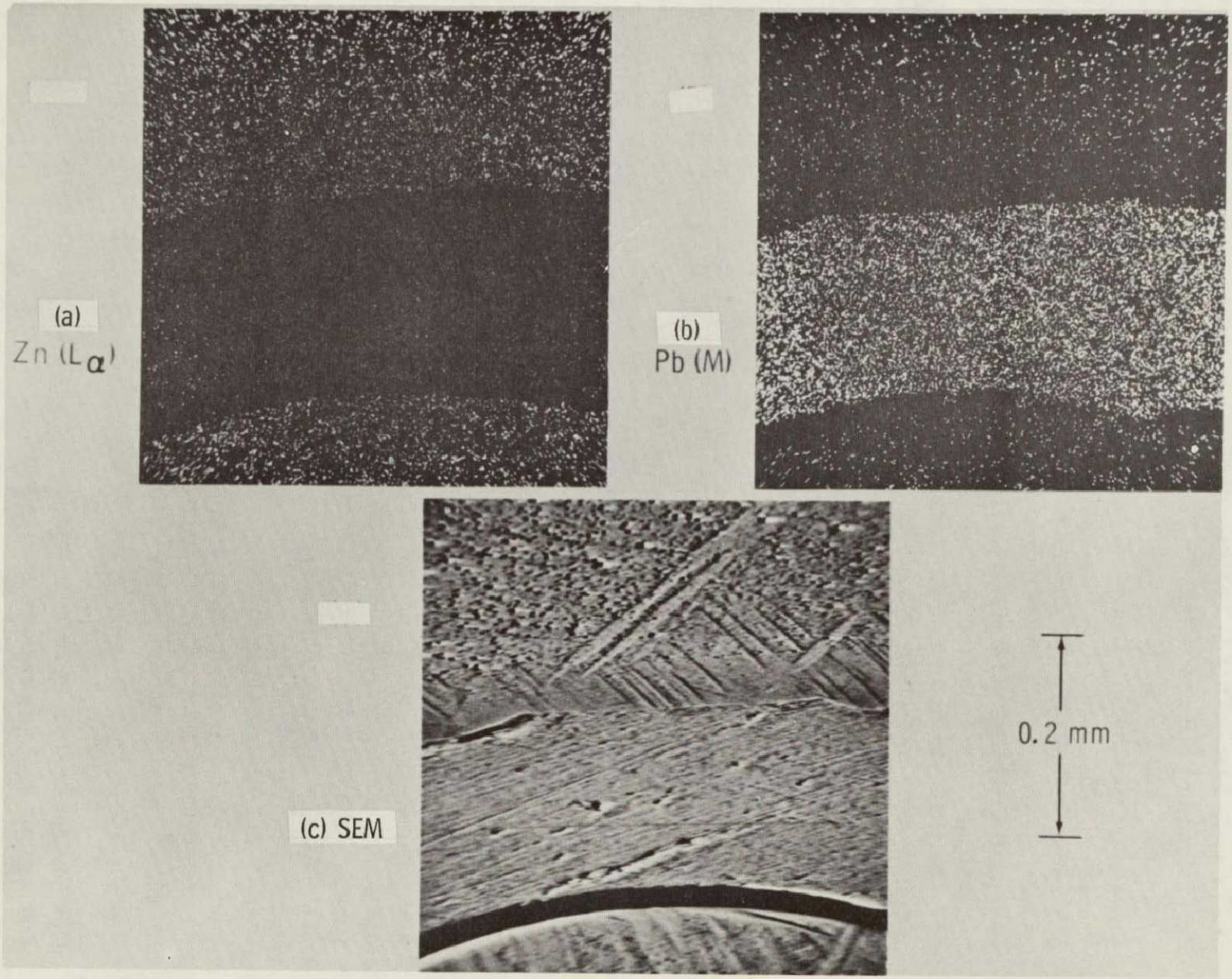

Figure IV-22. EDAX maps of PbZn interface in flight sample.

The microstructure of the Zn-rich region can be seen in Figure IV-23 for polished and etched surfaces of the flight sample. Many of the particles seen in the photomicrograph are Pb-rich as shown by the SEM photographs and EDAX maps of Figure IV-24 (flight sample) and Figure IV-25 (PT sample). The Pb dispersions in Zn appear to have a higher particle number density in the flight samples. The Pb particles of the flight sample also appear to be more uniform in size and spherical in shape. The particle alignment, evident in Figure IV-24(b), occurs in much of the flight sample and in less of the GBT samples. It seems reasonable to attribute the alignment of the microstructure in the flight sample to constitutional supercooling and subsequent nucleation and growth of Pb particles along supersaturated fronts. As previously observed, we would expect this phenomenon to be less evident in the GBT samples, because buoyancy forces acting on the individual particle and convective effects acting on the front would tend to destroy the alignment.

It should be noted that the one-g samples were processed in a manner as to encourage convective mixing between the Pb and Zn phases. In the one-g samples, the more dense liquid Pb was initially on top of the less dense zinc resulting in a flow of liquid Pb through the molted Zn. The residual Pb dispersions observed in the GBT samples indicate that total microscopic separation of the phases did not occur in one-g. In the following discussion, it will be shown that the Zn-rich portion of a GBT sample has a dilute and approximately constant concentration of Pb, part of which could be in the monotectic phase.

CHEMICAL AND DIFFUSIONAL ANALYSIS

One flight sample (B186) and one GBT 2 sample (B165) were cut into small sections of approximately 3 mm^3 each (i.e., approximately 20 mg/section) such that the distance of each section away from the PbZn interface could be determined. These small sample sections were chemically analyzed by means of atomic absorption spectroscopy. The results are shown in Figure IV-26. The Zn matrix of the GBT sample contains only a small (approximately 0.5 at.%) and constant concentration of Pb throughout the Zn matrix. This small concentration of Pb represents the combined influence of convective phase mixing during the heat-up and soak period and density sedimentation of molten Pb particles during cool-down portions of the experiment. In contrast, the flight sample contains a relatively large (maximum concentration of approximately 3.5 at.%) and monotonically decreasing concentration of Pb away from the Pb/Zn interface.

The data on the flight sample are consistent with the low-g immiscible-liquids diffusion model described previously and specified by equation (5).

Figure IV-23. Microstructure of flight PbZn sample (100X).

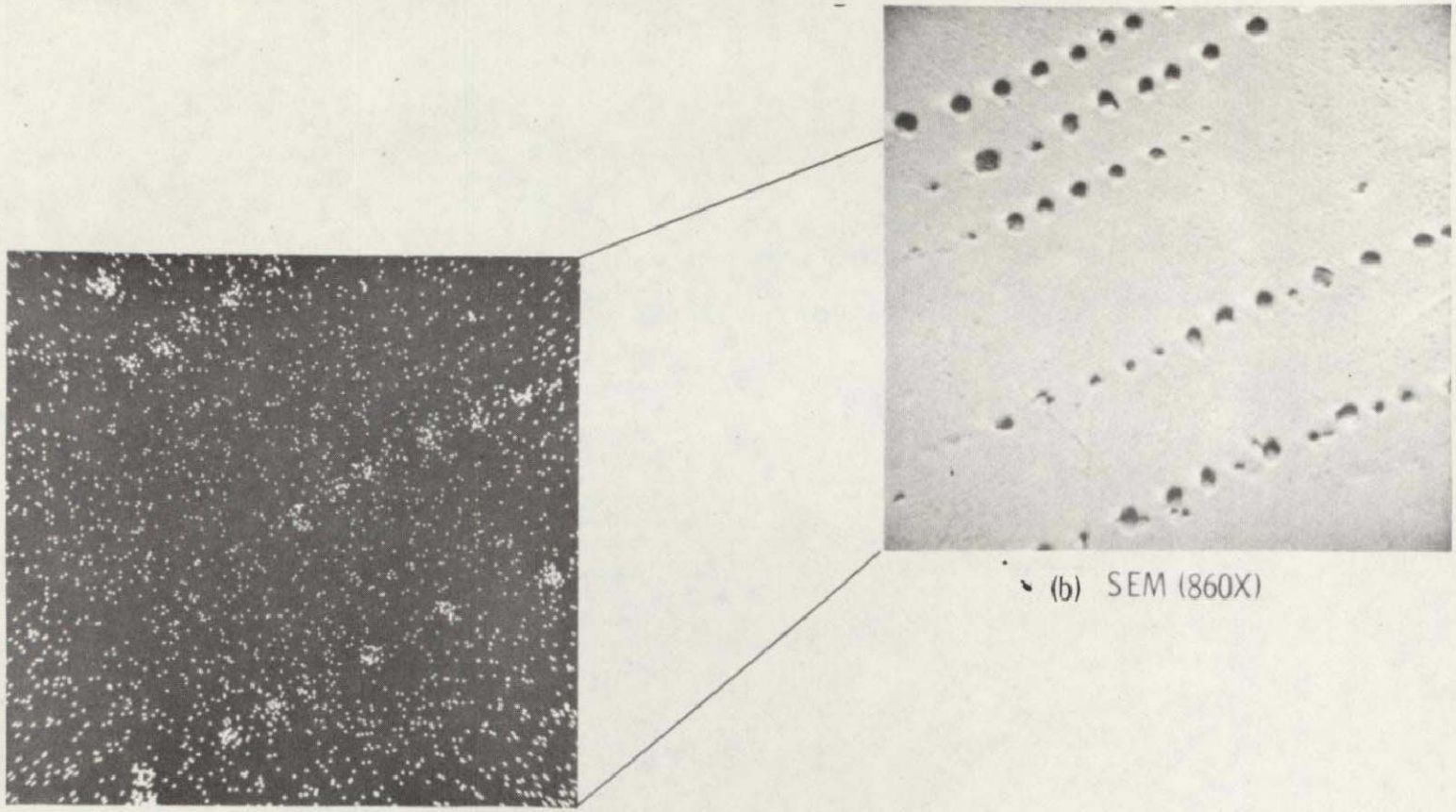

Figure IV-24. EDAX map of Zn matrix in flight sample.

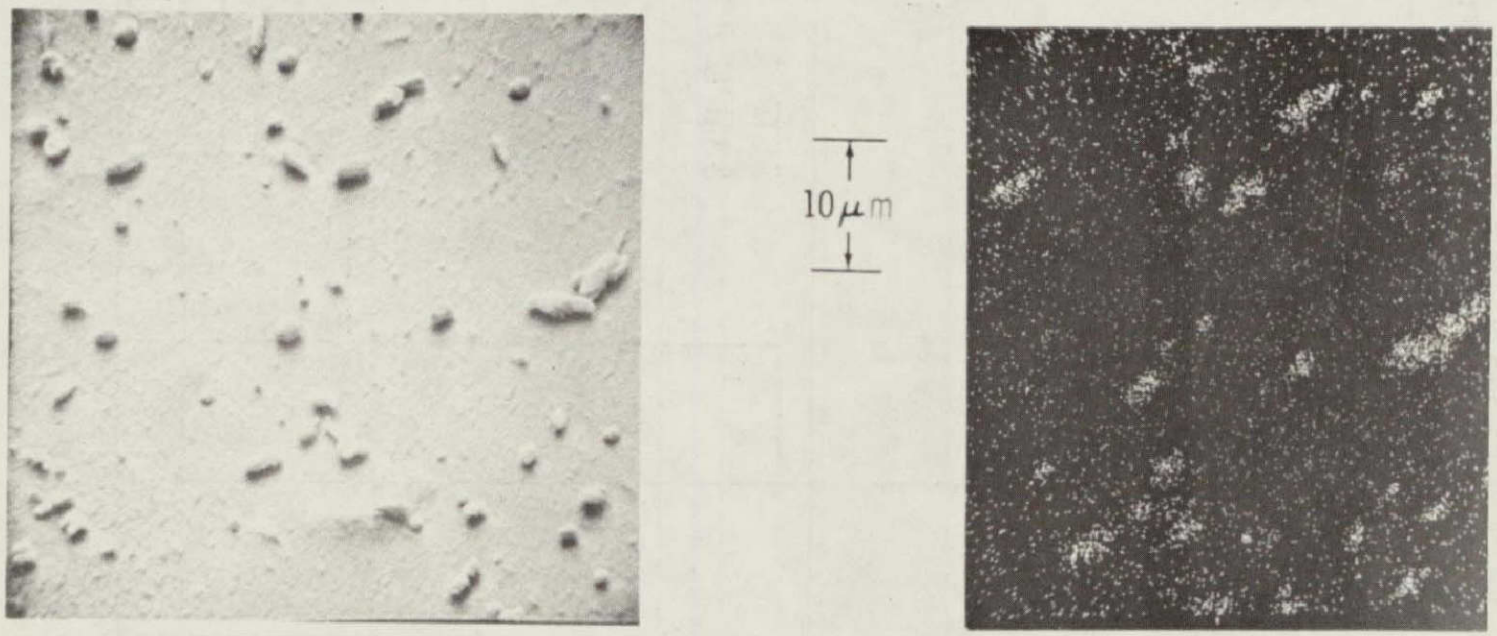

(a) SEM (1850X)

(b) EDAX Pb (Mα)

Figure IV-25. EDAX map of Zn matrix in PT sample.

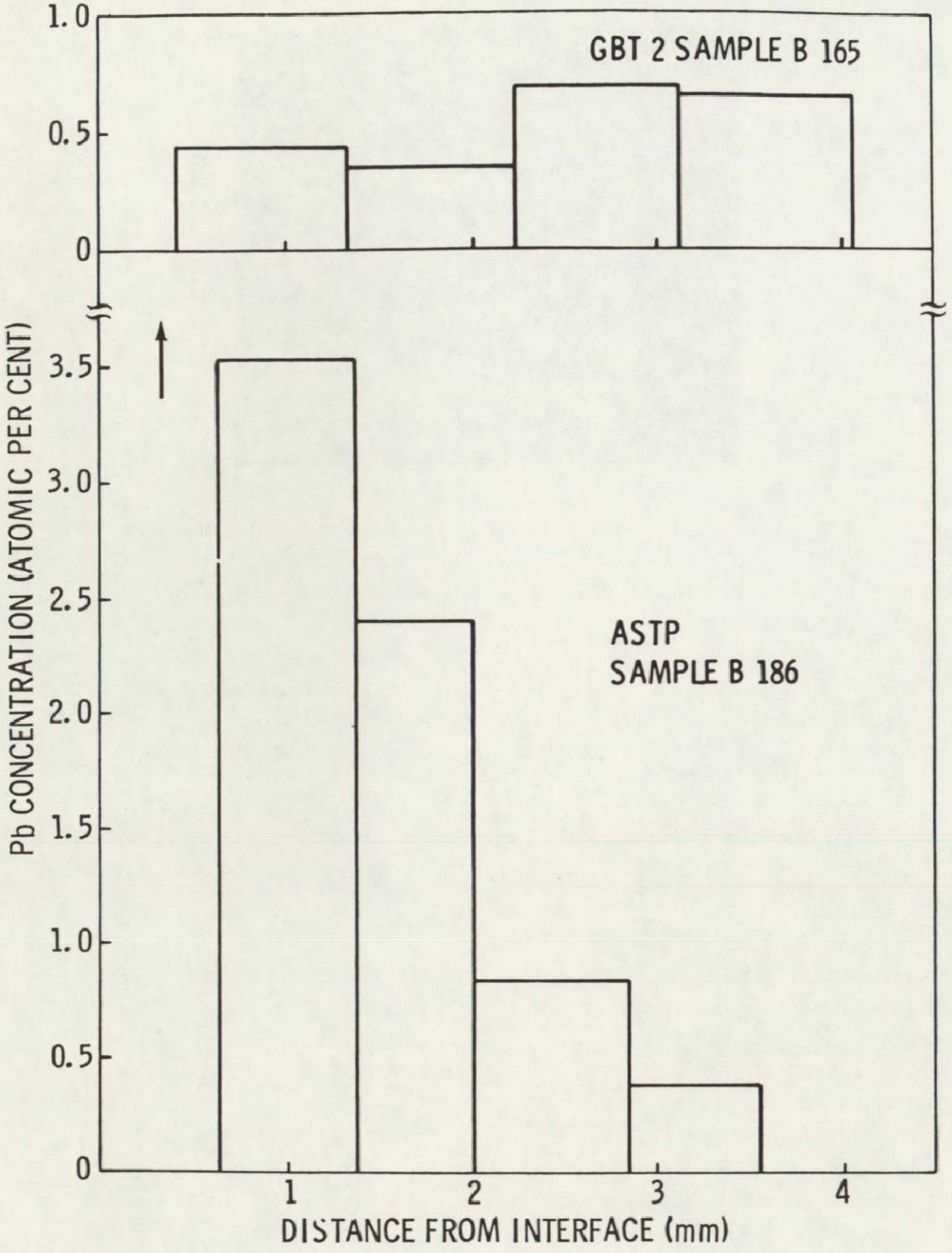

Figure IV-26. Compositional profiling of GBT and flight PbZn samples.

Equation (5) can be best fit to the data by assuming an equilibrium concentration at the interface C_o of 8 at.% and a diffusion coefficient of 2.4×10^{-6} cm^2/s. The theoretical immiscible-liquids diffusion curve is shown in Figure IV-27. After several attempts, it was concluded that the data could not be fit with a miscible-liquids diffusion model. The results of the chemical and diffusional analysis are therefore consistent with the microchemical and metallographic analysis in that the combined results show, in our low-g experiment, that Pb and Zn are still immiscible at 835°C and that the diffusion coefficient measured in the low-g sample is one or two orders of magnitude smaller than commonly expected. Thus, these experimental results would suggest that there is a significant inaccuracy in the published phase diagram of PbZn.

Pelzel [IV-13] has measured the rate of solution K in both immiscible and miscible liquid metals. His results appear to follow the diffusion models given previously, and he finds that K for the monotectic systems is of the same order of magnitude as in experiments where one of the phases is a solid reaction partner. He also finds that K is influenced by buoyance or gravitational effects. Using his published value of K for the diffusion of Pb into Zn at 500°C, it is estimated that this Earth-based experiment had an effective diffusion coefficient of $D \approx 3 \times 10^{-4}$ cm^2/s, which is two orders of magnitude greater than observed in our ASTP experiment. Thus, the combined results of our low-g experiment and Pelzel's one-g experiment would tend to support the conclusion that liquid metal diffusion is strongly influenced by thermal or density-driven convection in Earth-based experiments and that in our experiment the probability is high that the homogenization temperature of 835°C was not above the miscibility gap.

In summary, the results of our chemical and diffusional analysis would tend to indicate that the PbZn part of the experiment did not perform as initially anticipated for two reasons. First, the PbZn system is apparently still immiscible at 835°C which would limit the concentration gradient in the samples and greatly reduce the rate of solution K. Secondly, the diffusion coefficient D is much smaller than was initially expected. The results of the experiment do suggest that the low-g quiescent environment of space is an ideal environment for accurately determining diffusional and kinetic reaction rates that may be difficult, or perhaps in some cases impossible, to determine on the ground.

ELECTRICAL RESISTIVITY

The previous results and conclusions must be modified if the PbZn samples contained oxides at the interface, which would tend to prevent interdiffusion. The possible existence of oxides seems improbable since only the highest purity materials were used, the ampoules were sealed under highly pure

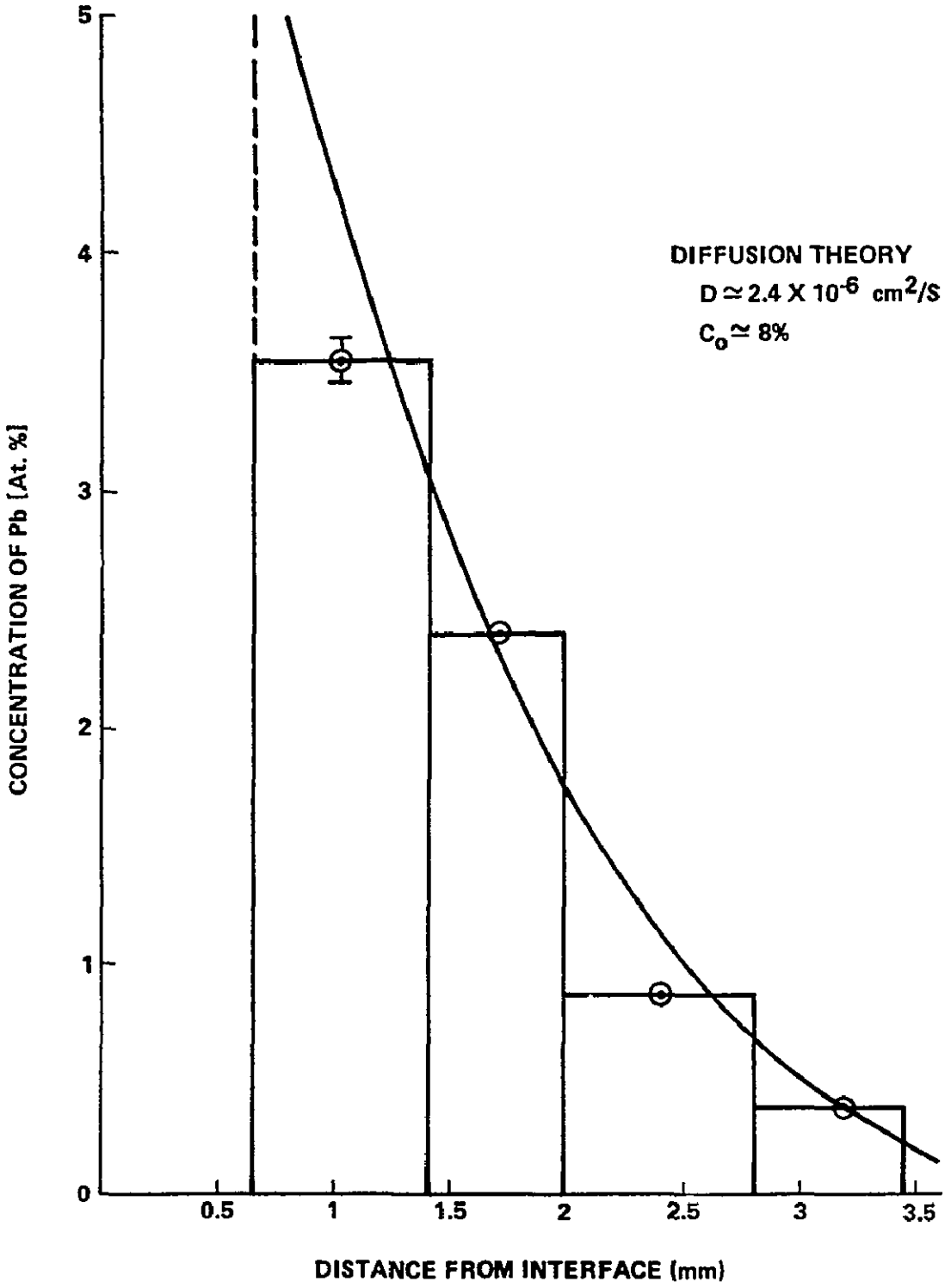

Figure IV-27. Diffusion profile for Pb in Zn in flight sample.

argon, and previous PT and GBT experiments did not indicate the presence of oxides. Moreover, the sedimentation of Pb through Zn during the initial stage of sample preparation would break up oxide films if present in the starting materials. To further test for the presence of oxides at the Pb/Zn interface, it was decided that a sensitive test would involve measuring the average resistivity of the material in the vicinity of the interface.

The resistivity of the materials was measured on the mounted, polished, and etched sample surfaces using a four-point probe. One flight sample (B186) and one GBT sample (B142) were selected for the test. The results of the measurements are presented in Figure IV-28 where each measurement point represents the average of 10 separate determinations. The absolute accuracy of the measurement is approximately 5 percent, and the relative accuracy between points is better than 1 percent. Both the ASTP and GBT resistivity values varied smoothly and continuously across the interface. In neither case was there any evidence of any oxide layer along the interface. The slightly larger resistivity values associated with the flight sample near the interface was probably caused by the higher concentration of Pb in the Zn matrix found by the chemical analysis.

CONCLUSIONS

The experiment plan for ASTP experiment MA-044 has essentially been implemented. As with other types of investigations, this experiment has led to unexpected observations that warrant continuation of certain efforts. On the basis of the results of the scheduled characterization tasks, the following conclusions have been reached.

Aluminum Antimonide Compound

Liquid-state homogenization of polycrystalline multiphase AlSb at low-g produces major improvements in macroscopic and microscopic homogeneity. The ASTP processed material contains an average of 4 and a maximum of 20 times less of the unwanted secondary phase. Very small amounts of an Al-rich phase are found only along parts of the grain boundaries in the flight samples, whereas the ground-processed counterparts show major grains of the Al-rich or Sb-rich phase not unlike the starting material except for the recrystallized grain structure.

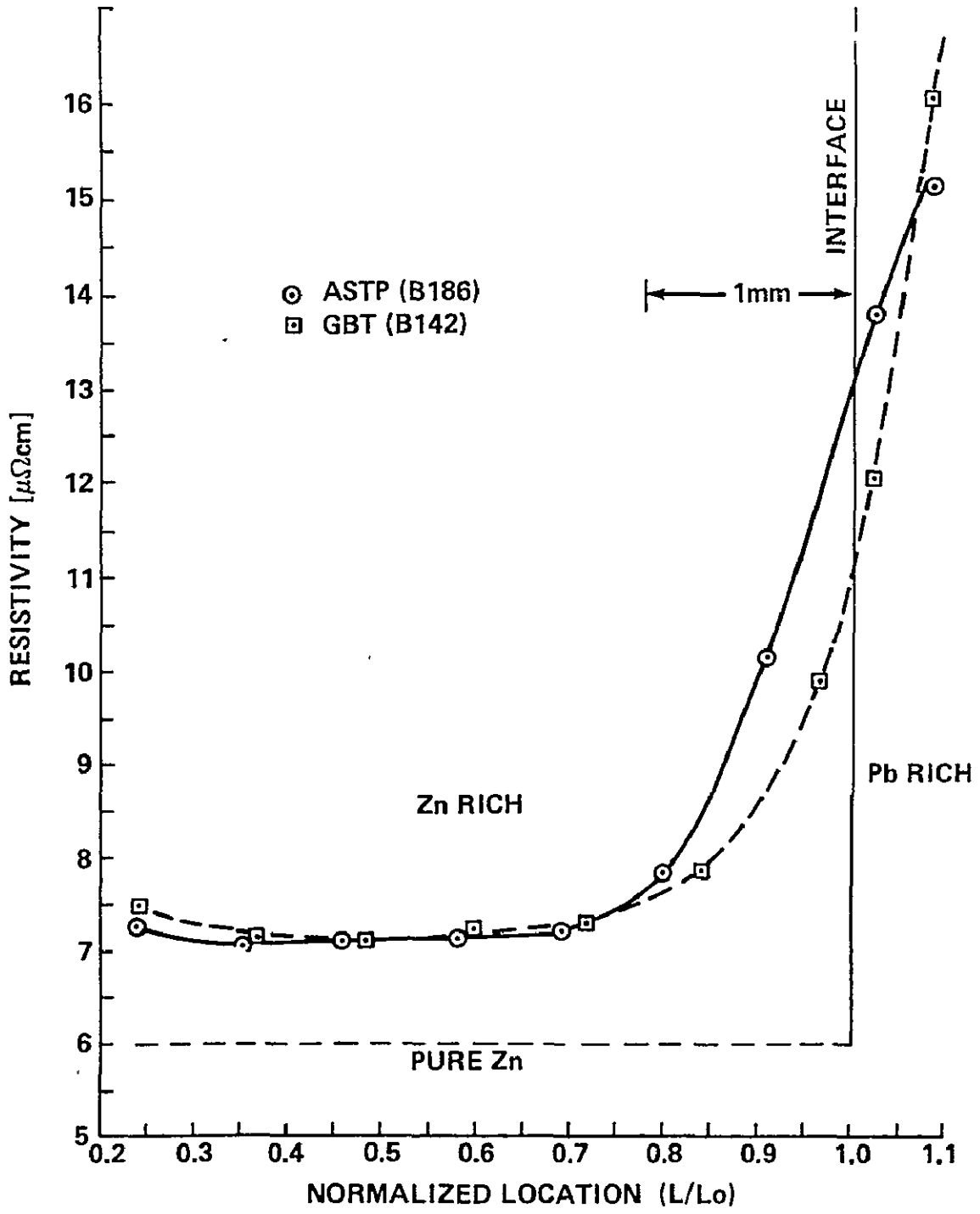

Figure 28. Electrical resistivity of PbZn samples.

A diffusional and liquid-state homogenization analysis indicates that gravity-induced convection can severely complicate the homogenization of AlSb melts on Earth and induce compositional and microstructural inhomogeneity during solidification.

Qualitative and semiquantitative energy dispersive X-ray and ion-microprobe mass analyses indicate the possibility of a homogeneity range for the AlSb compound and compositional variations in the secondary phases. A chemical analysis of a one-g sample indicates an overall approximate stoichiometric composition with a small, possibly gravity-induced, longitudinal variation in Al content.

These encouraging ASTP results show promise in the possible commercial utilization of space for the containerless zone melting and leveling of AlSb for solar cell applications, as well as for the development of other potentially useful material systems that involve constituents with large differences in density.

Lead-Zinc Immiscible

Incomplete liquid-state mixing of Pb and Zn was observed in the ASTP experiment, although the homogenization temperature of 835°C to 40°C above the miscibility gap described in the literature. In the flight samples, a dispersion of fine particles of superconducting Pb in the Zn matrix was observed, but the bulk of Pb remained in the same position as before the start of the experiment. Our results suggest that there is a significant inaccuracy in the published phase diagram for PbZn.

Compositional profiling of a low-g processed sample indicates a quasi-solid state diffusion of Pb into Zn with a diffusion coefficient of 2.4×10^{-6} cm^2/s, which is approximately two orders of magnitude smaller than expected from ground-based experiments.

Difficult-to-control convective mixing, sedimentation, and density gradients can hinder the analysis of diffusional or other kinetic processes in material systems carried out on Earth. The quiescent low-g conditions of orbital flight provide an ideal environment for studying and accurately measuring such processes by reducing or eliminating the competitive gravity-dependent variables.

ACKNOWLEDGMENTS

The authors wish to express their appreciation for the valuable contributions and support of the following MSFC employees: Mr. David Nicholas for SEM/EDAX, Mr. Forrest Wells for chemical analysis, Mr. Douglas Thomas for DIA, Mr. Ronald Harris for sample preparation, and Mr. Bill Pinkston for assistance with data analysis. Special appreciation is due the Metallic Materials Division of the Materials and Processes Laboratory for providing us with continued support in metallography and photography. The untimely death of Mr. Edward Ronning was deeply felt and cut short his valuable metallographic contributions. Dr. Guenther Otto of the University of Alabama in Huntsville kindly performed the X-ray diffraction analysis.

REFERENCES

IV-1. Proceedings Third Space Processing Symposium — Skylab Results. Vols. 1 and 2, Report M-74-5, June 1974.

IV-2. Modified from Hansen, or: Constitution of Binary Alloys. McGraw-Hill, New York, 1958, p. 1118.

IV-3. Lacy, L. L. and Otto, G. H.: The Stability of Liquid Dispersions in Low Gravity. AIAA/AGU Conference on Scientific Experiments of Skylab, AIAA Paper 74-1242, Nov. 1974.

IV-4. Lacy, L. L. and Otto, G. H.: Electrical Resistivity of Gallium-Bismuth Solidified in Free Fall. AIAA J., vol. 13, 1975, p. 219.

IV-5. Reger, J. L.: Experimental Development of Processes to Produce Homogenized Alloys of Immiscible Metals. Final Report, NASA Contract NAS8-27085, Jan. 1973.

IV-6. Otto, G. H.: Studies on Immiscible Alloys. Final Report, NASA Contract NAS8-27809, Jan. 1976.

IV-7. Willardson, R. K. and Beer, A. C., eds.: Semiconductors and Semimetals. Vol. 4, Academic Press, New York, 1968, p. 59.

IV-8. Rittner, E. S.: Use of p-n Junctions for Solar Energy Conversion. Physical Review, vol. 96, 1957, p. 1708.

IV-9. Lofershi, J. J.: Theoretical Considerations Governing the Choice of the Optimum Semiconductor for Photovoltaic Solar Energy Conversion. J. of Applied Physics, vol. 27, 1956, pp. 777-784.

IV-10. Ang, C. Y. and Lacy, L. L.: Monotectic and Syntectic Alloys: ASTP Experiment MA044. Postflight Preliminary Technical Report, NASA TM X-64956, Sept. 30, 1975.

IV-11. Ang, C. Y. and Lacy, L. L.: Apollo-Soyuz Preliminary Science Report. NASA TM X-58173, March 30, 1976.

IV-12. Giesecke, V. G. and Pfister, H.: Acts Cryst., vol. 11, 1958, p. 368.

IV-13. Pelzel, E.: Z. Metallkde, vol. 61, 1970, pp. 294-297.

SECTION V

QUANTITATIVE DETERMINATION OF ZERO-GRAVITY EFFECTS ON ELECTRONIC MATERIALS PROCESSING – GERMANIUM CRYSTAL GROWTH WITH SIMULTANEOUS INTERFACE DEMARCATION

EXPERIMENT MA-060

By H. C. Gatos,[1,2] A. F. Witt,[1,2]
M. Lichtensteiger,[1] and C. J. Herman[1]

1. Massachusetts Institute of Technology, Cambridge, Massachusetts
2. Co-Principal Investigators

TABLE OF CONTENTS

LIST OF ILLUSTRATIONS

LIST OF ILLUSTRATIONS (Continued)

LIST OF ILLUSTRATIONS (Continued)

LIST OF ILLUSTRATIONS (Concluded)

ABSTRACT

Experiment MA-060 was designed to establish the crystal growth and segregation characteristics of a melt in a directional solidification configuration under near zero-g conditions. The germanium (doped with gallium) system was selected because it has been extensively studied on Earth and because it lends itself to a very detailed macroscopic and microscopic characterization. The interface demarcation technique was incorporated into the experiment since it constitutes a unique tool for recording the morphology of the growth rate throughout solidification, and for establishing an absolute time reference framework for all stages of the solidification process. An extensive study has been performed of the germanium crystals grown during the Apollo-Soyuz Test Project mission. It was found that single crystal growth was achieved and that the interface demarcation functioned successfully. On the basis of the results obtained to date, there is no indication that convection driven by thermal or surface tension gradients was present in the melt. The gallium segregation, in the absence of gravity, was found to be fundamentally different in its initial and its subsequent stages from that of the ground-based tests. None of the existing theoretical models for growth and segregation can account for the observed segregation behavior in the absence of gravity. The results point strikingly to the acute need for extensive experimental and theoretical work on Earth before the far reaching implications of materials processing in space can be understood and exploited.

INTRODUCTION

Gravity-induced convection is always present in the melt undergoing solidification because of the unavoidable thermal gradients. It has also been established that thermal convection causes uncontrollable variations in the rate of crystal growth (or solidification), which in turn result in compositional inhomogeneities and structural defects. Thus, gravity adversely affects the key parameters of the crystal growth (solidification) process. Furthermore, thermal convection interferes with the study of the processing parameters (i.e., rate of solidification, growth interface characteristics, and others) and with the assessment of the relative importance of such parameters in the physical and chemical characteristics of the resulting solids. Since some key materials processing parameters remain essentially unaffected in the absence of gravity, space represents a unique environment and a striking opportunity for materials processing.

Our experiment of indium antimonide crystal growth in the Skylab mission demonstrated beyond doubt that under zero-g virtually ideal conditions of crystal growth can be established, which lead to chemical homogeneity never attained on Earth, and that crystal growth and segregation phenomena can be studied directly in the absence of convective interference.

The present experiment was designed, on the basis of the findings of the Skylab experiment, to obtain more refined fundamental and quantitative information on the crystal growth and segregation processes. The germanium (doped with gallium) system was selected because it has been most extensively studied on Earth for the last 30 years.

OBJECTIVES

The specific objectives of the present Apollo-Soyuz Test Project (ASTP) experiment were to establish the following under near zero-g conditions:

1. The absence or presence of convective phenomena

2. The surface tension (and/or wetting) characteristics of the melt

3. The microscopic growth rate behavior during directional solidification

4. The dopant segregation behavior and its dependence on the microscopic growth rate

5. The heat transfer characteristics of the solidification system.

EXPERIMENTAL APPROACH

To achieve the objectives listed, single crystals grown on Earth were partially melted and resolidified in space with simultaneous transmission of periodic current pulses across the crystal-melt interface.

The growth experiments in flight were carried out in the multipurpose furnace (Fig. V-1) originally designed for the Skylab mission [V-1] and modified to meet higher temperature requirements. The furnace had three tubular cavities into which the stainless steel cartridges containing the crystal assemblies were inserted. Heat levelers, lateral heat shields, and a heat extractor system controlled the heat flow from the heating element through the

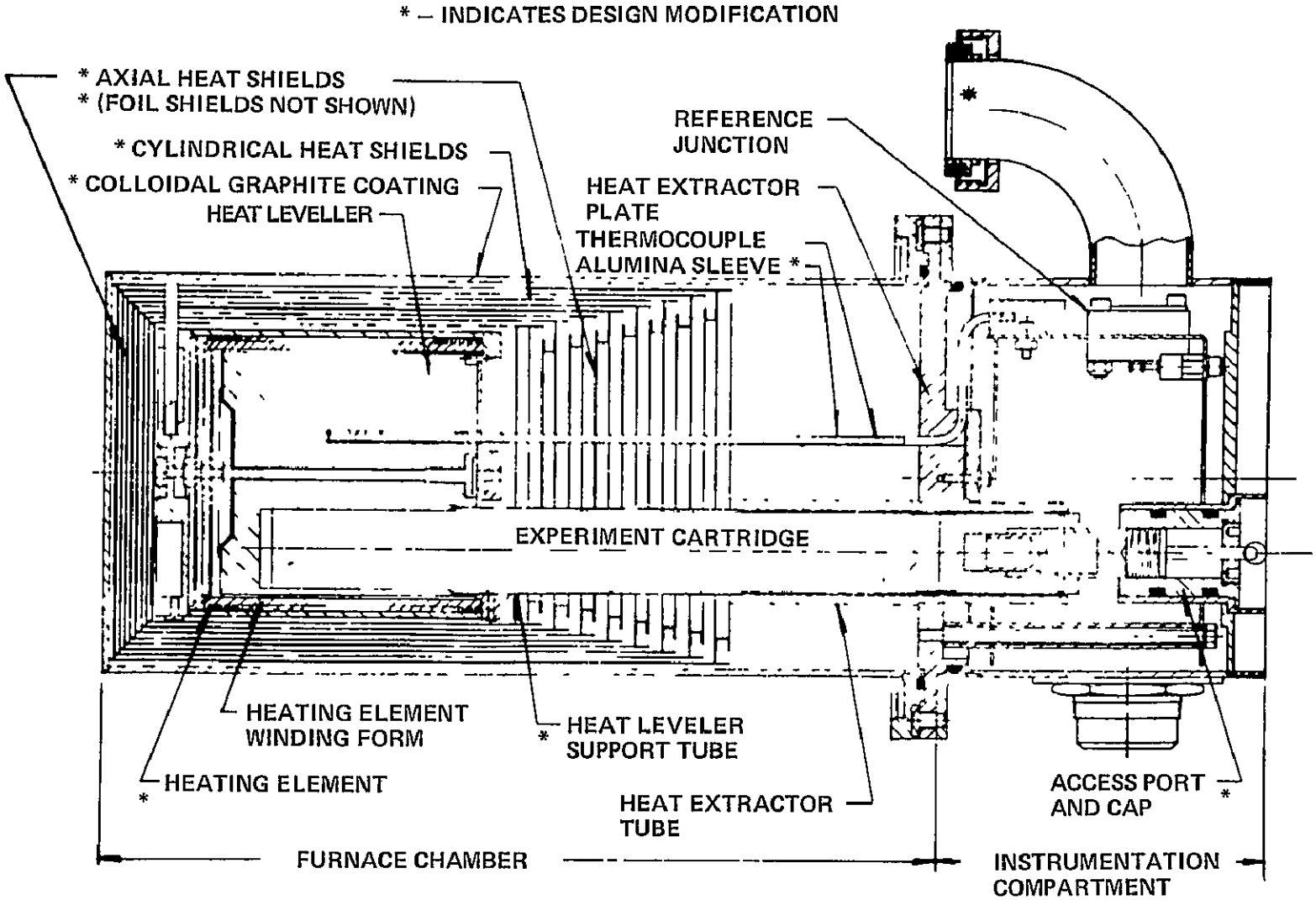

Figure V-1. Schematic of multipurpose furnace designed by Westinghouse for the ASTP crystal growth and solidification experiments.

crystal to the heat extractor plate. In this configuration melting was initiated upon appropriate power input at the crystal end located within the heating element, and the crystal-melt interface was stabilized after 6 cm of each of the original crystals were melted. Stabilization of the crystal-melt interface (thermal soaking) was achieved by reducing the power duty cycle to 90 percent. After thermal soaking (2 h) the power system was switched to the cool-down mode resulting in an average cooling rate of 2.4°C/min. This cooling rate was expected to yield a microscopic growth rate ranging from 5 μm/s at the beginning to 10 μm/s by the end of the controlled cool-down. Controlled cool-down was terminated after 1 h and 23 min (estimated regrowth length of approximately 4 cm); the growth system was subsequently switched to passive cool-down for a period of 1 h and 7 min after which helium was injected into the furnace to accelerate the cooling rate of the system.

To permit growth interface demarcation [V-2] by current pulsing, leads had to be attached to the encapsulated germanium crystals. This was achieved by means of graphite cups at both ends of the crystals to which platinum leads were attached (Fig. V-2). The platinum leads of the three growth systems were connected in series with a power supply that provided current pulses

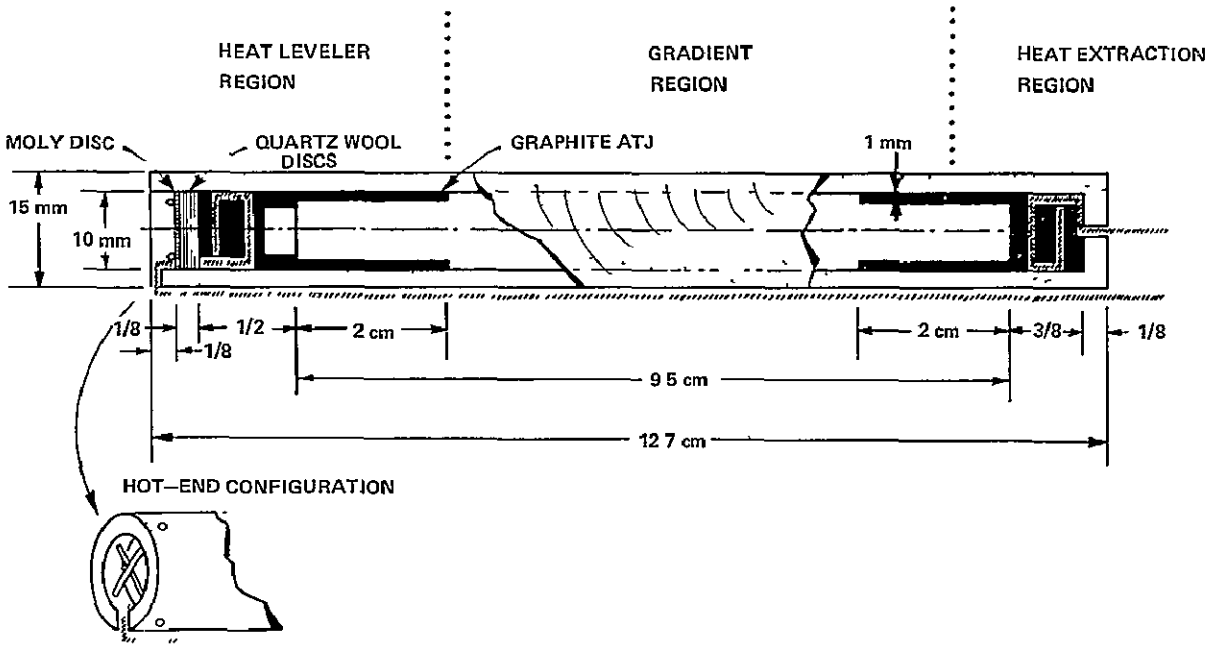

Figure V-2. Ampoule design permitting interface demarcation through current pulsing during regrowth.

(19.1 A/cm^2) of 55 ms duration at intervals of 4 s throughout the experiment, with the seed having a positive polarity. The specific cartridge design and the optimized procedure for interface demarcation were established during extensive ground-based tests, and information concerning this is presented in the appendices.

EXPERIMENTAL RESULTS AND DISCUSSION

The crystals grown in space were subjected to an exhaustive growth and segregation analysis after their return to the Massachusetts Institute of Technology, and this analysis was based on procedures established during ground-based tests. The primary analytical techniques were high resolution etching, Hall effect measurements, spreading resistance measurements, and ion-microprobe analysis. In view of the confined geometry that leads to stresses during growth, no defect analysis of the regrown material was pursued.

Surface Characterization

All crystals regrown in space could readily be removed from their quartz containers (Fig. V-3). In contrast, all crystals grown on Earth could only be isolated by dissolving the quartz containers in hydrogen fluoride (HF). This pronounced difference in behavior of the Earth and space-grown crystals can be understood on the basis of morphological characteristics of their surfaces. In interference contrast it was observed that the crystals grown in space exhibit an irregular network of narrow ridges on their surfaces (Fig. V-4) similar to that observed on indium-antimony (InSb) crystals grown on Skylab. In contrast, all crystals grown during ground-based tests in the same growth facility exhibited surface features that reflect the unavoidable irregularities of the inner walls of the quartz container in detail. It is therefore concluded that no wetting contact existed between the germanium (Ge) melts and the confining quartz ampoules during growth in space, while during growth on Earth the Ge melt is in wetting contact with its confinement. This conclusion is significant since it suggests that effective wetting inversion, first observed during growth of InSb on Skylab, is a phenomenon that may be expected to occur in a multitude of systems subjected to solidification in space. The implications of this effect on materials processing are far reaching with regard to processing technology and possibly with regard to the perfection of materials solidified in partial or total confinement.

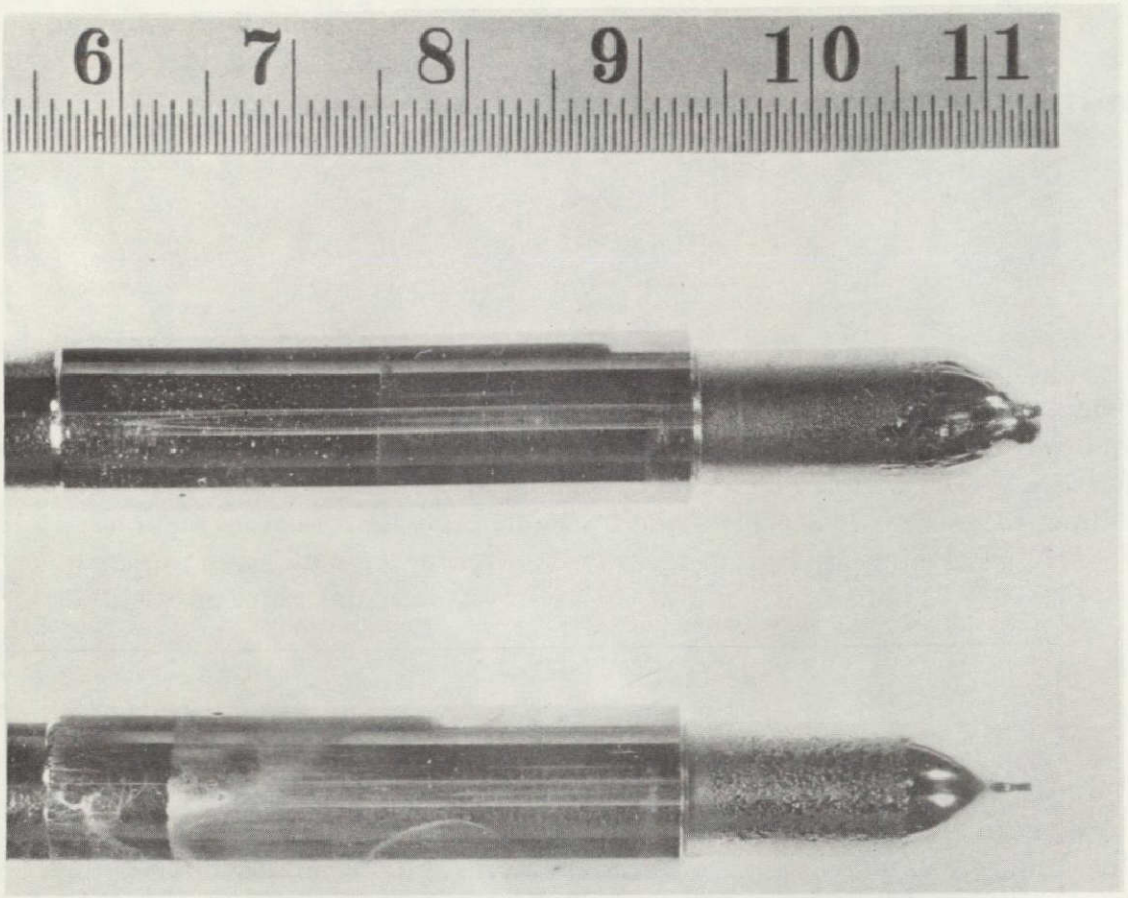

Figure V-3. Germanium crystals of <100> and <111> orientation, regrown in space, after removal from their quartz ampoules.

In all crystals the original regrowth interface was identified (Fig. V-3), which appeared as an abrupt increase (0.5 mm) in crystal diameter at the predicted distance of approximately 3.5 cm from the cold end of the crystals. Its location indicates the extent of back-melting in space and confirms on a macroscale the proper functioning of the multipurpose furnace.

From the morphological characteristics (absence of twin and grain boundaries) it is evident that single crystallinity in the peripheral region of the space grown Ge crystal of <111> orientation prevailed over the entire length of regrowth. In this respect growth in space and growth on Earth are conspicuously different, since all crystals regrown during ground-based tests never exhibited single crystallinity beyond regrowth of approximately 3 cm. The preservation of single crystallinity in the peripheral region (single crystal shell) is particularly remarkable in view of the high doping level for which interface instability due to constitutional supercooling and eventual interface breakdown is

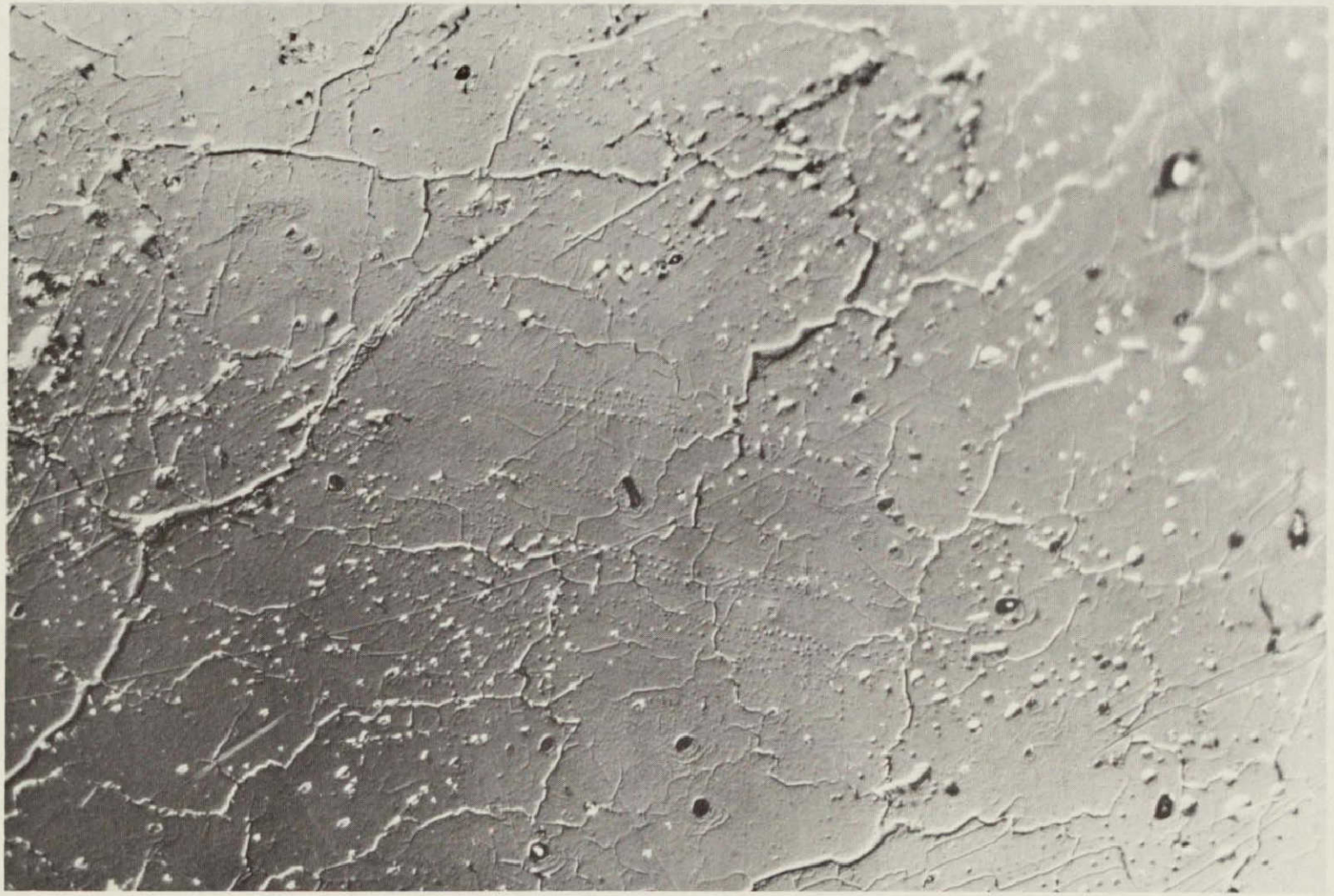

Figure V-4. Irregular ridge patterns on the surface of the <100> germanium crystal regrown in space (180X).

predicted, in fact observed, in the interior of the crystal. Single crystallinity in the peripheral region was not preserved on the space grown <100> crystal. In this case grain boundaries were first observed after growth of 3.5 cm, which compares favorably with ground-based tests where breakdown first occurred after approximately 2 cm of growth.

Bulk Characterization by High Resolution Etching

High resolution etching techniques were refined during ground-based testing to permit the detection of microscopic compositional fluctuations in Ge with a sensitivity of better than ±0.2 percent at gallium-dopant levels in excess of 10^{18} per centimeter. Bulk characterization by etching was performed on longitudinal center cuts of the regrown segments. The exposed surfaces were polished and etched (see the appendices). Figure V-5 shows an etched segment of the <111> Ge crystal regrown in space. Three regions can be identified: the original seed portion (top), a narrow region exhibiting microscopic compositional inhomogeneities, and a region exhibiting no compositional fluctuations (bottom). The latter growth region exhibits faint, but distinct, lines that are the current-induced interface demarcations formed at intervals of 4 s during regrowth. It can be seen that the spacing of consecutive demarcation lines converges to zero (zero growth rate) at the lower end of the bandlike region of perturbed growth and segregation. Thus, interface demarcation establishes that the formation of the growth region with compositional fluctuations (band below the original regrowth interface) took place during the 2 h thermal soak and preceded the controlled regrowth. Ground-based tests indicated that this growth band reflects thermal instability of the furnace and is attributed to a slight imbalance of heat input and heat loss during the early stages of thermal soak (see the appendices).

Etching analysis revealed further that the bulk of the controlled regrowth region of the <100> crystal is free of microscopic compositional fluctuations over a grown length in excess of 2.5 cm. For regrowth in the <111> direction minor compositional fluctuations of approximately 0.1 percent were observed associated with peripheral facet formation (Fig. V-6); the nature of there perturbations is not as yet understood.

Segregation inhomogeneities associated with interface breakdown due to constitutional supercooling were observed in all crystals after the advancing growth front had moved into the graphite cup. The breakdown in the space grown material is attributed to deteriorating thermal gradients caused by abrupt changes in the thermal conductivity of the confinement system (in going from

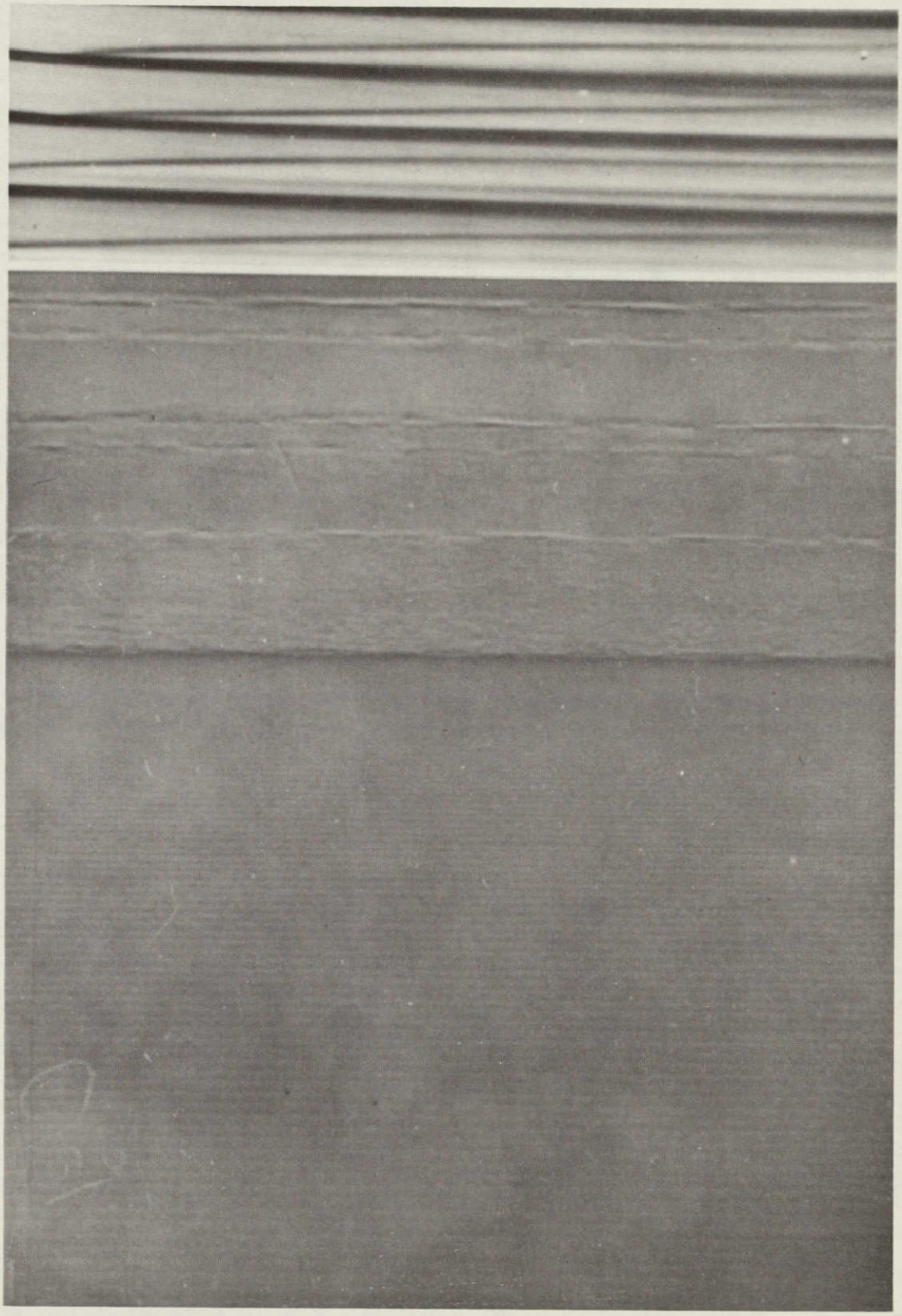

Figure V-5. Etched segment of the <111> germanium crystal regrown in space; observe the seed portion (top) and the controlled regrowth portion (bottom) separated by a band of uncontrolled growth and segregation (140X).

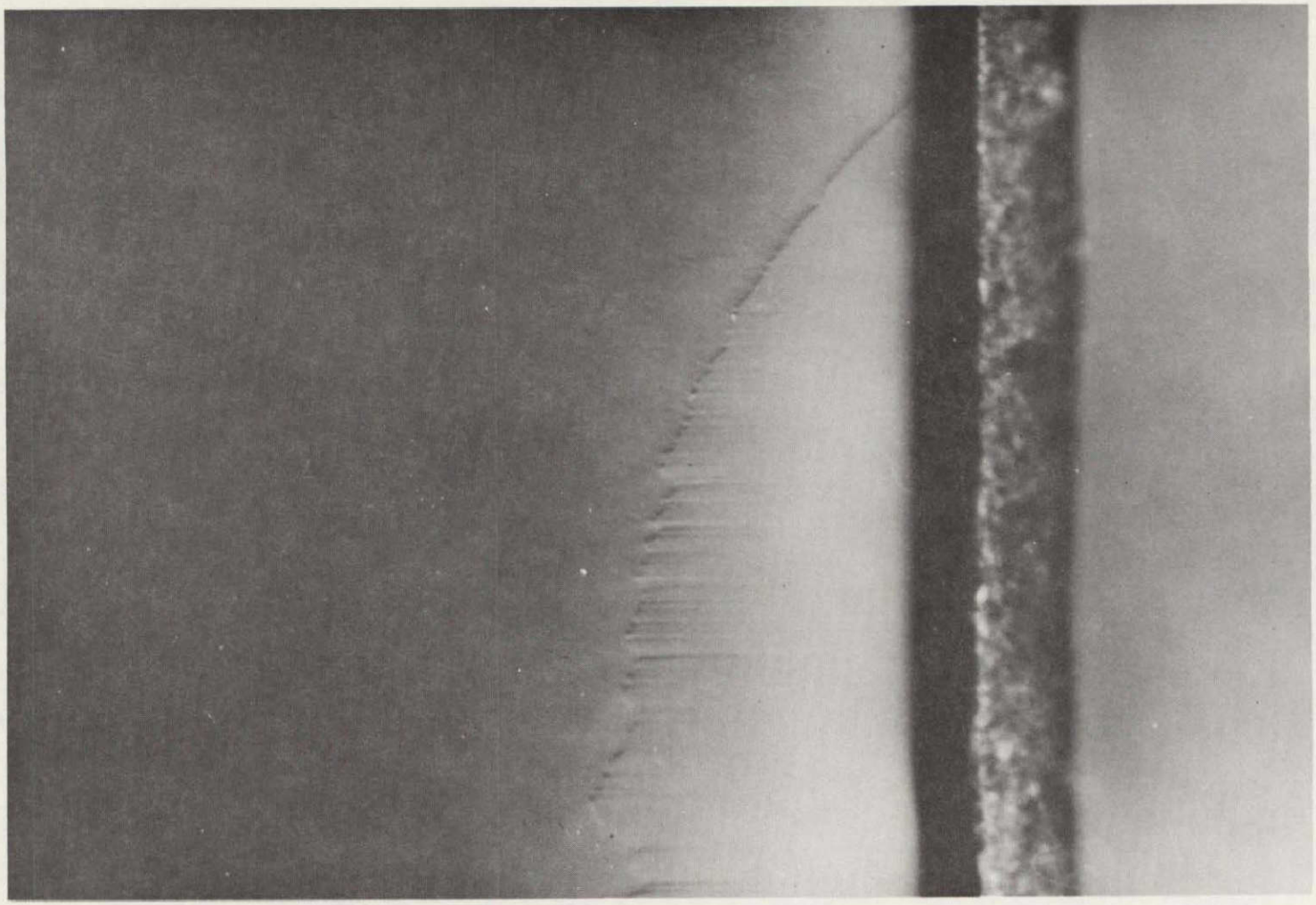

Figure V-6. Segregation inhomogeneities associated with peripheral facet formation in the <111> germanium crystal regrown in space (375X).

quartz to graphite) and the resulting changes in the growth interface morphology. It is important to note that the onset of instability occurs significantly earlier in the <111> crystal and is initiated at the facet to off-facet boundary. On occasions, the morphological characteristics of the unstable growth interface are much more regular and conforming to theoretical predictions in the space-grown crystals than in those grown on Earth (Figs. V-7 and V-8).

Growth Behavior on the Microscale

From interface demarcation lines introduced at intervals of 4 s, a quantitative growth rate analysis on a microscale was obtained for all space-grown crystals. The rate data for the crystals grown in the <111> direction are shown in Figure V-9. It can be seen that during the early stages of the cooling cycle, the microscopic rate of growth increases rapidly from zero to approximately 7 μm/s. After the initial transient region, the rate increase slows down and after approximately 2.5 cm of growth, the microscopic growth rate approaches a value of 10.5 μm/s. The growth rate behavior observed in space (for the cooling rate of 2.4°C/min) is virtually identical with that encountered during ground-based testing and indicates that the heat transfer characteristics of the system are the same in space and on Earth. This result indicates that in the growth configuration used, conductive heat transfer dominates and the contribution of laminar convection to heat transport, which is present in the ground-based tests, is negligible.

It should be pointed out that all existing theories of segregation assume an initial step function of the growth rate from zero to a finite and constant rate; since all real melt growth systems exhibit an initial transient growth behavior, no quantitative comparison between theory and experiment can be made. In view of these results, the development of a modified segregation theory has been initiated that considers the existence of initial growth rate transients under convection-free conditions.

Dopant Segregation Behavior

Quantitative compositional analyses of crystals regrown in space and on Earth have been obtained through spreading resistance measurements with a linear resolution of 5 μm. The results obtained for the initial regrowth region of crystals grown in the <111> direction are shown in Figure V-10. (These regions are the same as those shown in Figure V-5.) The measurements taken along the growth direction of a ground- and flight-grown sample identify three

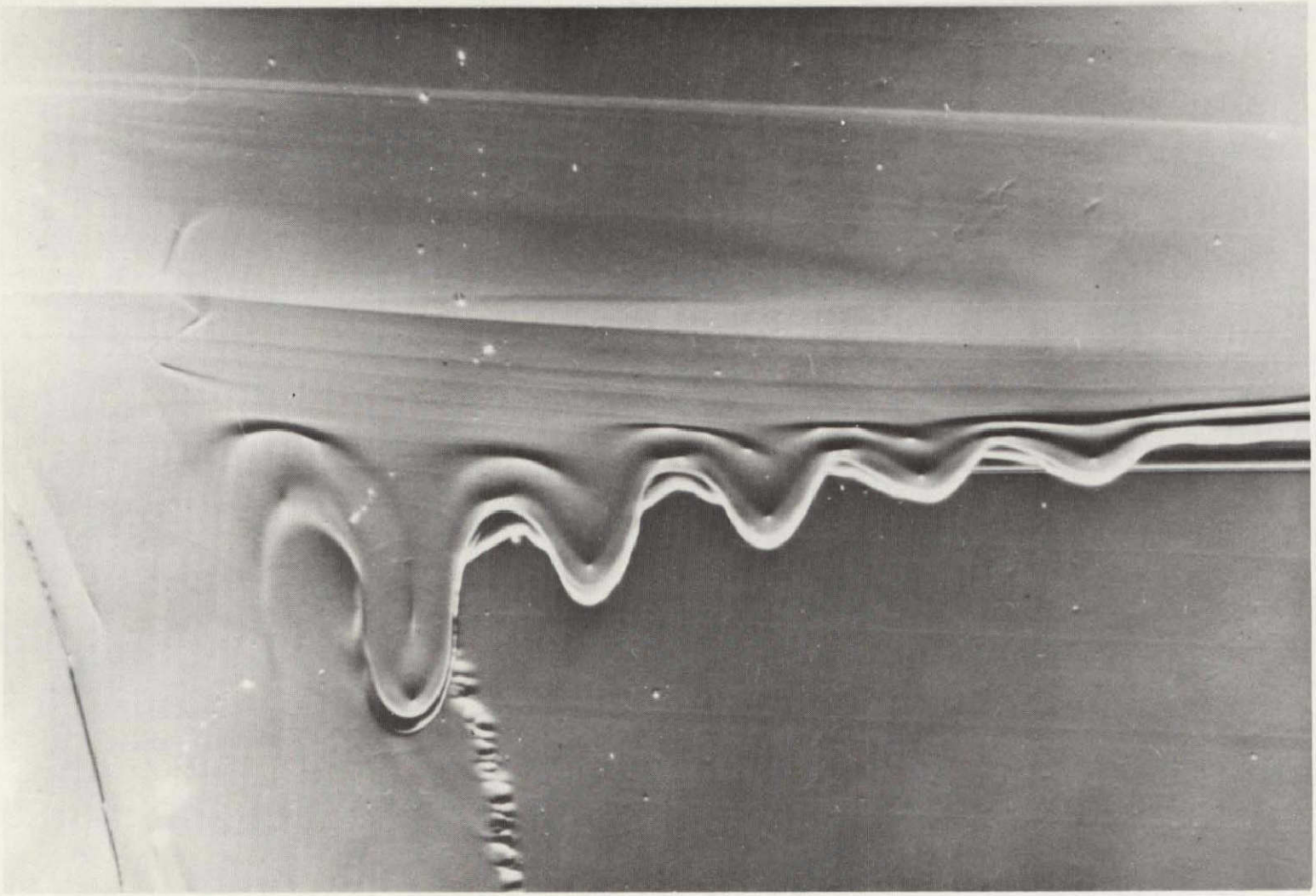

Figure V-7. Frontal interface breakdown during late stages of <111> germanium regrowth in space (compare with Figure V-8) (300X).

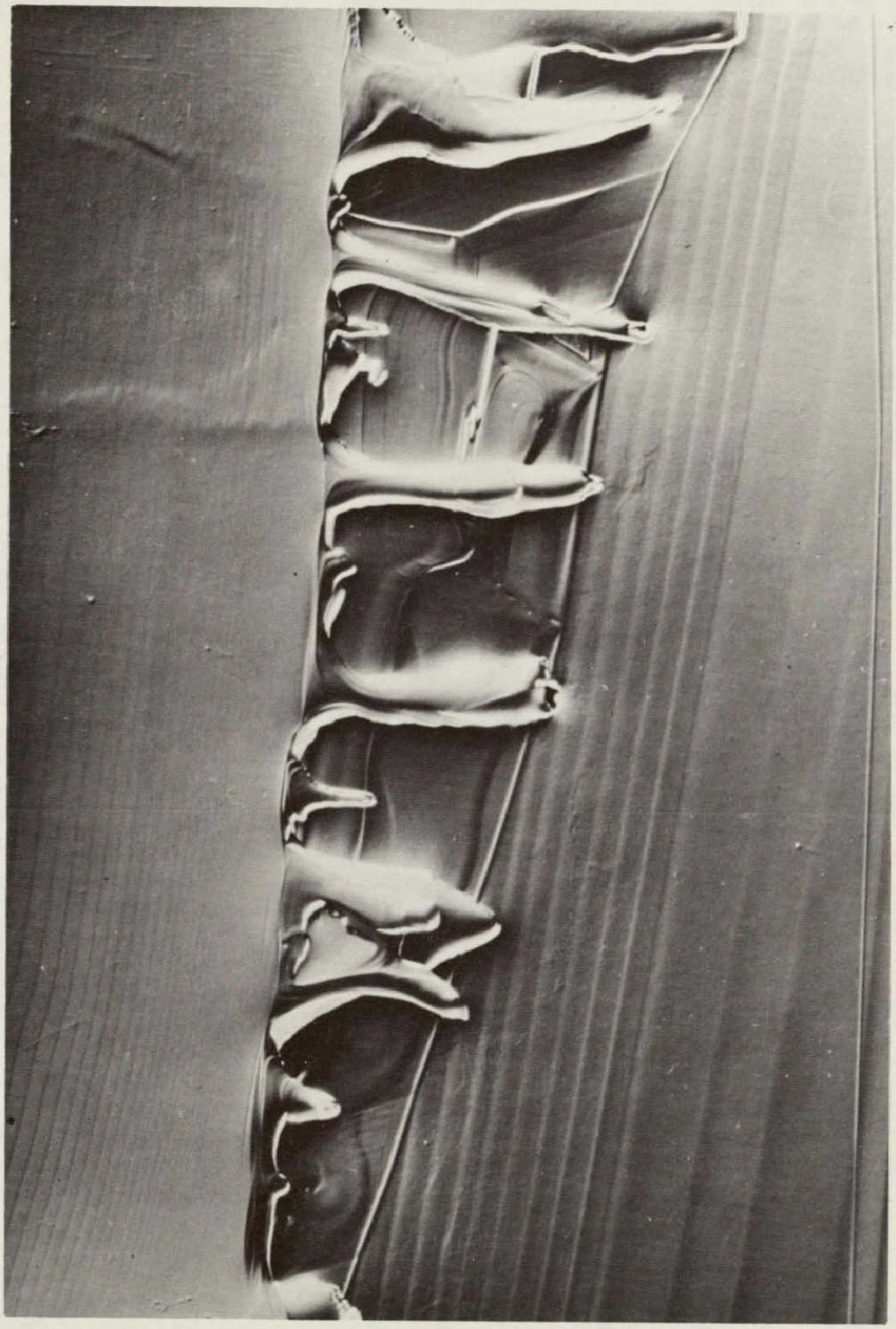

Figure V-8. Frontal interface breakdown during late stages of <111> germanium regrowth on Earth (300X).

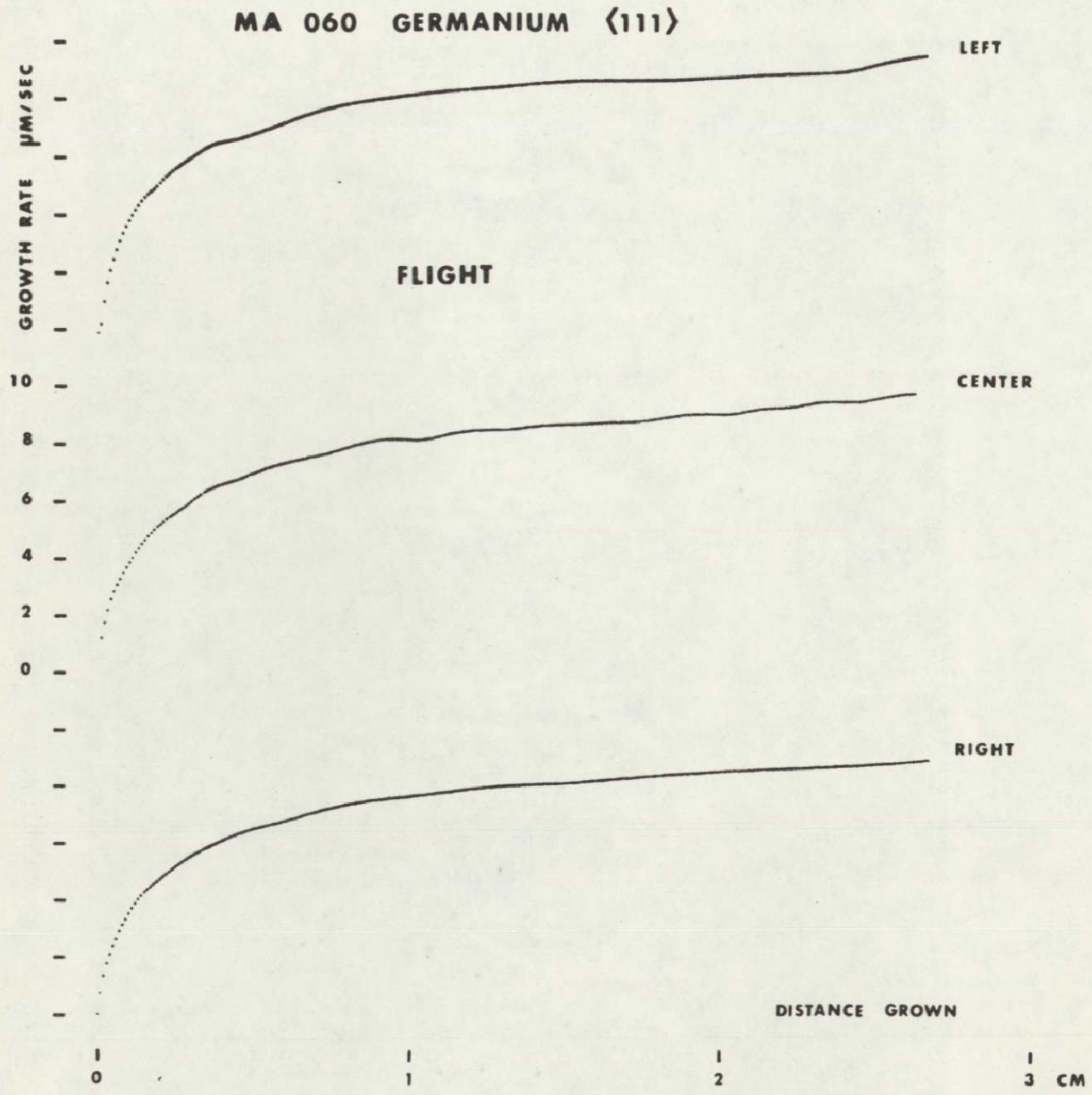

Figure V-9. Microscopic growth rates of the <111> germanium crystal regrown in space.

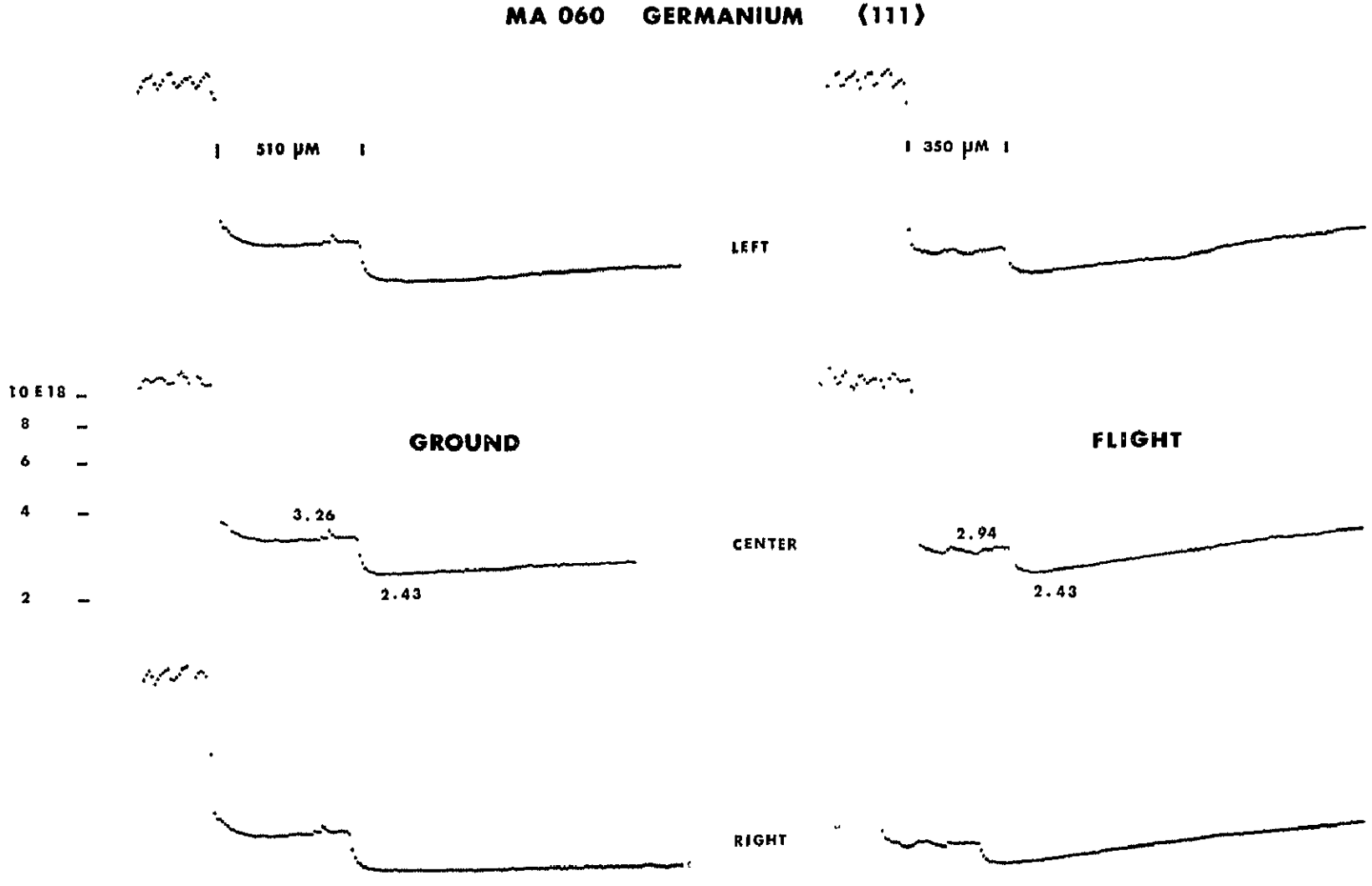

Figure V-10. Compositional profiles of the initial regrowth region in the <111> germanium crystal regrown in space; ground-based data shown for comparison.

regions: the seed regions on the left, characterized by pronounced compositional fluctuations; the bands of uncontrolled growth in the center; and the regrown regions with steadily increasing dopant concentration on the right. It is seen that the initial region in the space grown crystal exhibits a much more rapid dopant concentration increase than the crystal grown on Earth. This behavior reflects the effect of laminar convection on segregation. The results are not, however, as expected with regard to the absolute dopant concentration level. Taking the equilibrium distribution coefficient (k_o) of gallium (Ga) in Ge to be 0.087, as generally accepted, the dopant concentration in the initial regrowth region should assume a value of approximately 9×10^{17} per cubic centimeter instead of the presently measured value of 2.43×10^{18} per cubic centimeter. Since virtually identical initial dopant concentration levels were observed in both samples, it is assumed that the generally accepted value for k_o is erroneous.

The appearance of growth facets in the space-grown <111> crystal made it possible to study the facet segregation behavior in the absence of convective interference. The spreading resistance measurements (Fig. V-11) show that the dopant concentration on-facet is less than that of off-facet by a factor of 0.92. The tracings further show that the compositional change on-facet to off-facet takes place over a distance of approximately 30 μm.

Attempts to analyze quantitatively the initial segregation transient in the regrowth region of the space grown sample failed because of the existing growth rate transient, which is not considered in the theoretical treatments. In view of the unavailability of reliable values for k_o and D, the diffusion coefficient essential for a quantitative segregation analysis, appropriate experiments under zero-g conditions must be performed for the accurate determination of these constants.

Compositional analysis on a macroscale, covering the whole length of crystals regrown in space, is still being pursued. The results obtained to date are to a large extent unexpected and as yet unexplained. As seen in Figure V-12 the dopant concentration, as expected, increases steadily over a distance of approximately 1.5 cm from the original regrowth interface. At this distance k_{eff} approaches the value of 1, characteristic of diffusion-controlled steady-state segregation. However, with continuing growth and with a steadily increasing microscopic growth rate, the dopant concentration decreases instead of reaching the steady-state value. The dopant concentration continues to decrease over a distance of approximately 1 cm of growth. At this point interface breakdown takes place, due to constitutional supercooling, and a further analysis of the segregation behavior is not possible.

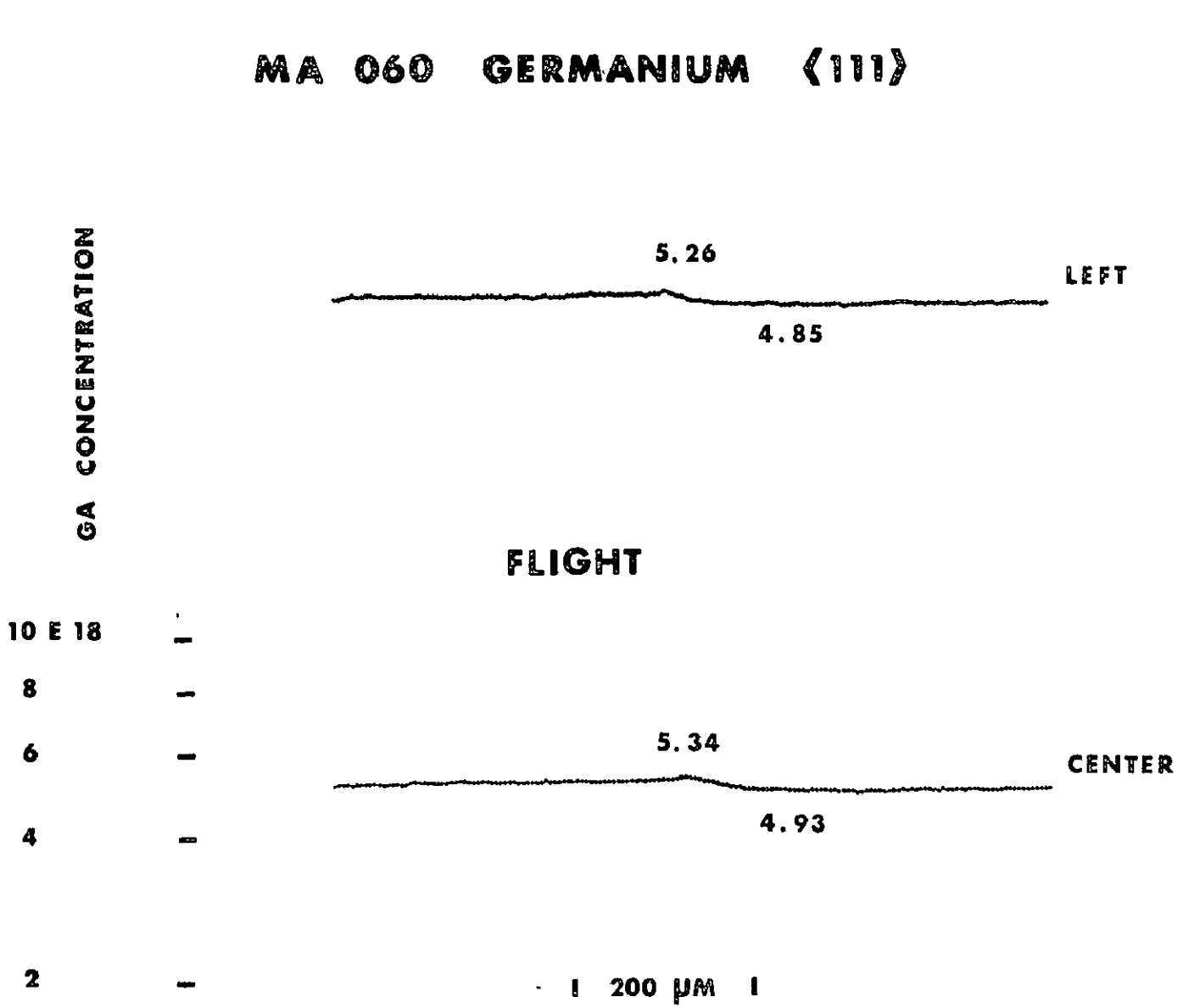

Figure V-11. Compositional profile of the off-facet to facet transition region in the <111> germanium crystal regrown in space.

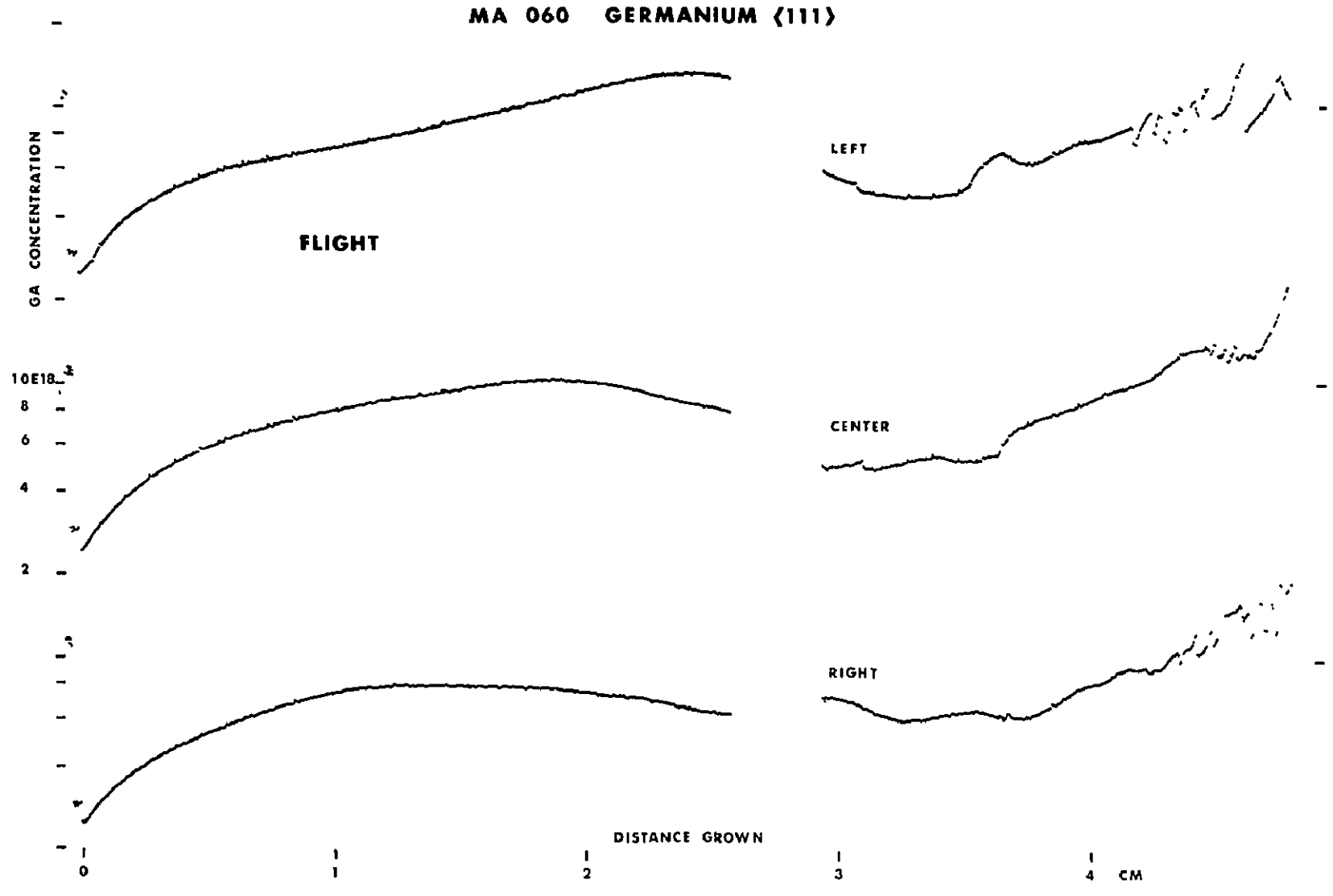

Figure V-12. Macroscopic compositional profile of the <111> germanium crystal regrown in space.

There are indications that the observed segregation anomaly is not characteristic of growth under zero-g conditions, but that it is a consequence of the particular geometry of the growth system.

In view of the potentially far reaching implications of these unexpected segregation effects, a complete understanding of their origin is of paramount importance.

SUMMARY

The present experiment revealed growth and segregation effects previously not observed on Earth. The bulk of these effects cannot be accounted for by an existing experimental or theoretical models of growth and segregation. This finding has fundamental implications in view of the fact that germanium is the most studied and best understood among all solids. It clearly implies that, although the uniqueness of outer space for materials processing is a truism, exploitation of the unprecedented opportunities of the zero-g environment necessitates the selection of systems and experimental apparatus that have been or can be exhaustively investigated on Earth, so that the effects of zero-g conditions on materials processing can be unambiguously indentified and quantitatively studied. It further implies that extensive research is essential following space experimentation, even on critically selected and well understood systems, to quantitatively understand the zero-g effects and establish sound guidelines for subsequent space processing. It is the belief of these investigators that materials processing within the Shuttle program, without major expansion of ground-based investigations on critically selected materials systems, is likely to evolve into a most expensive and unprofitable undertaking.

APPENDIX A

GROWTH OF GERMANIUM CRYSTALS FOR GROUND-BASED TESTS AND FLIGHT EXPERIMENTS

All germanium single crystals (23) used for the experiments were pulled from doped melts by the Czochralski technique under the following growth conditions:

Ge Charge:	240 g in ATJ graphite crucibles
Dopant Elements:	Ga, tin (Sn), and antimony (Sb) (all crystals were singly doped)
Doping Levels:	The melts were doped to achieve an average dopant concentration of approximately 10^{18} to 10^{19} per cubic centimeter in the grown crystals.
Seed Orientation:	<100> and <111>
Protective Gas Atmosphere:	H_2 at a pressure of approximately 760 760 mm Hg
Pulling Rate:	2 in./h for Ga doped crystals 1 in./h for Sb and Sn doped crystals
Seed Rotation:	10 rpm
Crucible Rotation:	0 rpm

The crystals (weight of approximately 130 g, length of approximately 15 cm, and diameter of approximately 1.5 cm) were centerless ground to a diameter of 1.046 cm and cut to a length of 9.5 cm. The diameter of both ends of all crystals was reduced to 0.843 cm over a length of 2.06 cm to permit the attachment of graphite cups which served as the current contacts for interface demarcation. The crystals were subsequently etched in CP-4 (five parts HNO_3, three parts HF, and three parts CH COOH, Br_2) to the desired diameter of 0.838 cm. Samples from both ends of all crystals were retained for the determination of the doping levels.

APPENDIX B

AMPOULE DESIGN AND ASSEMBLY

The ampoules confining the growth systems were made from heavy wall quartz (Amersil) tubing (inside diameter of 10 mm, outside diameter of 16 mm) which was centerless ground to 1.50 cm diameter and cut to a length of 12.7 cm. Prior to assembly the ampoules were etched with HF; rinsed with distilled H_2O, methanol, and acetone; and dried with hot filtered air. The graphite contact cups, machined to yield low contact resistance with the germanium crystals, were fired at 1600°C in a vacuum of 10^{-7} torr; subsequently platinum leads were attached as shown in Figure V-1.

After a discussion with the technical staff of Westinghouse, it was decided to use an open ampoule configuration (non-vacuum tight) with 0.04 in. Pt current leads and graphite cups at both ends of the crystals as contacting media (Fig. V-2). The inside length of the graphite cups was 2.0 cm and designed to ensure contact with the melt irrespective of the degree of back-melting. The mechanical contact design required precision machining of the graphite cups and the germanium crystals. The ampoule design was tested in ground-based experiments and was used for the flight experiment without modification.

APPENDIX C

PULSE POWER SUPPLY

From preliminary experiments it was concluded that growth characterization on a microscale through interface demarcation would require a power supply capable of delivering current pulses of the following characteristics (Fig. V-13):

Pulse Repetition Rate:	2 s
Pulse Duration:	$\geq$ 75 ms
Amplitude:	25 A independent of load resistance variations up to 1 Ω

The basic design criteria of the pulse power supply and its connection to the three growth ampoules in either parallel, series, or a multiplexed (sequential) configuration were evaluated jointly by members of the technical staff of Westinghouse and Massachusetts Institute of Technology.

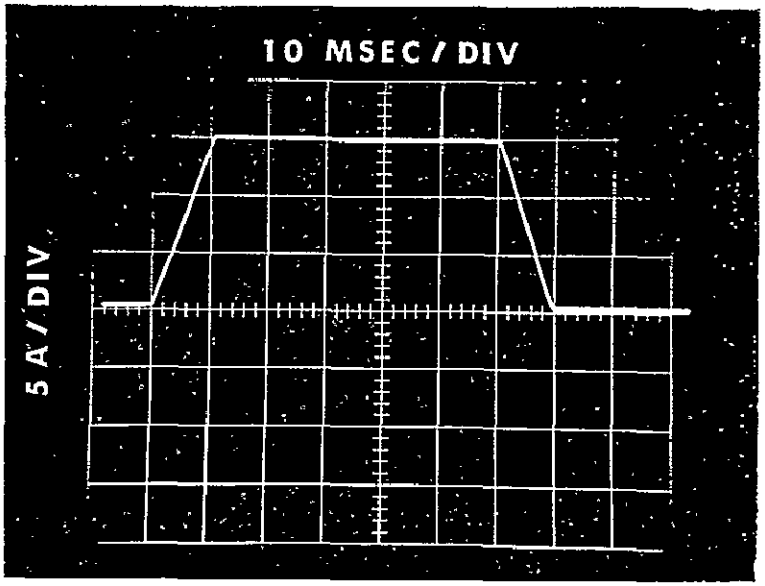

Figure V-13. Characteristics of pulses used for interface demarcation during flight experiment.

On the basis of the power available for MA-060, a prototype unit to be connected in series with the growth ampoules was designed that delivered 50 ms half-width constant current pulses of 15 A amplitude into a resistive load of up to 1 Ω with a nominal repetition rate of 4 s. The pulse transit time was degraded to 10 ms to minimize electrical isolation requirements for the spacecraft power bus.

APPENDIX D

SAMPLE PREPARATION FOR ETCHING ANALYSIS AND SPREADING RESISTANCE MEASUREMENTS

For bulk crystal analysis by interference contrast microscopy and spreading resistance measurements, all crystals were cut along the growth direction to obtain 0.2 cm thick slices containing the crystal axis. These center cuts were mounted on brass disks, as described in the following, and their surfaces were ground with 10 μm abrasive. All samples were subsequently mechanically polished to a Linde A surface finish and chemically polished with a modified Syton HT 30 solution (200 ml Syton HT 30, 200 ml H_2O, 5 ml H_2O_2, and 2 ml CH_3COOH). The samples were then etched by immersing them for 5 to 8 s in a solution of one part HF, one part CH_3COOH, and one part H_2O. For quantitative segregation analysis, the specimens were first subjected to spreading resistance measurements and subsequently investigated by interference contrast microscopy. With this procedure it was possible to determine the microscopic growth rate (from the spacing of consecutive interface demarcation lines) corresponding precisely to the region for which the dopant concentration profile was obtained through the spreading resistance measurements (the traces of the spreading resistance probe are visible in interference contrast). Photomicrographs were taken with Contrast Ortho Film (125 ASA).

APPENDIX E

SPREADING RESISTANCE MEASUREMENTS

The functional relationship between resistivity ρ and spreading resistance R_s with its application to the "spreading resistance probe" technique has been described by Mazur [V-3]. Resistivity and mobility data for germanium at 300° C have been analyzed by least-square methods and plotted as a function of impurity concentration by Sze and Irvin [V-4], which then establishes an exact correlation between spreading resistance and impurity concentration. Thus, spreading resistance measurements provide an elegant way of determining dopant impurity profiles on a microscale [V-5].

All measurements were performed with a single probe, which was calibrated against a small segment of the germanium <111> flight crystal, 0.4 cm × 0.4 cm × 0.2 cm in size, as a standard. Its resistivity and carrier concentration were determined by Hall effect measurements at 300° C using the Van der Pauw technique [V-6].

Center slices of 0.2 cm thickness were diamond-wheel cut from the ASTP flight and their corresponding ground-based test crystals. Due to the 2.5 cm traverse limit of the X-axis drive of the probe positioner, each slice had to be cut, which prevented continuous scanning of the sample surfaces.

Large area ohmic contact to the back side of all samples to be analyzed was made with an evaporated and microalloyed silver layer. The samples were pressure-bonded to brass disks with conductive silver paint.

Subsequently, the samples were polished and etched as described previously.

Reproducibility of the measurements taken on stabilized surfaces was better than 2 percent for the <111> germanium segments and approximately 5 percent for the <100> germanium segments (worst case). Occasional excessive data scatter on systematic drift of the data base could in all cases be traced to steps in the sample preparation.

The raw spreading resistance data were first converted to normalized resistances using a quadratic regression fit, correcting for additional distributed resistances in the external circuitry. From these values, resistivities were calculated without smoothing and fitted to a computer-generated expression for the concentration versus resistivity relationship employing a spline cubic interpolating polynomial. The resulting concentration values were plotted as a function of distance on a high speed digital plotter.

APPENDIX F

GROUND-BASED TESTS

Simulation Tests

The purposes of simulation tests were: (1) to study the thermal characteristics of the ampoule design, (2) to determine the cartridge design that would yield specified growth characteristics in the multipurpose furnace, and (3) to test growth interface demarcation.

The simulation tests indicated that the growth procedure used by Westinghouse resulted in Ge regrowth of 2.2 cm instead of the specified value of 3.0 cm. It was also observed that the intensity of interface demarcation (for pulses of 30 ms duration) over the first 1.5 cm of regrowth is too low to be detected by etching. Since growth experiments in the laboratory with the same pulse characteristics yielded detectable interface demarcation, it was concluded that current leakage in the simulation test arrangement was responsible for the lack of adequate interface demarcation.

To ensure detectable growth interface demarcation it was subsequently requested that the pulsing frequency be changed from 0.5 to 0.25 Hz and that the duration of the current pulses be increased from 30 to 60 ms.

Prototype Tests

These tests served to finalize ampoule and cartridge design as well as the pulse characteristics for interface demarcation; in addition, these tests were used to evaluate the detectability of interface demarcation in Sb and Sn doped germanium crystals. It was found that current pulses of 15 A and 60 ms duration lead to detectable interface demarcation in Ga doped crystals but not in Sb and Sn doped crystals. On the basis of these experiments, it was furthermore concluded that the desired regrowth rate (approximately 5 μm/s) could best be approximated at a cooling rate of 2.4°C/min.

Ground-Based Tests (GBT)

A total of three ground-based tests, each involving a melting and regrowth of three crystals in the prototype furnace, were carried out at MSFC. During these tests the cool-down rates, pulse characteristics, and pulse polarity was

tested. It was observed that furnace stability and the resulting regrowth characteristics were significantly affected by the lack of stable line voltage. In subsequent GBT experiments the furnace was battery operated and the pulse characteristics optimized at seed polarity (+), 0.25 Hz, 15 A, and 6 ms duration. The experiments further confirmed that a cooling rate of 2.4°C/min approximates the specified regrowth rate on Earth. The last GBT experiment, during which all specified growth and interface demarcation characteristics were applied, was performed in the prototype furnace after the actual launch of the ASTP mission. The results obtained during this test were used as reference for the space grown crystals.

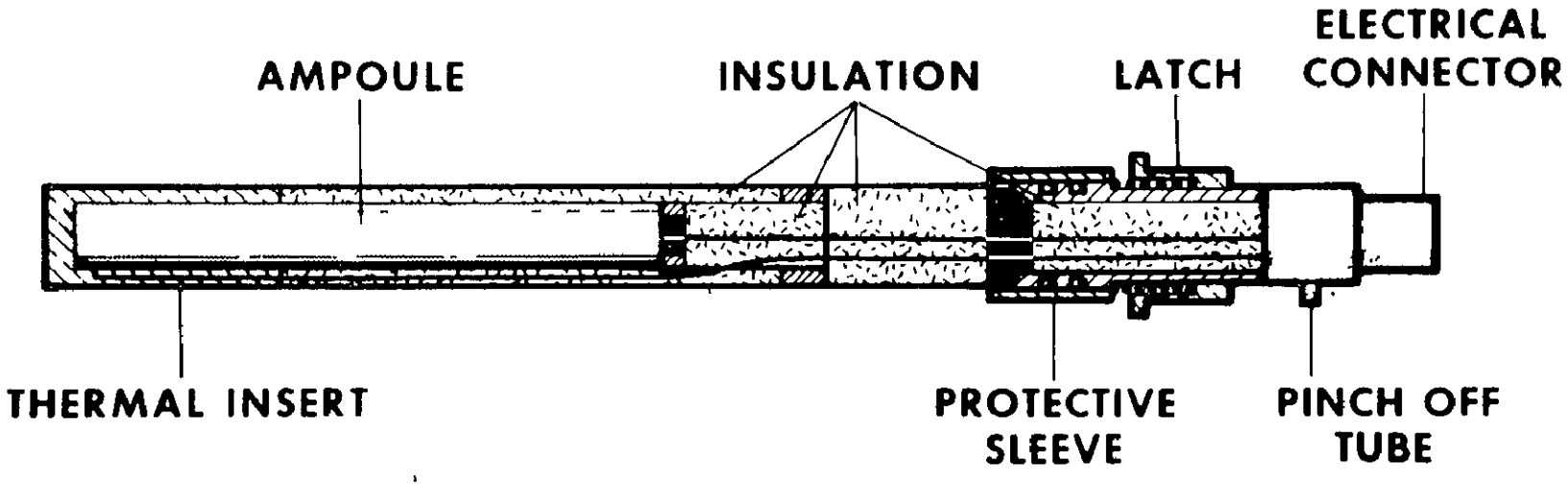

Figure V-14. Schematic of cartridge design for experiment MA-060.

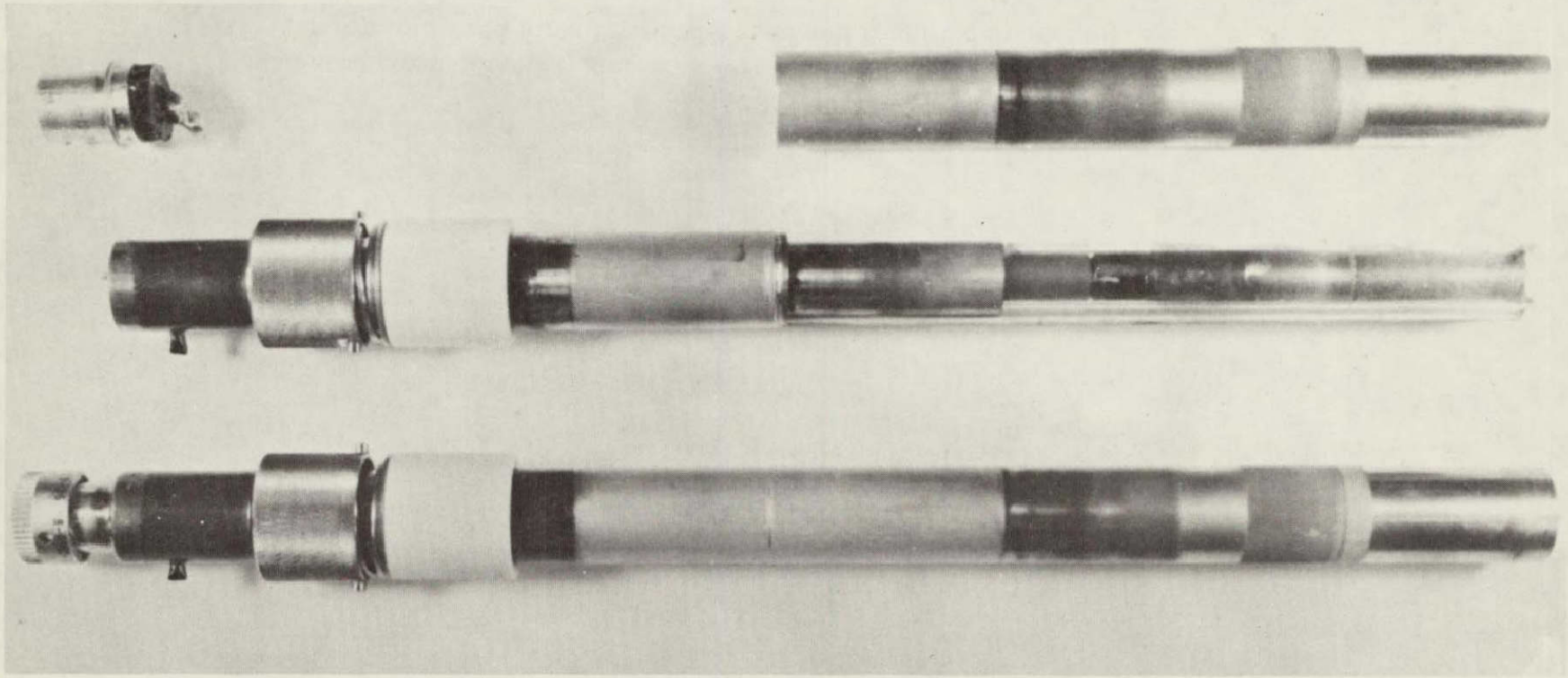

Figure V-15. Cartridges used for ground-based and flight experiments.

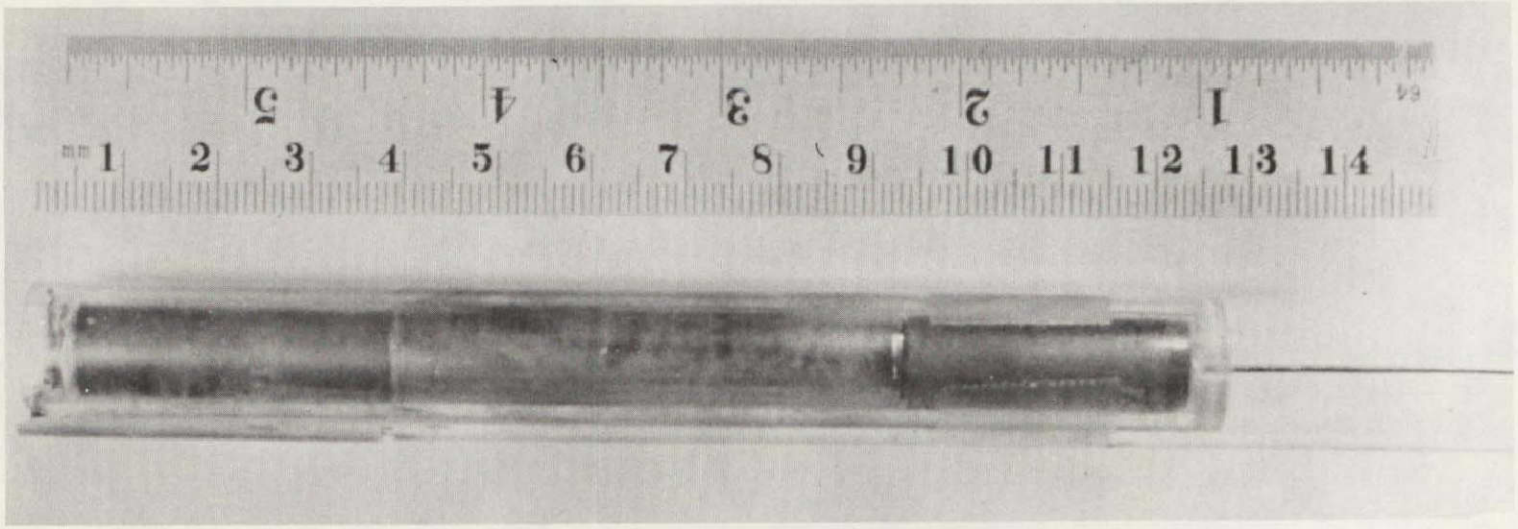

Figure V-16. Encapsulated germanium crystal used for simulation tests (the ampoule in the configuration shown was used for all ground-based and flight experiments).

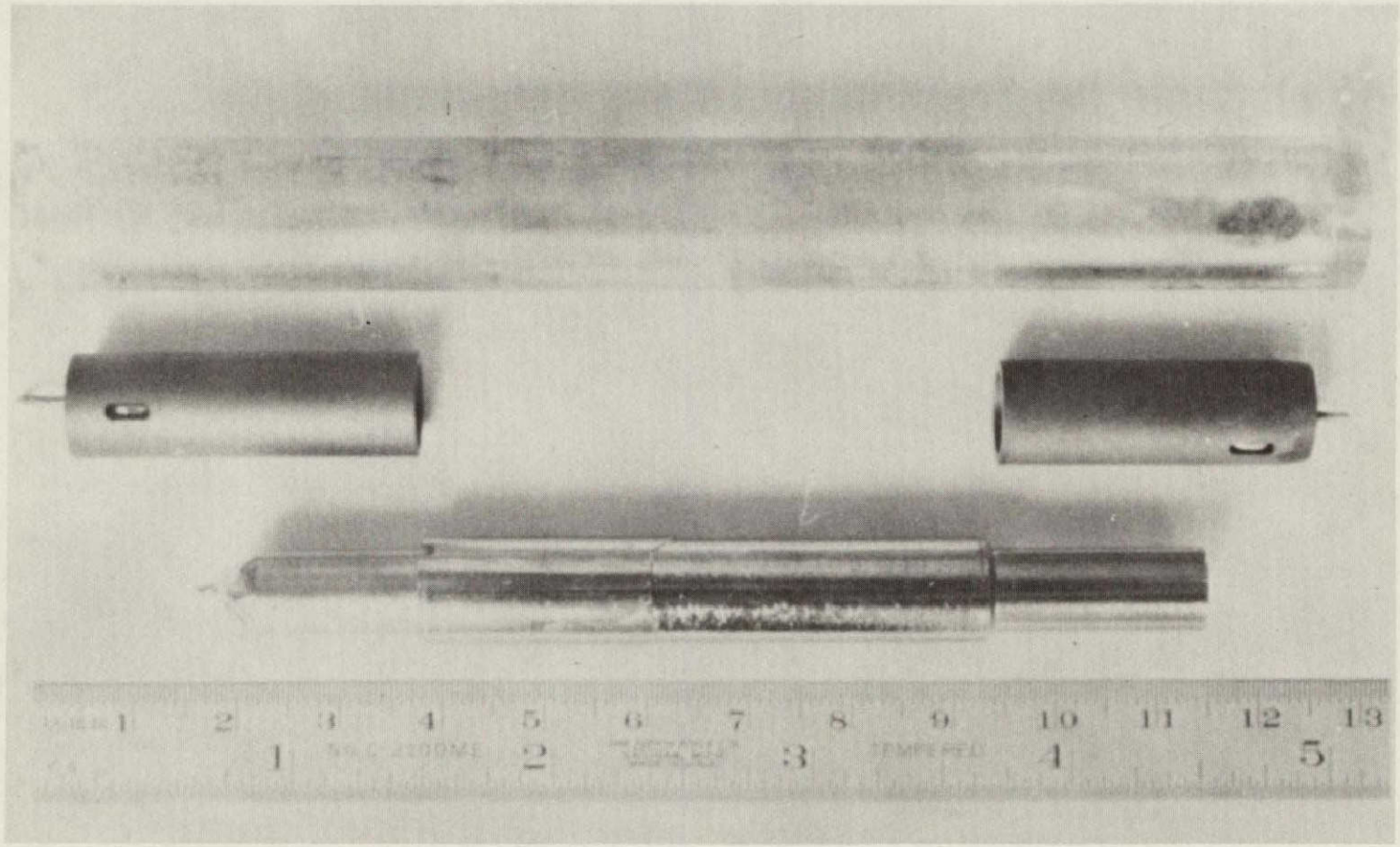

Figure V-17. Isolated germanium crystal regrown during simulation test (length of regrowth was 2.2 cm; the graphite cups which serve as contact material for current pulsing are also shown).

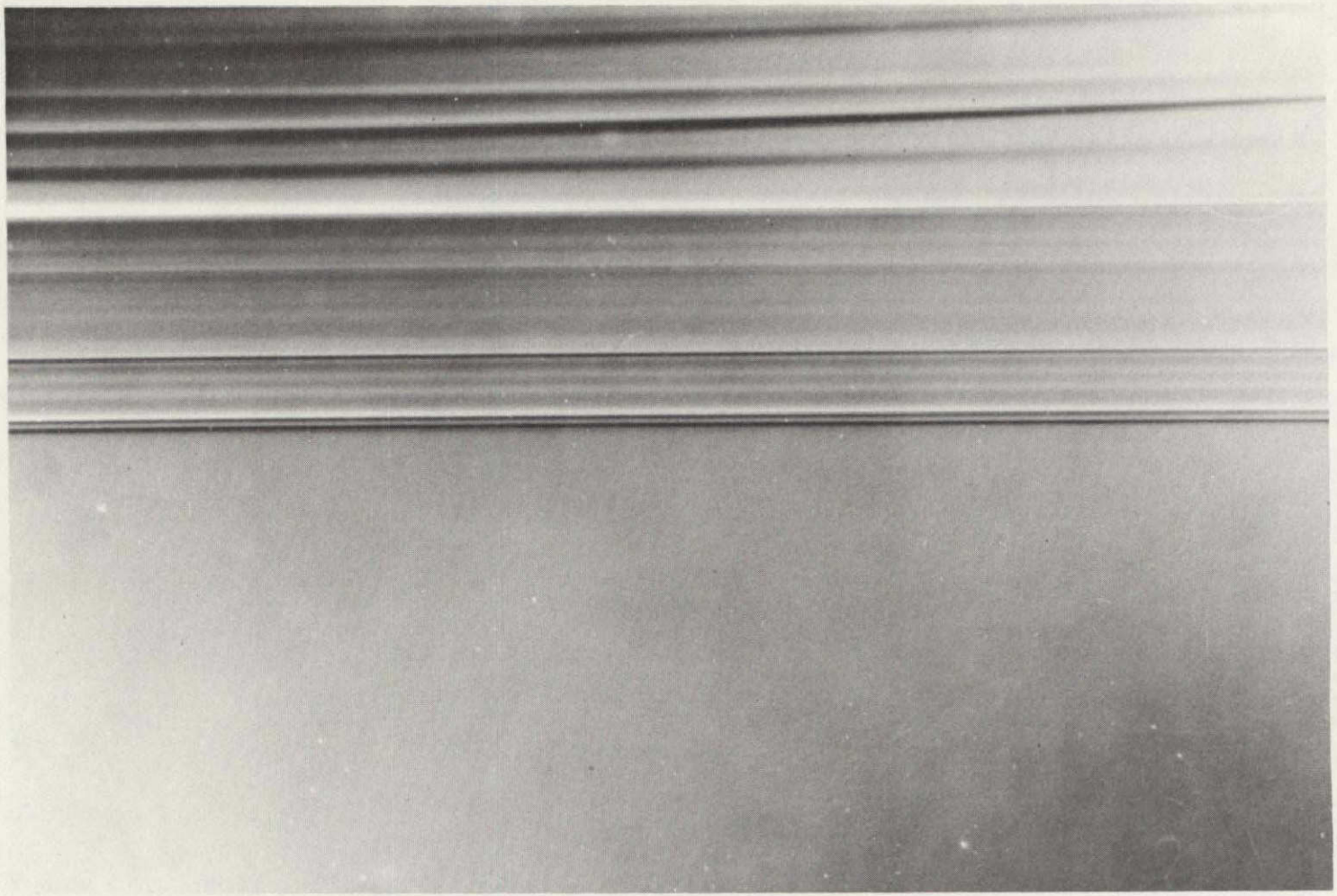

Figure V-18. Etched segment of germanium regrown during simulation test (notice the band of uncontrolled growth (200 μm) formed prior to passive cool-down; notice further that interface demarcation is not revealed by etching) (140X).

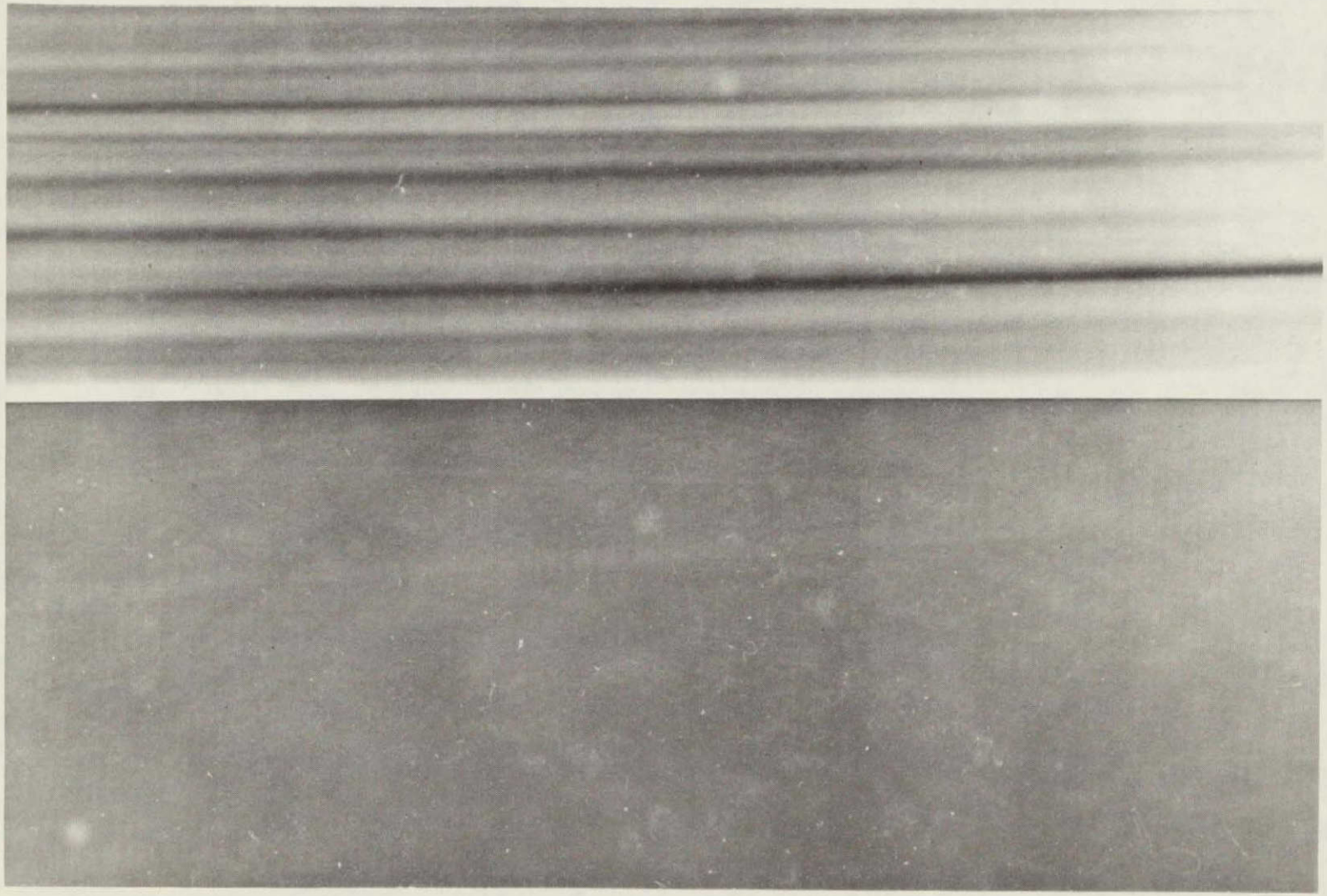

Figure V-19. Etched segment of the germanium crystal regrown during the prototype test (notice the absence of uncontrolled growth prior to controlled cool-down; the growth conditions involved a slight temperature increase prior to initiating the cool-down cycle) (140X).

Figure V-20. Interface demarcation achieved by current pulses of 15 A and 60 ms duration at a repetition rate of 4 s (the crystal shown was pulled, by the Czochralski technique, during ground-based testing).

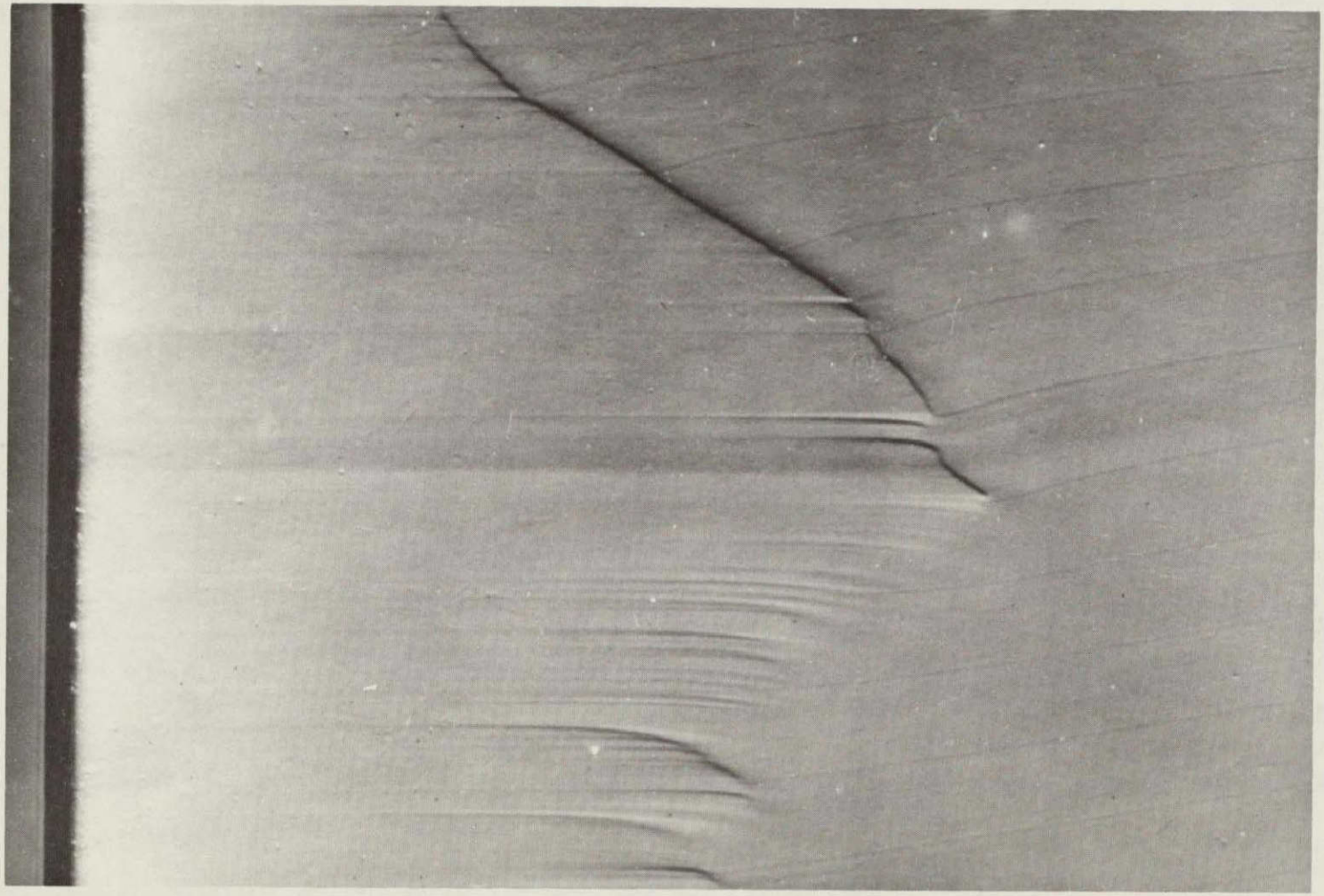

Figure V-21. Etched segment of a <111> germanium crystal regrown under conditions simulating the multipurpose furnace configuration (notice the pronounced interface demarcation achieved by current pulses with characteristics similar to those provided by the Teledyne-Brown pulsing unit).

Figure V-22. Etched segment of <111> germanium crystal regrown during ground-based testing (notice the well delineated interface demarcation achieved by current pulses of 15 A and a duration of 50 ms; the frequency of interface demarcation was decreased by a factor of two after a short period of regrowth).

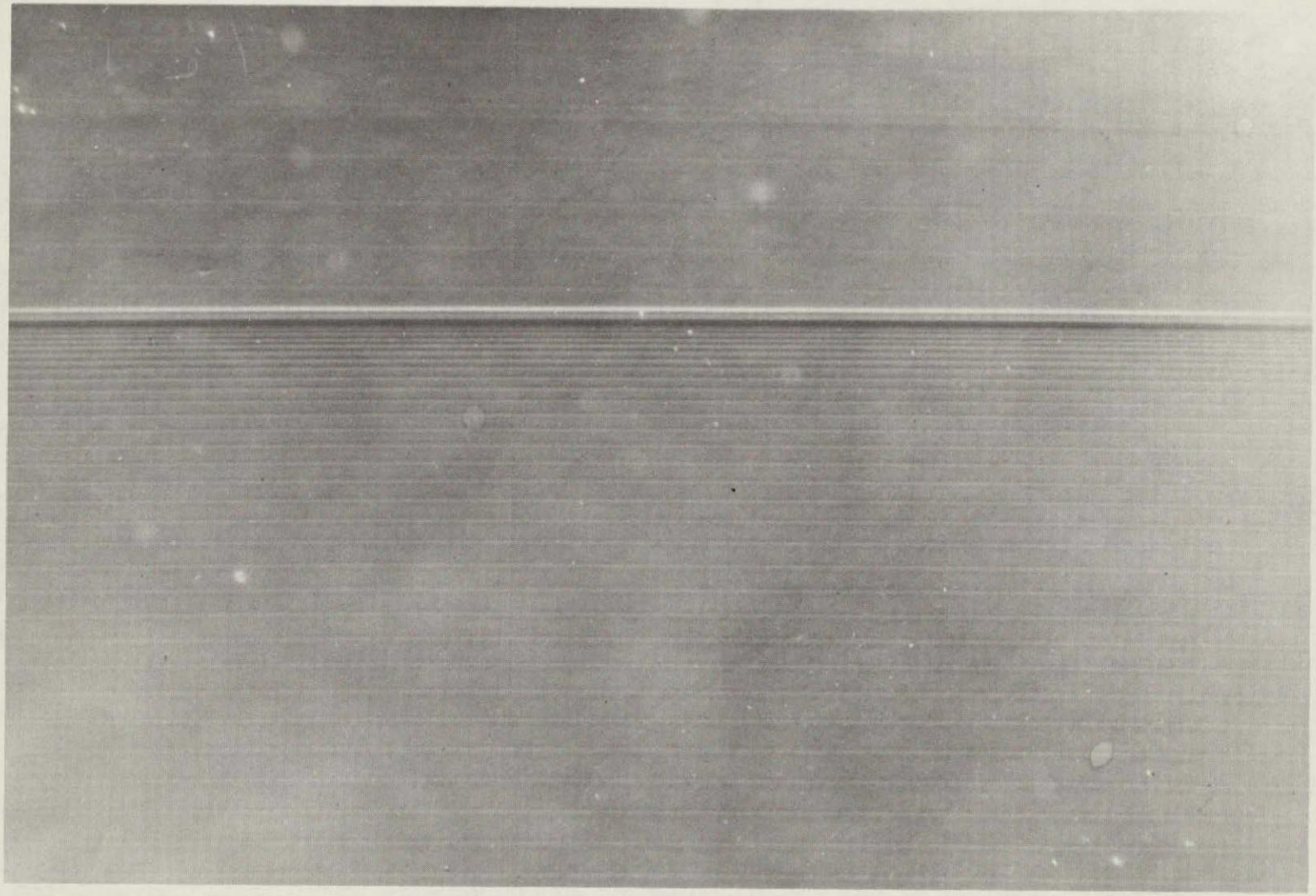

Figure V-23. Etched segment of <111> germanium crystal regrown during ground-based tests (the region depicted shows, through interface demarcation, the microscopic growth behavior associated with a thermal arrest of 1 h).

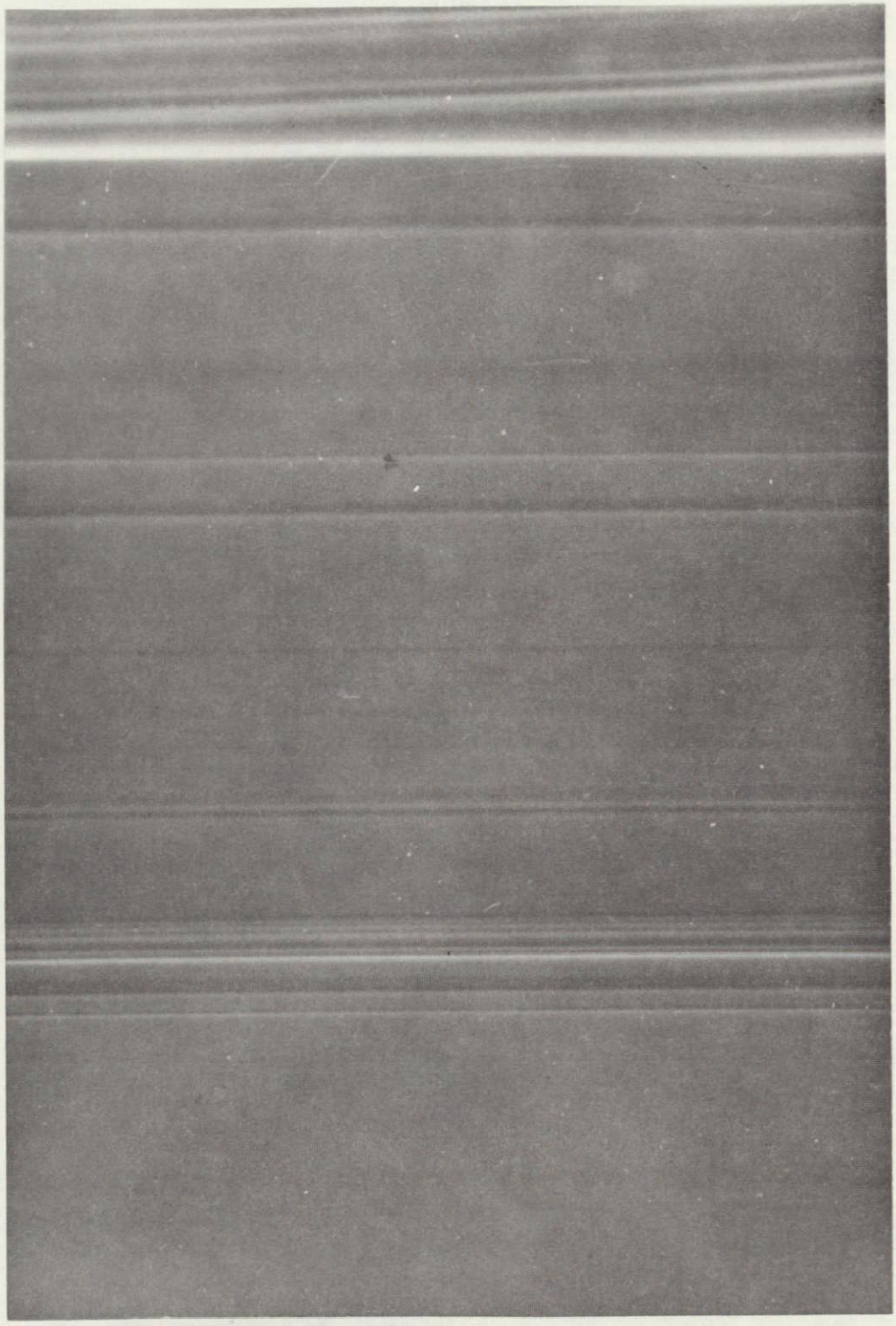

Figure V-24. Etched segment of a <100> germanium crystal regrown during ground-based tests at MSFC (notice the broad band of uncontrolled growth and segregation, 1000 μm, covering virtually all of the depicted region; this experiment was performed in the multipurpose furnace operated with line voltage) (110X).

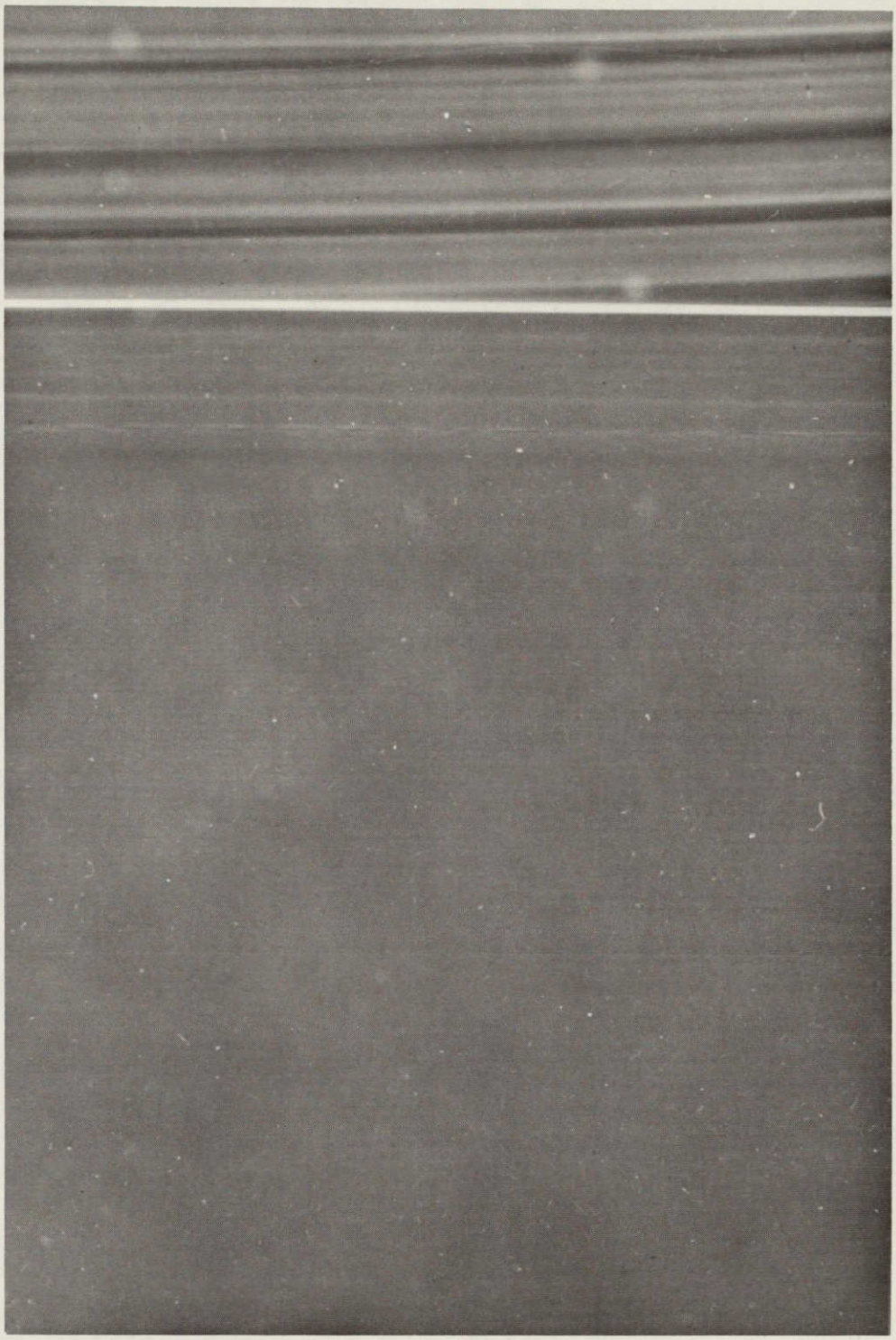

Figure V-25. Etched segment of a <100> germanium crystal regrown during ground-based tests at MSFC in the multipurpose furnace operated with battery power (notice that the band of uncontrolled growth and segregation immediately below the original regrowth interface has a width of 140 μm; compare with Figure V-24) (135X).

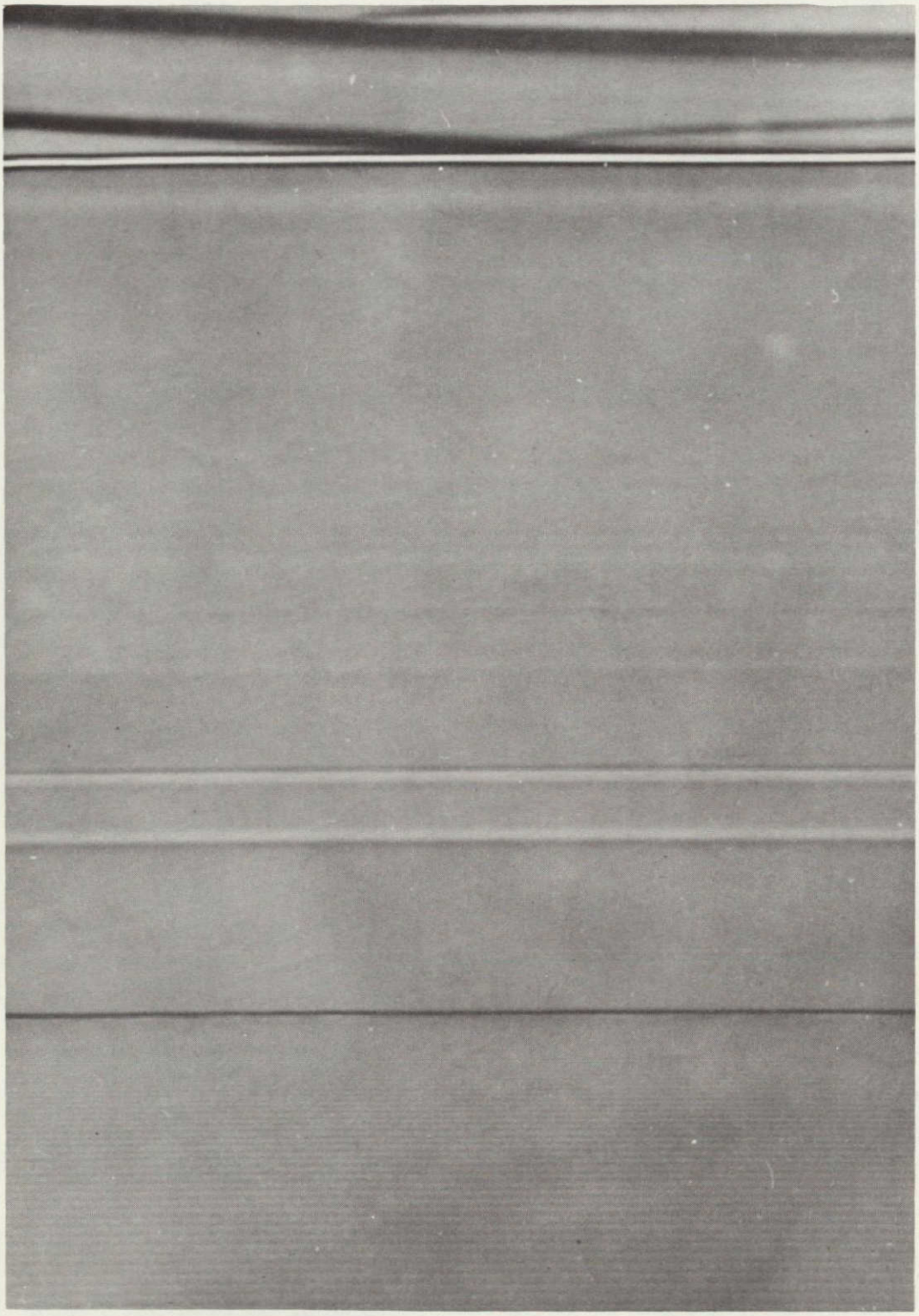

Figure V-26. Etched segment of a <111> germanium crystal regrown during the final ground-based test (GBT 3) (compare with Figure V-27) (210X).

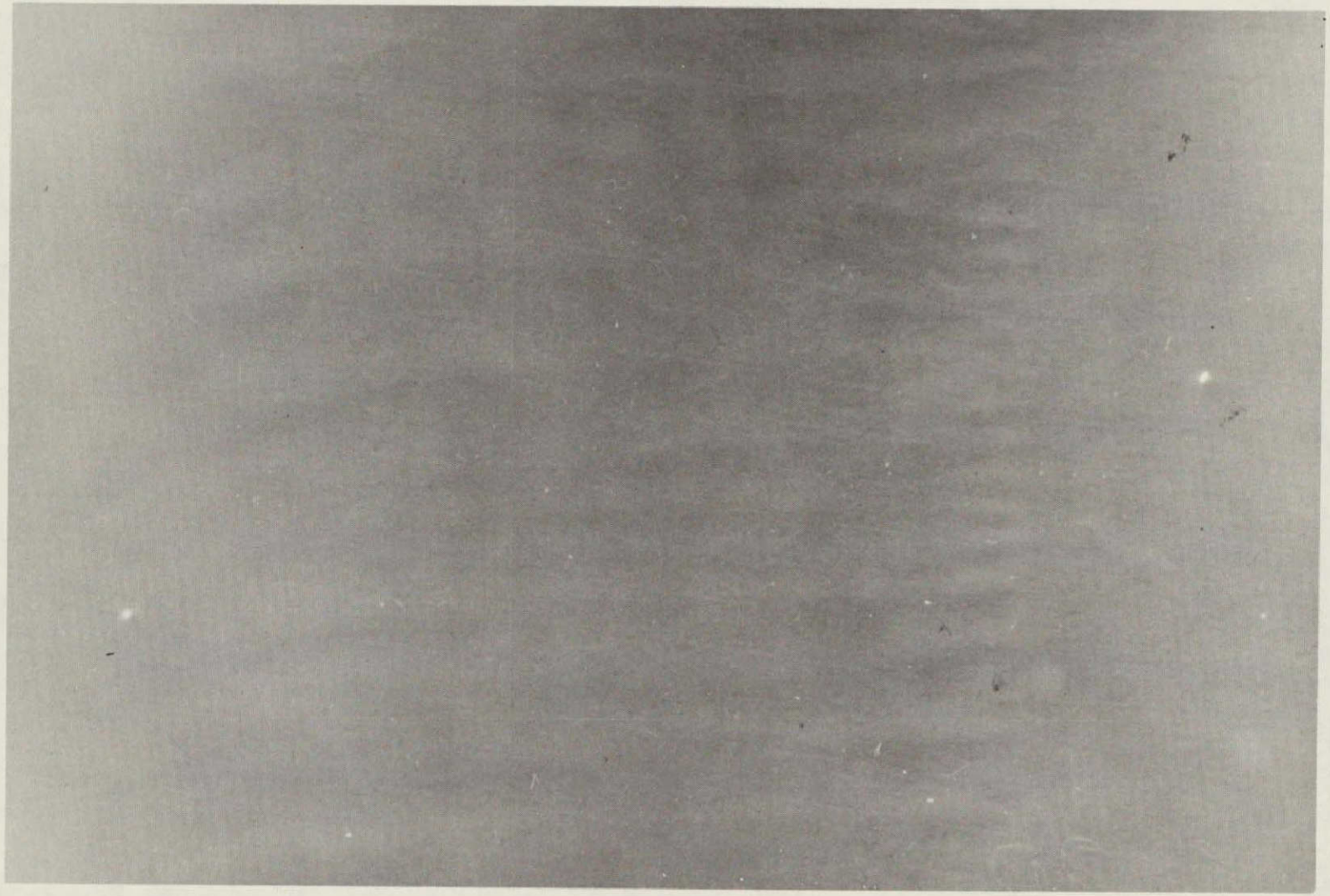

Figure V-27. Segregation inhomogeneities in <111> germanium crystal regrown during the final ground-based test (GBT 3) (the irregular dopant distribution appears after regrowth of approximately 1.0 cm; its origin is as yet unexplained).

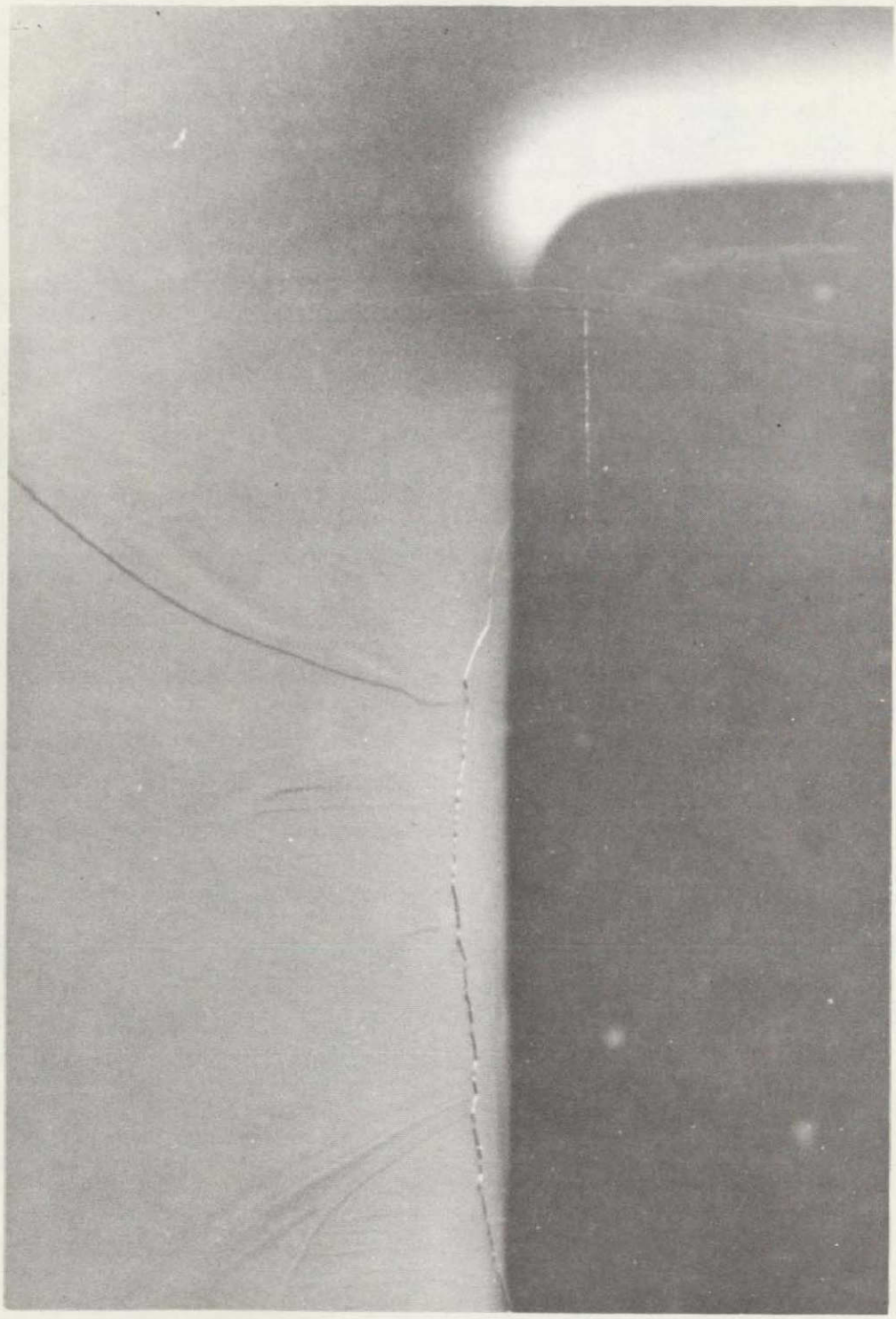

Figure V-28. Peripheral segregation inhomogeneity in the cup region of the <111> germanium crystal regrown during the final ground-based test (GBT 3) (observe the appearance of a grain boundary; compare with Figure V-30).

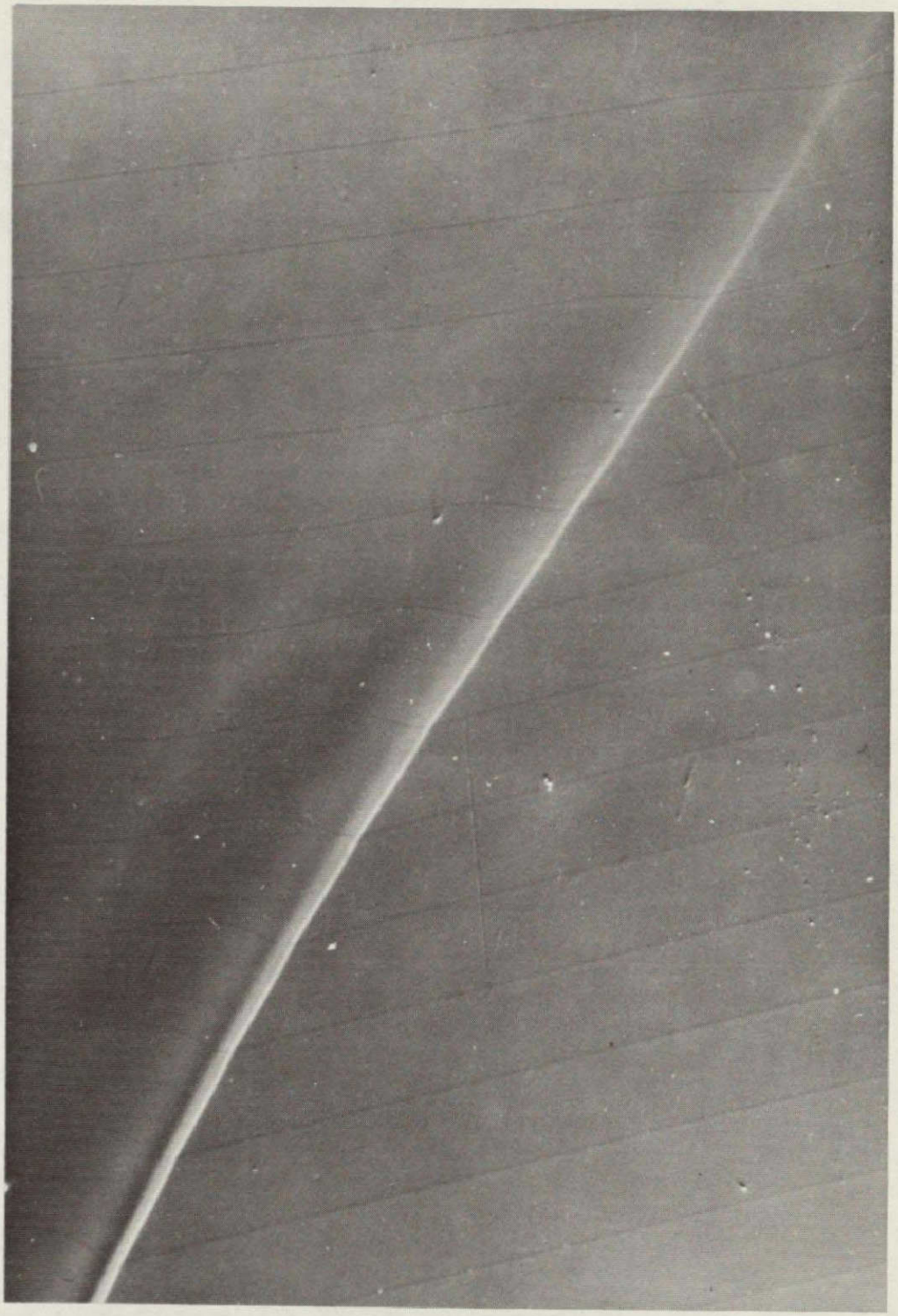

Figure V-29. Interface instability appearing in the central portion of the <111> germanium crystal regrown during the final ground-based test (GBT 3) (observe the development of severe growth interface distortion).

Figure V-30. Further development of interface instability and breakdown shown in Figure V-29.

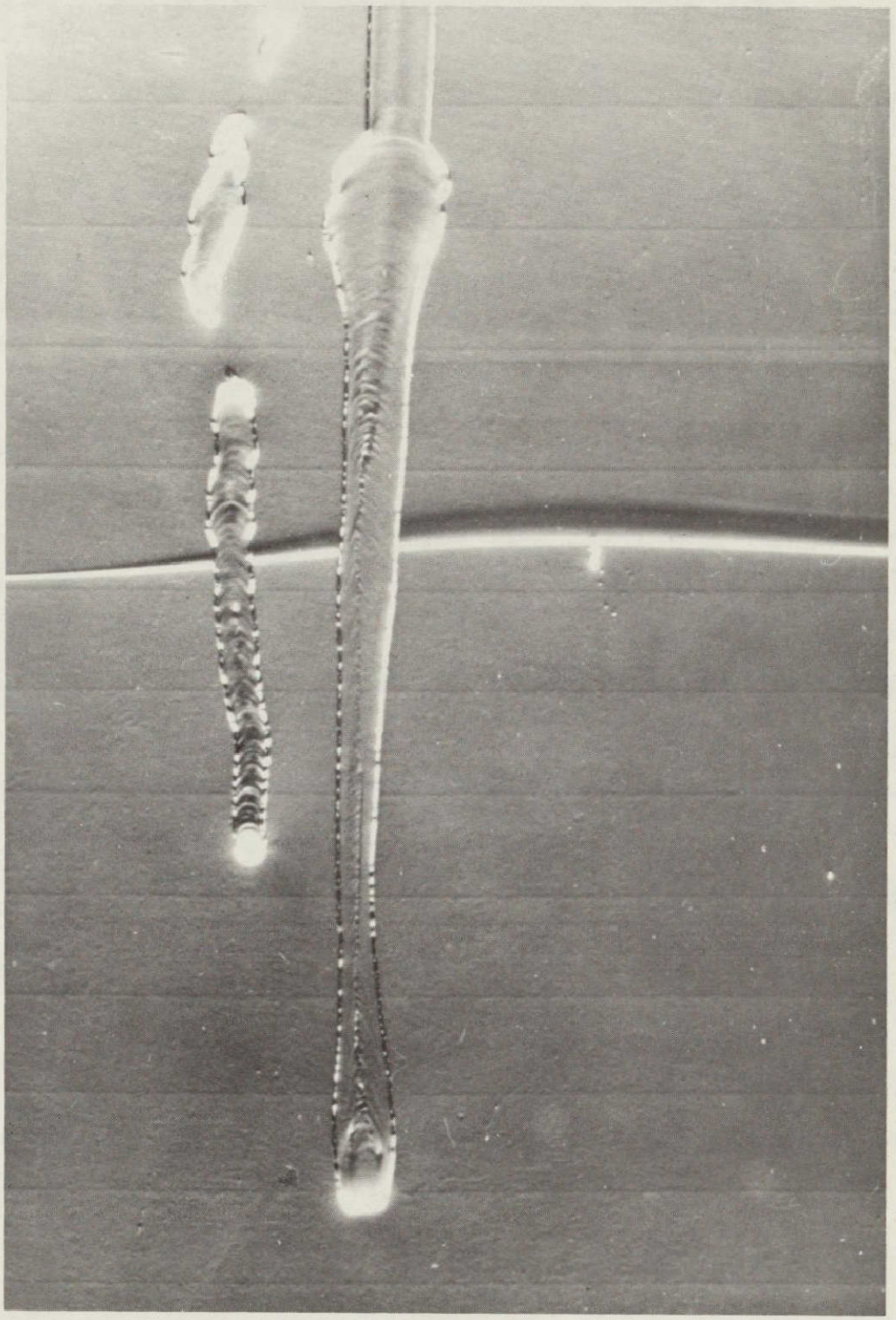

Figure V-31. Pronounced segregation inhomogeneity and phase segregation associated with the last stages of breakdown as depicted in Figures V-29 and V-30.

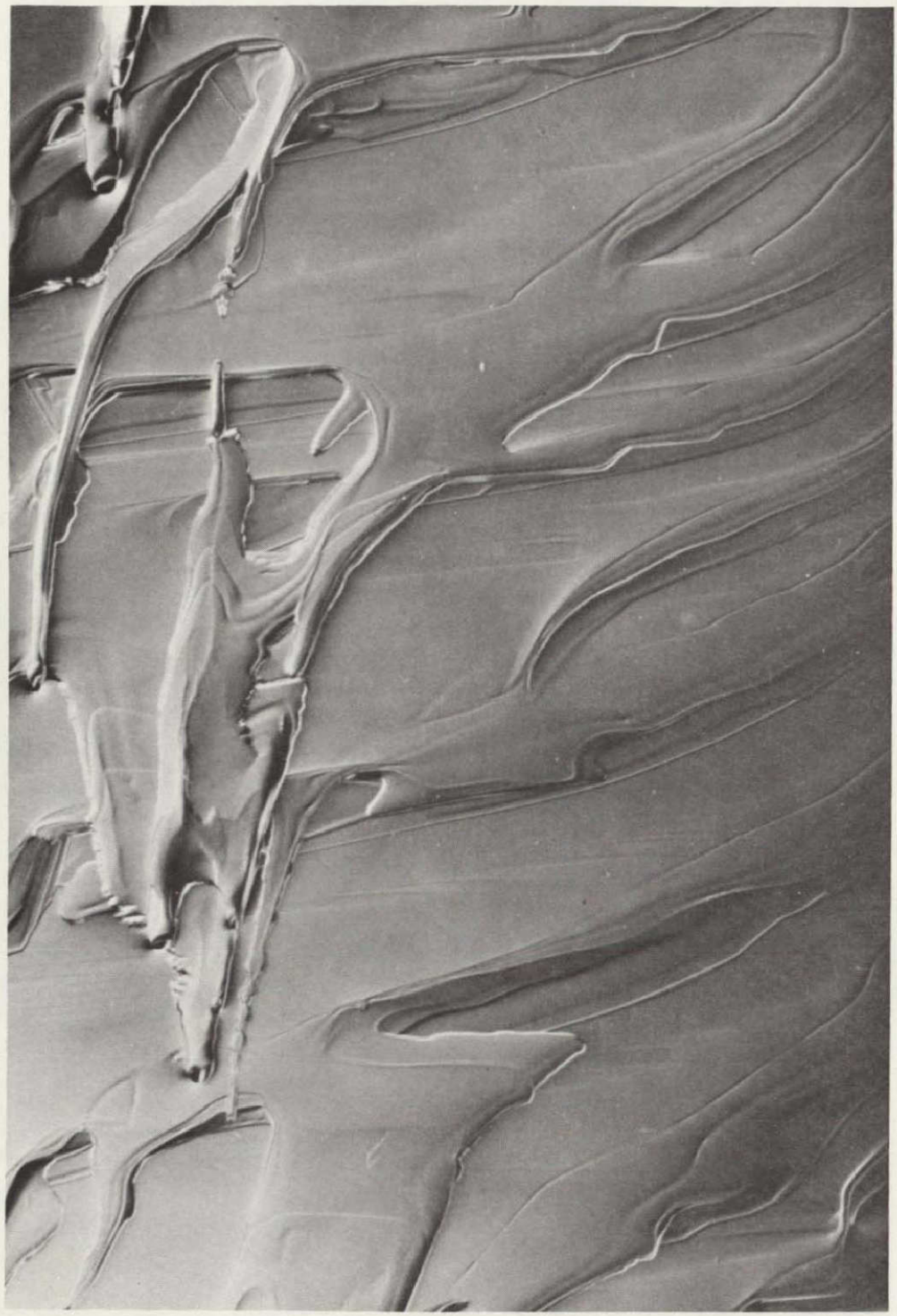

Figure V-32. Advanced stages of interface breakdown observed in the <111> germanium crystal regrown during the final ground-based test (GBT 3).

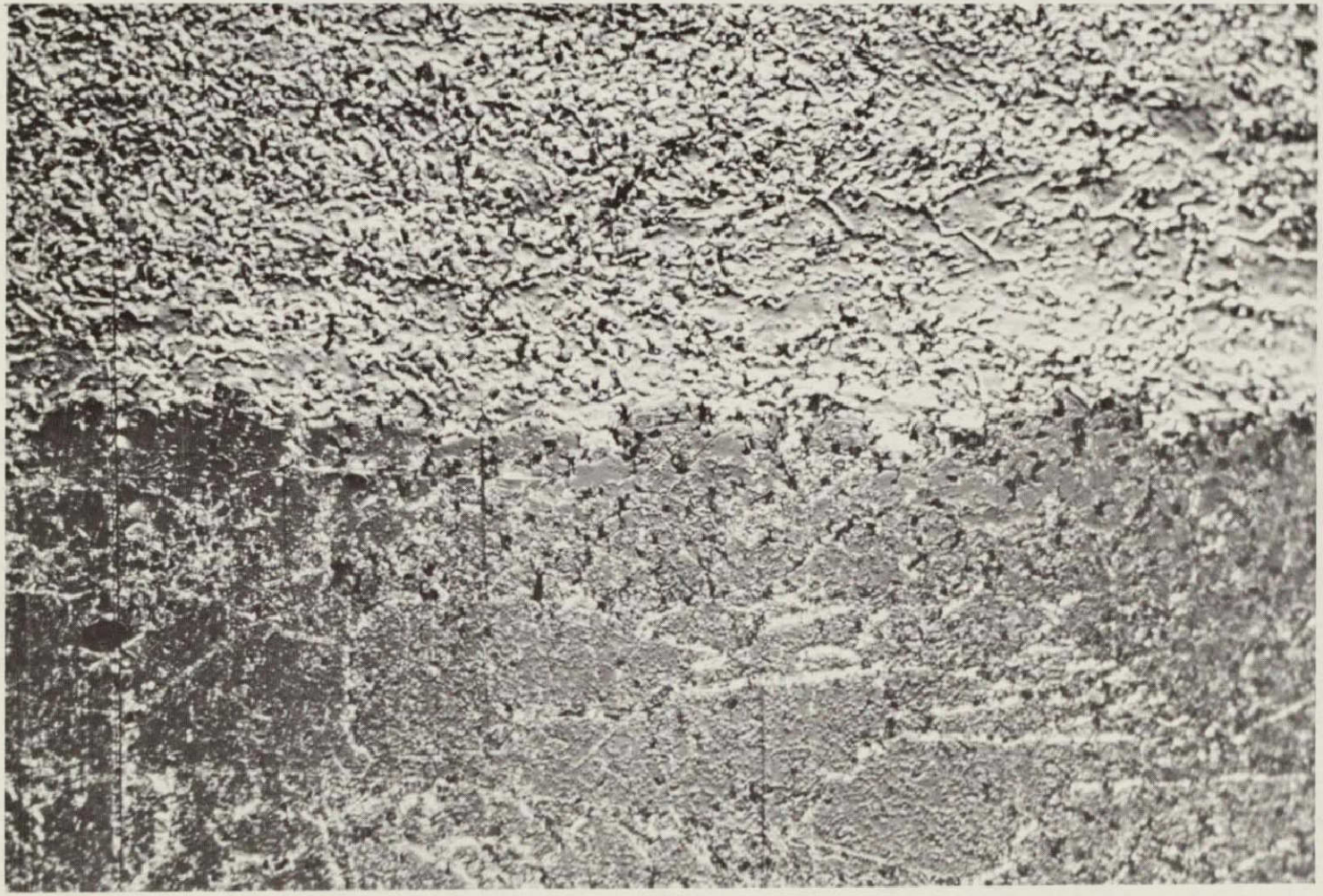

Figure V-33. Abrupt change in surface morphology observed in the <100> germanium crystal regrown during the final ground-based test (GBT 3).

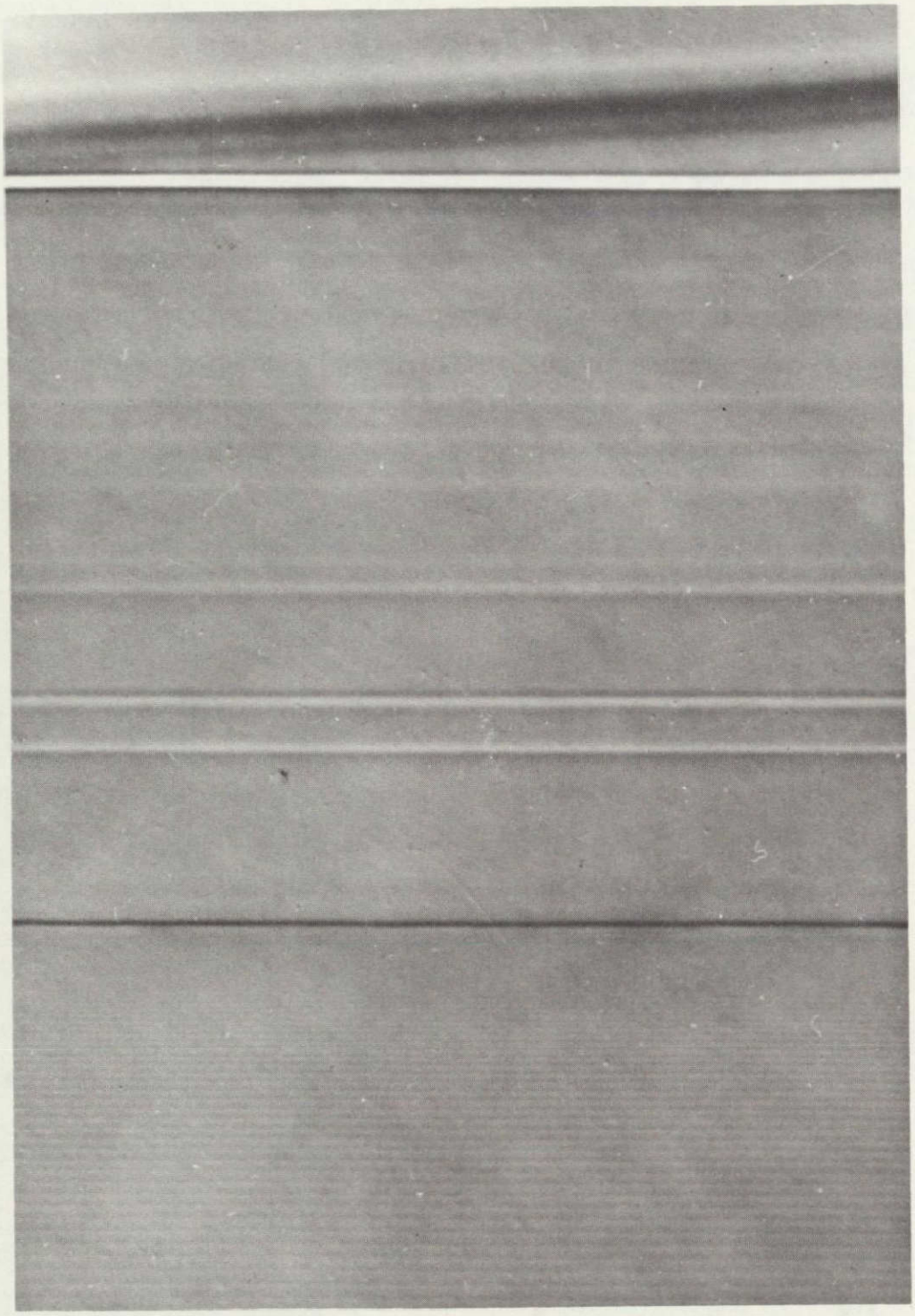

Figure V-34. Etched segment of <100> germanium crystal regrown during the final ground-based test (280X).

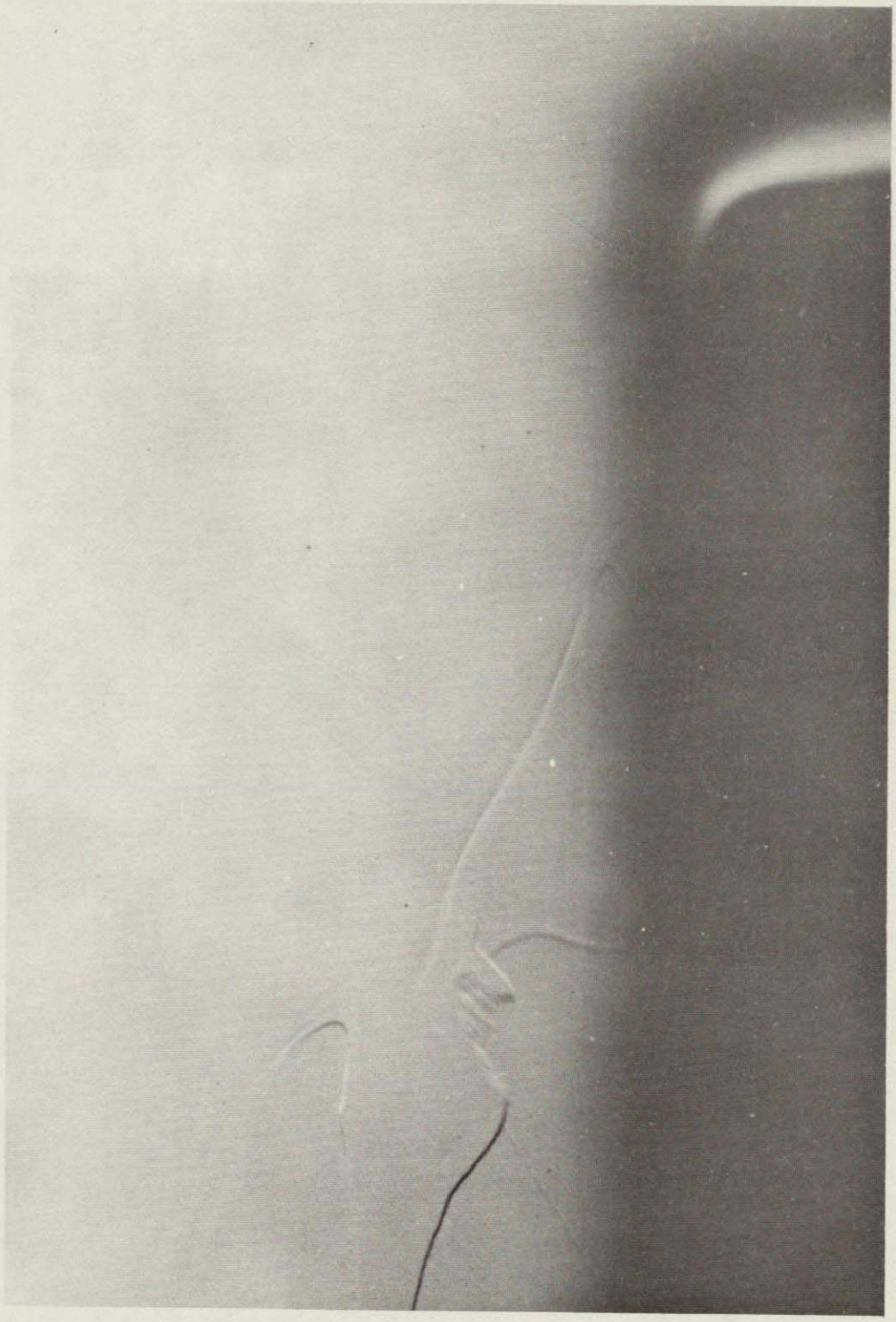

Figure V-35. Segregation inhomogeneities and interface breakdown in the <100> germanium crystal regrown during the final ground-based test (GBT 3).

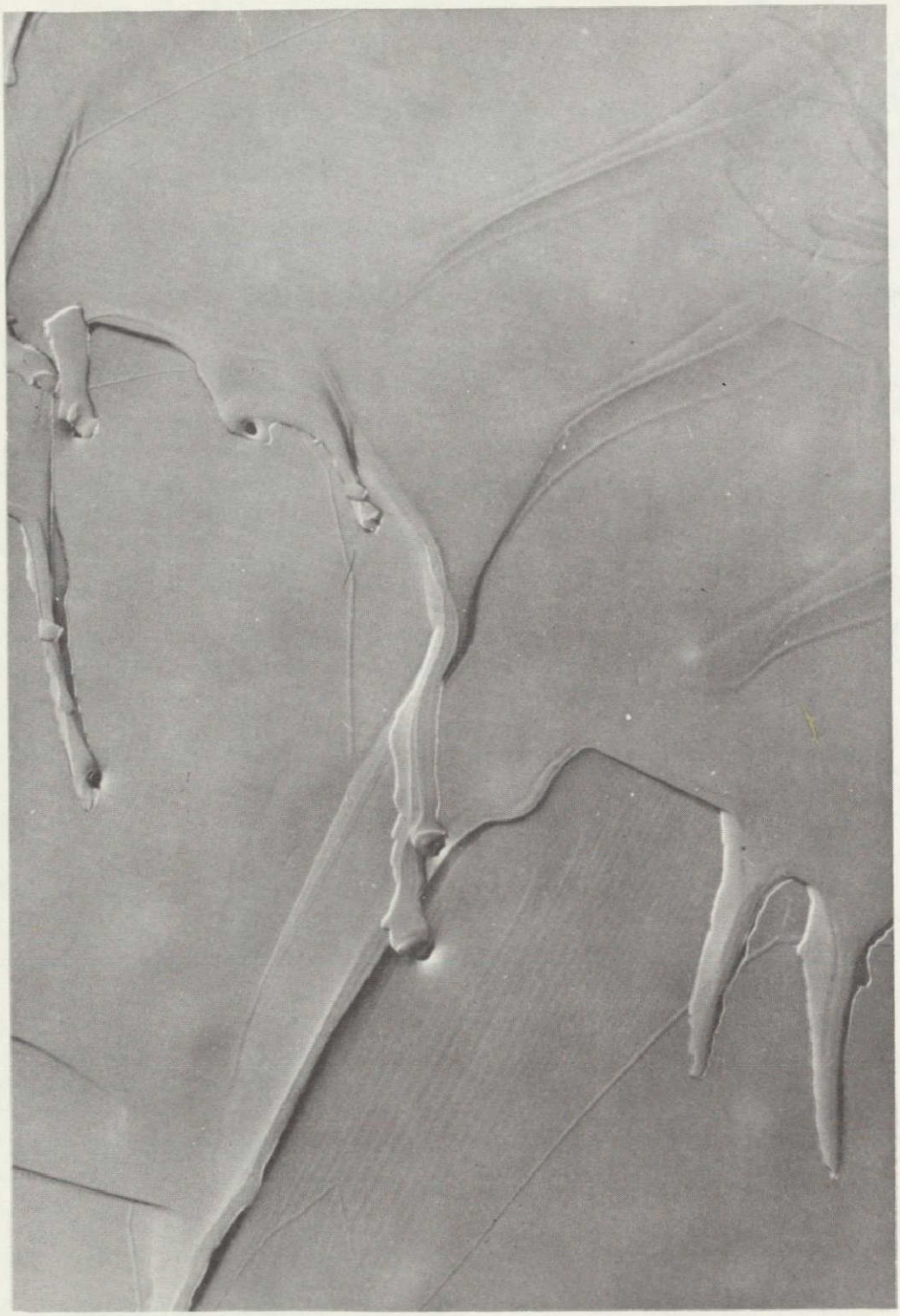

Figure V-36. Advanced stage of interface breakdown in the <100> germanium crystal regrown during the final ground-based test (GBT 3).

EXPERIMENT	CRYSTAL	DOPANT	ORIENTATION	I/F BAND WIDTH μM	REGROWN LENGTH CM	SEED POLARITY	PULSE WIDTH MSEC	PULSE REP. RATE SEC	SOAK TIME HRS	COOLING RATE °C/MIN	I/F DEMARCATION VISIBILITY
SIM 1	S-1	GA	111	200	2.3	NEG	30	2	2	PASSIVE	FAINT
SIM 2	S-2	SN	111	NONE VISIBLE	2.1	NEG	60	4	2	.6	NOT DETECTED
PROTOTYPE	P-1	GA	100	0	3.8	NEG	60	4	2	.6	FAINT
	P-2	SB	100		4.0	NEG	60	4	2	.6	NOT DETECTED
	P-3	SN	100		3.9	NEG	60	4	2	.6	NOT DETECYED
GBT 1	A-5	GA	100	998	4.1	NEG	60	4	5	1.2, 40 MIN 2.4, 20 MIN 1.2, END	GOOD
	B-6	RE-RUN IN GBT 3									
	C-1	RE-RUN IN GBT 2									
GBT 2	A-1	GA	100	140	3.7	POS, 30 MIN NEG, END	60	4	2		GOOD
	B-1	SB	100	OVER TEMP. TEST, USED AS FILLER						2.4, 30 MIN THERMAL ARREST 2.4, END	
	C-1	GA	111	2150	3.7	POS, 30 MIN NEG, END	60	4	2		GOOD
GBT 3	A-6	GA	100	336	4.1	POS	55	3.95	2	2.4	GOOD
	B-6	SB	100		3.6	POS	55	3.95	2	2.4	NOT DETECTED
	C-6	GA	111	511	4.0	POS	55	3.95	2	2.4	GOOD

Figure V-37. Tabulation of MA-060 ground-based tests.

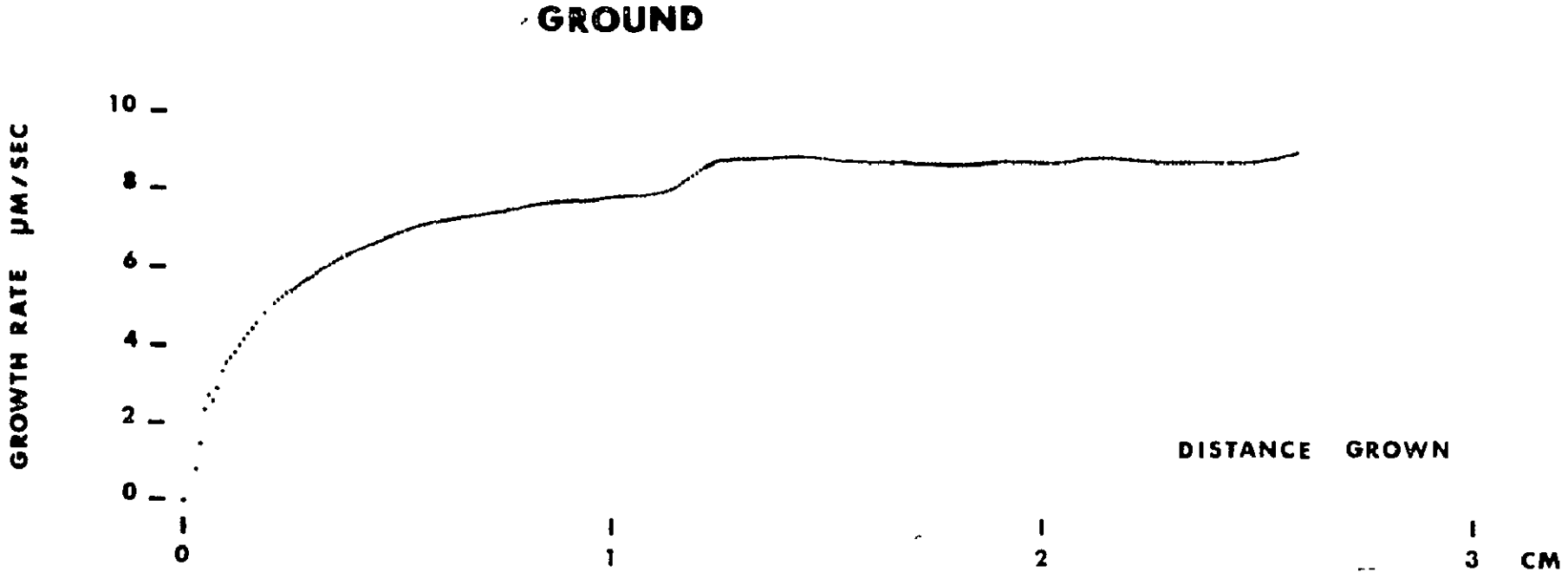

Figure V-38. Microscopic growth rates of the <111> germanium crystal regrown during the final ground-based test (GBT 3).

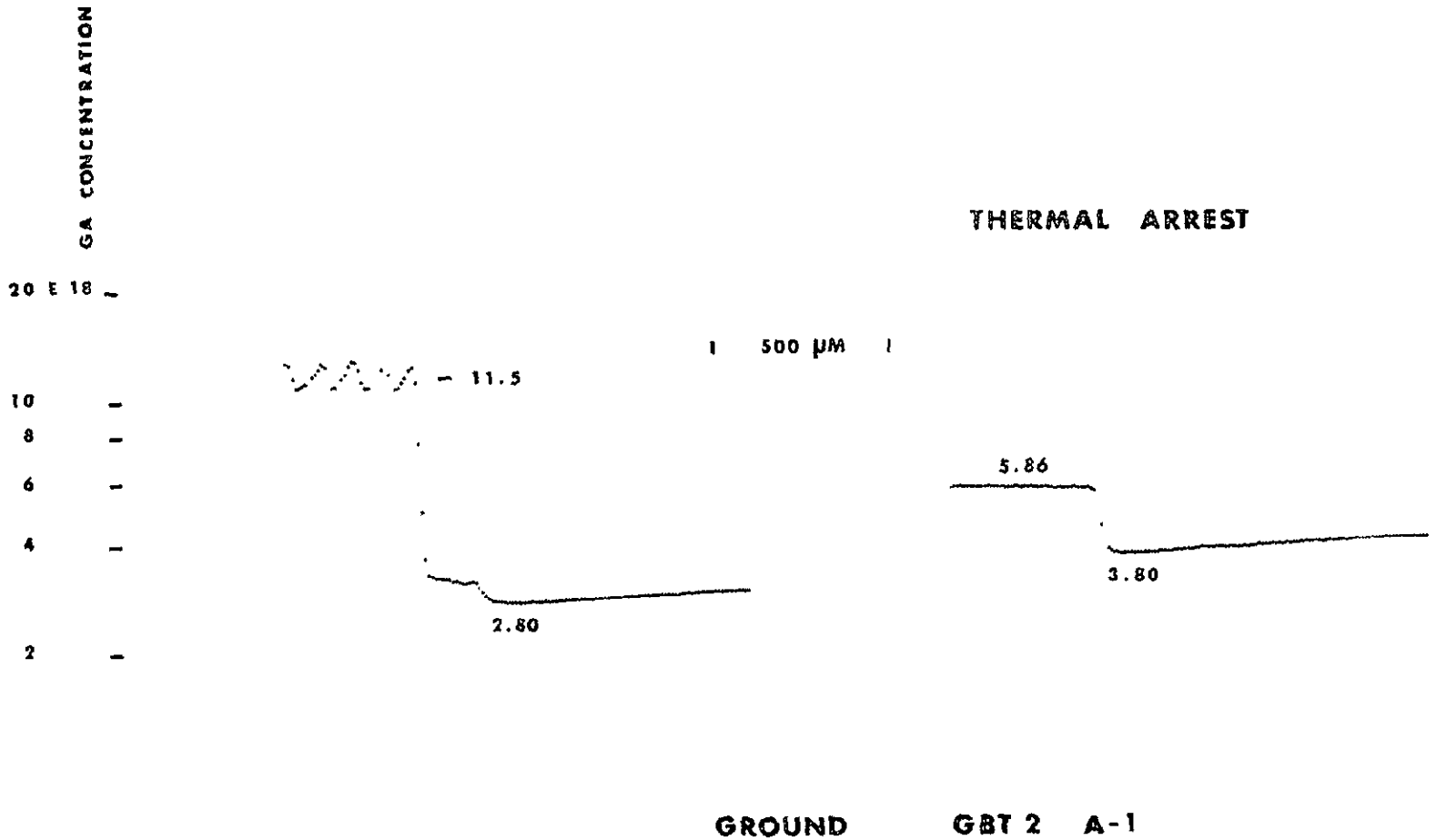

Figure V-39. Compositional profiles of the initial regrowth region and a thermal arrest in a <100> germanium crystal regrown during the second ground-based test (GBT 2).

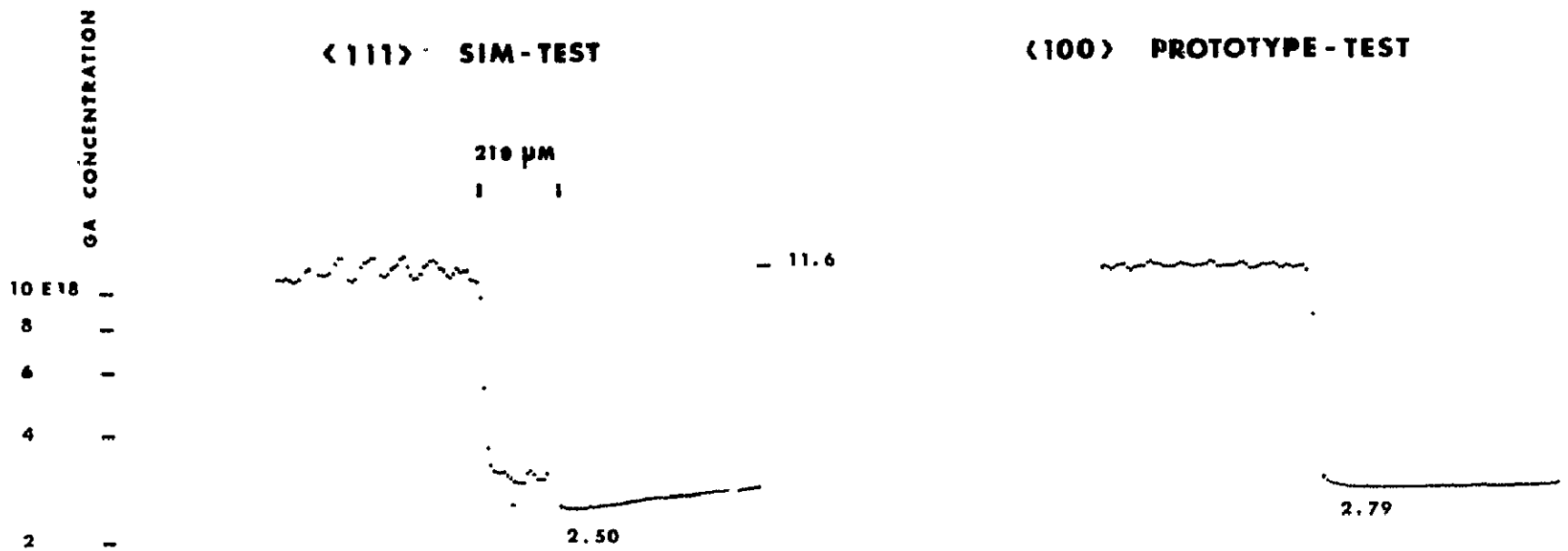

Figure V-40. Compositional profiles of the initial regrowth regions of germanium crystals regrown during simulation and prototype tests.

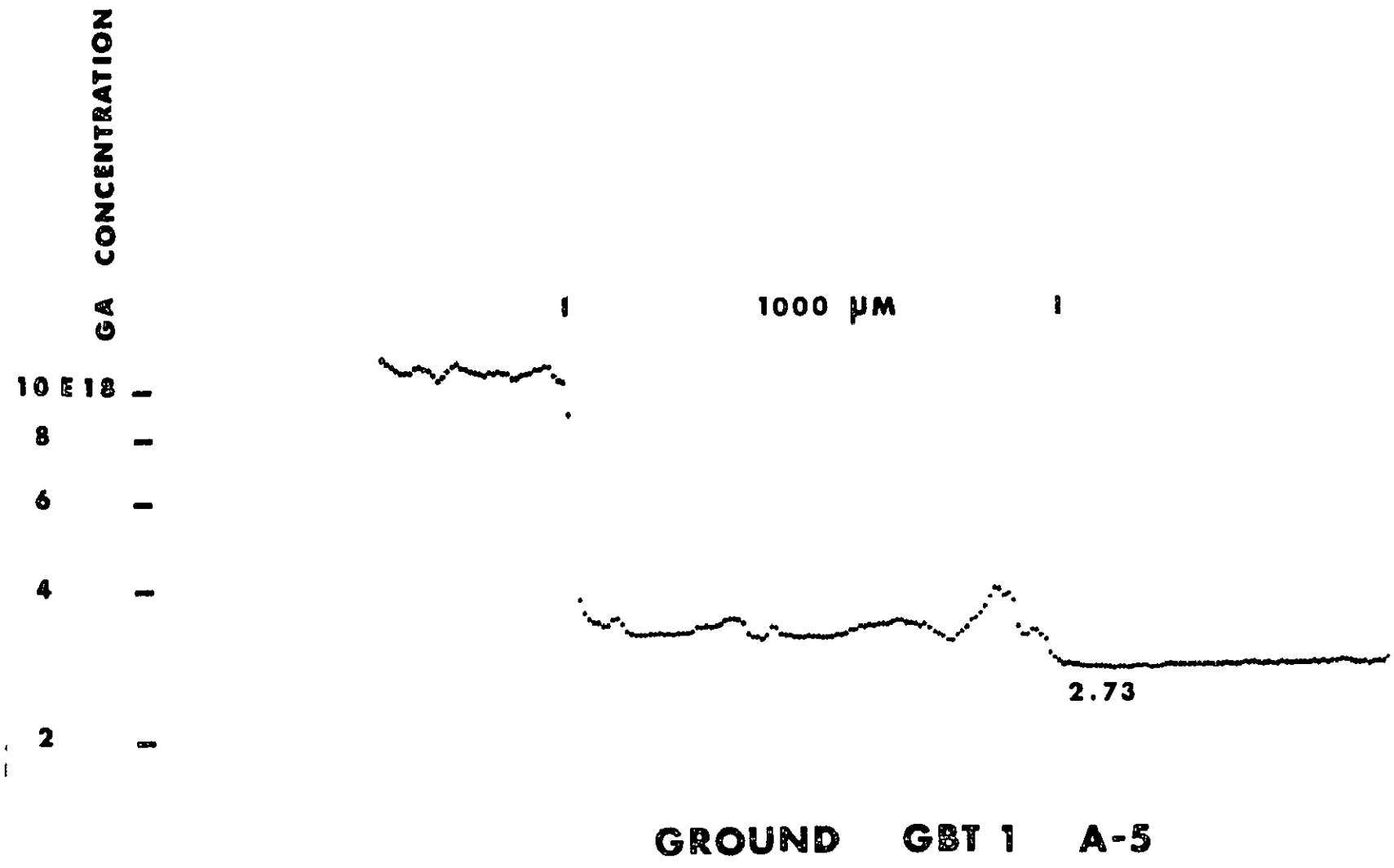

Figure V-41. Compositional profile of initial regrowth region in a <100> germanium crystal regrown during the first ground-based test (GBT 1) (notice the pronounced compositional fluctuations associated with uncontrolled growth, 1000 μm).

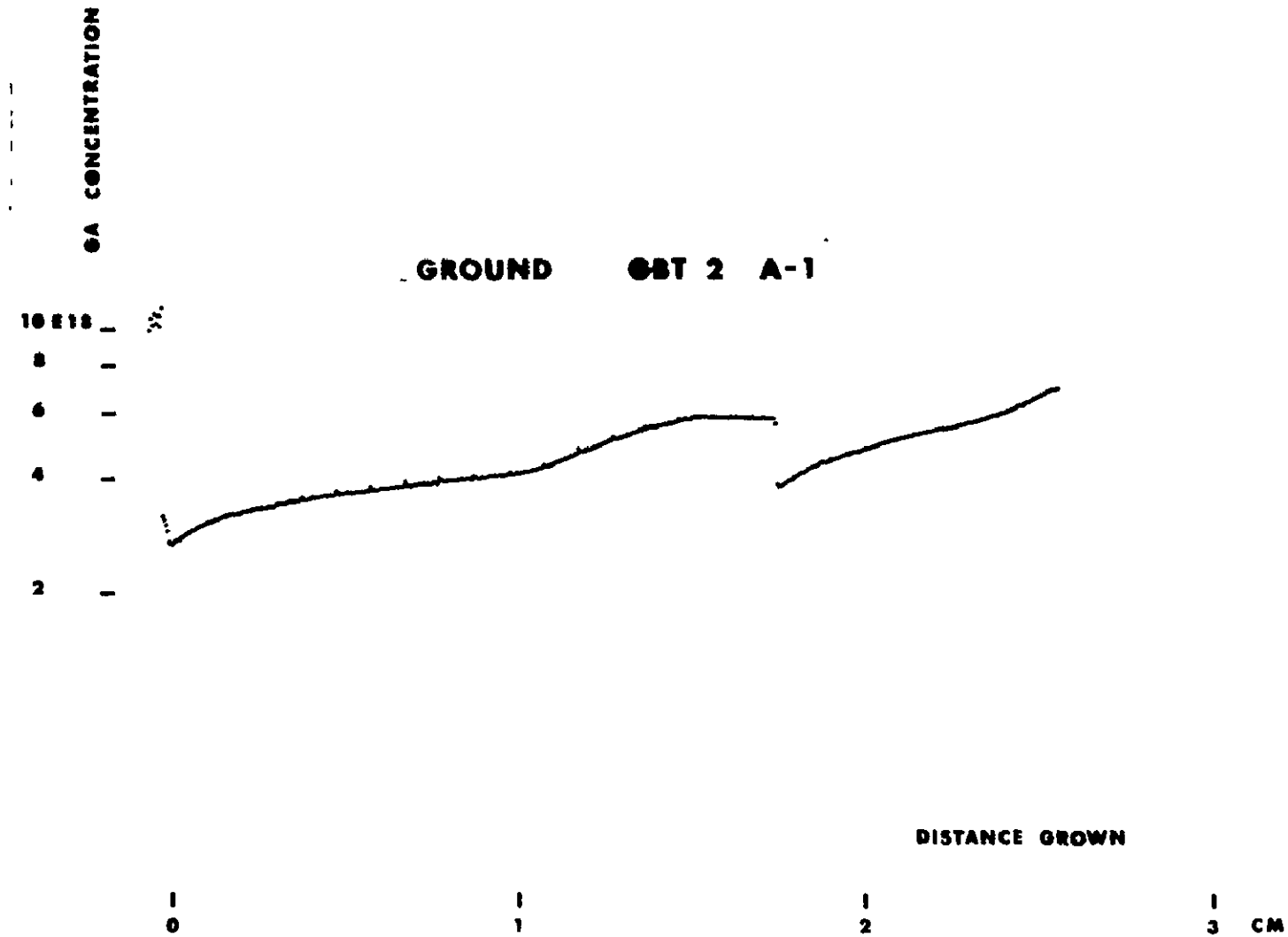

Figure V-42. Compositional profile in a <100> germanium crystal regrown with a thermal arrest of 1 h.

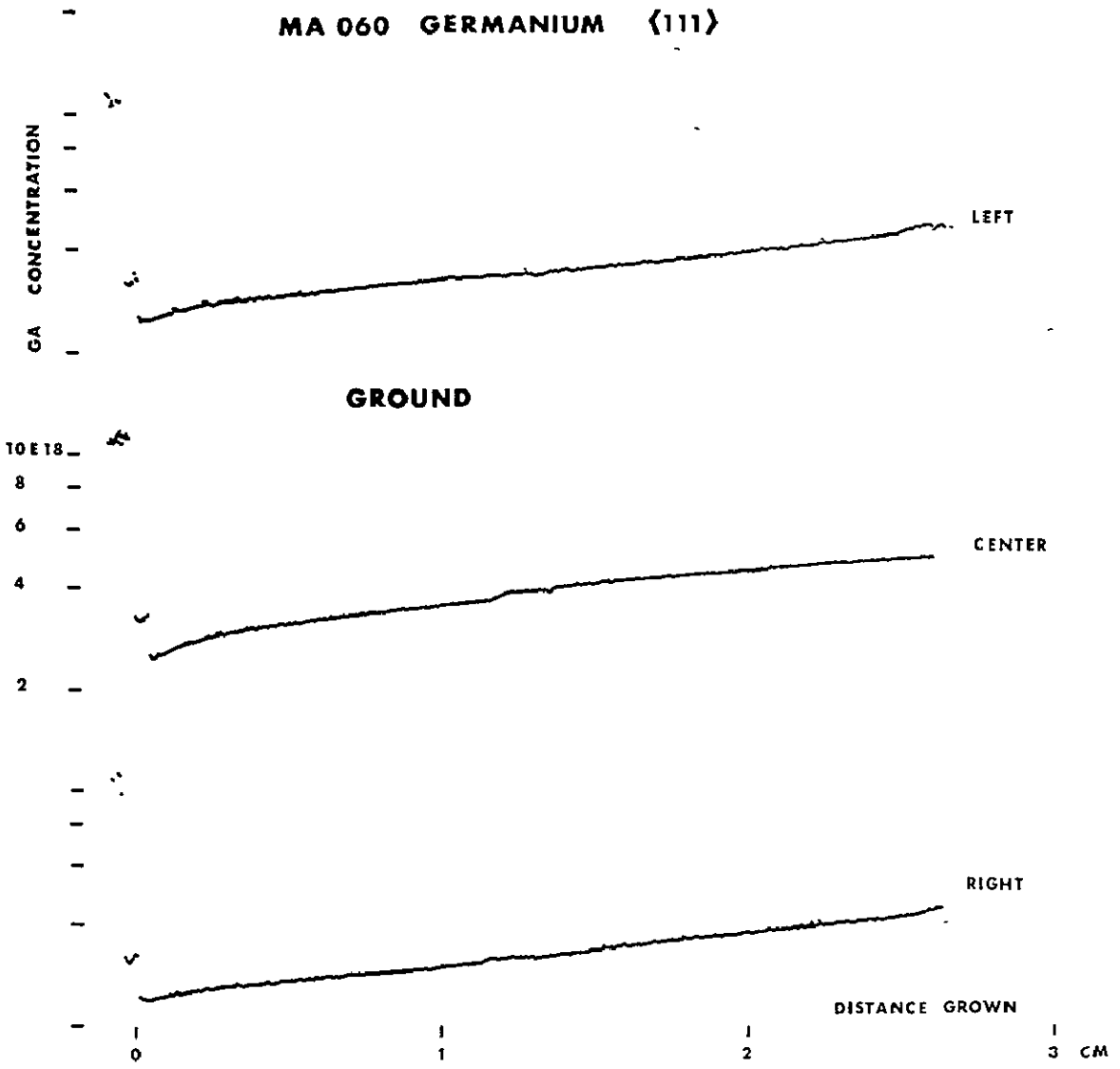

Figure V-43. Macroscopic compositional profiles of the <111> germanium crystal regrown during ground-based test (GBT 3).

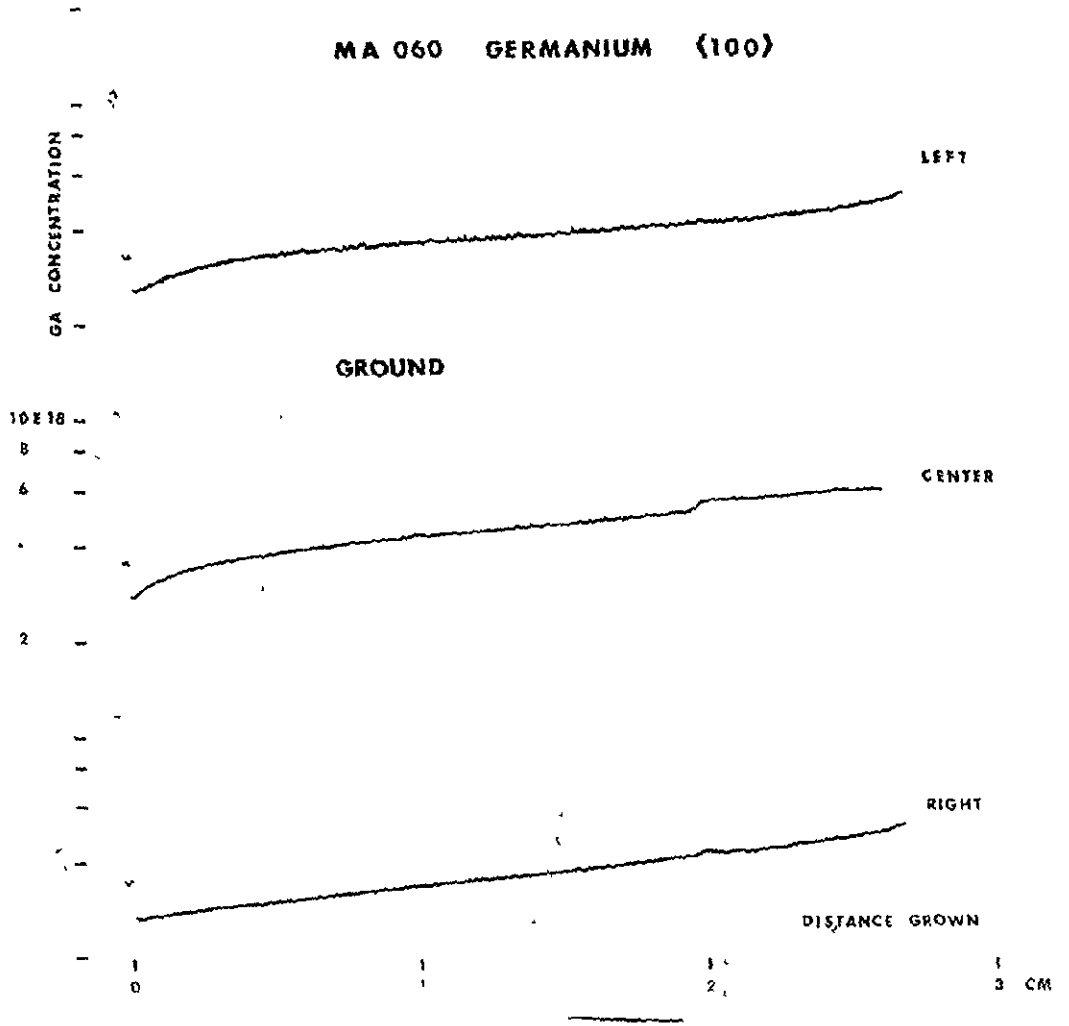

Figure V-44. Macroscopic compositional profiles of the <100> germanium crystal regrown during ground-based test (GBT 3).

ACKNOWLEDGMENTS

The authors are grateful to the National Aeronautics and Space Administration, particularly to the staff at Marshall Space Flight Center for their cooperation and enthusiastic support during all stages of the experiment. They are indebted to Mr. J. Baker for his skillful assistance with the characterization program and to Ms. M. Cretella and Messrs. D. Holmes and E. Martin for their valuable contributions to this work.

REFERENCES

V-1. Skylab Science Experiments. Vol. 38, Science and Technology, American Astronautical Society, 1975.

V-2. Witt, A. F.; Lichtensteiger, J.; and Gatos, H. C.: Experimental Approach to the Quantitative Determination of Dopant Segregation During Crystal Growth on a Microscale: Ga Doped Ge. J. Electrochem. Soc., vol. 120, 1973, pg. 1119.

V-3. Mazur, R. G. and Dickey, D. H.: J. Electrochem. Soc., vol. 113, 1966, p. 255.

V-4. Sze, S. M. and Irvin, J. C.: Solid State Electronics, vol. 11, 1968, p. 599.

V-5. Witt, A. F.; Lichtensteiger, M.; and Gatos, H. C.: J. Electrochem. Soc., vol. 120, 1973, p. 1119.

V-6. Van der Pauw, L. J.: Philips Res. Rep., vol. 13, 1958, p. 1.

BIBLIOGRAPHY

Brice, J. C.: The Growth of Crystals from Liquids. North-Holland Publishing Co., 1973.

Chalmers, B.: The Principles of Solidification. J. Wiley, 1964.

Gilman, J. J., Ed.: The Art and Science of Growing Crystals. J. Wiley, 1963.

Witt, A. F.; Gatos, H. C.; Lichtensteiger, M.; Cretella, M.; and Herman, C. J.: Crystal Growth and Steady-State Segregation under Zero Gravity: InSb. J. Electrochem. Soc., vol. 122, 1975, p. 276.

SECTION VI

ZERO-G PROCESSING OF MAGNETS

EXPERIMENT MA-070

By D. J. Larson, Jr.[1]

1. Principal Investigator, Grumman Aerospace Corporation, Bethpage, New York.

TABLE OF CONTENTS

LIST OF ILLUSTRATIONS

LIST OF ILLUSTRATIONS (Continued)

LIST OF ILLUSTRATIONS (Concluded)

ABSTRACT

The zero-g processing of magnets experiment (MA-070) was conducted during the Apollo-Soyuz Test Project to study contained solidification of high coercive strength magnetic materials in the low-g orbital environment. The magnetic compounds under study, manganese-bismuth (MnBi) copper-cobalt-cerium [$(Cu,Co)_5Ce$], are representative of magnetic alloy systems that have the potential for the development of high coercive strength and a high energy product.

The samples of 50 at.% bismuth and 50 at.% manganese solidified in the low-g environment demonstrated a substantial improvement in the macroscopic chemical homogeneity. The bismuth/manganese-bismuth directionally solidified eutectic flight samples exhibited markedly superior magnetic properties. Intrinsic coercive strengths in excess of 185 Koe have been measured in the low-g processed samples at 77 K. This exceeds the maximum previously published value (113 Koe) by 64 percent. The average value of inductance was improved by 76 percent, and the energy product was improved by 57 percent.

Additional results of this experiment indicate that, in the near-absence of the gravitational body force, contained fluids will assume a lowest energy configuration that differs significantly from that found terrestrially. These results are of significance to any orbital processing that involves controlled heat transfer to, or from, a contained fluid.

INTRODUCTION

Permanent magnets have an important but often overlooked role in present technology. In fact, since the magnets are usually located inside equipment, most people either are not aware of their presence or take them for granted. However, these permanent magnets are the key components in many devices that are important to our everyday life, such as telephone receivers, computers, radar, loud speakers, electrical meters, microphones, tape recorders, hearing aids, electric clocks, scientific instruments, magnetic door catches, and even childrens' toys [VI-1—VI-5].

In recent years, significant improvements in magnetic properties have developed through the discovery of the exceptionally high anisotropy constants in compounds of cobalt-platinum (CoPt) and manganese-bismuth (MnBi) and in the cobalt-rare Earth, CoR.E., (and yttrium) systems [VI-6—VI-8]. The magnitude of these improvements can be seen from Table VI-1, which compares the properties of some commercial magnets to experimentally determined values of high anisotropy magnets [VI-9].

TABLE VI-1. COMPARISON OF PROPERTIES OF COMMERCIAL MAGNETS AND EXPERIMENTALLY DETERMINED VALUES OF HIGH ANISOTROPY MAGNETS

Material	Energy Product $(BH)_{max}$, MGOe	Coercive Strength (H_c), KOe	Curie Temperature °C
Alnico	10	2	700 to 800
Barium Ferrite	4	3	723
CoPt	9	5	510
MnBi (Directionally Solidified)	7.3 (powders)	30	350
CoR (Co_5R)[a]	24	10[b]	870

a. Typical values.

b. Values as high as 28 KOe were obtained in chill cast specimens of cobalt-copper-samarium (Co_3Cu_2Sm) [VI-10].

The superior magnetic properties of the high anisotropy compounds are related to their crystal structures, since the anisotropy energy is a result of the coupling between the spin of an electron and its orbital motion. The electron orbits are strongly directional and are associated with the lattice symmetry.

Most of the high anisotropy compounds have a complex hexagonal lattice symmetry. The C-axis is the unique direction of easy magnetization, and the directions within the basal planes are uniformly hard to magnetize [VI-9]. The excess energy required to turn the direction of magnetization from an easy direction to a hard direction is the anisotropy energy. The anisotropy constant K is a measure of this energy and is related to the theoretical upper limit of the coercive strength H_A by

$$H_A = \frac{2K}{M_s} \quad ,$$

where M_s is the saturation magnetization [VI-11]. Values of K range from 5 to 12×10^7 ergs/cm^3 for Co_5R.E. type compounds [VI-4, VI-9], resulting in values of H_A from 150 to 250 KOe.

Besides the high anisotropy constants and coercive strength, it is also required that the permanent magnets have a high intrinsic magnetization ($4\pi M_s$) and a high Curie temperature (T_c).

Because of the brittleness and reactivity of most of the intermetallic high coercivity magnetic compounds, powder metallurgy techniques principally have been used to fabricate the high coercive strength magnets. Casting and solidification techniques have been possible only in a limited number of systems.

Fabrication of high coercive strength magnet materials from the liquid state could lead to a marked reduction in the number of processing steps and, hence, in cost. The magnets would have theoretical density, and the fine particles would be protected from environmental attack, would have a high degree of particle alignment, and would only require a minimal amount of final machining. The requirement of particle refinement and crystallographic and magnetic alignment has led several workers to consider directional solidification as a means of achieving this morphology.

In space, gravity-driven convection and gravitationally dependent elemental segregation are absent in the liquid state. This has important consequences in the directional solidification of eutectic alloys. When grown on Earth, the rod or lamellar structure of the eutectic usually contains many imperfections (faults or terminations) because of local thermal and compositional gradients resulting from convection. It has been suggested that eutectic solidification in the absence of gravity will produce better alignment and fewer imperfections as a result of the reduction of these convection currents. Directional solidification in the orbital would then improve the magnetic coercivity and, perhaps, the energy product. The work reported upon here was undertaken to test the effect of the reduction of gravitationally dependent elemental segregation and convection on high coercive magnetic composites.

EXPERIMENTAL PROCEDURE

Three sets of three samples were simultaneously processed in the course of this experiment. Three furnace cartridges, each housing three samples, were utilized. The sample arrangement within each furnace and cartridge is shown in Figures VI-1 and VI-2. Ampoules 1 and 2 were made from

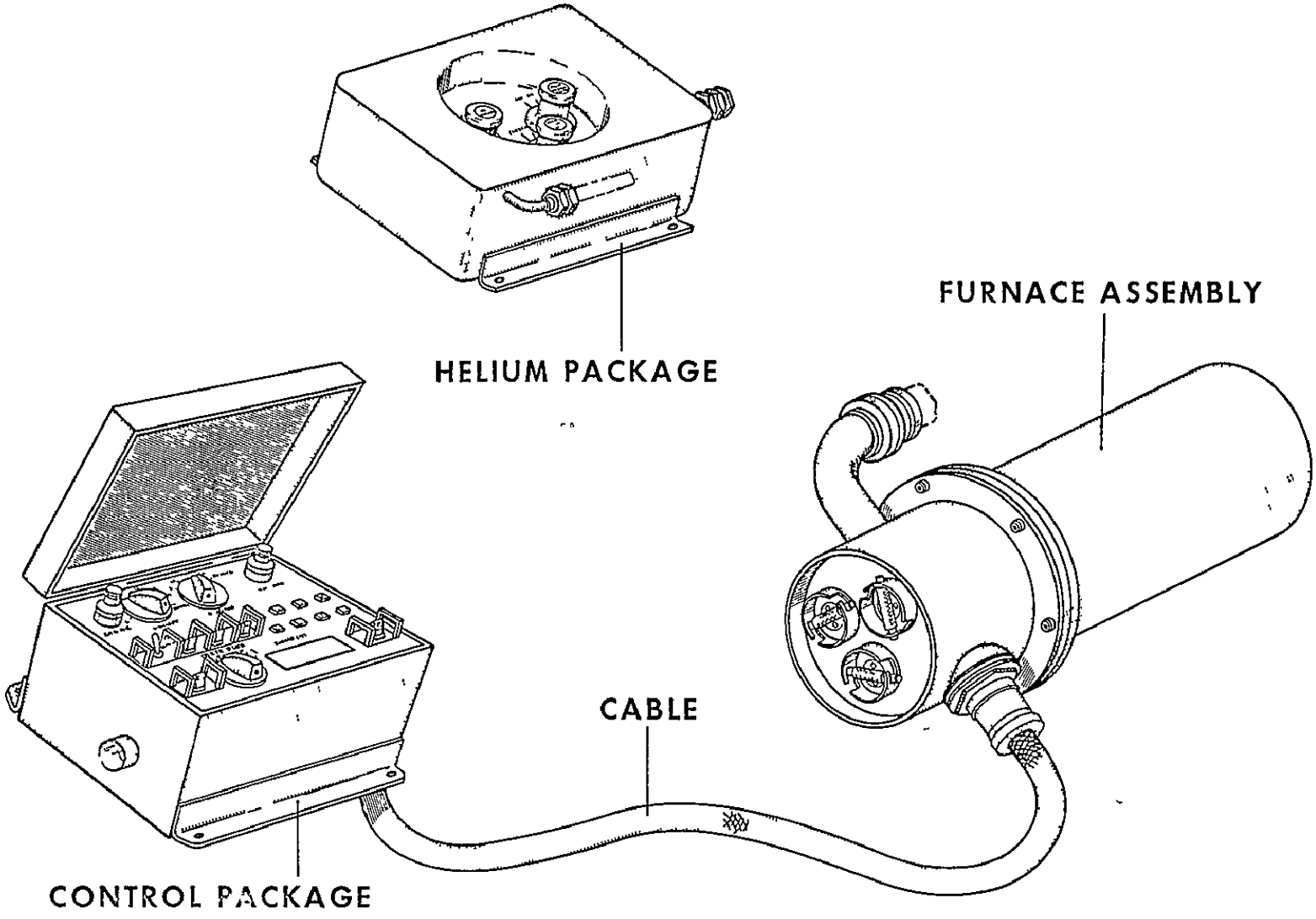

Figure VI-1. ASTP MA-010 multipurpose electric furnace system.

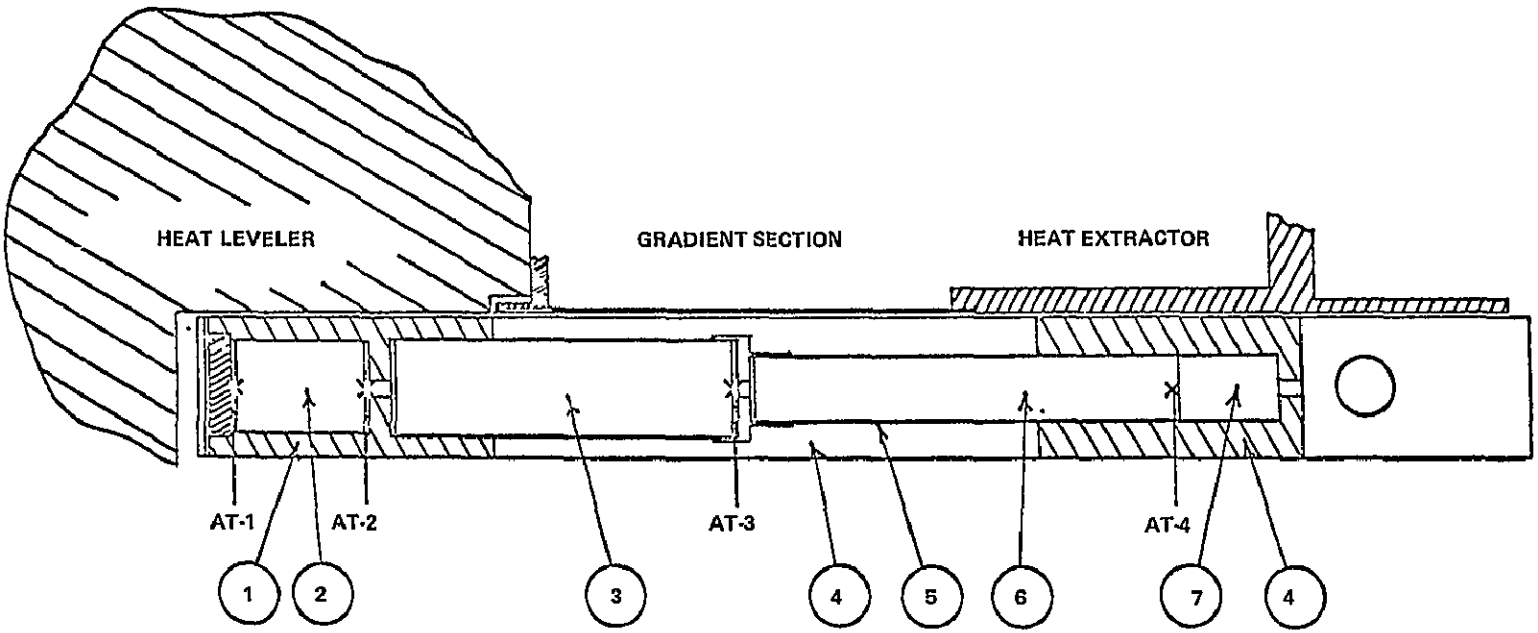

1. THERMAL INSERT, ZTA GRAPHITE
2. AMPOULE NO 1 (50 at % Bi, 50 at. % Mn)
3 AMPOULE NO 2 (8 at % Co, 92 at % Cu & Co)
4. INSULATION, FIBERFRAX
5 SUPPORT TUBE, 321 STAINLESS
6. AMPOULE NO 3 (99 4 at % Bi, 0 6 at. % Mn)
7 THERMAL INSERT, ZTA GRAPHITE

Figure VI-2. Furnace cartridge design for ASTP experiment MA-070.

pyrolytic boron nitride, and ampoule 3 was made from quartz fused silica. The thermal processing was conducted in the Westinghouse multipurpose furnace [VI-12] located in the Apollo-Soyuz Test Project (ASTP) docking adaptor.

Experiment planning was based on the thermal results from the prototype test. It was anticipated that the thermal environment for ampoule No. 1 (Fig. VI-2) would be essentially isothermal over the temperature range of solidification. Ampoule No. 2 was expected to be exposed to a thermal gradient of 30 K/cm ± 2 K/cm and ampoule No. 3 to a thermal gradient of 60 K/cm ± 3 K/cm. The flight samples were actually exposed to conditions substantially different from these, and these differences will be detailed in the following paragraphs.

The prototype test was the only thermal test of the furnace cartridge that was internally instrumented with thermocouples. The prototype furnace differed from the flight furnace in that it was a single-tube furnace. The flight furnace was a three-tube furnace with the tubes equidistant from the centerline of the furnace and arrayed at 120° angles from one another. This created a geometrical difference between the prototype ground-based and flight furnaces and led to the latter two experiments being conducted in thermal environments that were not radially symmetric. This will be considered further in the discussion on microstructures.

The longitudinal thermal profiles from the prototype test are shown in Figure VI-3. T_{HL} is the heat leveler temperature. The heat leveler temperature for the ground-based and flight tests are shown in Figure VI-4. The time to reach temperature for the flight test was slower than in the ground-based test, and the hold time was slightly shorter (45 min versus 60 min). The cooling rate was greater during the flight test. The differences in cooling rate after the helium injection are not very significant, since the samples are all completely solidified at this point.

The thermal history deduced for the type No. 1 flight ampoules is shown in Figure VI-5. Since thermal data of this type were not provided for the ground-based test, no direct comparison can be made. It is safe to conclude, however, that the cooling rate experienced by the flight samples was, on the average, 10 percent greater than that experienced by the ground-based samples. The difference in cooling rate was greatest for ampoule No. 1 and least for ampoule No. 3.

The thermal gradient was calculated as a function of time for ampoules No. 2 and 3. These calculations were made from analytical data presented in Reference VI-13. The variation of the thermal gradient, including the time

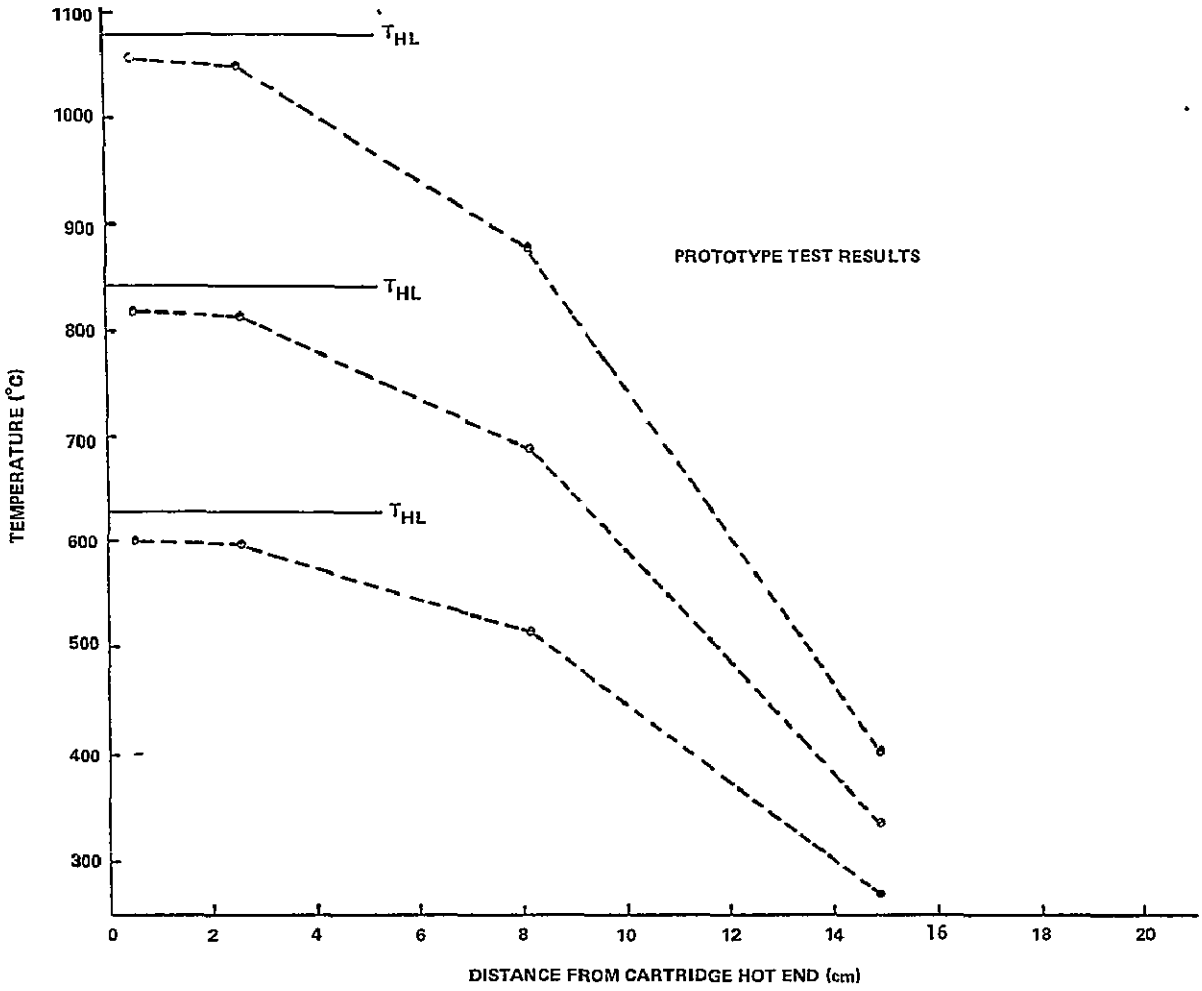

Figure VI-3. Longitudinal temperature distribution within the ASTP MA-070 experiment cartridges (prototype test results).

during which the samples in the No. 2 ampoules were directionally solidifying, is shown in Figure VI-6. The temperature gradient for ampoule No. 2 varies from approximately 30 K/cm at the onset of directional solidification to 23.5 K/cm at the conclusion of solidification.

The variation of the thermal gradient in ampoule No. 3 [VI-13] is shown in Figure VI-7 over the lifetime of the experiment and in Figure VI-8 over the duration of the directional solidification. The thermal gradient during the period of maximum superheat was 80 K/cm; however, over the period of solidification it varies from only 10.9 K/cm at the onset to 8.9 K/cm at the conclusion of solidification. This is approximately 80 percent lower than the thermal gradient anticipated from the prototype test.

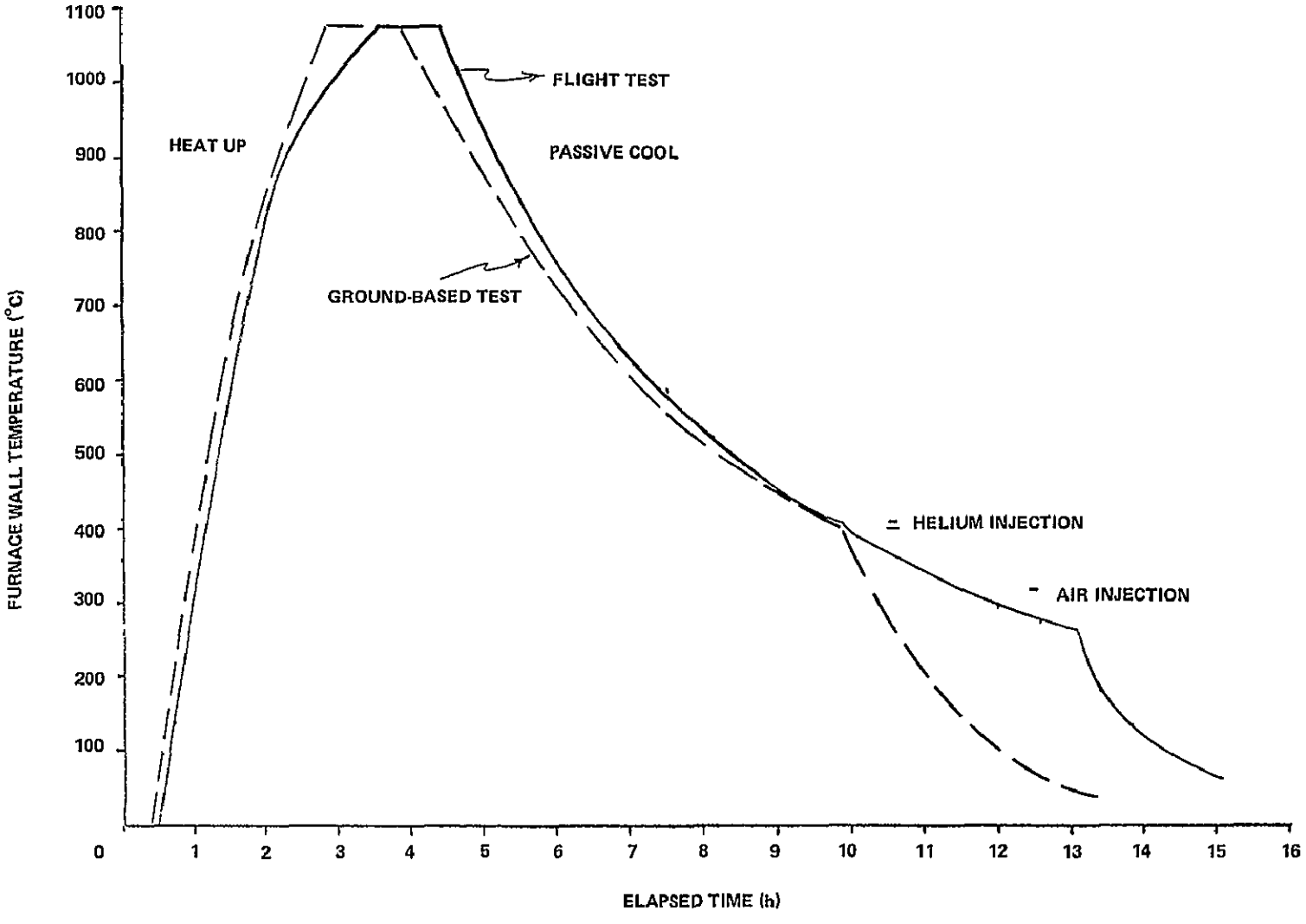

Figure VI-4. Furnace temperature versus elapsed time for the ASTP ground-based and flight tests.

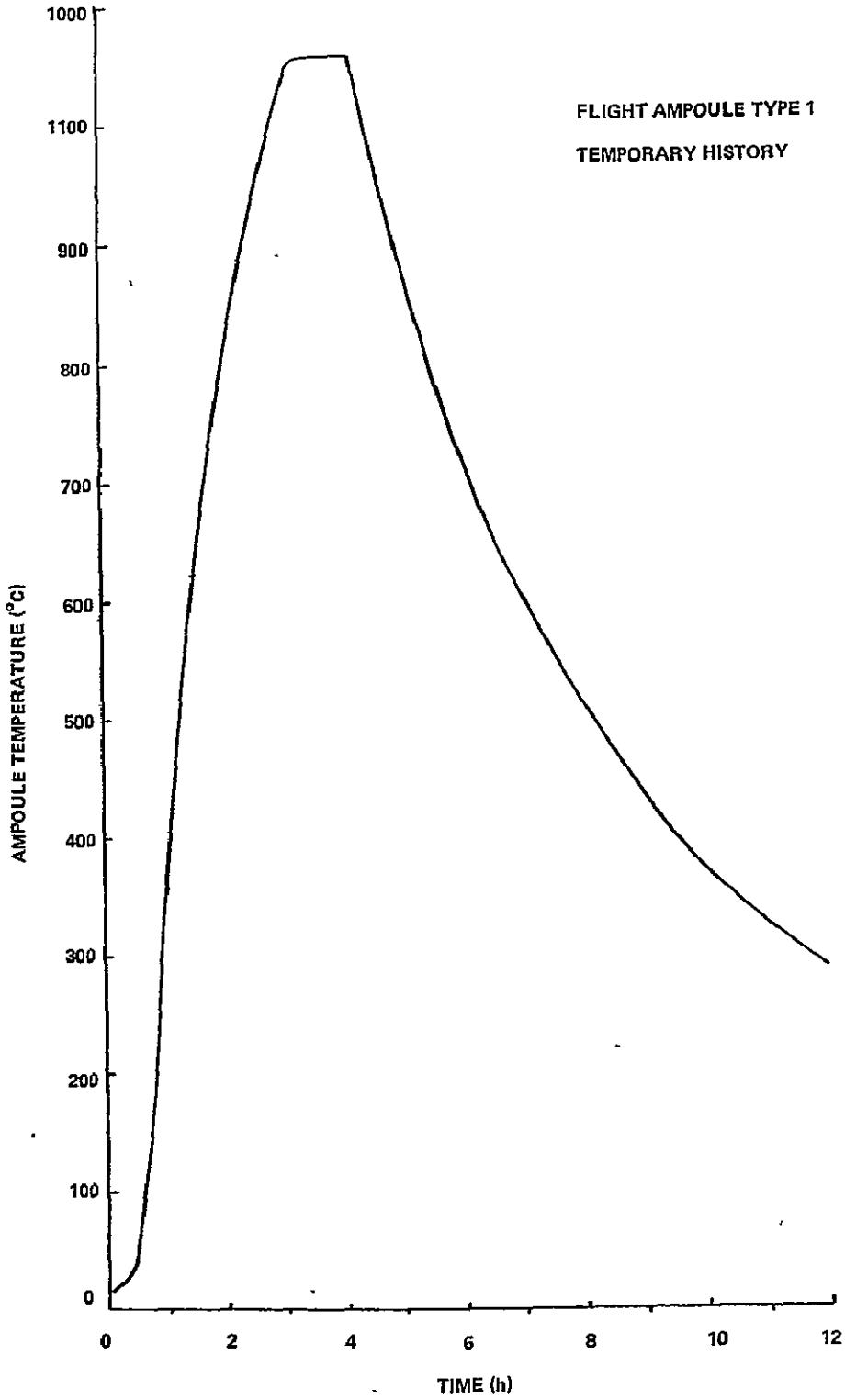

Figure VI-5. Temperature versus time for the type 1 ASTP flight ampoules.

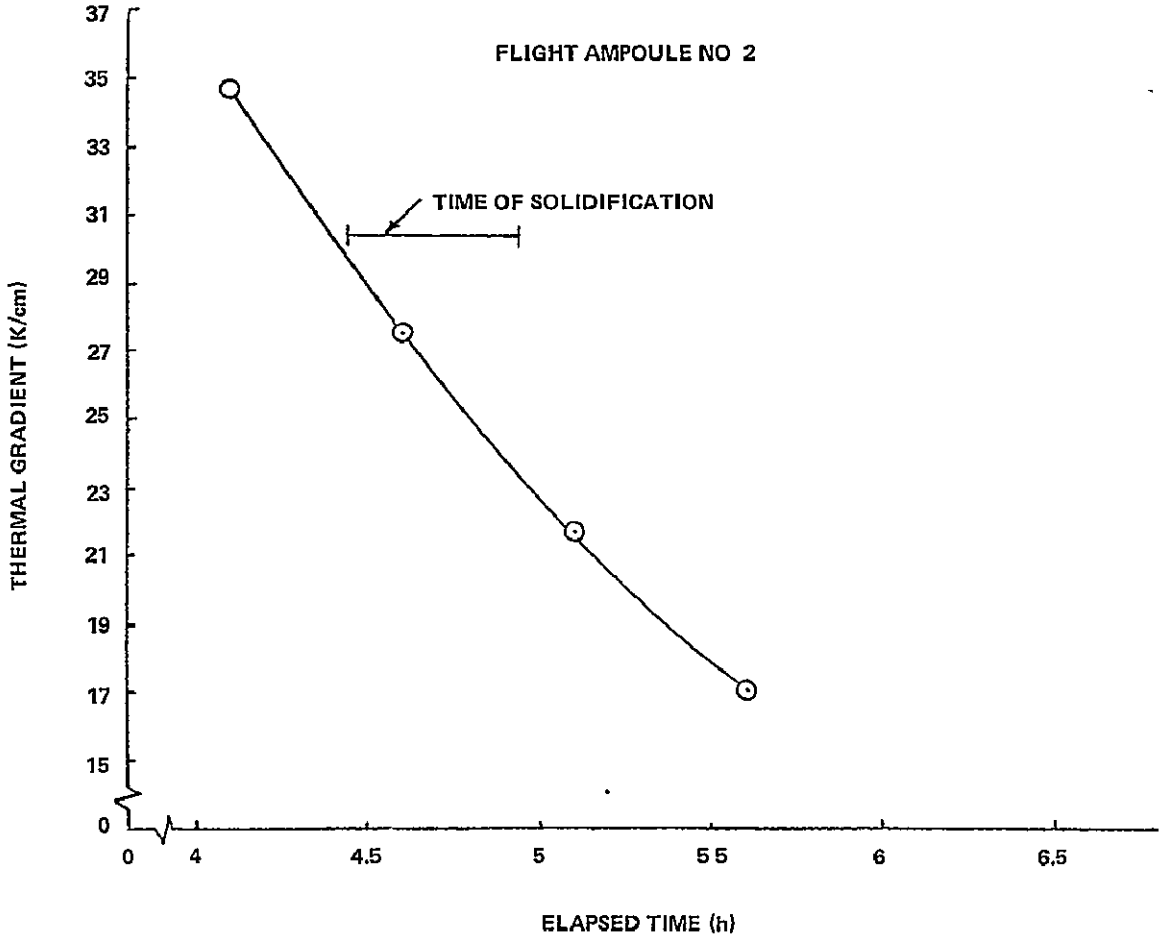

Figure VI-6. Thermal gradient versus time for the type 2 ASTP flight ampoules during the time of solidification.

EXPERIMENTAL RESULTS

Fluid Statics

The fluid state before and during thermally controlled solidification is of critical importance to successful plane-front solidification of single and polyphase alloys. This fluid state is complex and involves both static and dynamic components. Many of these fluid effects can be shown to be functionally dependent on gravity vector and level, so it would be anticipated that orbital processing would have a substantial influence upon them. The measurements required to conduct in situ and postflight dynamic analyses of the flight samples processed during the ASTP flight were deemed impossible. Thus, only static fluid analysis was conducted.

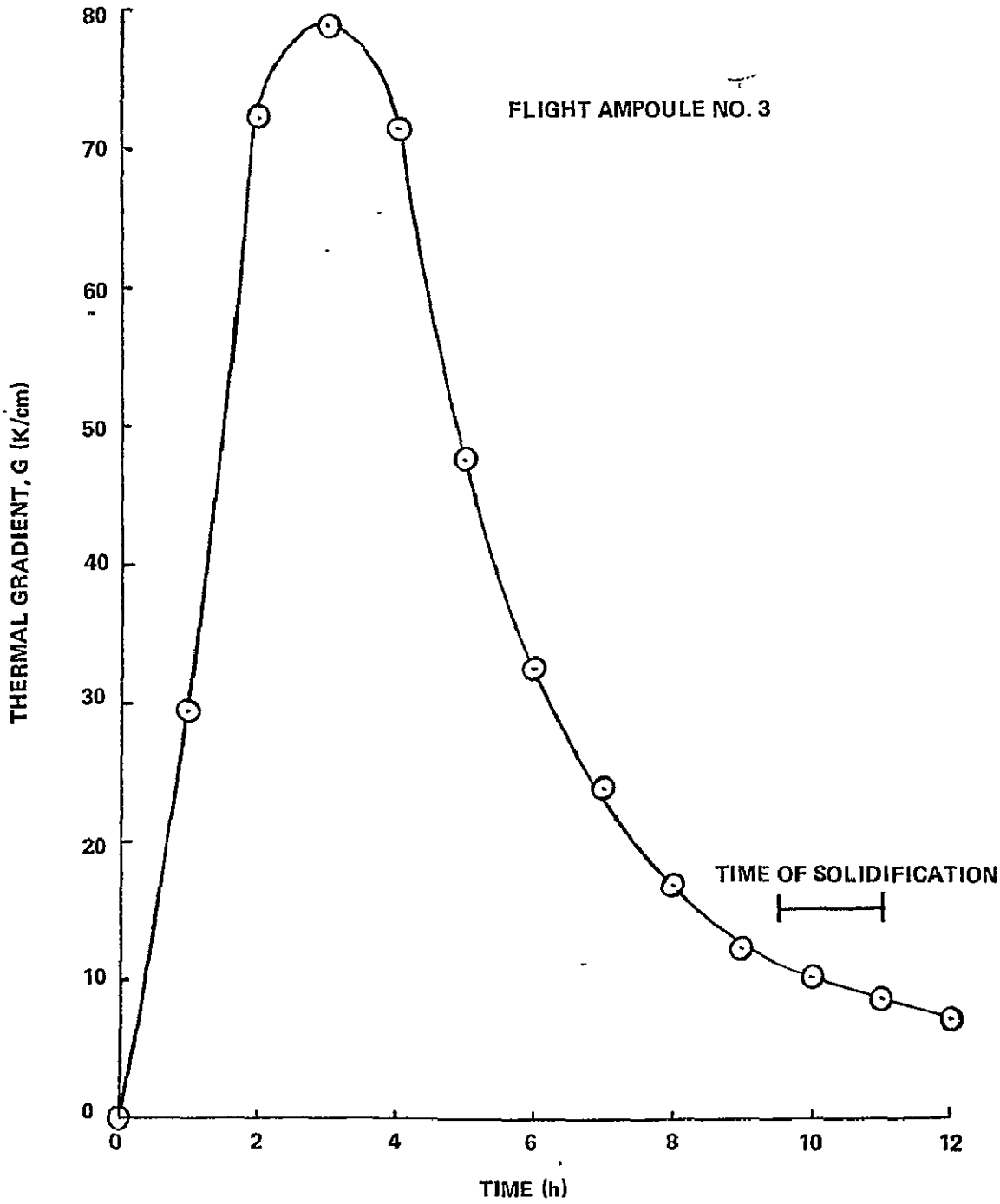

Figure VI-7. Thermal gradient versus time for the type 3 ASTP flight ampoules.

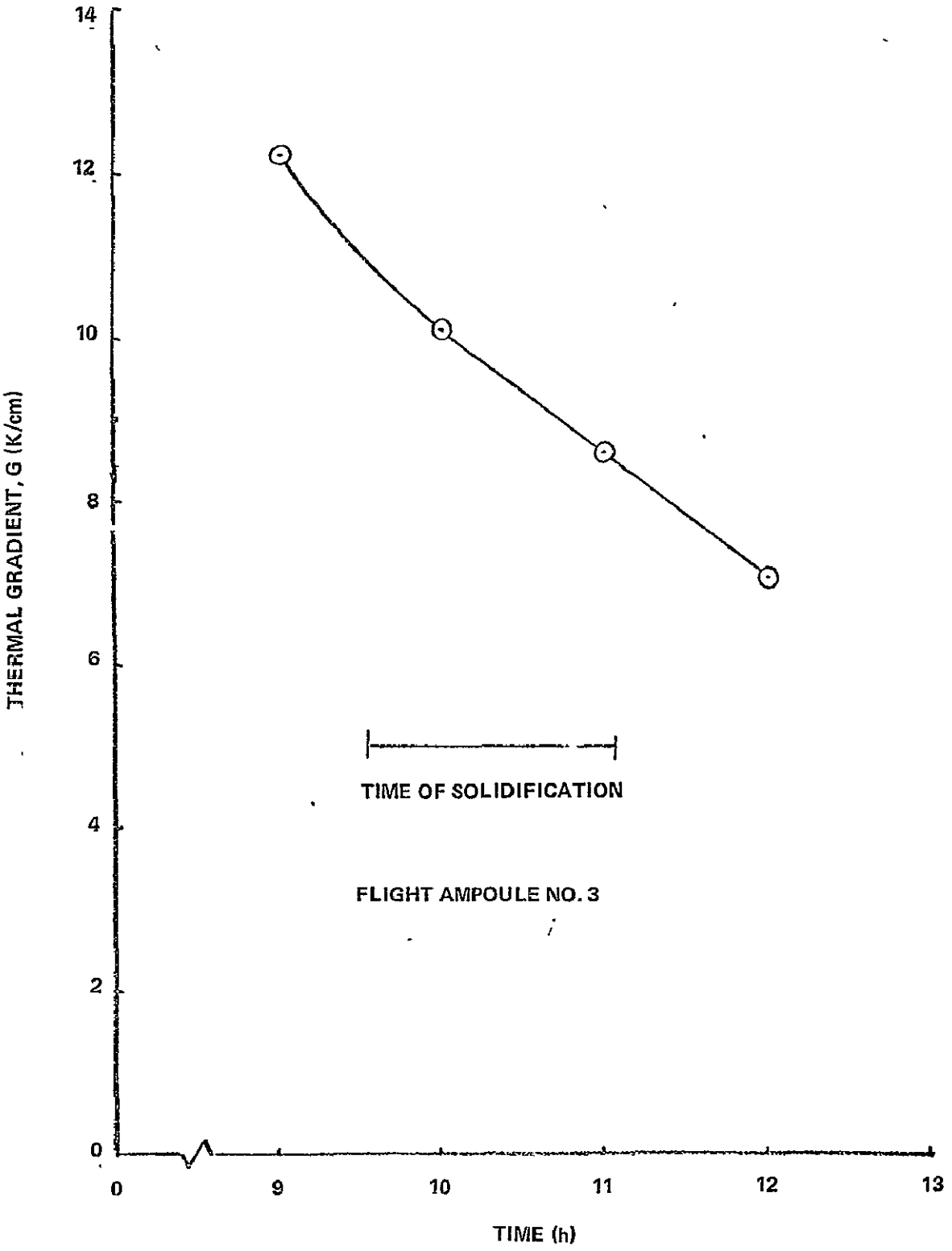

Figure VI-8. Thermal gradient versus time for the type 3 ASTP flight ampoules during the time of solidification.

Previous orbital plane-front solidification experiments conducted during Skylab indicated that the static fluid shape in the orbital environment was appreciably different from the static fluid shape documented terrestrially [VI-14, VI-15]. If the static fluid configuration is changed, the heat flux, thermal profile, and solid/liquid interface geometry may also change. Because these factors are critical to the plane-front solidification process, the success or failure of the experiment may depend on anticipating these changes. Prior work conducted in the drop tower facility at the NASA Lewis Research Center (LeRC) has identified the fluid-crucible variables that are of primary consideration in a reduced gravity environment [VI-16—VI-18]. The variables cited in the LeRC work are the fluid-crucible wetting angle θ, the thermal gradient G, the crucible taper, the fluid-crucible fill factor, the crucible diameter to length ratio D/L, the gravity vector $\vec{g}$, and the magnitude of the gravitational acceleration $|g|$ [VI-4—VI-6]. The LeRC results on fluid displacement are schematically presented in Figure VI-9, and the static fluid configurations and displacements within a cylindrical crucible are illustrated in Figure VI-10.

The fluid statics analysis of the samples was initiated while the flight ampoules were still in place in the experiment cartridges. Each cartridge was radiographed twice, at 90° angles, and the results were interpreted prior to the disassembly of the cartridges. A representative radiograph of the three cartridges is shown in Figure VI-11. Several points should be noted in Figure VI-11. These will be detailed in subsequent sections but may be summarized as follows:

- The No. 1 samples (Fig. VI-2) are of differing configurations, and the sample in the No. 9 cartridge has leaked from the inner to the outer crucible.

- The No. 2 samples appear similar, but the sample in the No. 8 cartridge appears higher than the other two.

- The No. 3 samples appear to be at differing heights. The sample in cartridge No. 9 is the highest and that in cartridge No. 8 is the lowest. It is apparent that some material has been lost from the No. 3 ampoule in cartridge No. 9, and subsequent analysis showed that some material had been lost for the No. 3 ampoule of cartridge No. 7 as well.

These displacement and configurational differences are all explainable on the basis of Figures VI-9 and VI-10.

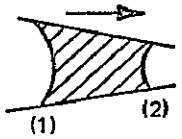

$\theta_1 = \theta_2 < 90°$
$\sigma_1 = \sigma_2$
TAPER AS SHOWN

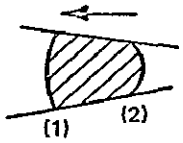

$\theta_1 = \theta_2 > 90°$
$\sigma_1 = \sigma_2$
TAPER AS SHOWN

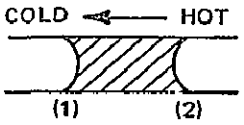

$\theta_1 = \theta_2 < 90°$
$\sigma_1 > \sigma_2$
NO TAPER

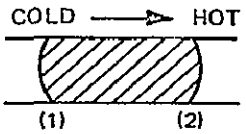

$\theta_1 = \theta_2 > 90°$
$\sigma_1 > \sigma_2$
NO TAPER

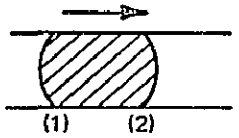

$\theta_1 > \theta_2 > 90°$
$\sigma_1 = \sigma_2$
NO TAPER

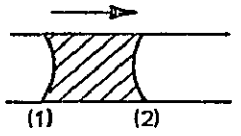

$\theta_2 < \theta_1 < 90°$
$\sigma_1 = \sigma_2$
NO TAPER

Figure VI-9. Results on fluid displacement in reduced gravity environment (σ is surface tension).

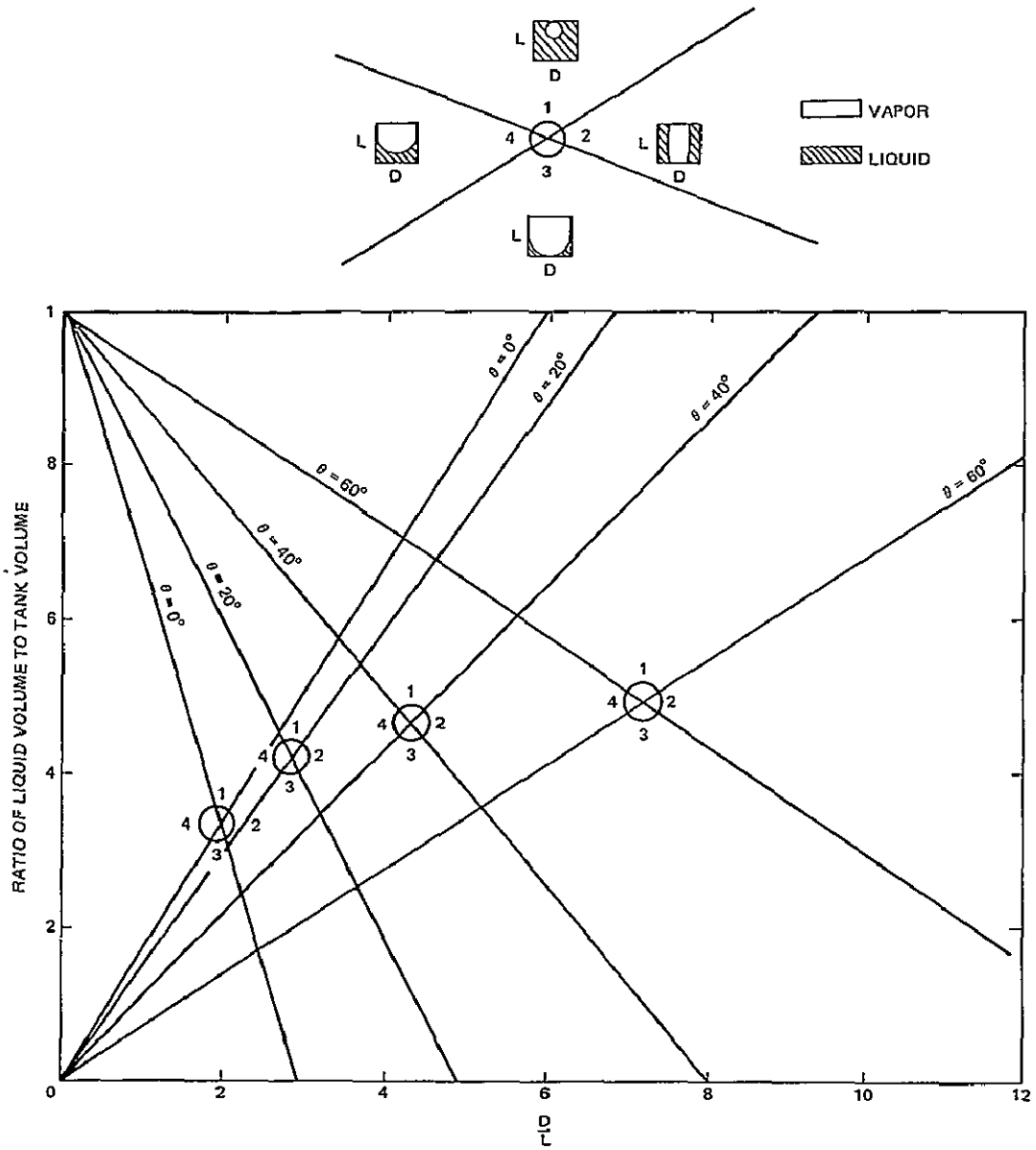

Figure VI-10. Wetting fluid configurations in a cylindrical crucible.

The fluid in ampoule No. 1 (50 at.% Bi, 50 at.% Mn) wet the inner crucible (pyrolytic boron nitride), and the crucible had a diameter to length ratio of approximately 0.71. The volumetric fill factors were varied within the No. 1 ampoules, and the samples were processed isothermally (G=0). The fill factor for the ampoule within cartridge No. 7 was 0.95, that within cartridge No. 8 was 0.90, and that within cartridge No. 9 was 0.85. It was anticipated

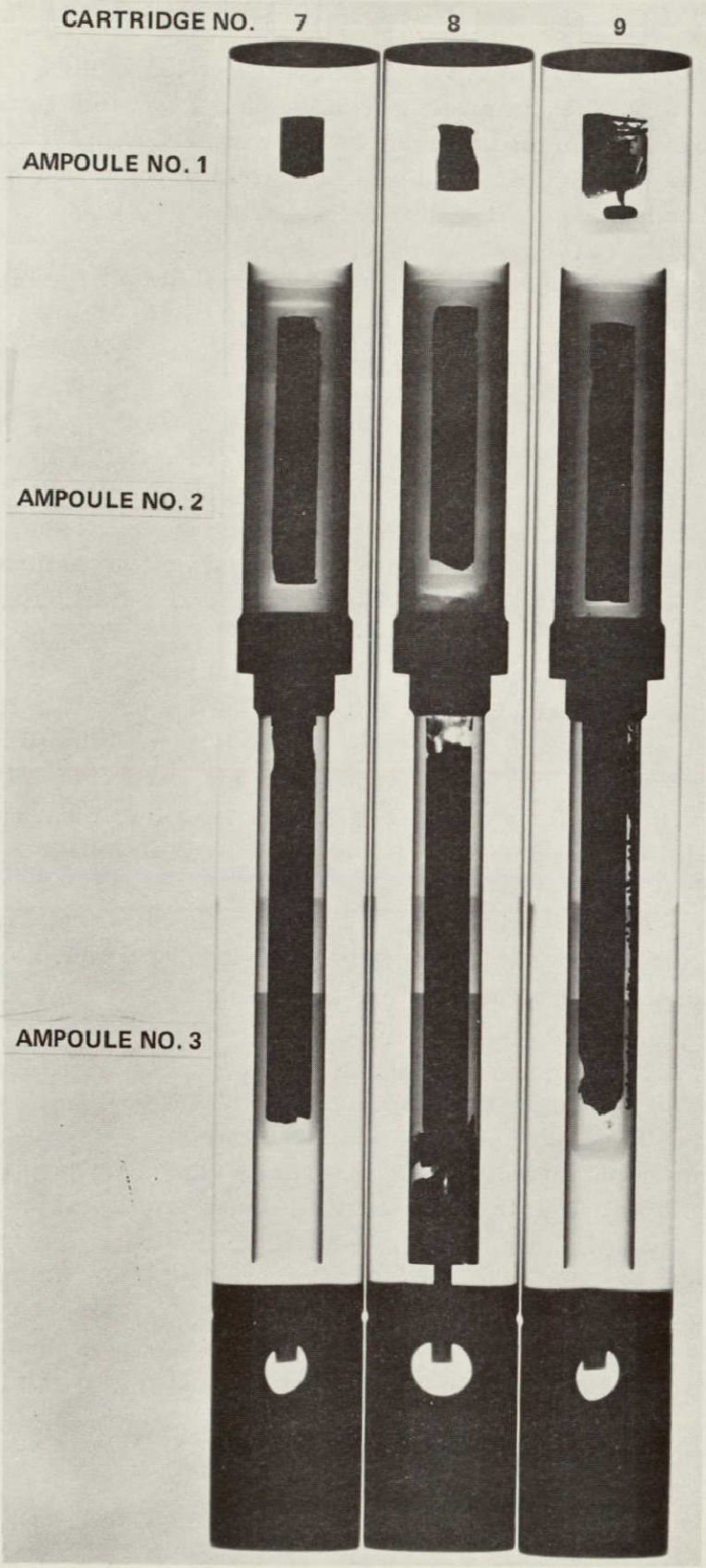

Figure VI-11. X-ray radiograph of the three ASTP MA-070 experiment flight cartridges (1X).

that variation from the type 1 to type 4 fluid configuration would be noted (Fig. VI-10). Unfortunately, the sample in cartridge No. 9 was lost through a vibrational failure; however, samples 7 and 8 were consistent with type 1 and intermediate type 1/type 4 behavior. This was indicative of a low wetting angle, as previously mentioned.

The No. 2 ampoules housed a wetting liquid within a crucible. These samples were processed in a thermal gradient of approximately 27 K/cm ± 2 K/cm. These samples were not totally melted but were melted back along the seed crystal such that at peak furnace temperature, the fluid was in contact with a seed crystal. Figure VI-9 shows that a wetting fluid would be expected to be displaced toward the colder end of a thermal gradient. This would be toward the seed crystal, and since this would be mechanically fixed, no fluid displacement would be expected. The upward displacement of sample No. 2 in cartridge No. 8 must be explained then on the basis of mechanical displacement of the entire seed crystal prior to the melting and solidification sequence.

The No. 3 ampoules were intended to demonstrate the behavior of an unconstrained (no seed crystal), nonwetting fluid (97.8 at.% Bi, 2.2 at.% Mn) in a thermal gradient. The thermal gradient varied from 80 to 10 K/cm over the course of the experiment. These fused silica ampoules had been backfilled with an inert gas (argon) to suppress the possibility of thermal cavitation of the bismuth-rich liquid. Apparently, in the backfilling operation a small amount of contaminant oxygen was allowed to enter the No. 3 ampoule of cartridge No. 8. This small amount of oxygen was sufficient to alter the fluid/crucible interfacial characteristics from a nonwetting to a wetting system with concomitant changes in the fluid displacement behavior.

As would be anticipated from Figure VI-9, the nonwetting fluid moved toward the hot end of the ampoule, whereas the wetting fluid moved in the opposite direction. This relative fluid displacement has been mentioned previously. The fluid displacements in the outermost ampoules resulted in the failure of the ampoules. The bismuth-rich fluid expands upon solidification. The movement of the fluid toward the hot end of the ampoule resulted in a condition, during the latter stages of solidification, whereby there was insufficient free volume in the ampoule to house the resultant solid. The pressure built up sufficiently within the ampoules to cause them to crack. This result should be a consideration in the planning of subsequent solidification experiments where the fluid expands on solidification.

Phase Relations and Microstructure

The thermal profile imposed upon the No. 3 ampoules substantially superheated the bismuth-rich liquid when the furnace was at peak temperature. This superheat necessitated the previously mentioned backfilling operation. To check the compatibility of the quartz ampoule with the superheated bismuth-rich liquid, quartz-bismuth samples were superheated within a differential thermal analysis (DTA) unit. These studies confirmed the compatibility of the bismuth and quartz even up to 1050 K and determined that a liquid phase transition took place in the liquid bismuth. Similar fluid state transitions have been reported for other semimetals [VI-19] but not for bismuth. The transition was found to demonstrate large temperature hysteresis and was rate sensitive. At 10 K/min the transition took place at 988 K (715°C) on heating and 858 K (585°C) on cooling.

The samples within the No. 1 ampoules (Fig. VI-2) were 50 at.% Bi and 50 at.% Mn. Three BiMn phase diagrams have been proposed [VI-20—VI-22], and we will comment on all of them. Ground-based work prior to the ASTP flight supported the liquidus results of References VI-21 and VI-22. Work performed in the analysis of the flight samples indicates that the phase diagram of Reference VI-22 is to be preferred, and this is shown as Figure VI-12. This conclusion is based upon qualitative metallographic evidence, and quantitative thermal and chemical analyses are in process. The quantitative data will determine if this preliminary conclusion is sound.

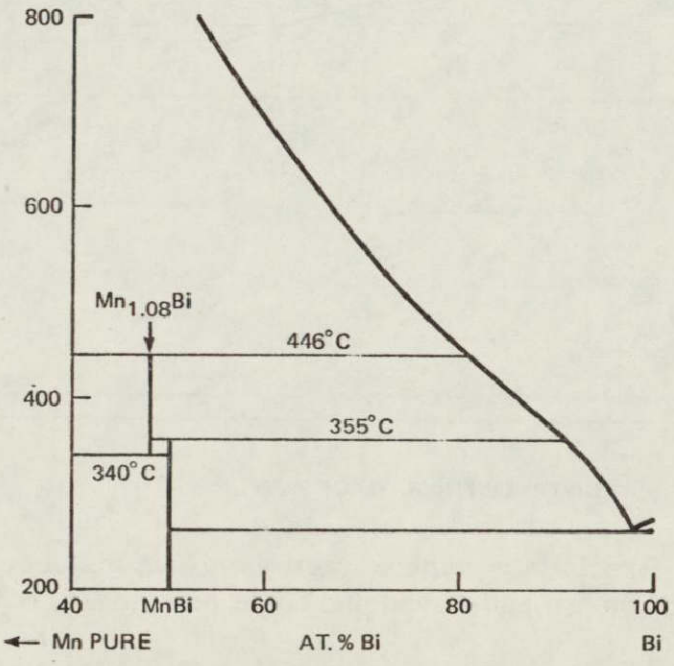

Figure VI-12. Proposed MnBi phase diagram segment [VI-22].

The samples in the No. 1 ampoules, henceforth to be referred to as No. 1 samples, were processed by isothermal lowering (G=0) from a temperature above the liquidus temperature. The ground-based samples demonstrated appreciable gravitationally dependent macrosegregation. This chemical macrosegregation resulted in almost all of the primary properitectic Mn particles being at the top of the sample. The volume fraction of the MnBi phase, determined by quantitative areal analysis, continuously decreased from the top of the ingot to the bottom. This variation, for a ground-based sample experiencing the same thermal cycle as the flight samples were exposed to, is shown in Figure VI-13. The average value for this sample was 29.5 vol.% of primary Mn and MnBi particles. The volume fraction of the primary MnBi phase in the flight samples was more uniformly distributed, and no primary Mn particles were identified. The average volume fraction of primary particles (Fig. VI-13) was 35.7 percent, which may be an indication that the properitectic Mn had reacted with the Bi-rich liquid to form MnBi. These measurements were made only on the tops and bottoms of the samples, because the samples are being conserved for detailed magnetic analysis. This will be discussed later.

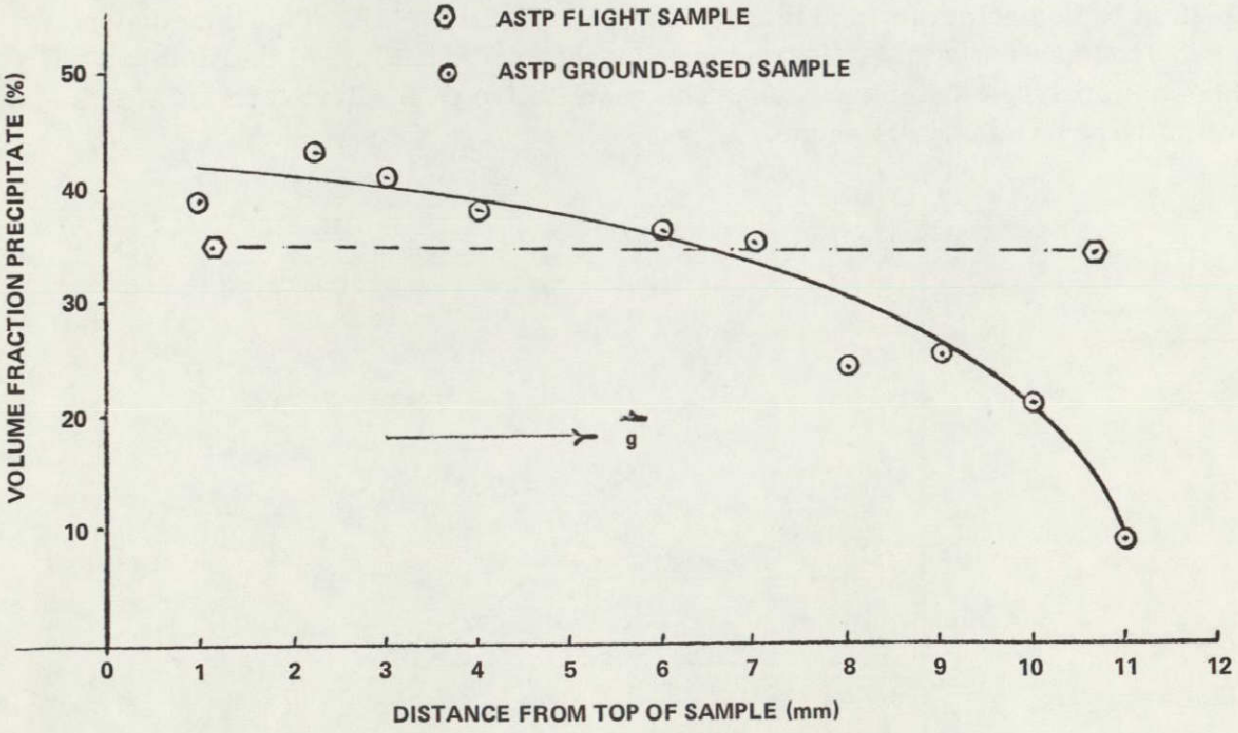

Figure VI-13. Precipitate volume fraction versus distance from top of the ground-based and flight samples.

The flight samples were found to have large primary MnBi particles, lying on or near the surface, transverse to the longitudinal direction of the samples. This was unexpected and was not typical of the ground-based samples. It is felt that this might indicate that the radial gradient experienced by the flight samples was greater than the longitudinal gradient, thus causing the primary crystallites to grow radially, in the direction of heat extraction. It may be that gravitationally dependent convective flow caused the thermal distribution to be more uniform in the ground-based samples, or at least prevented the primary crystallites from aligning.

Some of the ground-based and low-g primary MnBi crystallites appeared to be composed to two discretely different microstructural regions (Fig. VI-14), whereas others did not. This anomaly can be explained on the basis of the phase diagram shown in Figure VI-12. This phase diagram proposes two compositional modifications of MnBi. The first, MnBi (I), forms at 719 K (446°C) and is manganese-rich. The stoichiometric ratio proposed for this compound is $MnBi_{1.08}/Bi_{1.00}$. This phase decomposes eutectoidally to MnBi(II) plus Mn at 613 K (340°C). MnBi (I) forms directly from the melt between 719 K (446°C) and 628 K (355°C). MnBi (II) is equiatomic and forms directly from the melt between 628 K (355 °C) and the eutectic temperature 542 K (269°C).

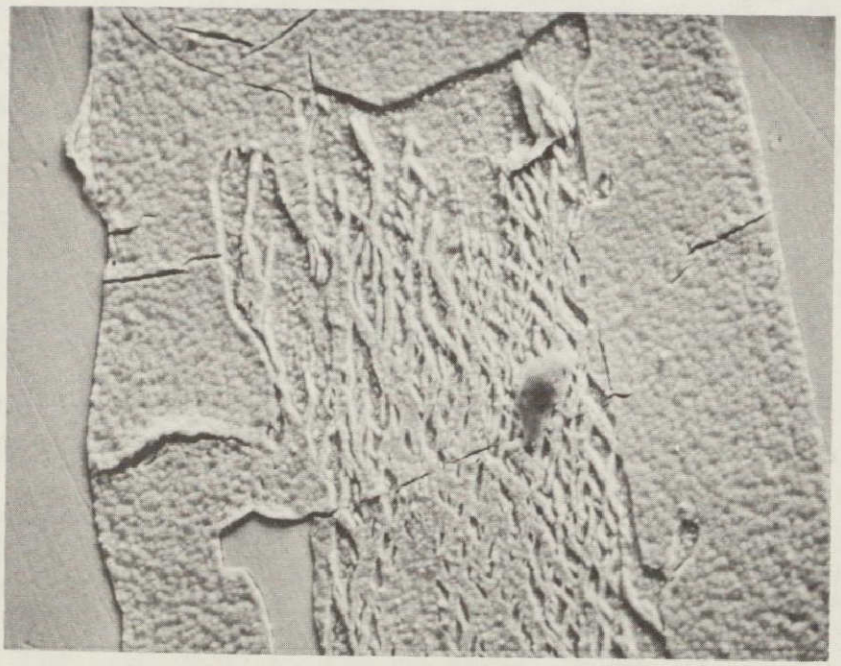

Figure VI-14. Primary MnBi crystallite showing discretely different morphological regions (900X).

Considering the flight samples, those crystallites forming between 719 K (446°C) and 628 K (355°C) would be expected to react with residual liquid between 628 K and 613 K to form MnBi (II). This reaction would be subject to the same diffusion barrier limitations common to all peritectic or peritectoid reactions and would not be expected to go to completion. The MnBi (I) core would then thermally decompose below 613 K (340°C) to Mn plus MnBi (II). The MnBi (II) formed via the peritectic reaction would then act as a heterogeneous nucleus for continued MnBi (II) precipitation below 628 K (455°C). Sections of those crystallites experiencing this sequence would be expected to have a duplex appearance. The MnBi (II) formed below 628 K (455°C), either via peritectic reaction [Fig. VI-15(a)] or proeutectic precipitation [Fig. VI-15(b)], would be expected to appear monolithic, whereas residual MnBi (II) would be expected to show some evidence of the eutectoid decomposition. Those crystallites forming below 628 K (355°C) would be expected to be monolithic throughout.

The secondary MnBi (II) crystallites were found to be almost normal to the primary MnBi crystallites in the low-g samples [Fig. VI-15(a)], whereas they were typically skewed in the one-g samples [Fig. VI-15(b)]. This may be an indication of decreased fluid motion, although other hypotheses may be proposed to explain this phenomenon.

In addition to morphological differences, the secondary crystallites were finer in the flight samples than in the ground-based samples. One might have expected the opposite to be true since the rate of cooling through this temperature range was slower for the flight samples than for the ground-based samples (Fig. VI-4).

The samples processed in the No. 2 ampoules were victimized by experimental limitations. The peak furnace temperature available was 1323 K (1050°C). To process most M_5R.E. compounds would have required a furnace temperature of 1773 K (1500 C) to 1873 K (1600°C). This experimental constraint required a serious alloy development program to be undertaken. The development program considered varying combinations of copper, cobalt, and iron as the metallic component (M) and varying combinations of cerium, samarium, and misch metal as the rare Earth (R.E.) component. The alloy development data were reported elsewhere.[2] In short, the maximum copper content, with cerium or misch metal alloying additions, provided the lowest liquidus temperatures but sacrificed magnetic performance to experimental expediency.

2. Larson, D. J., Jr.: ASTP MA-070 Experiment Final Report, in publication.

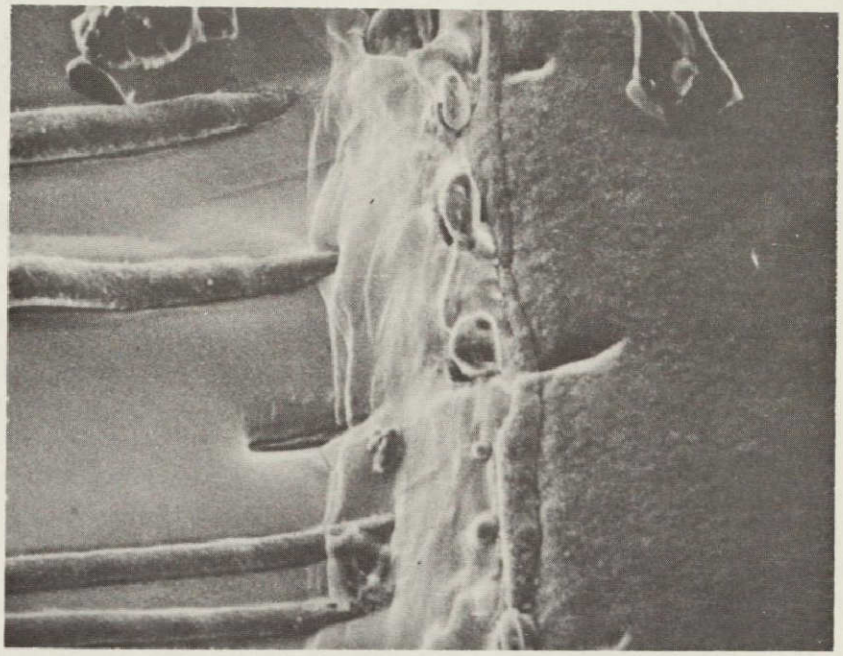

a. Flight sample (3750X).

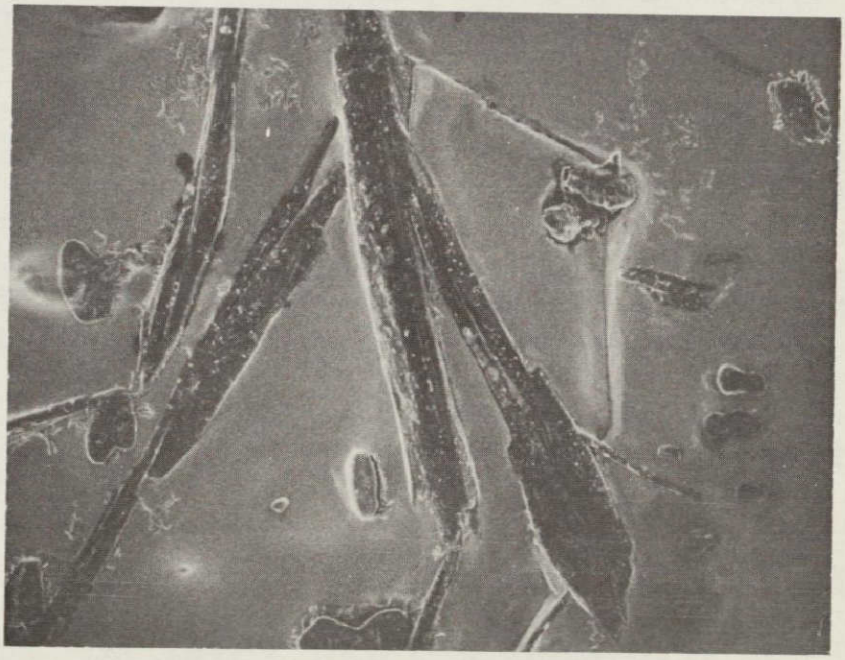

b. Ground-based sample (1500X).

Figure VI-15. Primary and secondary MnBi particles in the (a) low-g sample and (b) one-g sample.

In addition to thermal problems, there were crucible/fluid compatibility problems. In short, all rare Earth liquids are extremely reactive and, hence, difficult to contain. Ground-based and literature surveys identified pyrolytic boron nitride as the most promising crucible material. This crucible material did react with the melt but seemed to establish a stable reaction product at the crucible/fluid interface that acted as a barrier to further reaction. Ground-based studies showed that the copper-cerium fluid was the least reactive of the fluids investigated.

The thermal and compatibility considerations, in concert, demanded that we select the copper/copper-cerium eutectic as our eutectic composite material.

Analysis of the samples processed in the No. 2 flight ampoules indicated that the directional solidification aspects of the experiment were not achieved. The reaction product at the fluid/crucible interface acted as a heterogeneous nucleation point ahead of the advancing solid/liquid interface, and coordinated eutectic growth was not achieved. Crystallites grew into the melt from the crucible wall.

Directional solidification of high performance rare Earth magnetic composites in orbit is still considered to be an attractive possibility. Ideally, however, it would be conducted in a floating-zone, directional-solidification apparatus that could impose steep thermal gradients on the samples and achieve 2000 K (approximately 1750°C) in absolute temperature. This would eliminate most of the experimental constraints, and the experiment could be performed properly.

The samples in the No. 3 ampoules, henceforth referred to as the No. 3 samples, were 97.8 at.% Bi and 2.2 at.% Mn, the eutectic composition. These samples were totally melted and were solidified in a temperature gradient of approximately 10 K/cm. This was substantially lower than anticipated; however, coordinated eutectic growth was achieved.

The microstructure in the region of initiation of solidification of ground-based and flight samples consisted of large primary bismuth dendrites with Bi/MnBi(II) eutectic in the interdendritic regions. The eutectic in this region was not well aligned with the imposed thermal gradient; this is shown in Figure VI-16 for a ground-based sample. As the solidification progressed in the ground-based and flight samples, the primary bismuth dendrites became fewer in number and the interdendritic eutectic became progressively better aligned with the thermal gradient, as shown in Figure VI-17 for a ground-based sample. Ultimately, there was a transition from dendritic to coordinated growth in both sample sets, as shown in Figure VI-18 for a ground-based sample. It was the latter region of uniformly distributed, aligned, magnetic particles that was analyzed magnetically.

Figure VI-16. Primary bismuth dendrites and secondary MnBi/Bi eutectic within ground-based sample (650X).

Figure VI-17. Primary bismuth dendrites and secondary MnBi/Bi eutectic within ground-based sample (325X).

Figure VI-18. Transition from dendritic to coordinated growth within ground-based sample (75X).

The Bi/MnBi eutectic system is a doubly faceted system [VI-23]. The rod shape, in cross section, is dependent on the growth rate during solidification. At slow growth rates, the rods have a cross section reminiscent of a chevron, whereas at high rates the cross section is close to circular.

The rod cross section of both the ASTP ground-based and flight samples was chevron-like, as shown in Figure VI-19. This is consistent with the literature [VI-24]. The rod diameter, however, was smaller in the flight samples than in the ground-based samples. Particle sizes in the flight samples were typically 0.75 to 2.00 μm, whereas the ground-based samples were 2.0 to 4.0 μm. This is a somewhat surprising result, since it is generally understood that the rod diameter varies in a manner such that the square of the diameter (d^2) times the growth rate (R) is a constant over wide ranges of growth conditions [VI-25]. It was not anticipated that the growth rate would vary significantly between the ground-based and flight experiments, and the cause for this variation in d would seem to reside within the "constant." This constant was not expected to vary.

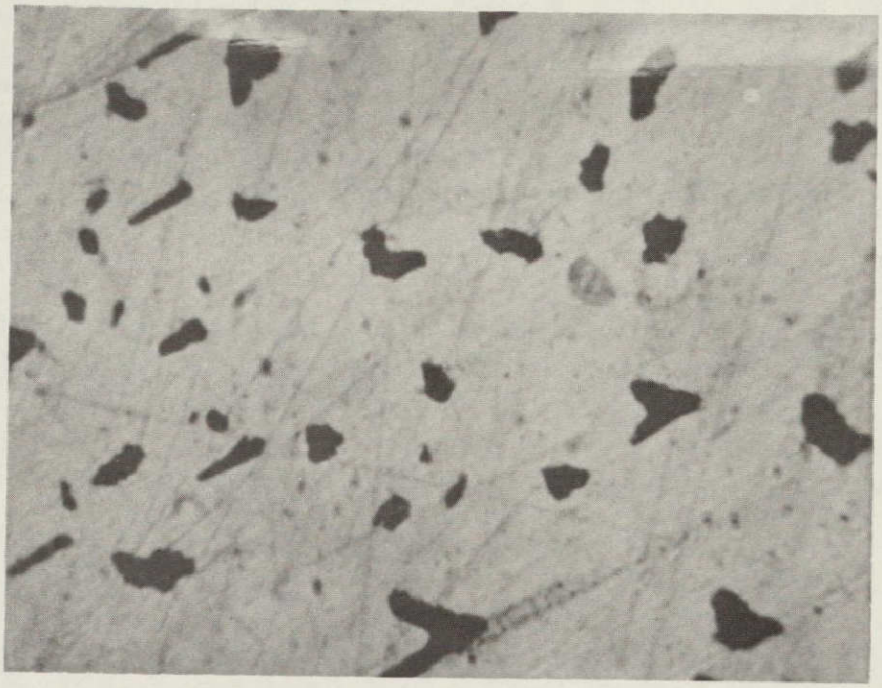

Figure VI-19. Transverse section of unidirectionally solidified MnBi/Bi eutectic (2000X).

Consideration of the various possibilities that would lead to a difference of this magnitude is continuing. One distinct possibility is thermotransport, which should be enhanced in a convectionless environment. This could impact both the solute profile ahead of the advancing interface, the diffusional coefficient in the aforementioned "constant," and the dendritic to coordinated transition. Although this would seem to be a likely source of difference, the lower limit of influence has been predicted analytically [VI-26], and the experimental parameters for our flight experiment would seem to predict only a small influence. Work in this area will be pursued.

The refinement of the particle size in the flight experiment was also reflected in the magnetic results. These will be detailed in the next section; however, it is important to note that the flight samples behaved magnetically like samples grown terrestrially approximately six times faster. This is equivalent to saying that if the ratio of the constant to the growth rate determined d^2, then for magnetic equivalence the flight samples should have a particle diameter approximately 40 percent of the ground-based value. This is reasonably consistent with the particle size data when the scatter bands are considered.

Another set of measurements was made to compare the flight samples with the ground-based samples. These measurements were of the MnBi lattice parameter. It was assumed in these measurements that all of the MnBi that we were dealing with had 4 atoms/unit cell and was of a D^4_{6h}-$P6_3/mmc$ hexagonal structure. The bismuth was assumed to have 2 atoms/unit cell and to be a D^5_{3d}-$R\bar{3}m$ structure. It was assumed that the bismuth rhombohedral angle (α) was 57°14' throughout this study.

Measurements utilizing the MnBi $\{10\cdot0\}$ and $\{21\cdot0\}$ reflecting planes were used to calculate the lattice parameters of the MnBi. Because of the low volume fraction and crystallographic anisotropy of the samples, it was impossible to consistently utilize other than these lines. The lattice parameter measured from the ground-based samples, in the coordinated growth region, was α_o = 4.255 ± 0.003 Å. This value did not vary, within our experimental error, over the length of the coordinated growth region. The value measured for the coordinated growth region of one of the flight samples was 4.306 ± 0.003 Å. This difference is well beyond our experimental error and is worth considering further.

Slow cooled bulk MnBi samples have been reported to have a_o lattice parameters varying from 4.25 to 4.27 Å. Rapidly cooled bulk samples, and samples quenched from high temperatures, have a_o parameters as high as 4.33 Å (quenched from 673 K). The lattice parameter from the flight sample would indicate that it is equivalent to a sample quenched from an intermediate temperature or grown at a higher growth rate. This is consistent with our magnetic and particle size conclusions.

Magnetic Analysis

The optimum morphological array for a magnetic composite consists of fine, elongated, single-domain magnetic particles aligned in a matrix, with the easy axis of magnetization parallel to the particle axis [VI-27]. The greater the magnetocrystalline anistropy constant for the magnetic phase is, and the finer the discrete magnetic particles [VI-28] are, the higher the magnetic coercivity is.

Directional solidification of magnetic composites is promising because the particle size of the magnetic phase in a rod eutectic is typically of the order of 1 μm, the finely dispersed magnetic phase is protected from contaminating

environmental effects, and the easy axis of magnetization of the magnetically anisotropic dispersed phase is frequently the crystallographic growth direction of the magnetic phase. Directional solidification of magnetic composites thus offers the potential for protection, alignment, and refinement of the dispersed magnetic phase.

As mentioned previously, this condition was not achieved in the No. 2 samples and the magnetic performance of the ground-based and flight samples was essentially the same. The measured intrinsic coercivity (H_{ci}) of the magnetic phase was found to be 1.04 KOe in both cases, within experimental error. As mentioned previously, the evolution of new experimental hardware is required to accomplish successfully our original goal of processing high performance rare earth magnetic composites.

The No. 3 samples, however, were successfully processed and because of their high performance, particularly at cryogenic temperatures, all measurements were made at the Francis Bitter National Magnet Laboratory of the Massachusetts Institute of Technology, where the author was tendered guest scientist status.

A bitter magnet is shown schematically in Figure VI-20 and a typical magnet facility is shown in Figure VI-21. The large cooling capability is required because 5 to 10 MW of power is run through these magnets, depending on which unit is being utilized.

A standard two-coil pickup was used to make measurements on the full length of the coordinated growth region. Sample sizes were approximately 2.5 cm long and 5 mm in diameter. A flux integration technique was used to map the B-H curves. The coil circuit used is shown schematically in Figure VI-22 and the integrator circuit is shown schematically in Figure VI-23. The H axis was calibrated from the known calibrated field parameters and B was calibrated using a VP grade pure nickel standard. Measurements were made with this diagnostic system at 295, 245, and 77K. Thermal loss problems precluded making lower temperature measurements with this apparatus. Measurements were made up to field strengths of 185 kG.

A typical set of B-H loops for ground-based material, as a function of test temperature, is shown in Figure VI-24. These curves are typical of directionally solidified MnBi dispersed in a Bi matrix. The duplex curve at 77 K was analyzed using the theory of superposition, and the data are reported in the manner of Reference VI-24. The duplex loop reduces to two simple B-H loops, as shown in Figure VI-25.

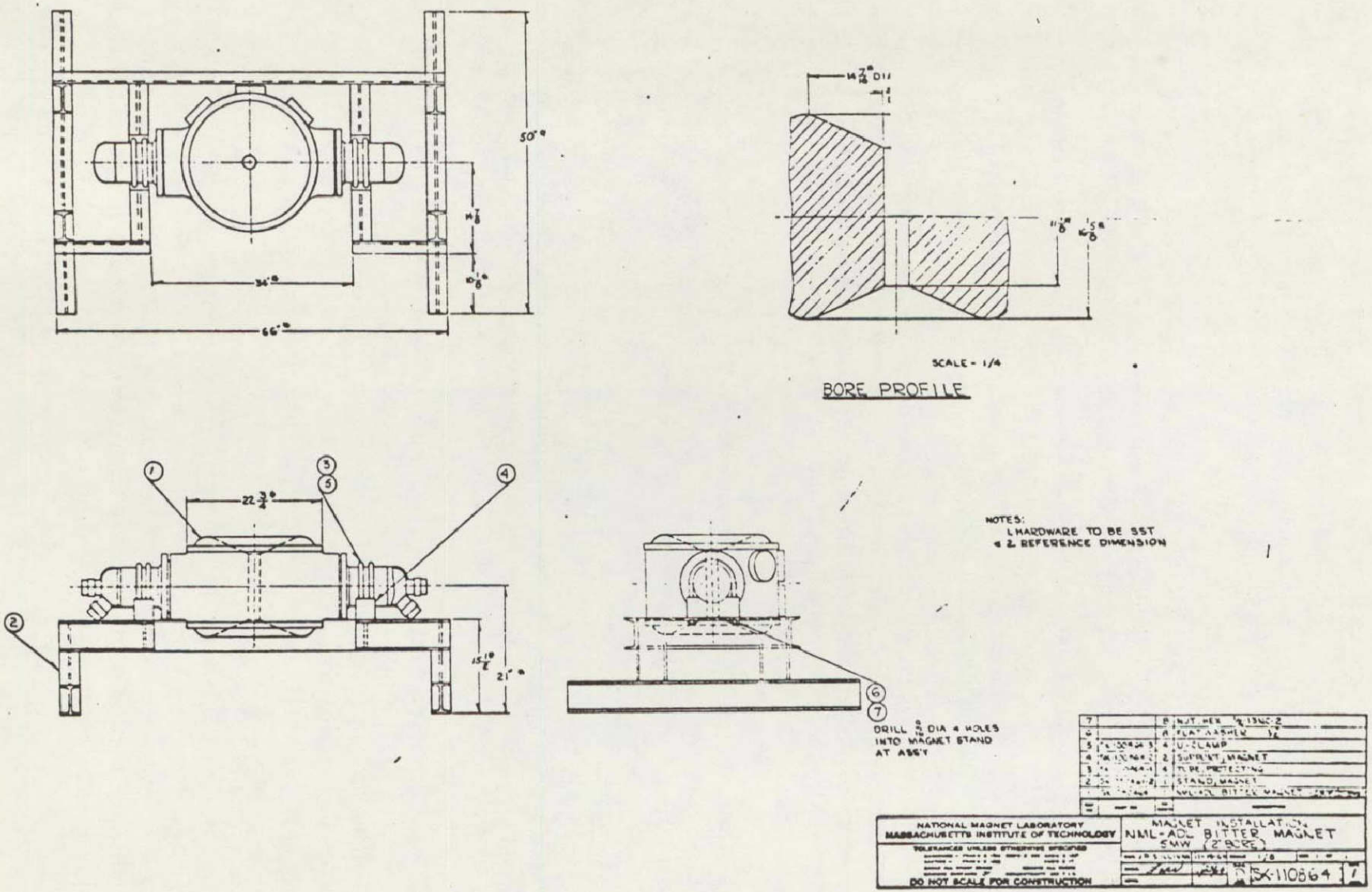

Figure VI-20. Schematic diagrams of NML-ADL bitter magnets.

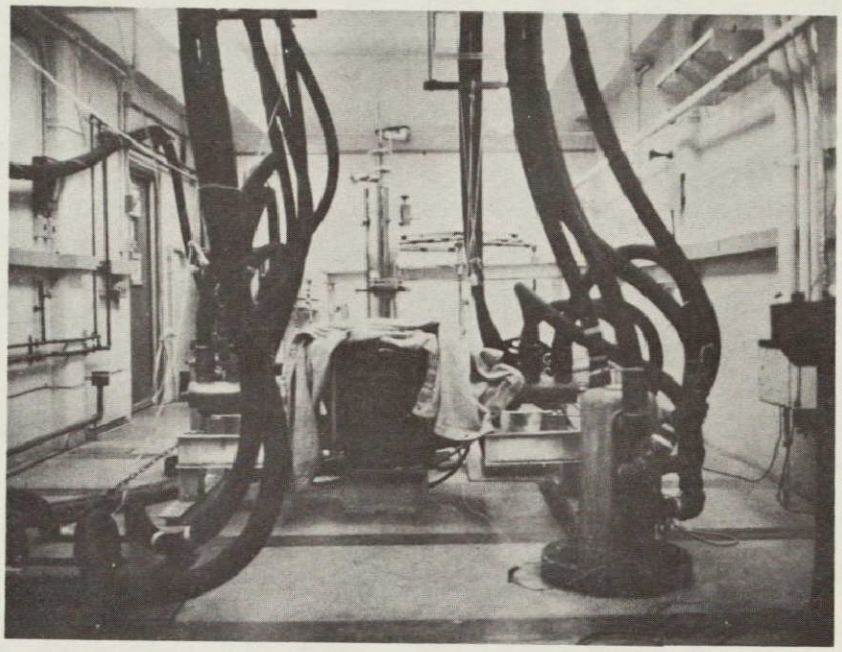

Figure VI-21. NML bitter magnet installation.

The apparatus previously described was relatively insensitive and did not offer the possibility of further reduction in sample size for more selective analyses within the coordinated growth region. Fortunately a low frequency vibrating sample magnetometer was made available, and Figure VI-26 shows the general facility and the gear box that changed the rotary motion to a vertical displacement in the field. The measurement technique and hardware is fully described in Reference VI-29. This apparatus substantially increased our resolution and allowed us to reduce our sample sizes by a factor of five. This allowed us to make measurements transverse to the magnetic flux lines and to selectively analyze the region of coordinated growth. This also allowed us to utilize the world's largest continuous field magnet (235 kG) and to include measurements at 4.2 K in our study.

Our average room temperature data for ground-based, flight, and literature samples are presented in Figure VI-27. The literature data shown in Figure VI-27 has been taken from Reference VI-24. The square root of the growth rate was selected as the abcissa, because it is a solidification parameter that should be proportional to the intrinsic coercive strength (H_{ci}). It should be pointed out, however, that the literature data presented were measured on samples that were grown in a thermal gradient (G) an order of magnitude greater

Side By Side
MATCHED COIL SYSTEM

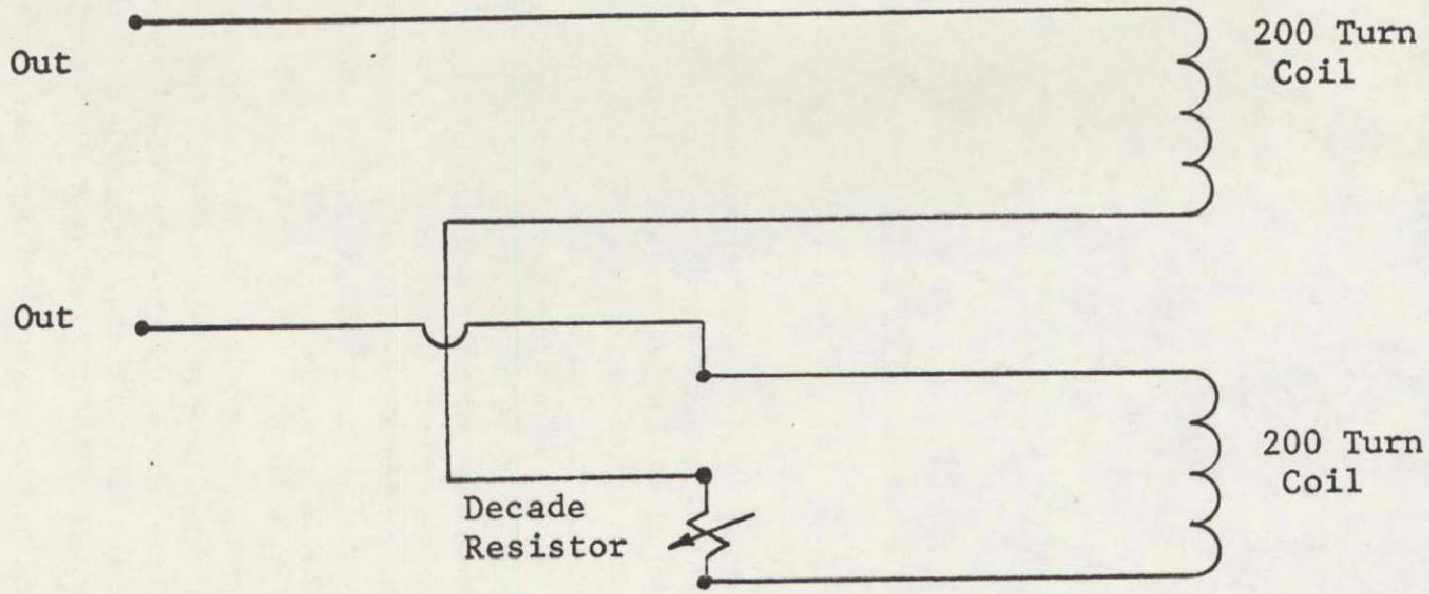

Figure VI-22. Schematic diagram of pickup coil circuit.

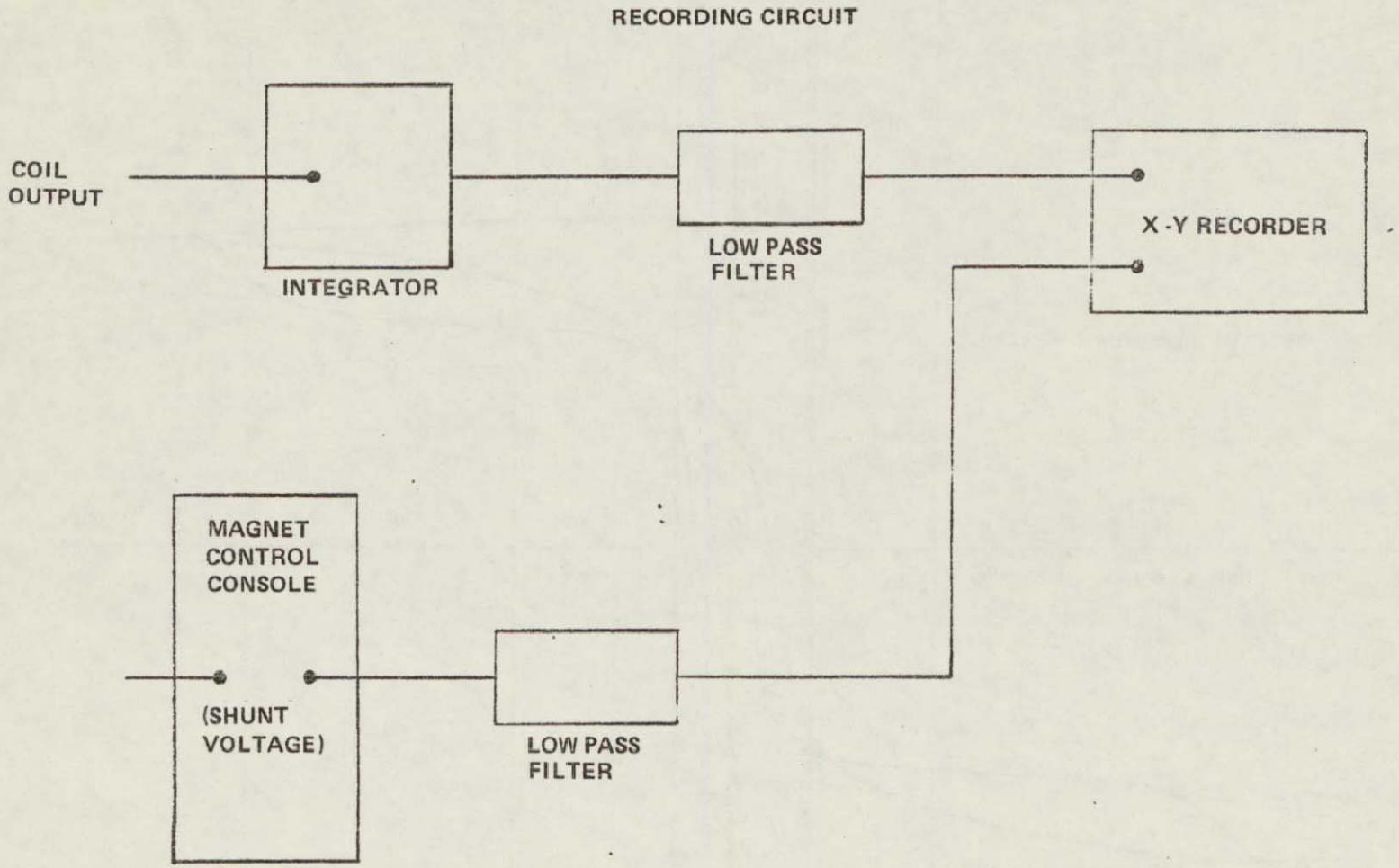

Figure VI-23. Schematic diagram of integrator circuit.

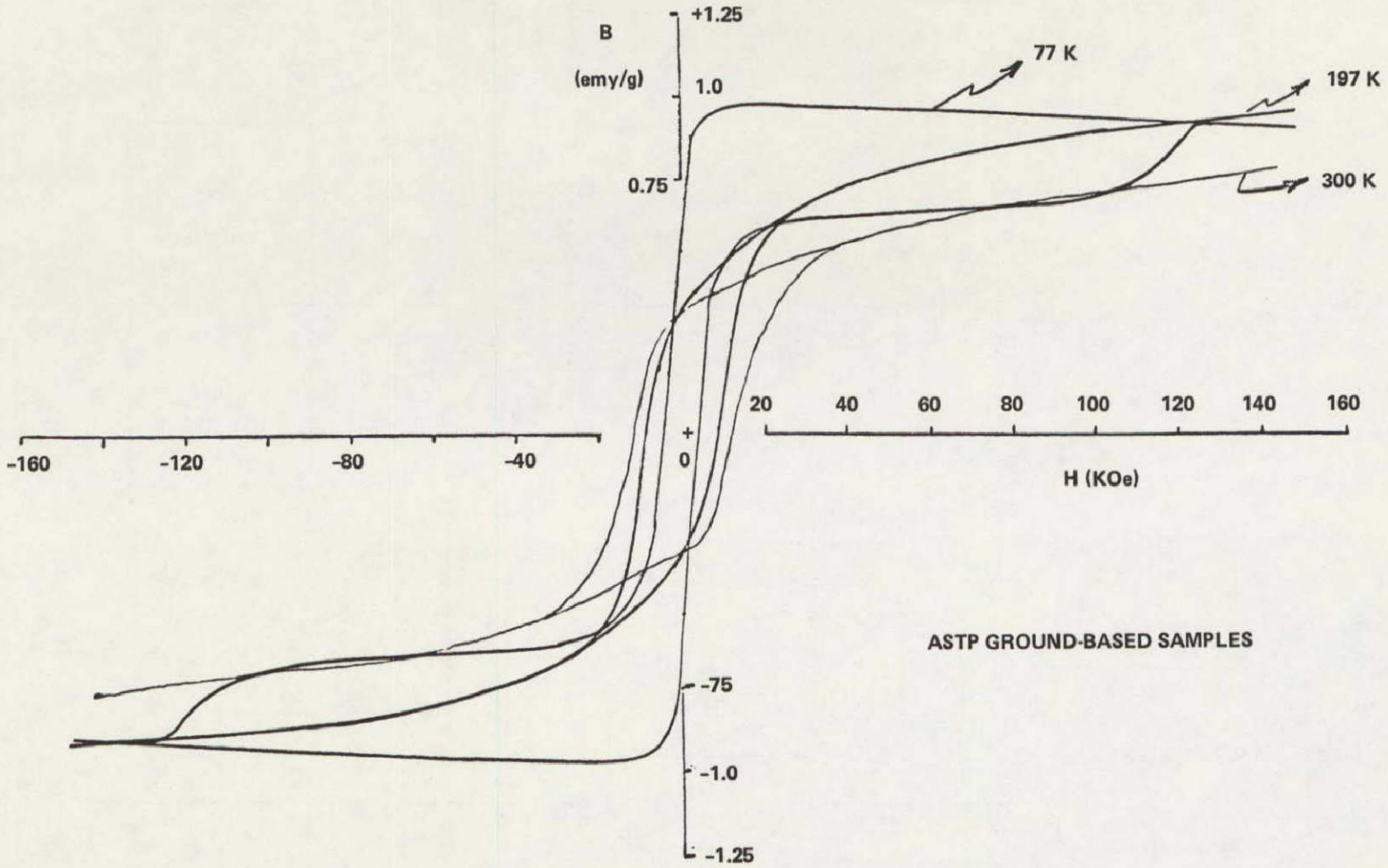

Figure VI-24. MnBi/Bi eutectic composite B-H behavior at 295, 197, and 77 K.

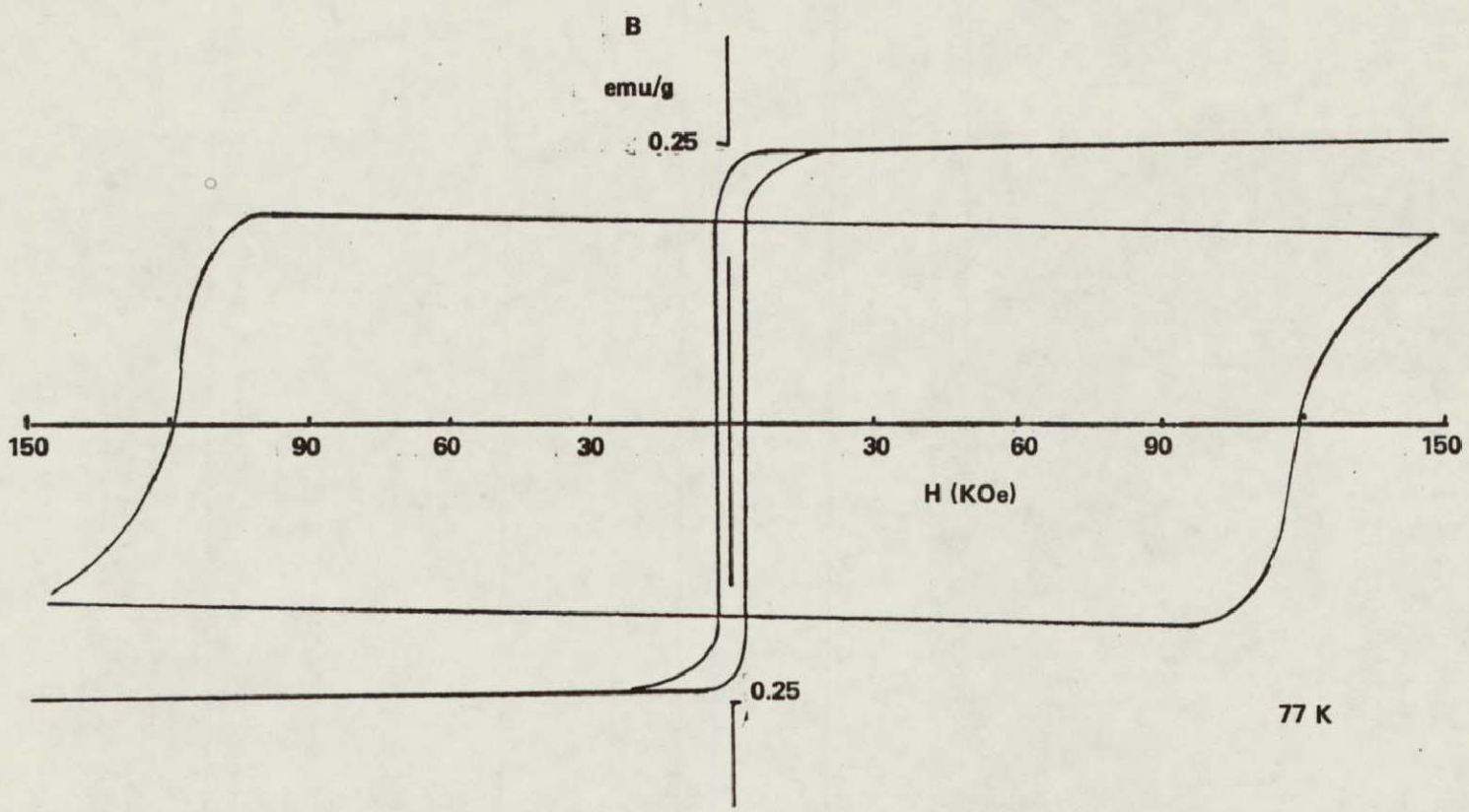

Figure VI-25. B-H component loops at 77 K.

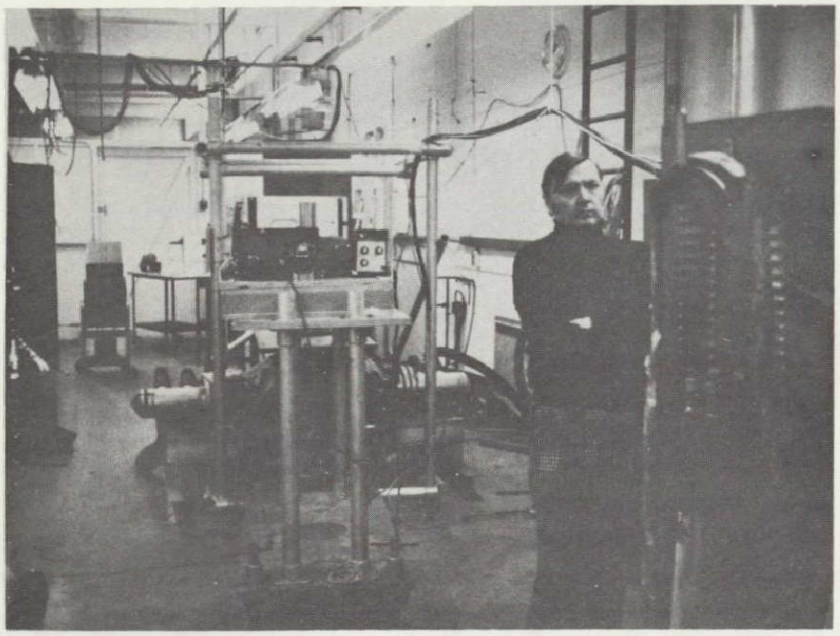

(a)

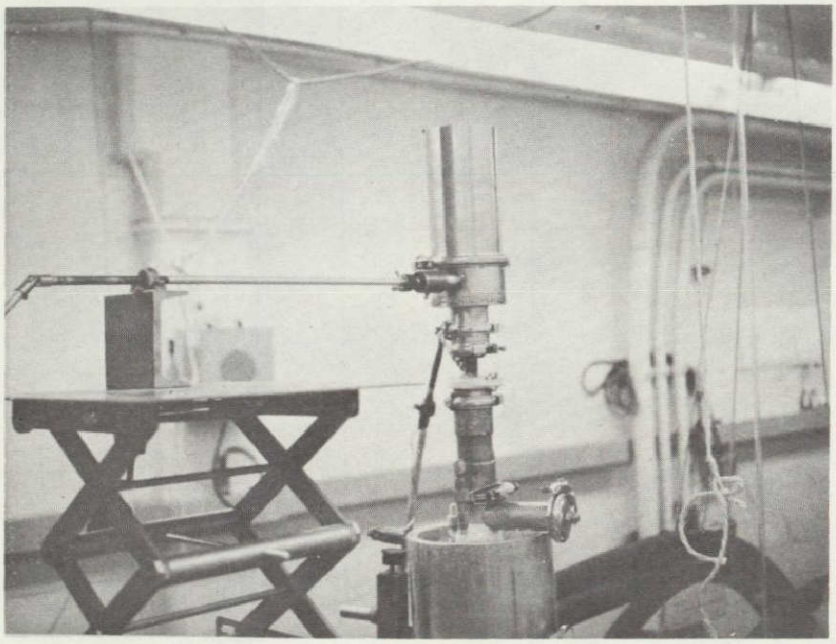

(b)

Figure VI-26. Low frequency vibrating sample magnetometer, (a) installation and (b) gear mechanism.

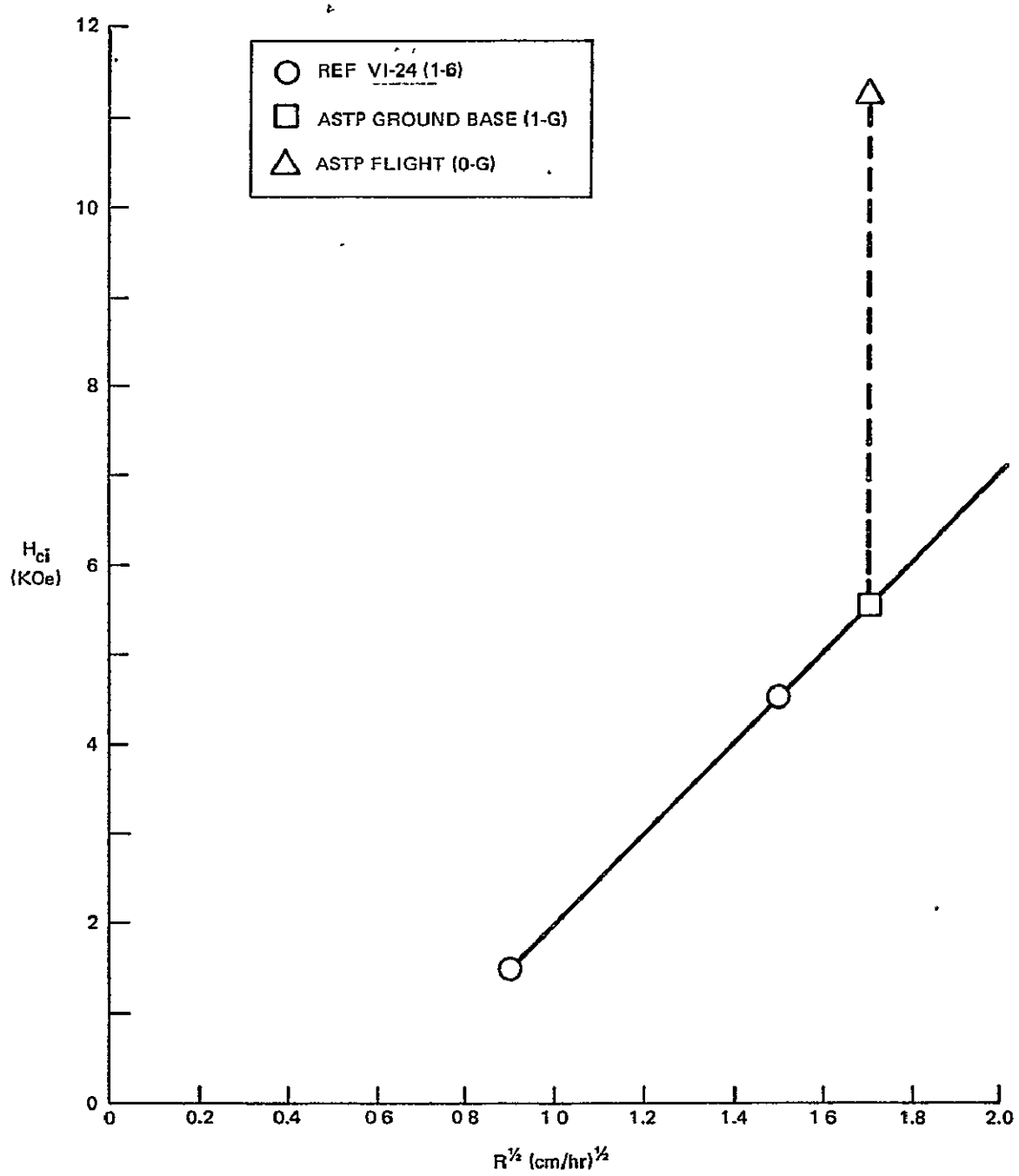

Figure VI-27. Intrinsic coercive strength (H_{ci}) versus the square root of the growth rate $(R)^{1/2}$ for as-grown MnBi/Bi eutectic composites.

than that of our experimentation. Although a steeper thermal gradient might be expected to impact the physical properties, no definitive study has been made to date to quantify this effect. To that extent, the comparisons are imprecise.

Representative B-H loops for ground-based samples have been shown for the eutectic composite at 299 K, 197 K, and 77 K in Figure VI-24. The configuration at 4.2 K is virtually identical to that at 77 K, except that the intrinsic coercive strength is slightly lower.

The magnetic anisotropy energy [VI-30] and the intrinsic coercive strength of the room temperature magnetic phase have been shown to decrease with temperature. These values are reported to reach zero at 85 K and 80 K, respectively. Neutron diffraction measurements [VI-31] have suggested that small positive values may be found even at very low temperatures. Our H_{ci} data for the ground-based and flight samples support the latter contention down to 4.2 K. Representative curves showing the temperature dependence of the room temperature magnetic phase from ground-based and flight samples is shown in Figure VI-28.

At temperatures below room temperature, a second magnetic component appears with extremely high coercivity [VI-24]. No magnetic property data as a function of growth rate have been published at cryogenic temperatures, so our low temperature data for our flight samples have been superimposed on the temperature dependence results of Reference VI-32. This is shown in Figure VI-29. The literature data shown in Figure VI-29 are from samples grown at 75 cm/h. It has been reported that the low temperature component appears only in samples grown at freezing rates in excess of 75 cm/h [VI-24]; however, our flight data for samples grown at 3 cm/h are not consistent with this conclusion.

The average values of intrinsic coercive strength are shown in Table VI-2 for the ASTP ground-based and flight samples. Work has continued, however, in the analysis of selected sample sections. An unexpected result, confirmed by other experts,[3] on MnBi behavior is illustrated in Figure VI-30. Sections of this type from the coordinated growth regions of the flight samples demonstrate the high field coercivity associated with the low temperature component but show positive field "collapse" upon field reduction.

Thermal cycling of this sample showed that the positive field "collapse" occurred at lower positive fields at 4.2 K than at 77 K. Restated, these results show a wider hysteresis in field strength at 4.2 K than at 77 K.

Some samples were heat treated at 90 percent of the absolute melting point for a period of 24 h and were furnace cooled. This heat treatment has been reported to substantially improve the room temperature intrinsic coercive

3. Personal communication with C. D. Graham, Jr., and M. R. Notis.

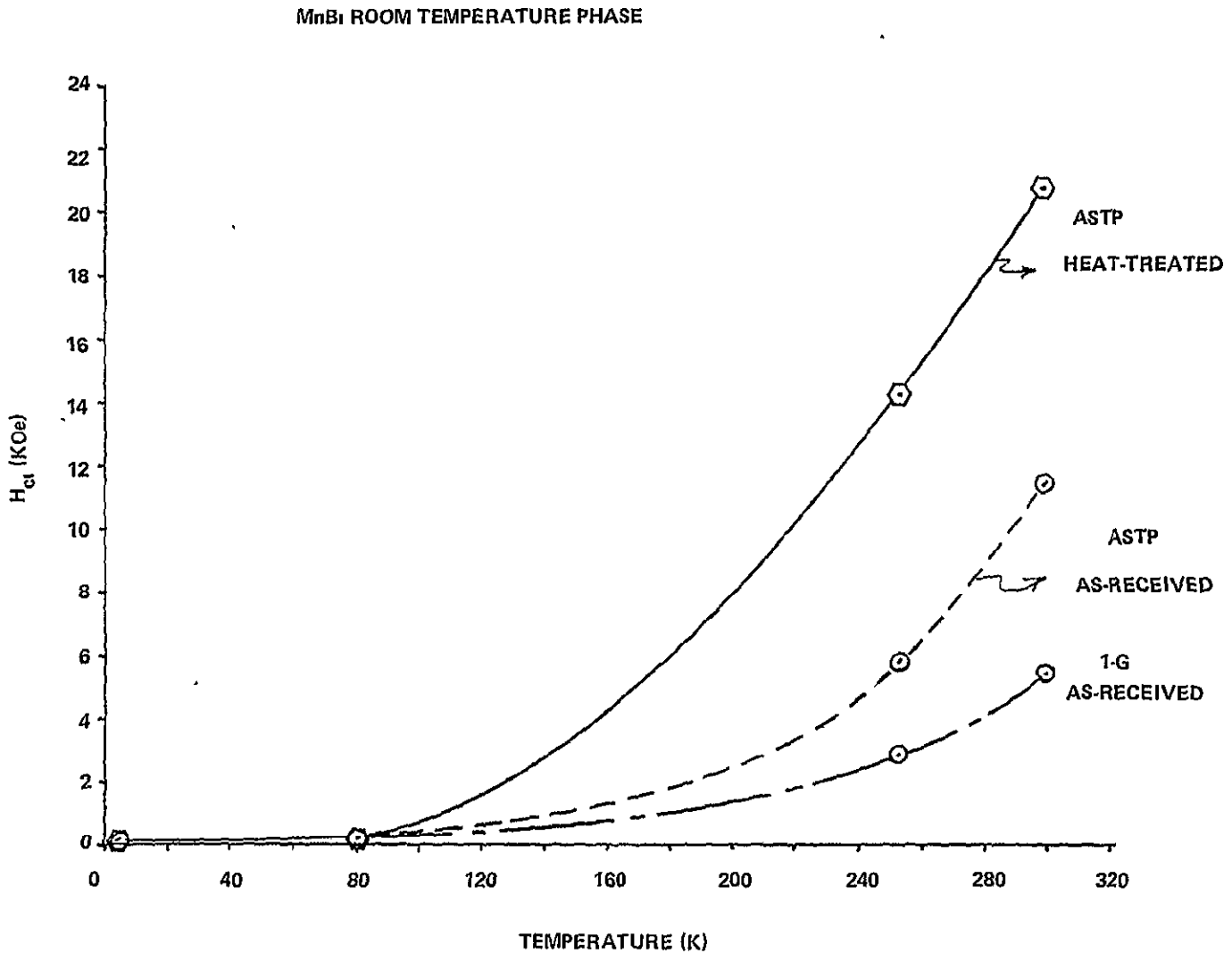

Figure VI-28. Intrinsic coercive strength (H_{ci}) versus temperature for the room temperature MnBi phase.

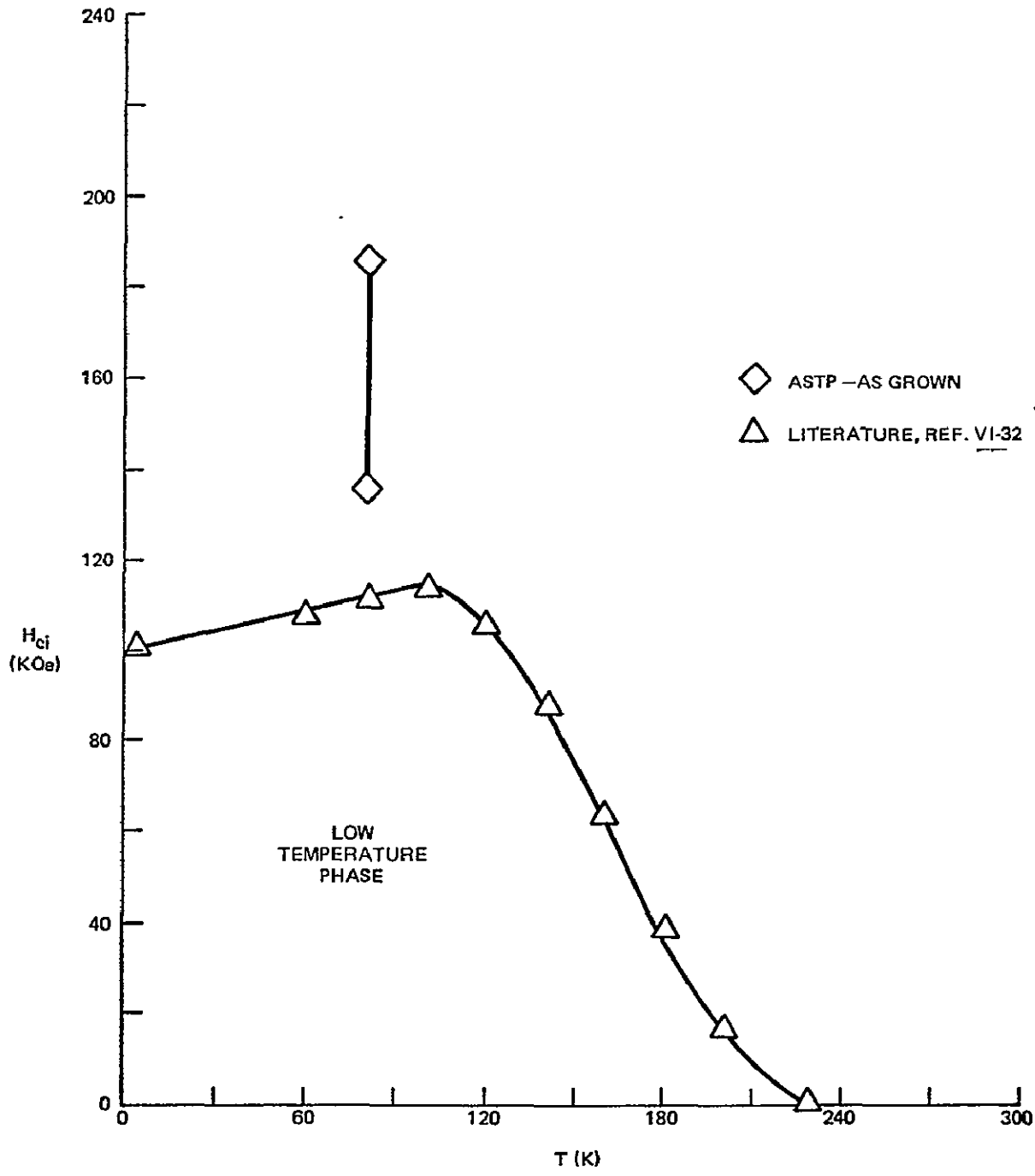

Figure VI-29. Intrinsic coercive strength (H_{ci}) versus temperature for the room temperature MnBi phase.

TABLE VI-2. AVERAGE VALUES OF INTRINSIC COERCIVE STRENGTH

Sample	Temperature (K)	Intrinsic Coercive Strength (KOe)
ASTP (1-g)	295	5.5
ASTP (0-g)		
8C	295	10.92
	253	5.88
	77	135
9C	295	13.93
	253	10.94
	77	185 145
10C	295	10.24
	77	117.5
	4.2	102
ASTP (0-g) Heat-treated	295	20.8
	243	13.08
	77	110
	4.2	102

strength. The H_{ci} of this sample increased from 11.47 KOe to 20.8 KOe, an 80 percent improvement. The heat treatment squared the B-H loop and increased the room temperature H_{ci}, as reported in Reference VI-24. The temperature behavior of the room temperature component of the heat-treated flight sample is shown in Figure VI-28. Essentially, the magnitudes are different, but the behavior as a function of temperature is consistent.

The heat-treated value of intrinsic coercive strength as a function of rod diameter is shown in Figure VI-31. Rod diameter has been selected for the abcissa in this case because the thermal-mechanical state of the composite should be equilibrated. The results indicate that the heat treatment is a determining factor in the final value of H_{ci}. Our data points are entirely consistent with those presented in the literature for similar heat treatments.

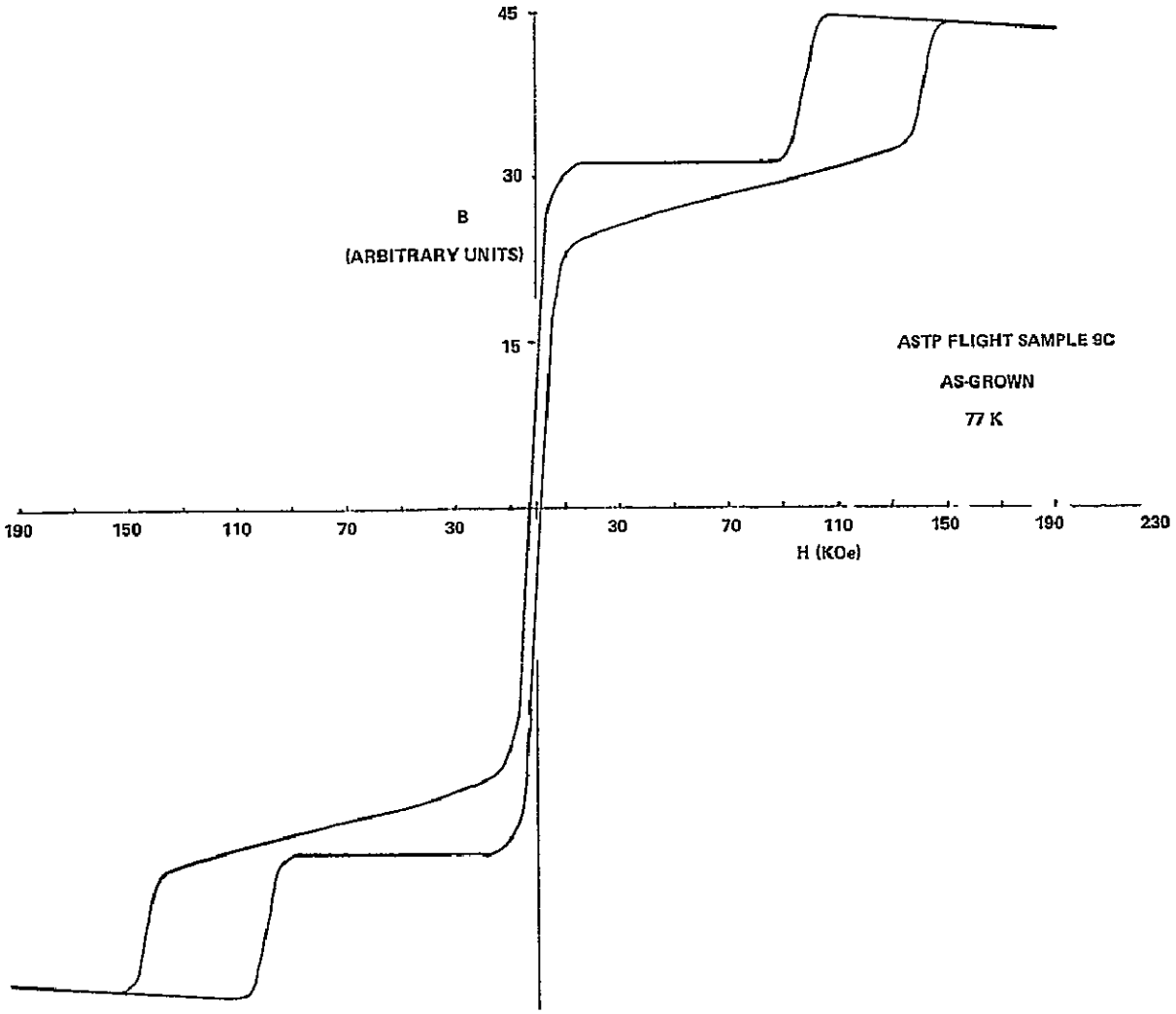

Figure VI-30. B-H loop for as-grown ASTP flight sample 9C at 77 K.

One last room temperature measurement was conducted on the heat treated sample. A B-H curve, with the rods transverse to the magnetic field, was measured and is shown in Figure VI-32. As may be seen, the sample was not saturated even at the highest field strength (223 kG). This was entirely expected, because theoretical estimates [VI-33] of the coercivity in a transverse field predicted that saturation would not occur until 200 to 250 KOe. It would appear that a field of 250 kG would be barely adequate for saturation studies.

In addition to intrinsic coercive strength, we have also measured the magnetization of the ASTP ground-based and flight samples. The average magnetization for magnetic MnBi/Bi eutectic composites is reported in the literature to be 0.6 emu/g [VI-24]. The average value for the ASTP flight samples was 1.05 emu/g. This is a substantial improvement over the previously

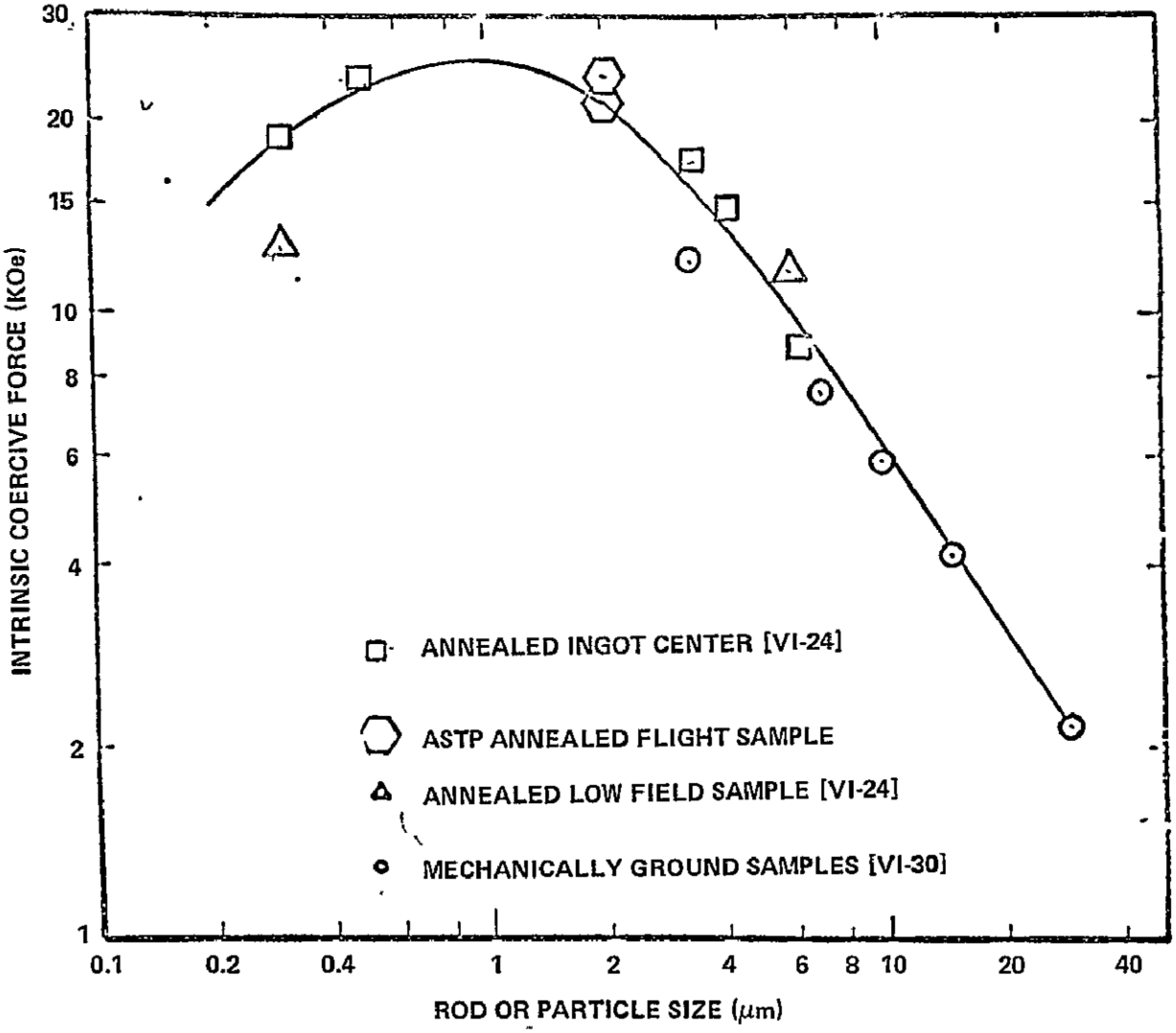

Figure VI-31. Intrinsic coercive strength at room temperature versus MnBi particle size for heat-treated MnBi/Bi eutectic composites and mechanically ground MnBi particles.

mentioned value; however, magnetizations an order of magnitude greater were measured within these samples on their first exposures to a magnetic field. These results were not possible to reproduce, and subsequent measurements gave the value quoted above. This variation in magnetization has been alluded to in the literature [VI-32] but remains unexplained. It indicates that although our average value of magnetization has shown improvement over the literature value, an additional improvement may well be possible with proper processing.

In summary, we may conclude that orbital processing of the eutectic MnBi/Bi composite has led to enhanced values of critical magnetic parameters

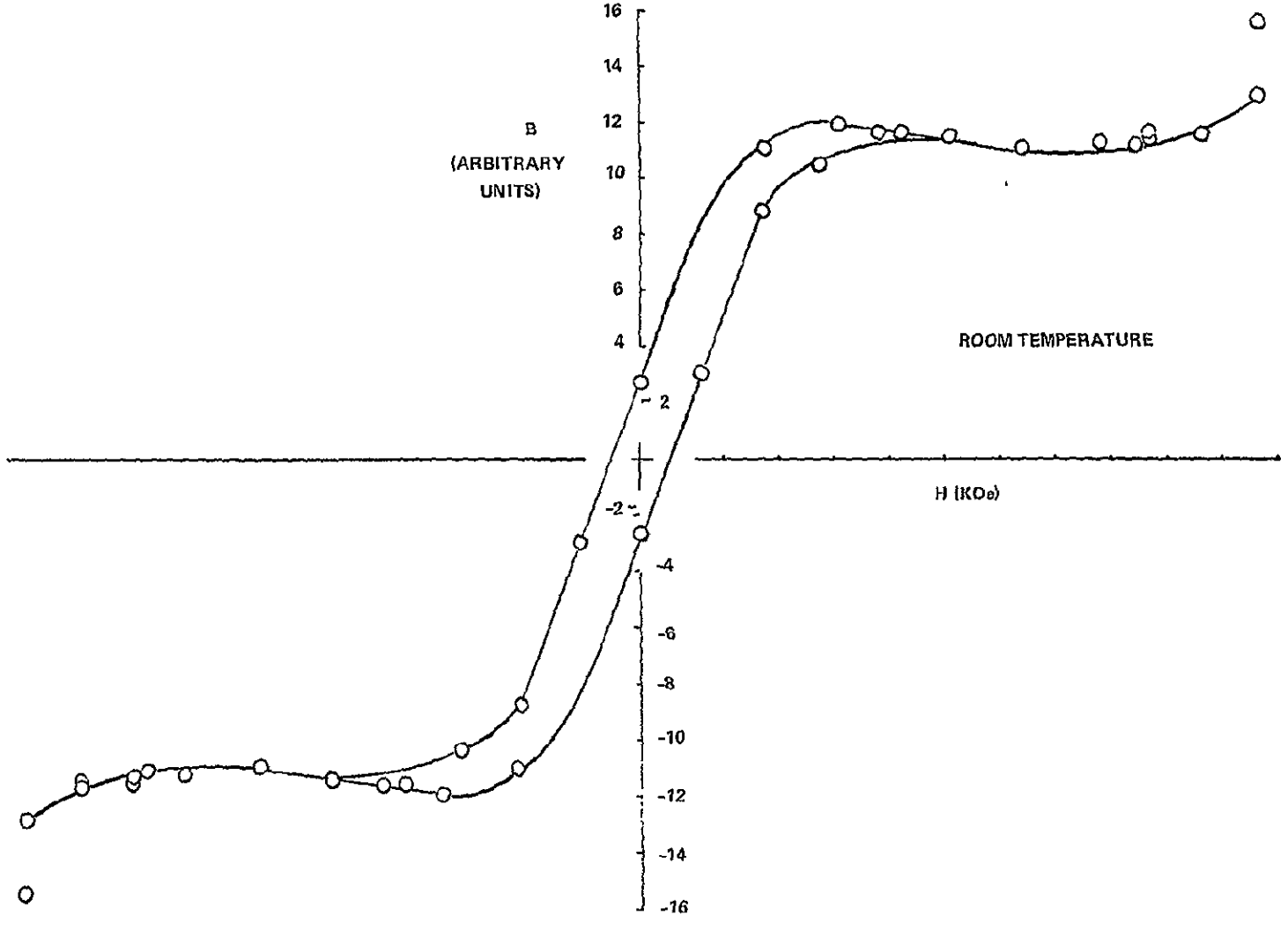

Figure VI-32. Room temperature B-H loop with transverse field for ASTP flight sample 11C (heat-treated).

B and H through particle refinement and alignment. The average improvement within these parameters was 60 percent. The precise reason for these improvements has not been ascertained to date; however, it seems reasonable to presume that the reduction of detrimental gravitationally dependent phenomena during solidification has resulted in these improvements in the as-received composites.

The magnetic results from the as-received No. 1 samples showed duplex behavior at room temperature. This behavior could be the result of a shift in the onset temperature of the low temperature magnetic component from 240 to 295 K or from particle size effects. In addition, substantial differences in magnetic behavior were noted depending on the orientation of the sample in the field. Since the microstructural analysis of the flight samples has shown that the microstructure is complex but nonrandom and that there are substantial differences in the MnBi particle size, it was decided to defer the magnetic analysis of these samples until all of the necessary magnetic analyses of the aligned, constant particle size eutectic samples are completed.

SUMMARY AND CONCLUSIONS

The intent of this project was to study the contained solidification of magnetic materials in a low-g environment. Although the work is not yet complete, the following conclusions may be drawn:

- Fluid static configurations in low-g were appreciably different than those in one-g but were found to agree well with theory.
- Bismuth undergoes a liquid phase transition, with large hysteresis, at 988 K on heating and 858 K on cooling.
- The MnBi phase diagram presented by Reference VI-24 is preferred.
- Macroscopic chemical segregation due to gravitationally dependent buoyancy forces is minimal in low-g.
- The number and size distribution of orbitally processed primary crystals are significantly different in the flight samples.
- The intrinsic coercive strength of as-grown low-g MnBi/Bi eutectic samples greatly exceeds any values previously reported for this magnetic composite (greater than 60 percent).

- The solidification product from the orbital processing of the Bi/MnBi faceted rod eutectics differs in particle size, lattice parameter, and magnetic properties from equivalently processed terrestrial samples.

RECOMMENDATIONS FOR FUTURE WORK

The data generated in this program suggest that additional work is justified in the following areas:

- Directional solidification should be conducted, in orbit, that minimizes the impact of thermotransport. This will allow a conclusion to be made as to whether thermotransport was a significant factor in the ASTP processing and the ASTP sample performance.

- If thermotransport is shown to have an enhanced role in the convectionless environment, it should be incorporated into the analytical models for directional solidification in the low-g environment. This model should then be experimentally tested.

- Analytical and hardware development should be pursued that would allow floating-zone directional solidification to be accomplished on Shuttle.

- Orbital processing of magnetic composites should be pursued to determine whether the substantial improvement in magnetic performance is limited to the MnBi/Bi eutectic composite or whether it is more general in scope.

REFERENCES

VI-1. Polgreen, G. R.: New Applications of Modern Magnets. MacDonald, London, 1966.

VI-2. Lee, E. W.: Magnetism. Pelican, London, 1963.

VI-3. Iden, D. J.; Ehrenfried, C. E.; and Garrett, H. J.: Magnetism and Magnetic Materials. AIP Conference Proceedings, no. 5, 1971, p. 1026.

VI-4. Strnat, K. J.: The Recent Development of Permanent Magnetic Materials Containing Rare Earth Metals. AFML-TR-69-299, June 1970.

VI-5. Becker, J. J.; Luborsky, F. E.; and Martin, D. L.: IEEE Trans. Mag., Mag. 4, 1968, p. 84.

VI-6. Hoffer, G. and Strnat, K.: IEEE Trans. Mag., Mag. 2, 1966, p. 487.

VI-7. Strnat, K. et al.: J. Appl. Phys., vol. 38, 1967, p. 1001.

VI-8. Buschow, K. H. J. and Velge, W. A. J. J.: Z. Angew. Physik, vol. 26, 1969, p. 157.

VI-9. Strnat, K. J.: Cobalt, no. 36, 1967, p. 133.

VI-10. Nesbitt, E. A.: J. Appl. Phys., vol. 40, 1969, p. 1259.

VI-11. Faltermayer, E.: Fortune, vol. 86, 1972, p. 99.

VI-12. Prototype Test Report for MA-010 Experiment Cartridges. Westinghouse Electric Corporation, Astronuclear Laboratory, Technical Report WANL-TME-2867, May 1975.

VI-13. Thermal Analysis of the Apollo Soyuz Test Project MA-070 Experiment in the Flight Environment. Teledyne Brown Engineering, Technical Letter ASD-EP44-22740 (SO-E017-Par III) H72, January 21, 1976.

VI-14. Witt, A. F.; Gatos, H. C.; Lichtensteiger, M.; Lavine, M. C.; and Herman, C. J.: Steady State Growth and Segregation Under Zero Gravity: InSb. Proceedings of the Third Space Processing Symposium-Skylab Results, NASA TM X-70252, 1974, pp. 275-288.

VI-15. Hasemeyer, Earl A.; Lovoy, Charles V.; and Lacy, L. L.: Skylab Experiment M566 Copper-Aluminum Eutectic. Proceedings of the Third Space Processing Symposium-Skylab Results, NASA TM X-70252, 1974, pp. 457-461.

VI-16 Clodfelter, Robert G. and Lewis, Roger C.: Fluid Studies in a Zero Gravity Environment. Wright-Patterson AFB, Technical Note 61-84, June 1961.

VI-17. Clodfelter, Robert G.: Fluid Mechanics and Tankage Design for Low Gravity Environments. Wright-Patterson AFB, ASD-TDR-63-506, September 1963.

VI-18. Clodfelter, Robert G.: Low Gravity Pool Boiling Heat Transfer. Wright-Patterson AFB, APL-TDR-64-19, March 1964.

VI-19. Vezzoli, Gary C.: Electrical Resistance of Liquid Sulfur to 420°C and of Liquid Selenium to 700°C. American Ceram. Soc. J., vol. 55, 1972, p. 2.

VI-20. Siebe, P.: Z. Anorg. Chem., vol. 108, 1919, pp. 161-171.

VI-21. Willis, B. T. M. and Rooksby, H. P.: Proc. Phys. Soc. (London), vol. 67B, 1954, pp. 290-296.

VI-22. Chen, T. and Stutius, W. E.: The Phase Transformation and Physical Properties of the Mn Bi and $Mn_{1.08}$ Bi Compounds. IEEE Transactions on Magnetics, MAG-10, 1974, p. 3.

VI-23. Hunt, J. D. and Jackson, K. A.: Eutectic Solidification. Trans. Met. Soc. AIME, vol. 236, 1966, p. 843.

VI-24. Boulbes, J. C.; Kraft, R. W.; Notis, M. R.; and Graham, C. D. Jr.: Proceedings of the Conference on in situ Composites. Lakeville, Connecticut, 1972, National Materials Advisory Board Special Publication 308.

VI-25. Cline, H. E., and Livingston, J. E.: High Speed Directional Solidification of Sn-Pb Eutectic Alloys. Trans. Met. Soc. AIME, vol. 245, 1969, pp. 1987-1992.

REFERENCES (Concluded)

VI-26. Verhoeven, J. D.; Warner, J. C.; and Gibson, E. D.: Met. Trans., vol. 3, 1972, pp. 1437-1441.

VI-27. Albright, D. L.; Conrad, G. P., II; and Kraft, R. W.: Magnetic Behavior of a Eutectic Alloy Featuring and Aligned Array of Iron Rods. J. Appl. Phys., vol. 38, 1967, p. 2219.

VI-28. Stoner, E. C. and Wohlfarth, E. P.: A Mechanism of Magnetic Hysteresis in Heterogeneous Alloys. Phil. Trans. Roy. Soc., vol. 240, 1948, p. 74.

VI-29. Foner, S.: Rev. Sci. Instr., vol. 30, 1959, p. 548.

VI-30. Guillaud, C.: Thesis, University of Strasbourg, 1943.

VI-31. Roberts, B. W.: Phys. Rev., vol. 104, 1956, p. 607.

VI-32. Boulbes, J. C.: M.S. Thesis, Lehigh University, 1972.

VI-33. Noothoven van Goor, J. M. and Zijlstra, H.: J. Appl. Phys., vol. 39, 1948, p. 5471.

SECTION VII

CRYSTAL GROWTH FROM THE VAPOR PHASE

EXPERIMENT MA-085

By H. Wiedemeier,[1,2] H. Sadeek,[1] F. C. Klaessig,[1]
M. Norek,[1] and R. Santandrea[1]

1. Rensselaer Polytechnic Institute, Troy, New York
2. Principal Investigator

TABLE OF CONTENTS

LIST OF ILLUSTRATIONS

LIST OF ILLUSTRATIONS (Concluded)

LIST OF TABLES

ABSTRACT

The positive effects of microgravity on crystal quality and the fundamental properties of the vapor transport reaction were established by analyzing the results of three transport experiments on multicomponent systems performed during the Apollo-Soyuz Test Project mission. The systems employed were $GeSe_{0.99}Te_{0.01}$ - GeI_4 (A), $GeS_{0.98}Se_{0.02}$ - $GeCl_4$ (B), and GeS-$GeCl_4$-Ar (C).

The crystallographic analysis is based on a direct comparison of space and ground-based (prototype) crystals employing X-ray diffraction, microprobe, microscopic, and chemical etching techniques. The results demonstrate a considerable improvement of the space-grown crystals in terms of chemical and crystalline homogeneity, surface morphology, and bulk perfection relative to ground specimens. The confirmation of greater mass transport rates than predicted for microgravity by present vapor transport models is of basic scientific and practical importance for the improvement of transport models and techniques on Earth and for the development of a transport model for space conditions. The internal consistency and agreement between our Apollo-Soyuz Test Project and Skylab results obtained for different compounds, transport agents, and temperature gradients strongly support the validity of these observations. The combined findings of improved crystal quality and high mass transport rates are of technological significance for space processing applications.

INTRODUCTION

Crystal growth by chemical vapor transport is of technological importance for the production of bulk and layer type single crystalline materials used in various electronic devices. It is well known that the performance characteristics of electronic materials are critically dependent on their degree of chemical homogeneity and crystalline perfection. These material properties are affected by the transport and growth conditions of a given chemical system. Complete control of these growth parameters under ground-based conditions is limited due to the presence of gravity-driven convection. Under otherwise optimal growth conditions on Earth, convective interference with the transport process causes crystalline imperfections.

Crystal growth in a microgravity environment in the absence of convective interference should produce crystals of improved quality and yield fundamental data for the vapor transport process. These expectations were confirmed

confirmed by the results of Skylab experiment M556. In the Skylab experiments [VII-1, VII-2] representative compounds of IV-VI materials, GeSe and GeTe, were transported with GeI_4 as a transport agent. The single crystals grown in space are of considerably improved structural perfection compared to corresponding ground-based specimens. The second major result of the Skylab studies is the observation of greater mass transport rates in microgravity than predicted for a diffusion type transport process. In view of the far reaching scientific and technological implications of the observations, the Skylab results served as a basis for the definition of the Apollo-Soyuz Test Project (ASTP) experiments. The primary objectives of experiment MA-085 performed on the Apollo-Soyuz mission were to extend and generalize microgravity crystal growth for a class of compounds and to characterize the unexpected gas motion observed on Skylab. For this purpose, new compounds and solid solutions were transported with different transport agents in higher temperature gradients. In addition, inert atmosphere was employed in one of the transport ampoules. Details of the experimental design and chemical systems are discussed in the following paragraphs.

This report is based on the present analysis of three transport experiments performed in space. The data demonstrate improved crystalline perfection for the space-grown material relative to ground-based samples. These results confirm the Skylab observations and extend the conclusions drawn to more complex systems. In addition, the mass transport rates observed in space are considerably greater than predicted by theory. The latter results not only confirm Skylab data, but provide experimental evidence for the cause of the higher than expected mass fluxes.

In view of the technological importance of single crystals for solid state devices and because of their high yield to weight ratio, crystal growth by vapor transport is a primary candidate for space processing applications. It is a definite purpose of our ground-based and microgravity transport studies to provide the scientific and technical basis for actual space manufacturing. In addition, knowledge gained from these space experiments will be of practical use for the improvement of crystal growth techniques on Earth.

GROUND-BASED STUDIES

Basic Theory

In a chemical transport reaction [VII-3], a gaseous transport agent reacts at a given temperature with the solid source material to form exclusively gaseous products. This process is represented by the following reaction:

$$x\,A(s) + y\,B(g) = z\,C(g) + \ldots \quad . \qquad (1)$$

The number of different gaseous products formed depends on the particular chemical system. The vapor species migrate in the reaction vessel from the source to the condensation region where, at different temperature, the reverse reaction occurs with formation of the solid. The necessary concentration gradient is established by means of a temperature gradient that yields different equilibrium constants for reaction (1) and, thus, different partial pressures of the gaseous species in the source and condensation zone of the system. According to reaction (1), the solid A is transported via the gas phase by means of a chemical reaction which is distinctly different from a transport by sublimation. Under optimal experimental conditions, well defined single crystals of the source material are obtained by the condensation reaction. Depending upon the thermodynamic properties of the transport reaction, a chemical transport can occur from high to low temperature or vice versa. This aspect is of practical importance with respect to the choice of transport agent and condensation temperature. The transport reaction is performed in evacuated sealed ampoules of fused silica that are conventionally subjected to the desired temperature gradient in a horizontal two-zone tubular resistance furnace.

The migration of gas phase species can be described by diffusion and by gravity-driven convection. In a gravitational field and temperature gradient, both transport modes occur simultaneously. It is a unique feature of the vapor transport technique to select experimental conditions such that one or the other mode can be predominant. Under ground-based conditions the convective contribution to the overall transport process can be minimized, but not eliminated. Based on present models for diffusive and convective gas motion [VII-3], the material flux from the source to the condensation region is affected by the pressure in the transport ampoule. At very low pressures of transport agent, the mass transport rate is controlled by the rate of the heterogeneous solid-gas phase reaction in the source and/or condensation region. Under these conditions the material flux is proportional to the concentration of transport agent. At medium pressures the transport rate is inversely proportional to the total pressure. The overall transport is diffusion controlled in this range. At higher pressures the material flux increases with increasing total pressure indicating the predominance of the convective transport mode. For the conditions of the diffusion and convection controlled transport modes, the heterogeneous solid-gas phase reactions in the source and condensation zone are fast.

Transport Properties of IV-VI Compounds

Mass transport rate studies on GeTe [VII-4] and GeSe [VII-5] confirmed the general shape of flux versus total pressure curves predicted by the previously mentioned models. Details of the experimental procedures and results have been discussed previously [VII-4, VII-5]. The most important observation of these studies is the decrease in crystal perfection with increasing contribution of the convective component to the overall transport process. Transport studies in our laboratory on GeS using $GeCl_4$ as a transport agent and different temperature gradients show the diffusion and convection controlled transport regimes in agreement with these systems [VII-4, VII-5]. In particular, the changes in crystal morphology and habit of GeS as a function of transport mode reveal the negative effects of convective interference on crystal quality. The ground-based studies and the solid solution properties of these binary systems led to the definition of mixed systems for two of the three transport experiments performed on the ASTP mission. The chemical composition of the mixed systems is given by the formulas $GeSe_{0.99}Te_{0.01}$ (A) and $GeS_{0.98}Se_{0.02}$ (B), respectively. The third transport ampoule (system C) contained GeS and a mixture of $GeCl_4$ and argon. Quantitative mass transport rate studies in terms of flux as a function of pressure were performed in our laboratory on these systems in the temperature gradient 604° →507°C. The transport agent employed was GeI_4 for system (A) and $GeCl_4$ for systems (B) and (C). The flux is calculated from the amount of crystals recovered, the cross section of the ampoule, and the duration of the experiment. The pressure is computed for the mean temperature of the gradient from the amount of transport agent added, assuming ideal conditions and $GeI_4(g)$ or $GeCl_4(g)$, respectively. In system (C), the partial pressure of argon in the ampoule was approximately twice the pressure of the transport agent $GeCl_4$. The flux is plotted as a function of transport agent pressure to be consistent with systems (A) and (B), as represented in Figure VII-1. For comparative purposes the flux results of the GeS-$GeCl_4$ system are also included in Figure VII-1. The flux curves of all systems have the same shape as observed earlier [VII-5]. The diffusion controlled region at lower pressures shows a decrease in flux with increasing pressure. The range of predominantly convective transport is characterized by an increase in flux with increasing pressure. The leveling of the flux curve for system (A) at higher pressures is due to the precipitation of the transport agent, thus establishing a constant saturation pressure in the ampoule. The flux curves in Figure VII-1, determined in our laboratory, serve as a basis for the evaluation of the space experiments. For the direct comparison of mass transport rates and crystals obtained on Earth and in space, a set of three ampoules containing the same amount of starting materials and transport agent as the corresponding ampoules used on the ASTP mission were processed in the prototype furnace. This furnace and the prototype transport conditions were identical to the furnace and conditions employed in space, except for gravity.

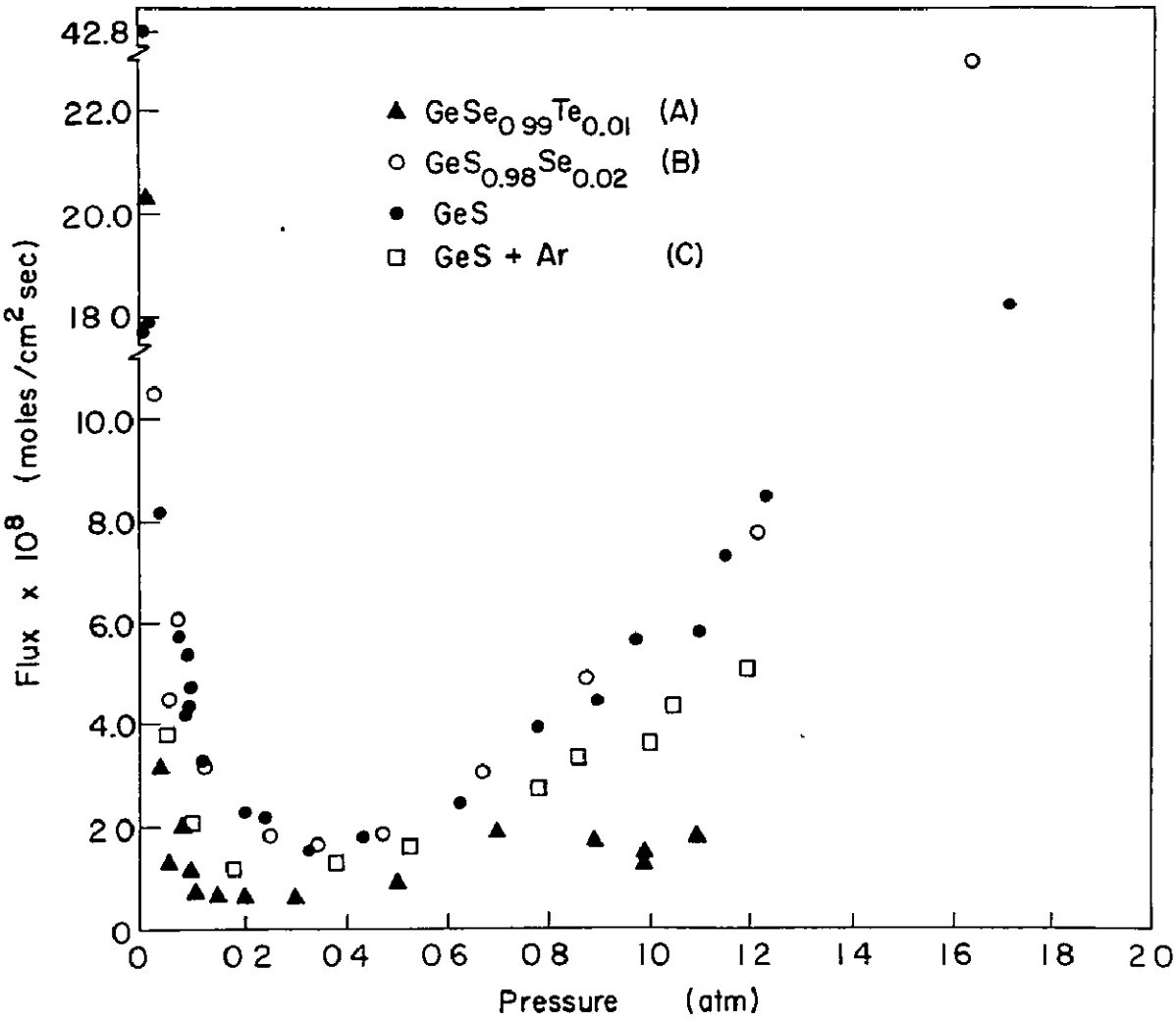

Figure VII-1. Mass transport rates in terms of flux versus pressure of transport agent for the temperature gradient 604°→507°C determined under ground-based conditions.

EXPERIMENTAL ASTP PROCEDURES

Apparatus

The transport experiments were performed in the multipurpose electric furnace which consisted essentially of a cylindrical furnace chamber and an instrumentation compartment. The furnace chamber contained three tubular reaction cavities for the individual metal cartridges and quartz ampoules discussed later. Since the furnace was heated resistively (one zone) at the source

region, the desired temperature gradient and stability were achieved by heat shields surrounding the quartz ampoules in the metal cartridges and by appropriate heat shields in the furnace. The temperature gradient employed for these experiments in space was 604°→507° C with a shallow gradient in the hot zone and a nearly linear gradient between the hot and cold zone of the reaction chamber. During the performance of the transport experiments, the furnace temperatures were constantly monitored at the outside of the metal cartridges in the hot and cold zones. The difference between furnace temperature and actual ampoule temperature was calibrated under identical ground-based conditions using thermocouples.

Ampoule and Sample Preparation

The transport ampoules were made of fused silica tubing of 13.7 mm inner diameter and 150 mm in length. Close to the rounded end, the ampoules contained two thin silica rods to hold the source material in place. The other ampoule end was sealed after loading at a pressure of 10^{-6} torr or less. Prior to loading, the cleaned ampoules [VII-4, VII-5] were outgassed at a temperature of approximately 1000°C for 10 h and a vacuum of 10^{-6} torr. The polycrystalline starting materials were synthesized by repeated annealing at approximately 600°C of stoichiometric mixtures of the binary compounds GeS, GeSe, and GeTe. The latter were prepared from high purity elements (99.999 percent) by annealing and subsequent sublimation of the produce [VII-4, VII-5]. The crystallographic identity of all materials was established by X-ray diffraction techniques. High purity GeI_4 (99.999 percent) and $GeCl_4$ (99.999 percent) were used as transport agents. Ultrahigh purity argon was employed as the inert gas in one system. The ampoule designated 3A in this experiment contained 1.50 g of $GeSe_{0.99}Te_{0.01}$ and 123.5 mg of GeI_4. Ampoule 3B was loaded with 1.50 g of $GeS_{0.98}Se_{0.02}$ and 59.1 mg of $GeCl_4$. The third ampoule (3C) contained 1.50 g of GeS, 61.8 mg of $GeCl_4$, and 1.91 atm of argon at the mean temperature of the gradient. The ampoules used for the ground-based prototype tests (2A, 2B, and 2C) were of the same dimensions and contents. The chemical transport reactions for the binary compounds and the experimental conditions employed for the ASTP mission are summarized in Table VII-1. The transport reactions of the mixed systems are analogous. The total pressures in terms of $GeI_4(g)$ or $GeCl_4(g)$ are calculated for the mean temperature of the gradient and ideal gas conditions. The partial pressure of argon in ampoule 3C is twice the pressure of the transport agent $GeCl_4$. Thus the total pressure in ampoule 3C is approximately three times the pressure in ampoule 3B.

TABLE VII-1. TRANSPORT REACTIONS AND EXPERIMENTAL CONDITIONS

$GeSe(s) + GeI_4(g) = 2\ GeI_2(g) + 1/2\ Se_2(g)$	
$GeTe(s) + GeI_4(g) = 2\ GeI_2(g) + 1/2\ Te_2(g)$	
$GeS(s) + GeCl_4(g) = 2\ GeCl_2(g) + 1/2\ S_2(g)$	
ΔT: 604° → 507°C	
$GeSe_{0.99}Te_{0.01}$ (3A)	$P(GeI_4(g)) = 0.70$ atm
$GeS_{0.98}Se_{0.02}$ (3B)	$P(GeCl_4(g)) = 0.94$ atm
GeS (3C)	$P(GeCl_4(g)) = 0.96$ atm
	$P(Ar) = 1.91$ atm

Heating Cycle and Return of Ampoules

The transport ampoules were enclosed in hermetically sealed metal cartridges that were inserted into the multipurpose furnace by the astronauts. Details of the cartridges have been described previously [VII-1]. After a heating period of approximately 2 h the desired temperature gradient was achieved and maintained for 16 h. After termination of the experiment, cooling of the cartridges to ambient temperatures occurred over a period of approximately 4 h during which a helium quench was employed.

After opening the cartridges at the George C. Marshall Space Flight Center, none of the ampoules showed any mechanical damage and the residual source material in all ampoules was firmly attached to the ampoule wall in the source region. The ampoules were brought to our laboratory at Rensselaer Polytechnic Institute for analysis of these experiments.

RESULTS AND DISCUSSION

The analysis of the transport experiments performed on the ASTP mission is based on X-ray diffraction, microprobe, microscopic, and chemical etching techniques and on mass transport rate measurements. The results to date are summarized in the following paragraphs.

Crystallographic Identification of Transport Products

The crystallographic identification of space-grown crystals was established by means of Debye-Scherrer and Laue X-ray diffraction techniques. For the Debye-Scherrer method, randomly selected crystals were finely powdered, sealed in thin-walled glass capillaries, and exposed to CuKα radiation in a 114.59 mm diameter camera. For the Laue method, individual single crystal platelets were mounted on the crystal holder of a conventional Laue camera and exposed to CuKα radiation. The results in terms of lattice parameters (Debye-Scherrer) and crystallographic orientation of as-grown predominant faces (Laue) are summarized in Table VII-2 together with corresponding data for ground-based (prototype) crystals.

TABLE VII-2. CRYSTALLOGRAPHIC PARAMETERS OF ASTP AND GROUND-BASED CRYSTALS

System	Lattice Parameters (Å)			Orientation
	a_o	b_o	c_o	
$GeSe_{0.99}Te_{0.01}$ (Ground-Based)	4.385 ± 0.008	3.838 ± 0.007	10.791 ± 0.019	(001)
$GeSe_{0.99}Te_{0.01}$ (ASTP 3A)	4.386 ± 0.008	3.839 ± 0.007	10.793 ± 0.020	(001)
$GeS_{0.98}Se_{0.02}$ (Ground-Based)	4.301 ± 0.009	3.651 ± 0.008	10.431 ± 0.020	(001)
$GeS_{0.98}Se_{0.02}$ (ASTP 3B)	4.302 ± 0.012	3.652 ± 0.010	10.432 ± 0.022	(001)
GeS (Ground-Based)	4.299 ± 0.008	3.649 ± 0.007	10.428 ± 0.019	(001)
GeS (ASTP 3C)	4.301 ± 0.006	3.651 ± 0.005	10.430 ± 0.015	(001)

A comparison of the data in Table VII-2 shows that the lattice constants of the respective systems are in excellent agreement. There is no change in the orientation of predominant native faces of single crystals. Within the detection limits of X-ray diffraction techniques, there is no measurable effect of microgravity on the crystallographic parameters of space-grown crystals. These results are expected in view of the relative magnitude of chemical bonding and gravitational forces.

Transmission Laue photographs of $GeSe_{0.99}Te_{0.01}$ ground (2A) and space (3A) crystals indicate considerable differences as shown in Figure VII-2. The diffraction pattern of the ground-based crystal, Figure VII-2(a), reveals striations and multiplicity of individual diffraction spots. This indicates a high degree of strain and structural inhomogeneities of the ground specimen. The Laue pattern of the space crystal, Figure VII-2(b), reveals the two-fold symmetry of the predominant (001) oriented growth face. The considerably better defined diffraction spots indicate improved crystallographic perfection compared to the ground-based sample.

Corresponding diffraction patterns of $GeS_{0.98}Se_{0.02}$ ground (2B) and space (3B) crystals in Figure VII-3 demonstrate a pronounced improvement in crystallinity of the space sample, Figure VII-3(b), relative to the ground specimen, Figure VII-3(a). The rather well defined diffraction spots of the space crystal, Figure VII-3(b), reveal a considerable degree of crystallographic perfection that has not been observed for ground crystals obtained under these conditions.

Laue diffraction patterns of GeS ground (2C) and space (3C) crystals in Figure VII-4, grown in the presence of argon, indicate some degree of strain in both cases. Since crystals obtained under these conditions are considerably thinner than those of systems (A) and (B), it is presently difficult to decide whether the observed strain is caused by mechanical handling of the sample or by the inclusion of argon into the crystal lattice.

The combined results of the diffraction studies for systems (A) and (B) demonstrate the distinctly improved structural homogeneity and perfection of the crystals obtained in the microgravity environment.

Chemical Homogeneity of Crystals

In order to examine the chemical homogeneity of the solid solutions (systems A and B), the distribution of Te in GeSe (A) and of Se in GeS (B) was

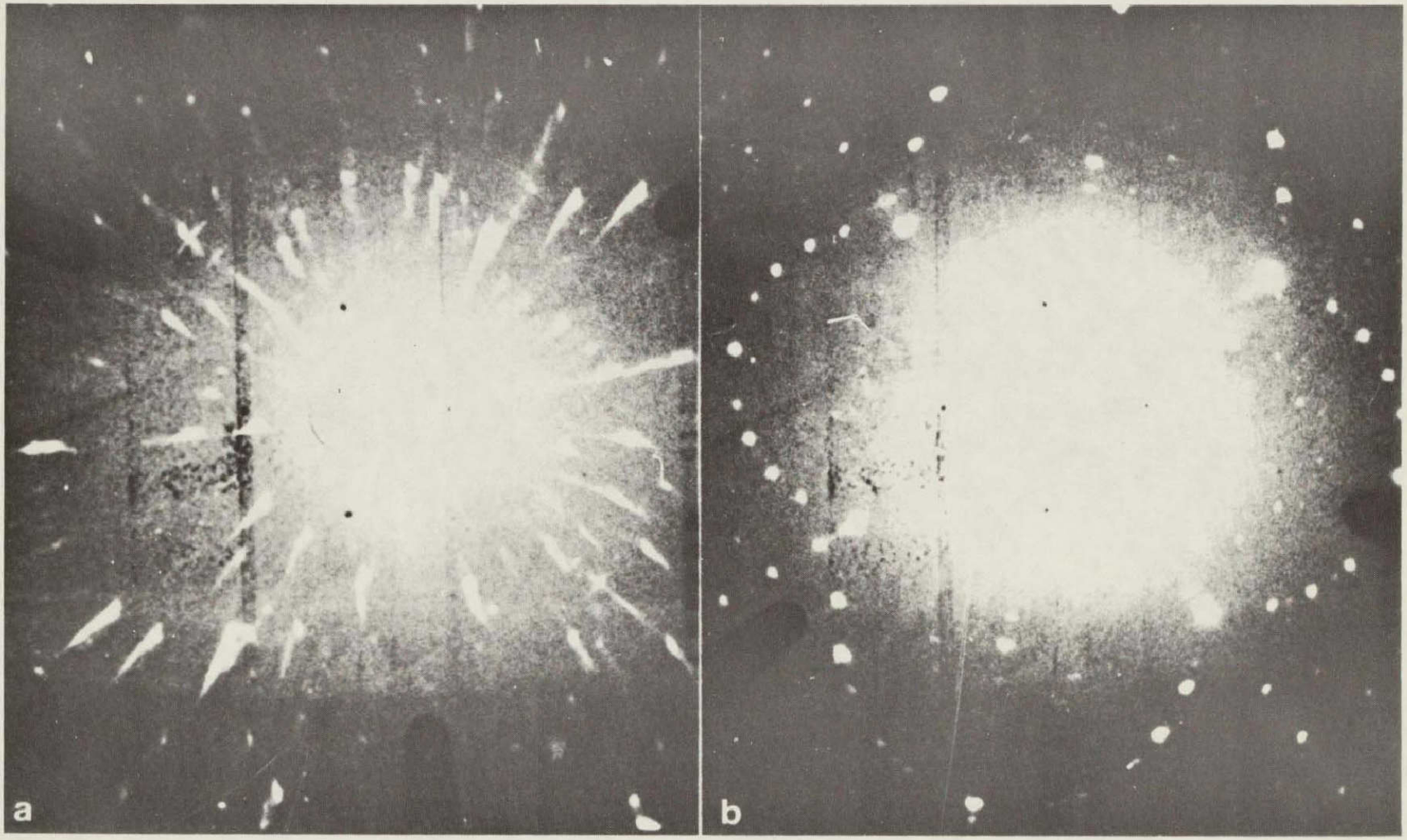

Figure VII-2. Laue X-ray diffraction transmission photographs of (001) oriented $GeSe_{0.99}Te_{0.01}$ (system A) single crystal platelets: (a) ground-based (prototype), (b) space-grown.

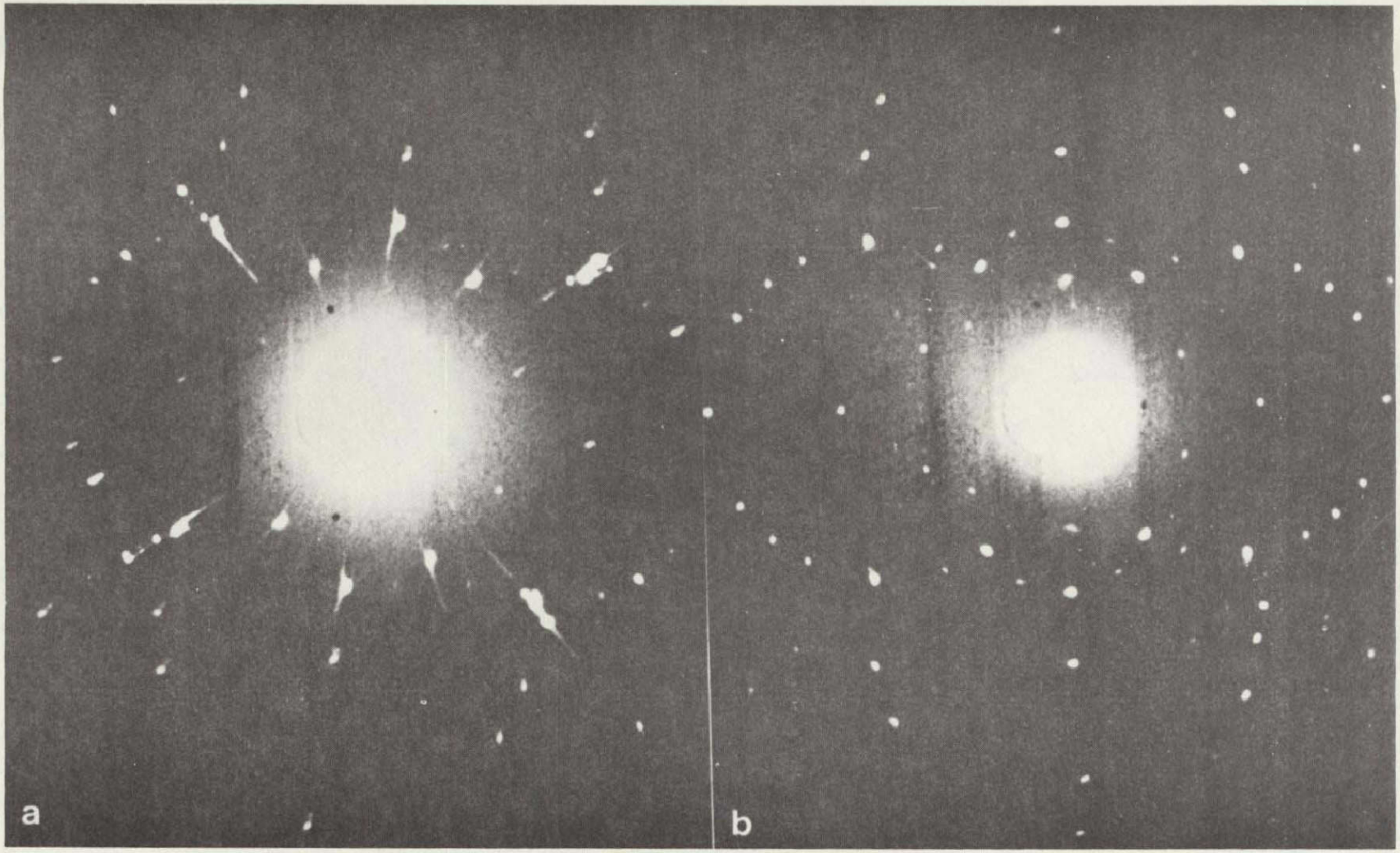

Figure VII-3. Laue X-ray diffraction transmission photographs of (001) oriented $GeS_{0.98}Se_{0.02}$ (system B) single crystal platelets: (a) ground-based (prototype), (b) space-grown.

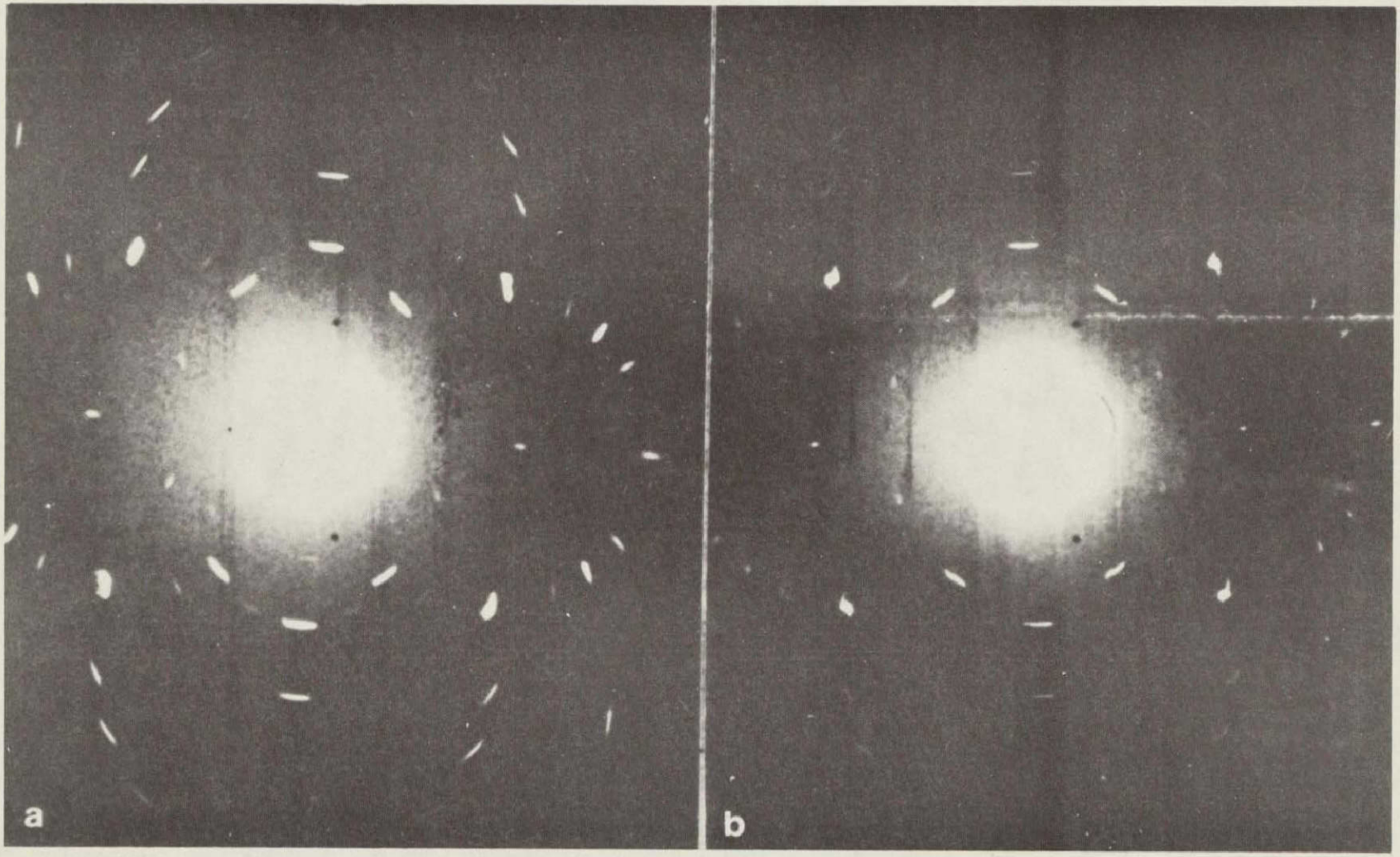

Figure VII-4. Laue X-ray diffraction transmission photographs of (001) oriented GeS (system C) single crystal platelets: (a) ground-based (prototype), (b) space-grown.

determined using an electron microprobe analyzer (EPA model 400S). For this purpose, cleaved faces of ground-based (prototype) and space crystals were used. The relative concentration of Te (in GeSe) and of Se (in GeS) was measured along three directions parallel to the a- and b-axes of the (001) oriented crystal platelet. Along each direction, intensity measurements were performed at several locations. The results are summarized in Table VII-3. The individual data listed are the averages of points along a given direction. The error limits represent the maximum deviation in atomic concentration of individual points from the mean value for all points along that direction. Stoichiometric GeTe and GeSe, respectively, were used as reference samples.

Based on the relative magnitude of the deviations in concentration from the average values, the distribution of Te in the solid solution of starting composition $GeSe_{0.99}Te_{0.01}$ is considerably more homogeneous in the space crystals (3A) than in the ground-based crystals. The differences in homogeneity are

TABLE VII-3. DISTRIBUTION OF Te AND Se IN GROUND-BASED AND SPACE CRYSTALS

System	Concentration (at.%)		
	Average All Data	Average Parallel a-Axis	Average Parallel b-Axis
$GeSe_{0.99}Te_{0.01}$ (Ground-Based)	1.83 ± 0.6	2.03 ± 0.5 1.71 ± 0.6 1.78 ± 0.4	1.59 ± 0.4 2.07 ± 0.3 1.81 ± 0.4
$GeSe_{0.99}Te_{0.01}$ (ASTP 3A)	1.56 ± 0.1	1.59 ± 0.03 1.52 ± 0.08 1.56 ± 0.02	1.58 ± 0.04 1.57 ± 0.06 1.58 ± 0.02
$GeS_{0.98}Se_{0.02}$ (Ground-Based)	0.395 ± 0.092	0.371 ± 0.068 0.399 ± 0.061 0.399 ± 0.028	0.374 ± 0.034 0.402 ± 0.020 0.422 ± 0.015
$GeS_{0.98}Se_{0.02}$ (ASTP 3B)	0.462 ± 0.048	0.470 ± 0.014 0.448 ± 0.020 0.470 ± 0.007	0.459 ± 0.046 0.471 ± 0.009 0.463 ± 0.007

approximately one order of magnitude. The corresponding improvement in the distribution of Se in the space crystal (3B) compared to the ground specimen for the solid solution of starting composition $GeS_{0.98}Se_{0.02}$ is less pronounced, but is measurable. The deviation of the average values from the nominal concentration of Te and Se in the starting materials is due to slightly different transport properties of the binary components of the mixed systems.

In view of the relative differences in atomic radii between S, Se, and Te and due to the individual crystal structures of GeS and GeSe (orthorhombic) and GeTe (rhombohedral), one would expect a more homogeneous mixing to occur in the GeS-GeSe system than in the GeSe-GeTe system. Any improvement in the degree of homogeneity as a result of microgravity conditions should thus be more pronounced for GeSe-GeTe than for GeS-GeSe solid solutions. The experimental observations are in agreement with these expectations.

Morphological Characterization of Crystals

Before we discuss the microscopic investigation of individual single crystals, we will examine a macroscopic view of the deposition pattern of transport agent (GeI_4) on the ampoule walls of the A-system (Fig. VII-5) which shows significant differences. The transport agent in the space ampoule, Figure VII-5(a), is condensed in the form of well developed, transparent, single crystal platelets and a few needles. The GeI_4 deposition in the ground-based ampoule, Figure VII-5(b), shows dendritic type material with a distinct curvature of individual dendrites. The length of these dendrites is up to approximately 8 mm. The absence of any distinct curvature in the deposition pattern of the space ampoule, Figure VII-5(a), reflects the more homogeneous gas motion in the microgravity environment.

Optical photomicrographs of representative $GeSe_{0.99}Te_{0.01}$ (A) ground (prototype) and space crystals show qualitative differences in surface morphology, as illustrated in Figure VII-6. The majority of the prototype crystals, Figure VII-6(a), reveal ragged edges, intergrowth, and stepped surfaces. The space crystals, Figure VII-6(b), have smoother surfaces and generally better defined edges. The average dimensions of the ground specimens range from approximately 2 mm to 8 mm in edge length. The slightly smaller sizes of the space material are in agreement with the lower transport rates in microgravity observed for this system (Table VII-4).

Optical photomicrographs of representative $GeS_{0.98}Se_{0.02}$ (B) ground (prototype) and space crystals in Figure VII-7 reveal distinct morphological differences. The prototype crystals, Figure VII-7(a), show considerable

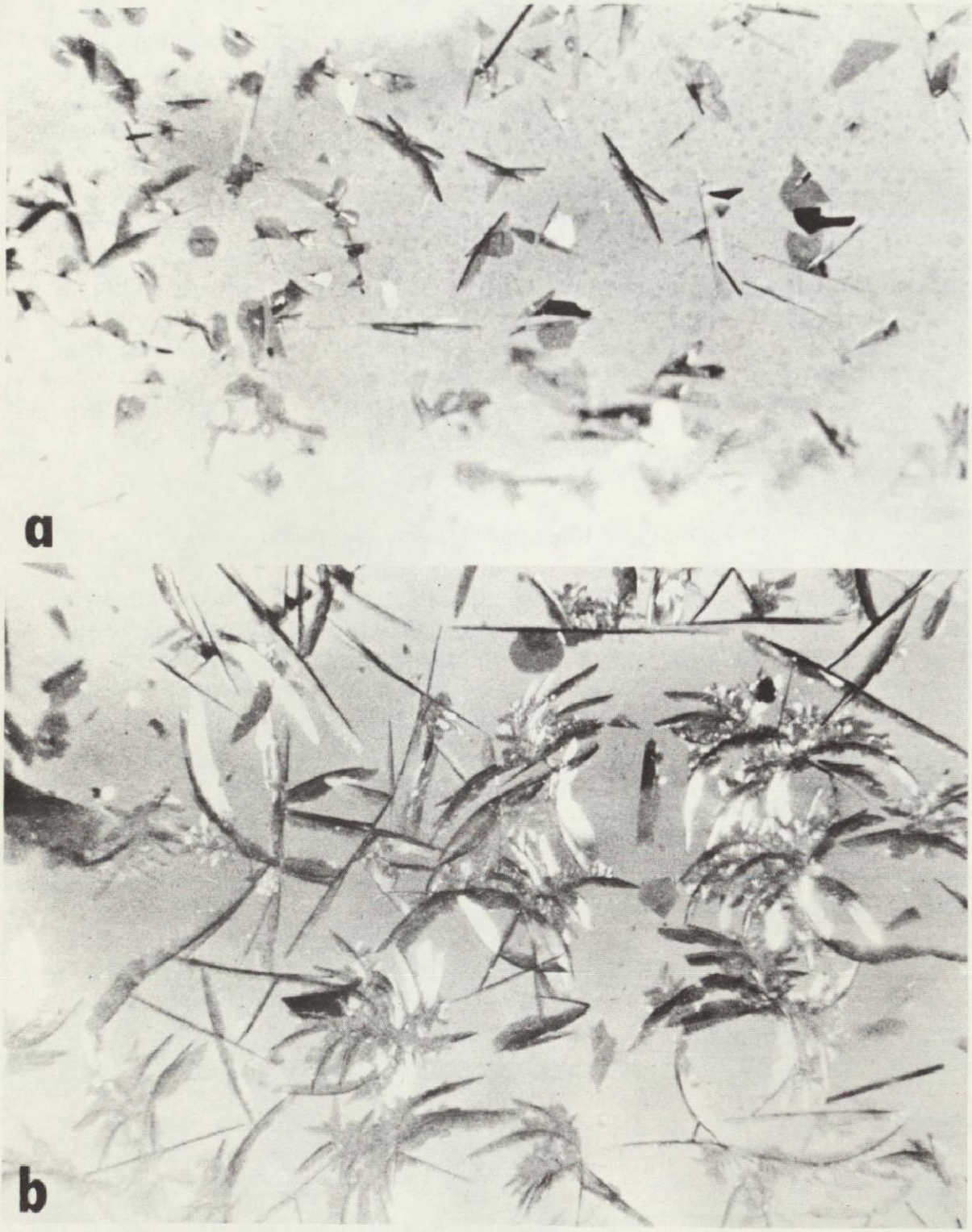

Figure VII-5. Deposition pattern of transport agent GeI_4 (system A) on ampoule walls: (a) observed in microgravity, (b) under ground-based (prototype) conditions.

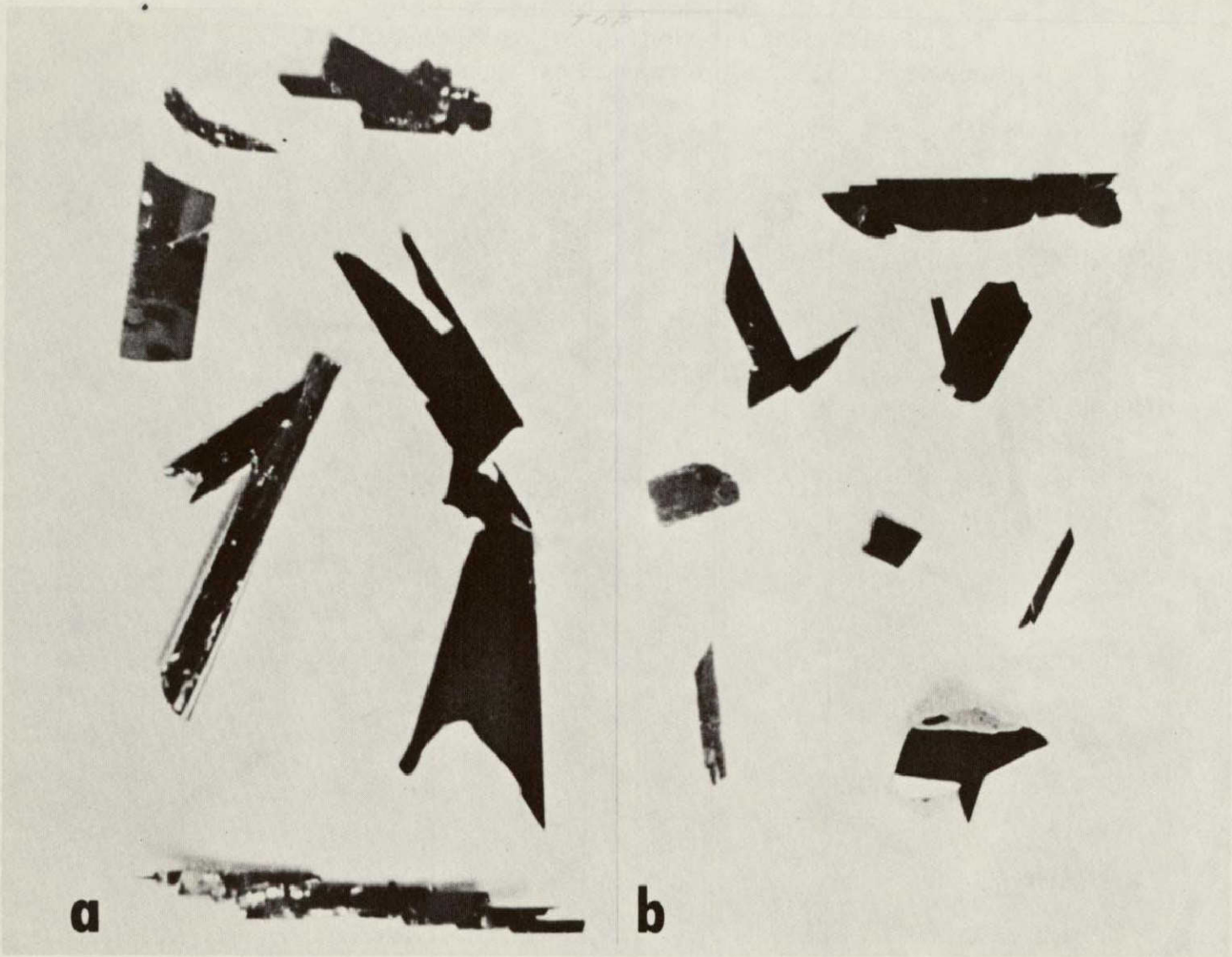

Figure VII-6. Representative crystals of $GeSe_{0.99}Te_{0.01}$ (system A): (a) ground-based (prototype), (b) space-grown).

Figure VII-7. Representative crystals of $GeS_{0.98}Se_{0.02}$ (system B): (a) ground-based (prototype), (b) space-grown.

TABLE VII-4. MASS TRANSPORT RATES UNDER GROUND-BASED AND MICROGRAVITY CONDITIONS

System	Mass Flux [(moles/cm^2 · s) × 10^{-9}]		
	One-g	Microgravity	Extrapolated Difference Mode
$GeSe_{0:99}Te_{0.01}$ (A)	7.9	4.2	1.4
$GeS_{0.98}Se_{0.02}$ (B)	22.1	22.1	6.5
GeS + Ar (C)	15.0	13.0	2.8

aggregation, undefined edges, and rough surfaces. The morphological improvement in terms of surfaces and edges of the space crystals is evident from Figure VII-7(b). The average dimensions of the space material range from approximately 1 mm to 7 mm in edge length. In view of the fact that the transport rates for system (B) (Table VII-4) are the same under ground and space conditions, the external morphological differences reflect the absence of convective interference in the microgravity environment. Similar differences in growth habits were observed for GeS crystals (system C).

The external morphological differences of native faces and edges of typical $GeSe_{0.99}Te_{0.01}$ (A) ground and space crystals are shown in the scanning electron photomicrographs (400X) of Figure VII-8. The well defined surfaces and edges of the space crystal, Figure VII-8(a), are contrasted by the rough and partially damaged faces of the ground crystal, Figure VII-8(b). The majority of ground crystals appear to have at least one edge damaged, whereas most of the space crystals have well developed edges. These results confirm similar observations of the Skylab experiments and indicate homogeneous nucleation which could occur more frequently under microgravity conditions than on Earth.

Scanning electron photomicrographs (400X) of native surfaces of $GeS_{0.98}Se_{0.02}$ (B) space, Figure VII-9(a), and ground (prototype), Figure VII-9(b), crystals reveal significant morphological differences. The degree of surface perfection of the space material, Figure VII-9(a), is considerably improved compared to the ground specimen, Figure VII-9(b). Since the transport rates of the system (B) are the same under ground-based and microgravity conditions (Table VII-4), the greater crystalline perfection of the space material is attributed to the absence of convective interference.

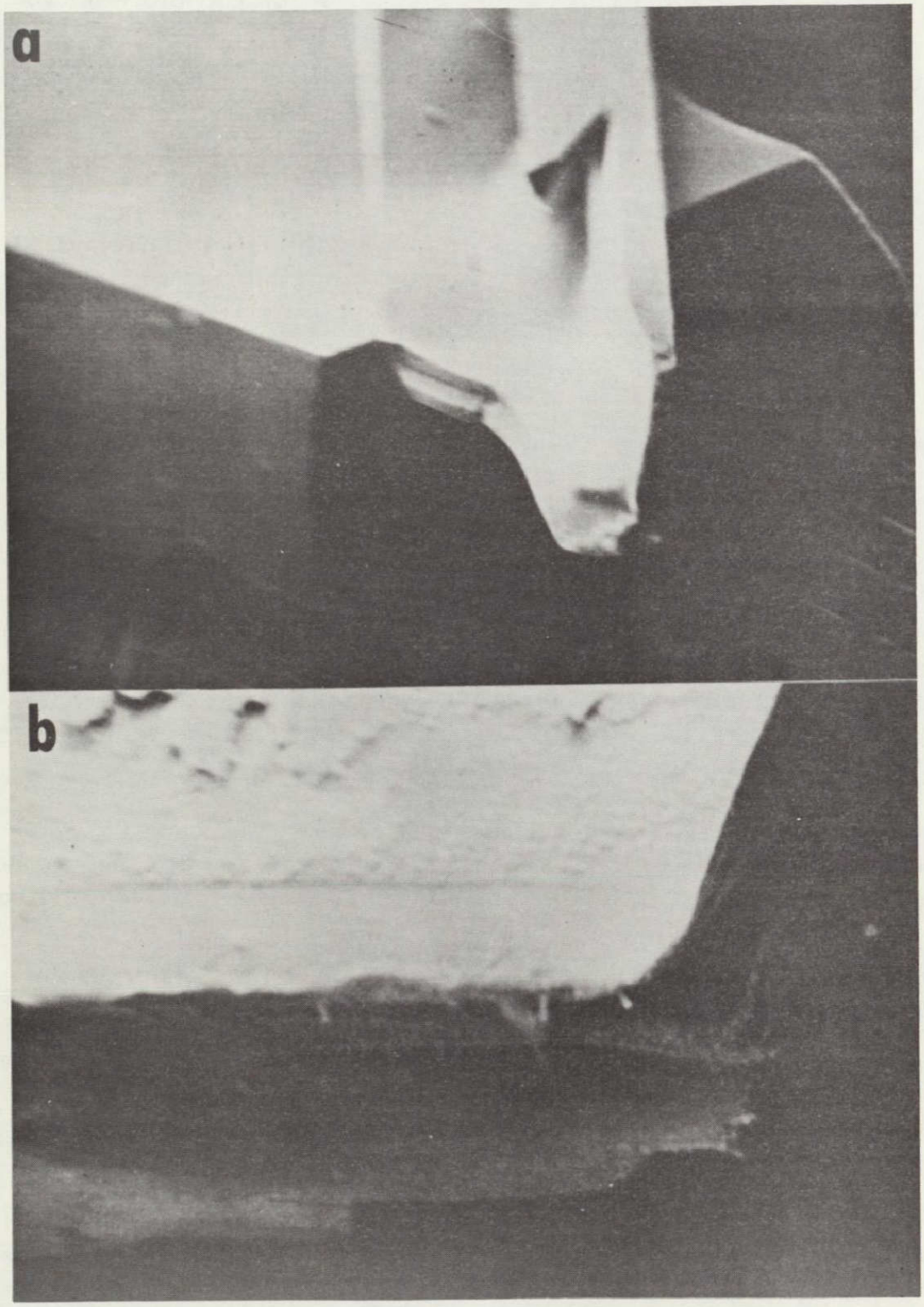

Figure VII-8. Scanning electron photomicrographs (400X) of native faces and edges of $GeSe_{0.99}Te_{0.01}$ (system A) crystals: (a) microgravity, (b) ground-based (prototype) grown.

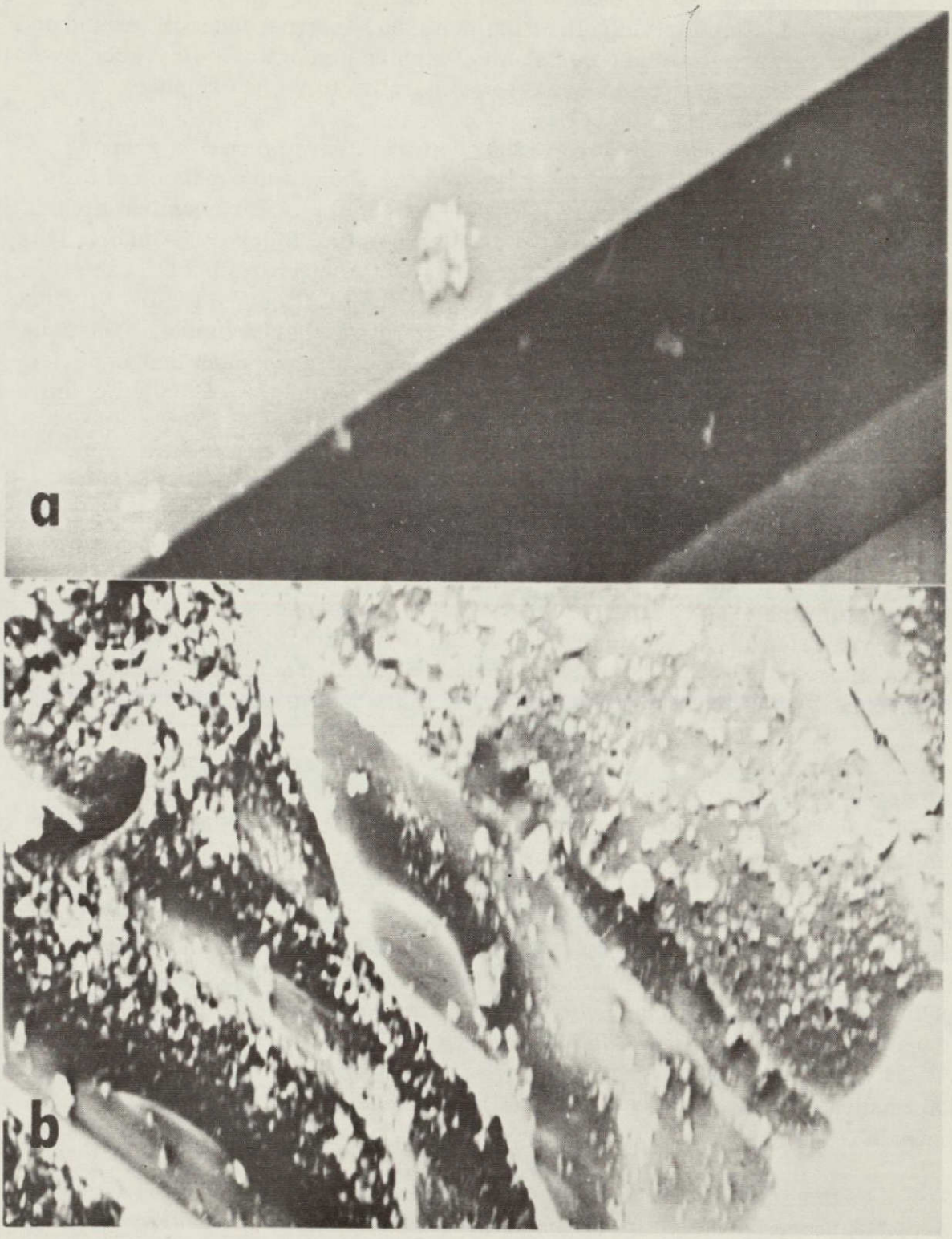

Figure VII-9. Scanning electron photomicrographs (400X) of native faces of $GeS_{0.98}Se_{0.02}$ (system B) crystals: (a) microgravity, (b) ground-based (prototype) grown.

In order to investigate the effects of microgravity on the degree of crystalline perfection for the bulk of the material, internal faces of ground and space crystals were examined by chemical etching and optical microscopy. For this purpose crystal platelets were cleaved parallel to the (001) plane.

An optical photomicrograph (200X) of the cleaved face of a ground (prototype) crystal of $GeSe_{0.99}Te_{0.01}$ (system A) shows the presence of large cavities in the bulk of the material, Figure VII-10(a). After chemical etching, the same area of the crystal is covered with etch pits, Figure VII-10(b). It is interesting to note that the areas which appear to be mirror smooth at this magnification, Figure VII-10(a), show a high etch pit density, Figure VII-10(b). Etch pits along the walls of the main cavity are also clearly visible. The concentration of etch pits indicates the degree of structural or chemical imperfections in the ground-based material. Similar observations were made for the majority of investigated crystals.

Application of the same cleaving and etching procedures to space-grown crystals of system (A) yields distinctly different results, as shown in Figure VII-11. The photomicrograph (200X) of the cleaved crystal reveals that the bulk of the space material is structurally very uniform, Figure VII-11(a). The photomicrograph (200X) after etching of the cleaved space crystal platelet, Figure VII-11(b), is practically free of etch pits indicating a high degree of microhomogeneity. The line pattern of the crystal is due to cleavage, showing (001) planes of different depth with respect to the native surface.

Similar differences in etch patterns were observed for ground (prototype) and space-grown $GeS_{0.98}Se_{0.02}$ (B) crystals, as shown in Figures VII-12 and VII-13. For comparative purposes, a ground crystal of above average quality has been selected as indicated by the cleavage pattern (200X), Figure VII-12(a). (The majority of B-type ground crystals contain cavities and elongated channels in the bulk of the material.) Chemical etching of the cleaved (001) face yields large etch pits and lines, Figure VII-12(b) (200X), which are indicative of crystallographic imperfections. This is contrasted by optical photomicrographs (200X) of cleaved and etched (001) faces of space crystals of this system (Fig. VII-13). Except for a few isolated etch pits in the crystal plane, Figure VII-13(b), the bulk of the material is practically unaffected by chemical etching. This indicates a high degree of crystalline homogeneity of the space-grown material.

Optical photomicrographs (200X) of cleaved and etched (001) faces of GeS (C) ground (prototype) and space crystals are shown in Figures VII-14 and VII-15. While the cleaved faces of the prototype, Figure VII-14(a), and space,

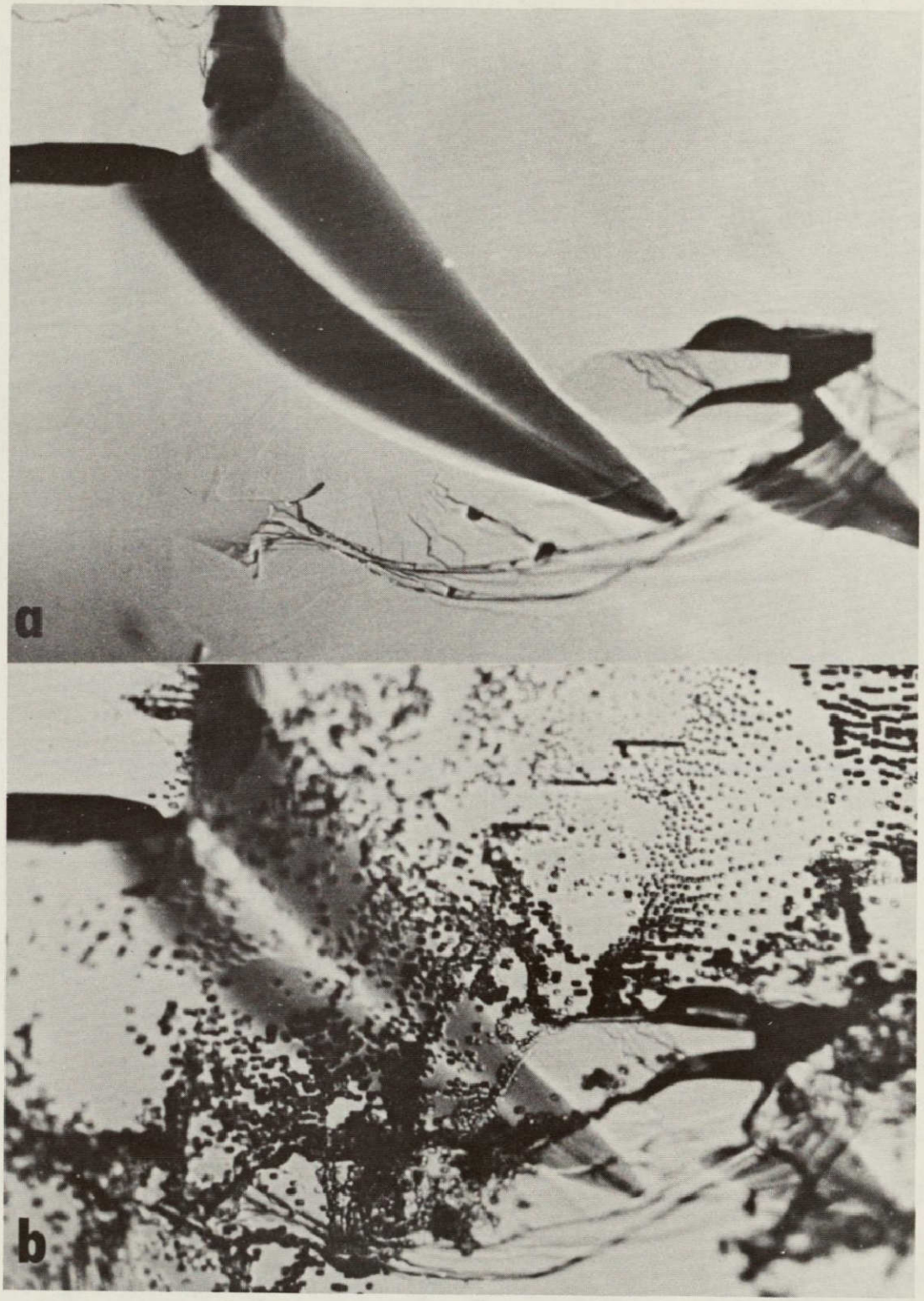

Figure VII-10. Optical photomicrographs (200X) of a cleaved and etched (001) face of a ground-based (prototype) $GeSe_{0.99}Te_{0.01}$ (system A) crystal platelet: (a) cleaved, (b) cleaved and etched.

Figure VII-11. Optical photomicrographs (200X) of a cleaved and etched (001) face of a space-grown $GeSe_{0.99}Te_{0.01}$ (system A) crystal platelet: (a) cleaved, (b) cleaved and etched.

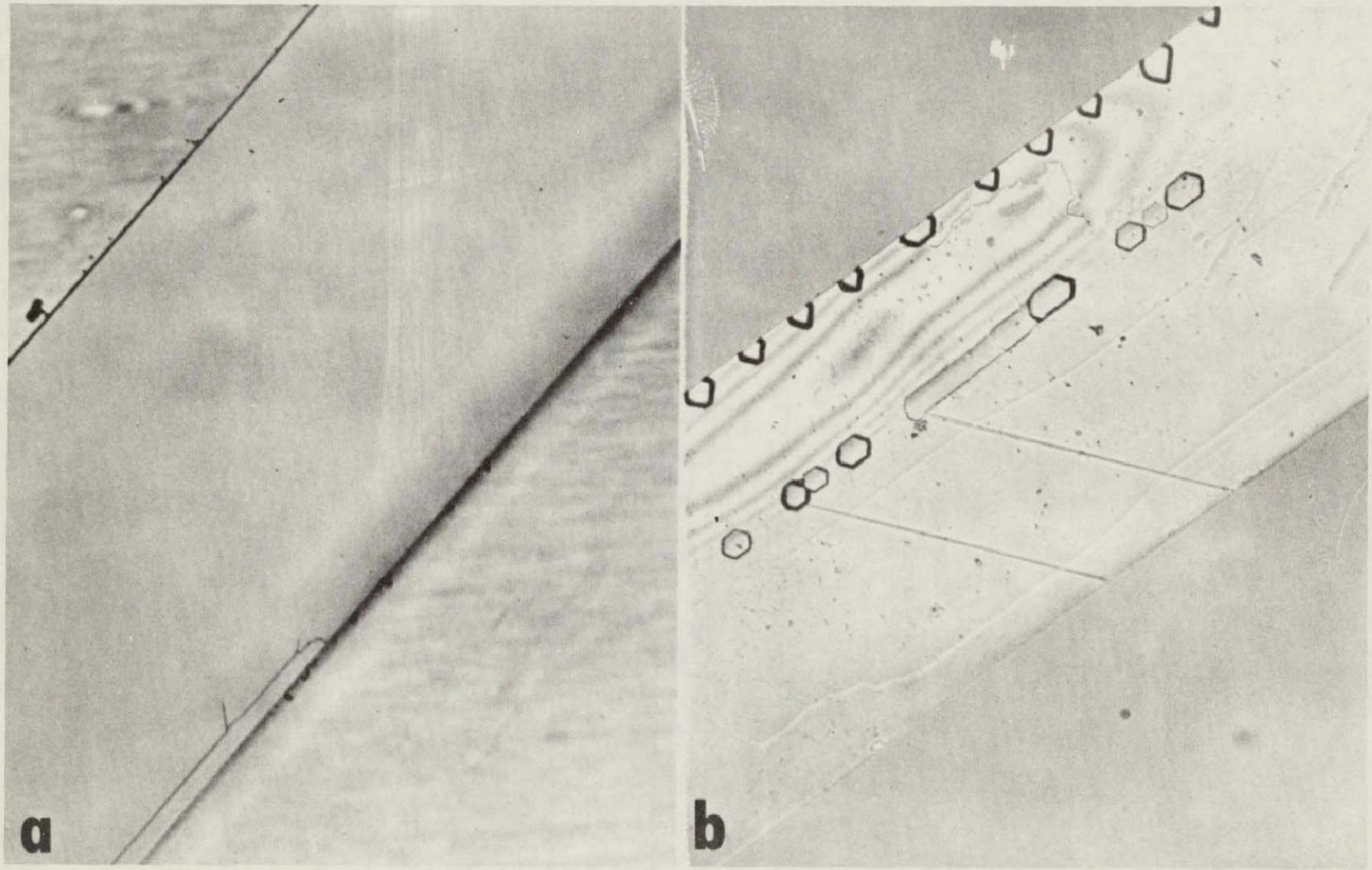

Figure VII-12. Optical photomicrographs (200X) of a cleaved and etched (001) face of a ground-based (prototype) $GeS_{0.98}Se_{0.02}$ (system B) crystal platelet: (a) cleaved, (b) cleaved and etched.

Figure VII-13. Optical photomicrographs (200X) of a cleaved and etched (001) face of a space-grown $GeS_{0.98}Se_{0.02}$ (system B) crystal platelet: (a) cleaved, (b) cleaved and etched.

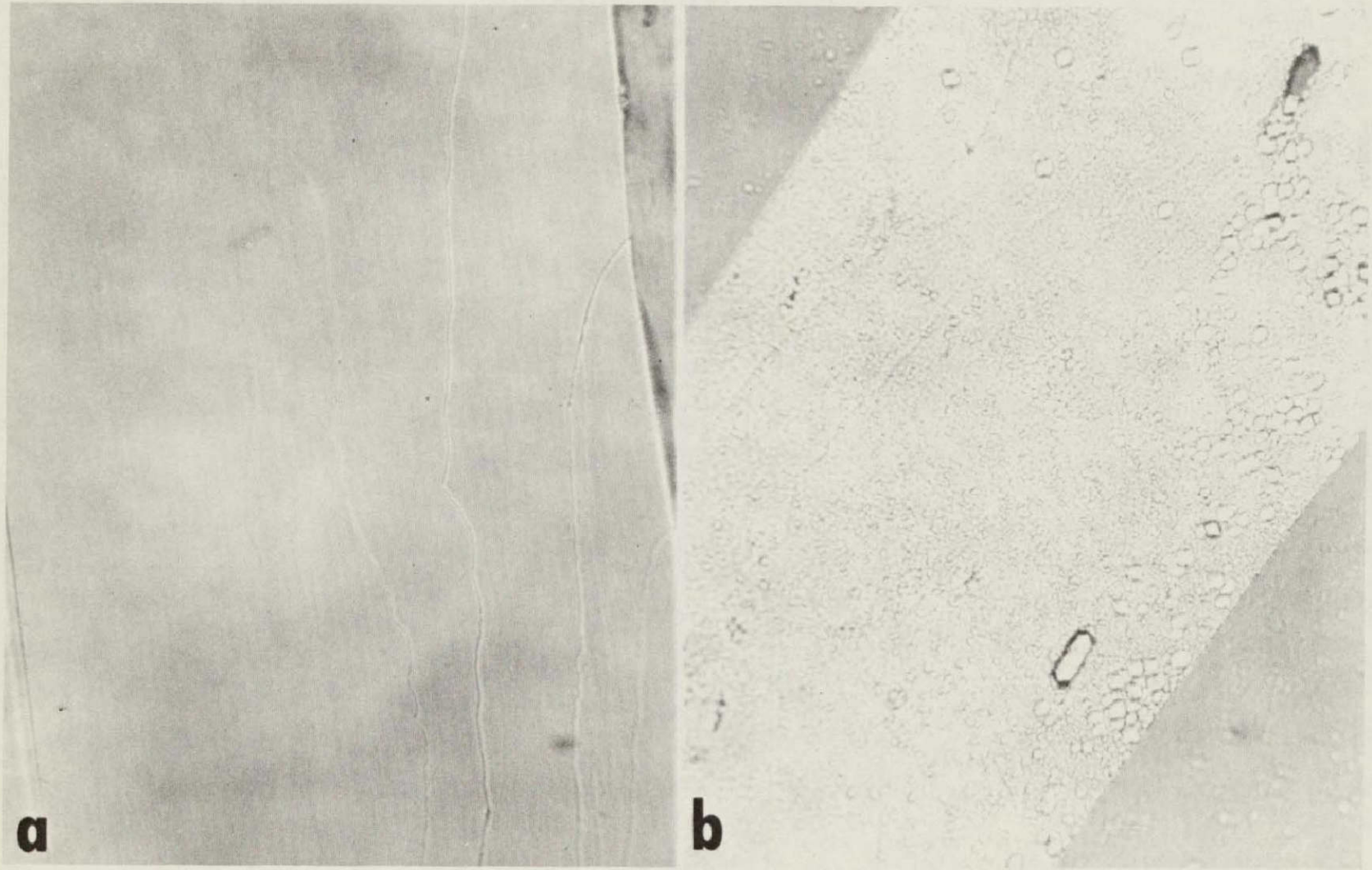

Figure VII-14. Optical photomicrographs (200X) of a cleaved and etched (001) face of a ground-based (prototype) GeS (system C) crystal platelet: (a) cleaved, (b) cleaved and etched.

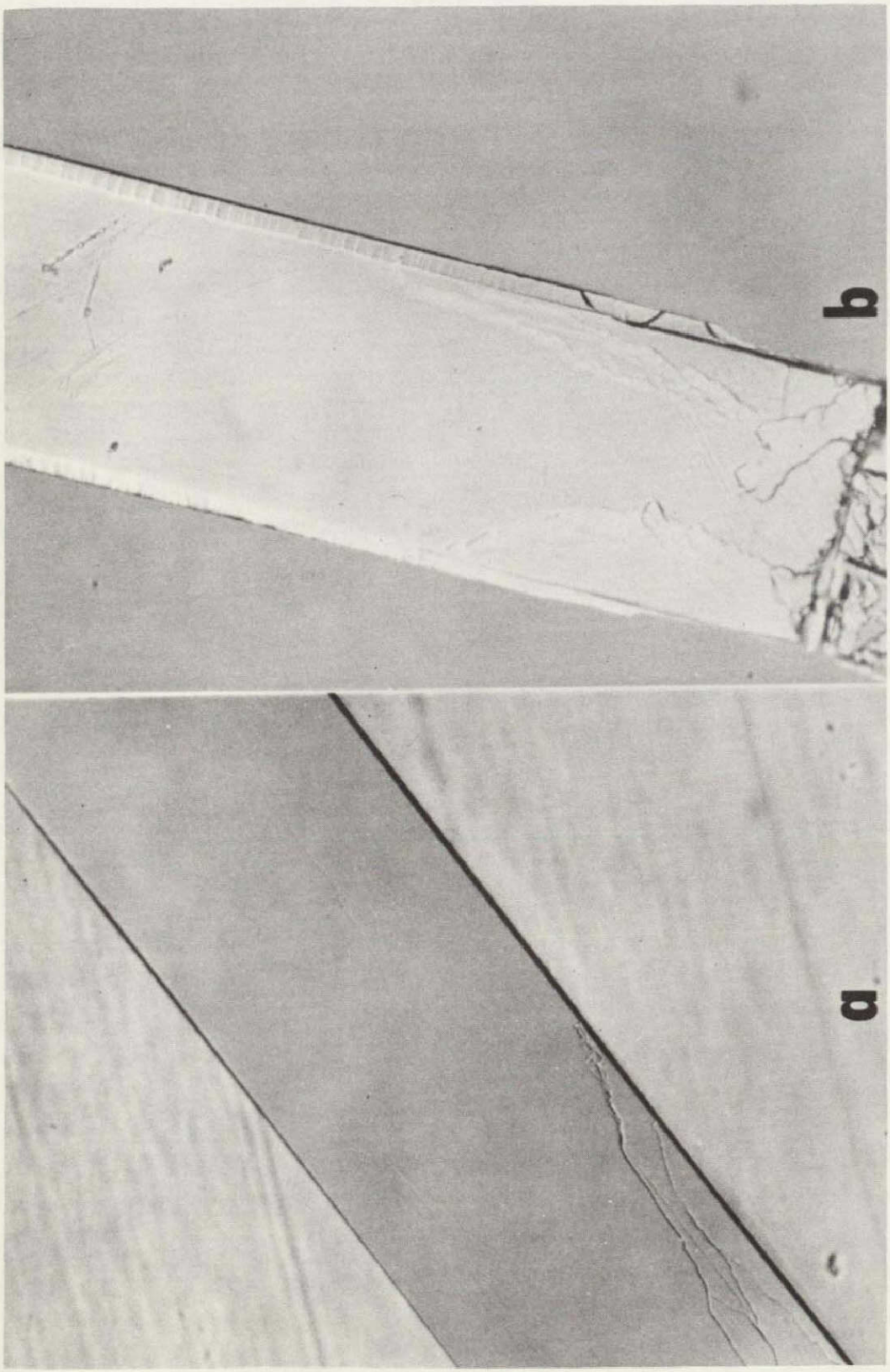

Figure VII-15. Optical photomicrographs (200X) of a cleaved and etched (001) face of a space-grown GeS (system C) crystal platelet: (a) cleaved, (b) cleaved and etched.

Figure VII-15(a), crystals appear to be of comparable quality, the corresponding etched faces of the ground, Figure VII-14(b), and space, Figure VII-15(b), crystals reveal measurable differences. The prototype material shows a high density of etch pits of different sizes, Figure VII-14(b). The etch pits of the space sample, Figure VII-15(b), are concentrated in the lower section of the crystal and along the edges, while the major part of the plane has a considerably lower pit density than the ground crystal. It was observed that the GeS space crystals (system C) grown in the presence of argon were of slightly lower crystallographic quality than the space crystals of systems (A) and (B) which were produced in the absence of inert atmosphere. Studies are in process to determine whether these differences are due to the incorporation of argon into the GeS lattice.

The previously reported differences in cleavage and etch patterns for the three systems were observed for the majority of investigated space and ground crystals. The combined results of the morphological studies demonstrate the considerably improved crystallographic perfection of the crystals grown in the microgravity environment.

Mass Transport Rates

The determination of the mass transport rates observed in microgravity is based on the mass of the transported crystals and on the mass loss of the source materials. The same procedures were applied to determine the fluxes of the prototype ground-based systems. The experimental uncertainties connected with the recovery of crystals were combined to yield lower values for the mass flux observed in microgravity. The extrapolated values are based on a graphical extrapolation of the diffusion controlled region of the respective ground-based experimental flux curves shown in Figure VII-1. For this purpose flux versus pressure data were plotted in double logarithmic scales, and the resulting straight line was extended to the flux corresponding to the pressure employed in the ASTP experiments. This is shown for system (A) in Figure VII-16 and for system (B) and GeS in Figure VII-17. The data of the diffusion controlled region selected for the extrapolation are close to the minimum of the individual flux curves (Fig. VII-1) in order to obtain upper values for the predicted fluxes. The extrapolations are based on the assumptions that vapor transport in microgravity is by gas phase diffusion and that other known non-gravity caused transport effects, e.g. streaming, are included in this procedure. The predicted flux value for system (C) was obtained analytically from the extrapolated identical values for system (B) and GeS (Fig. VII-17) and the argon pressure in system (C), considering the different molecular weights of

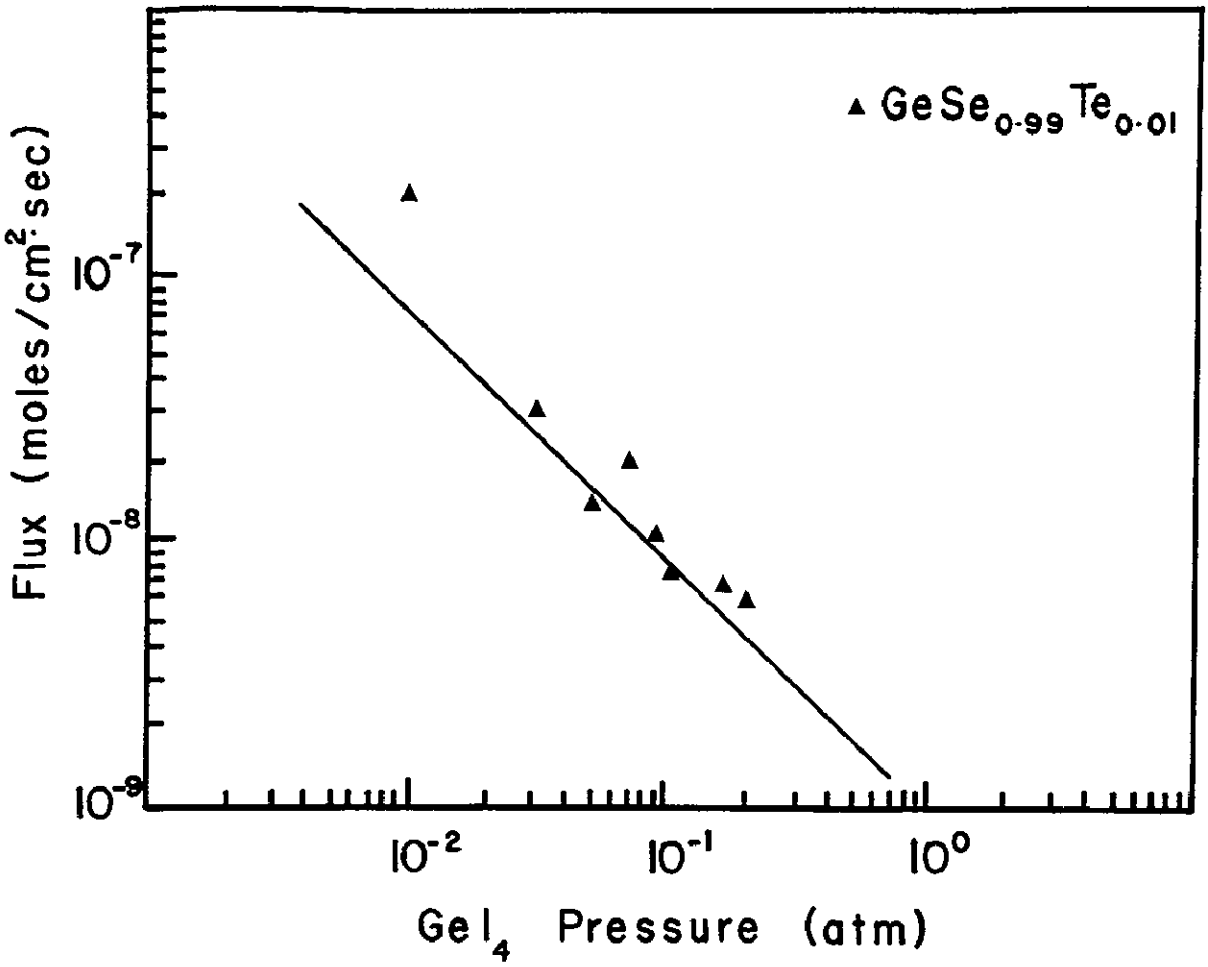

Figure VII-16. Extrapolation of flux versus pressure data of the diffusion branch of the ground-based flux curve (Fig. VII-1) for system (A).

argon and $GeCl_4$. The mass transport properties of system (B) and GeS (Fig. VII-1 and VII-17) and the transport agent ($GeCl_4$) pressures of systems (B) and (C) (Table VII-1) are the same within limits of error. This allows a direct comparison of the effect of argon on the mass flux between systems (B) and (C). In view of the applied evaluation procedures, any differences between observed and predicted (extrapolated) fluxes for microgravity are minimized and well outside error limits. The numerical transport results are listed in Table VII-4.

A comparison of the data in Table VII-4 reveals a rather significant result. For system (A) the flux observed in microgravity is lower than under prototype ground-based conditions but is approximately three times greater than predicted for a purely diffusion type transport. These observations are consistent with the Skylab results. For system (B) the prototype ground-based and microgravity fluxes are the same, but the latter is more than three times greater

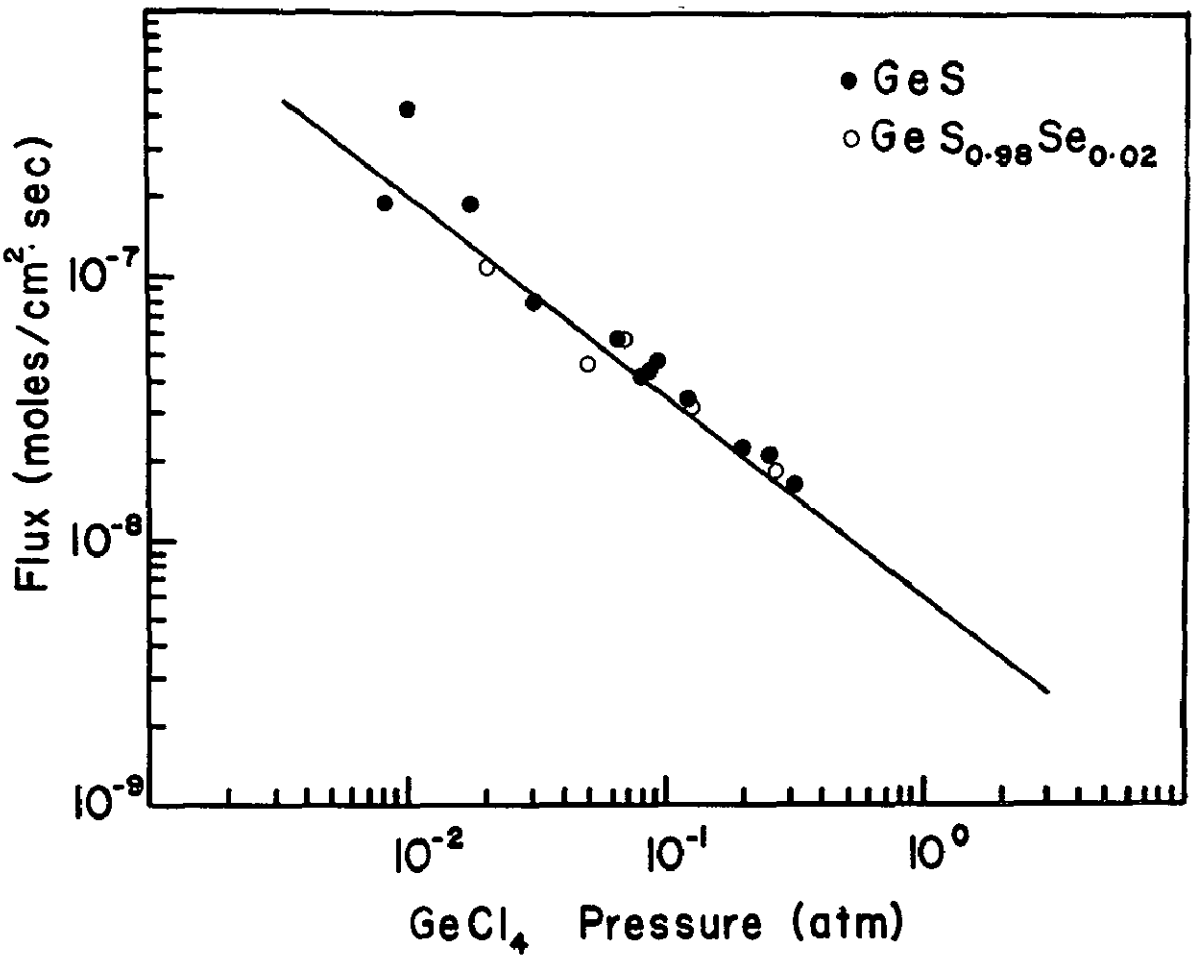

Figure VII-17. Extrapolation of flux versus pressure data of the diffusion branch of the ground-based flux curves (Fig. VII-1) for system (B) and GeS.

than the transport rate predicted by theory. The pressure of transport agent $GeCl_4$ employed for ASTP system (B) is different from the GeI_4 pressure of the corresponding Skylab experiment for which the same ground and space fluxes were observed. This indicates the importance of the chemical properties of the transport system for flux considerations. For system (C) the prototype ground-based and microgravity fluxes are the same within error limits, and the latter is nearly five times greater than predicted. A comparison of the individual flux data of systems (B) and (C) demonstrates that the effect of argon on the mass transport rate is the same under ground-based (prototype) and microgravity conditions. The observed decrease in flux upon addition of argon is in good agreement with ground-based inert atmosphere studies, as shown in Figure VII-1. These combined results have two important consequences. First, the greater than predicted transport rates observed in microgravity are not

caused by gravity fluctuations or any other conditions typical for spacecraft operations. Secondly, the effect of argon on the mass flux is independent of gravity and, thus, affects the inherent physicochemical properties of the transport system. These observations are of primary importance for the explanation of the unexpected flux results.

In view of the rather unconventional nature of the transport phenomena in microgravity, it is necessary to demonstrate independently the validity of the discrepancies between the flux values actually observed in space and those predicted on the basis of a diffusion type transport. For this purpose, different transport models developed by Schäfer [VII-3], Lever [VII-6], Mandel [VII-7], and Faktor [VII-8] have been employed. These models are for vapor transport by diffusion and differ essentially in the treatment of the so-called streaming effect or flow factor and in the thermodynamic calculation of partial pressure gradients. Based on these diffusion models, flux versus pressure curves were computer for the temperature gradients and transport agents of the ASTP, Skylab 3, and Skylab 4 experiments. The "theoretical" flux curves were fitted to the diffusion branch of the experimental ground-based curves (Fig. VII-1 for the ASTP mission and accordingly for the Skylab missions) to obtain optimal fit. This procedure yielded the numerical constants required for the calculation of the fluxes for the specific ASTP and Skylab conditions. The results of these computations for the different models are listed in Table VII-5 together with the observed and extrapolated fluxes. A comparison of these data shows that the flux values obtained from the model computations agree within a factor of two with our extrapolated values. In no case are the transport rates predicted by the models greater than the observed fluxes. In view of the uncertainties associated with thermodynamic calculations of partial pressures and transport effects, the agreement between the model calculations and extrapolation procedures is close. However, because of these uncertainties our extrapolated data represent the best flux values for comparison. The combined data demonstrate unambiguously that the transport rates observed in microgravity cannot be explained on the basis of an exclusively diffusion type process. The internal consistency and close agreement between the flux results of the ASTP and Skylab missions obtained for different chemical systems, eight pressures, two transport agents, and three temperature gradients strongly support the validity of these observations. The combined results lead to the conclusion that the greater than predicted mass transport rates in the microgravity environment are due to nongravity caused transport effects. These unexpected phenomena are related to thermochemical effects of gas phase reactions that have not been considered in present vapor transport models.

TABLE VII-5. MASS TRANSPORT RATES OBSERVED AND PREDICTED FOR MICROGRAVITY CONDITIONS

System	Mass Flux [(moles/cm^2 · s) × 10^{-9}]					
	Observed	Extrapolated	Schafer	Lever	Mandel	Faktor
ASTP Experiments 604°→507°C						
$GeSe_{0.99}Te_{0.01}$ (A)	4.2	1.4	2.5	2.7	2.6	3.1
$GeS_{0.98}Se_{0.02}$ (B)	22.1	6.5	8.9	9.1	9.1	9.5
GeS + Ar (C)	13.0	2.8	3.6	3.7	3.2	5.2
SL-3 Experiments 524°→422°C						
GeSe (A)	5.0	0.5	0.80	0.89	0.86	1.1
GeSe (B)	10.0	2.5	3.4	3.7	3.6	4.2
GeTe (C)	3.0	0.5	0.84	0.87	0.87	0.92
SL-4 Experiments 412°→346°C						
GeSe (A)	0.8	0.15	0.14	0.14	0.14	0.15
GeSe (B)	1.8	0.35	0.39	0.30	0.30	0.30
GeTe (C)	1.0	0.40	0.79	0.79	0.79	0.79

The latter conclusion is supported by the analysis and application of models for convective vapor transport on Earth which have been developed by Schäfer [VII-3] based on the Hagen-Poiseuille equation and by Klosse and Ullersma [VII-9] following a hydrodynamic approach and the Navier-Stokes equation. An important difference between these two models is their treatment of the convective boundary layer, the fluid layer immediately in contact with the growing crystal and through which mass must diffuse. The model based on Hagen-Poiseuille [VII-3] does not consider a boundary layer. In the hydrodynamic model [VII-9] the thickness of the boundary layer depends on the aspect ratio of the enclosure. Preliminary applications of these convection models to our experimental ground-based flux curves show systematic deviations. The

mass fluxes predicted by the first model [VII-3] for convective transport are greater than observed. The second model [VII-9] agrees with our experimental results in the initial convection range and predicts lower fluxes than observed at higher pressures. These deviations from our experimental ground-based data are related to the treatment of the boundary layer in these models [VII-3, VII-9]. In addition, the above convection models [VII-3, VII-9] do not consider possible thermal effects of gas phase reactions on mass transport and on the boundary layer. Theoretical and experimental studies are continued to further analyse present vapor transport models through systematic applications of these models to different transport systems investigated in our laboratory. The immediate purpose of these efforts is the extension of ground-based convection models to agree with experimental results. These modifications combined with our space and continued ground experiments will lead to the development of a transport model for microgravity conditions.

In view of these results, the transport phenomena observed for the ASTP and Skylab mission experiments are of far reaching scientific and technological significance. The improvement of ground-based transport models is of basic and practical value for crystal growth theories and techniques on Earth. A transport model for space conditions based on microgravity experiments is of primary importance for actual space processing applications.

SUMMARY AND CONCLUSIONS

The original objectives of experiment MA-085 were to investigate the effects of microgravity on the morphology of single crystals of mixed systems and to determine the mass transport rates of these systems using the chemical transport technique. For this purpose three vapor transport experiments were performed during the ASTP mission employing three chemical compounds, two transport agents, and one inert gas in one common temperature gradient. The analysis of these experiments is based on a direct comparison of X-ray diffraction, microprobe, scanning electron and optical microscopy, and chemical etching studies of crystals obtained under ground-based (prototype) and microgravity conditions. The results demonstrate a considerable improvement in structural and chemical homogeneity, surface morphology, and bulk perfection of the space-grown materials compared to ground-based specimens. In addition to the positive crystallographic results, the confirmation of greater mass transport rates in microgravity than predicted by present transport models represents the second major achievement of experiment MA-085.

The excellent agreement between our ASTP and Skylab results demonstrates the validity of the observed crystal growth and transport properties in space for a class of technologically useful materials. This confirms our initial predictions concerning the suitability of the vapor transport technique for the growth of higher quality crystals and for the observation of unexpected phenomena in the microgravity environment. These results are of basic scientific and practical importance for the modification of transport models on Earth. The production of high quality crystals at high mass transport rates is of technological significance for space processing applications.

ACKNOWLEDGMENTS

The authors express their sincere appreciation to the National Aeronautics and Space Administration for the opportunity to participate in the Apollo-Soyuz Test Program. We would like to thank the scientific and technical staff of the George C. Marshall Space Flight Center and the astronautics of the ASTP mission who made the performance of these experiments possible.

REFERENCES

VII-1. Wiedemeier, H.; Klaessig, F. C.; Wey, S. J.; and Irene, E. A.: Proceedings of Third Space Processing Symposium Skylab Results. vol. 1, no. M-74-5, June 1974, p. 235.

VII-2. Wiedemeier, H.; Klaessig, F. C.; Irene, E. A.; and Wey, S. J.: J. Crystal Growth, vol. 31, 1975, p. 36.

VII-3. Schäfer, H.: Chemical Transport Reactions. Academic Press, New York, 1964.

VII-4. Wiedemeier, H.; Irene, E. A.; and Chaudhuri, A. K.: J. Crystal Growth, vol. 13/14, 1972, p. 393.

VII-5. Wiedemeier, H. and Irene, E. A.: Z. Anorg. Allg. Chem., vol. 400, 1973, p. 59.

VII-6. Lever, R. F.: J. Chem. Phys., vol. 37, 1962, p. 1078.

VII-7. Mandel, G.: J. Chem. Phys., vol. 37, 1962, p. 1177.

VII-8. Faktor, M. M.; Garrett, I.; and Heckingbottom, R.: J. Crystal Growth, vol. 9, 1971, p. 3.

VII-9. Klosse, K. and Ullersma, P.: J. Crystal Growth, vol. 18, 1973, p. 167.

SECTION VIII

ZERO-GRAVITY GROWTH OF NaCl-LiF EUTECTIC

EXPERIMENT MA-131

By A. S. Yue,[1] C. W. Yeh,[1] and B. K. Yue[1]

1. University of California, Los Angeles, California

TABLE OF CONTENTS

LIST OF ILLUSTRATIONS

LIST OF ILLUSTRATIONS (Concluded)

ABSTRACT

Continuous and discontinuous lithium fluoride fibers embedded in a sodium chloride matrix have been produced in space and on Earth, respectively. The production of continuous fibers in a eutectic mixture was attributed to the absence of convection current in the liquid during solidification in space. Image transmission and optical transmittance measurements of transverse sections of the space-grown and Earth-grown ingots were made with a light microscope and a spectrometer. It was found that better optical properties were obtained from samples grown in space. This was attributed to a better alignment of lithium fluoride fibers along the growth direction.

INTRODUCTION

When certain binary eutectic mixtures solidify, one of the two phases can form fibers or platelets in a matrix of the second phase. For example, when an eutectic liquid of sodium chloride (NaCl) and sodium fluoride (NaF) solidifies, fibers of NaF [VIII-1] form a matrix of NaCl. Similarly, when a liquid of NaCl and lithium fluoride (LiF) solidifies, LiF will form the fiber phase in the NaCl matrix.

Fiberlike and platelike eutectics produced on Earth are limited in perfection by the presence of a banded structure [VIII-2, VIII-3], discontinuity [VIII-4], and faults [VIII-5, VIII-6] due, at least in part, to vibration and convection currents in the melt during solidification. The presence of these defects renders the solid-state eutectic devices inefficient and useless [VIII-7].

If the solidification process is performed in a space environment, where there are no vibration and convection currents in the melt, there is reason to believe that continuous fiberlike eutectic microstructures can be produced. The electric, thermomagnetic, optical, and superconducting characteristics of such eutectics will be strongly anisotropic, which suggests the possibility of exciting device applications. A Skylab experiment [VIII-1] of NaCl-NaF eutectic demonstrated that continuous fibers of NaF embedded in an NaCl matrix have been grown by the directional solidification technique in space.

OBJECTIVES

The objectives of this project were to: (1) prepare, in a space experiment, fiberlike LiF-NaCl eutectic with continuous LiF fibers embedded in the NaCl matrix (this eutectic of continuous LiF fibers cannot be produced on Earth

because of the presence of convection currents and vibration in the melt during solidification); (2) extract a few fibers from an ASTP-grown NaCl-LiF eutectic ingot and also from Earth-grown ingots and determine whether the extracted fibers were continuous or discontinuous; (3) calculate the interfiber spacing of the LiF fibers; and (4) measure transmittance versus wavelength curves of ASTP-grown and Earth-grown ingots, both along and perpendicular to the fiber axes.

EXPERIMENTAL PROCEDURE

NaCl, 29 wt.% LiF eutectic ingots were prepared from 99.96 percent NaCl and 99.99 percent Lif obtained from Research Organic-Inorganic Chemical Corporation, Sun Valley, California. The salt ingots were melted and solidified in an induction furnace under an argon atmosphere. After solidification, each ingot was machined to the shape and dimensions depicted by the sample in Figure VIII-1.

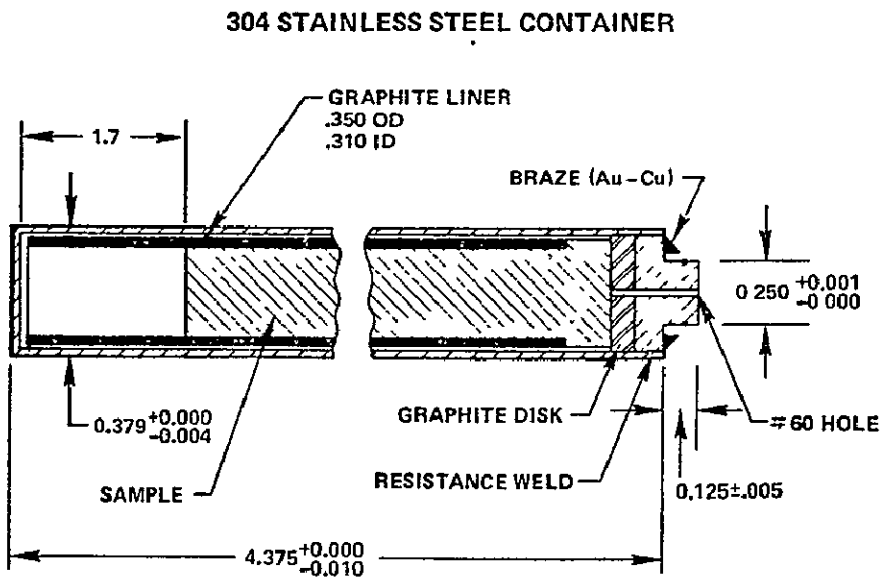

THE SOLIDIFICATION EXPERIMENT WAS CARRIED OUT IN A MULTIPURPOSE ELECTRIC FURNACE [VIII-8] AT A FREEZING RATE OF 0.6°C/min AND A TEMPERATURE GRADIENT OF 50°C/cm THE PROCEDURE FOR CONDUCTING THE EXPERIMENT IS AUTOMATIC

Figure VIII-1. Sketch of an ampoule.

To hold the salt ingot, a graphite crucible was machined from a high purity graphite rod, 0.5 in. in diameter and 12 in. long, obtained from Ultra Carbon Corporation, Bay City, Michigan, to the dimensions of 4 in. in length, 0.350 in. outside diameter, and 0.310 in. inside diameter. Since graphite is a very fragile material, a special method was employed to machine the crucibles. Beginning with a 0.5 in. rod mounted in a lathe, the 0.310 in. hole was drilled so as to be concentric with the graphite rod. Then a 0.31 in. brass rod was inserted into the 0.310 in. hole to give the graphite tube support, while the outer diameter was machined from 0.5 in. to 0.35 in. in diameter. The graphite crucibles were cut to 4.375 in. in length and calcined in vacuum at 950°C for 25 h.

The salt ingot-graphite crucible assembly was then loaded into a 304 stainless steel container having the dimensions shown in Figure VIII-1. The steel container was made from 0.375 in. outside diameter and 0.355 in. inside diameter stainless steel tubing obtained from Tube Sales Co., Los Angeles, California, with a stainless steel plug heliarc-welded to one end of the tube. After loading the ingot-crucible assembly, the inner wall of the stainless steel container was coated with a graphite paste where the salt ingot is exposed to the container. Then a calcined graphite disk (0.010 in. thick) was placed over the end of the ingot. The graphite paste and disk were employed to prevent a reaction between the container and the salt when the salt was later remelted and resolidified. The container was then sealed by heliarc welding a cap in place, with a No. 60 vent hole as shown in Figure VIII-1.

There were three groups of samples involved. All were prepared initially at the University of California, Los Angeles (UCLA). The first set was retained at UCLA for later comparison (group A). The second set was sent to Westinghouse Laboratories to be regrown in a prototype furnace for comparison with the space-grown samples (group B). The third set of the three samples went from UCLA to the Apollo-Soyuz space vehicle for growth in space (group C).

The resolidification experiment in the Apollo-Soyuz vehicle was carried out in a multipurpose electric furnace [VIII-8]. One-half of the eutectic sample in this experiment adjacent to the graphite disk was left unmelted, and the remaining portion of the sample was melted and resolidified unidirectionally toward the empty space of the ampoule, as indicated in Figure VIII-1.

RESULTS

The experimental results are presented in five parts. The first part concerns the macrostructure and microstructures of the samples that were grown in the Apollo-Soyuz vehicle and on Earth. The second part concerns the extraction of continuous LiF fibers embedded in an NaCl matrix. The third part calculates the interfiber spacing of the LiF fibers of the ASTP-grown NaCl-LiF eutectic. The fourth part concerns the image the transmission of the NaCl-NaF eutectic, and the fifth part concerns the optical transmittance.

Macrostructures and Microstructures

After the space experiment the three ampoules were brought to us by Dr. Ang of Aerospace Corporation and were given three identity numbers (131-07, 131-08, and 131-09).

Figure VIII-2 is a macrophotograph showing the appearance of the three ampoules after the space experiment. The surfaces of the stainless steel cylinders and plugs were in perfect condition.

Figure VIII-3 is a macrophotograph of the three ASTP-grown samples taken out of the ampoules by grinding off the welded ends of each stainless steel cylinder. A careful inspection of the surface of the samples revealed no reaction between the NaCl-LiF eutectic and the graphite container. In sample 18, one transverse fracture surface occurred at the head portion of the sample, as revealed in Figure VIII-3. However, the fracture, which occurred after resolidification, did not interrupt the growth pattern of the sample.

Figure VIII-4 is a macrophotograph of the solidified sample, 131-09, showing the shape of the melt-back interface. The resolidified portion of the sample is on the right of the interface, and the unmelted portion of the sample is on the left of the interface. In this particular sample, the remelt-back interface is 0.28 cm (0.11 in.) from the left end of the sample, whereas the same melt-back distances of the other two samples are approximately 0.51 cm (0.20 in.). This may indicate a slight offset in the positioning of the heat zones in the furnace. An enlarged portion of the solid-liquid interface is given in Figure VIII-5, which shows the beginning of the solidification process. The elongated LiF phases grew in a direction perpendicular to the conical solid-liquid interface. This indicates that the direction of heat extraction during the onset of solidification was not parallel to the growth direction as intended. At a distance not far away from the initial solid-liquid interface as evidenced in

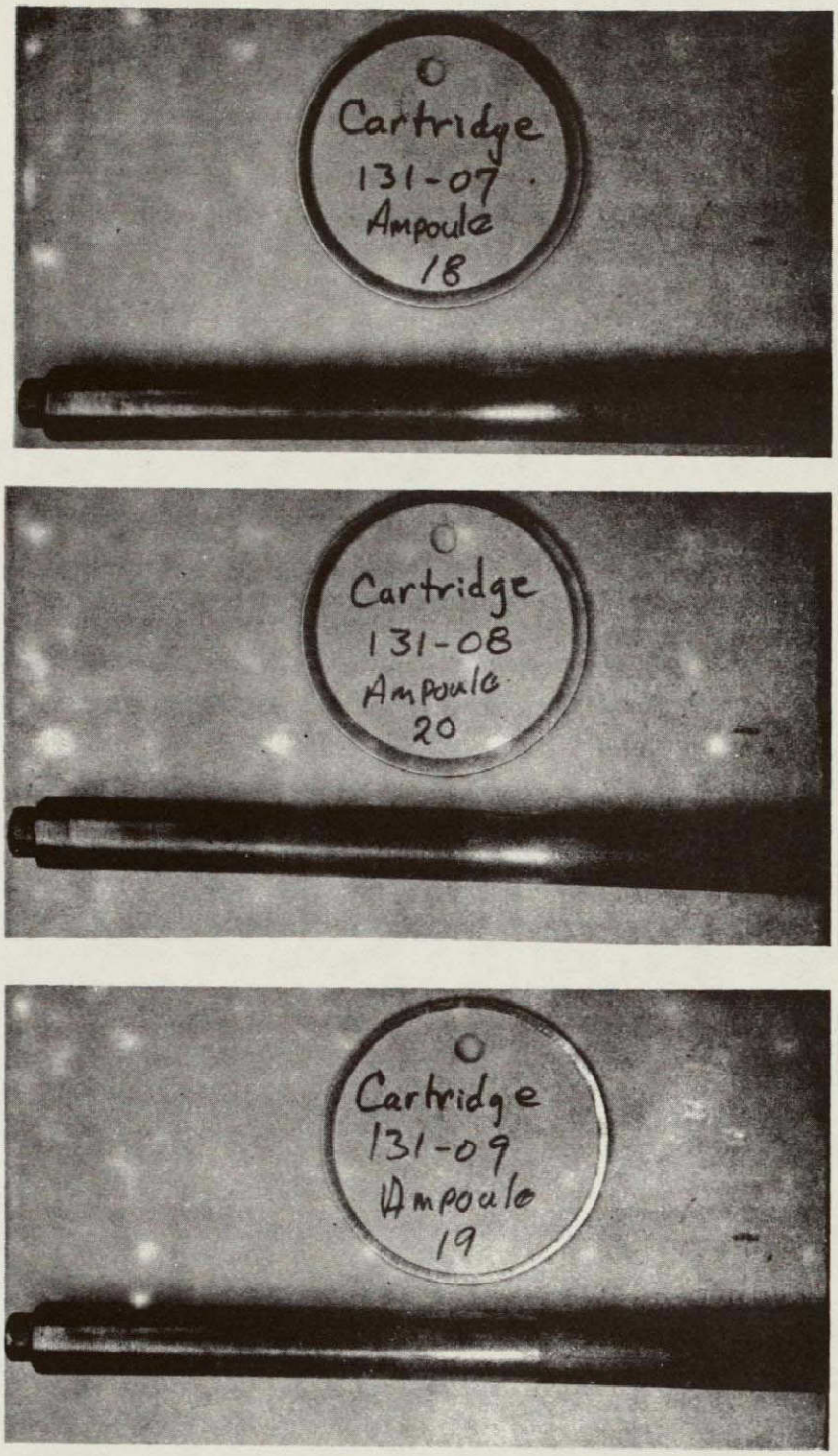

Figure VIII-2. Macrophotograph of the three ASTP ampoules (1X).

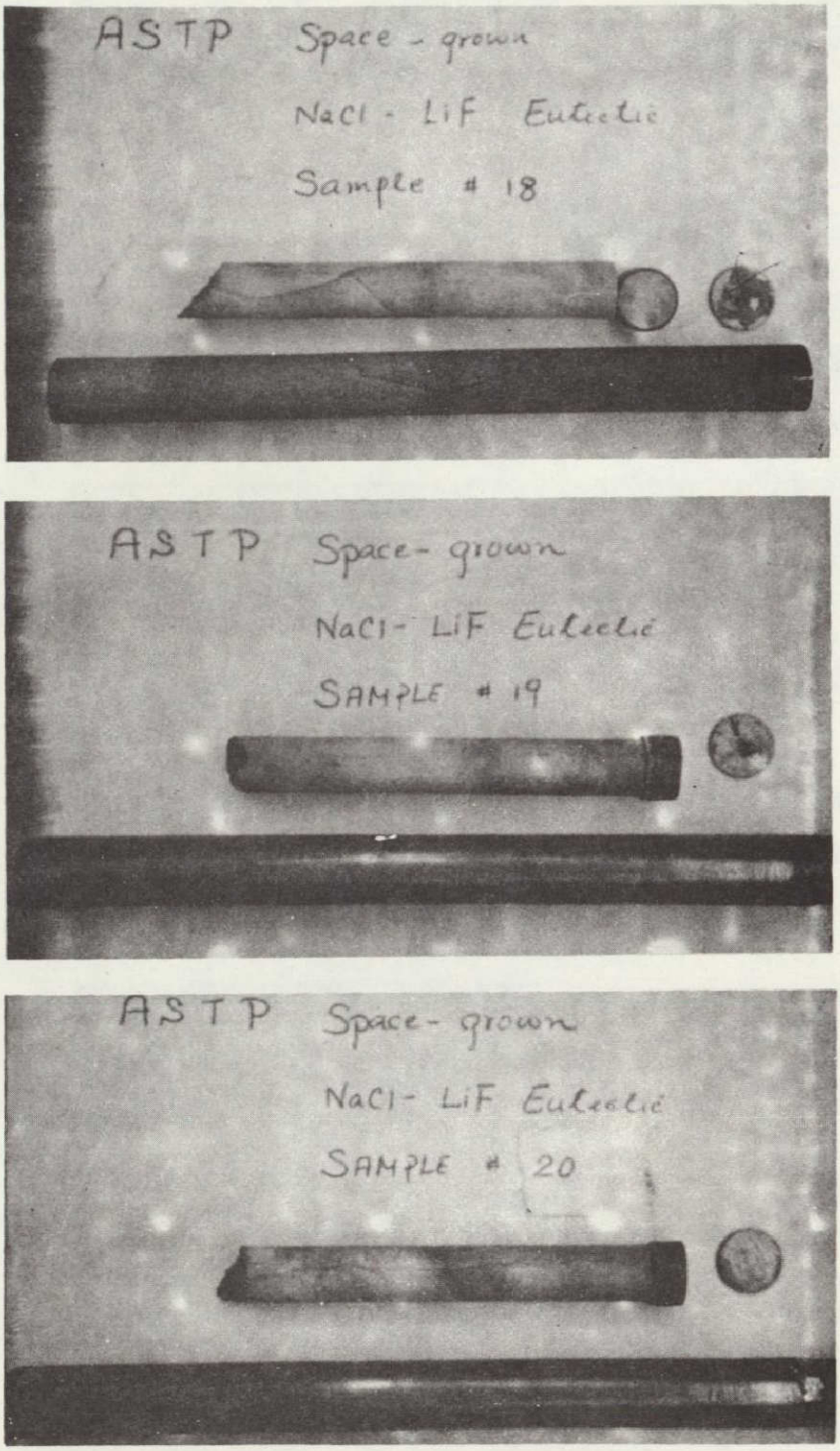

Figure VIII-3. Macrophotograph of ASTP-grown NaCl-LiF eutectic.

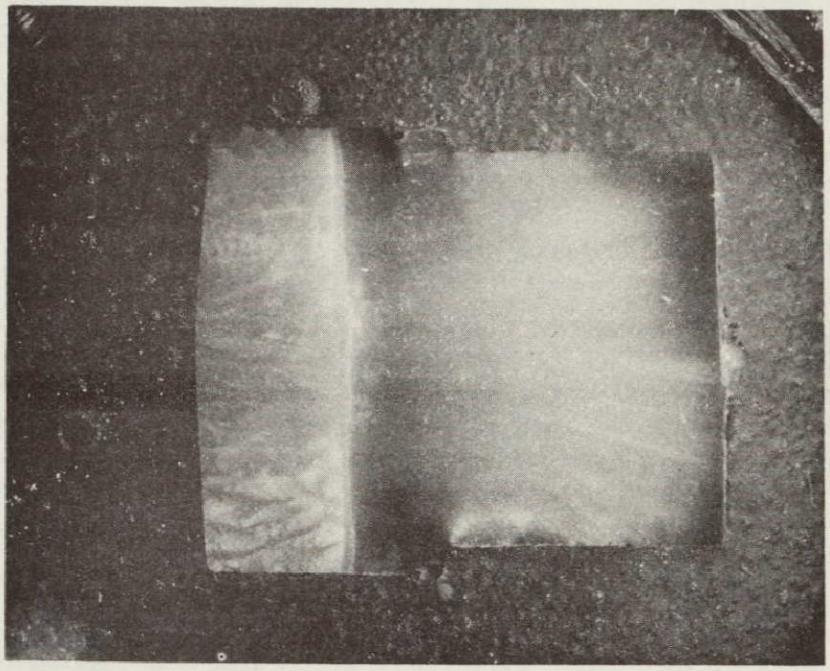

Figure VIII-4. Macrophotograph showing the original shape of the solid-liquid interface of the ASTP-grown NaCl-LiF eutectic (6.4X).

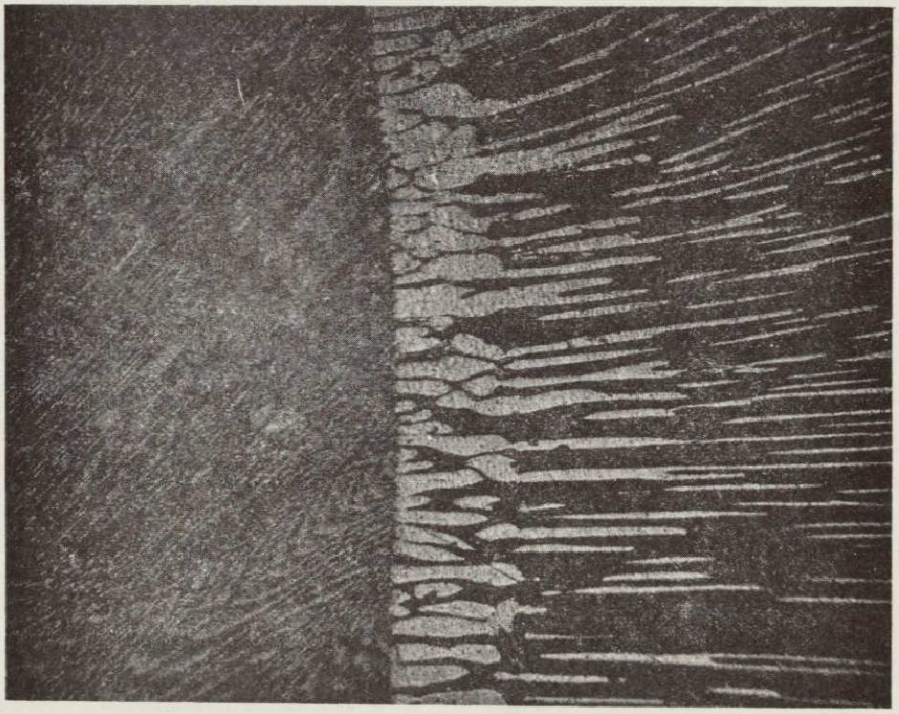

Figure VIII-5. Enlarged portion at the original solid-liquid interface (80X).

in Figures VIII-4 and VIII-5, the LiF fibers began to divert toward the periphery of the ingot. Figure VIII-6(a) is a representative photomicrograph of a longitudinal section of 131-09 showing the long continuous fibers. The eutectic microstructure that resulted when the NaCl-LiF eutectic was grown on Earth with convection current is shown in Figure VIII-6(b), which shows that the solidified LiF fibers are short and discontinuous. A representative photomicrograph of a transverse section of a sample is shown in Figure VIII-7, which reveals the shapes of the fibers which are preferentially round. A scanning electron photomicrograph (SEM) showing the shapes of LiF fibers grown on Earth protruding from the continuous NaCl matrix is given in Figure VIII-8, which is the perspective view of the round LiF fibers. Figure VIII-9 shows a corresponding SEM view of the ASTP-grown ingot showing that all the LiF fibers are aligned in one direction.

Single-grain eutectic was not produced in the presence of microgravity in space as evidenced in Figure VIII-10, which is a transverse section of sample 131-07. Many grains are present throughout the entire cross section. Evidence supporting this is given in Figure VIII-11(a), which is a picture taken from sample 131-07 grown in space. Filtered light from a Bausch and Lomb microscope was directed at the lower end of the sample. Because of good alignment of LiF fibers along the sample axis, light was transmitted from the lower end and propagated through the ingot at a longer distance with a much stronger intensity than the sample grown on Earth, as evidenced in Figure VIII-11(b). Light was not transmitted through the upper portion of the ASTP sample, because in that portion of the sample, the fibers did not align with the sample axis.

Lithium Fluoride Fibers

Figure VIII-12 is a photograph of an ASTP-grown ingot taken when the LiF fibers were suspended in a methyl alcohol. From Figure VIII-12, it is evident that the LiF fibers are continuous and straight. When the Earth-grown NaCl-LiF eutectic ingot was immersed in the same solution, LiF fibers could also be extracted from the NaCl matrix. However, the extracted fibers were short and discontinuous as indicated in Figure VIII-13, which agreed with predictions (sample from group A). In view of this analysis, it is tentatively concluded that continuous LiF fibers have been produced in space.

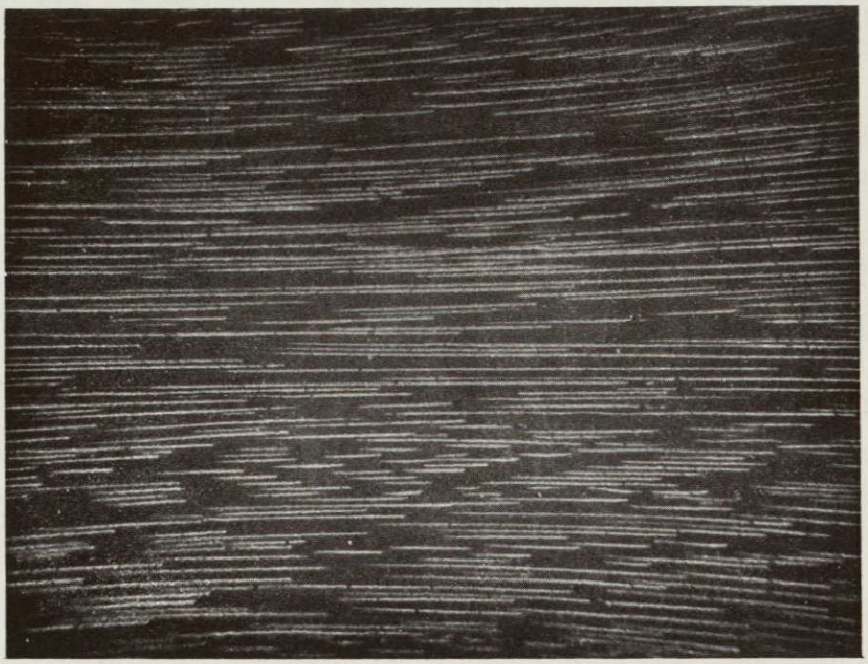

(a)

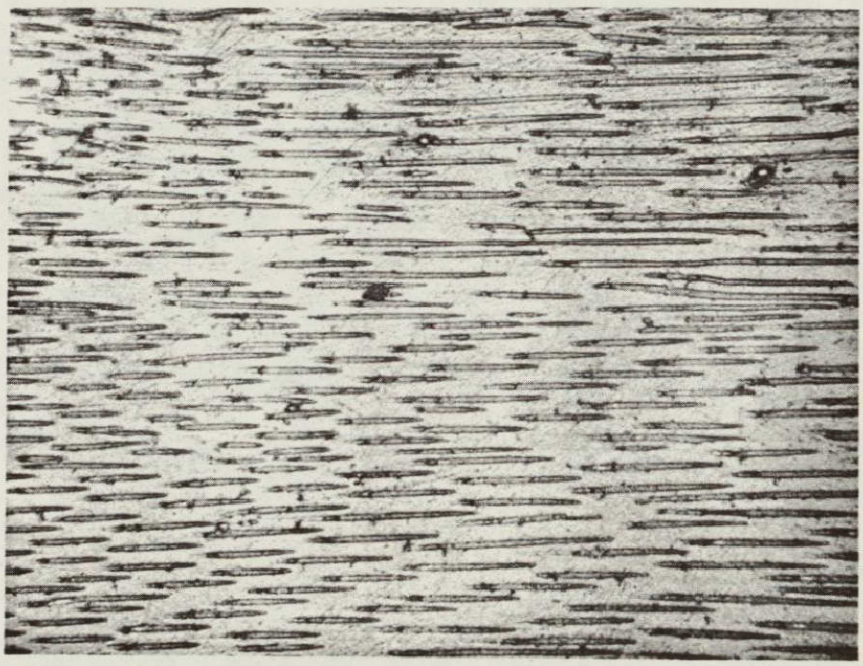

(b)

Figure VIII-6. Photomicrographs of a longitudinal section of the NaCl-LiF eutectic showing (a) continuous LiF fibers (56X) and (b) discontinuous LiF fibers (210X).

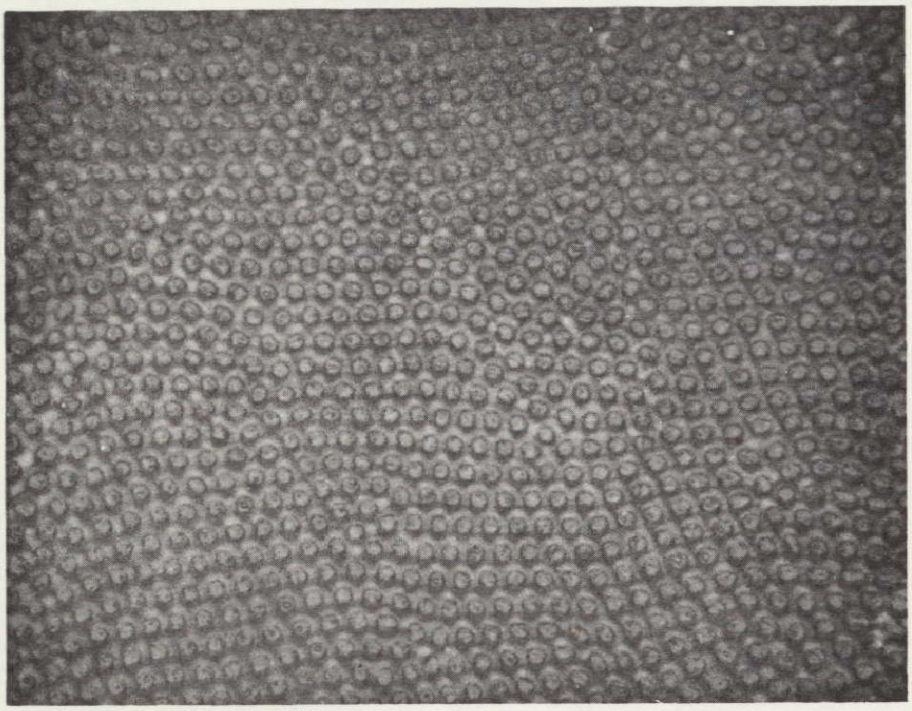

Figure VIII-7. Photomicrograph of the transverse section showing shapes of LiF fibers (410X).

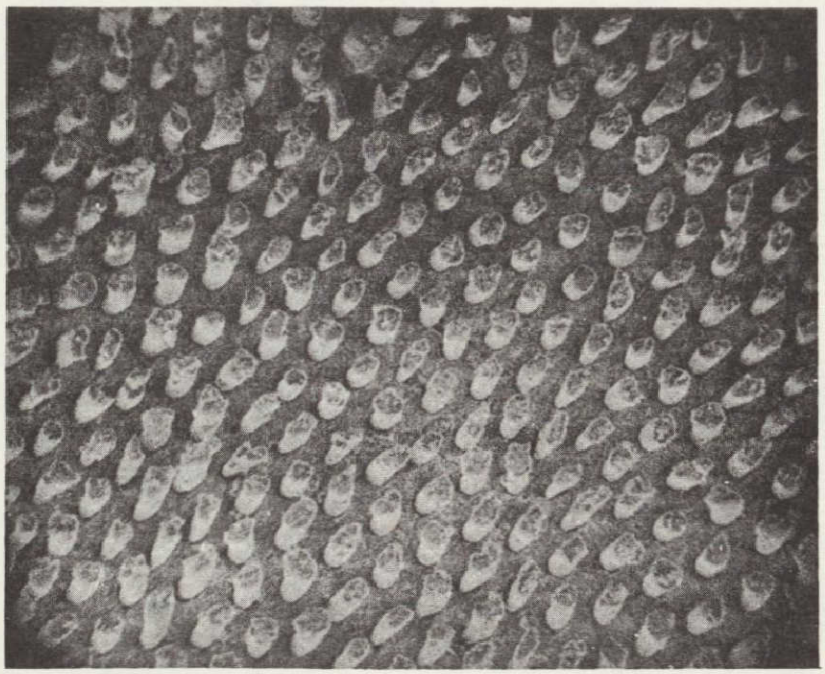

Figure VIII-8. Scanning electron photomicrograph of the Earth-grown LiF fibers (940X).

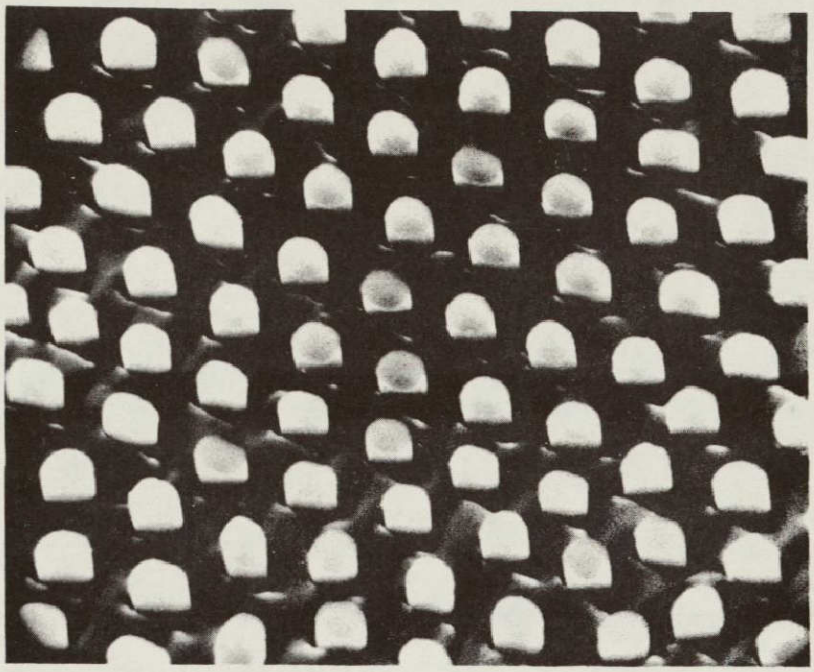

Figure VIII-9. Scanning electron photomicrograph of the ASTP-grown LiF fibers (1900X).

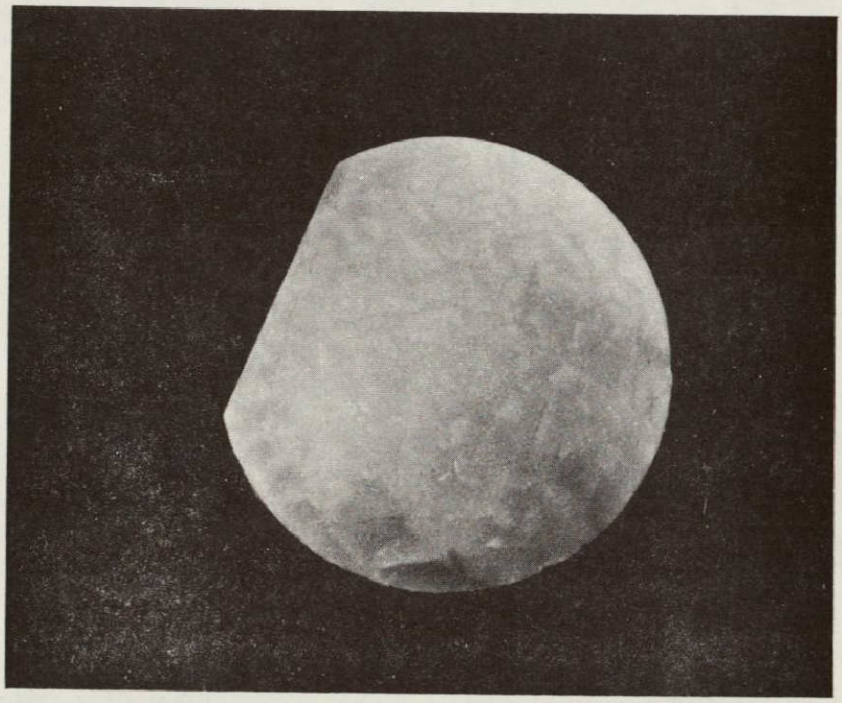

Figure VIII-10. Macrophotograph of the transverse section of the NaCl-LiF eutectic showing grains and subgrains, sample No. 10 (7.2X).

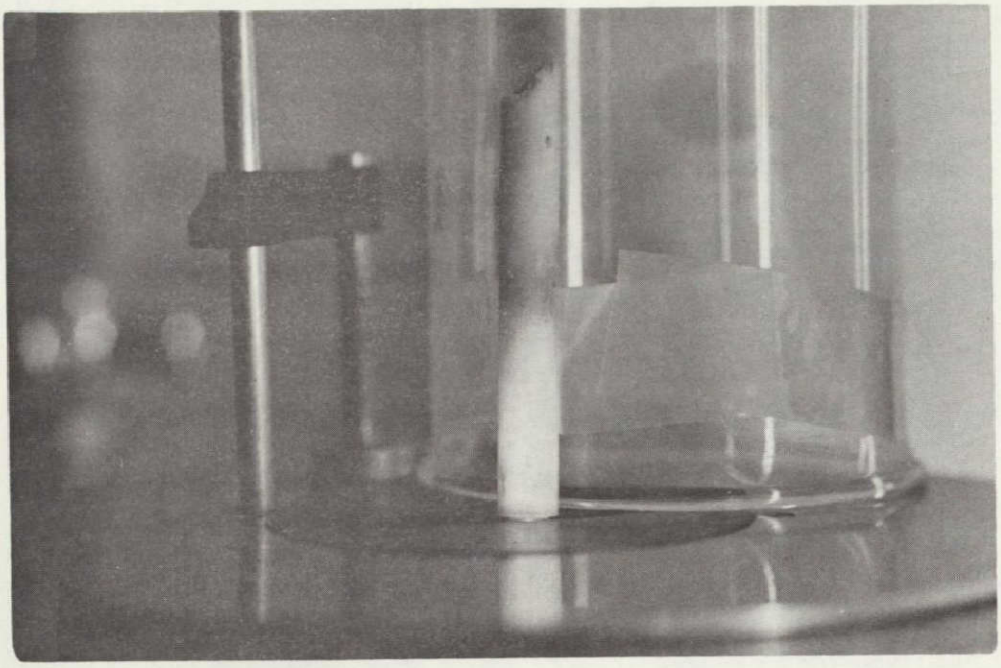

(a)

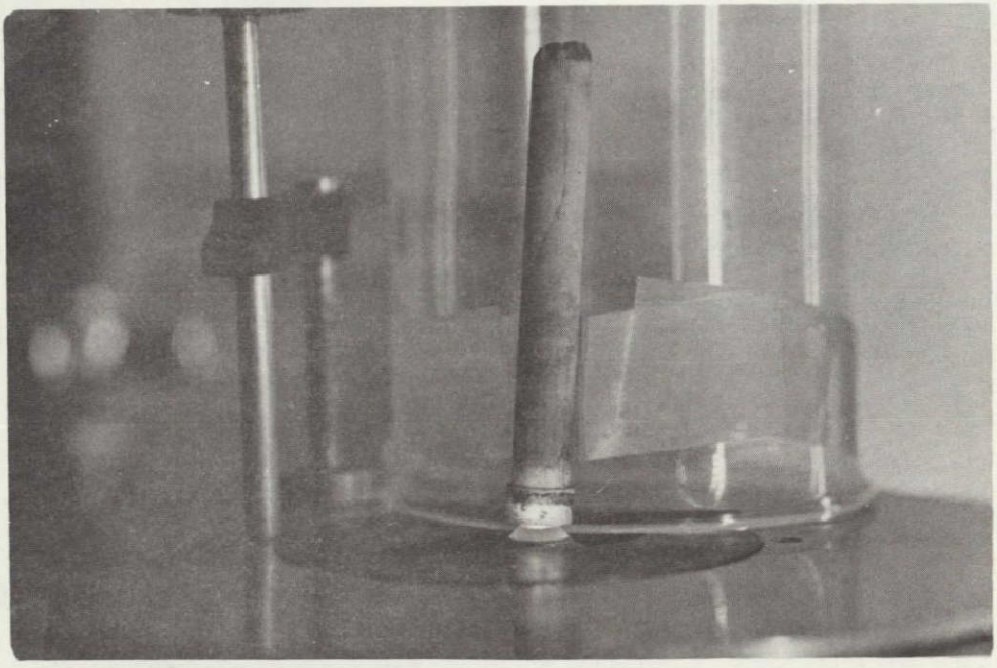

(b)

Figure VIII-11. Macrophotographs of (a) ASTP-grown and (b) Earth-grown NaCl-LiF eutectic.

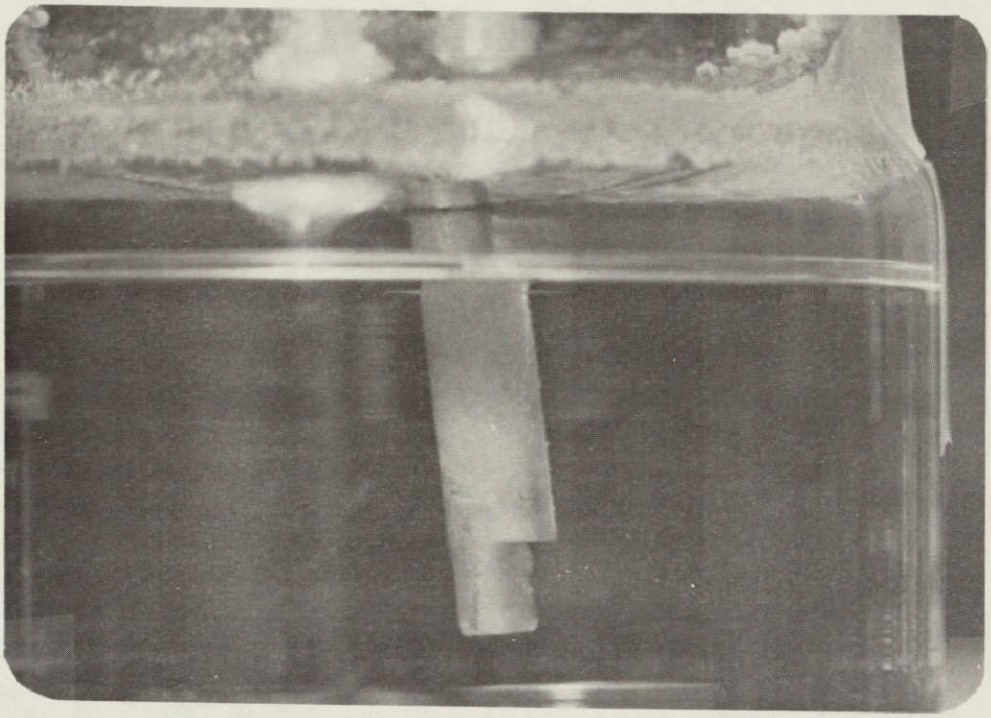

Figure VIII-12. ASTP-grown ingot with continuous LiF fibers (2X).

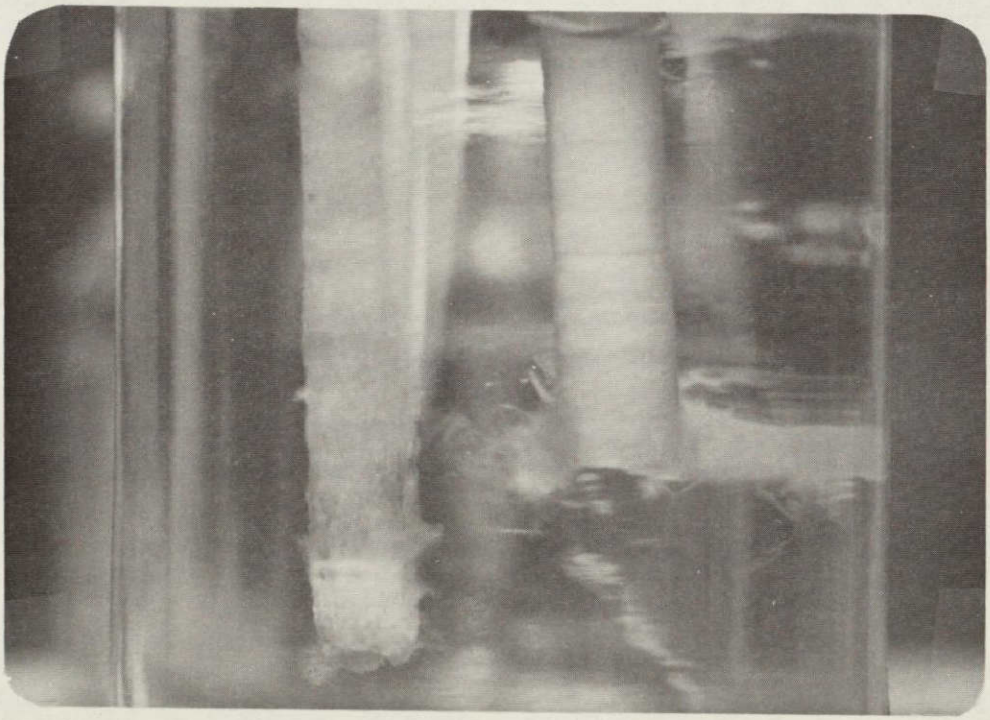

Figure VIII-13. Discontinuous and randomly oriented fibers of the Earth-grown ingot end (2X).

Interfiber Spacing

The measured interfiber distances in ASTP-grown, phototype furnace-grown, and Earth-grown ingots at growth rates of approximately 4.5 μm/s are as follows:

Interfiber Distance (μm)		
ASTP-Grown	Prototype Furnace-Grown	Earth-Grown
6.68 (131-07)	6.92 (131-01)	4.5 (UCLA)
5.41 (131-08)	7.35 (131-02)	
6.41 (131-09)	6.70 (131-03)	

The average diameter of the fiber of prototype furnace-grown and ASTP-grown ingots is 3.6 μm. These measurements indicate that there is no significant difference in interfiber spacing between the ASTP-grown and the prototype furnace-grown ingots. The interfiber spacing of the Earth-grown eutectic is smaller than that of the ASTP-grown ingot because the Earth-grown eutectic had a faster freezing rate during growth.

Image Transmission

Image transmission properties similar to those of fiber optic materials have been obtained by others with an NaCl-LiF eutectic [VIII-9]. Since the eutectic in that case had discontinuous LiF fibers, far better results will be obtained if the same eutectic can be produced in space with continuous fibers. Two cylindrical sections 2 mm long were cut from ASTP-grown and Earth-grown (group A) samples. Image transmission experiments were made on these two samples. The results are given in Figure VIII-14. Figure VIII-14(a) shows that an image was transmitted from a source (a sheet of paper containing the word "solar") through the length of the sample (2 mm) to its surface. The transmitted image has the same dimensions as the source, indicating that the LiF fibers are perpendicular to the plane of the paper. However, the transmitted image is not as clear as the original image of the source, indicating that there is a loss through transmission. Some loss is common to all fiber optics materials [VIII-10]. A transmitted image was also observed from a sample grown on Earth, as seen in Figure VIII-14(b). However, the image is unclear and the dimensions of the letters "S" and "E" are larger than those of the source, indicating that the fibers are diverged away from the source.

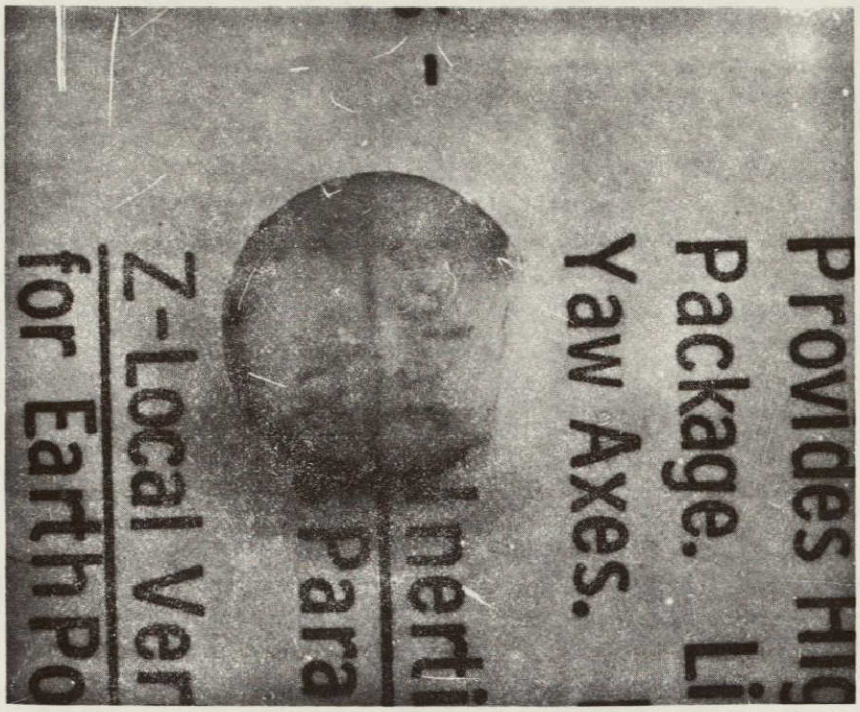

(a)

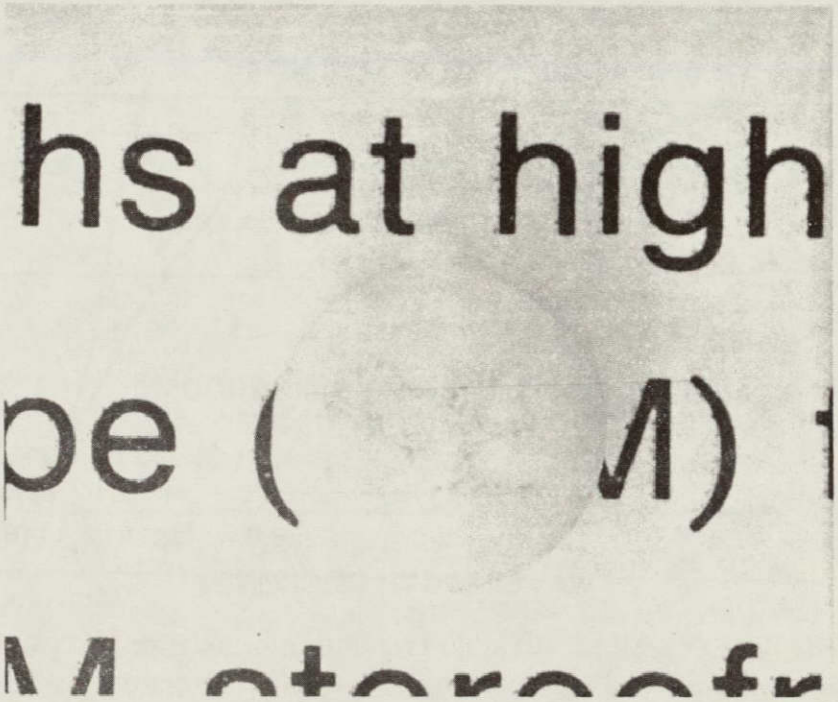

(b)

Figure VIII-14. Image transmission macrophotograph of (a) ASTP-grown and (b) Earth-grown NaCl-LiF eutectics, 2 mm sample thickness (5.3X).

Optical Property

Image transmission properties similar to those of fiber optic materials were obtained with an NaCl-NaF eutectic [VIII-9]. This eutectic was found to be a far-field infrared transmitting medium for wavelengths longer than the interfiber distance. Since the NaCl-NaF eutectic used for optical measurement has discontinuous NaF fibers embedded in an NaCl matrix, better results should be observed if continuous fibers are obtained. This was indeed the case as demonstrated in the Skylab experiment [VIII-1]. Similar experiments comparing transmission properties of NaCl-LiF eutectic grown in space and on Earth were performed for ASTP. The far-field infrared transmission of transverse sections of three NaCl-LiF eutectic samples is compared in Figure VIII-15. The ASTP space-grown sample is shown to have the highest transmittance over nearly the entire wavelength range, indicating that it has the highest percentage of fibers parallel to the growth direction. The transmittance result also shows that the sample grown in the Westinghouse prototype furnace has a lower transmittance than the eutectic sample grown at UCLA over part of the wavelength range.

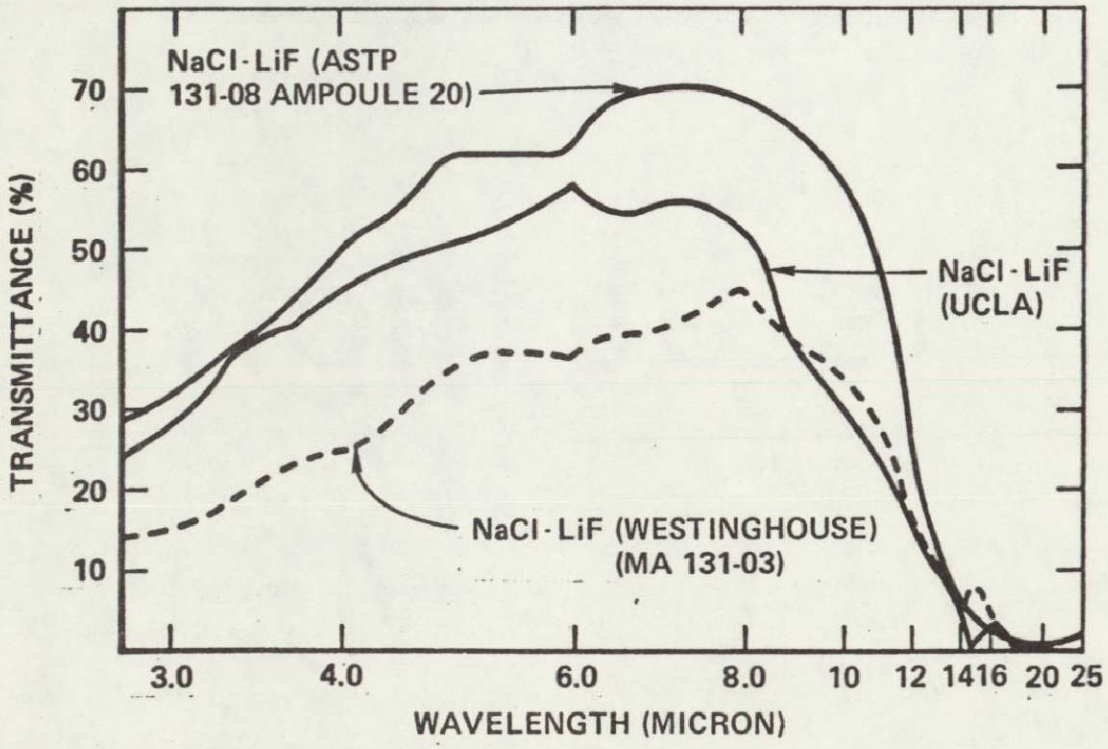

Figure VIII-15. Far-field infrared transmission curves of transverse sections of NaCl-LiF eutectics grown on earth and in space, 0.0211 in. sample thickness.

The effect of thickness on the transmission curve is shown in Figures VIII-16 and VIII-17 for the Westinghouse prototype furnace and the ASTP space-grown samples, respectively. In both cases, the thinner the sample is, the higher the transmittance is for a fixed wavelength. This observation is in agreement with absorption laws, as expected.

Figures VIII-18(a) and VIII-18(b) show plots of the transmittance versus wavelength of a longitudinal section of a UCLA-grown sample (group A) using polarized light with an electric field parallel and perpendicular to the fiber axes, respectively. Figures VIII-19(a) and VIII-19(b) show the same curves for the ASTP-grown sample (131-07). In both cases, the transmittance is lower over a range of wavelength measured. It is difficult to explain this peculiar phenomenon at the present time.

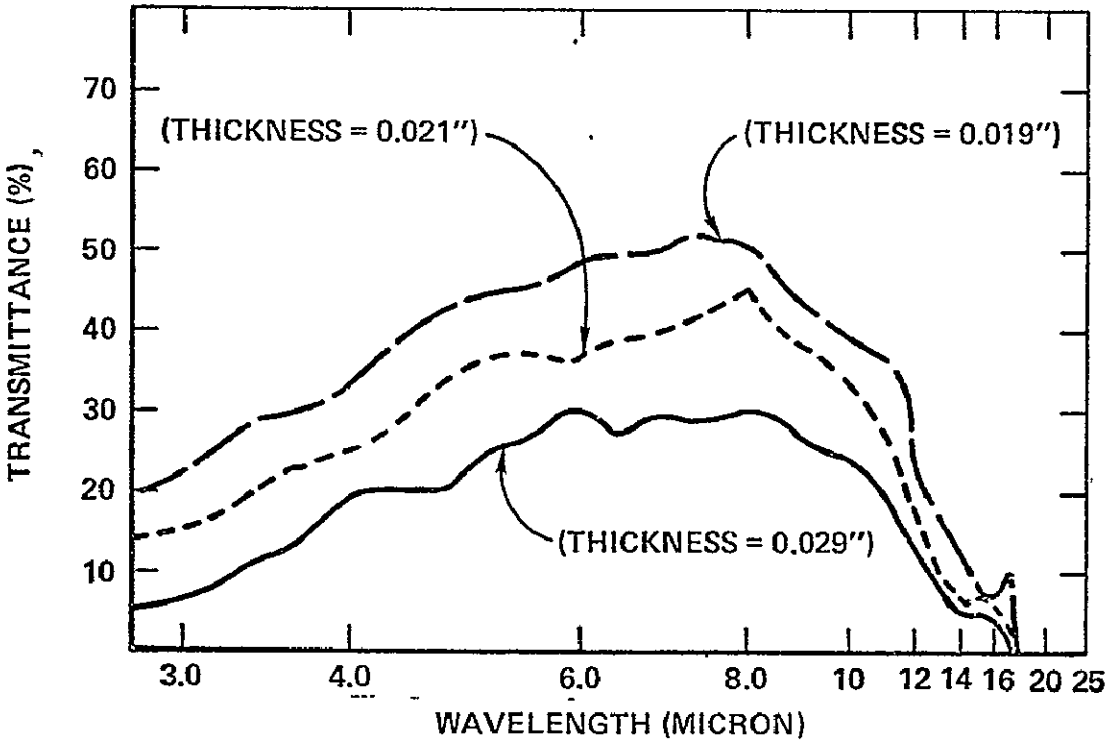

Figure VIII-16. Far-field infrared transmittance curves of transverse sections of NaCl-LiF eutectics with different thickness, sample No. 131-03.

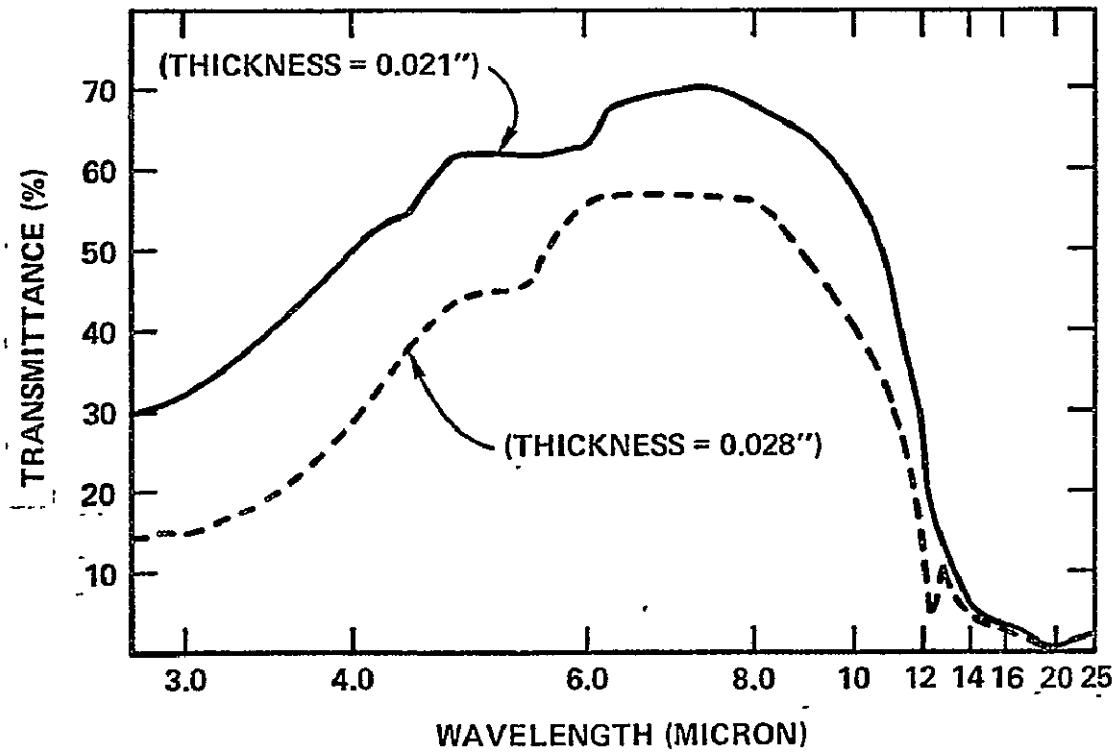

Figure VIII-17. Far-field infrared transmittance curves of transverse sections of NaCl-LiF eutectics with different thickness, sample No. 131-08.

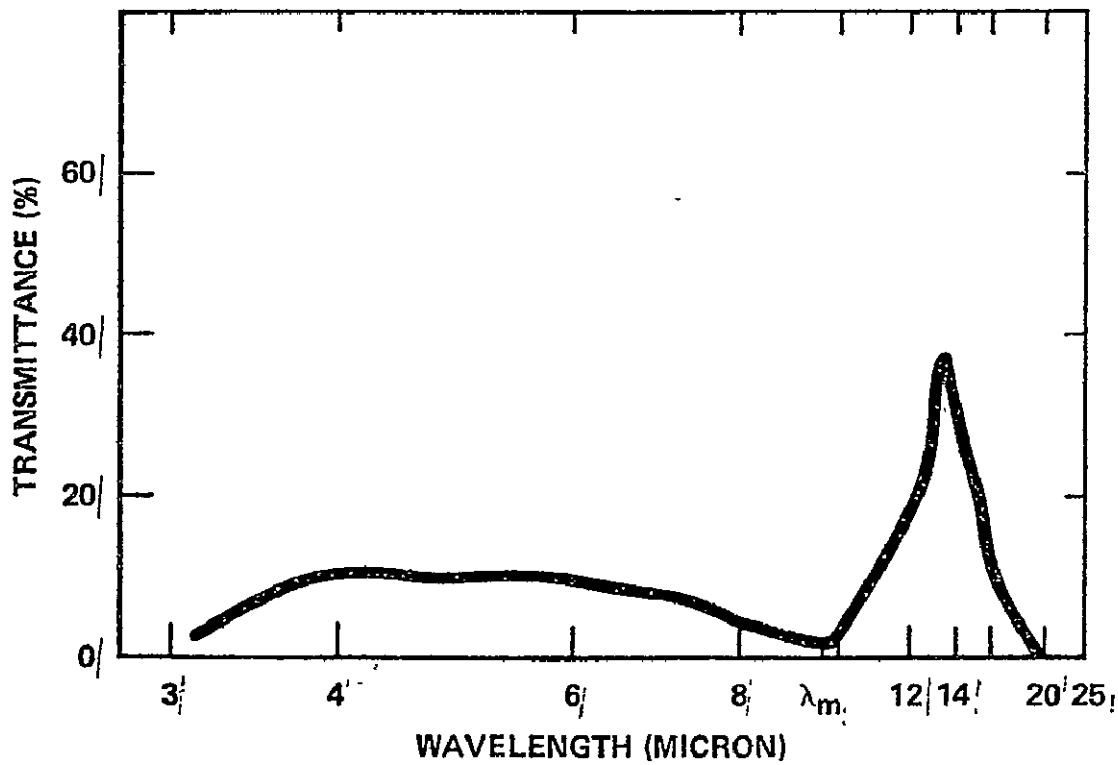

Figure VIII-18(a). Far infrared transmittance curve of a longitudinal section of NaCl-LiF eutectic grown on Earth, electric field parallel to fiber axis.

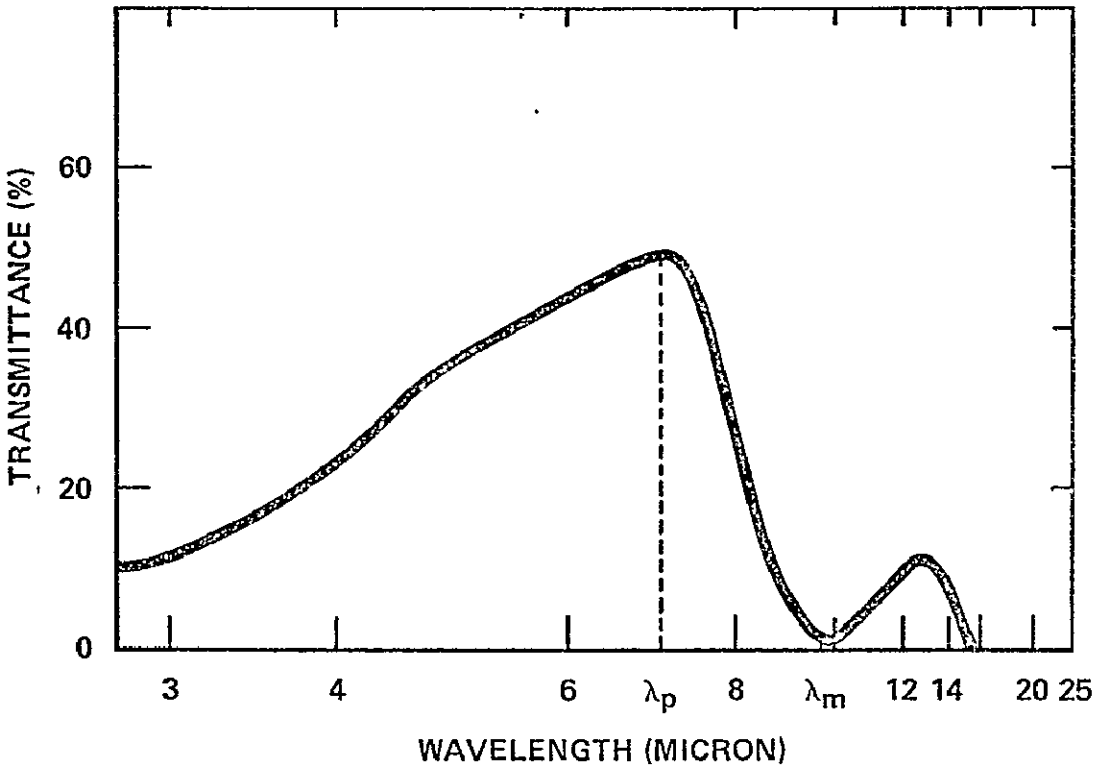

Figure VIII-18(b). Far infrared transmittance curve of a longitudinal section of NaCl-LiF eutectic grown on Earth, electric field perpendicular to fiber axis.

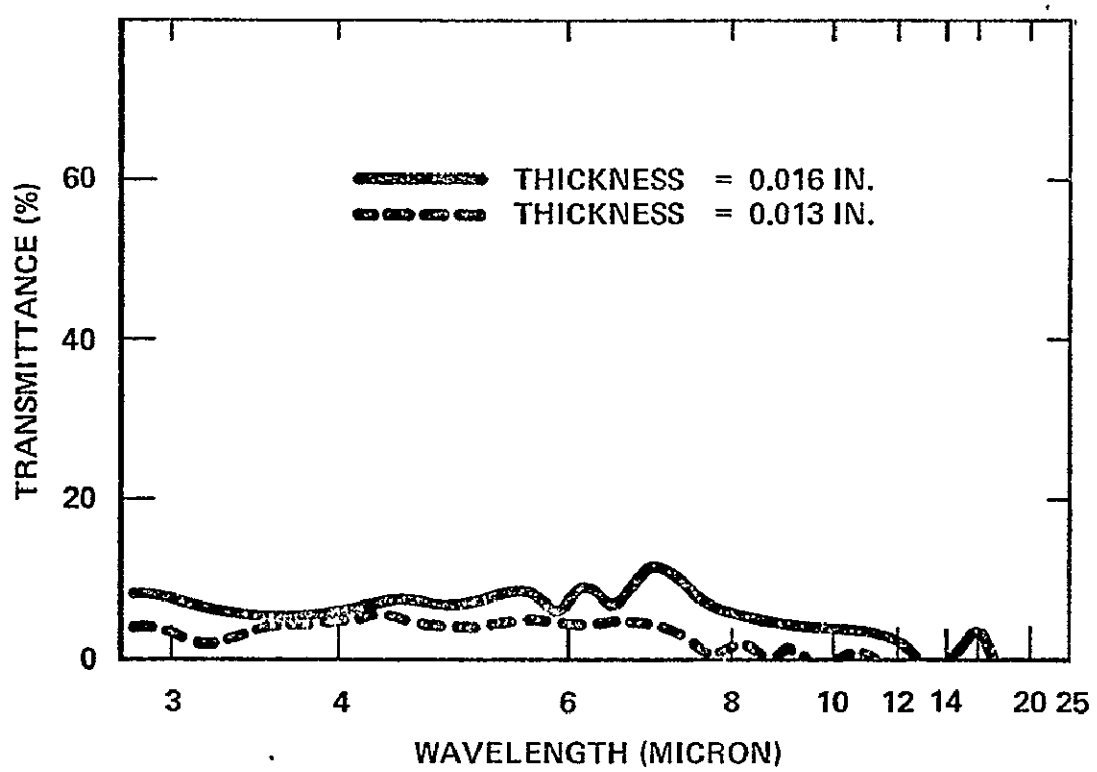

Figure VIII-19(a). Far infrared transmittance curves of a longitudinal section of NaCl-LiF eutectic (131-07) of varying thicknesses, electric field parallel to fiber axis.

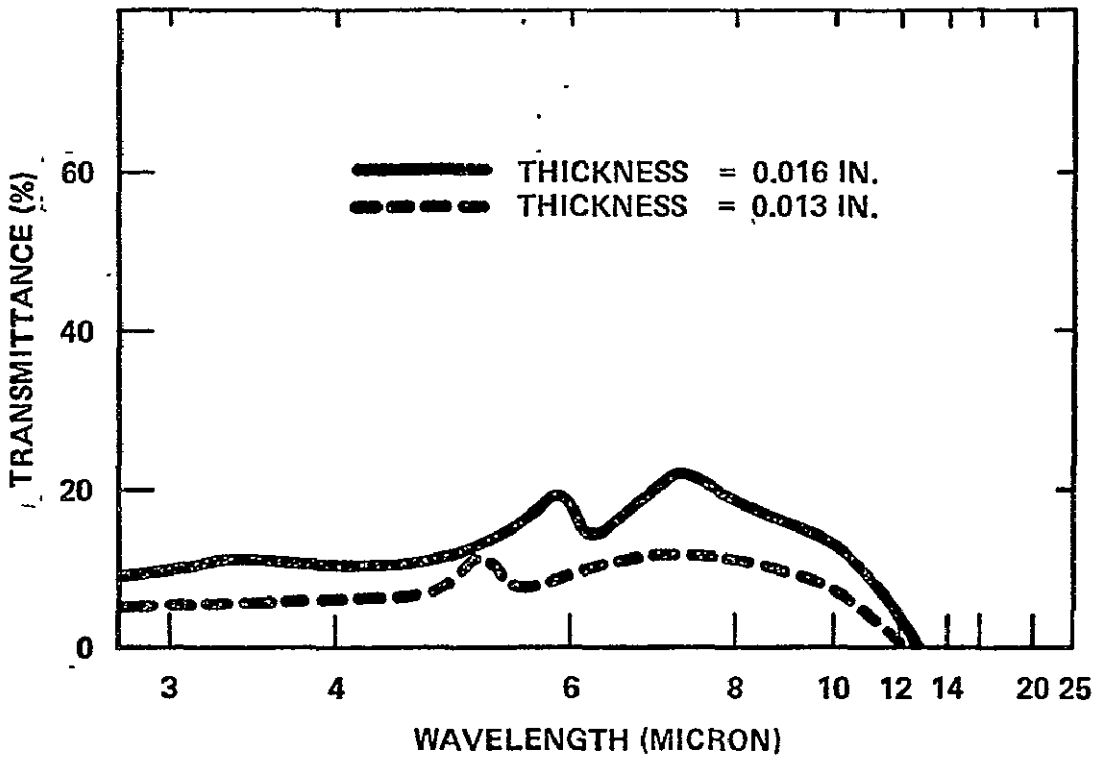

Figure VIII-19(b). Far infrared transmittance curves of a longitudinal section of NaCl-LiF eutectic (131-07) of varying thicknesses, electric field perpendicular to fiber axis.

DISCUSSION

LiF Fibers

In a zero-g environment, there is no gravity-driven convection current in the liquid during solidification and there is no difficulty in mixing two liquid phases of different densities. Furthermore, vibration levels in the spacecraft will be far lower than those on Earth. Consequently, a homogeneous eutectic mixture consisting of continuous fibers can be produced in a space environment, and microstructure sensitive to convection currents and vibration can develop undisturbed. Accordingly, the success in producing continuous LiF fibers as evidenced in Figure VIII-12 is primarily due to the absence of convection current in the melt during resolidification in space.

Optical Transmittance

Pure sodium chloride and sodium fluoride crystals, as is known from previous work [VIII-1], have approximately 95 percent transmittance per centimeter of thickness, up to 15 and 9 μm respectively, in the far infrared wavelength region. Beyond these ranges of wavelengths, these crystals have zero transmittance because of the optical modes of lattice vibration of ionic crystals. If a thin piece of NaCl-LiF eutectics is cut along its fiber axis (longitudinal section), as illustrated in Figure VIII-20, and is measured from 2 to 20 μm wavelength with an infrared spectrometer, typical transmittance versus wavelength curves with a polarized beam parallel and perpendicular to the fiber axes are as given in Figures VIII-18(a) and VIII-18(b), respectively. For the electric field parallel to the fiber axes, the transmittance is near zero over a range of wavelength approximately less than λ_m (10 μm), a maximum wavelength. When the electric field is perpendicular to the fiber axes, the percentage of transmittance increases over a range of wavelengths less than λ_m and reaches a maximum value at a wavelength of 7.2 μm, which is designated

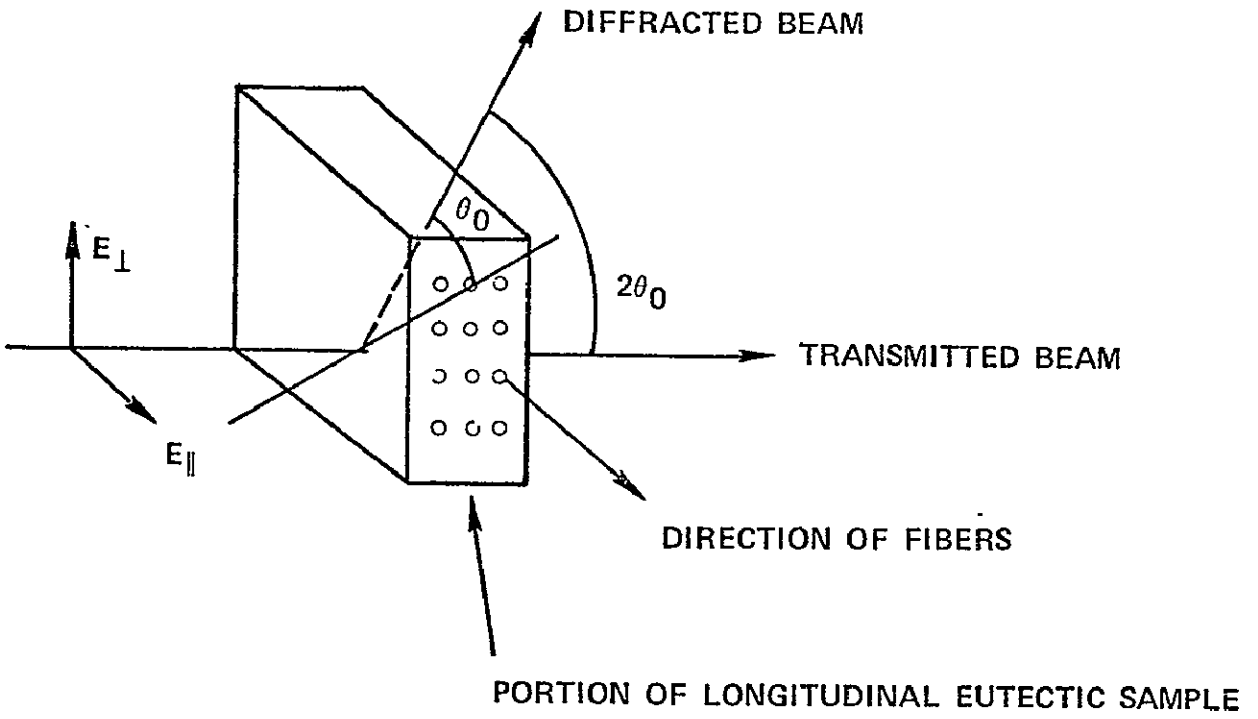

Figure VIII-20. Diagram illustrating quantities discussed in analyzing scattering measurements for transmission through a longitudinal sample section.

λ_p, a peak wavelength, as indicated in Figure VIII-18(b). Since a thin NaCl-LiF eutectic sheet has these characteristics it can be used as a polarizer and a modulator. It can switch on and off the light at a specified wavelength when the electric field is rotating. An explanation has been advanced to account for this phenomenon in terms of two-dimensional Bragg scattering and the polarization effect of Rayleigh scattering [VIII-11].

CONCLUSIONS

The following conclusions can be drawn from this report:

1. Continuous LiF fibers regularly arranged in a portion of the NaCl matrix which has been resolidified unidirectionally in a space environment have been produced.

2. Larger transmittance over a wider wavelength and better image transmission were obtained for transverse sections of the ASTP-grown ingots.

RECOMMENDATIONS

The following recommendations are made:

1. To design decanting experiments to study the interface morphology in the scientific laboratory to be used in the early flights of the Space Shuttle.

2. To etch out LiF fibers from the NaCl matrix for the study of multiple channel electron intensifiers.

3. To make an extensive study on the composition of LiF and NaCl phases using an electron microprobe.

REFERENCES

VIII-1. Yue, A. S. and Yu, J. G.: Thermophysics and Heat Transfer Conference, AIAA/ASME, July 15-17, 1974, AIAA Paper No. 74-646.

VIII-2. Yue, A. S. and Clark, J. B.: Trans. TMS-AIME, 1961.

VIII-3. Lemkey, F. D. and Thompson, E. R.: Met. Trans., vol. 2, 1971, p. 1537.

VIII-4. Yue, A. S.: Trans. TMS-AIME, vol. 224, 1962, p. 1010.

VIII-5. Crossman, F. W. and Yue, A. S.: Met. Trans., vol. e, 1971, p. 1545.

VIII-6. Kraff, R. W. and Albright, D. L.: Trans. TMS-AIME, vol. 221, 1961, p. 95.

VIII-7. Weiss, H.: Met. Trans., vol. 2, 1971, p. 1513.

VIII-8. Seidensticker, R.: Third Space Processing Symposium, April 30-May 1, 1974, Marshall Space Flight Center, Alabama.

VIII-9. Batt, J. A.; Douglas, F. C.; and Galasso, F. S.: Optical Properties of Unidirectionally Solidified NaF-NaCl Eutectic. Ceramic Bulletin, vol. 48, 1969, pp. 622-626.

VIII-10. Payne, D. N. and Gambling, W. A.: Opto-Electronics, vol. 5, 1973, p. 297.

VIII-11. Yue, A. S.; Allen, F. G.; and Yu, J. G.: Zero-Gravity Growth of NaF-NaCl Eutectics. NASA Contract No. NAS-8-28310, January 1976.

SECTION IX

GERMANIUM-SILICON SOLID SOLUTIONS

EXPERIMENT MA-150

By V. S. Zemskov,[1] V. N. Kubasov, I. N. Belokurova, A. N. Titkov, I. L. Shulpina, V. I. Safarov, and N. B. Guseva

TABLE OF CONTENTS

LIST OF ILLUSTRATIONS

LIST OF ILLUSTRATIONS (Concluded)

INTRODUCTION

An experiment on melting and directional crystallization of an antimony (Sb) doped germanium silicon (GeSi) solid solution was designed for the Apollo-Soyuz Test Project (ASTP) to study the possibility of using zero-g conditions for obtaining solid-solution monocrystals with uniformly distributed components.

Solid-solution monocrystals obtained in the zero-g environment in the absence of ejecting forces and thermal convection were expected to have a more homogeneous and even distribution of components compared to those obtained under normal gravity conditions.

It was anticipated that the absence of convectional mixing and the occurrence of mass transfer in the melt caused by diffusion only would create conditions for stationary crystal growth and provide a compositional segregation consistent with these conditions [IX-1]. Also, in the absence of uncontrollable convective mixing, laminar distribution of components in a monocrystal is not likely to occur [IX-2].

Sb-doped GeSi solid solutions present a favorable material for studying the previously mentioned processes, because the distribution coefficient of Si in Ge, which is $K_{Si} > 1$, and that of Sb, which is $K_{Sb} < 1$, render the possibility of investigating the behavior of components with different distribution coefficients.

Since the Sb-doped GeSi solid solution is a semiconducting material, the precision techniques that are widely used in studying semiconducting materials can be used also for a detailed investigation of component distribution in crystal volume and for crystal structure defect analyses.

PREPARATION AND EXECUTION OF THE EXPERIMENT

Cylindrical specimens of Sb-doped GeSi solid solution, which will be referred to as "ingots," were prepared for the experiment. The ingots were made of monocrystals obtained by means of crystal pulling from the melt, which was continually being fed with Si [IX-3]. All monocrystals had the following identical characteristics: <111> orientation growth, Si content from 0.7 to 1.0 % at. wt., Sb content from 1 to 2×10^{17} at. cm^{-3}, dislocation density in {111} face from 10^3 to 10^4 cm^{-2}, laminar distribution of components with Si content fluctuations in the layers ranging to approximately 0.1 % at. wt., and heterogeneity associated with the crystal face effect.

The monocrystals were ground so that the ingot diameter should not be smaller than the internal diameter of the quartz ampoule by more than 1.2 mm, and the crystallographic <111> orientation should coincide with the ingot axis. The length of the ready ingot was 38 ± 0.1 mm.

The pipes used to fabricate the ampoules were made of quartz that contained total impurities of not more than 1.2×10^{-3} wt.%. Before inserting the ingots, the internal surface of the ampoules was graphitized by acetone pyrolysis.

A schematic diagram of an ampoule with an ingot inside is shown in Figure IX-1. To increase the mechanical strength of the ampoule, the walls of its rounded end, situated in the hot zone of the furnace, were made thicker than those of the remainder of the ampoule. The corresponding end of the ingot had

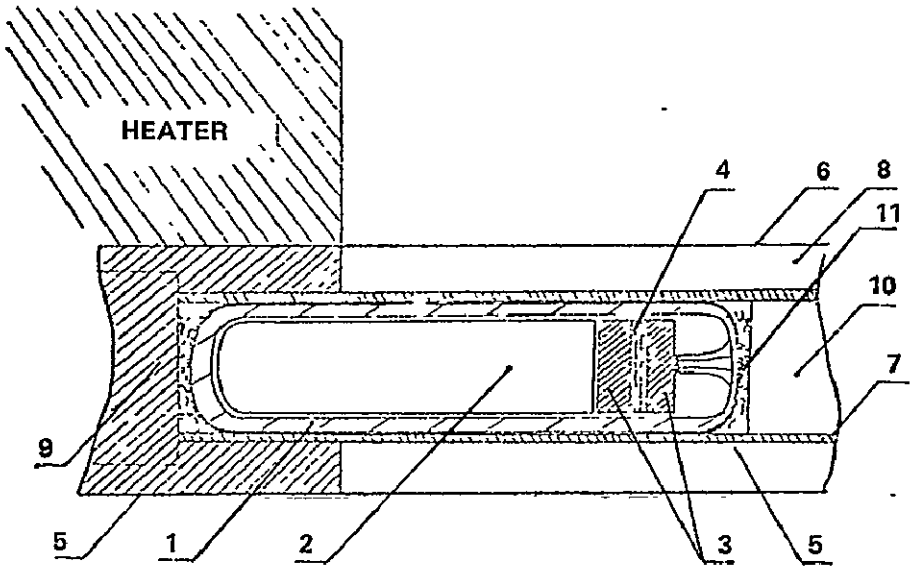

1. QUARTZ AMPOULE: OUTSIDE DIAMETER, 11.5 ± 0.1, LENGTH, 52 + 0.05, - 1.0 mm
2. INGOT: DIAMETER, 9 5 ± 0.1 mm; LENGTH, 38 ± 0.1 mm
3. GRAPHITE SPACERS
4. SPACER CONSISTING OF FOUR LAYERS OF QUARTZ CLOTH
5. COPPER FOIL
6. STAINLESS STEEL CARTRIDGE
7. STAINLESS STEEL PIPE
8. HEAT INSULATION
9. GRAPHITE INSERT WITH AMPOULE NO. 1
10. COPPER INSERT WITH AMPOULE NO. 3
11. QUARTZ PIPE

Figure IX-1. Schematic diagram of an ampoule with an ingot of GeSi solid solution.

a spherical shape matching the internal surface of the ampoule. At the other end of the ampoule, where sealing had to be performed, the specimen has a plane face. Two spacers that were of the same diameter as that of the specimen and that were made of high purity graphite that had been additionally annealed in vacuum at a temperature of approximately 1773 K (approximately 1500°C) were located at the plane face, and another spacer consisting of four layers of quartz cloth was located between the two graphite spacers. The sealing of the ampoules was performed at a near-vacuum pressure of 1×10^{-4} torr to make the quartz pipe press the graphite spacers tightly to the specimen.

The ampoules with the ingots were transferred to the United States for insertion into cartridges of a specific design. Both ends of the ampoules were wrapped with copper foil to create necessary conditions for heat transfer inside the cartridge.

The experiment on melting and crystallization of GeSi solid solution was conducted in a three-chamber multipurpose furnace [IX-4]. According to the preset program of the experiment, the ampoule containing the solid solution was placed in the furnace gradient zone in which the following thermal conditions were to be maintained:

1. A temperature of 1323 K (1050°C) at the hot end, and a temperature of 973 K (700°C) at the cold end.

2. A thermal gradient along the ampoule from 30 to 40 K/cm (30 to 40°C/cm), when the specimen is in the molten state, and from 10 to 40 K/cm (10 to 40°C/cm) during the cool-down phase.

Such temperature distribution in the gradient zone would be expected to restrict the melting of the ingot to no more than two-thirds of its length, so that the rest of it served as a seed for crystallization of the melt.

For the purpose of developing the required thermal mode and perfecting the ampoule and cartridge designs, ground-based thermal simulation experiments using prototypes of the flying ampoules and furnace were performed in the United States. There experiments aided in obtaining the desired temperatures at the hot and cold ends of the furnace. However, during these experiments, the distribution of the temperature along the ampoules with the solid solution was such that the thermal gradient did not exceed 20 K/cm (20°C/cm) at any point along the ingot. Under these thermal conditions, complete melting of the entire ingot could be expected.

During the experiment in the zero-g environment, as well as during the ground-based thermal simulation tests, the temperature cycles were kept in conformity with the program.

CRYSTAL STUDY TECHNIQUES

The first step upon experiment completion, both in thermal simulation tests and during the mission, was an X-ray defectoscopic analysis of the cartridges which was performed to detect changes in their internal parts and, above all, any injury to the ampoules and crystals. The cartridges then were opened, and the surface, contour, and macrostructure of the crystals were visually inspected. Next, structural perfection of the crystals and the distribution of their components in longitudinal sections and cross sections were investigated.

For that purpose, the specimens were prepared and oriented by means of X-ray techniques so that the {110} planes of their longitudinal sections and {100} planes of their cross sections had a convenient orientation for investigation. The preparation scheme for monocrystals grown in <111> orientation is presented in Figure IX-2.

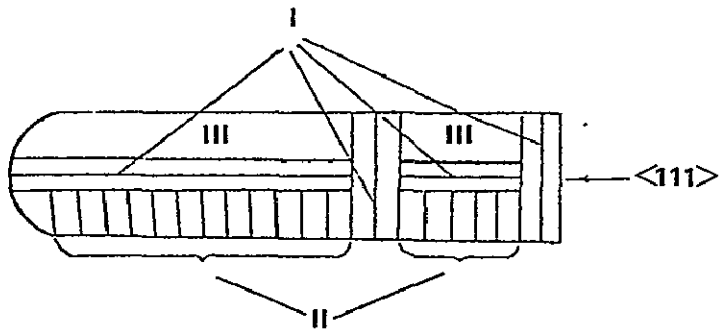

I AND III ARE SERIES OF SAMPLES THAT WERE SUBJECTED TO X-RAY-TOPOGRAPHICAL, SPECTRAL, ELECTROPHYSICAL, AND METALLOGRAPHIC ANALYSES.
II IS A SERIES OF SAMPLES FOR INVESTIGATION OF ELECTROPHYSICAL PROPERTIES.

Figure IX-2. Schematic of crystal sample preparation.

To determine Si content in crystals, photoluminescence spectra were analyzed [IX-5]. Since the size of the investigated area was less than or equal to 0.11 mm^2, a high topographic resolution was obtained. The error in Si content determination was $\leq$ 0.1 % at. wt.

Specific resistance was measured by means of conventional four- and two-probe compensation techniques and the spreading resistance method [IX-6].

The distribution of Sb along the crystals was determined by measurements of carrier concentration using the Hall effect method. Samples for these measurements were cut out of series II semiplates (Fig. IX-2) in regions that were adjacent to the center of the crystal.

The crystal structure was investigated by means of the X-ray diffraction topography methods of Berg-Barrete-Newkirk and Lang [IX-7]. For the Berg-Barrete-Newkirk method, a specific camera was used [IX-8]. This camera enables a geometry of crystal survey capable of providing a linear resolution reaching the value of 3 μm and an angular resolution reaching the value of 5' for Cu K_α radiation. The depth of the crystal working layer was from 5 to 25 μm. For the Lang method, a standard camera with crystal scanning was used. The linear resolution for Mo K_α and Ag K_α radiation used with that camera was 5 μm.

The detection of dislocations by chemical etching allowed an evaluation of microheterogeneities and macroheterogeneities of GeSi solid solutions in the investigated crystal face. The detection of dislocations was performed by chemical etching in ferrocyanide [IX-9] in {111} or {110} face, which had been previously polished in a solution. A metallographic microscope with 90X or 120X enlargement was used to study the density of the dislocations and their distribution in the investigated face of the crystal.

RESULTS

Ingot Macrostructure

For the purpose of studying the zero-g ($<6 \times 10^{-3}$ g) effect on melting and crystallization of GeSi solid solution and comparing the obtained results with those of other studies on identical crystals obtained under normal gravity conditions, four experiments on Earth and one in space were performed.

The post-experiment defectoscopic analysis of the flight cartridges revealed no damage to the internal parts of the cartridges; all the ampoules and crystals remained intact. A visual inspection of the crystals, after the cartridges had been opened, showed no macroirregularities, such as cracks, scratches, or bubbles.

The results of a preliminary examination of the macrostructure of all crystals obtained under both normal-gravity and zero-g conditions are summarized in Table IX-1.

TABLE IX-1. RESULTS OF EXTERNAL EXAMINATION OF GeSi SOLID-SOLUTION CRYSTALS OBTAINED DURING GROUND-BASED EXPERIMENTS AND UNDER ZERO-G CONDITIONS

Experiment	Cartridge No.	Melted Portion of Ingot (%)	Structure
Ground No. 1	MA-150-01	100	Polycrystalline
	MA-150-02	100	Polycrystalline
	MA-150-03	100	Polycrystalline
Ground No. 2	MA-150-04	-	-
	MA-150-05	100	Polycrystalline
	MA-150-06	100	Monocrystalline
Ground No. 3	MA-150-07	100	Monocrystalline
	MA-150-08	100	Monocrystalline
	MA-150-09	100	Polycrystalline
Ground No. 4	MA-150-10	Was not melted, opened after dynamic tests	
	MA-150-11	60	Monocrystalline
	MA-150-12	80	Monocrystalline
Space	MA-150-16	100	Polycrystalline
	MA-150-17	90	Polycrystalline
	MA-150-18	100	Monocrystalline

The macrophotographs of space-grown crystals are shown in Figure IX-3. According to the contour of the crystals, a conclusion can be made that the ingot MA-150-16 melted completely and was measurably superheated. Both ends of the crystal had a typical spherical contour, which has never been observed in ground-based crystals. The entire surface of the ingot in cartridge MA-150-18

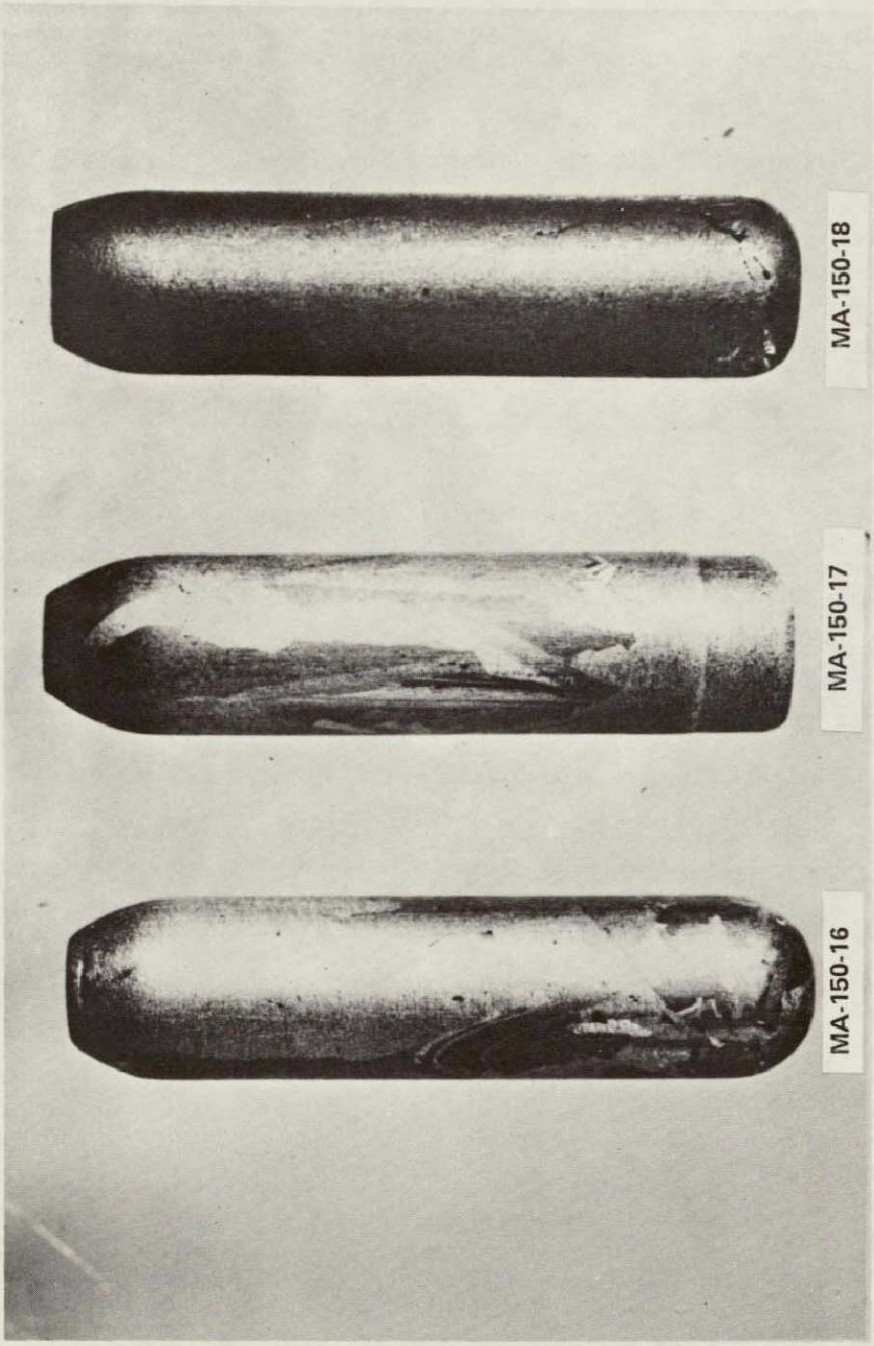

Figure IX-3. General view of space-grown crystals.

melted also, but the ingot was less superheated than MA-150-16. The ends of crystal MA-150-18 also had a spherical shape but with a smaller curvature radius compared to that of MA-150-16. A portion of the ingot MA-150-17, approximately 4 cm long, looked unmelted, supposedly an indication that this crystal preserved its seed. Subsequent etching of the crystals showed that MA-150-18 had a monocrystalline structure, whereas MA-150-16 and Ma-150-17 were polycrystals.

It should be noted that all space-grown crystals, both monocrystals and polycrystals, had a specific surface contour (Fig. IX-4) never observed in ground-based crystals. Such a contour would indicate that wetting of the graphitized ampoule walls by the melt does not occur during crystallization under zero-g conditions.

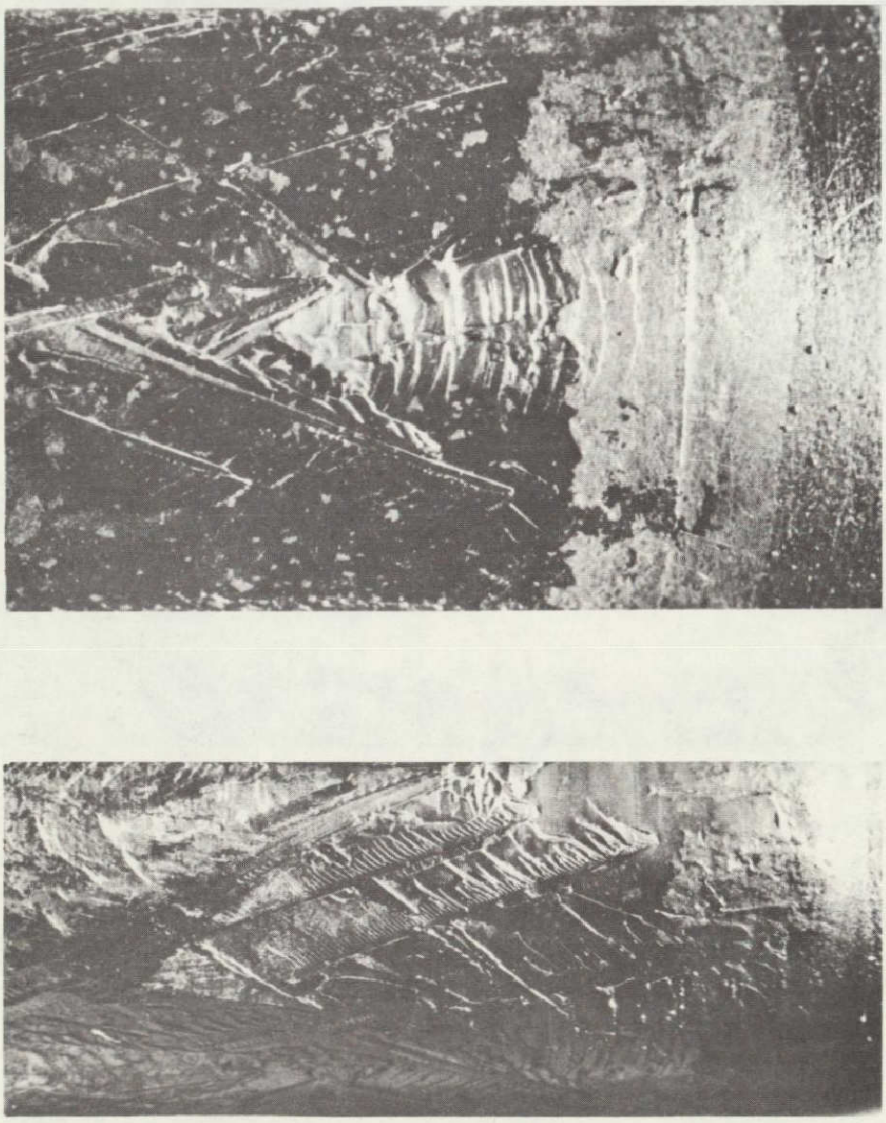

Figure IX-4. Surface of space-grown crystal MA-150-17, areas near the seed.

Two groups of crystals, each containing two ingots, were selected for subsequent measurements. The basic data on these crystals are given in Table IX-2.

TABLE IX-2. BASIC DATA ON CRYSTALS SELECTED FOR MEASUREMENTS

Group	Crystal No.	Obtained Under Conditions	Presence of Seed	Orientation	Notes
I	MA-150-18	Space	No	<110>	—
	MA-150-07	Ground	No	<100>	—
II	MA-150-17	Space	Yes	<111>	4 mm long seed
	MA-150-12	Ground	Yes	<111>	7 mm long seed

Monocrystals Obtained Without Seeding

Si DISTRIBUTION

Si distribution in the space-grown monocrystal MA-150-18 is shown in Figure IX-5. Figure IX-5(a) shows Si distribution along one edge of the crystal. and Figure IX-5(b) shows Si distribution along the other edge. As observed from Figure IX-5, a decrease of Si content with the increase of distance from the point of original crystallization is the basic characteristic of admixtures with $K > 1$. A considerable scattering of Si concentration was noticed in the initial region of the crystal. It is also evident from Figure IX-5 that Si distribution throughout the crystal diameter was heterogeneous. The variance of Si concentration along the diameter was decreasing toward the end of the crystal. Si distribution in the longitudinal section through the center of the crystal is not shown, but it was identical to that shown in Figure IX-5(a). Si distribution throughout the diameter of the ground-based crystal MA-150-07, in regions located close to the onset and termination of crystallization, proved to be virtually uniform and, by its form, in agreement with the laws of normal directional crystallization (Fig. IX-6).

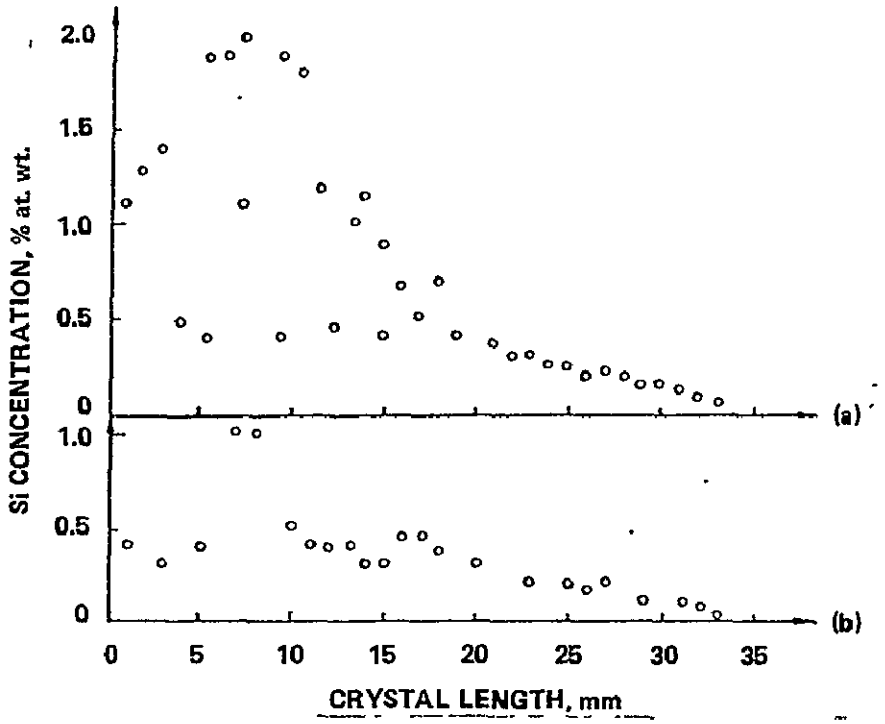

Figure IX-5. Si distribution in space-grown monocrystal MA-150-18; (a) at the left side of the crystal and (b) at the right side of the crystal.

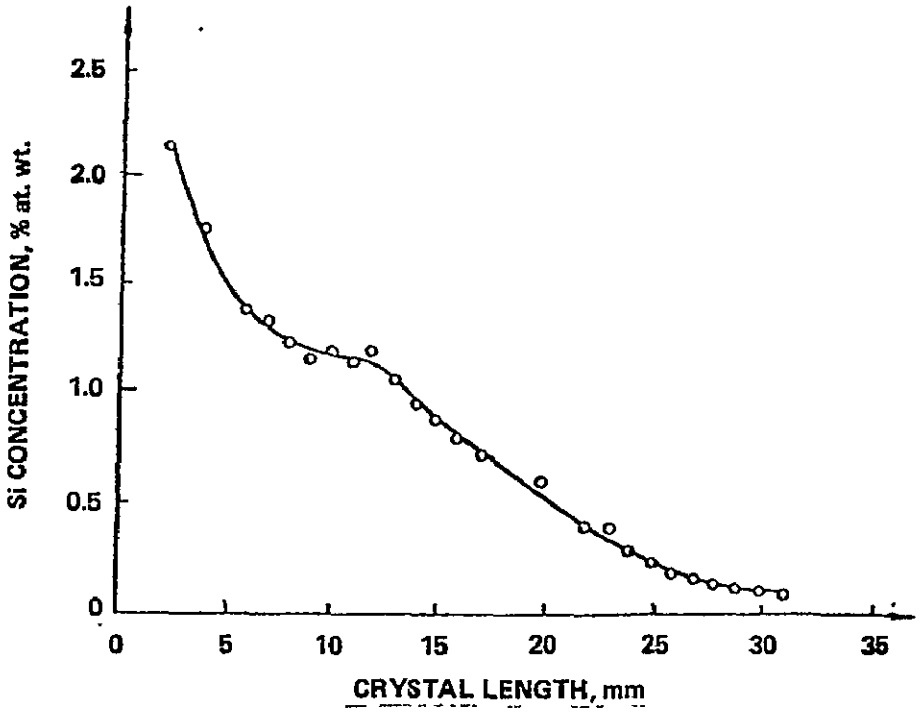

Figure IX-6. Si distribution in ground-based monocrystal MA-150-07.

Sb DISTRIBUTION

The changes in specific resistance along the space-grown crystal MA-150-18 and ground-based crystal MA-150-07, measured on series II samples (Fig. IX-2), are shown in Figure IX-7. For the space-grown crystal, the specific resistance remained virtually constant along approximately 20 mm and decreased abruptly only at the end of the crystal. For the ground-based crystal, the specific resistance decreased monotonically from the beginning to the end of the crystal. Consequently, the nature of the changes indicates that Si distribution was uniform throughout a large portion of crystal MA-150-18.

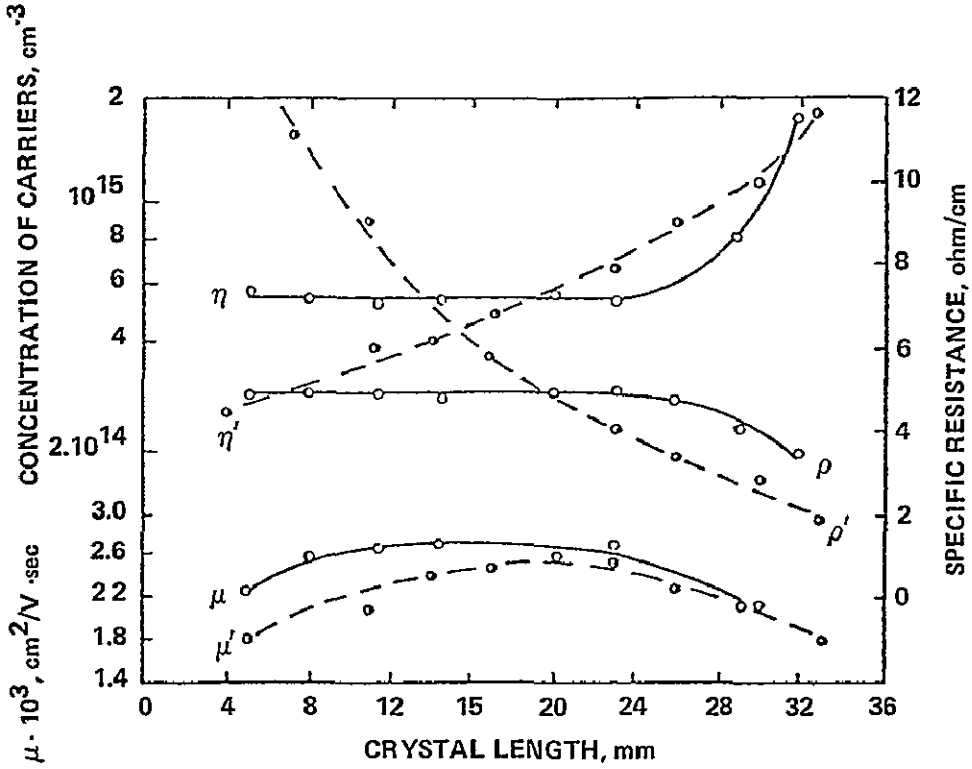

Figure IX-7. Change in specific resistance, concentration, and mobility of charge carriers in crystals MA-150-18 (ρ, η, μ) and MA-150-07 (ρ', η', μ').

Sb content determination by measurements of carrier concentration performed using the Hall effect method showed that in crystal MA-150-18 Sb was distributed uniformly (Fig. IX-7), whereas in the ground-based crystal MA-150-07 the concentration of Sb increased along the entire length of the crystal from beginning to end. It is interesting to note that such uniformity of Sb distribution, which occurred during GeSi solid-solution crystallization under zero-g conditions, has been never obtained under Earth conditions unless special techniques capable of providing uniform distribution of admixtures in a crystal were used.

An analysis of charge carrier distribution curves showed that Sb concentration in the area with uniform Sb distribution in the space-grown crystal was 6×10^{14} at.cm^{-3}, whereas it could have been equal to Sb concentration in the melt, i.e., approximately 2×10^{17} at.cm^{-3}, if ideal stationary conditions of growth and segregation depending only on the diffusion in the melt near the crystallization front were obtained in the zero-g environment. On the other hand, the value of approximately 6×10^{14} at.cm^{-3} is in good agreement with the value of the Sb distribution coefficient if we accept that this coefficient is equal to the coefficient of Sb distribution in Ge (3×10^{-3}) for a solid solution low in silicon and that the crystal grows from a melt with an Sb concentration of approximately 2×10^{17} cm^{-3}, which is close to the Sb concentration in the original ingot.

Changes in the Hall mobility of carriers along both space-grown crystals and crystals obtained during the ground-based experiments were of a similar nature (Fig. IX-7).

However, the distribution of Sb throughout the space-grown crystal was nonuniform, Sb concentration changing from one edge of the cross section to the other by two or three times. The nonuniformity was obvious from measurements of specific resistance of crystal MA-150-18 along its three parallel lines, going along the edges and the center of the crystal, and from the nature of spreading-resistance changes in the cross sections.

CRYSTAL STRUCTURE

Monocrystals MA-150-07 and MA-150-18 had a dendritic structure at the beginning of the crystal, Figures IX-8(a) and IX-8(b); as crystallization continued, the dendritic structure changed to a block structure, Figure IX-9(a) and IX-9(b). This transition is clearly seen in photographs of the longitudinal section of the region of initial crystallization, Figures IX-10(a) and IX-10(b). Both space-grown and ground-based crystals had zones of local deformation centers, situated mainly in the region of initial crystallization and concentrated near the lateral surface of the crystals, Figures IX-10(a) and IX-10(b), whereas the central portion of the crystals was almost completely free of such defects. However, an extensive region of microtensions probably caused by local deformation centers was observed in the central part. Crystal MA-150-18 had a different number of centers of local deformation near different lateral surfaces. The reason for these defects could be seizure of separate drops of the melt caused by irregular crystal growth, an indication of the presence of microheterogeneities in the composition of the crystal.

Figure IX-8(a). X-ray topograph of the cross section of the initial region of crystal MA-150-07 (12X).

Blocks in different cross sections along the length of the crystals differed in size and orientation. This difference can be attributed to microheterogeneities in the composition of the solid solution resulting from radial thermal gradients in the multipurpose furnace.

Microphotographs in Figures IX-11(a) and IX-12 show the distribution of dislocations in {110} planes of the longitudinal section and cross section of monocrystal MA-150-18. A region with a high density of dislocations, i.e., a

Figure IX-8(b). X-ray topograph of the cross section of the initial region of crystal MA-150-18 (12X).

region that had the most heterogeneous Si distribution, was observed in the beginning of the crystal where Si content was the highest. Distribution of dislocations throughout the longitudinal section of this portion of the crystal, Figure IX-11(a), was in line with its structure, as shown by X-ray diffraction topography, Figure IX-10(a). Local defects are clearly seen in this region, Figure IX-11(b). The density of dislocations diminished with a decrease in Si content, and their distribution throughout the longitudinal section became more uniform.

Figure IX-9(a). X-ray topograph of the cross section of the central portion of crystal MA-150-07 (12X).

A cellular structure, which indicates the presence of concentration supercooling at the front of crystallization, is clearly seen in the cross section of the central part of the crystal (Fig. IX-12). [The X-ray topograph is given in Figure IX-9(a).]

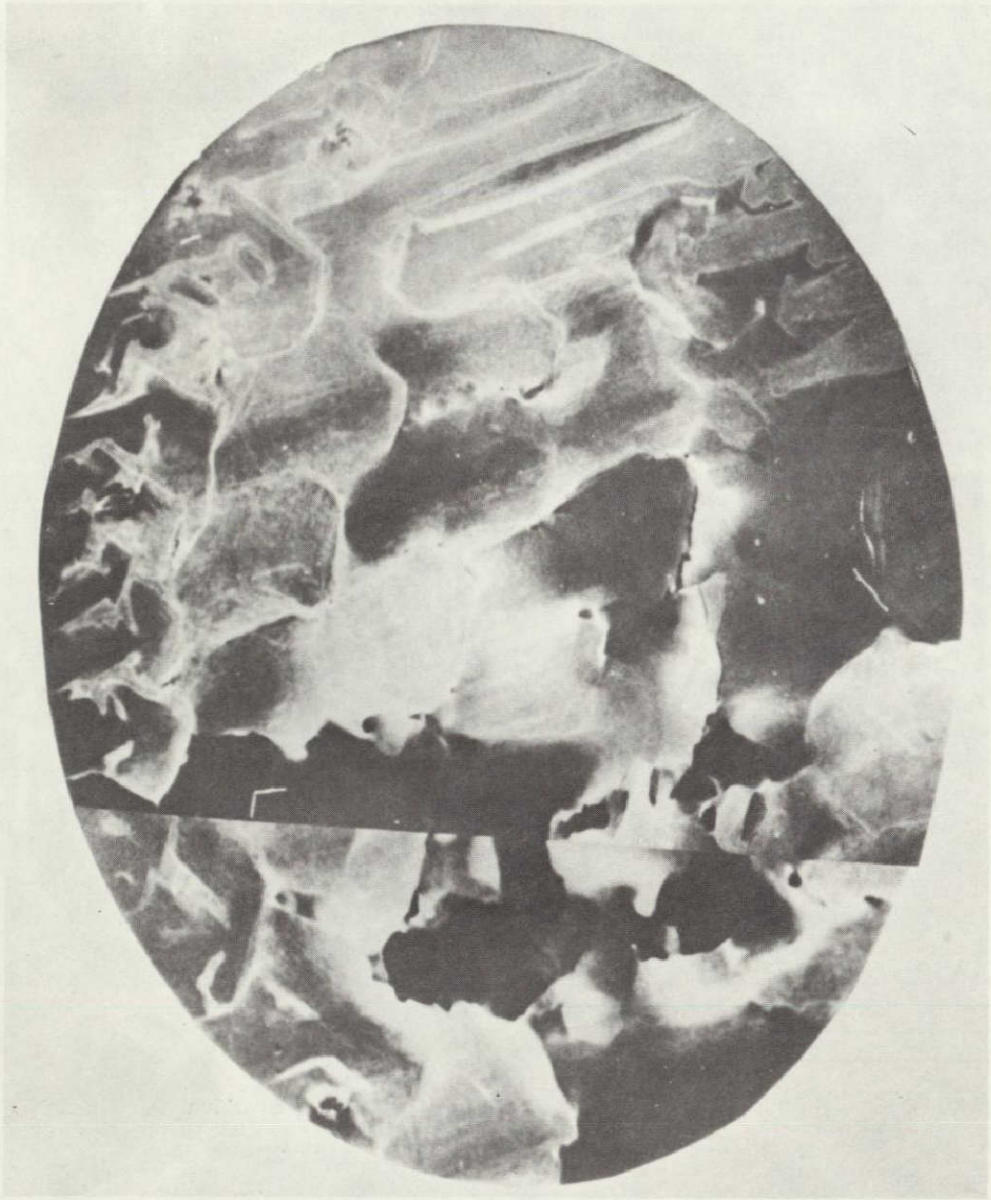

Figure IX-9(b). X-ray topograph of the cross section of the central portion of crystal MA-150-18 (12X).

Crystals Obtained by Seeding

Si DISTRIBUTION

The change in Si content throughout the ground-based crystal MA-150-12, which had an approximately 7 mm long seed, is shown in Figure IX-13. The pictured curve consists of several differing segments that characterize the

Figure IX-10(a). X-ray topograph of the longitudinal section of crystal MA-150-07 (12X).

Figure IX-10(b). X-ray topograph of the longitudinal section of crystal MA-150-18 (12X).

Figure IX-11(a). Distribution of dislocations in {110} plane of the longitudinal section of crystal MA-150-18.

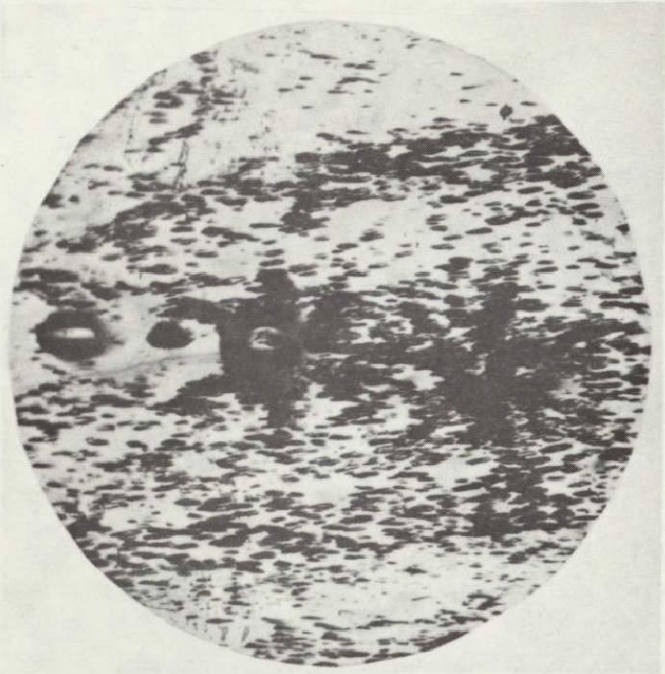

Figure IX-11(b). Centers of local deformation.

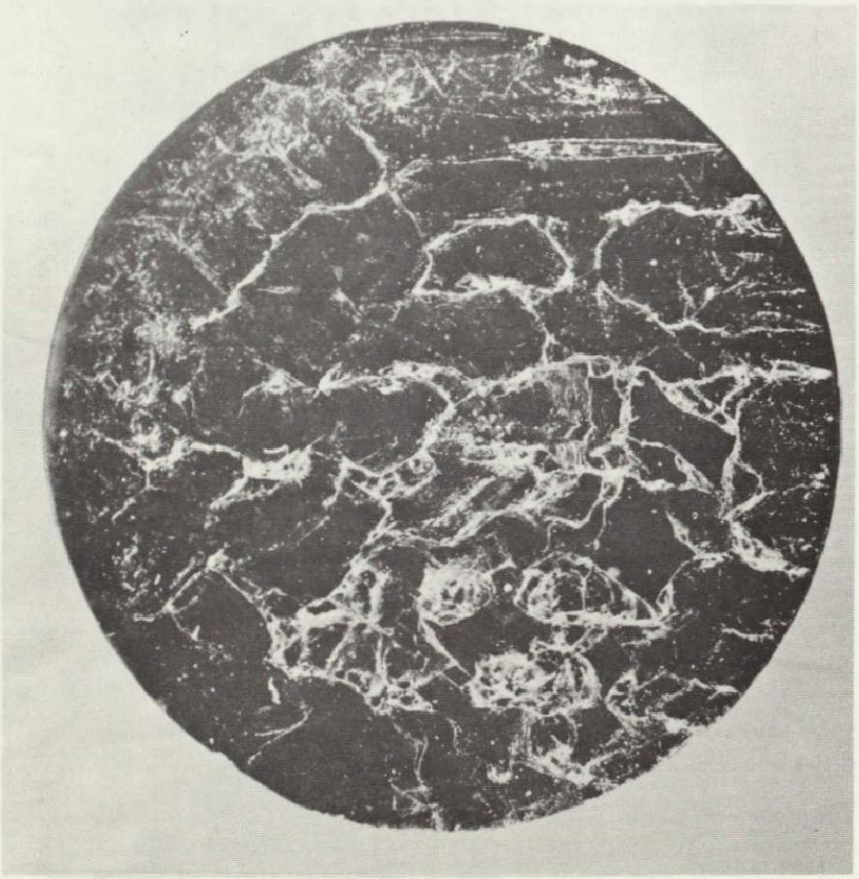

Figure IX-12. Distribution of dislocations in {110} plane of the cross section of crystal MA-150-18.

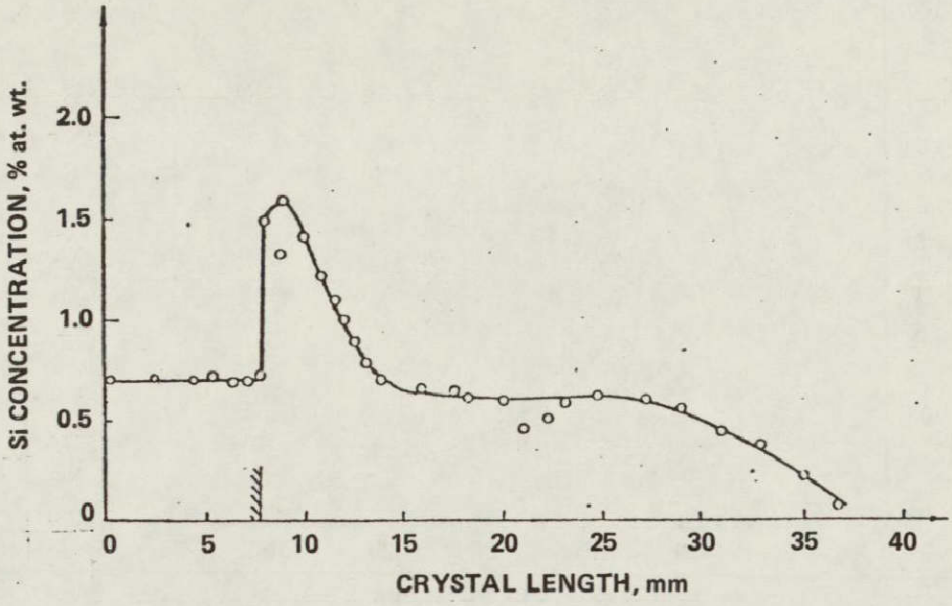

Figure IX-13. Si distribution in ground-based crystal MA-150-12.

recrystallization process. The initial segment of the Si distribution curve corresponds to the approximately 7 mm long unmelted part of the ingot, which served as a seed for crystallization. Si concentration in this region was constant and equalled 0.7 % at. wt. At the interface of melting and subsequent crystallization, Si concentration abruptly increased to a value of 1.6 % at. wt. In the remaining part of the crystal, the concentration of Si decreased gradually, as the crystallization of the melt was in progress. In the ground-based experiment, the effective coefficient of Si distribution in Ge during crystallization was evaluated from the curve in Figure IX-13. The obtained value of 2.3 agrees with published data on values of K for nonequilibrium conditions of crystallization. Si distribution throughout the cross sections of the crystal was practically uniform. Si concentration variance throughout the diameter did not exceed 20 percent.

Si distribution in the region of the seed of space-grown crystal MA-150-17 looks unusual (Fig. IX-14). An increase in Si concentration is observed in two regions, in that of the seed and in that located at some distance from the crystallization boundary. In the section between them, approximately 2 mm long, Si concentration could not be estimated. The anomalous change of composition in the region of the seed can be attributed to regeneration of the seed, namely, to melting of its single spots.

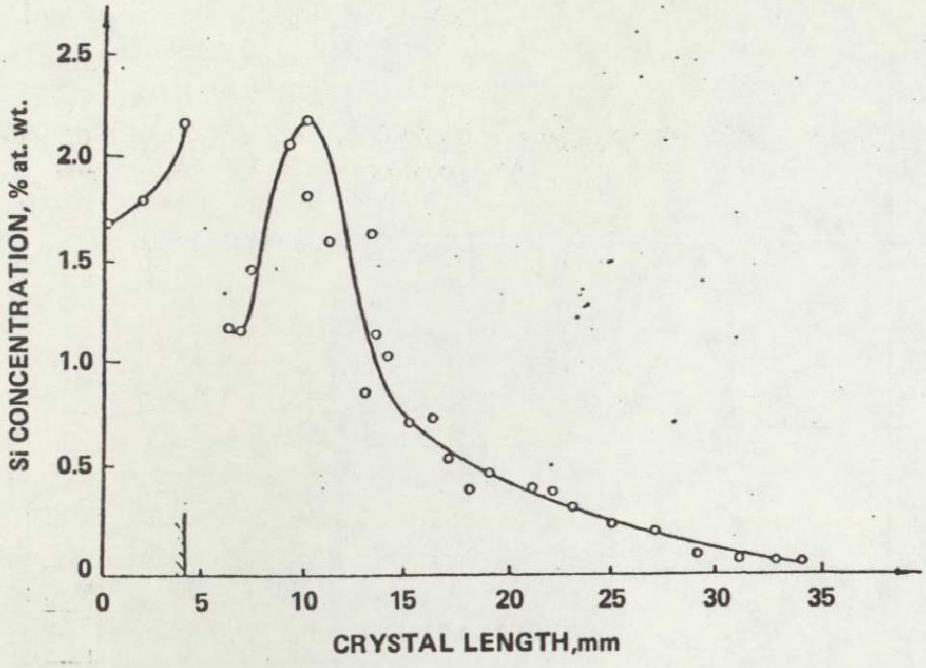

Figure IX-14. Si distribution in space-grown crystal MA-150-17.

Si distribution throughout the cross section of the recrystallized region, which had a polycrystalline structure, was identical to that of the space-grown monocrystal MA-150-18. A change in Si concentration from one edge toward the other was observed in both crystals.

Sb DISTRIBUTION

Changes in specific resistance and charge-carrier concentration throughout the length of crystals grown by seeding both under zero-g (MA-150-17) and Earth (MA-150-12) conditions are shown in Figure IX-15. The curves for specific resistance and carrier concentration in the crystals were of the same type as those for monocrystals grown without seeding, except for the region of the seed. The seed region of crystal MA-150-12 had the same specific resistance and carrier concentration as the original ingot. The space-grown crystal MA-150-17 had the same specific resistance value as the original ingot only in the end face that was adjacent to the graphite spacer and located in the cold end of the furnace. Strictly speaking, it was only this zone that served as a seed. After that zone, the specific resistance increased abruptly in a 4 mm long region with an outward contour of a seed. The increase in specific resistance and the nature of Si distribution in this region indicate that, although the seed preserved its original contour, it probably underwent partial melting and recrystallization during the experiment.

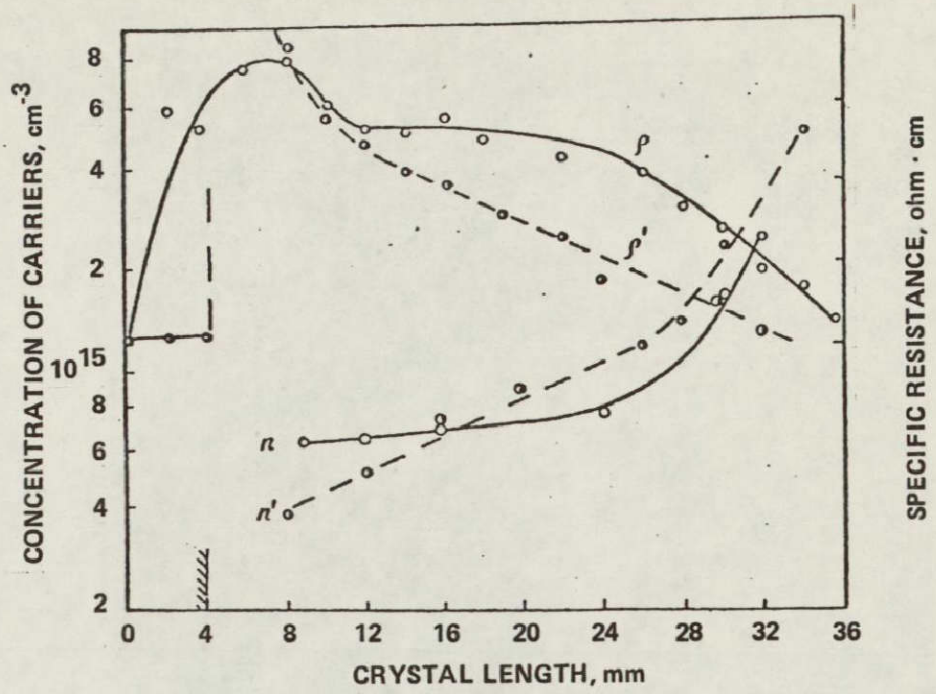

Figure IX-15. Changes in specific resistance and concentration carriers for crystals MA-150-17 (ρ, η) and MA-150-12 (ρ', η').

CRYSTAL STRUCTURE

The most interesting part of the investigation of the structure of the space-grown crystal MA-150-17 was the study of the structure of its seed in comparison with the structure of the seed and the region of original recrystallization in the ground-based ingot MA-150-12.

Figure IX-16(a) shows the outward appearance of the portion of crystal MA-150-12 that includes the seed, the boundary of melting, and the recrystallized part of the crystal, the diameter of which was somewhat larger than that of the seed. The distribution of dislocations in the $\{110\}$ plane is shown in Figure IX-16(b), and the X-ray topograph of the seeding boundary of this crystal is shown in Figure IX-17.

The crystallization interface had a concave (in the direction of the seed) shape and a steplike construction. The region near the crystallization interface had a high density of dislocations and numerous centers of local deformation. X-ray topography revealed a laminar structure of the seed, never observed in GeSi solid-solution monocrystals obtained under zero-g conditions.

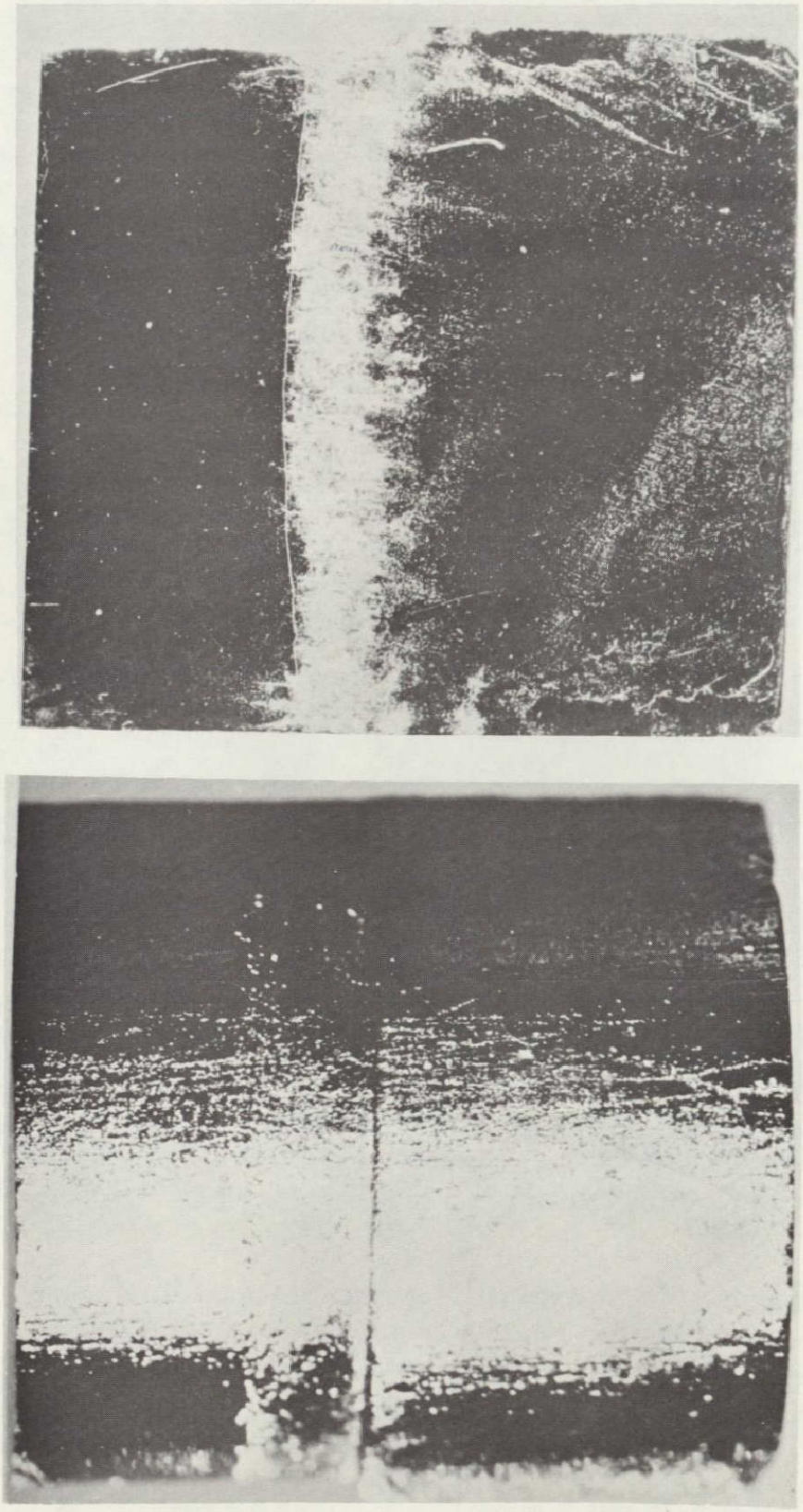

Figure IX-16. Region of the seeding boundary of crystal MA-150-12; (a) outward appearance and (b) distribution of dislocations.

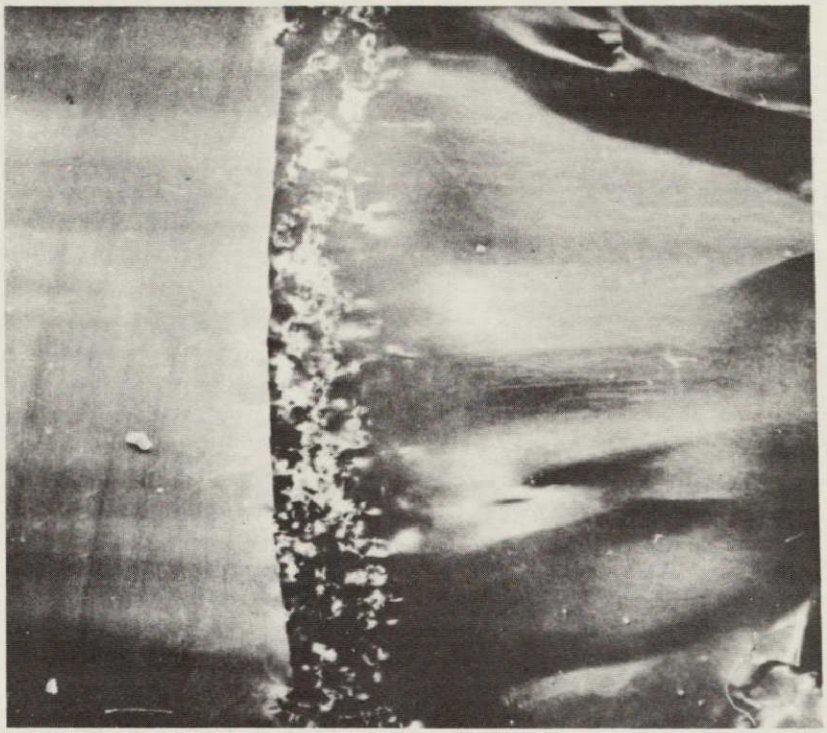

Figure IX-17. X-ray topograph of the seeding boundary region of crystal MA-150-12 (12X).

The outward appearance of the end of crystal MA-150-17 is shown in Figure IX-18(a). Figure IX-18(a) shows a sharp boundary line between the seed and the recrystallized portion, which, similar to that of crystal MA-150-12, had a slightly enlarged diameter. However, the macrostructure and the X-ray topograph of this region, Figures IX-18(b) and IX-19, are fundamentally different from those of the ground-based crystal, Figures IX-16(b) and IX-17. The region of the seed in crystal MA-150-17 is of a heterogeneous structure characterized by centers of local deformation situated close to each other. Outside this region local deformation centers are observed in single groups, but not everywhere. Further, formation of a block structure with strong microtensions and macrotensions occurred; the monocrystal changed to a polycrystal.

A detailed investigation of the seed showed that portions of its surface that were adjacent to the graphite spacer began melting in hexagon corners, Figure IX-20(a). The center of the seed surface was distorted. An X-ray topograph of the surface of a sample taken from the other side of the seed, Figure IX-20(b), showed that, following the hexagon corners, other portions of

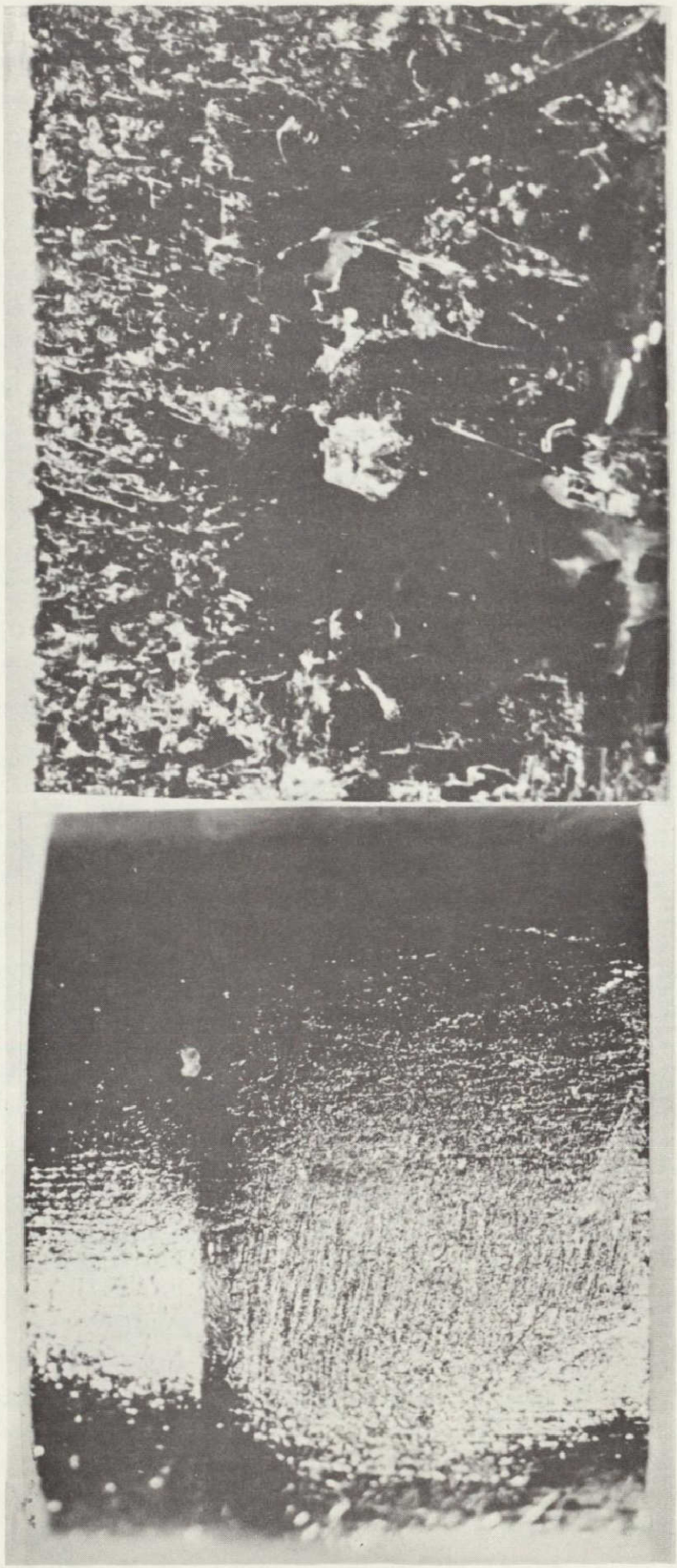

Figure IX-18. Region of the seeding boundary of crystal MA-150-17; (a) outward appearance and (b) distribution of dislocations.

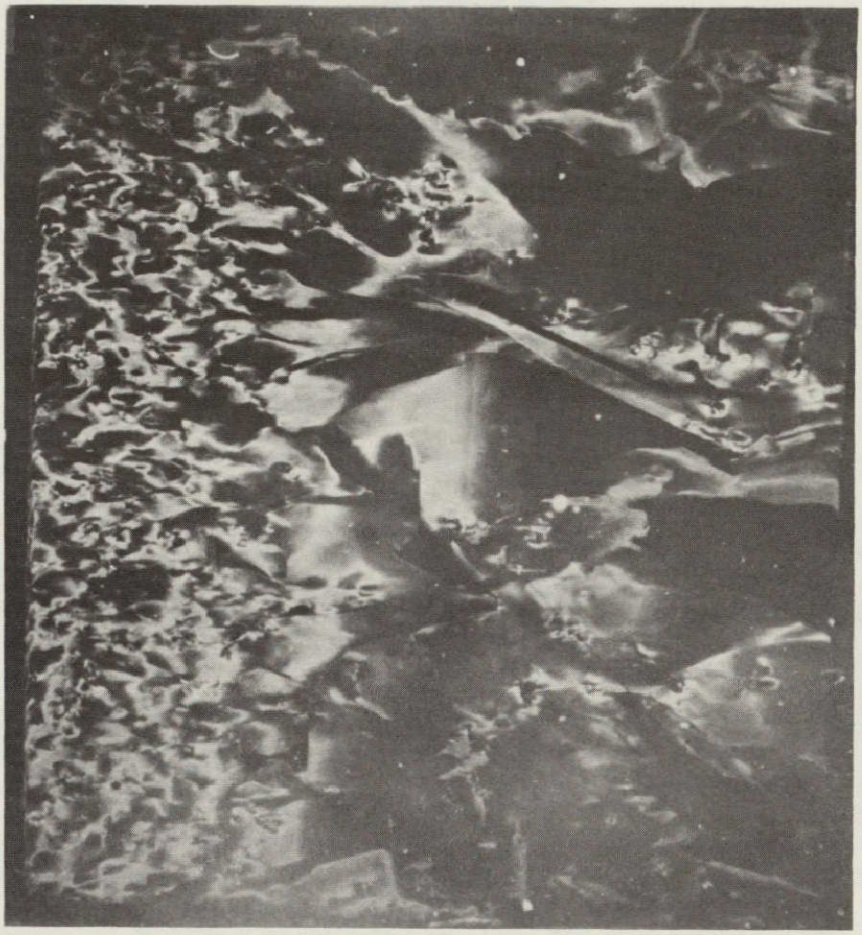

Figure IX-19. X-ray topograph of the seeding boundary region of crystal MA-150-17 (12X).

the crystal along the hexagon sides started melting, but the melting occurred locally, in isolated areas only. The spreading of the melting throughout a section of the crystal is shown in Figure IX-20(c), which is a photograph of the portion of the seed adjacent to the region shown in Figure IX-19. It should be noted that the radial spreading of the melting regions was unsymmetrical. Considering that microheterogeneities of Si distribution in the layers of the original ingot were approximately 0.1 % at. wt., it was possible to determine the thermal gradient of the seed region in the longitudinal direction and across the crystal by the size of the regenerated seed. The gradient was approximately 1 K/cm.

Thus, crystal MA-150-17, obtained under zero-g conditions, had no recrystallization boundary. Recrystallization started gradually, 2 to 3 mm behind the line visible on the outward surface, and developed consecutively both along the crystal growth and in the radial direction.

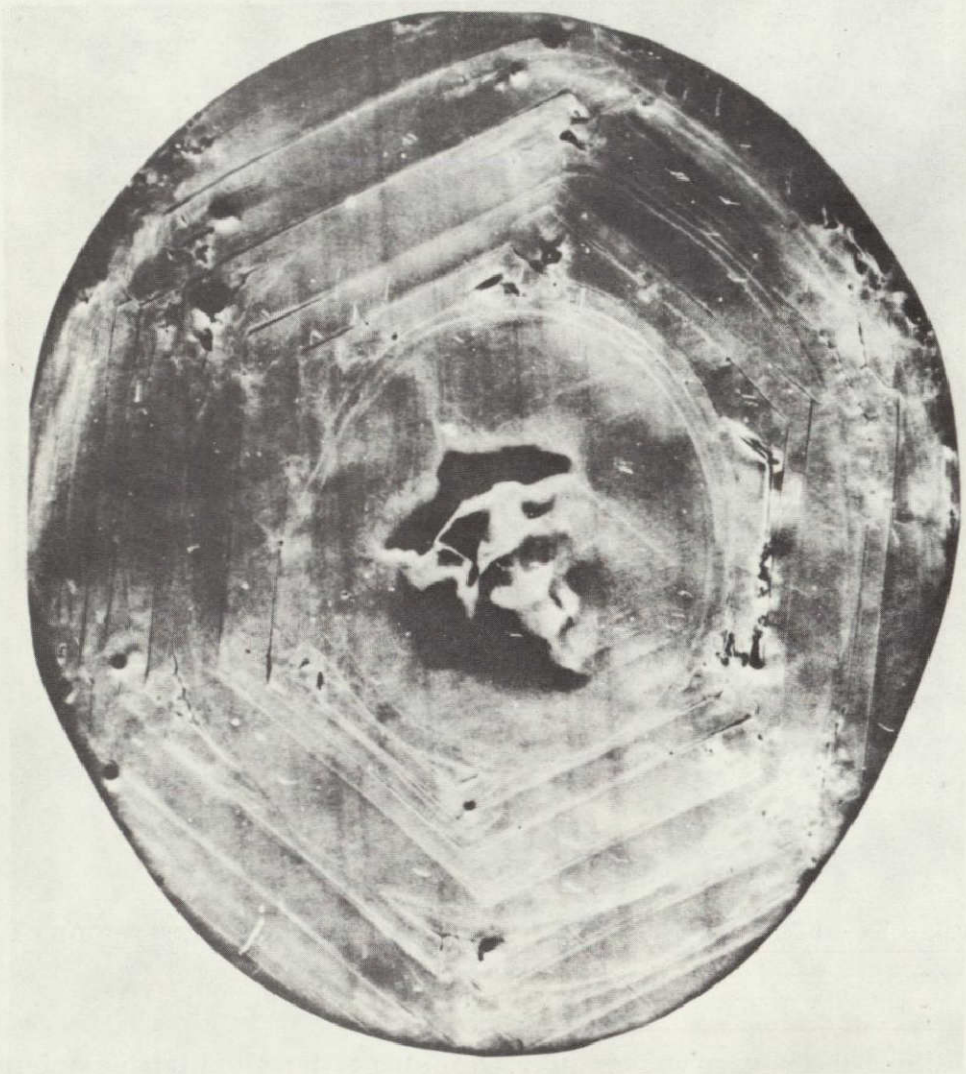

Figure IX-20(a). X-ray topograph of crystal MA-150-17 seed surface adjacent to the graphite spacer (12X).

SUMMARY AND CONCLUSIONS

The investigation of GeSi solid-solution crystals obtained under zero-g conditions in the multipurpose furnace experiment during the ASTP mission gave the following results.

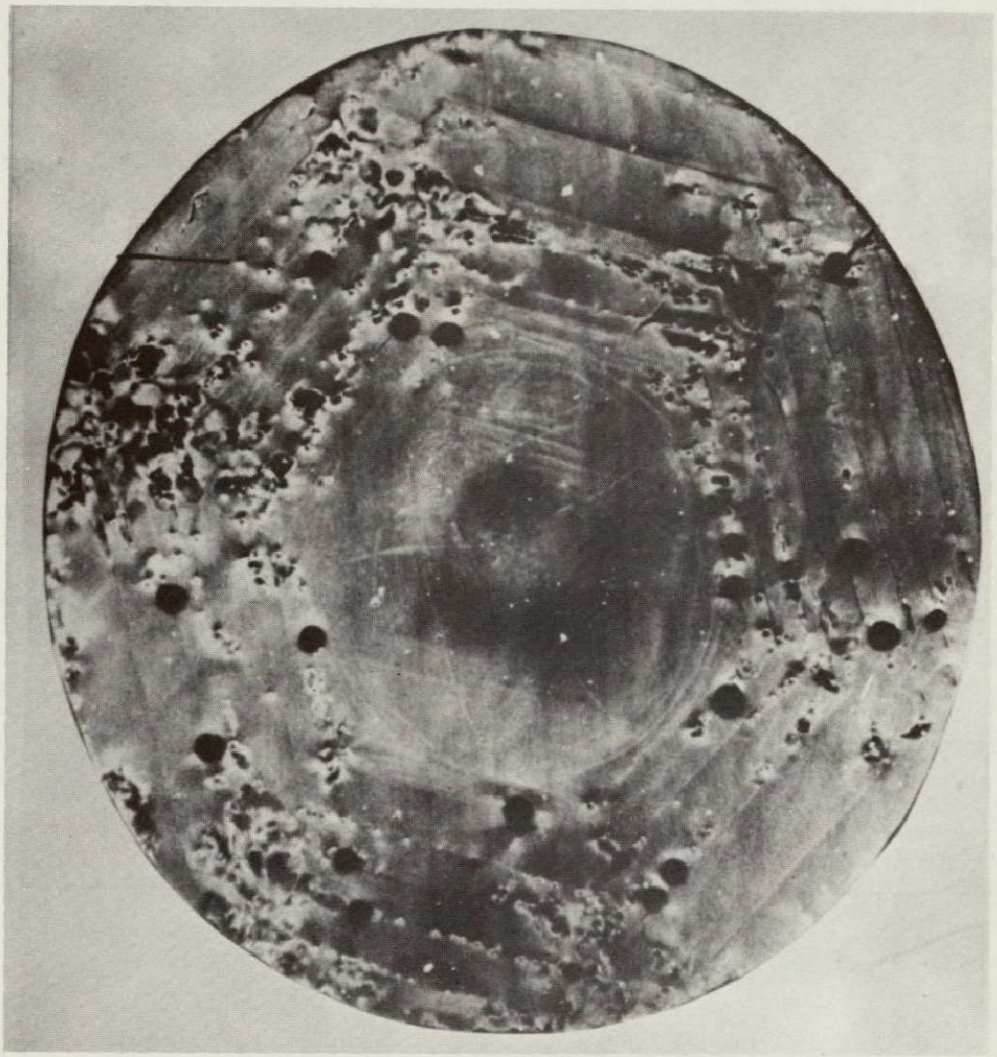

Figure IX-20(b). X-ray topograph of the other side of the specimen shown in Figure IX-20(a); the thickness of the specimen is approximately 1 mm (12X).

Under zero-g conditions, monocrystals of Sb-doped GeSi solid solution were obtained with and without seeding by means of directional crystallization in ampoules.

The analysis of Si and Sb distribution in crystals and of their structures resulted in a series of conclusions concerning melting and crystallization under zero-g conditions.

Figure IX-20(c). X-ray topograph of the seed surface adjacent to the region of crystal MA-150-17 shown in Figure IX-19 (12X).

During melting and crystallization under zero-g conditions, convective mixing is either absent or so negligible that it does not affect the process. The following facts support this conclusion.

1. Absence of laminar distribution of crystal components.

2. Cellular structure, which indicates the presence of concentration supercooling at the crystallization front.

3. Regeneration of the seed, which could occur in the zero-g environment only, in the absence of mixing; under Earth conditions, complete melting of the seed would have occurred.

Crystallization in the zero-g environment did not occur under ideal stationary growth and segregation conditions, which would have been expected considering that directional crystallization occurs in the absence of convective mixing.

Crystallization under zero-g conditions revealed the heterogeneous nature of Si and Sb distribution in the cross sections of crystals. The presence of the radial thermal gradient in the multipurpose furnace could be one of the reasons for such Si and Sb distribution.

The structure of space-grown crystals correlates with the nature of heterogeneities of Si and Sb distribution in crystals.

The type of surface morphology and the contour observed in space-grown crystals have been never observed in ground-based crystals and indicate the absence of wetting of the graphitized walls of the ampoule by the melt during melting and crystallization.

All original ingots melted completely, an indication that the temperature distribution along the ampoule with GeSi solid solution did not satisfy the optimal conditions preplanned for the experiment. In the area where the cold end of the ampoule was located and where a part of the ingot had to stay unmelted to serve as a seed, the temperature was 1211 K (938°C) and higher.

The regeneration of the seed proves that the thermal gradient in the region of the seed was not higher than 1 K/cm, causing local melting of the seed, a change in its structure, and formation of a polycrystalline structure during subsequent crystallization. Such thermal conditions were unfavorable for the growth of monocrystals.

ACKNOWLEDGMENTS

The authors wish to express their sincere gratitude to Cosmonaut A. Leonov, Astronauts T. Stafford, D. Slayton, and V. Brandt, and to all U.S. and U.S.S.R. engineers and scientists who contributed to the execution of the multipurpose furnace experiment.

REFERENCES

IX-1. Tiller, W. A.; Jackson, K. A.; Rutter, J. W.; and Chalmers, B.: Acta Metallurgica, vol. I, 1953, p. 428.

IX-2. Lodix, R. and Parker, R.: Rost monokristallov (Monocrystal Growth). M., Mir, 1974.

IX-3. Belokurova, I. N.; Kekua, M. G.; Petrov, D. A.; and Suchkova, A. D.: Izv. AN SSSR, OTN, Metallurgiya i toplivo, vol. I, 1959, p. 9.

IX-4. Chi, J. W. H.; Seidensticker, R. G.; and Duncan, C. S.: AIAA/ASME 1974 Meeting, Thermophysics and Heat-Transfer Conference, Boston, Massachusetts, July 15-17, AIAA Paper 74-650.

IX-5. Gross, E. F.; Sokolov, N. A.; and Titkov, A. N.: FFT, vol. 14, 1972, p. 2004.
Pokrovskiy, Ya. E.; Svistunova, K. I.; and Alkeyev, N. V.: FTT, vol. 14, 1972, p. 3306.
Safarov, V. I. and Titkov, A. N.: FTT, 1972, p. 458.

IX-6. Gupta, D. C. and Chan, J. Y.: Rev. Sci. Instr., vol. 41, 1970, p. 176.

IX-7. Pryamyye metody issledovaniya defektov v kristallakh (Direct Methods of Crystal Defect Studies). M., Mir, 1965.

IX-8. Gross, Ya. G.; Pokrovskiy, E. P.; Bolotovskiy, D. M.; Kol'yev, E. K.; and Shul'pina, I. L.: Pribory i tekhn. eksperimenta, vol. 4, 1972, p. 231.

IX-9. Travleniye poluprovodnikov (Etching of Semiconductors). M., Mir, 1965.

APPROVAL

APOLLO-SOYUZ TEST PROJECT – COMPOSITE OF MSFC FINAL SCIENCE REPORT

The information in this report has been reviewed for security classification. Review of any information concerning Department of Defense or Atomic Energy Commission programs has been made by the MSFC Security Classification Officer. This report, in its entirety, has been determined to be unclassified.

This document has also been reviewed and approved for technical accuracy.

Eugene C. McKannan

EUGENE C. MCKANNAN
Manager, Space Processing Application Task Team

James T. Murphy

J. T. MURPHY
Director, Advanced Projects Office

☆U S GOVERNMENT PRINTING OFFICE 1977—740-049/120 REGION NO 4

DISTRIBUTION

DA01/W. R. Lucas
PF01/B. O. Montgomery
PF11/W. R. Adams
FA21/R. A. Reeves
FA21/R. P. Chassay
EH01/R. J. Schwinghamer
JA01/R. E. Pace
EH01/C. E. Cataldo
EH11/R. L. Gause
EH11/J. C. Horton
EH12/R. S. Snyder
EH12/M. H. Johnston
EH12/C. S. Griner
EH12/B. R. Aldrich
EH12/A. M. Priester
EH12/L. H. Berge
EH15/W. A. Wall
EH15/R. A. Taylor
EH21/H. W. Herring
EH21/J. H. Hess
EH21/W. B. McPherson
EH14/A. F. Whitaker
EH31/J. E. Curry
EH22/E. A. Hasemeyer
EH34/R. L. Nichols
EH35/P. C. Rhodes
EH35/F. E. Scott
EH35/B. H. Nerren
EH35/R. H. Harwell
EH35/W. J. Patterson
EH41/J. R. Williams
ES01/C. A. Lundquist
ES01/M. P. L. Siebel
ES12/B. R. Facemire
ES12/C. F. Schafer
ES12/J. M. Zwiener
ES12/M. C. Davidson
ES12/R. C. Ruff
ES12/G. M. Arnett
ES11/W. C. Snoddy
ES24/I. C. Yates
ES24/E. W. Urban
ES24/L. L. Lacy
ES32/K. S. Clifton
ES33/R. L. Kroes
EL55/A. Boese
PA01/J. T. Murphy
ER01/J. B. Dozier
EA01/J. E. Kingsbury
ES01/L. F. Belew
ES31/R. Naumann
PF11/(25 copies)
AS61L/(8 copies)
AS61/(2 copies)
CC01/W. E. Guilian
AT01/A. D. Smith
Hqts/ESS/J. Bredt
JSC/TN3/T. Giuli
NASA Scientific & Technical
Information Facility
P. O. Box 8757
Baltimore/Washington
International Airport,
MD 21240